NUREG/CR-3664
BNL-NUREG-51746

DO NOT MICROFILM
COVER

A DESCRIPTION AND ASSESSMENT OF RAMONA-3B MOD.0 CYCLE 4: A COMPUTER CODE WITH THREE-DIMENSIONAL NEUTRON KINETICS FOR BWR SYSTEM TRANSIENTS

W. Wulff, H.S. Cheng, D.J. Diamond, and M. Khatib-Rahbar

Manuscript Completed — October 1981
Date Published — January 1984

DEPARTMENT OF NUCLEAR ENERGY, BROOKHAVEN NATIONAL LABORATORY
UPTON, LONG ISLAND, NEW YORK 11973

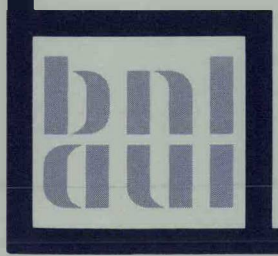

Prepared for the U.S. Nuclear Regulatory Commission
Office of Nuclear Regulatory Research
Contract No. DE-AC02-76CH00016

MASTER

DISTRIBUTION OF THIS DOCUMENT IS UNLIMITED

DISCLAIMER

This report was prepared as an account of work sponsored by an agency of the United States Government. Neither the United States Government nor any agency thereof, nor any of their employees, makes any warranty, express or implied, or assumes any legal liability or responsibility for the accuracy, completeness, or usefulness of any information, apparatus, product, or process disclosed, or represents that its use would not infringe privately owned rights. Reference herein to any specific commercial product, process, or service by trade name, trademark, manufacturer, or otherwise does not necessarily constitute or imply its endorsement, recommendation, or favoring by the United States Government or any agency thereof. The views and opinions of authors expressed herein do not necessarily state or reflect those of the United States Government or any agency thereof.

DISCLAIMER

This report was prepared as an account of work sponsored by an agency of the United States Government. Neither the United States Government nor any agency thereof, nor any of their employees, makes any warranty, express or implied, or assumes any legal liability or responsibility for the accuracy, completeness, or usefulness of any information, apparatus, product, or process disclosed, or represents that its use would not infringe privately owned rights. Reference herein to any specific commercial product, process, or service by trade name, trademark, manufacturer, or otherwise does not necessarily constitute or imply its endorsement, recommendation, or favoring by the United States Government or any agency thereof. The views and opinions of authors expressed herein do not necessarily state or reflect those of the United States Government or any agency thereof.

DISCLAIMER

Portions of this document may be illegible in electronic image products. Images are produced from the best available original document.

NOTICE

PORTIONS OF THIS REPORT ARE ILLEGIBLE. It has been reproduced from the best available copy to permit the broadest possible availability.

NUREG/CR-3664
BNL-NUREG-51746
AN, R-4
NUREG/CR--3664
DE84 010607

A DESCRIPTION AND ASSESSMENT OF RAMONA-3B MOD.0 CYCLE 4: A COMPUTER CODE WITH THREE-DIMENSIONAL NEUTRON KINETICS FOR BWR SYSTEM TRANSIENTS

W. Wulff, H.S. Cheng, D.J. Diamond, and M. Khatib-Rahbar

Contributors:
Core and Systems Code Development Group
D.J. Diamond (Group Leader)
J. Colman
H.R. Connell
D.I. Garber
S.V. Lekach
C.J. Ruger

Independent Contributors:
A.L. Aronson
M. Khatib-Rahbar
M.M. Levine
M.S. Lu
L. Neymotin
W. Wulff

DEPARTMENT OF NUCLEAR ENERGY
BROOKHAVEN NATIONAL LABORATORY
JANUARY 1984

PREPARED FOR THE
U.S. NUCLEAR REGULATORY COMMISSION
OFFICE OF NUCLEAR REGULATORY RESEARCH
CONTRACT NO. DE-AC02-76CH00016
FIN A-3014

E&B

DISTRIBUTION OF THIS DOCUMENT IS UNLIMITED

NOTICE

This report was prepared as an account of work sponsored by an agency of the United States Government. Neither the United States Government nor any agency thereof, or any of their employees, makes any warranty, expressed or implied, or assumes any legal liability or responsibility for any third party's use, or the results of such use, of any information, apparatus, product or process disclosed in this report, or represents that its use by such third party would not infringe privately owned rights.

The views expressed in this report are not necessarily those of the U.S. Nuclear Regulatory Commission.

Available from
GPO Sales Program
Division of Technical Information and Document Control
U.S. Nuclear Regulatory Commission
Washington, D.C. 20555
and
National Technical Information Service
Springfield, Virginia 22161

ABSTRACT

This report documents the physical models and the numerical methods employed in the BWR systems code RAMONA-3B. The RAMONA-3B code simulates three-dimensional neutron kinetics and multichannel core hydraulics of nonhomogeneous, nonequilibrium two-phase flows. RAMONA-3B is programmed to calculate the steady and transient conditions in the main steam supply system for normal and abnormal operational transients, including the performances of plant control and protection systems.

Presented are code capabilities and limitations, models and solution techniques, the results of developmental code assessment and suggestions for improving the code in the future.

TABLE OF CONTENTS

TABLE OF CONTENTS (cont'd)

TABLE OF CONTENTS (cont'd)

TABLE OF CONTENTS (cont'd)

TABLE OF CONTENTS (cont'd)

TABLE OF CONTENTS (cont'd)

TABLE OF CONTENTS (cont'd)

TABLE OF CONTENTS (cont'd)

TABLE OF CONTENTS (cont'd)

LIST OF FIGURES

LIST OF TABLES

LIST OF TABLES

FOREWORD

The RAMONA-3B code was developed under the sponsorship of the U.S. Nuclear Regulatory Commission from the RAMONA-III code by the Core and Systems Code Development Group of the Reactor Safety Research Division in the Department of Nuclear Energy at Brookhaven National Laboratory.

D.J. Diamond, as Principal Investigator and Leader of the Core and Systems Code Development Group, directed the implementation of the models for simulating decay heat (D.J. Diamond and D.I. Garber), boron transport (D.I. Garber), post-CHF vapor generation (C.J. Ruger), plant protection systems (S.V. Lekach and C.J. Ruger), the BNL cross-section feedback model (D.I. Garber) and the Bankoff-Jones slip correlation, (D.I. Garber). D.J. Diamond and M.M. Levine had the responsibility for assessing, accepting and implementing the models developed under subcontract with Scandpower for the simulation of heat transfer through fuel cladding, fluid dynamics in recirculation loops, jet pumps and steam separators.

Scandpower A/S staff in Norway, particularly J. Rasmussen, O. Oye, L. Moberg and T. Sauar contributed from time to time as consultants to the development of RAMONA-3B, and their assistance is gratefully acknowledged.

Independent contributors of the Reactor Safety Research Division supported the RAMONA-3B development. The steam line module has been developed and verified by W. Wulff. L. Neymotin developed and implemented (along with S.V. Lekach and P. Saha) the heat transfer package for post-CHF conditions. M. Khatib-Rahbar developed the model for the pressure regulator. M.S. Lu and W. Wulff contributed to the developmental code assessment regarding slip and vapor generation models and analysis of Peach Bottom-2 Turbine Trip Tests. M.M. Levine acted as technical consultant on new modeling for the steam separators.

H.R. Connell, J. Colman and A.L. Aronson have adapted the Scandpower code to BNL's computer, implemented many code modifications and provided programming support.

This report has four authors: W. Wulff wrote Chapters 1, 3, 4, 8 and all but Sections 6.2, 6.6.1 and 6.7.1 of Chapter 6. H.S. Cheng wrote Chapter 2 and the three sections in Chapter 6 which are related to neutron kinetics. M. Khatib-Rahbar wrote Chapter 5 on plant controls and plant protection systems. D.J. Diamond wrote Chapter 7 on developmental code assessment. The drafting of this report necessitated many detailed derivations for assessment of models and numerical methods, since no complete documentation was available for either the antecedent code RAMONA-III, or for the modeling development work for RAMONA-3B. The authors acknowledge gratefully the information concerning RAMONA-3B supplied by D. I. Garber, C. J. Ruger and S. V. Lekach. The authors also express their appreciation to P. Saha for his review of, and many improvements to, the manuscript.

This program was carried out under the sponsorship of the Analysis Development Branch in the Reactor Safety Research Division of the U.S. Nuclear Regulatory Commission, Washington, D.C. N. Zuber acted as program monitor and

contributed significantly with technical advice and guidance. Assistance by F. Odar of the NRC during the initial phase of the program is also gratefully acknowledged. R. J. Cerbone, Associate Chairman in the Department of Nuclear Energy at BNL, coordinated much of the code development and the assembly of this report.

NOMENCLATURE

A	Cross-sectional area of flow channel
A_h	Heat transfer area
A_i, A_{i-1}	Constants for simplified thermal neutron diffusion
A_{ijk}	Surface area of neutron kinetics mesh cell
$A_1', A_1, \ldots, A_4$	Constants for neutron kinetics boundary conditions
$\underline{\underline{A}}, [A]$	Coefficient matrices for two-group neutron diffusion equations
$\underset{\approx}{A}$	Coefficient matrix for implicit finite difference form of state equations, Eq. 6.5.2
a	Parameter for pressure effect on slip, Eq. 4.4.66
a	Weighting factor for average fast flux, Eqs. 6.2.68 and 6.2.69
a_f	Fuel temperature coefficient for two-group neutron kinetics parameters
a_i	Polynomial coefficients for thermophysical property correlations, Section 4.4.2.5
a_i	Relative yields of delayed neutrons, Eq. 2.6.6
a_ℓ	Moderator temperature coefficient for two-group neutron kinetics parameters
a_n^c	Polynomial coefficients of quadratic void feedback correlation for controlled fuel types
a_n^o	Polynomial coefficients of quadratic void feedback correlation for uncontrolled fuel types
a_t	Weighting factor for average thermal flux
a_x	Constant for xenon reactivity feedback
$a_{11}, a_{12}, a_{21}, a_{22}$	Coefficients for relaxation parameters, Eqs. 6.7.14 to 6.7.17
B	Boron injection source strength
B_g^2	Geometric buckling for neutron flux of group g
B_i, B_{i-1}	Constants for simplified thermal neutron diffusion formulation
b	Exponent on void fraction for slip correlation, Eq. 4.4.66

$\tilde{b}$	Parameter for cell-averaged fast flux, Eq. 6.2.68
b_i	Polynomial coefficients for thermophysical property correlation
b_{m1}, b_{m2}	Parameters defined by Eqs. 6.2.62 and 6.2.63
b_t	Parameter for cell-averaged thermal flux, Eq. 6.2.71
b_x	Constant for xenon reactivity feedback
b_1, b_2	Parameters defined by Eqs. 6.7.18 and 6.7.19
b_{11}, b_{12}, b_{1m}	Parameters defined by Eqs. 6.2.57, 6.2.58 and 6.2.59
b_{21}, b_{22}	Parameters defined by Eqs. 6.2.60 and 6.2.61
C_B	Boron concentration in ppm
C_{crit}	Critical flow factor, Section 5.2.1.5
C_i, C_m	Delayed neutron precursor concentrations, Sections 2.3.4 and 6.2
C_i	Capacitance of i-th computational cell in steam line, Eq. 6.4.41
C_{ref}	Coefficient defined in Eq. 2.5.29
C_{TRB}	Turbine mass flow impedance
C_o	Boron reactivity feedback constant, 1.1×10^{-11}
$C_1, \ldots, C_{27}$	User-specified constants
$\underset{\approx}{C}$	Coefficient matrix for implicit finite difference form of state equations under initial conditions, Eq. 6.5.2
c, c_p	Specific heat, specific heat at constant pressure
c_B	Mass fraction of boron in liquid phase
$\bar{c}_B$	Liquid mass-weighted, volume-averaged boron concentration, Eq. 6.4.75
$\tilde{c}_B$	Liquid mass flux-weighted, area-averaged boron concentration, Eq. 6.4.75
c_t	Parameter for cell-averaged thermal neutron flux, Eq. 6.2.71
$\tilde{c}$	Parameter for cell-averaged fast neutron flux, Eq. 6.2.69
$\mathscr{C}$	Closed contour for momentum equation

D, D_1	Diffusion coefficients for fast neutrons
$, D_2$	Diffusion coefficients for thermal neutrons
$[D]$	Diffusion coefficient matrix
$D/D\tau$	Substantial derivative, $\partial/\partial\tau + \vec{v} \cdot \nabla$
$D_i/D\tau$	Substantial derivative for phase i, $\partial/\partial\tau + \vec{v}_i \cdot \nabla$, $i=\ell,g$
d_h	Hydraulic diameter
$d_{i,\ell}, d_{j,\ell}, d_{k,\ell}$	Effective fast neutron diffusion coefficients, Eqs. 6.2.47, 6.2.48 and 6.2.49
E	Exposure or burnup (neutron kinetics, Chapter 2 and Sections 6.2, 6.6 and 6.7)
E	Deviation of measured pressure from pressure set point (Chapter 5)
$\underset{\sim}{E}$	Vector functions for explicit finite-difference integration, Eq. 6.5.3
$\underset{\sim}{e}_c$	Computational error, Section 6.7.3.1
$\underset{\sim}{e}_T$	Truncation error, Section 6.7.3.1
$e_1, \ldots, e_4$	Constants in Newton-Raphson iteration, Eqs. 6.4.63 and 6.4.67
F	Fission density (characterizing type of fuel), Eqs. 2.7.3 and 6.2.103
$\langle F^j \rangle$	Average fission density due to j-th isotope, steady state
F_Γ	Relaxation function for approaching thermal equilibrium, Eq. 6.4.63
$\underset{\sim}{F}$	Vector function of state variables, Eqs. 6.3.36 and 6.5.1
$f(x)$	General function symbol, Eq. 6.4.36
f, f_i	Darcy friction factor, Darcy friction factor in i-th steam line segment
$f(p,\alpha)$	Bankoff-Jones function for pressure and void fraction effects on slip ratio
f_w	Ratio of flow area to total area of fuel bundle
$\tilde{f}$	Normalized control rod density, $0 \leq \tilde{f} \leq 1$

f^*	Correction factor for boron reactivity feedback
G	Mass flux, ρv
$G(x)$	Transfer function (Chapter 5)
$\underset{\sim}{G}$	Nonlinear vector function of state variables $\underset{\sim}{y}$ and secondary variables $\underset{\sim}{x}$, Eq. 6.4.4
g	Magnitude of gravitational acceleration
g_z	Axial component of gravity, $\vec{g} \cdot \hat{k}$
g_1, g_2	Parameters defined by Eqs. 6.2.82 and 6.2.85
$\vec{g}$	Gravitational acceleration
$\underset{\sim}{g}$	General nonlinear vector function, Eq. 6.6.5
$H(\tau,\tau_h), H(\tau,\infty)$	Decay heat history integral, Eqs. 2.7.6 and 2.7.14
H_o	Fraction of delayed total fission energy
$h, \Delta h$	Enthalpy, subcooling enthalpy, h_f-h
$h(\tau-\tau')$	Delayed energy released per fission and per unit of time, from fission products
$\overline{h}_c$	Convective heat transfer coefficient
h_x, h_y, h_z	Neutron kinetics mesh spacings in x-, y-, and z-directions
I	Total number of delayed neutron precursor groups, normally I=6
I_{PM}	Moment of inertia for pump and motor rotor assembly
i	Index; spatial position, neutron group
J, J_1	Fast neutron current
J_{B1}, J_{B2}	Fast and thermal neutron currents, respectively, at the boundary
J_2	Thermal neutron current
$[J_B]$	Vector of boundary neutron current
j	Spatial index
$\vec{j}$	Volumetric flux
$\vec{j}_g, j_g$	Vapor volumetric flux, $\alpha \vec{v}_g$

$\vec{j}_\ell, j_\ell$	Liquid volumetric flux, $(1-\alpha)\vec{v}_\ell$
$\vec{j}_m, j_m$	Mixture volumetric flux, $\vec{j}_\ell + \vec{j}_g$
K	Total energy released per fission, 3.204×10^{-11} J
$\overline{K}$	Gain of Proportional Integrating Differentiating Controller (PID)
K_{CV}	Valve coefficient
k	Thermal conductivity
k_{eff}	Effective multiplication factor of reactor core
k_∞	Infinite multiplication factor, Eq. 6.2.97
$\hat{k}$	Unit vector in flow direction
L	Length
L/A	Length over area ratio, geometric inertia parameter
L_{CB}	Length of steam line bypass pipe
L_{LVL}	Two-phase mixture level elevation above horizontal interface between upper downcomer and steam dome
L_1, L_2	Fast and thermal neutron diffusion lengths, respectively
$\mathcal{L}_T, \mathcal{L}_B, \mathcal{L}_S$	Fast neutron leakage from top, bottom and side, respectively
M	Total mass in reactor vessel
M_F	Maximum magnitude of second derivative
M_f	Number of concentric zones in fuel pellet
M_o	Cardinal number of relief valve node in steam line
M_1	Cardinal number of bypass branch node in steam line
M_2	Number of computational cells in main steam line
M^2	Fast neutron migration area
$\mathcal{M}$	Momentum of coolant along closed contour $\mathcal{C}$
m	Mass in computational cell
N	Isotopic number density
N_c	Total number of flow channels in core

N_{CB}	Number of computational cells in bypass of steam line
N_{CEL}	Total number of computational cells in reactor vessel
N_{cl}	Number of concentric zones in fuel cladding
N_{Nu}	Nusselt number, $\bar{h}_c d_h / k_{fl}$
N_{Pr}	Prandtl number, $\mu c_p / k$
N_{Re}	Reynolds number, Gd/μ
N_{RCL}	Number of recirculation loops
N_S	Number of straight channel segments in closed contour
N_{SEP}	Number of steam separators
n	Number of reflector-facing surfaces for a boundary cell of neutron kinetics calculations
P	Normalized power distribution for xenon reactivity feedback model
Pu	Plutonium isotope
p	Pressure
$\langle p \rangle_{syst}$	System pressure, Eq. 4.4.87
$\langle p \rangle^{\circ}_{syst}$	Initial system pressure
$p_{i,j,k}$	Parameter, defined by Eq. 6.2.90
$Q_{i,j,k}$	Parameter, defined by Eq. 6.2.99
$q_{i,j,k}$	Parameter, defined by Eq. 6.2.101
$\vec{q}$	Heat flux vector
q'	Linear heating rate in flow channel, $\xi q''_w$
q"	Radial heat flux, positive in outward direction
q''_w	Wall heat flux
q''_z	Axial heat flux
q'''	Volumetric thermal power generation rate density
q'''_d	Delayed power generation rate density
q'''_f	Power generation rate density in fuel element

q'''_{ℓ}	Power generation rate density in liquid
q'''_{1b}	Power generation rate density in core bypass
q'''_{p}	Prompt power generation rate density
q'''_{o}	Rated volumetric power density
R	Ratio of h_x^2 over h_z^2, Eq. 6.2.41
R_{ci}	Inner cladding radius
R_{co}	Outer cladding radius
R_f	Radius of fuel pellet
RW	Flow impedance
r	Radial coordinate
r_i	Radial position, inner surface of fuel pellet zone with index i; i=1,...,M_f; r_1=0; Eq. 6.3.7
r_j	Radial position of j-th cladding zone interface, j=0,...,N_{c1}, Eq. 6.3.9
$r_{i,m}$,$r_{j,m}$	Center positions of pellet and cladding zones, respectively
Δr_c	Radial increment (zone width) in fuel cladding
$\underline{r}$	Position vector
$\tilde{r}$	Fast neutron function, defined by Eq. 6.2.70
$\tilde{r}_t$	Thermal neutron function, defined by Eq. 6.2.71
S	Slip, Eq. 4.4.64
S_{BF}	Constant source for fast flux boundary conditions
S_{BT}	Constant source for thermal flux boundary conditions
S_{CV}	Fractional valve position
S_{max}	Maximum valve position
S_{min}	Minimum valve position
s	Laplace transform of time
$\tilde{s}$	Transient fast flux function, Eq. 6.2.91
s_c	Cladding thickness, R_{co}-R_{ci}

T	Absolute temperature (Kelvin)
T_{EL}	Electrical torque of pump motor
T_{RCP}	Recirculation pump torque
TR_m	Trim signal
TR_ℓ	Lagged signal
t, t°	Relative temperature (centigrade), initial temperature
$t_{f,i}$	Temperature at pellet zone interface, Eq. 6.3.20
$\bar{t}_{f,i}, \bar{t}_{c,j}$	Zone area-averaged temperature in pellet and fuel cladding, respectively, Eqs. 6.3.18 and 6.3.20
$\underset{\sim}{\bar{t}}$	Column vector of pellet and cladding temperatures
U	Uranium isotope
$\bar{U}_{1b}$	Overall coefficient of heat transfer between heated channel and bypass channel
u	Internal energy
$u_m \rho_m$	Internal energy per unit of volume in computational cell
V	Volume, volume of computational cell
V_1	Volume of liquid in reactor vessel and recirculation loop
V_2	Volume of vapor in reactor vessel
V^*	Volume of system exclusive of steam dome, $V^* = V_{syst} - V_{DOM}$
$\dot{V}$	Time rate of volume change, Eq. 4.4.52
$\vec{v}, v$	Velocity vector, velocity
v_1	Average fast neutron velocity
v_2	Average thermal neutron velocity
W	Mass flow rate, $W=AG$
$(Wh)_m$	Mixture enthalpy flow rate, $(Wh)_m = A[G_\ell h_\ell + G_g h_g]$
w	Axial velocity component
w^o	Vapor velocity relative to stagnant liquid
X	Dimension of active core in x-direction

x	x-coordinate in rectangular Cartesian core representation, Chapter 2 and Sections 6.2, 6.6 and 6.7
x	Flow quality, Eq. 4.4.48
$\underset{\sim}{x}$	Argument vector of nonlinear function, secondary state variable
$\underset{\sim}{x}^0$	Initial guess.for solution to nonlinear equations
$\underset{\sim}{x}^k$	k-th iterant of $\underset{\sim}{x}$
$\underset{\sim}{x}^*$	Solution vector of nonlinear equation
Y	Core dimension in y-direction
Y_M	Miropolskiy two-phase flow factor
$\underset{\sim}{Y}$	State variable vector in implicit finite difference equations
$\underset{\sim}{y}$	State variable vector in ordinary differential equations (state equations)
y^0	Initial state variable vector $\underset{\sim}{y}$
$\underset{\sim}{Z}^0$	Initial-value vector for secondary state variables, Eq. 6.6.2
z	Axial coordinate
z_j	Cell center position of j-th computational cell in steam line
z_λ	Location of boiling incipience
Δz	Axial increment

Greek Symbols

α	Vapor void fraction
$\alpha_{ij}, [\alpha]$	Two-group albedo matrix, Eq. 2.3.22
β	Total delayed neutron fraction
β_i, β_m	Neutron fractions from i-th, m-th delayed precursor groups
β_{11}, β_{22}	Fast and thermal albedos, Eq. 2.5.18
$\tilde{\beta}$	Covariance parameter, Eq. 4.4.180
Γ_a, Γ_v	Vapor generation rate, per unit of interface area and per unit of volume, respectively

γ	Ratio of fast slowing-down cross section to thermal absorption cross section (asymptotic thermal over fast flux ratio)
γ_j	Constants in Newton-Raphson iterations, Eqs. 6.6.58 and 6.6.59
Δ, δ	Increments
ΔL	Length of computation cell in steam line
$\Delta\tau$	Time increment, integration step size
$\Delta\tau_A$	Time step limit to control truncation error
$\Delta\tau_N$	Time step for neutron kinetics calculations
$\Delta\tau_S$	Time step limit to assure stability
δ_i^j, δ_{ij}	Kronecker delta, $\delta_{ij}=0$ for $i\neq j$, $\delta_{ij}=1$ for $i=j$
$\delta_B^T, \delta_B^B, \delta_B^S$	Kronecker deltas for top, bottom and side boundary cells
$\delta_{x\ell}, \delta_{y\ell}$	Kronecker deltas for boundary nodes with x=X/2, y=Y/2
$\delta\Sigma_{Lg}$	Additions to fast (g=1) and thermal (g=2) total cross sections due to transverse leakage
$\delta\Sigma_g(c_B,\alpha)$	Changes in fast (g=1) and thermal (g=2) absorption cross sections due to boron injection
$\delta\Sigma_X$	Changes in thermal absorption and fission cross sections due to xenon poisoning
ϑ	Interpolant, Eq. 4.4.36
ϵ	Relative pipe roughness
ϵ_1, ϵ_i	Relative computational error
Z	Flow impedance, Eq. 4.4.133
ζ	Form loss coefficient (nondimensional)
$\zeta_{i,j,k}$	Neutron kinetics function defined by Eq. 6.2.43
η	Parameter defined by Eq. 6.2.65
η_c	Fraction of total fission energy absorption outside fuel pellet, which is absorbed in coolant channel
η_{dw}, η_{pw}	Fractions of delayed and prompt fission energy absorption outside of fuel pellet
η_i	Fast flux gradient at node interface, Eq. 2.3.7

θ	Angular coordinate
θ_c	Ratio of net inward thermal to net outward fast neutron fluxes at the boundary: θ_{CB} at bottom, θ_{CS} at sides, θ_{CT} at top of core
θ_i	Phase angle of i-th eigenvalue, $\tilde{\sigma}_i$
ι	Inertia multiplier, Eq. 4.4.150
κ	Polytropic expansion coefficient
κ_1, κ_2	Parameters defined by Eqs. 6.2.86 and 6.2.84, respectively
Λ_2	Thermal neutron leakage rate density vector with x, y and z components $\Lambda_{2,i}$, $\Lambda_{2,j}$ and $\Lambda_{2,k}$
$\overline{\Lambda}$	Average thermal neutron leakage, Eq. 6.2.46
λ	Lipschitz constant
λ_{eff}	Effective linear extrapolation length, Eq. 2.3.30, λ^B_{eff} for bottom, λ^S_{eff} for sides and λ^T_{eff} for top of core
λ_i, λ_m	Decay constant for i-th and m-th group of delayed neutron precursors
λ_1, λ_2	Linear extrapolation lengths for fast (1) and thermal (2) neutrons
$\tilde{\lambda}_i$	Eigenvalues of Jacobian for system of ordinary differential equations
μ	Dynamic viscosity
$\tilde{\mu}$	Function defined by Eq. 6.2.64
ν	Kinematic viscosity
ν_1, ν_2	Mean number of fast (1) and thermal (2) neutrons in group
ν_d	Number of delayed neutrons per fission
$\overline{\nu}$	Fission density-weighted average of ν_1 and ν_2, Eq. 2.6.5
$\tilde{\nu}$	Normalized mass flux, Eq. 4.4.23
ξ	Heated perimeter
ξ_h	General notation for mesh spacing h_x, h_y and h_z
ξ_i	Reciprocal thermal neutron diffusion length

$\bar{\xi}_m$	Average delayed neutron precursor concentrations, Eq. 6.2.53, m=1,...,I.
π_m	Parameter defined by Eq. 6.2.83
ρ	Mass density
ρ_c	Round-off error
ρ_s	Radius of neighborhood around solution vector
ρ_o	Initial mass density
$\bar{\rho}$	Average mass density
(ρc)	Volumetric heat capacity
Σ	Macroscopic neutron cross section
Σ_L	Thermal leakage cross section, Eq. 6.2.46
Σ_{f1}, Σ_{f2}	Macroscopic fission cross sections for fast and thermal neutrons
Σ_1, Σ_2	Total macroscopic cross section for fast and thermal neutrons
Σ_{21}	Macroscopic slowing-down cross section for fast neutrons
σ	Surface tension
σ_{ag}	Microscopic absorption cross sections of Boron-10 for fast (g=1) and thermal (g=2) neutrons, respectively
$\tilde{\sigma}_i$	Eigenvalues of integrating algorithm
τ	Time
τ_{cv}	Time constant for valve action
$\tau_d, \tau_i, \tau_\ell, \tau_m$	Time constants of derivative and integral controllers, lag element and signal delay, respectively
Φ	Average diffusion density, Eq. 6.2.52
$[\Phi]$	Two-group flux vector
$\bar{\Phi}$	Average thermal flux
$\tilde{\Phi}$	Unknown variable in Newton-Raphson iteration, Eq. 6.4.66
ϕ	Volumetric expansion functions, Eqs. 4.4.115, 4.4.117 and 4.4.119

ϕ_μ	Viscous dissipation function
φ_1, φ_2	Fast and thermal neutron fluxes, respectively
$\overline{\varphi}$	Average fast flux in computational cell
X	Unknown variable in Newton-Raphson iteration, Eq. 6.4.64
χ	Function defined by Eq. 4.4.108
Ψ	Fast diffusion density, Eq. 6.2.50
$\overline{\Psi}$	Average fast diffusion density in a cell
ψ	Function defined by Eq. 4.4.109
Ω, Ω_p	Under-relaxation parameter for the initial, steady fast flux (Eq. 6.6.4) and fission density (Eq. 6.6.19), respectively
Ω_1, Ω_2	Parameters defined by Eqs. 2.5.13 and 2.5.14, respectively
$\Omega^{(n)}$	Parameter defined by Eq. 6.7.5
ω	Angular velocity
$\omega_o, \omega_1, \omega_2$	Relaxation parameters of inner iterations for transient calculations, Eqs. 6.7.11, 6.7.12 and 6.7.13

General Subscripts

a	Absorption of neutrons
B	Boron
B	Boundary nodes
b,B	Core bottom
CB	Bypass in steam line
CE	Core exit
CHF	Critical burnout condition
CI	Core inlet
CON	Condenser
CU	Carry-under
CV	Control valve

c	Cladding
cap	Full capacity
ch	Coolant channel
ci	Inner cladding surface
co	Outer cladding surface
crit	Critical flow
DC	Downcomer
DCI	Downcomer inlet
DIF	Jet pump diffuser
DOM	Vapor dome in vessel
d	Decay heat, delayed neutron power density
dw	Direct (delayed) heating in coolant
E	Exposure, burnup
ECC	Emergency core cooling injection
EL	Electric
eff	Effective
FB	Film boiling
FC	Forced convection
FW	Feedwater
f	Fission, fuel
f	Saturated liquid (water properties)
fg	Equilibrium phase change
fℓ	Fluid (subcooled liquid or saturation)
G 5.9	Groeneveld 5.9
g	Neutron energy group index, g=1 for fast group, g=2 for thermal-group
g	Saturated vapor (water properties)

gp	Gas gap between fuel pellet and fuel cladding
HDR	Steam line header
HN	Homogeneous nucleation
h	Heating
INJ	Injection
I	Midpoint of boundary cell
i	Index
JT	Jet pump
j	Flow channel index (hydraulics), y-coordinate index (neutron kinetics)
k	Node index (hydraulics), z-coordinate index (neutron kinetics)
L	Neutron leakage
LVD	Low-void regime in vapor dome
LVL	Two-phase mixture level in dome
ℓ	Liquid
l,l'	Spatial indices of cell, cell interface
lb	Liquid in bypass
MB	Modified Bromley
MSFB	Minimum stable film boiling
M_0	Safety and relief valve node
M_1	Bypass branch node
M_2	Node upstream of turbine stop valve
m	Two-phase mixture (thermohydraulics), delayed neutron precursor (neutron kinetics)
N	Neutron kinetics
NB	Nucleate boiling
N_{CB}	Node upstream of steam bypass valve
NZZ	Jet pump nozzle

n	Index in void feedback polynomial
PM	Recirculation pump and motor combination
p	Prompt fission energy
ph	Interphase
pw	Prompt heating of coolant
RCL	Recirculation loop
RCP	Recirculation pump
RSE	Riser exit
RSR	Riser
ref	Reference (full load)
rated	Full-load normal operation
S	Side
SCT	Jet pump suction
SL	Steam line
SR	Safety and relief valve
sat	Saturation
T	Top Boundary cell in core, its surfaces
TB	Transition boiling
TRT	Jet pump throat
t	Thermal
v	Vapor
w	Wall, outer cladding surface (thermohydraulics), water (neutron kinetics)
x,y,z	x-, y-, z-coordinates
o	Reference, initial, rated
1,2	Fast and thermal, respectively (neutron kinetics)
1,2	Upstream and downstream of abrupt cross-sectional area change

Superscripts

B	Bottom boundary nodes or surfaces
c	Core section of a reactor, or controlled fuel types
j	Isotopic index for fissionable nuclides
k	Iteration count
(m)	Eigenvalue iteration index for steady-state neutron kinetics
n	Time step index, or exponent of void feedback polynomial as shown in Eq. 2.4.2
(n)	Inner iteration index for steady-state neutron kinetics
(p)	Power-void iteration index for steady-state neutron kinetics
r	Reflector surrounding the reactor core
S	Side boundary nodes or surfaces
T	Top boundary nodes or surfaces
o	Initial guess, initial value
+,-	Above and below two-phase mixture level, just downstream and abstream of flow cross section, respectively
$\overline{\quad}$	Integral mean
'	Differentiation with respect to pressure, along the saturation lines

Other Symbols

< >	Control system average (line, area, volume)

1. INTRODUCTION AND EXECUTIVE SUMMARY

This report documents the models and the solution techniques in the BWR plant transient code RAMONA-3B at the time of its documentation in October 1981. The RAMONA-3B computer code descriptions, the instructions for preparing input data, and the definitions of output data listings are presented in an attendant User's Guide (Connell, Neymotin, Saha and Slovik, 1984).

RAMONA-3B was developed from RAMONA-III of Scandpower, Norway. Publication and distribution of this report have been delayed until an agreement was reached between the U.S. Nuclear Regulatory Commission and Brookhaven National Laboratory (BNL) on the one side and Scandpower on the other, regarding the distribution of RAMONA-3B to U.S. organizations.

Since the drafting of this report in October 1981, significant improvements have been made to the RAMONA-3B code. These improvements will be described in detail in a forthcoming, separate report by P. Saha et al. (1984). They strongly reduce or eliminate the limitations as described in this report regarding the predictions of mixture level motions, wall friction, boron transport and decay heat. Work is now in progress to improve the steam separator model, to simulate processes in the balance-of-plant and to simulate control systems for feedwater and recirculation flows.

Updated versions of RAMONA-3B are now available, at no cost and through BNL, to U.S. organizations for the analysis of U.S. reactors.

We present in this chapter first the code objectives, then we summarize the capabilities and the limitations of RAMONA-3B and describe the major modeling features as well as the general code structure. The details of models and solution methods are documented in Chapters 2 through 6. The developmental assessment of RAMONA-3B at BNL is described in Chapter 7. The report is concluded with an overall summary of recommendations for future code improvements.

1.1 RAMONA-3B Code Objectives

The RAMONA-3B code is designed to predict the neutron kinetics parameters in the reactor core and the thermohydraulics parameters in the pressure vessel, the recirculation loops and the steam lines of a Boiling Water Reactor (BWR) power plant, as it operates under steady-state or transient conditions. Specifically, RAMONA-3B should simulate normal and abnormal operational plant transients* in the pressure and temperature ranges between cold standby and full power conditions, plant transients which are induced by a full or partial

* As defined in Chapter 14 of Final Safety Analysis Reports.

reactor scram, the withdrawals of control rods, a main steam isolation valve closure, a turbine trip, a recirculation pump trip, a steam line break, a change in feedwater conditions or a failure of the pressure regulator. RAMONA-3B is programmed to simulate any combination of plant control actions related to the main steam supply system, and the consequences of such control actions.

RAMONA-3B is the only BWR systems code currently available which is designed to predict local, three-dimensional distributions of fission power, neutron kinetics parameters, fuel and cladding temperatures, vapor void and axial coolant velocities in any one of many core flow channels. The detailed core predictions in the context of a BWR systems code are combined in RAMONA-3B with the capability to describe phase separation and liquid subcooling or superheating in the two-phase coolant mixture anywhere in the reactor vessel. These unique features in RAMONA-3B afford the detailed study of the effects from individual control rod motion and their system interactions.

RAMONA 3-B is programmed to predict the critical power ratio under steady state conditions, i.e., the measure of safety margin against the appearance of burnout conditions anywhere in the reactor core. RAMONA-3B is also programmed to simulate the conditions of burnout, transition or film boiling during transients.

RAMONA-3B is designed to predict acoustical effects in the steam lines, following a sudden valve closure or opening, and the consequences from pressure and steam mass flow oscillations in the steam lines on the conditions in the pressure vessel. Finally, the RAMONA-3B code is programmed to predict the transient distributions of boron concentrations in the pressure vessel, and the effects of boron on the fission power.

RAMONA-3B is intended to accommodate standard plant controls for system pressure regulation and the following plant protection systems: the safety and relief valves, the main steam isolation valve, the High Pressure Coolant Injection (HPCI) system, and the Reactor Core Isolation Cooling (RCIC) system, including boron injection.

In the next two sections is a summary of the capabilities and limitations, showing the extent to which RAMONA-3B currently meets the above objectives.

1.2 Summary of RAMONA-3B Capabilities

In this section are listed the transients which RAMONA-3B is deemed, or has been shown, of being capable to simulate. The first list below is assembled on the basis of modeling features in RAMONA-3B, and also includes transients for which the code has not yet been tested. The transients which RAMONA-3B has executed successfully during developmental assessment are summarized in the second listing below. A RAMONA-3B code application for licensing

has been scheduled for fiscal year 1982. This application deals with the anticipated transient with partial reactor scram (partial ATWS).

The RAMONA-3B code has the unique capability of predicting, in the context of a complete BWR Main Steam Supply Systems code, the local, detailed, three-dimensional fission power distributions, the details of neutron kinetics parameters, heat generation, fuel temperatures, vapor void distributions and local axial velocity distributions in a multichannel reactor core description. In addition, the RAMONA-3B code accounts for unequal velocities of vapor and liquid in the boiling two-phase mixture and for subcooling, saturation or superheating in the liquid phase while implying saturation for the vapor. Moreover, RAMONA-3B has individual reactor component modeling and also reflects the judicious elimination of unimportant but computationally expensive processes (acoustic effects) found normally in large systems codes.

Thus, RAMONA-3B is in principle capable of predicting efficiently and accurately the effects from processes particularly important for BWR simulations. RAMONA-3B predicts the effects from local thermohydraulics parameters, such as vapor void fraction, and from individual control rod positions on both the local fission power and fuel temperature as well as on the overall system response. There is currently no other systems code available which offers this comprehensive combination of capabilities in a single computer program.

As pointed out in the Foreword, RAMONA-3B evolved from modifications of the RAMONA-III code which was orignally developed and programmed by Scandpower A/S, Kjeller, Norway and then obtained by Brookhaven National Laboratory for use and modification on behalf of the U.S. Nuclear Regulatory Commission. The documentation presented here does not account for all the differences between the actual coding in RAMONA-3B and the model descriptions by Scandpower, since such an account is impractical in view of the original code structure. Presently there is no document available for quality assurance of FORTRAN coding in RAMONA-3B. Since standard criteria for computational stability are approximated in the original RAMONA-III code and in some of its modifications, the code may encounter computational instabilities under untested circumstances. For further details see Chapters 3, 4 and 6. It is recommended that RAMONA-3B be further assessed for the transients listed below in Section 1.2.1. Transients already successfully executed by BNL are summarized in Section 1.2.2.

1.2.1 RAMONA-3B Modeling Capabilities

(a) RAMONA-3B can simulate all steady-state conditions between zero-power, hot standby conditions and full power conditions, with the recirculation pumps running at full power, nominal stator voltage and A.C. frequency.

The following summary contains the sixteen BWR normal and abnormal operational transients which RAMONA-3B is programmed to simulate. RAMONA-3B needs to be tested, assessed and documented for these transients. The transients are grouped together on the basis of their primary disturbances.

1.2.1.1 Transients with Reactivity Changes

RAMONA-3B can simulate the consequences from:

(b) gradual or sudden withdrawals or insertions of control rods, either during startup from hot standby conditions, during power range operations, or during setback and shut-off maneuvers, while the recirculation pump motors operate at nominal stator voltage and nominal A.C. frequency, or at zero stator voltage.

(c) accidental dropping of a single control rod, a cluster of rods or an arbitrary combination of rods.

(d) full or partial reactor scram.

(e) boron injection.

(f) transients which induce a change in moderator (coolant) density or temperature (e.g., void collapse due to pressure rise in the core).

1.2.1.2 Transients with System Pressure Change

RAMONA-3B can predict the consequences from:

(g) electrical load rejection with fast closure of the turbine control valve.

(h) turbine failure with closure of turbine stop valve.

(i) closure of main steam isolation valve.

1.2.1.3 Transients with Coolant Inventory Decrease

RAMONA-3B can simulate the transients caused by:

(j) a failure of the pressure regulator.

(k) faulty opening of safety or relief valves.

(l) loss of feedwater flow.

(m) loss of electrical power at the recirculation pump motor.

1.2.1.4 Transients with Coolant Temperature Changes

RAMONA-3B simulates the following events:

(n) the failure of the feedwater flow controller.

(o) the change of feedwater temperature if this change can be represented by a specified, single linear change of temperature between two specified temperature levels (loss of feedwater preheating).

1.2.1.5 Transients with Changes in Coolant Mass Flow Rate

RAMONA-3B can predict the consequences from:

(p) the trip of both recirculation pumps.

(q) the seizure of both recirculation pumps.

1.2.2 Documented Capabilities of RAMONA-3B

RAMONA-3B has successfully executed the following two transients:

(a) Reactor Scram with the control rods of only half of the core entering the core (Half ATWS), accompanied by either a turbine trip or a Main Steam Isolation Valve closure.

(b) Turbine Trip with bypass flow, at three power levels.

Both transients are documented in Chapter 7 of this report. The Turbine Trip Test predictions have been compared with experimental results.

Scandpower has also performed a number of developmental code assessment calculations. However, since their documentation is incomplete, we have not included Scandpower's assessment results in this report.

1.3 Summary of RAMONA-3B Limitations

The following code limitations are inferred from the assessment of the models and the numerical methods in RAMONA-3B. The impact of these limitations in quantitative terms has not yet been determined and should be part of independent code assessment.

Some of the limitations summarized in this section may restrict the code capabilities as summarized in Section 1.2, most likely for long-term simulations (when countercurrent flow and flow reversals occur at low-flow conditions, for example). As it is impossible without extensive code assessment to identify the conditions generated from all combinations of malfunctions and whence the resulting limitations, we summarize in this section generic limitations. This enables the code user to infer the impact from the code limitations on a particular transient of interest.

RAMONA-3B simulates processes only in the pressure vessel, in a recirculation loop (representing all recirculation loops) and in a steam line (representative of all steam lines), but not in the containment building, nor the suppression pool, nor in the balance of the plant. Simulated are only the plant control and protection functions which are related to the main steam supply system.

The simplifications adapted for the numerical solution and integration techniques have not yet been tested. Also a priori computational stability and accuracy under all possible conditions cannot be assured, although the code has successfully executed a number of transients.

The importance and a quantitative assessment of the limitations listed below are given in Chapters 3 for fuel modeling (gap conductance effects), in Chapter 4 for hydraulics and system component simulations and in Chapter 5 for control system simulations. The reader is also referred to Chapter 6, particularly to Sections 6.3.3 and 6.8 for control of computational errors.

The RAMONA-3B code cannot be expected to reliably predict the consequences from:

(a) the effects of burnup on fuel gap conductance.

(b) start-up from cold standby conditions.*

(c) loss of coolant accidents, caused by either a small or a large break.

(d) jet pump failures due to a pipe break inside the reactor vessel.

(e) start-up of one or all recirculation pumps.

(f) load-following maneuvers controlled by recirculation pump speed (A.C. voltage and frequency).

(g) general variations of feedwater temperatures or failure of feedwater preheater.

(h) malfunctions of shutdown cooling system (RHRS).

(i) failure of recirculation flow control.

(j) loss of condenser vacuum.**

(k) fuel cladding failure.

(l) single recirculation pump failure.

(m) single jet pump failure.

(n) flashing in jet pumps or recirculation loops.

---

*Corrected in MOD 0 Cycle 7

**Does not affect Turbine Trip Transient

(o) pipe break in a single steam line.

(p) critical two-phase flow.

(q) counter-current flow limitations

RAMONA-3B can presently predict the fuel pellet temperature distribution only to within ± 20 percent of total fuel temperature difference, under both transient and steady-state conditions, because of its modeling assumptions related to thermal conduction. Long-term transients (ten minutes or more), where the thermal energy stored in the pressure vessel walls and structural components can affect the coolant energy are not presently adequately simulated. Rapid transients in fuel cladding temperature (burnout) are not accurately predicted because of simplifying assumptions in cladding property descriptions and numerical methods.

Transients in which the coolant level in the vessel either rises above the vapor separators or below their liquid discharge ports are not treated accurately. RAMONA-3B has no provision for computing the state of superheated vapor anywhere in the system. This affects the simulation of transients with rapid pressure rises (above approximately 10 bar/s) or with prolonged conditions of burnout in the core. RAMONA-3B is not modeled to account for acoustical effects in the coolant, and it cannot predict flow reversal.

This completes the summary of code capabilities and limitations. Technical details of modeling assumptions and of numerical techniques related to these capabilities and limitations are found in:

Section 2.3.1 for neutron kinetics modeling,
3.2 for thermal conduction modeling,
4.2 for thermohydraulic modeling,
6.3.1.1, 6.4., 6.6, 6.7.3.1.2 and 6.7.3.1.3 for numerical methods.

The reader's attention is directed toward the list of recommendations for future code improvements, given in Chapter 8. A number of minor code modifications can effectively eliminate several of the code limitations.

As indicated earlier, the reader should know that significant improvements have been made to the RAMONA-3B code since the writing of this report (Saha et al., 1984). These improvements include a collapsed water level tracking capability, an expanded wall friction factor package, including the laminar flow regime, and reactivity edits. A number of corrections have also been made in the areas of decay heat predictions, momentum equation, boron transport and level tracking calculations. The improved level tracking calculation does allow the mixture level to rise above or fall below its normal range, and it includes the effect of steam condensation on feedwater and/or safety injection water when the level drops below the feedwater sparger. Work is presently under way to implement the simulations of a feedwater and recirculation control system, suppression pool temperature calculation, and a balance-of-plant as

modeled by MINET (Van Tuyle, 1984) into the RAMONA-3B code. Two separate recirculation loops will also be modeled in the near future. In addition, improvements are being made in the steam separator model and the reverse flow calculation in the reactor vessel. Rather than extensively modify this report, these improvements are to be documented in a separate report (Saha et al., 1984).

1.4 Primary Modeling Features in RAMONA-3B

This section presents the summary of modeling characteristics in RAMONA-3B for neutron kinetics, thermal conduction and thermohydraulics. More details are presented in Sections 2.1, 3.1 and 4.1.

1.4.1 Neutron Kinetics Models

A 1-1/2 group, coarse mesh diffusion model in a three-dimensional rectangular coordinate system is used to predict transient three-dimensional fission power distributions in the core. Six delayed neutron groups are accounted for. Decay heat from fission products is computed in RAMONA-3B from ANS Standard 5.1 (1978). All feedback mechanisms between neutron kinetics and thermohydraulics are modeled.

The prompt neutron equations are integrated with an implicit "box" method. The delayed neutron equations are explicitly integrated.

1.4.2 Thermal Conduction

Thermal energy storage in, and its conduction and convection from, structural components are ignored in RAMONA-3B. Thermal energy storage and conduction in fuel elements (pellet, gas gap and fuel cladding), each one representing all the fuel in a computational cell of the three-dimensional mesh for neutron kinetics calculations, is computed with a discrete-parameter model. Axial conduction and the temperature dependencies of heat capacity in fuel pellet and cladding and of thermal conductivity in the cladding are ignored. The gap conductance is a prescribed function of fuel pellet temperature.

The conduction equations are numerically integrated by an iterative predictor-corrector method for the pellet and by a successive substitution procedure for the cladding.

1.4.3 Thermohydraulics

RAMONA-3B has models for two-phase flows with unequal phasic velocities, subcooled or superheated liquid phase and with transient boron concentration. Four equations of vapor mass, mixture mass, momentum and energy conservation

describe the coolant dynamics in the vessel. Two equations of vapor mass and momentum conservation describe the acoustic effects from valve closures in the (adiabatic) steam lines. One boron mass conservation equation is used to predict the transport of boron.

A single pressure is used in the entire system to compute all phasic properties. This technique eliminates efficiently the effects from unimportant acoustic effects in the vessel and contributes significantly to the computing economy in RAMONA-3B.

One closed-contour momentum equation each is used to predict the individual axial velocities in a chosen number of parallel core flow channels. This method increases significantly the computing speed.

The partial differential equation of mixture mass conservation is integrated by a simple quadrature in space. This method also significantly increases computing speed without loss in accuracy.

Without these three advanced modeling features, RAMONA-3B would not be able to compute three-dimensional neutron kinetics and thermohydraulics for multichannel core geometries in the context of a systems code and produce results at acceptable costs.

RAMONA-3B accounts for nonequilibrium vapor generation, unequal phase velocities, wall shear and heat transfer for single-phase and two-phase flow conditions. The prediction of slip is deemed reliable for low and moderate vapor void fractions ($\alpha < 0.6$), that of wall shear for forced turbulent flow, and that of heat transfer for forced turbulent convection in single-phase flows and for nucleate boiling in churn-turbulent two-phase flow. New modeling is needed for laminar flows, film flows, dispersed droplet flows and the flow of superheated vapor.

RAMONA-3B has individual component modeling to accommodate BWR systems of U.S. design. All recirculation loops and all steam lines are represented in RAMONA-3B by a single recirculation loop with a single jet pump and a single steam line, respectively. The steam separator model is arbitrary and requires improvements for the prediction of carry-under.

The thermohydraulics equations and the boron transport equations are integrated by the Euler-Cauchy method; the acoustics in the steam line are predicted by a fourth-order Runge-Kutta method, coupled with the Simpson rule to control the time step from specified error bounds. The implementation of the first-order Euler-Cauchy method in RAMONA-3B can be expected to work most of the time but not always because the stability criteria as implemented in RAMONA-3B are not universal. (See Section 6.9 for necessary improvements.)

1.4.4 Systems Controls

RAMONA-3B has simplified but adequate models for the plant control and plant protection systems which affect directly the main steam supply system. Specifically, RAMONA-3B simulates the actions of the pressure regulator, the

Safety and Relief Valves (SRV), the Main Steam Isolation Valve (MSIV), and of the plant protection system, i.e., the sensors for neutron flux, water level and system pressure, and the trip logic for control rod and valve responses.

Numerical methods for systems control simulations consist of explicit Euler-Cauchy integrations and first-order backward time differencing (lag elements, proportional-integral-differential controller) and of MAX/MIN statements for limiters.

1.5 Code Structure

The RAMONA-3B code consists of over one hundred FORTRAN SUBROUTINE and FUNCTION subprograms. It is divided into two major program sets, one for neutron kinetics calculations, the other one for thermohydraulics calculations. A minor program module contains the steam line dynamics simulation.

The neutron kinetics package contains the small set of subprograms for computing the thermal conduction in fuel elements. The thermohydraulics package includes the procedures for predicting boron transport.

The RAMONA-3B code structure is not optimized within the major program set for the thermohydraulics calculation. There is no modular separation into mathematical procedures and into procedures for computing derivatives of state variables, for computing constitutive relations for mass, momentum and energy transfer, nor for computing particular, component-related processes. The plant control and plant protection systems simulation is not programmed in a separate module. Only the steam line module has separate subprograms each for initial conditions, derivatives of state variables, constitutive relations, mathematical procedures and program execution control.

Details of the programming in RAMONA-3B are to be found in the User's Guide (Connell, Neymotin, Saha and Slovik, 1984), which also contains the descriptions for the arrangement of input data and the detailed explanations of the output listing.

1.6 Overview of Code Development

RAMONA-3B evolved from RAMONA-III. RAMONA-III was developed by Scandpower Inc. in Kjeller, Norway as an outgrowth from RAMONA-I (with point kinetics) (Bakstad and Solberg, 1968), and from RAMONA-II (with one-dimensional neutron kinetics) (Holt and Rasmussen, 1968). RAMONA-III also contains program features from other codes for steady-state neutron kinetics (PRESTO) and for thermohydraulics (ANDYCAP), also developed at the Institutt for Atomenergi in Kjeller, Norway.

RAMONA-III was acquired from Scandpower by Brookhaven National Laboratory in 1978 on behalf of the U.S. Nuclear Regulatory Commission. BNL then modified and expanded the RAMONA-III code extensively for the purpose of accommodating specific system components of BWR power plants in the United States, and of simulating processes which were beyond the capabilities of RAMONA-III. The modified code is called RAMONA-3B.

Brookhaven National Laboratory implemented in RAMONA-3B existing procedures for

a) decay heat calculations

b) computing the critical power ratio,

c) computing the slip in accordance with the Bankoff-Jones correlation,

d) calculating feedback effects on neutron cross sections, and for

e) independent verification of global mass and energy conservation.

Brookhaven National Laboratory also developed and implemented models for

f) steam line dynamics,

g) boron transport,

h) post-CHF heat transfer,

i) plant control and plant protection systems, i.e.: pressure regulator, Safety and Relief Valves (SRVs), Main Steam Isolation Valves (MSIVs), Turbine Stop Valve (TSV), High Pressure Core Injection (HPCI) and Reactor Core Isolation Cooling (RCIC).

Brookhaven National Laboratory subcontracted with Scandpower to develop models for simulating thermal conduction in the fuel cladding and fluid flow dynamics in the recirculation loop, including the jet pump, and in the steam separators. BNL incorporated the respective program modules from Scandpower into RAMONA-3B. The Recirculation Pump Data in RAMONA-3B were obtained from General Electric.

Brookhaven National Laboratory also developed a plotting package and deleted a number of coding errors from the original code. Finally, BNL performed code calculations for developmental code assessment. The steam line module was assessed by comparing its results with exact solutions, with other code results, and with experiments. RAMONA-3B was assessed as a whole at BNL by comparison with test data from the Peach Bottom turbine trip tests. BNL demonstrated the capability of RAMONA-3B to simulate, in principle, a partial scram transient (Half ATWS). Details of this assessment are presented in Chapter 7 of this report.

1.7 Organization of Report

This report was prepared on the basis of all available (but incomplete) code documentation on RAMONA-III, of reports on code modifications and on code listings, as obtained from Scandpower Inc.

The detailed technical part of this report presents the modeling in RAMONA-3B in Chapters 2, 3 and 4 for neutron kinetics, thermal conduction in solid structures and coolant thermohydraulics, respectively. Chapter 6 presents first the finite difference formulation of these models, in the same order, and then the solution techniques employed in RAMONA-3B for computing first the steady-state and then the transient conditions. Chapter 5 presents the complete description of control models and the solution methods for their implementation. Chapter 7 describes the details of the developmental code assessment carried out at BNL. The summary of Chapter 8 contains the list of recommendations for future code improvements.

Equations are numbered by Arabic numerals, the first two numbers indicating the chapter and primary section in which they appear first. Assumptions are numbered by Arabic numbers for their respective chapters and within the chapter by lower-case Roman numerals. The sections covering the consequences from assumptions have the same labels as the assumptions.

The models for neutron kinetics, thermal conduction and thermohydraulics have been derived by the authors of this report. The derivations were started from first principles as published in standard texts, and carried out to lead to the formulations used in RAMONA-3B and documented by Scandpower. The derivations showed clearly the assumptions implied in the models, and they served to assess the capabilities and limitations of the code. Where major assumptions are implied, the model derivation has been presented separately from the description of its implementation in RAMONA-3B. Minor differences between the authors' derivations and the RAMONA-3B formulations are stated as part of the derivations.

2. MODELING OF NEUTRON KINETICS AND POWER GENERATION

2.1 Scope and Objectives

One of the most salient characteristics of boiling water reactors is the strong space-time effect on the power distribution in the reactor core because of the strong void feedback and the need for frequent movement of control rods for operational maneuvering. Therefore, a rigorous analysis of many BWR transients and accidents often requires a knowledge of the three-dimensional transient power distribution in the reactor core. RAMONA-3B is unique in that it provides a capability for predicting the three-dimensional transient power distribution. In fact, it is currently the only BWR system code which has such a capability.

The source terms for the thermohydraulic equations in the core are derived from the fission induced power distribution which, in turn, is determined from the neutron flux distribution. The most rigorous theoretical description of the neutron flux behavior is given by the Boltzmann transport equation. Unfortunately, the solution of the transport equation for a light water reactor (LWR) must be obtained by numerical means which are prohibitively expensive (especially for time-dependent three-dimensional problems) because of excessive computer time and memory requirements. It has been found satisfactory in many practical applications to describe the neutron flux behavior in a nuclear reactor by means of a multigroup neutron diffusion theory model, a low order approximation to the formally exact Boltzmann transport equation. In this model, multiple energy groups are used to represent the energy dependence of the neutron flux, the diffusion theory approximation (Fick's law) is used to represent neutron transport, and up to six delayed neutron precursor groups are used to represent the delayed neutrons.

For large reactors such as modern LWRs, even multigroup diffusion theory is very expensive to use for calculating the three-dimensional power distribution. Two decades of experience have indicated that two or three energy groups are, in most situations, sufficient to represent the neutrons, particularly for light water reactors. Consequently, RAMONA-3B employs a two-group diffusion theory model to describe the neutron kinetics.

The two-group diffusion theory model is based on the division of all neutrons into two classes depending on whether their energy is greater or less than some arbitrary cut-point in the continuous energy spectrum ranging from 10^{-4} eV to 10^{7} eV. The cut-point is generally taken to be about 1 eV above which upscattering is negligible. It is assumed that within given regions of the reactor (generally corresponding to given compositions) the energy distribution of neutrons belonging to the two groups is independent of position. This implies that the cut-point is assumed to remain constant during the course of a transient. This is generally true for transients of interest with RAMONA-3B, but not for long-term transients such as due to fuel depletion (burnup). The adequacy of the two-group diffusion theory model for LWRs is intrinsically related to the unique moderating property of hydrogen and has been demonstrated by a wide range of experimental and operating experience.

Thus, the two-group diffusion theory forms the basis for the neutron kinetics of RAMONA-3B. However, it is not sufficient to consider the neutron kinetics alone if one wishes to realistically predict the transient behavior of a light water reactor. One must also consider the associated problems of heat transfer and fluid flow as well as the coupling of the latter (thermohydraulics) to the neutron kinetics. The coupling comes about because nuclear fission reactions generate a tremendous amount of heat that can result in changes in core geometry, density of the constituent materials (coolant in particular), and temperature of these materials. These effects, in turn, change the local nuclear reaction rates, and hence, influence the subsequent kinetic behavior of the reactor. These feedback effects are generally represented by empirical constitutive relations often referred to as feedback models.

The objectives of this chapter are to describe the governing equations of the neutron kinetics in RAMONA-3B and the associated initial conditions and boundary conditions, and to describe the power generation rate for thermohydraulics. The basic assumptions and approximations leading to the 1-1/2-group, coarse-mesh, diffusion equations employed by RAMONA-3B are discussed in Sections 2.2 and 2.3. The feedback models which relate the diffusion equation parameters to the thermohydraulic variables are described in Section 2.4. A general discussion on how to obtain the two-group diffusion equation parameters is also given. Section 2.5 discusses the boundary condition parameters and Section 2.6 treats other neutron kinetics parameters. The calculation of power generation is described in Section 2.7. The finite difference equations and the numerical schemes for their solutions are not discussed in this chapter and will be given in Chapter 6.

2.2 General Approach

2.2.1 The Two-Group Diffusion Theory Model

The general approach to the neutron kinetics for LWRs is the two-group diffusion theory model. Let $\varphi_1(\underline{r},\tau)$ and $\varphi_2(\underline{r},\tau)$ denote the fast and thermal (i.e., slow) neutron fluxes, respectively. The corresponding neutron densities are given by $\varphi_1(\underline{r},\tau)/v_1$ and $\varphi_2(\underline{r},\tau)/v_2$, v_1 and v_2 being the average speed of neutrons in the two groups (subscript 1 referring to the higher energy group, i.e., the faster group of neutrons).

The total reaction rate at any location and time is given by the product of fluxes and appropriate macroscopic cross sections $\Sigma_g(\underline{r},\tau)$ where the subscript g (g=1,2) refers to the energy group. The $\Sigma_g(\underline{r},\tau)$ are sums of the macroscopic cross sections for each nuclide present. These macroscopic cross sections are the product of nuclide number densities, $N(\underline{r},\tau)$, and the corresponding microscopic cross sections, $\sigma_g(\tau)$. The time dependence of σ_g arises from the fact that it is an average over the thermal motion of the nuclei present and over the assumed energy distribution of the neutrons. Thus, the feedback effects change the Σ_g by virtue of altering the values of the group averaged microscopic cross sections as well as the material concentrations, $N(\underline{r},\tau)$.

The selection of the thermal cutoff at 1 eV is such that neutrons in the thermal group do not scatter up into the fast group, but neutrons in the fast group will slow down into the thermal group. The symbol $\Sigma_{21}(\underline{r},\tau)$ is customarily used to denote a cross section for slowing down from group 1 to group 2. Thus, the source for the thermal group is the slowing down density expressed as $\Sigma_{21}(\underline{r},\tau)\ \varphi_1(\underline{r},\tau)$. The symbol $\nu_g \Sigma_{fg}$ will indicate the cross section for the production of ν_g fast neutrons due to fission of a fissionable isotope (e.g., ^{235}U) in group g. Σ_{fg} is the fission cross section for the isotope and ν_g is the mean number of neutrons produced by that fission. A fraction β of the ν_g neutrons produced in fission appears only after a beta-decay of one of the fission products. There are a number of these fission products which are lumped together as six "precursor groups." The fraction of fission neutrons appearing from the i^{th} such group will be designated by β_i ($\beta = \sum_i \beta_i$). The concentration of the i^{th} precursor group will be denoted by $c_i(\underline{r},\tau)$, and λ_i will represent the decay constant (the probability of decay per second) of the i^{th} precursor group.

The leakage rate of neutrons in group g out of a unit volume is given by the divergence of neutron current. In the diffusion theory approximation, the neutron current is approximated so that the leakage is $-\nabla\cdot D_g(\underline{r},\tau)\nabla\varphi_g(\underline{r},\tau)$, where $D_g(\underline{r},\tau)$ is the diffusion coefficient for group g. The coefficient depends on the number densities, temperatures and nuclear cross sections of the materials at point $\underline{r}$.

The general two-group diffusion theory equations are derived from the fundamental conservation law which states that the rate of change of the neutron density is equal to the rate at which neutrons are produced within a volume of interest minus the rate at which they are absorbed or escape from the volume; namely (Henry 1975, Chapter 7):

$$\frac{\partial}{\partial\tau}\left[\frac{\varphi_1(\underline{r},\tau)}{v_1}\right] = \sum_j (1-\beta^j)\left[\nu_1^j\Sigma_{f_1}^j(\underline{r},\tau)\,\varphi_1(\underline{r},\tau) + \nu_2^j\Sigma_{f_2}^j(\underline{r},\tau)\,\varphi_2(\underline{r},\tau)\right]$$

$$+\sum_i \lambda_i c_i(\underline{r},\tau) - \Sigma_1(\underline{r},\tau)\,\varphi_1(\underline{r},\tau) + \nabla\cdot D_1(\underline{r},\tau)\ \nabla\varphi_1(\underline{r},\tau) \qquad (2.2.1a)$$

$$\frac{\partial}{\partial\tau}\left[\frac{\varphi_2(\underline{r},\tau)}{v_2}\right] = \Sigma_{21}(\underline{r},\tau)\,\varphi_1(\underline{r},\tau) - \Sigma_2(\underline{r},\tau)\,\varphi_2(\underline{r},\tau) + \nabla\cdot D_2(\underline{r},\tau)\ \nabla\varphi_2(\underline{r},\tau) \qquad (2.2.1b)$$

and the corresponding balance equation for the delayed neutron precursors is

$$\frac{\partial c_i(\underline{r},\tau)}{\partial \tau} = \sum_j \beta_i^j \left[\nu_1^j \Sigma_{f_1}^j(\underline{r},\tau)\,\varphi_1(\underline{r},\tau) + \nu_2^j \Sigma_{f_2}^j(\underline{r},\tau)\,\varphi_2(\underline{r},\tau)\right] - \lambda_i c_i(\underline{r},\tau). \tag{2.2.1c}$$

$$i = 1,2,\ldots I$$

We have assumed that neutrons from fission appear only in group 1. The assumption is valid for the two-group approximation since the lowest energy of fission neutrons is well above the thermal cutoff of 1 eV. We have also considered the general case where there are several fissionable isotopes (represented by the index j) in the reactor core.

It should be pointed out that the indicated space and time dependence of the cross sections and diffusion coefficients stem from the feedback effects due to fission heating which depends on the neutron fluxes. Equations 2.2.1 are really nonlinear and the nonlinearity presents a further difficulty for their solutions. The difficulty is circumvented in practice by solving the neutron kinetics equations in tandem with the thermohydraulics equations. Thus with the fission rate known at some initial time τ, material temperatures and densities at some slightly later time, $\tau+\Delta\tau$, are computed under the assumption that the fission rate stays constant during the time interval $\Delta\tau$. The new temperatures and densities are then used to estimate the behavior of the diffusion theory parameters during $\Delta\tau$, and Eqs. 2.2.1 are solved during the interval as a set of linear equations with time-dependent coefficients. The fission rate at $\tau+\Delta\tau$ is then used as the starting point for another cycle. It is, of course, possible to iterate this process. Indeed, this is what is normally done for the initial steady-state solutions. However, during a transient, changes in material properties are generally so much slower than changes in the neutron fluxes that this is not necessarily a good strategy. Instead, the time step size, $\Delta\tau$, is reduced appropriately if the tandem-strategy is found unacceptable. (RAMONA-3B employs a predictor-corrector procedure to determine if the time step size needs to be reduced.)

A further simplification of Eqs. 2.2.1 is made in practice: the spatial dependence of cross sections and diffusion coefficients is reduced to the dependence on material compositions which correspond to the nodalization structure for the thermohydraulics calculation. The thermohydraulic nodalization structure is, in general, coarser (simpler) than the neutronic mesh grid for the neutron flux. Hence, such a simplification is a profitable strategy. This simplification is also totally consistent with modeling the feedback effects due to the thermohydraulics.

For the convenience of future discussions, the two-group diffusion theory equations (2.2.1) are cast in more compact matrix form as follows:

$$\frac{\partial}{\partial\tau}\begin{bmatrix}\frac{1}{v_1} & 0\\ 0 & \frac{1}{v_2}\end{bmatrix}\begin{bmatrix}\varphi_1\\ \varphi_2\end{bmatrix} = \begin{bmatrix}\nabla\cdot D_1\nabla - \Sigma_1 & 0\\ \Sigma_{21} & \nabla\cdot D_2\nabla - \Sigma_2\end{bmatrix}\begin{bmatrix}\varphi_1\\ \varphi_2\end{bmatrix}$$

$$+\begin{bmatrix}1\\ 0\end{bmatrix}\sum_j (1-\beta^j)\left\{\begin{bmatrix}\nu_1^j\Sigma_{f_1}^j & \nu_2^j\Sigma_{f_2}^j\end{bmatrix}\begin{bmatrix}\varphi_1\\ \varphi_2\end{bmatrix}\right\} + \sum_i \begin{bmatrix}1\\ 0\end{bmatrix}\lambda_i c_i \tag{2.2.2}$$

$$\frac{\partial c_i}{\partial\tau} = \sum_j \beta_i^j \left\{\begin{bmatrix}\nu_1^j\Sigma_{f_1}^j + \nu_2^j\Sigma_{f_2}^j\end{bmatrix}\begin{bmatrix}\varphi_1\\ \varphi_2\end{bmatrix}\right\} - \lambda_i c_i \; ; \qquad i = 1,2,\ldots I$$

or

$$\frac{\partial}{\partial\tau}[V]^{-1}[\Phi] = [A][\Phi] + \sum_j [\chi_p^j](1-\beta^j)[F^j]^T[\Phi] + \sum_i [\chi_i]\lambda_i c_i$$

$$\frac{\partial c_i}{\partial\tau} = \sum_j \beta_i^j [F^j]^T[\Phi] - \lambda_i c_i \; ; \qquad i = 1,2,\ldots I \tag{2.2.3}$$

where the superscript T indicates a transpose so that $[F]^T$ is the row vector, row $[\nu_1\Sigma_{f1}\ \nu_2\Sigma_{f2}]$; and other terms in Eqs. 2.2.3 are defined by comparison with Eqs. 2.2.2. Note that the notations for $[\chi_p]$ and $[\chi_i]$ are both equal to the vector column [1,0] and hence superfluous. They are introduced so that Eqs. 2.2.3 have the general multigroup form.

Equations 2.2.3 are to be solved subject to the boundary conditions at the outer boundary (S):

$$\nabla\varphi_g(\underline{r}) + \frac{1}{\lambda_g}(\underline{r})\,\varphi_g(\underline{r}) = 0 \qquad \text{for } \underline{r}\in S \tag{2.2.4}$$

and the initial conditions at $\tau=0$:

$$-[A][\Phi] = \frac{1}{k_{eff}}[\chi_p][F]^T[\phi] \quad . \tag{2.2.5}$$

Note that Eq. 2.2.5 is an eigenvalue problem, so an eigenvalue $1/k_{eff}$ is introduced. Physically, k_{eff} can be interpreted as the effective multiplication factor (or criticality factor) of the reactor defined as the ratio of total productions of neutrons to the total losses of neutrons. Thus, $k_{eff} = 1.0$ when the reactor is exactly critical. This is the desirable initial condition to start a reactor transient.

A real reactor is geometrically complex and materially heterogeneous. To solve the group diffusion equations (2.2.3) for a complex three-dimensional light water reactor, one needs literally in excess of a hundred thousand spatial mesh points to represent the heterogeneities of the system. Obviously, this is impractical, particularly for transient calculations. The usual remedy for this problem is to seek coarse-mesh solutions of Eqs. 2.2.3. In this approximation, we partition the reactor into a reasonable number of coarse-mesh volumes, customarily referred to as "nodes." However, another degree of approximation is necessary before the coarse-mesh approximation can be made. Namely, the geometrical complexity and material heterogeneity must be homogenized by means of some spatial averaging procedure known as "homogenization." This procedure yields a set of equivalent homogenized two-group parameters for the coarse-mesh nodes.

2.2.2 Homogenization and Energy Averaging

In practice, the homogenized two-group parameters are rarely generated for each coarse-mesh region. Rather, they are calculated for each so-called "fuel cell" (or "fuel type" as called in RAMONA-3B). A fuel cell is defined to be a collection of unit cells and a unit cell may be a fuel bundle or a fuel element, its cladding, and associated coolant. There may be only several different fuel cells in a fresh core, (although an exposed core may contain two dozen or more such fuel cells).

The homogenization is usually carried out by first obtaining a fine-mesh, multigroup transport (or diffusion) theory solution for the fuel cell of interest using zero current boundary conditions, then flux-weighting the multigroup cross sections to obtain the equivalent two-group parameters for the homogenized fuel cell. For example, the average total cross section for group g for the fuel cell is prescribed as follows:

$$\bar{\Sigma}_{t_g} = \frac{\int_{\text{fuel cell}} dV \int_{\Delta E_g} dE\ \Sigma_t(\underline{r},E)\ \varphi(\underline{r},E)}{\int_{\text{fuel cell}} dV \int_{\Delta E_g} dE\ \varphi(\underline{r},E)} \tag{2.2.6}$$

where $\varphi(\underline{r},E)$ is the fine-mesh, multigroup flux solution for the fuel cell obtained from the detailed auxiliary calculations usually performed in a lattice physics code such as the ARMP package, and ΔE_g is the energy width of the group g. The first integration is the homogenization procedure and the second integration is the energy averaging procedure known as "group collapsing."

The other cross section types are calculated in the same way as $\bar{\Sigma}_{tg}$, except for the average diffusion coefficient, which is usually obtained as follows:

$$\bar{D}_g = \frac{\int_{\text{fuel cell}} dV \int_{\Delta E_g} dE\, \varphi(\underline{r},E)}{\int_{\text{fuel cell}} dV \int_{\Delta E_g} dE\, \frac{\varphi(\underline{r},E)}{D(\underline{r},E)}} \qquad (2.2.7)$$

where $D(\underline{r},E)$ is the diffusion coefficient at position $\underline{r}$ and energy E.

The spatial homogenization and group collapsing are routinely done in the lattice physics calculations. Thus, the equivalent two-group parameters required for the group diffusion equations (2.2.3) are the product of a lattice physics code and a core burnup code to determine the material distribution in the core as a result of burnup. A successful scheme for obtaining these parameters is given in (Cokinos 1980, Chapter 2) and (Kohut 1981, Chapter 2).

It should be mentioned, in passing, that the two-group parameters (i.e., cross sections and diffusion coefficients) must be generated for different reactor conditions (state points) at various void fractions, fuel temperatures, coolant temperatures, fuel burnups (exposures) with and without the presence of control rods. These data points are then used to derive the various feedback coefficients associated with the two-group parameters. We shall discuss the details later in Section 2.4.

2.3 The 1-1/2-Group, Coarse-Mesh, Diffusion Model

RAMONA-3B employs the so-called "1-1/2-group, coarse-mesh, diffusion theory model" for neutron kinetics. In this section we shall discuss how this simple model was developed from the more rigorous two-group diffusion theory model. In so doing, we address the assumptions and approximations that must be made, and assess their implications and limitations.

2.3.1 The 1-1/2-Group, Coarse-Mesh, Diffusion Equations

The idea of using the 1-1/2-group approximation is intrinsically related to the desire of seeking accurate coarse-mesh solutions to the two-group diffusion equations (2.2.1) for a large three-dimensional LWR core. Note that the fast neutrons do not see the small heterogeneities due to their much longer mean free path (mfp). For example, for the Peach Bottom-2 core at the end of cycle 2, the fast neutron mfp is about 37 cm in the bottom of the core with no voids, 50 cm at the midplane with 40% voids, and about 65 cm in the top of the core with 67% voids. In contrast, the thermal neutron mean free path is much shorter, about 10-20 cm. This suggests that much is to be gained if one could solve Eqs. 2.2.1 for the fast flux only and then derive the thermal flux from

the fast flux by some means. This is precisely how the 1-1/2-group approximation came about.

To derive the 1-1/2-group diffusion equations, we retain the divergence term only for the fast flux φ_1 in Eqs. 2.2.1 and assume that

(i) the divergence term for the thermal flux φ_2 can be either neglected (the standard option in RAMONA-3B) or approximated by some known function, $\Lambda_2(\underline{r},\tau)$.

For simplicity, we further assume that

(ii) the average neutron speeds, v_1 and v_2, are independent of space and time, and

(iii) a single set of the delayed neutron parameters, β_i and λ_i, can be defined such that they too are independent of space and time.

Assumption (i) is the essence of the 1-1/2-group model and its validity depends on the problem at hand. The assumption is generally good for a homogeneous region of large size (much larger than the thermal neutron diffusion length so that the thermal neutron leakage is insignificant). It is bad for small regions and near any large material discontinuities. Fortunately, this assumption is self-consistent with the coarse-mesh representation of the reactor.

Assumption (ii) is generally valid, but should be substantiated by calculations of the variation in v_1 and v_2, and the sensitivity of transients to this variation.

Assumption (iii) may not be valid for an exposed core with nonuniform burnup (exposure) distributions. One of the LWR operating strategies is to maintain the exposure distribution as uniform as practicable; however, calculations are recommended in order to substantiate that the spatial dependence will not be important. It is clear that β_i and λ_i can be assumed to be independent of time. These parameters will be discussed further in Section 2.6.2.

With these assumptions, the two-group diffusion equations (2.2.1) reduce to

$$\frac{1}{v_1}\frac{\partial\varphi_1(\underline{r},\tau)}{\partial\tau} = \nabla\cdot D_1\nabla\varphi_1(\underline{r},\tau) - \Sigma_1\varphi_1(\underline{r},\tau) + (1-\beta)\left[\nu_1\Sigma_{f_1}\varphi_1(\underline{r},\tau) + \nu_2\Sigma_{f_2}\varphi_2(\underline{r},\tau)\right] + \sum_i \lambda_i c_i(\underline{r},\tau) \qquad (2.3.1a)$$

$$\frac{1}{v_2}\frac{\partial\varphi_2(\underline{r},\tau)}{\partial\tau} = \Lambda_2(\underline{r},\tau) - \Sigma_2\varphi_2(\underline{r},\tau) + \Sigma_{21}\varphi_1(\underline{r},\tau) \qquad (2.3.1b)$$

and

$$\frac{\partial c_i(\underline{r},\tau)}{\partial \tau} = \beta_i\left[\nu_1\Sigma_{f_1}\varphi_1(\underline{r},\tau) + \nu_2\Sigma_{f_2}\varphi_2(\underline{r},\tau)\right] - \lambda_i c_i(\underline{r},\tau); \qquad (2.3.1c)$$

$$i = 1,2,\ldots I.$$

Equations 2.3.1 are the basic 1-1/2-group, coarse-mesh, diffusion equations. We have retained the argument $(\underline{r},\tau)$ to indicate that they are meant to apply to three-dimensional time-dependent problems. We have also dropped the argument for the two-group parameters to indicate that they are the homogenized constants for a coarse-mesh representation of the reactor, even though they are fully time dependent.

Note that the spatial part of the group 2 flux equation becomes trivial without having to deal with the divergence term. Thus we can use a coarse-mesh grid to calculate the fast flux accurately. Once the fast flux is obtained, the problem is reduced to obtaining the thermal flux accurately from the fast flux. This is the central theme of the neutron kinetics model in RAMONA-3B. The success of the model hinges on how one can minimize the impact of the fundamental assumption (i) regarding the thermal neutron leakage. Because of its fundamental importance, we shall discuss this subject in the following section.

2.3.2 Simplified Treatment of Thermal Neutron Diffusion

As stated in assumption (i), the thermal neutron diffusion in space is approximated by the function $\Lambda_2(\underline{r},\tau)$; namely;

$$\nabla\cdot D_2\nabla\varphi_2(\underline{r},\tau) = \Lambda_2(\underline{r},\tau). \qquad (2.3.2)$$

Here $\Lambda_2(\underline{r},\tau)$ is assumed known from either a simple analytical treatment or an auxiliary precalculation for a typical coarse-mesh node of interest. It is this treatment of $\Lambda_2(\underline{r},\tau)$ which will have a great impact on the accuracy of the present model. A judicious choice of the nodalization structure is important in that it can help relieve the impact of the Λ_2 treatment.

In the simplest case, one can set $\Lambda_2(\underline{r},\tau)$ to zero, thus completely neglecting the thermal neutron diffusion. In fact, this is the standard option in RAMONA-3B. Physically, this implies that the majority of thermal neutrons in a coarse-mesh node stay within the volume and only a negligible number of thermal neutrons escape the volume by diffusion near the nodal boundary. Thus, the larger the size of the coarse-mesh node, the better this simplest treatment of Λ_2 is because of very short thermal neutron diffusion length (about 2-5 cm). However, one should not use a nodal size so large as to render the treatment of the fast flux divergence term inaccurate. (RAMONA-3B employs a finite-difference scheme to treat this term.) Obviously, there is an optimum range of

nodal size that is a good compromise for both the fast and thermal neutron fluxes. One must keep this in mind if he chooses to use this option in RAMONA-3B.

There is, in RAMONA-3B, an option for determining the $\Lambda_2(\underline{r},\tau)$ function that has not been verified as to its correctness. It is based on the basic idea of the coarse-mesh formulation, that the size of the coarse-mesh volume (node) is sufficiently large for thermal neutrons so that the thermal flux distribution becomes separable within the coarse-mesh volume. Thus, the three-dimensional thermal neutron leakages can then be treated separately in each spatial dimension as a one-dimensional slab problem. The following derivation is based on this idea and provides the formulas which must be verified as being present in RAMONA-3B.

Consider two adjacent slabs of sufficient thickness, each of which has homogeneous material properties of its own. In what follows, we shall consider only the steady-state diffusion equation for thermal neutrons in say, the x-dimension. The derived formula for Λ_2 is then assumed to apply at each time step during a transient. The thermal neutron diffusion equation at steady state may be written

$$D_2 \frac{d^2\varphi_2(x)}{dx^2} + \Sigma_{21}\varphi_1(x) - \Sigma_2\varphi_2(x) = 0. \qquad (2.3.3)$$

If φ_1 is assumed known, the solution of Eq. 2.3.3 consists of a general solution and a particular solution of the form:

$$\varphi_2(x) = Ae^{-\frac{x}{L2}} + Be^{\frac{x}{L2}} + \left(\frac{\Sigma_{21}}{\Sigma_2}\right)\varphi_1 \qquad (2.3.4)$$

where L_2 is the thermal neutron diffusion length defined as

$$L_2 = \sqrt{\frac{D_2}{\Sigma_2}}\ , \qquad (2.3.5)$$

and A,B are the constants associated with the general solution to be determined.

Note that Eq. 2.3.4 is applicable to the slab i of interest and its neighbor (i-1) as sketched in Fig. 2.1. The interface is defined to be at x=0 for convenience. There are four unknown constants (A_j, B_j, A_{j-1} and B_{j-1}) to be determined. We need four boundary conditions to determine them. The first two are the continuity of the thermal neutron flux and its current at the interface:

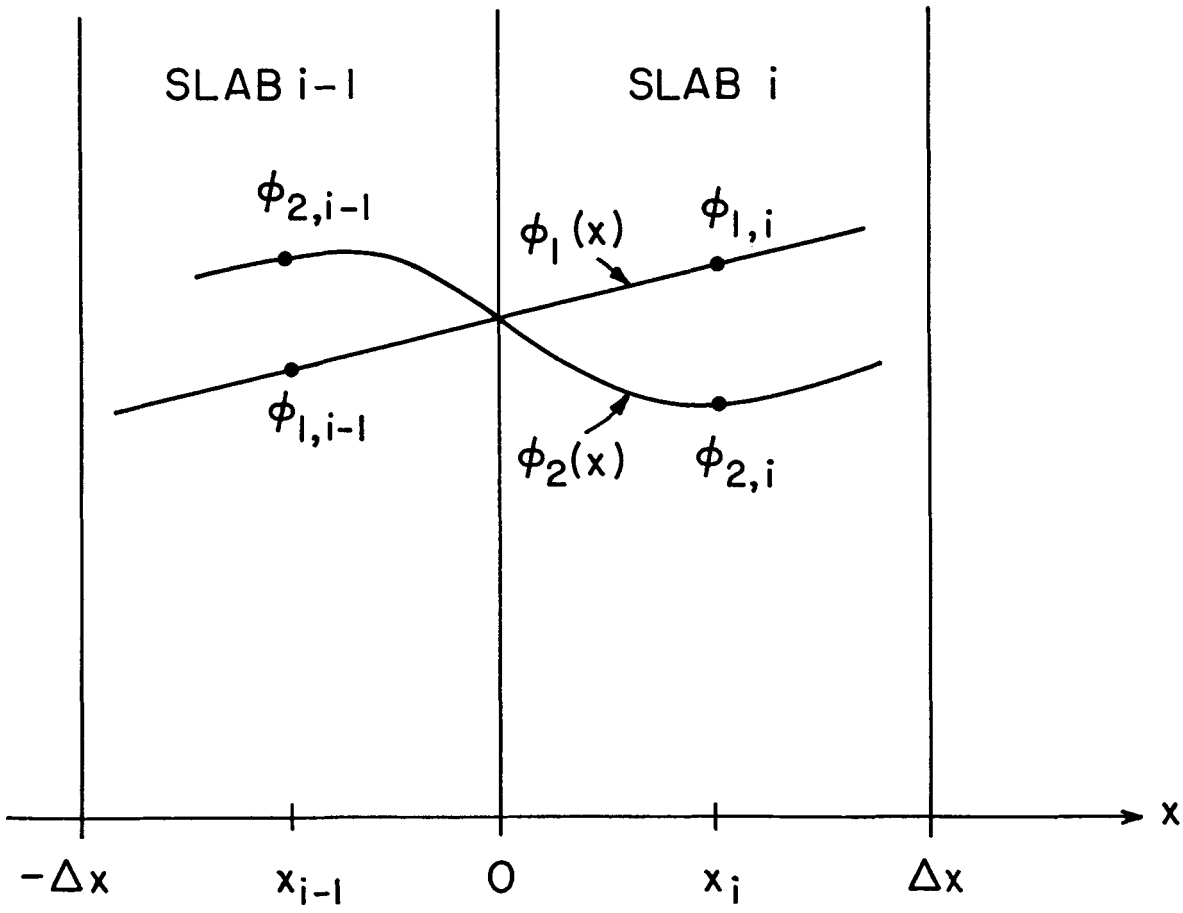

Figure 2.1 Simplified Treatment of Thermal Neutron Diffusion

$$(1)\quad \varphi_{2,i}\Big|_{x=0} = \varphi_{2,i-1}\Big|_{x=0}$$

$$(2)\quad D_{2,i}\,\frac{d\varphi_{2,i}}{dx}\Big|_{x=0} = D_{2,i-1}\,\frac{d\varphi_{2,i-1}}{dx}\Big|_{x=0} \quad .$$

The other two boundary conditions are derived from the assumption that, at the center of each slab, the thermal flux has reached its asymptotic form:

$$\varphi_2(x) = \left(\frac{\Sigma_{21}}{\Sigma_2}\right)\varphi_1(x)$$

whence

$$\frac{d\varphi_2(x)}{dx} = \left(\frac{\Sigma_{21}}{\Sigma_2}\right)\frac{d\varphi_1(x)}{dx} \quad .$$

This is a good assumption if $\Delta x >> L_2$, a condition required of the coarse-mesh formulation. Applying this to both slabs, we obtain the two additional boundary conditions:

$$(3)\quad \frac{d\varphi_{2,i}}{dx}\Big|_{x=\frac{\Delta x}{2}} = \left(\frac{\Sigma_{21}}{\Sigma_2}\right)_i \frac{d\varphi_{1,i}}{dx}\Big|_{x=\frac{\Delta x}{2}}$$

$$(4)\quad \frac{d\varphi_{2,i-1}}{dx}\Big|_{x=-\frac{\Delta x}{2}} = \left(\frac{\Sigma_{21}}{\Sigma_2}\right)_{i-1} \frac{d\varphi_{1,i-1}}{dx}\Big|_{x=-\frac{\Delta x}{2}} \quad .$$

In order to apply the above two boundary conditions, it is further assumed that the fast flux φ_1 varies linearly across the interface, as shown in Fig. 2.1, so that the fast flux gradient can be expressed in terms of the fast fluxes at the center of the slabs.

In summary, the use of the boundary conditions (3) and (4) invokes two assumptions. This is not necessary because we can utilize the central thermal fluxes of the slabs which are being calculated by RAMONA-3B. Thus, a better approach would be to use the following boundary conditions:

$$(3)' \quad \varphi_{2,i}(x)\Big|_{x=\frac{\Delta x}{2}} = \bar{\varphi}_{2,i}$$

$$(4)' \quad \varphi_{2,i-1}(x)\Big|_{x=-\frac{\Delta x}{x}} = \bar{\varphi}_{2,i-1} \quad .$$

We recommend this for future improvement. In what follows, we shall present the result for Λ_2 based on the boundary conditions (1), (2), (3) and (4) as they are actually implemented in RAMONA-3B.

For ease of writing, define the following quantities:

$$\xi_i = \frac{1}{L_{2,i}} \tag{2.3.6}$$

$$\eta_i = \frac{\varphi_{1,i} - \varphi_{1,i-1}}{\Delta x} \tag{2.3.7}$$

$$\gamma_i = \left(\frac{\Sigma_{21}}{\Sigma_2}\right)_i \tag{2.3.8}$$

where $\varphi_{1,i}$ represents the flux at $x=x_i$ (cf. Fig. 2.1). Applying the flux solution (2.3.4) to the four boundary conditions, we obtain the following four equations for the four unknowns (A_i, B_i, A_{i-1}, B_{i-1}):

$$A_i + B_i + \gamma_i \frac{1}{2}\left(\varphi_{1,i} + \varphi_{1,i-1}\right) = A_{i-1} + B_{i-1} + \gamma_{i-1} \frac{1}{2}\left(\varphi_{1,i} + \varphi_{1,i-1}\right) \tag{2.3.9}$$

$$D_{2,i}\left(-\xi_i A_i + \xi_i B_i + \gamma_i \eta_i\right) = D_{2,i-1}\left(-\xi_{i-1} A_{i-1} + \xi_{i-1} B_{i-1} + \gamma_{i-1} \eta_i\right) \tag{2.3.10}$$

$$A_i = e^{\frac{\Delta x}{L2}} B_i \tag{2.3.11}$$

$$A_{i-1} = e^{-\frac{\Delta x}{L2}} B_{i-1} \quad . \tag{2.3.12}$$

For a coarse-mesh representation, $\Delta x/L_2 \geq 6$ is usually chosen. Thus, we see from Eqs. 2.3.11 and 2.3.12 that A_i is much larger than B_i and A_{i-1} is much smaller than B_{i-1}. (For $\Delta x/L_2 = 6$, $e6 = 403$, $e^{-6} = 0.00248$.) Taking advantage of this and solving Eqs. 2.3.9 and 2.3.10 for B_{i-1} and B_i, we obtain

$$B_{i-1} = \frac{\frac{1}{2}\left(\varphi_{1,i} + \varphi_{1,i-1}\right)\left(\gamma_i - \gamma_{i-1}\right)D_{2,i}\xi_i + \eta_i\left(D_{2,i}\xi_i - D_{2,i-1}\xi_{i-1}\right)}{\left(D_{2,i}\xi_i + D_{2,i-1}\xi_{i-1}\right)}, \quad (2.3.13)$$

$$B_i = \left(\frac{1+e^{-\frac{\Delta x}{L_2}}}{1+e^{\frac{\Delta x}{L_2}}}\right) B_{i-1} - \frac{\left(\varphi_{1,i} + \varphi_{1,i-1}\right)}{2\left(1+e^{\frac{\Delta x}{L_2}}\right)}\left(\gamma_i - \gamma_{i-1}\right),$$

$$\approx e^{-\frac{\Delta x}{L_2}}\left[B_{i-1} - \frac{1}{2}\left(\varphi_{1,i} + \varphi_{1,i-1}\right)\left(\gamma_i - \gamma_{i-1}\right)\right] . \quad (2.3.14)$$

We are interested in the net outward currents (i.e., leakage) at the boundaries of the slab i. At the left boundary (x=0), we have

$$J^L_{2,i} = D_{2,i}\left.\frac{d\varphi_{2,i}}{dx}\right|_{x=0} = D_{2,i-1}\left.\frac{d\varphi_{2,i-1}}{dx}\right|_{x=0}$$

$$= D_{2,i-1}\left(-\xi_{i-1}A_{i-1} + \xi_{i-1}B_{i-1} + \gamma_{i-1}\eta_i\right) . \quad (2.3.15)$$

The term with A_{i-1} can be neglected because of Eq. 2.3.12. Thus, the net outward current at the left boundary of slab i becomes

$$J^L_{2,i} = D_{2,i-1}\left(\xi_{i-1}B_{i-1} + \gamma_{i-1}\eta_i\right) \quad (2.3.16)$$

where B_{i-1} is given by Eq. 2.3.13.

Similarly, we can derive the net outward current (to the right) at the right boundary of slab i. In this case, we have

$$J^R_{2,i} = - D_{2,i} \left. \frac{d\varphi_{2,i}}{dx} \right|_{x = \Delta x} ,$$

$$= - D_{2,i} \left(-\xi_i A_i e^{-\frac{\Delta x}{L2}} + \xi_i B_i e^{\frac{\Delta x}{L2}} + \gamma_i \eta_{i+1} \right) \qquad (2.3.17)$$

where η_{i+1} is the fast flux gradient at the right boundary which, by the linear approximation, may be written

$$\eta_{i+1} = \frac{\varphi_{1,i+1} - \varphi_{1,i}}{\Delta x} . \qquad (2.3.18)$$

Here we have assumed that the mesh spacing Δx is everywhere constant. Using Eq. 2.3.11 for A_i and Eq. 2.3.14 for B_i, we obtain the net outward current at the right boundary of slab i:

$$J^R_{2,i} = - D_{2,i} \left[\xi_i B_{i-1} - \frac{\xi_i}{2} \left(\varphi_{1,i} + \varphi_{1,i-1} \right) \left(\gamma_i - \gamma_{i-1} \right) + \gamma_i \eta_{i+1} \right] . \qquad (2.3.19)$$

The Λ_2 function as defined by Eq. 2.3.2 for the slab i of interest is then given by

$$\Lambda_{2,i} = \frac{J^L_{2,i} - J^R_{2,i}}{\Delta x} . \qquad (2.3.20)$$

A similar expression can be derived for $\Lambda_{2,j}$ in the y-direction and for $\Lambda_{2,k}$ in the z-direction. By virtue of the separability assumption discussed earlier, we can then express the total Λ_2 function as the sum of its three components:

$$\Lambda_2 = \Lambda_{2,i} + \Lambda_{2,j} + \Lambda_{2,k} . \qquad (2.3.21)$$

2.3.3 Boundary Conditions

In a BWR, surrounding the active fuel region of the core is the coolant which acts as a reflector for both fast and thermal neutrons. A reflector can significantly affect the characteristics of the neutron population within the

core. It is, therefore, important to represent correctly the effects produced by a reflector. This can be done simply by including the reflector as a part of the overall reactor when performing the neutron flux calculations. However, such a procedure is computationally costly since fine meshes are usually required to represent the reflector in a finite-difference approximation.

RAMONA-3B overcomes this problem by excluding the reflector but, instead, applying appropriate boundary conditions at the core-reflector interfaces. The most general approach for the two-group approximation is to use a matrix albedo $[\alpha]$ defined as a current-to-flux ratio at the boundary:

$$[\alpha] \triangleq \begin{bmatrix} \alpha_{11} & 0 \\ \alpha_{21} & \alpha_{22} \end{bmatrix} = \frac{[J_B]}{[\Phi_B]} \tag{2.3.22}$$

where $[J_B]$ is the boundary current vector and $[\Phi_B]$ is the boundary flux vector. In neutron diffusion theory, the current vector is given by

$$[J_B] = - [D][\nabla\Phi]\,|_B \approx [D]\,\frac{[\Phi_I] - [\Phi_B]}{\xi/2} \tag{2.3.23}$$

where $[\Phi_I]$ is the adjacent interior flux vector and ξ is the mesh spacing next to the boundary of interest. On the (x,y) plane, ξ is equal to Δx and in the z-direction it is equal to Δz.

Eliminating the boundary current vector $[J_B]$ from Eqs. 2.3.22 and 2.3.23, and then solving for the boundary flux vector $[\Phi_B]$ yields

$$[\Phi_B] = \left([I] + \frac{\xi}{2}\,[D]^{-1}[\alpha]\right)^{-1}[\Phi_I] \tag{2.3.24}$$

where $[I]$ is the unity vector. Carrying out the matrix inversion, we obtain the two-group boundary fluxes as follows:

$$\varphi_{B_1} = \frac{\varphi_{I_1}}{\left(1 + \frac{\xi}{2}\,\frac{\alpha_{11}}{D_1}\right)} \tag{2.3.25}$$

$$\varphi_{B_2} = \frac{-\frac{\xi}{2}\,\frac{\alpha_{21}}{D_2}}{\left(1 + \frac{\xi}{2}\,\frac{\alpha_{11}}{D_1}\right)\left(1 + \frac{\xi}{2}\,\frac{\alpha_{22}}{D_2}\right)}\,\varphi_{I_1} + \frac{1}{\left(1 + \frac{\xi}{2}\,\frac{\alpha_{22}}{D_2}\right)}\,\varphi_{I_2} \tag{2.3.26}$$

The above relations between the boundary fluxes and the interior (center) fluxes are important since only the center fluxes are calculated and these must be related to the boundary fluxes before the boundary conditions can be applied.

In the 1-1/2-group, coarse-mesh, diffusion model employed by RAMONA-3B, Eq. 2.3.25 is utilized to treat the boundary condition for the fast neutron flux in terms of the fast boundary current:

$$J_{B_1} = \alpha_{11}\varphi_{B_1} = \frac{\alpha_{11}\,\varphi_{I_1}}{1+\frac{\xi}{2}\frac{\alpha_{11}}{D_1}} \quad . \tag{2.3.27}$$

It is assumed that the fast neutron flux extrapolates linearly to zero at some distance λ_1 beyond the boundary, where λ_1 is known as the "fast extrapolation length." This assumption is consistent with the homogeneous boundary conditions given by Eq. 2.2.4. It can be readily shown that α_{11}, in diffusion theory, is simply

$$\alpha_{11} = \frac{D_1}{\lambda_1} \quad . \tag{2.3.28}$$

With this α_{11}, the boundary current reduces to

$$J_{B_1} = \frac{D_1\,\varphi_{I_1}}{\lambda_1 + \frac{\xi}{2}} \quad . \tag{2.3.29}$$

For convenience, let us define

$$\lambda_{eff} = \lambda_1 + \frac{\xi}{2} \; ; \quad \xi = \Delta x \text{ or } \Delta z \quad , \tag{2.3.30}$$

so that we may write $J_{B_1} = D_1\,\varphi_{I_1}/\lambda_{eff}$. This boundary current is then used to treat the fast flux divergence term, $\nabla \cdot D_1 \nabla \varphi_1$, in the boundary nodes only.

For the thermal neutron flux, the general relation as given by Eq. 2.3.26 is not used in RAMONA-3B. Instead, the thermal neutron boundary condition is taken into account by introducing a source term, $\delta_B S_B \varphi_1(\underline{r},\tau)$, in the balance equation (2.3.1b):

$$\frac{1}{v_2}\frac{\partial \varphi_2(\underline{r},\tau)}{\partial \tau} = \Lambda_2(\underline{r},\tau) - \Sigma_2\varphi_2(\underline{r},\tau) + \Sigma_{21}\varphi_1(\underline{r},\tau) + \delta_B S_B \varphi_1(\underline{r},\tau) \, . \tag{2.3.31}$$

Physically, we may interpret the introduced source term as the additional thermal neutrons reflecting back into the core from the reflector per fast neutron leaking into the reflector. Note that δ_B is unity in the boundary nodes only and zero elsewhere.

Before we go on to discuss the derivation of this source term, a caution is in order. If the option of non-zero Λ_2 is invoked, care must be taken to insure that the Λ_2 treatment discussed in the previous section does not include all the external boundaries for, otherwise, the thermal neutron leakage (or in-leakage) may be doubly accounted for.

To derive S_B in the introduced source term, we define a parameter, θ, as the ratio of the net inward thermal neutron current ($-J_{B_2}$) to the net outward fast neutron current (J_{B_1}) at the boundary surface of interest:

$$\theta \equiv \frac{-J_{B_2}}{J_{B_1}} \quad . \tag{2.3.32}$$

Thus, upon using Eqs. 2.3.29 and 2.3.30, we obtain

$$-J_{B_2} = \theta J_{B_1} = \frac{\theta D_1 \varphi_{I_1}}{\lambda_{eff}} \quad . \tag{2.3.33}$$

Note that $-J_{B_2}$ is the number of thermal neutrons per unit surface area leaking into the boundary node of interest from the reflector; whereas the introduced source term as it appears in Eq. 2.3.31 is the number of thermal neutrons per unit volume leaking into the boundary node from the reflector. Note also that $\varphi_1(\underline{r},\tau)$ in the source term is the interior (center) fast neutron flux of the boundary node; namely, φ_{I_1}. Thus, we have

$$S_B \varphi_{I_1} = \frac{-J_{B_2}}{\xi} = \frac{D_1 \theta \varphi_{I_1}}{\lambda_{eff} \xi}$$

whence

$$S_B = \frac{D_1 \theta}{\lambda_{eff} \xi} \quad , \tag{2.3.34}$$

where ξ is the mesh spacing of the boundary node. Note that RAMONA-3B imposes that the mesh spacings on the (x,y) plane be equal (i.e., $\Delta x = \Delta y$). Hence, $\xi = \Delta x$ for the side (radial) boundary nodes and $\xi = \Delta z$ (the mesh spacing in the axial direction) for both the bottom and top boundary nodes.

Equation 2.3.34 is directly applicable to the bottom and top boundary nodes which all have only one surface facing the reflector. For the side

(radial) boundary nodes, one must consider the possibility that some of the boundary nodes may have more than one surface facing the reflector. Thus, the right-hand side of Eq. 2.3.34 should carry a number n for the side boundary nodes to account for the multiple reflector-facing surfaces (i.e., missing neighbors as they are called in RAMONA-3B).

Furthermore, the side boundary conditions may vary along the axial direction primarily because of the void distribution. Steam voids significantly affect the diffusion coefficient which dictates the parameter λ_{eff}, as we shall discuss later in Section 2.5.1. The axial variation of the side boundary condition is taken into account via a first-order Taylor series expansion for $1/\lambda_{eff}$:

$$\frac{1}{\lambda^S_{eff}} = \left(\frac{1}{\lambda^S_{eff}}\right)_{ref} + \frac{\partial}{\partial D_1}\left(\frac{1}{\lambda^S_{eff}}\right)_{ref}\left(D_1 - D_1^{ref}\right) \qquad (2.3.35)$$

where the notation "ref" represents the reference condition chosen for determining the single set of the side boundary condition parameters as required by RAMONA-3B, and the superscript S has been used to stand for the side boundary nodes.

The source term for the side boundary nodes can then be written

$$S^S_B = \left(\frac{n}{\lambda^S_{eff}}\right)\left(\frac{\theta_S}{\Delta x}\right) D^S_1 \ , \qquad (2.3.36)$$

where θ_S is the current ratio defined by Eq. 2.3.32 for the side boundary nodes with their fast diffusion coefficients being D^S_1.

Considering all the boundary nodes in three dimensions, we can summarize the source term as follows:

$$\delta_B S_B = \delta^B_B \frac{D^B_1 \theta_B}{\lambda^B_{eff}\Delta z} + \delta^T_B \frac{D^T_1 \theta_T}{\lambda^T_{eff}\Delta z} + \delta^S_B \frac{D^S_1 n \theta_S}{\lambda^S_{eff}\Delta x} \ . \qquad (2.3.37)$$

Recall that the parameter, λ^S_{eff}, includes the void effect through Eq. 2.3.35 where the coefficient $\partial/\partial D_1(1/\lambda^S_{eff})_{ref}$ and D_1^{ref} are also required input for RAMONA-3B. Determination of the boundary condition parameters will be discussed later in Section 2.5.

2.3.4 Initial Conditions

Appropriate initial conditions are necessary to start a transient calculation. The governing equations for the initial conditions of neutron kinetics can be derived from Eqs. 2.3.1 by setting the time derivatives to zero:

$$\begin{cases} -\nabla\cdot D_1 \nabla \varphi_1(\underline{r}) + \Sigma_1 \varphi_1(\underline{r}) = \frac{1}{k_{eff}} \left[\nu_1 \Sigma_{f_1} \varphi_1(\underline{r}) + \nu_2 \Sigma_{f_2} \varphi_2(\underline{r})\right] & (2.3.38a) \\ -\Lambda_2(\underline{r}) + \Sigma_2 \varphi_2(\underline{r}) = \Sigma_{21} \varphi_1(\underline{r}) + \delta_B S_B \varphi_1(\underline{r}) & (2.3.38b) \\ C_i(\underline{r}) = \frac{\beta_i}{\lambda_i} \left[\nu_1 \Sigma_{f_1} \varphi_1(\underline{r}) + \nu_2 \Sigma_{f_2} \varphi_2(\underline{r})\right] \quad ; & (2.3.38c) \end{cases}$$

$$i = 1,2,\ldots,I.$$

Here again, for simplicity, we have dropped the argument for all the cross sections and diffusion coefficients, keeping in mind that they are actually time dependent and space dependent in a coarse-mesh sense.

The first two equations in Eq. 2.3.38 define an eigenvalue problem of the form:

$$\begin{bmatrix} (-\nabla\cdot D_1 \nabla + \Sigma_1) & 0 \\ -(\Sigma_{21} + \delta_B S_B + \Lambda_{21}) & (-\Lambda_{22} + \Sigma_2) \end{bmatrix} \begin{bmatrix} \varphi_1 \\ \varphi_2 \end{bmatrix} = \frac{1}{k_{eff}} \left\{ \begin{bmatrix} \nu_1\Sigma_{f_1} & \nu_2\Sigma_{f_2} \end{bmatrix} \begin{bmatrix} \varphi_1 \\ \varphi_2 \end{bmatrix} \right\} \quad (2.3.39)$$

or

$$[A][\Phi] = \frac{1}{k_{eff}} [F]^T[\Phi] \ . \quad (2.3.40)$$

Here we have decomposed the Λ_2 function into a term depending on $\varphi_1(\underline{r})$ and another depending on $\varphi_2(\underline{r})$ for the sake of generality:

$$\Lambda_2(\underline{r}) = \Lambda_{21}\varphi_1(\underline{r}) + \Lambda_{22}\varphi_2(\underline{r}) \ . \qquad (2.3.41)$$

Naturally, $\Lambda_{21} = \Lambda_{22} = 0$ if the option of $\Lambda_2 = 0$ is invoked.

Note that an eigenvalue $1/k_{eff}$ has been introduced to assure that a desired initial condition exists. The parameter k_{eff} is often interpreted as the effective multiplication factor (or criticality factor) of the reactor of interest. It can be determined either by solving the eigenvalue equation (2.3.40) for the fundamental eigenvalue or from the ratio of total production of neutrons to total loss of neutrons using the eigenfunction $[\Phi]$. The latter approach is used by RAMONA-3B to obtain k_{eff}.

The desired initial condition to start a reactor transient is that the reactor is exactly critical ($k_{eff} = 1.0$). In practice, it is not always possible to obtain this desired condition from solving Eq. 2.3.40 because of the uncertainties in the two-group parameters used and the method employed to solve the eigenvalue equation. The usual practice is to calculate k_{eff} to within 0.5% of unity, then divide both $\nu_1\Sigma_{f1}$ and $\nu_2\Sigma_{f2}$ by the calculated k_{eff} to make the reactor exactly critical prior to the transient calculation.

We shall defer the discussion of the solution method used to solve the eigenvalue equation until Chapter 6. It is important to point out that the initial value problem is not closed unless the coupling between the neutron kinetics and thermohydraulics is considered. This coupling is due to the thermohydraulic feedback effects on the two-group neutron diffusion parameters. The coupling at the initial steady state is established by solving successively the eigenvalue equation and the thermohydraulics equations (to be discussed in Chapters 3 and 4) until a converged fission power distribution (or thermohydraulic heat source distribution) is obtained. To do this we need a feedback model for representing the thermohydraulic effects on the two-group diffusion parameters. We shall discuss this in the next section.

2.4 Feedback Models

The two-group cross sections and diffusion coefficients (hereafter called two-group parameters for brevity) are functions of space and time as a consequence of their dependence on the material composition, density and temperature. The material composition changes due to fuel depletion (often referred to as burnup or exposure), fission product buildup (especially xenon), soluble boron injection, and the control rod movement including reactor scram. The density changes with steam voids and temperatures which, in turn, change with the thermohydraulic conditions. The material temperature changes due to fission heating.

Thus, in general, the two-group parameters should be represented as a function of nine variables: the void fraction α, the coolant temperature T_ℓ,

the fuel temperature T_f, the control fraction f_d, the liquid boron concentration c_B, the xenon concentration X_e, the fuel type F, the exposure E, and the exposure-weighted void fraction α_E (customarily called history-dependent void). Symbolically, we can express the two-group parameters as

$$\Sigma = \Sigma(\alpha, T_\ell, T_f, f_d, c_B, X_e, F, E, \alpha_E) \ . \tag{2.4.1}$$

For convenience, we call Eq. 2.4.1 the feedback model for linking the neutron physics and thermohydraulics.

The functional form of the feedback model is by and large empirical in that experimental evidence and practical experience dictate its choice. In this sense, the feedback models are analogous to the constitutive relations used in thermohydraulics. In RAMONA-3B there are three different such choices called, respectively, the BNL1 option, the BNL2 option and the ScP1 option. We shall describe the BNL2 option in the following and leave a description of other options to Appendix 2.1.

The BNL2 option represents the two-group parameters in the following form:

$$\Sigma = (1 - f_d)\sum_{n=1}^{3} a_n^o \alpha^{n-1} + f_d \sum_{n=1}^{3} a_n^c \alpha^{n-1} + a_\ell (T_\ell - T_{\ell o})$$

$$+ a_f\left(\sqrt{T_f} - \sqrt{T_{fo}}\right) + \delta\Sigma(c_B,\alpha) + \delta\Sigma_x + \delta\Sigma_L \ . \tag{2.4.2}$$

The first two terms account for the effect of void feedback and the presence of control rods. The third term with a_ℓ accounts for the effect of moderator temperature feedback. The term involving a_f takes into account the effect of Doppler feedback. The term $\delta\Sigma(c_B,\alpha)$ accounts for the effect of standby soluble boron injection should it occur. The term $\delta\Sigma_x$ attempts to account for the effect of fission product poisoning. Finally, the term $\delta\Sigma_L$ accounts for the effect of transverse leakage of neutrons if fewer than three dimensions are used to represent the core.

Note that the effect of exposure (burnup) is not explicitly represented in Eq. 2.4.2 because the effect of exposure does not change during the course of most BWR transients of interest to RAMONA-3B. (Exposure accumulates appreciably only in a duration of months or years.) Thus, for intended applications of RAMONA-3B, the exposure can be assumed to be constant in time and its effect should be taken into account in generating the coefficients for Eq. 2.4.2. Note also that the fuel type dependence has been suppressed in Eq. 2.4.2 for the sake of simplicity. One must keep in mind that the coefficients in Eq. 2.4.2 must be generated for all fuel types that are present in the core.

2.4.1 Void Feedback

The effect of void feedback differs substantially between the uncontrolled (control rod out) condition and the controlled (control rod in) condition in a BWR. Therefore, the quadratic representation of the void feedback must be given for both the uncontrolled and controlled conditions as shown in Eq. 2.4.2. The quadratic coefficients, a_n^o (n=1,2,3), are for the uncontrolled state and a_n^c (n=1,2,3) for the controlled state. These coefficients must be generated for each of nine two-group parameters (D_1, D_2, Σ_1, Σ_2, Σ_{21}, $\nu_1\Sigma_{f1}$, $\nu_2\Sigma_{f2}$, ν_1, ν_2). To this end, one must obtain first these nine two-group parameters by performing the so-called lattice physics calculations (as discussed in Section 2.2.2) for all uncontrolled fuel types or fuel cells (a fuel cell is usually a fuel bundle or a multiple of fuel bundles) and all controlled fuel types for at least three void fractions (usually chosen to be α=0, 0.4 and 0.7). The calculations use nominal values for all other variables in Eq. 2.4.1. The data obtained at the three void fractions are then used to determine the quadratic coefficients, a_n^o and a_n^c for each of the two-group parameters. Of course, one can generate the two-group parameters for many more void fractions, then least-square fit them to the quadratic form. This is rarely done in practice because of the large computing expense required.

It should be mentioned that the quadratic void feedback model was selected after a parametric study (Lu and Cheng 1976) had shown that the void feedback follows a quadratic law up to a void fraction of 0.75. For $\alpha > 0.75$, a higher order term may be necessary. We recommend this for future improvement.

2.4.2 Moderator Temperature Feedback

The effect of moderator temperature feedback is generally of much less importance than that of the void feedback. It is sufficient for most situations to represent the moderator temperature feedback via a linear dependence on the moderator (coolant) temperature T_ℓ as shown in Eq. 2.4.2.

To determine a_ℓ, one first selects an appropriate reference moderator temperature $T_{\ell o}$ (usually 286°C, the saturation temperature at 70 bars), a reference void fraction (usually 0.40) and a reference fuel temperature (usually 922 K or 1200°F); then generates the two-group parameters at these reference conditions. Keeping the reference void fraction and fuel temperature constant, one then selects another moderator temperature somewhat lower than $T_{\ell o}$ (usually 220°C) and generates another set of the two-group parameters at the perturbed conditions. The moderator temperature coefficient, a_ℓ, is then given by

$$a_\ell \approx \frac{\Sigma(T_{\ell o}) - \Sigma(T^*_{\ell o})}{T_{\ell o} - T^*_{\ell o}} \qquad (2.4.3)$$

where $T^*_{\ell o}$ is the perturbed moderator temperature, and $\Sigma(T_{\ell o})$ represents symbolically any of the two-group parameters generated with the reference moderator temperature $T_{\ell o}$.

2.4.3 Doppler Feedback

Neutrons with an energy spectrum ranging from about 1 eV to 5.53 keV are called "epithermal or resonance neutrons." The absorption cross section of these epithermal neutrons exhibits a complex resonant structure within the resonance energy spectrum. Nuclear fission heating results in an increase in the epithermal absorption cross section due to Doppler broadening of the resonant structure. The increased epithermal absorption decreases the reactivity in the core. The reduction in the reactivity due to an increase in the fuel temperature (as a result of fission heating) is called the "Doppler feedback." The Doppler reactivity coefficient (i.e., the change in reactivity due to an increase in fuel temperature) is always negative and very important for a severe power excursion such as a rod drop accident since the Doppler feedback acts promptly on the reactivity.

The Doppler feedback affects primarily the fast group cross sections (Σ_1, Σ_{21}, $\nu_1\Sigma_{f1}$) and has little effect on the fast diffusion coefficient, D_1. Consequently, the Doppler feedback effect is taken into account only in these three cross sections. The coefficients a_f, called the "fuel temperature coefficients," are simply the changes in these cross sections with respect to a change in the fuel temperature. The coefficient a_f is negative for Σ_{21} and $\nu_1\Sigma_{f1}$, but positive for Σ_1. A parametric study (Lu and Chang 1976) indicated that the Doppler effect on the cross sections follows a linear dependence on the square root of the fuel temperature over a wide range of reactor conditions. Consequently, such a linear model is employed as shown in Eq. 2.4.2.

To determine a_f, one first selects a reference fuel temperature T_{fo} (usually 922 K or 1200°F) along with a reference moderator temperature (usually 286°C) and a reference void fraction (say, 0.40), then generates a set of fast group cross sections at these reference conditions. Keeping the reference moderator temperature and void fraction constant, one then selects another fuel temperature (T^*_{fo}) somewhat higher than T_{fo} (say, 1172 K or 1650°F) and generates another set of the fast group cross sections at the perturbed conditions. The fuel temperature coefficient, a_f, can then be determined as follows:

$$a_f \approx \frac{\Sigma(T_{fo}) - \Sigma(T^*_{fo})}{\sqrt{T_{fo}} - \sqrt{T^*_{fo}}} \quad . \tag{2.4.4}$$

Here again $\Sigma(T_{fo})$ is used to represent symbolically any of the fast group cross sections generated with the reference fuel temperature T_{fo}.

It is important to note that the present Doppler feedback model, as given in Eq. 2.4.2, does not consider the effect of voids on the fuel temperature coefficients, a_f. As a matter of fact, a_f does vary with the void fraction (Diamond and Cheng 1979). In general, one should account for the void effect on a_f. We recommend this for future improvement. Moreover, the fuel temperature coefficients, a_f, also depend on the control fraction, f_d (Diamond and Cheng 1979). Such dependence on the control density, while not ignorable,

is of secondary importance for most anticipated transients in a BWR, but may be important for a severe power excursion such as a rod drop accident.

2.4.4 Boron Reactivity Feedback

For BWRs, a standby liquid control system (SLCS) is provided to inject soluble boron into the reactor vessel in case the normal control rod system experiences difficulty in shutting down the reactor. Since boron is a strong neutron absorber (especially for thermal neutrons), the boron injection, when it occurs, will decrease the reactivity in the core. This boron reactivity feedback is represented by the term $\delta\Sigma(c_B,\alpha)$ in Eq. 2.4.2.

The boron effect is taken into account in the fast and thermal absorption cross sections only as follows:

$$\delta\Sigma_g(c_B,\alpha) = C_o\ \sigma_{ag}(1-f^*)\ f_w(1-\alpha)\ \bar{\rho}_\ell\ c_B; \qquad (2.4.5)$$

$$g = 1,2$$

where

α = average void fraction in the thermohydraulic node,

$\bar{\rho}_\ell$ = average liquid (water) density defined at each boron computational cell as the arithmetic average of the cell inlet and outlet densities (kg/m^3),

c_B = boron concentration computed for each boron computation cell (ppm),

C_o = 0.11×10^{-10}, a constant involving Avogadro's number, the natural abundance and atomic weight of Boron-10, and conversion factors to obtain the correct units,

σ_{ag} = microscopic absorption cross section of Boron-10 (typically, σ_{a1} = 22∿48 barns, σ_{a2} = 1300∿3500 barns, depending on the neutron spectrum in the water of a fuel cell),

f_w = the ratio of bundle hydraulic flow area to total bundle cross-sectional area,

f^* = a correction factor to allow for conservatism and/or uncertainties (use zero if there is no uncertainty).

The last three quantities (σ_{ag}, f_w and f^*) are required input for RAMONA-3B. Note that the σ_{ag} should be those corresponding to the hardened water spectrum in a fuel cell, and hence depend on the boron concentration, c_B.

2.4.5 Xenon Reactivity Feedback

As a result of fuel burnup, fission products build up in the core. These fission products are neutron absorbers. Hence, their presence decreases the reactivity in the core. This reduction in the core reactivity is often called "fission product poisoning." Among all the fission products xenon stands out as the strongest thermal neutron absorber and is the major single contributor to the poisoning. Since xenon has relatively little effect on the fast neutron cross sections, only the poisoning effect on the thermal cross sections are considered in the xenon reactivity feedback, represented by the term $\delta\Sigma_x$ in Eq. 2.4.2.

The problem of xenon buildup is a transient problem by itself. The xenon concentration tends to approach an equilibrium condition after a while. For the sake of modeling the xenon reactivity feedback, it is usually assumed that the xenon buildup has reached its equilibrium condition. The equilibrium xenon concentration depends on the operating power level as well as the power distribution within the core.

The correction for equilibrium xenon in the core assumes that the cross sections, as otherwise supplied, are evaluated at a core average power density q_o''' corresponding to rated power. The correction for the nonuniformity of the power distribution and/or an operating power level different from rated power is

$$\delta\Sigma_x = a_x \left[\frac{1 + b_x}{1 + b_x \left(\frac{q_o'''}{q'''} \right)} - 1 \right] \qquad (2.4.6)$$

where q''' is the local power density, b_x is a fitting constant and a_x depends on whether Σ_x is the absorption cross section (Σ_2) or the ν-fission cross section ($\nu_2\Sigma_{f2}$):

$a_x = \Delta(\Sigma_2)_{xe}$, the change in Σ_2 due to xenon poisoning at the rated power density,

$a_x = -\Delta(\nu_2\Sigma_{f2})_{xe}$, the negative change in $\nu_2\Sigma_{f2}$ due to xenon poisoning at the rated power density.

Both a_x and b_x are required input for RAMONA-3B. They may be obtained from a lattice physics calculation at the rated condition.

2.4.6 Transverse Leakage Correction

Although RAMONA-3B is a three-dimensional code for neutron kinetics, it can be used to calculate a one-dimensional (axial) problem. In this case, the neutron leakage in the other two dimensions (x,y), called "transverse leakage," should be accounted for, if it is important. Such a correction is not very significant for BWRs of large size (e.g., Peach Bottom-2), but may be important for smaller BWRs.

The transverse leakage correction is simply an approximate way of representing the leakage (divergence) term of the governing equations in the transverse directions. That is,

$$\begin{aligned} \delta\Sigma_{L_g}\varphi_g &= -\nabla\cdot D_g\,\varphi_g\Big|_{(x,y)}\,, \\ &\approx -D_g\nabla^2\varphi_g\Big|_{(x,y)}\,. \end{aligned} \tag{2.4.7}$$

If we define a parameter, B_g^2, called "buckling" as

$$B_g^2 = \left.\frac{-\nabla^2\varphi_g}{\varphi_g}\right|_{(x,y)}\,, \tag{2.4.8}$$

we obtain the transverse leakage corrections as follows:

$$\delta\Sigma_{L_g} = D_g B_g^2\,;\quad g=1,2\,. \tag{2.4.9}$$

Thus, the problem becomes how to estimate the bucklings, B_g^2 (g=1,2). The best way is to evaluate B_g^2 with Eq. 2.4.8 if the detailed flux distributions in the transverse directions are available. Since the transverse leakage corrections are not of prime importance, they are often estimated from a homogeneous reactor theory (Glasstone 1956, Chapter 7):

$$B_g^2 = \left(\frac{\pi}{X+2\lambda_g}\right)\left(\frac{\pi}{Y+2\lambda_g}\right)^2\,;\quad g=1,2 \tag{2.4.10}$$

where X is the effective dimension of the active reactor core in the x-direction, Y is that in the y-direction, and λ_g is the linear extrapolation length for the g^{th} group of neutrons. The determination of λ_g will be discussed next in Section 2.5.1.

2.5 Boundary Condition Parameters

We have discussed the boundary conditions in Section 2.3.3 where a set of boundary condition parameters have been defined; namely, the effective linear extrapolation length for the fast flux (λ_{eff}), the thermal-to-fast current ratio (θ), and the coefficient $\partial/\partial D_1$ ($1/\lambda_{eff}$). These parameters must be input by the user for RAMONA-3B at present. Thus, it is necessary for the code user to know how to determine these parameters.

The parameter λ_{eff} is related to the linear extrapolation length, λ_1, for the fast flux as given by Eq. 2.3.30. The determination of λ_1 is a well known subject in reactor physics. Simple analytical formula for λ_1 can be found in any textbook (e.g., Glasstone and Edlund 1956). We shall present one such formula later in Section 2.5.1.

Because of the special way of treating the thermal flux boundary condition in RAMONA-3B, the subject of determining the parameter θ is not a common one in reactor physics. There is no simple analytical expression for θ available in open literature or any textbook. Scandpower Inc. has developed an auxiliary code called "ALBMO" with which one can generate data for the parameter θ at the initial steady-state condition. They are then assumed to apply and hold constant during the transient calculation. However, the use of the ALBMO code is cumbersome and time-consuming in that it involves generating a flux file from a fine-mesh calculation with another 2-group diffusion theory code (MD2 or MD1) and generating a cross-section file with RAMONA-3B or PRESTO using a mirror symmetry boundary condition (Borresen 1978). Furthermore, one must do these extra calculations for every new problem at hand. Clearly this is not a practical and efficient approach. The laborious effort involved tends to discourage the user from using it.

In this section we shall present a simple method for deriving an analytical formula for the thermal-to-fast current ratio θ, with which the user can readily estimate the value for θ from the two-group parameters in the core and reflector. The method is based on some simplifying assumptions tailored to the 1-1/2-group, coarse-mesh, diffusion model employed by RAMONA-3B. It has been found to work well for the RAMONA-3B code, but should not be taken to apply to the general 2-group, fine-mesh, diffusion calculation. In this case, the best approach is to represent the reflector explicitly as part of the reactor core.

2.5.1 Linear Extrapolation Lengths

In order to determine the effective extrapolation length λ_{eff} defined by Eq. 2.3.30, we must know how to determine the linear extrapolation length λ_1 for the fast neutron flux. For the purpose of deriving the boundary condition parameters, it is a good approximation to represent the core and reflector as semi-infinite slabs because of the large size of modern LWRs. For convenience, let us assume that the core-reflector interface is at x=0. The linear extrapolation length λ_1 is defined as

$$\lambda_1 = - \left. \frac{\varphi_1}{\frac{d\varphi_1}{dx}} \right|_{x=0} . \qquad (2.5.1)$$

Physically, λ_1 is the distance beyond the interface (x=0) where the fast neutron flux is zero (inside the reflector). In neutron diffusion theory, Eq. 2.5.1 can be expressed as (Glasstone and Edlund 1956, Chapter 5, p. 133):

$$\lambda_1 = 2D_1 \left(\frac{1 + \beta_{11}}{1 - \beta_{11}} \right) \qquad (2.5.2)$$

where β_{11} is an albedo defined as

$$\beta_{11} = \left. \frac{1 + \frac{2D_1}{\varphi_1} \frac{d\varphi_1}{dx}}{1 - \frac{2D_1}{\varphi_1} \frac{d\varphi_1}{dx}} \right|_{x=0} . \qquad (2.5.3)$$

For a finite reflector of thickness T, β_{11} is given by (Glasstone and Edlund 1956, p. 133)

$$\beta_{11} = \frac{1 - 2 \left(\frac{D_1^r}{L_1^r} \right) \coth \left(\frac{T}{L_1^r} \right)}{1 + 2 \left(\frac{D_1^r}{L_1^r} \right) \coth \left(\frac{T}{L_1^r} \right)} \qquad (2.5.4)$$

where the superscript r denotes the reflector and L_1^r is the fast neutron diffusion length defined as

$$L_1^r = \sqrt{\frac{D_1^r}{\Sigma_1^r}} . \qquad (2.5.5)$$

If T is very large ($\geq$ 30 cm) as is the case for modern LWRs, β_{11} reduces to

$$\beta_{11} \simeq \frac{1 - 2 \left(\frac{D_1^r}{L_1^r} \right)}{1 + 2 \left(\frac{D_1^r}{L_1^r} \right)} . \qquad (2.5.6)$$

Note that we have used the fast flux in the reflector to evaluate β_{11}. This is permissible because of the continuity of the neutron flux and current across the interface.

Substituting Eq. 2.5.6 into Eq. 2.5.2, we obtain a very interesting result:

$$\lambda_1 \simeq L_1^r \quad . \tag{2.5.7}$$

Thus, λ_1 is approximately equal to the fast neutron diffusion length in the reflector.

In general, we do not need the thermal neutron linear extrapolation length λ_2 unless Eq. 2.4.10 is used to estimate the thermal buckling B_2^2. In this case, λ_2 can be determined by a similar approach; namely,

$$\lambda_2 \approx L_2^r = \sqrt{\frac{D_2^r}{\Sigma_2^r}} \quad , \tag{2.5.8}$$

which is the thermal neutron diffusion length in the reflector.

2.5.2 Thermal-To-Fast Current Ratios, θ

For the determination of the thermal flux boundary condition parameters, the group-to-group coupling as well as the core-reflector coupling is important. Thus, one should consider the two-group diffusion equations for a reflected core. However, the subject of interest here is not to seek the two-group flux solutions for the reflected core as this is the main mission of the neutron kinetics model of RAMONA-3B. Rather, the main thrust is to find the proper relationship between the thermal and fast neutron currents at the boundary so that the effect of the reflector on the midpoint thermal flux of the boundary nodes is properly acocunted for in accordance with the thermal boundary conditions discussed in Section 2.3.3.

We shall adopt the same approach as that used for the simplified treatment of thermal neutron diffusion as discussed in Section 2.3.2. It is based on the basic idea of the coarse-mesh formulation that the sizes of the coarse-mesh boundary node and the reflector are sufficiently large for thermal neutrons so that the thermal flux distributions become separable within the coarse-mesh volumes. Thus, the three-dimensional thermal neutron leakages (or in-leakages) can be treated separately in each spatial dimension as a one-dimensional slab problem.

We make the following simplifying assumptions:

(i) The boundary node of interest and its adjacent reflector are thermally thick so that they can be represented as two-region slabs

with the interface located at the origin (x=0), for convenience. We assume that the boundary node occupies the space $x \geq 0^+$ and the reflector occupies the other space $x \leq 0^-$.

(ii) The boundary node and its adjacent reflector are homogeneous so that the two-group parameters can be treated as constant in each region.

(iii) The source term, called S, for the fast neutron flux is assumed to be constant in the boundary node and zero in the reflector:

$$\begin{aligned} S &= \text{constant} \quad && \text{for } x \geq 0^+ \\ &= 0 && \text{for } x \leq 0^- \ . \end{aligned} \tag{2.5.9}$$

(iv) The boundary condition parameters are a weak function of time so that the time rate of change of fluxes can be ignored.

Assumption (i) is a good approximation within the framework of the coarse-mesh formulation of RAMONA-3B because the sizes of the boundary node and the reflector are much larger than the thermal neutron diffusion length ($2 \sim 3$ cm).

Assumption (ii) is true or made true by the homogenization procedure discussed in Section 2.2.2. Again, this is consistent with the coarse-mesh formulation of RAMONA-3B.

Assumption (iii) is essential for the present approach. It is made to obtain a simple analytical formula for θ. The assumption is also consistent with the coarse-mesh formulation which applies a piecewise constant for the neutron flux and power density in each coarse-mesh node. Furthermore, the assumption is in keeping with the design and operating strategy for BWRs to maintain the power distribution in the core as uniform as practicable.

Assumption (iv) is commonly made for deriving the boundary conditions in reactor physics primarily due to practical considerations. The validity of this assumption is subject to question if the core condition near the boundary changes drastically due to, for example, the control rod movement. However, some of the time-dependent effects can be restored if the boundary condition parameters are allowed to change during the transient calculation due to the change in the two-group parameters in the boundary nodes as this can be readily done if simple analytical expressions are available for the boundary condition parameters.

Under the above assumptions, the governing equations for the two-region slabs can be written

$$- D_1^c \frac{d^2\varphi_1^c}{dx^2} + \Sigma_1^c \varphi_1^c = S \tag{2.5.10a}$$

$$- D_2^c \frac{d^2\varphi_2^c}{dx^2} + \Sigma_2^c \varphi_2^c = \Sigma_{21}^c \varphi_1^c \tag{2.5.10b}$$

$$- D_1^r \frac{d^2\varphi_1^r}{dx^2} + \Sigma_1^r \varphi_1^r = 0 \qquad (2.5.10c)$$

$$- D_2^r \frac{d^2\varphi_2^r}{dx^2} + \Sigma_2^r \varphi_2^r = \Sigma_{21}^r \varphi_1^r \qquad (2.5.10d)$$

where the superscript c denotes the core (boundary node), the superscript r represents the reflector, and

$$S = \frac{1}{k_{eff}} \left(\nu_1^c \Sigma_{f1}^c \varphi_1^c + \nu_2^c \Sigma_{f2}^c \varphi_2^c \right) \approx \text{constant} \qquad (2.5.11)$$

in the coarse-mesh boundary node of interest.

Equations 2.5.10a through 2.5.10d are a set of inhomogeneous, ordinary differential equations. The complete solutions of these equations take the form:

$$\varphi_1^c(x) = \frac{S}{\Sigma_1^c} + A_1 e^{x/L_1^c} + A_1' e^{-x/L_1^c} \qquad (2.5.12)$$

$$\varphi_2^c(x) = C_o + C_1 e^{x/L_1^c} + C_1' e^{-x/L_1^c} + A_3 e^{x/L_2^c} + A_3' e^{-x/L_2^c} \qquad (2.5.13)$$

$$\varphi_1^r(x) = A_2 e^{-|x|/L_1^r} + A_2' e^{|x|/L_1^r} \qquad (2.5.14)$$

$$\varphi_2^r(x) = C_2 e^{-|x|/L_1^r} + C_2' e^{|x|/L_1^r} + A_4 e^{-|x|/L_2^r} + A_4' e^{|x|/L_2^r} \qquad (2.5.15)$$

where the A's are the homogeneous solution constants and the C's are the particular solution constants, and

$$L_g^c = \sqrt{\frac{D_g^c}{\Sigma_g^c}} \quad ; \qquad g = 1,2 \tag{2.5.16}$$

$$L_g^r = \sqrt{\frac{D_g^r}{\Sigma_g^r}} \quad ; \qquad g = 1,2. \tag{2.5.17}$$

We can simplify the general solutions as follows. First, the neutron flux in the reflector must vanish at the outer boundary of the reflector. This requires that $A_2' = A_4' = C_2' = 0$ since the reflector is very thick in terms of the neutron diffusion lengths.

Next, we apply the boundary condition (2.5.1) for the fast flux $\varphi_1^c(x)$ to obtain

$$A_1' \approx A_1 \left(\frac{\lambda_1 - L_1^c}{\lambda_1 + L_1^c} \right) \tag{2.5.18}$$

which implies that A_1' is insignificant relative to A_1 since $\lambda_1 \approx L_1^c$. For simplicity, we will drop the A_1' term and hence the C_1' term.

In the 1-1/2-group, coarse-mesh approximation, the thermal neutron diffusion (divergence term) is assumed to be negligible. This means that the A_3 and A_3' terms (which correspond to the thermal neutron diffusion) must be secondary to the asymptotic term related to the particular solution (C_0 and C_1 terms). In the interest of maintaining consistency with the 1-1/2-group approximation, it is acceptable to neglect both the A_3 and A_3' terms. However, we shall retain the A_3 term to preserve at least some contribution of the thermal neutron diffusion near the boundary for the A_3 term contributes more significantly to the center flux of the boundary node.

With these approximations and simplifications, the flux solutions reduce to

$$\varphi_1^c(x) \approx \frac{S}{\Sigma_1^c} + A_1 e^{x/L_1^c} \quad , \tag{2.5.19}$$

$$\varphi_2^c(x) \simeq C_o + C_1 e^{x/L_1^c} + A_3 e^{x/L_2^c} \quad , \tag{2.5.20}$$

$$\varphi_1^r(x) = A_2 e^{-|x|/L_1^r} \quad , \tag{2.5.21}$$

$$\varphi_2^r(x) = C_2 e^{-|x|/L_1^r} + A_4 e^{-|x|/L_2^r} \quad . \tag{2.5.22}$$

We can determine the particular solution constants (C_o,C_1,C_2) by substituting Eqs. 2.5.20 and 2.5.22 into Eqs. 2.5.10b and 2.5.10d, respectively. This gives rise to the following results:

$$C_o = \left(\frac{S}{\Sigma_1^c}\right) \gamma^c \tag{2.5.23}$$

$$C_1 = \frac{A_1 \gamma^c}{1 - \left(\frac{L_2^c}{L_1^c}\right)^2} \tag{2.5.24}$$

$$C_2 = \frac{A_2 \gamma^r}{1 - \left(\frac{L_2^r}{L_1^r}\right)^2} \tag{2.5.25}$$

where

$$\gamma^c = \frac{\Sigma_{21}^c}{\Sigma_2^c} \quad , \tag{2.5.26}$$

$$\gamma^r = \frac{\Sigma_{21}^r}{\Sigma_2^r} \quad . \tag{2.5.27}$$

The four homogeneous solution constants (A_1,A_2,A_3,A_4) can be determined by the four boundary conditions (i.e., the continuity of the flux and current) at the core-reflector interface (x=0):

$$(1) \quad \varphi_1^c(o) = \varphi_1^r(o) \quad ,$$

$$(2) \quad \varphi_2^c(o) = \varphi_2^r(o) \quad ,$$

$$(3)\quad D_1^c \left.\frac{d\varphi_1^c}{dx}\right|_{x=0} = D_1^r \left.\frac{d\varphi_1^r}{dx}\right|_{x=0} ,$$

$$(4)\quad D_2^c \left.\frac{d\varphi_2^c}{dx}\right|_{x=0} = D_2^r \left.\frac{d\varphi_2^r}{dx}\right|_{x=0} .$$

Applying the flux solutions (2.5.19) through (2.5.22) to the above four boundary conditions, then solving the resultant four algebraic equations for the four unknowns (A_1, A_2, A_3, A_4), we obtain

$$A_1 = -\left(\frac{S}{\Sigma_1^c}\right)\left(\frac{\Omega_1}{1+\Omega_1}\right) , \tag{2.5.28}$$

$$A_2 = \left(\frac{S}{\Sigma_1^c}\right)\left(\frac{1}{1+\Omega_1}\right) , \tag{2.5.29}$$

$$A_3 = \frac{\left(\frac{S}{\Sigma_1^c}\right)\Omega_2}{(1+\Omega_1)(1+\Omega_2)} \left\{ \frac{\gamma^r}{1+\frac{L_2^r}{L_1^r}} - \gamma^c \left[\frac{\left(1 - \frac{\Omega_1}{\Omega_2}\cdot\frac{L_2^c}{L_1^c}\right) - (1+\Omega_1)\left(\frac{L_2^c}{L_1^c}\right)^2}{1-\left(\frac{L_2^c}{L_1^c}\right)^2} \right] \right\} \tag{2.5.30}$$

$$A_4 = \frac{\left(\frac{S}{\Sigma_1^c}\right)}{(1+\Omega_1)(1+\Omega_2)} \left\{ \gamma^c \left[1 + \frac{\Omega_1\left(\frac{L_2^c}{L_1^c}\right)}{1+\frac{L_2^c}{L_1^c}} \right] - \gamma^r \frac{\left(1+\Omega_2\frac{L_2^r}{L_1^r}\right)}{\left[1-\left(\frac{L_2^r}{L_1^r}\right)^2\right]} \right\} \tag{2.5.31}$$

where

$$\Omega_1 = \frac{D_1^r}{D_1^c}\cdot\frac{L_1^c}{L_1^r} , \tag{2.5.32}$$

$$\Omega_2 = \frac{D_2^r}{D_2^c}\cdot\frac{L_2^c}{L_2^r} . \tag{2.5.33}$$

In the definition of the thermal-to-fast current ratio, the net current is defined to be positive in the outward direction and negative in the inward direction. Since the axial reflectors consist of more than 60% of structural materials (stainless steel), both the fast and thermal neutrons leak out of the core (i.e., the fast and thermal fluxes have slopes of the same sign) at the axial boundaries. Thus, the thermal-to-fast current ratios, θ_T and θ_B, at the top and bottom boundaries are given by

$$\theta_{T,B} = \frac{D_2^r \left.\frac{d\varphi_2^r}{dx}\right|_{x=0}}{D_1^r \left.\frac{d\varphi_1^r}{dx}\right|_{x=0}} \quad . \tag{2.5.34}$$

Note that, because of the continuity of the fluxes and currents, it does not matter whether the reflector fluxes or the core fluxes are used. Using Eqs. 2.5.21 and 2.5.22, we obtain

$$\theta_{T,B} = \frac{\left(\frac{D_2^r}{D_1^r}\right)\left(\frac{L_1^r}{L_2^r}\right)}{(1+\Omega_2)} \left[\gamma^c \left(1 + \frac{\Omega_1 \frac{L_2^c}{L_1^c}}{1 + \frac{L_2^c}{L_1^c}} \right) - \gamma^r \left(\frac{1}{1 + \frac{L_2^r}{L_1^r}} \right) \right] \quad . \tag{2.5.35}$$

For the side (radial) parameter θ_S, we recognize the fact that fast neutrons leak out of the core; whereas thermal neutrons are reflected back into the core. This is due to the unique characteristics of the side (radial) reflector consisting of pure hot water. Thus, we have

$$\theta_S = - \frac{D_2^r \left.\frac{d\varphi_2^r}{dx}\right|_{x=0}}{D_1^r \left.\frac{d\varphi_1^r}{dx}\right|_{x=0}} \quad , \tag{2.5.36}$$

whence

$$\theta_S = \frac{\left(\frac{D_2^r}{D_1^r}\right)\left(\frac{L_1^r}{L_2^r}\right)}{(1+\Omega_2)} \left[\gamma^r \left(\frac{1}{1 + \frac{L_2^r}{L_1^r}} \right) - \gamma^c \left(1 + \frac{\Omega_1 \frac{L_2^c}{L_1^c}}{1 + \frac{L_2^c}{L_1^c}} \right) \right] \quad . \tag{2.5.37}$$

Thus, given the two-group parameters for the reflectors and the boundary nodes in the core, one can determine the boundary condition parameters. The importance of the core-reflector coupling is evident in the parameters, θ_T, θ_B and θ_S. We recommend that, for input preparation, the two-group parameters of the core needed for θ_S be those of the side boundary node at the mid-core with approximately 40% voids.

2.5.3 The Coefficient, C_{ref}

For brevity, we denote the coefficient in Eq. 2.3.35 by C_{ref}; that is

$$C_{ref} = \frac{\partial}{\partial D_1}\left(\frac{1}{\lambda^s_{eff}}\right)_{ref} = -\frac{1}{\left(\lambda^s_{eff}\right)^2}\cdot\frac{\partial\lambda^s_{eff}}{\partial D_1} \quad . \tag{2.5.38}$$

From Eqs. 2.3.30, 2.5.7 and 2.5.5, we have

$$\lambda^s_{eff} = \sqrt{\frac{D^r_1}{\Sigma^r_1}} + \frac{\Delta x}{2} \quad . \tag{2.5.39}$$

Using the above expression in Eq. 2.5.38, we obtain

$$C_{ref} = -\frac{0.5\left(\frac{L^r_1}{D^r_1}\right)}{\left(\lambda^s_{eff}\right)^2} \quad . \tag{2.5.40}$$

We see that C_{ref} is always negative and changes with the mesh spacing Δx selected for the core representation.

2.5.4 Two-Group Reflector Parameters

In this section we provide a typical set of the two-group reflector cross sections and diffusion coefficients applicable to a typical operating condition of a BWR. This is desirable because the reflector compositions do not vary significantly from one class of BWRs to another.

In a BWR the axial reflectors are approximately a mixture of 60% stainless steel and 40% water (or two-phase mixture). The water of the bottom reflector is at a hot operating condition with no voids, while that of the top reflector consists of about 70% voids. The side (radial) reflector is pure water at near saturation.

Multigroup integral transport calculations have been performed for a two-region slab of core and reflector to obtain first a set of 8-group (with 5 thermal groups) cross sections, using the integral transport theory code HAMMER (Rothenstein, 1977) with an 84-group cross section library based on ENDF/B-IV data. The obtained 8-group cross sections were then used to calculate the two-group reflector parameters by means of the discrete ordinate transport code TWOTRAN-II (Lathrop, 1973) using the weighting scheme described in Section 2.2.2. The results are listed in Table 2.1 for the axial and side reflectors.

Table 2.1 Typical Two-Group Reflector Parameters

	Top	Bottom	Side
D_1	1.0051	0.90379	1.6851
D_2	0.36378	0.30612	0.24624
Σ_1	0.011155	0.016686	0.03634
Σ_2	0.09437	0.10081	0.010407
Σ_{21}	0.008397	0.01388	0.03598

2.6 Neutron Kinetics Parameters

The neutron kinetics parameters consist of the average neutron velocities, v_g (g=1,2), and the delayed neutron parameters, β_i and λ_i (i=1,2,...I).

2.6.1 Average Neutron Velocities

In the formulation of the 1-1/2 group, coarse-mesh, diffusion model, a set of average neutron velocities was defined so that they become effectively constant in space and time. In order to minimize the impact of this assumption, the average (effective) neutron velocities should be determined as follows:

$$\left\langle \frac{1}{v_g} \right\rangle = \frac{\int_{\Delta E_g} \int_{core} \frac{1}{v_g} \varphi_g (\underline{r},E)\, dE\, dV}{\int_{\Delta E_g} \int_{core} \varphi_g (\underline{r},E)\, dE\, dV} \quad , \qquad (2.6.1)$$

$$g = 1,2$$

where ΔE_g is the energy width of group g, and the spatial integral covers the entire reactor core. Here we have introduced the energy dependence of the group fluxes since each group flux has its own energy spectrum. These energy spectra can be obtained from the multigroup neutron spectrum calculations in a lattice physics code.

Note that the particular definition (2.6.1) results naturally from energy and space averaging of the general two-group diffusion equations (2.2.1). The average inverse velocities, $\langle 1/v_g \rangle$ (g=1,2), are all that are actually needed to solve the neutron kinetics equations. However, RAMONA-3B requires as input the average neutron velocities, v_g (g=1,2). Thus, they should be obtained as the reciprocals of $\langle 1/v_g \rangle$ (g=1,2).

Note also that we have suppressed the time dependence of the group spectra, φ_g (g=1,2), under the assumption that they do not change appreciably during a transient. This is nearly true for most reactor transients of short duration. With this assumption and the averaging (2.6.1), the neutron velocities become effectively constant in space and time. Typical values for the neutron velocities in a BWR are:

$$v_1 = 1.81 \times 10^7 \text{ cm/sec}$$

$$v_2 = 3.65 \times 10^5 \text{ cm/sec} \quad .$$

2.6.2 Delayed Neutron Parameters

In the 1-1/2-group, coarse-mesh diffusion formulation, we have made the assumption that a single set of the delayed neutron parameters, β_i and λ_i ($i=1,2,\ldots,I$), can be defined such that they are independent of space and time. In this section we shall discuss how this is usually done and provide the most recently published delayed neutron data for various fissionable isotopes that may be present in a BWR.

It is obvious from the general two-group diffision equations (2.2.1) that, in order to get rid of the isotope dependence (j), we simply define an average β_i as follows:

$$\beta_i\ (\underline{r},\tau) = \frac{\sum_j \beta_i^j \sum_{g=1}^{2} \nu_g^j\ \Sigma_{fg}^j\ \varphi_g\ (\underline{r},\tau)}{\sum_{g=1}^{2} \nu_g\ \Sigma_{fg}\ \varphi_g\ (\underline{r},\tau)} \tag{2.6.2}$$

where

$$\nu_g \Sigma_{fg} = \sum_j \nu_g^j\ \Sigma_{fg}^j \quad . \tag{2.6.3}$$

Note that we have retained the space- and time-dependence of β_i for the sake of generality. However, if β_i^j are independent of j, the argument $(\underline{r},\tau)$ of β_i then drops out. This is not quite true in reality, and hence β_i will have some dependence on space and time. We shall show that such dependence is a weak one so that the assumption of constant β_i and λ_i can be justified in most situations.

First of all, observe that the space- and time-dependence of β_i stems from that of the neutron fluxes, φ_g, the ν-fission cross sections, $\nu_g\Sigma_{fg}$, and the isotopic dependence of β_i^j. The effect of the first two tends to cancel each other for they appear both in the numerator and denominator of Eq. 2.6.2. The effect of the isotopic dependence becomes important only if the exposure distribution in the core is very nonuniform. Furthermore, the delayed neutron effect tends to be dominated by a particular fissionable isotope (i.e., ^{235}U) in a LWR.

The physical definition of the total β is the fraction of delayed neutrons per fission:

$$\beta = \frac{\nu_d}{\bar{\nu}} \tag{2.6.4}$$

where ν_d is the delayed neutrons per fission and

$$\bar{\nu} = \frac{\nu_1 \Sigma_{f1} \varphi_1 + \nu_2 \Sigma_{f2} \varphi_2}{\Sigma_{f1} \varphi_1 + \Sigma_{f2} \varphi_2} \quad . \tag{2.6.5}$$

While the individual β_i will influence the delayed neutron concentrations, c_i $(i=1,2,\ldots,I)$, it is the total β which is of primary importance for the transient behavior of the neutron fluxes. It is, therefore, advantageous to define the so-called relative delayed neutron yield, a_i, as

$$a_i = \frac{\beta_i}{\beta} \tag{2.6.6}$$

so that the transient neutron fluxes become relatively insensitive to a_i. In fact, the customary way of reporting the delayed neutron data in the literature is to report a_i rather than β_i and the decay constants λ_i, or the half-life $(1/\lambda_i)$.

The delayed neutron data for most fissionable isotopes have been extensively reviewed and evaluated (Tuttle 1975). A recent review of the delayed neutron data has also been made (Walker and Weaver 1979). The evaluated delayed neutron data for ^{235}U, ^{238}U, ^{239}Pu, ^{240}Pu, ^{241}Pu, and ^{242}Pu are summarized in Table 2.2.

To obtain the total β for a BWR core, we make use of the data in Table 2.2 and calculate β_i with Eq. 2.6.2, then sum:

$$\beta = \sum_i \beta_i \quad . \tag{2.6.7}$$

Since the calculation of β_i by Eq. 2.6.2 calls for a knowledge of the neutron spectrum, this calculation is typically a part of the lattice physics calculations for the generation of the two-group parameters. For BWRs, the value of β is about 0.00738 at beginning-of-life (BOL) and decreases progressively to about 0.00546 at end-of-cycle 2 (EOC2) due to plutonium buildup.

Table 2.2 Delayed Neutron Parameters[a]

Fission Nuclide	ν_d (Neutron/Fission)	Total β	Group i	Fractional Yield a_i	Decay Constant $\lambda_i(s^{-1})$
^{235}U	0.01654 ± 0.0002	0.0068 ± 0.0002	1	0.038 ± 0.004	0.0127 ± 0.0003
			2	0.213 ± 0.007	0.0317 ± 0.0012
			3	0.188 ± 0.024	0.115 ± 0.004
			4	0.407 ± 0.010	0.311 ± 0.012
			5	0.128 ± 0.012	1.40 ± 0.12
			6	0.026 ± 0.004	3.87 ± 0.55
^{238}U	0.04508 ± 0.0006	0.0161 ± 0.0008	1	0.013 ± 0.001	0.0132 ± 0.0004
			2	0.137 ± 0.003	0.0321 ± 0.0009
			3	0.162 ± 0.030	0.139 ± 0.007
			4	0.388 ± 0.018	0.358 ± 0.021
			5	0.225 ± 0.019	1.41 ± 0.10
			6	0.075 ± 0.007	4.02 ± 0.32
^{239}Pu	0.00655 ± 0.00012	0.0022 ± 0.0001	1	0.038 ± 0.004	0.0129 ± 0.0003
			2	0.280 ± 0.006	0.0311 ± 0.0007
			3	0.216 ± 0.027	0.134 ± 0.004
			4	0.323 ± 0.015	0.331 ± 0.018
			5	0.103 ± 0.013	1.26 ± 0.17
			6	0.035 ± 0.007	3.21 ± 0.38
^{240}Pu	0.00960 ± 0.0011	0.00291 ± 0.0002	1	0.028 ± 0.004	0.0129 ± 0.0006
			2	0.273 ± 0.006	0.0313 ± 0.0007
			3	0.192 ± 0.078	0.135 ± 0.016
			4	0.350 ± 0.030	0.333 ± 0.046
			5	0.128 ± 0.027	1.36 ± 0.30
			6	0.029 ± 0.009	4.04 ± 1.16
^{241}Pu	0.0160 ± 0.0016	0.0051 ± 0.0005	1	0.010 ± 0.003	0.0128 ± 0.0002
			2	0.229 ± 0.006	0.0299 ± 0.0006
			3	0.173 ± 0.025	0.124 ± 0.013
			4	0.390 ± 0.050	0.352 ± 0.018
			5	0.182 ± 0.019	1.61 ± 0.15
			6	0.016 ± 0.005	3.47 ± 1.7
^{242}Pu	0.0228 ± 0.0025	0.0069 ± 0.0008	1	0.004 ± 0.001	0.0128 ± 0.0003
			2	0.195 ± 0.032	0.0314 ± 0.0013
			3	0.161 ± 0.048	0.128 ± 0.009
			4	0.412 ± 0.153	0.325 ± 0.020
			5	0.218 ± 0.087	1.35 ± 0.09
			6	0.010 ± 0.003	3.70 ± 0.44

[a] From Tuttle 1975

2.7 Power Generation

The thermohydraulic calculations in RAMONA-3B require the volumetric heat generation rate, $q'''(\underline{r},\tau)$, or the power density in each thermohydraulic computational cell. The power density at any point in the reactor is the sum of two components. One component, called "prompt fission heat," is the amount of energy released promptly in the fission process and is proportional to the fission rate. The other component, called "decay heat," is the amount of energy released by the decay of fission products. It is delayed relative to the prompt fission heat, and hence depends on the fission rate history.

Using the subscripts p and d to denote the prompt and delayed components, respectively, we may write

$$q'''(\underline{r},\tau) = q_p'''(\underline{r},\tau) + q_d'''(\underline{r},\tau) \quad . \tag{2.7.1}$$

2.7.1 Prompt Fission Heat

The prompt power density is related to the fission density, $F(\underline{r},\tau)$:

$$q_p'''(\underline{r},\tau) = K(1-H_o)\ F(\underline{r},\tau) \tag{2.7.2}$$

where

$$F(\underline{r},\tau) = \Sigma_{f1}\varphi_1(\underline{r},\tau) + \Sigma_{f2}\varphi_2(\underline{r},\tau) \quad . \tag{2.7.3}$$

Note that $KF(\underline{r},\tau)$ is the total fission energy density and H_o is the fraction of this energy density which is delayed.

The constant K is the total energy released per fission, usually taken to be 200 MeV/fission (ANS 5.1, 1978). Converting it to joules per fission for RAMONA-3B, we obtain

$$K = 3.2041 \times 10^{-11} \text{ joules/fission} \ .$$

2.7.2 Decay Heat

The amount of delayed energy released at time τ due to the decay of fission products per fission at time τ' per unit time, denoted by $h_f(\tau-\tau')$, is a measured quantity and has been tabulated as a function of time for different fissionable nuclides (ANS 5.1, 1978).

Using the approach similar to that for the treatment of the delayed neutron fraction β, we assume that an average set of $h_f(\tau-\tau')$ can be defined for a reactor so that it is independent of space. Thus, if the reactor has been operated for a given time, τ_h, prior to the start of a reactor transient at $\tau=0$, the delayed power density is given by

$$q'''_d(\underline{r},\tau) = \int_{-\tau_h}^{\tau} F(\underline{r},\tau')\, h_f(\tau-\tau')\, d\tau' \quad . \tag{2.7.4}$$

If we further assume that the reactor has been in operation at a constant power density q'''_{τ_h} for the time period τ_h with the initial power distribution at $\tau=0$, we can rewrite Eq. 2.7.4 as

$$q'''_d(\underline{r},\tau) = q'''_{\tau_h}(\underline{r})\, H(\tau,\tau_h) + \int_0^{\tau} F(\underline{r},\tau')\, h_f(\tau-\tau')\, d\tau' \tag{2.7.5}$$

where

$$H(\tau,\tau_h) = \frac{1}{K}\int_{-\tau_h}^{0} h_f(\tau-\tau')\, d\tau' \quad . \tag{2.7.6}$$

From the definition of $H(\tau,\tau_h)$, we see that the fraction of the total fission energy which is delayed is obtained from an infinite irradiation, i.e.,

$$H_0 = H(0,\infty) \, . \tag{2.7.7}$$

H_0 is approximately 0.07.

The contribution of the second term in Eq. 2.7.5 is generally small, less than 5% for $\tau < 1000$ seconds. Hence, we can treat this term approximately as follows. For $0 \leq \tau' \leq \tau$, we approximate the fission density $F(\underline{r},\tau')$ as

$$F(\underline{r},\tau') \approx \gamma(\tau)\, F(\underline{r},\tau) \quad , \tag{2.7.8}$$

where

$$\gamma(\tau) = \frac{\frac{1}{\tau}\int_0^\tau q'''(\tau')\,d\tau'}{q'''(\tau)} \tag{2.7.9}$$

and $q'''(\tau)$ is the total core power density; namely,

$$q'''(\tau) = \int_{core} q'''(\underline{r},\tau)\,dV \quad . \tag{2.7.10}$$

This approximation (Eq. 2.7.8) is important for transients in which the reactor does not shut down after a reactor trip due to failure of the control rod insertion. It takes into account that the reactor will reach a new quasi-steady state power distribution after a short time and at the same time (through the use of $\gamma(\tau)$) protects against errors incurred if $F(\underline{r},\tau)$ exhibits oscillations with high amplitude.

From Eq. 2.7.6, it can be shown that

$$H(\tau,\tau_h) = H(\tau,\infty) - H(\tau+\tau_h,\infty) \quad , \tag{2.7.11}$$

and that

$$\frac{1}{K}\int_0^\tau h_f(\tau-\tau')\,d\tau' = H(o,\infty) - H(\tau,\infty) \quad . \tag{2.7.12}$$

Using Eqs. 2.7.8, 2.7.11 and 2.7.12, we obtain

$$\begin{aligned} q_d'''(\underline{r},\tau) = {} & q_{\tau_h}'''(\underline{r})\,[H(\tau,\infty) - H(\tau+\tau_h,\infty)] \\ & + K\gamma(\tau)\,F(\underline{r},\tau)\,[H(o,\infty) - H(\tau,\infty)] \quad . \end{aligned} \tag{2.7.13}$$

We see that a single function $H(\tau,\infty)$, if it can be defined, is all that is needed to compute the delayed power density $q_d'''(\underline{r},\tau)$. We define this single

function to be an average for the three major fissionable isotopes (^{235}U, ^{238}U, and ^{239}Pu):

$$H(\tau,\infty) = \frac{\sum_{j=1}^{3} \langle F^j \rangle \, H^j(\tau,\infty)}{\sum_{j=1}^{3} \langle F^j \rangle} \qquad (2.7.14)$$

where the superscript j refers to a fissionable isotope and $\langle F^j \rangle$ is the total fission density due to isotope j at steady state (τ=0); namely,

$$\langle F^j \rangle = \int_{core} \left[\Sigma_{f1}^j \varphi_1 (\underline{r},o) + \Sigma_{f2}^j \varphi_2 (\underline{r},o) \right] dV \quad . \qquad (2.7.15)$$

The $H^j(\tau,\infty)$ used in RAMONA-3B for the three isotopes is obtained from the ANS Standard (ANS 5.1, 1978) with a multiplier of 1.02 applied to account for the effect of neutron capture by fission products. A more accurate value for this factor is available (ANS 5.1, 1978), but since it changes by only 1.3% in 1000 seconds, the constant value is recommended.

The weighting factors, $\langle F^j \rangle \Big/ \sum_{j=1}^{3} \langle F^j \rangle$, in Eq. 2.7.14 must be supplied by the user as input to RAMONA-3B. They can be determined by Eq. 2.7.15. If we assume that only ^{235}U is present in the core, the decay power will be slightly overestimated (ANS 5.1, 1978). (The user also specifies τ_h, the duration of the fuel exposure prior to the transient and the average power level q'''_{τ_h} at which the fuel was exposed.)

2.7.3 Location of Heat Deposition

RAMONA-3B takes into account the fact that the fission energy is deposited as thermal energy both inside the fuel pellet where the fission takes place and outside the pellet due to neutron slowing-down and gamma ray attenuation. It also provides for differences in the heat deposition location for the prompt and delayed power densities, separately.

For each thermohydraulic node, there corresponds a volumetric heat generation rate, q'''_f, in the fuel which is assumed to be constant across the pellet and zero in the clad. Let η_{pw} and η_{dw} be the fractions of the prompt and delayed power densities that are deposited outside the pellet. For a thermohydraulic node of volume V, the average value of q'''_f is given by

$$\bar{q}_f'''(\tau) = \frac{(1-\eta_{pw})\int_V q_p'''(\underline{r},\tau)\,dV + (1-\eta_{dw})\int_V q_d'''(\underline{r},\tau)\,d\underline{V}}{\pi r_f^2 \Delta z N_r} \qquad (2.7.16)$$

where r_f is the radius of the fuel pellet, Δz is the height of the volume, and N_r is the total number of fuel rods in the Volume V.

The heat deposition outside the fuel consists of the direct heating in the coolant (i.e., the water within a bundle channel box) and that in the bypass water. If η_c is the fraction of the total heat deposition outside the fuel that is deposited in the coolant, then $(1-\eta_c)$ of the total heat deposition is in the bypass water. This fraction η_c is about 0.5 for BWRs.

The average volumetric heat generation rate due to the direct heating in the coolant of the thermohydraulic volume V is

$$\bar{q}_\ell'''(\tau) = \frac{\eta_c}{A_c \Delta z}\left[\eta_{pw}\int_V q_p'''(\underline{r},\tau)\,dV + \eta_{dw}\int_V q_d'''(\underline{r},\tau)\,dV\right] \qquad (2.7.17)$$

where A_c is the flow area in the volume V.

The average volumetric heat generation rate in the bypass water of the bypass channel is given by

$$\bar{q}_{\ell b}'''(\tau) = \frac{(1-\eta_c)}{A_b \Delta z}\left[\eta_{pw}\int_{core} q_p'''(\underline{r},\tau)\,dV + \eta_{dw}\int_{core} q_d'''(\underline{r},\tau)\,dV\right] \qquad (2.7.18)$$

where A_b is the flow area of the bypass channel. Note that the integrals extend over the entire radial plane of the core. In reality, there is one bypass region per coolant channel in a BWR, and hence, there are many bypass regions in the core. RAMONA-3B lumps all the bypass regions into a single bypass channel and we must inegrate accordingly all the prompt and delayed power densities in the core.

The three fractions $(\eta_{pw},\eta_{dw},\eta_c)$ must be specified in order to compute the average volumetric heat generation rates $(\bar{q}_f''',\bar{q}_\ell''',\bar{q}_{\ell b}''')$. Studies (Thorlaksen 1976 and Moberg et al. 1981) have shown that these fractions are functions of void

fraction. (Linear functions are generally adequate.) Since the transient peak power for certain BWR transients is sensitive to these fractions (Moberg et al. 1981 and Cheng and Diamond 1978), a careful choice of these fractions is in order. Typical values used in BWR safety analyses are $\eta_{pw} = \eta_{dw} = 0.03 \sim 0.04$ and $\eta_c = 0.5$.

2.8 Summary and Recommendations

In this chapter we have described the modeling details of the neutron kinetics and power generation in RAMONA-3B. The fundamental assumptions invoked in the development of the 1-1/2 group, coarse-mesh, diffusion model for neutron kinetics were discussed, and their limitations were assessed.

The importance of the coupling between neutron kinetics and thermohydraulics was stressed, and the feedback models for establishing this coupling were described.

The initial conditions and boundary conditions required to specify a transient problem were also discussed. In particular, a method of determining the boundary condition parameters was provided, thus eliminating the need for arbitrary adjustment of these parameters as is often done in practice.

The neutron kinetics parameters were uniquely defined, and the usual methods for determining them were described. Typical values for these kinetics parameters were also given.

The volumetric heat generation rates required for thermohydraulic calculations were defined and the methods used to compute them were described. In particular, the decay heat model was discussed in detail. The direct heating fractions in the normal coolant and the bypass water were also defined and their typical values were given.

We recommend for future improvements the following refinements:

(1) The new ScP feedback model should be implemented in RAMONA-3B for future applications. The BNL1 option should be deleted, but the BNL2 option should be retained.

(2) A higher order term (e.g., cubic term) should be included for the void feedback for the case of $\alpha > 0.75$ (post-CHF applications).

(3) The void dependence and control-state dependence of the Doppler feedback coefficients should be included to treat the Doppler feedback effect more accurately.

(4) A linear void dependence of the direct heating fractions should be considered.

(5) An edit of various reactivity components (void reactivity, Doppler reactivity, control reactivity, etc.) is highly desirable for it will provide legitimate reactivity input for point kinetics that is still widely used in many system codes. Moreover, it is extremely helpful for understanding the characteristics of a transient. It is, however, not a trivial task. A similar capability has been implemented in the BNL version of the 3-D neutron kinetics code, MEKIN-B (Aronson et al. 1980), and can be used as a guide to the installation in RAMONA-3B.

(6) Because of the importance of thermal neutron diffusion in certain situations, a better treatment of the thermal neutron diffusion would be desirable and is recommended.

(7) The microscopic absorption cross sections, σ_{a1} and σ_{a2}, of Boron-10 required for the boron reactivity calculation should be obtained with a hardened neutron spectrum in the water of a typical fuel cell. Since the hardness of the neutron spectrum depends on the boron concentration in the water, the cross sections (σ_{a1} and σ_{a2}) are, in general, functions of the boron concentration, C_B.

APPENDIX 2.1

RAMONA-3B Feedback Model Options

This appendix describes the three feedback options mentioned in Section 2.4. These options are quite similar in that they all employ a quadratic law for the void feedback, a linear law (in terms of the average coolant temperature) for the moderator temperature feedback, and a linear law (in terms of the square root of the average fuel temperature) for the fuel temperature (Doppler) feedback.

The two BNL options differ in the representation of the control rod effect on the two-group parameters with the BNL1 option being a simplification of the BNL2 option. Since the BNL2 option is more realistic, we recommend that the BNL1 option be deleted to avoid confusion.

The principal differences between the BNL2 option and the ScP1 option are the following:

(1) The BNL2 option uses the void fraction (α) to represent the void feedback, whereas the ScP1 option uses the coolant density (ρ) to describe the void feedback. Since both options apply a quadratic law to the two-group parameters, they are, in effect, equivalent and constitute no difference in the void feedback effect.

(2) The BNL2 option defines two separate void feedback coefficients for both the uncontrolled (rod-out) and controlled (rod-in) fuel types. This is necessary because the void feedback for the controlled fuel types is three times more negative than that for the uncontrolled fuel types. The ScP1 option defines a single set of the void feedback coefficients for the uncontrolled fuel types only and accounts for the control rod effect via a correction to the thermal (group 2) absorption and fission cross sections only. (The control rod effect on other two-group parameters is neglected.) Thus, the BNL2 option is superior to the ScP1 option in the representation of the control rod effect.

(3) The BNL2 option defines two separate mean numbers of neutrons per fission (i.e., ν_1 and ν_2) for the fast and thermal groups, respectively. The ScP1 option defines a single constant ν for both the fast and thermal groups of neutrons. Since $\nu_1 \neq \nu_2$ in general, the BNL2 option is also superior to the ScP1 option in this respect.

(4) The BNL2 option does not account for the void effect on the Doppler feedback, while the ScP1 option does. However, the ScP1 option does not consider the Doppler effect on $\nu\Sigma_{f_1}$, while the BNL2 option does. Since the Doppler reactivity coefficient varies with the void fraction (about 25% difference between α=0 and α=0.4, (Cheng 1978)), the ScP1 option is better than the BNL2 option in the representation of the Doppler feedback.

In summary, the BNL2 option is superior in the modeling of the control rod effect and the mean numbers of neutrons per fission, whereas the ScP1 option is better in the description of the Doppler feedback. For the void feedback, both options employ a quadratic law and constitute no difference.

A new ScP option (Moberg 1980) was developed by Scandpower Inc. under the sponsorship of BNL for the purpose of improving the deficiencies of the ScP1 option as outlined above. The deficiency regarding the mean numbers of neutrons per fission is removed. The Doppler feedback on $\nu\Sigma_{f_1}$ is also included (previously neglected). Also, separate void feedback coefficients are now utilized for both the uncontrolled and controlled fuel types. The quadratic representation for the void feedback still remains. The new ScP option has not been implemented in RAMONA-3B. We recommend that it be implemented and used in the future applications of RAMONA-3B.

3. MODELING OF THERMAL CONDUCTION IN SOLID STRUCTURES

This chapter covers the formulation of the RAMONA-3B models for thermal conduction in solids, particularly in fuel elements. Presented are the modeling assumptions and their implications, the governing field and constitutive equations and recommendations for possible improvements. The numerical techniques used for the predictions of steady-state and transients are presented in Chapter 6. Section 6.3 covers the discretization of the equations presented here, while Sections 6.6 and 6.7.1 describe the numerical methods, respectively, for the steady-state and for the transients. The coupling of the algorithms for thermal conduction with the algorithms for neutron kinetics and thermohydraulics is described in Section 6.7.3.

The conduction models presently incorporated in RAMONA-3B were developed and programmed by Scandpower (1977). The model descriptions and assessments presented here are in part taken and derived from Scandpower documentation and in part derived from the program listing, since the available documentation is incomplete. As pointed out in Chapter 1, the documentation for the original RAMONA-III code as obtained from Scandpower was incomplete so that an assessment with regard to quality assurance was impossible. Therefore, the thermal conduction models as implemented here have not been assessed with regard to potential coding errors. Furthermore, there exists to our knowledge no documented comparison with exact analytical solutions.

3.1 Scope of Thermal Conduction Modeling

The purpose of thermal conduction models is to account for thermal energy storage in, and release from, structural components and for the transport of thermal energy from the fuel pellets, where heat is being generated (see Section 2.4), to the coolant in the core (see Section 4.4) and also from the coolant through vessel and piping walls to the containment. Conduction models link neutron kinetics with thermohydraulics models and provide such surface temperatures of solid structures as are required for computing convective heat transfer from structures to coolant or from structures to the environment in the containment.

The RAMONA-3B code has conduction models for the fuel elements to predict storage and transport of energy in the fuel pellets, the gas gap and the fuel cladding. This model is designed for predicting operational transients near normal operating conditions as discussed in Section 3.2.

The RAMONA-3B code does not take into account the thermal inertia due to energy storage in structural components, such as the pressure vessel, vessel intervals and core structures other than fuel and fuel cladding. The significance of omitting these effects is summarized in Section 3.2 below and discussed in detail in Section 3.3.1.

3.2 Code Capabilities and Limitations

This section is a summary of RAMONA-3B code capabilities and limitations arising from the modeling assumptions and the solution techniques which are used to predict the thermal response of structural components in a BWR reactor system. The capabilities related to thermal response modeling are potentially limited further by modeling assumptions for neutron kinetics and thermohydraulics. For the overall summary of capabilities and limitations see Sections 1.2 and 1.3 of this report.

The models in RAMONA-3B for the storage and transport of thermal energy in solid structures are suitable to predict operational transients in the range between hot stand-by and full-power conditions. These models are also suitable to predict other thermohydraulic transients with characteristic times* in the range of approximately one second to one minute and with fuel conditions (mean temperature, burn-up and fission gas concentrations) near initial conditions.

The models in RAMONA-3B for the storage and transport of thermal energy in solid structures are not suitable for slow transients that allow large temperature variations in the pressure vessel because thermal energy storage in solid components other than fuel pins is not accounted for. These models are also inadequate for the simulation of rapid reactivity insertions and of rapid thermal transients in the fuel cladding (change in boiling length, dryout), with characteristic times* on the order of 0.05 second, since the correlations for thermophysical properties are inadequately represented at present. Moreover, the models as presently implemented in RAMONA should be used with care in the area of stability analyses.

RAMONA-3B is not designed to predict core quenching as there are no models for radiative heat transfer and because axial conduction near the quench front is not accounted for.

For details of modeling assumptions, see Section 3.3 below. The assumptions implied in the development of finite difference equations for thermal conduction are presented in Section 6.3.

3.3 Assumptions and Their Consequences

This section presents the eleven modeling assumptions which are implied in the RAMONA-3B models for thermal conduction in solid structures. The consequences resulting from these assumptions have been inferred on the basis of order of magnitude estimates, rather than on sensitivity calculations. We present at first the assumptions related to solid structures in general, and then those related to fuel elements.

*Time span of main events during the transient.

In addition to the eleven modeling assumptions presented here, there are also three simplifying assumptions implied in the development of the finite-difference analogues used in numerically integrating the field equations for thermal conduction. These assumptions restrict the code capabilities further, as discussed in Section 6.3.2.

3.3.1 Structural Components

For the storage and transport of thermal energy in solid structures, namely the pressure vessel, the core shroud, the separator assembly, the top guide, the fuel support structures, the guide tubes, the jet pumps, the steam dryer and the feedwater sparger, there is no model in RAMONA-3B. This fact is equivalent to the two assumptions stated below.

3.3.1.1 Modeling Assumptions for Conduction in Structural Components

Assumption (3-i) The stored energy in the above structural components is negligible.

Assumption (3-ii) Heat transfer across the above structural components is negligible.

3.3.1.2 Consequences from Modeling Assumptions for Structural Components

Concerning Assumption (3-i), one needs to recognize that the pressure vessel with a typical mass of 6.8×10^5 kg and the internal structures with the mass of approximately 1.6×10^5 kg have a combined heat capacity of 389 MWs/°C. This heat capacity is more than seven times as large as the heat capacity of all the uranium oxide and five times as large as that of the fuel elements.

When the mean temperature of all structural components changes at the rate 0.5°C/s, as a consequence of pressure fluctuations with attendant changes in coolant (saturation) temperature for example, then the thermal energy released or absorbed by these structures equals approximately the decay heat release.

The pressure vessel has a time constant of approximately ten minutes under nonboiling conditions and approximately one minute when boiling occurs at the vessel wall. All other components have time constants below one minute and constitute one quarter of structural heat capacities.

This means that RAMONA-3B is restricted to transients with rapid changes of coolant temperature that cannot be followed by the vessel and structural component temperatures and to slow transients with fission power levels well above decay heat levels.

Concerning Assumption (3-ii), heat transfer across structural components is expected to affect the prediction of core inlet subcooling because of heat transfer from the core through the core shroud into the downcomer and jet

pumps which are filled with subcooled liquid. Incorrect predictions of core inlet subcooling affect the boiling length and thereby the void fraction in the core, which in turn affects strongly the reactivity feedback and the axial variation of fission power generation. Heat transfer across the vessel walls may be important in simulations of long-term heat rejection.

3.3.2 Fuel Elements

3.3.2.1 Modeling Assumptions for Conduction in Fuel Elements

The thermal energy storage and conduction in the fuel pins, consisting of the fuel pellets, of the gas gap between pellets and cladding and of the fuel cladding is modeled with the following nine assumptions.

Assumption (3-iii) Fuel and cladding are rigid, retaining their cylindrical geometries. Possible variations in time of the gas gap width can be taken into account by a temperature-dependent gap conductance (see Assumption (3-xi) below).

Assumption (3-iv) Curvature effects are ignored in gas gap and fuel cladding, which are modeled as plane-parallel slabs.

Assumption (3-v) The volumetric concentration of heat generation rate, q_f as defined in Eq. 2.7.16 and used later in Eqs. 3.4.2 and 3.4.22 is uniformly distributed over the fuel pellet cross-section. Gamma heat generation is ignored in the gas gap, $q'''_{gp} = 0$, and in the cladding, $q'''_c = 0$.

Assumption (3-vi) Axial and azimuthal conduction in the fuel pellet, gas gap and cladding are negligible: $\partial t/\partial z = 0$, $\partial t/\partial \Theta = 0$.

Assumption (3-vii) The volumetric heat capacities for fuel, $(\rho c)_f$, and cladding, $(\rho c)_c$ are constants. The same values apply everywhere in the core and at all times.

Assumption (3-viii) The volumetric heat capacity of the gas in the gas gap, $(\rho c)_{gp}$, is negligible.

Assumption (3-ix) The thermal conductivity of the fuel pellet, $k_f(t)$, depends on temperature only.

Assumption (3-x) The thermal conductivity, k_c of the fuel cladding material is a fixed constant, applied everywhere in the core and at all times.

Assumption (3-xi) The thermal conductance $(k/\delta)_{gp}$ of the gas gap is the same everywhere in the core and can be specified by the code user as a quadratic power polynomial in average fuel pellet temperature t_f.

Additional assumptions are implied in the application of numerical methods for integrating the field equations of thermal conduction. These assumptions affect the accuracy of the computer results and are discussed in Section 6.3.2. Computational accuracy is also affected by the approximation for thermal conductivity of fuel pellets which is assessed in Section 3.4.1.3.

3.3.2.2 Consequences from Conduction Modeling Assumptions for Fuel Elements (Assumptions 3-iii through xi)

Assumption (3-iii), implying rigidity of fuel and cladding enables RAMONA to compute only transients in which neither the gas gap between fuel pellet and cladding changes in width, nor the fuel cladding swells to block (in part) the coolant flow. This assumption limits the use of RAMONA-3B to operational transients, provided the heat transfer regimes of dryout or burnout are not encountered, and provided that no significant (long-term) fuel degradation occurs.

Assumption (3-iv) concerning curvature effects in gas gap and cladding imposes no additional restriction on the RAMONA-3B code. By virtue of Assumption (3-iii), the mean gap radius is at least thirty times the gap width and the mean cladding radius is approximately sixteen times as large as the clad thickness.

Assumption (3-v) implies that the heat generation rate is uniformly distributed over the fuel pellet cross section and thereby limits the use of the RAMONA code to transients with fuel at the Beginning of Life (BOL). Toward the End of Life (EOL) the heat generation rate is known to concentrate around the periphery of the fuel pellet and to reduce the difference between fuel pellet centerline and surface temperatures by up to five percent (Wulff 1980, p. 24 and Moody and Lahey 1977, p. 257). Assumption (3-v) also implies negligible heat generation in the cladding. Gamma absorption in the fuel cladding is approximately 1.5% of fission power and is responsible for rapid cladding temperature responses to changes in reactivity.

Assumption (3-vi) implies primarily the neglection of axial conduction in fuel pellets and cladding. Axial conduction is unimportant during operational transients, but it may be important under conditions of dryout or burnout where local hot spots develop along the fuel pin. Axial conduction is important during fuel quenching in the reflooding phase after a Loss of Coolant Accident (LOCA). Assumption (3-vi) also implies axisymmetric temperature distributions in the fuel element. This is always justified except during reflooding of the core after a large-break LOCA, with radiative heat transfer between fuel pins and channel box. Notice that LBLOCA simulation is not the objective of RAMONA-3B.

Assumption (3-vii) imposes constant volumetric heat capacities for fuel and cladding. The volumetric heat capacity of uranium dioxide varies 110% in the range between 290°C (≈560°F) and 2,440°C (≈4,430°F), i.e., between minimum fuel surface and maximum fuel centerline temperatures. The volumetric heat capacity of Zircaloy cladding material varies 25% in the range of possible cladding temperatures between start-up and burnout conditions.

The volumetric heat capacity does not affect steady-state temperature predictions. However, the time constant of thermal responses depends linearly on the volumetric heat capacity. Assumption (3-vii) is entirely inconsistent with the objective of computing transient fuel element temperature distributions through the discrete-parameter representation in the RAMONA-3B code. Assumption (3-vii) restricts the use of RAMONA-3B to transients which are weakly affected by fuel temperature variations, that is, to slow operational transients within a narrow fuel temperature range, in the vicinity of the fuel temperature at

which the volumetric heat capacities have been specified by the user. Because of Assumption (3-vii) the RAMONA-3B code should not be used for reliable predictions of transient fuel temperatures.

Assumption (3-viii) is justified because the heat capacity of the gas in the gas gap is insignificant under all conditions.

With Assumption (3-ix) RAMONA-3B accounts for the primary variation of fuel thermal conductivity, namely for its temperature dependence but it neglects the effects from changes in fuel density and porosity (cracking) with progressive burn-up. Assumption (3-ix) is justified for all transients with fixed fuel composition and structure throughout the entire core.

Assumption (3-x) implies temperature-independence of thermal conductivity for the cladding material. The thermal conductivity of Zircaloy cladding material varies by 50% in the temperature range between 100°C (≈210°F) and 590°C (≈1100°F).

The thermal conductivity of the cladding affects strongly the predicted cladding outer surface temperature and hence the boiling heat transfer. It also affects the thermal response time constant of the cladding which is of the order of 1/10 of a second.

Thus, Assumption (3-x) is in conflict with the objectives of predicting three-dimensional distributions of neutron kinetic and thermohydraulic parameters in the core. Assumption (3-x) does not permit the accurate prediction of reactor transients with characteristic times of the order of 0.1 second.

Assumption (3-xi) imposes uniformly over the entire core the same quadratic dependence of gas gap conductance on fuel temperature. RAMONA therefore cannot account for differences in fuel type, in degree of burn-up and fission gas concentrations, nor for fuel expansion relative to its cladding.

The gap conductance varies 30% between fuel assemblies with 7x7 and 8x8 arrays, it varies 100% with linear fission power density between 33 kW m^{-1} (≈10 kW ft^{-1}) and 61 kW m^{-1} (≈18.5 kW ft^{-1}) (Lahey and Moody 1977, pp. 255 and 256) and it varies 200% with xenon concentration between the xenon mole fractions of 0.2 and 0.4 (McDonald and Thompson, 1976, p. 306)

To account only for the temperature dependence of the gap conductance is not adequate for the reliable prediction of three-dimensional neutron kinetics and thermohydraulic parameters since the above effects can be represented only by core-wide averages. Thus, Assumption (3-xi) imposes the same limitation on the use of RAMONA-3B as Assumption (3-x) above.

It should be noted that Assumptions (v), (vii), (x) and (xi) can readily be relaxed, with relatively little programming effort, hardly any significant penalty on computing time, but with considerable benefit regarding the applicability of RAMONA-3B.

3.4 Governing Equations of Thermal Conduction

In this section are presented the conduction equations, the constitutive equations and the initial and boundary conditions which constitute the thermal conduction model in RAMONA-3B for the fuel elements. As indicated in Section 3.1, RAMONA-3B ignores thermal energy transport in other structural components.

This section presents the analytical formulations, based on Assumptions (3-iii) through (3-xi) in Section 3.3. The transformation from the analytical to the finite difference formulations is discussed later in Section 6.3. The methods for solving the finite-difference equations are described in Sections 6.6 and 6.7 for steady-state initial conditions and for transients, respectively.

Below we present first the formulations for transient conduction and then we specialize the description of transients to model the steady-state conditions.

3.4.1 Description of Transient Conduction

Consider the composite of fuel pellets, gas gap and cladding shown in Figure 3.1. Concentric, right circular cylindrical surfaces with radii R_f, R_{ci} and R_{co} bound the fuel pellets and the cladding. Nuclear reactions generate heat in the fuel pellets. Heat is stored in fuel and clad and is conducted from the fuel, across the gas gap, through the cladding and convected from the cladding outer surface by forced convection with or without boiling.

3.4.1.1 Field Equations of Thermal Conduction

Conservation of thermal* energy and Fourier's law yield the conduction equation (Slattery 1972, pg. 307)

$$\rho c \frac{\partial t}{\partial \tau} = \nabla (k \nabla t) + q''' \quad , \tag{3.4.1}$$

where ρ, c, k, t, q''' and τ designate density, specific heat (strictly speaking, specific heat at constant strain, however the specific heat at constant pressure is used justifiably), thermal conductivity, centigrade temperature, volumetric heat generation rate from nuclear fission and decay, and time, respectively. Because of Assumption (3-vi) in Section 3.3.2.1, Eq. 3.4.1 becomes for the fuel pellets (subscript f):

$$(\rho c)_f \frac{\partial t_f}{\partial \tau} = \frac{1}{r} \frac{\partial}{\partial r} \left(r k_f \frac{\partial t_f}{\partial r} \right) + q'''_f \qquad \text{for } 0 \le r < R_f,\ \tau > 0. \tag{3.4.2}$$

*Contributions from mechanical energy are insignificant (Boley and Winer 1960, Chapter 2).

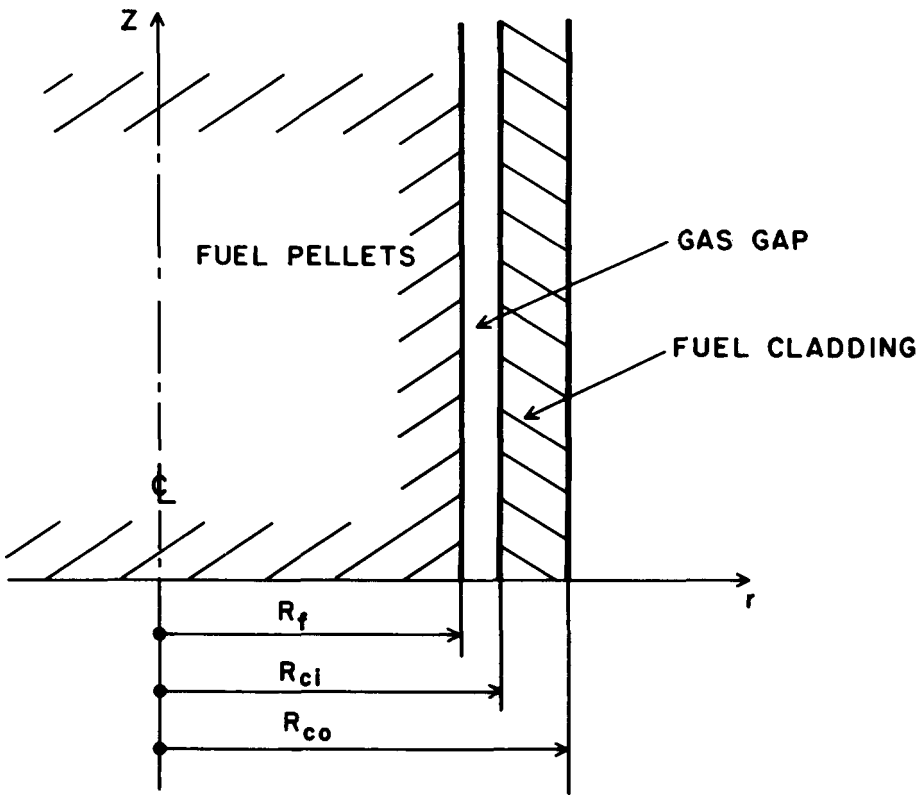

Figure 3.1 Fuel Element Geometry

Because of Assumptions (3-iv, v, and viii), Eq. 3.4.1 reads for the gas gap (subscript g):

$$\frac{\partial}{\partial r}\left(k_{gp}\frac{\partial t_{gp}}{\partial r}\right) = 0, \qquad R_f < r < R_{ci}, \text{ all } \tau. \tag{3.4.3}$$

Assumptions (3-iv and v) simplify Eq. 3.4.1 for the fuel cladding (subscript c):

$$(\rho c)_c \frac{\partial t_c}{\partial r} = \frac{\partial}{\partial r}\left(k_c \frac{\partial t_c}{\partial r}\right), \qquad R_{ci} < r < R_{co}, \ \tau > 0. \tag{3.4.4}$$

Equations 3.4.2 through 3.4.4 are the field equations which govern the storage and transport of thermal energy in the fuel element. They can be integrated for specified initial and boundary conditions, provided that constitutive descriptions are given for (ρc), k and q'''. The heat generation rate q'''_f for the fuel pellet is predicted from neutron kinetics and defined by Eq. 2.7.16 in Chapter 2. Below we define first the boundary conditions which couple Eqs. 3.4.2 through 3.4.4 among each other and Eq. 3.4.4 with the coolant temperature field. After that, in Subsection 3.4.1.3, we discuss the constitutive relations for thermal conduction.

3.4.1.2 Boundary Conditions for Thermal Conduction in Fuel Elements

The boundary conditions imposed on Eqs. 3.4.2 through 3.4.4 are the continuity conditions for heat flux and for temperatures. Specifically, they are:

$$\frac{\partial t_f}{\partial r} = 0 \qquad \text{at } r = 0 \tag{3.4.5}$$

$$\left.\begin{aligned} k_f \frac{\partial t_f}{\partial r} &= k_{gp}\frac{\partial t_{gp}}{\partial r} && (3.4.6)\\ t_f(R_f) &= t_{gp}(R_f) && (3.4.7)\end{aligned}\right\} \quad \text{at } r = R_f$$

$$\left.\begin{aligned} k_{gp}\frac{\partial t_{gp}}{\partial r} &= k_c \frac{\partial t_c}{\partial r} && (3.4.8)\\ t_{gp}(R_{ci}) &= t_c(R_{ci}) && (3.4.9)\end{aligned}\right\} \quad \text{at } r = R_{ci}$$

$$-k_c \frac{\partial t_c}{\partial r} = \bar{h}_c\left[t_c(R_{co}) - t_{fl}\right] \qquad \text{at } r = R_{co} \tag{3.4.10}$$

The new symbols $\bar{h}_c$ and t_{fl} designate the convective heat transfer coefficient and the coolant temperature (fluid). Observe that the temperature continuity requirements in Eqs. 3.4.7 and 3.4.9 are necessary and imply that neither mass transfer at the positions $r = R_f$ and $r = R_{ci}$, nor the Kundsen effect of rarefied gases (McDonald and Thompson 1960) are taken into account.

Equation 3.4.3 is integrated and then combined with Eqs. 3.4.6 through 3.4.9 to yield

$$\frac{k_{gp}}{\delta}\left[t_c(R_{ci}) - t_f(R_f)\right] = k_f \left.\frac{\partial t_f}{\partial r}\right|_{R_f} \tag{3.4.11}$$

$$= k_c \left.\frac{\partial t_c}{\partial r}\right|_{R_{ci}} , \tag{3.4.12}$$

where

$$\delta = R_{ci} - R_f$$

is the gap width. Thus, Eqs. 3.4.11 and 3.4.12 replace Eqs. 3.4.3 and 3.4.6 through 3.4.9 and Eqs. 3.4.2, 3.4.4, 3.4.5, and 3.4.10 through 3.4.12 define the conduction process, provided the constitutive relations for (ρc), (k_{gp}/δ), k, h_c and q'''_f are specified and provided that the initial conditions for t_f and t_c are given.

3.4.1.3 Constitutive Descriptions for Thermal Conduction

This subsection presents material properties for fuel, cladding and gas gap which are related to conduction. These properties are the volumetric heat capacity (ρc) for fuel and cladding, the thermal conductivities k for fuel and and cladding, and the thermal conductance $(k/\delta)_{gp}$ of the gas gap. The convective heat transfer coefficient h_c in Eq. 3.4.10 is defined in Section 4.4.2.1, by Eqs. 4.4.30, 4.4.32, 4.4.35 and 4.4.39, respectively for single-phase liquid flow, for subcooled boiling and for transition and film boiling.

The Volumetric Heat Capacity $(\rho c)_f$ of the Fuel must be specified by the code user as a fixed constant (see Assumption (3-vii) in Sections 3.3.2.1 and 3.3.2.2). The value currently used in RAMONA-3B* corresponds to $t_f = 492°C$† and is

$$(\rho c)_f = 3.157 \times 10^6 \ \mathrm{J\,m^{-3}\,C^{-1}} . \tag{3.4.13}$$

Consult MATPRO (McDonald and Thompson 1976), Appendix A, Page 9 for reliable data on specific heat c_f. The fuel density ρ_f is 10,968 and 10,420 kg m^{-3} at 100% and 95% of theoretical fuel density, respectively (Lahey and Moody 1977, p. 252).

*ROCF on Input Data Card No. 720 000.
†At 95% of theoretical fuel density. The FSAR lists $(t_f)_{avg.}$ 650°C.

The Volumetric Heat Capacity of the Cladding must also be specified by the code user. A fixed constant applies everywhere in the core and at all times (see Assumption (3-vii) in Sections 3.3.2.1 and 3.3.2.2). The value currently used in RAMONA-3B* corresponds to $t_c = 307°C$ and is

$$(\rho c)_c = 2.127 \times 10^6 \text{ J m}^{-3} \text{ C}^{-1}. \tag{3.4.14}$$

MATPRO (McDonald and Thompson 1976) lists specific heats c_c for most cladding materials on Page 151 in Appendix B. For Zircaloy-2 use $\rho_c = 6{,}570.3$ kg m^{-3} (Lahey and Moody 1977, p. 252).

The Thermal Conductivity for the Fuel is defined in RAMONA by

$$k_f = \frac{C_1}{1 + C_2 t_f}, \tag{3.4.15}$$

where C_1 and C_2 are user-specified† constants and t_f is the local centigrade temperature. RAMONA-3B has currently

$$C_1 = 8.5 \text{ W m}^{-1} \text{ C}^{-1} \tag{3.4.16}$$

and

$$C_2 = 0.002°\text{C}^{-1}. \tag{3.4.17}$$

As discussed in Sections 3.3.2.1 and 3.3.2.2 under Assumption (3-ix), the effects of fuel density (burn-up) are ignored in RAMONA-3B. Table 3.1 below shows a comparison of RAMONA-3B-computed thermal conductivities with data published in a revised version of MATPRO (Hagrman, Reyman and Mason 1980, pp. 41-43). The RAMONA-3B results are specific to the choices for C_1 and C_2 in Eqs. 3.4.16 and 3.4.17.

*RCCA on Input Card No. 720 000.

†E1 and E2 on Input Card No. 391 000.

Table 3.1 Comparison of RAMONA-Computed Thermal Conductivity of Fuel With MATPRO Data

Temperature t_f(C)	Thermal Conductivity k_f of Fuel ($W\ m^{-1}\ C^{-1}$)		
	RAMONA-3B (Eqs. 3.4.15-17)	MATPRO	
		95% TD*	98% TD*
277	5.85	6.31	6.91
726	3.46	3.57	3.67
2,227	1.56	2.22	2.62

The Thermal Conductivity of Cladding Material must be specified by the user as a single constant which applies to the cladding at all locations in the core and at all times (see Assumption (3-x) in Sections 3.3.2.1 and 3.3.2.2). The value currently used in RAMONA-3B** is

$$k_c = 13.85\ W\ m^{-1}\ C^{-1} \tag{3.4.18}$$

This equals the thermal conductivity of Zircaloy (-2 or 4) at the temperature of 141°C (the average cladding temperature in the core is 300°C and calls for k_c= 15.80 W m-1 C-1), according to MATPRO-Version 11 (Hagrman, Reymann and Mason 1980, p. 217), where standard expressions can be found to compute the thermal conductivity for cladding materials.

The Thermal Conductance of the Gas Gap between fuel and cladding is defined in RAMONA-3B by a bounded quadratic power polynomial

$$\frac{k_{gp}}{\delta} = \text{Min}\left\{C_3 + C_4 \bar{t}_f + C_5 \bar{t}_f^2,\ C_6\right\} \tag{3.4.19}$$

where C_3, C_4, C_5 and C_6 are user-specified constants and $\bar{t}_f$ is the cross-sectional average of the fuel temperature.

*TD stands for theoretical fuel density.
**RCLA on Input Data Card No. 391 000.
†For its actual approximate evaluation see Section 6.3.4.

The values currently used in RAMONA-3B are*

$$C_3 = C_6 = 5.678 \times 10^3 \text{ W m}^{-2} \text{ C}^{-1} \tag{3.4.20}$$

$$C_4 = C_5 = 0 \tag{3.4.21}$$

The dimensions of C_4 and C_5 are W m^{-2} C^{-2} and W m^{-2} C^{-3}, respectively. The fixed gap conductance defined by Eqs. 3.4.19 through 3.4.21 represents fresh fuel in an 8x8 BWR/6 fuel bundle, operating with the linear power generation rate of 44 kW m^{-1}. Notice also that Eq. 3.4.19 has no continuous derivative at the temperature $\bar{t}_f$ at which the quadratic polynomial reaches the maximum value C_6. See Chapter 6 for the effect of this discontinuity on the solution process.

This completes the presentation of constitutive descriptions related to thermal conduction and energy storage in fuel elements. The convective heat transfer coefficient $\bar{h}_c$ is discussed in Section 4.4.2.1.

3.4.2 Steady-State and Initial Conditions

Transients are computed with the RAMONA-3B code by starting from steady-state initial conditions. The RAMONA-3B code can also be employed to find steady-state operating conditions.

Steady-state thermal conditions in the fuel pin are uniquely defined by specifying a fixed heat generation rate q'''_f (in Eq. 3.4.2) and a fixed coolant temperature t_{f1} (in Eq. 3.4.10). The steady-state temperature distributions are computed for these boundary conditions by setting $\partial/\partial\tau$ equal to zero in Eqs. 3.4.2 and 3.4.4. For the fuel pellets one obtains

$$\frac{d}{dr}\left(rk_f \frac{dt_f}{dr}\right) = -rq'''_f, \qquad \text{for } 0 \le r < R_f,\ \tau \le 0, \tag{3.4.22}$$

and for the cladding one gets

$$\frac{d}{dr}\left(k_c \frac{dt_c}{dr}\right) = 0, \qquad \text{for } R_{ci} < r < R_{co},\ \tau \le 0. \tag{3.4.23}$$

Equations 3.4.22 and 3.4.23 can be integrated**, subject to the boundary conditions given by Eqs. 3.4.5, 3.4.10, 3.4.11 and 3.4.12, using the constitutive relations in Eqs. 3.4.13 through 3.4.21.

*See GCA0, GCAI, GCA2 and GCAMAX on Input Data Card No. 391 000.

**Closed-form integration is possible but, while useful for code verification, not compatible with the steady-state solution of finite-difference analogues for Eqs. 3.4.2 and 3.4.4.

3.5 Summary and Recommendations for Improvement

The models in RAMONA-3B for the prediction of thermal phenomena in the fuel pins are completely specified by Eqs. 3.4.22 and 3.4.23, and by Eqs. 3.4.5, through 3.4.12 and Eqs. 3.4.15 through 3.4.21 for the steady-state initial conditions and by Eqs. 3.4.2 and 3.4.4 through 3.4.21 for the transients.

The applicability of RAMONA-3B can be considerably enhanced by removing the restrictions of Assumptions (3-v, vii, x and xi) regarding the dependence of transport properties on temperature. The thermal transport properties and the gap conductance (see Section 3.4.1.3) should be computed as functions of position and local conditions in the core to account for variations in fuel types, burn-up, fission gas composition and to render the conduction modeling consistent with three-dimensional neutron kinetics modeling.

The thermal interaction between structural components other than fuel pins and the coolant should be accounted for with simple, lumped-parameter descriptions of storage and transport of thermal energy in such components.

The conduction models in RAMONA-3B should be verified by comparison with exact analytical solutions.

4. MODELING OF THERMOHYDRAULICS

This chapter presents the formulation of the models in RAMONA-3B for the dynamics of coolant flows in the BWR reactor vessel, the recirculation loops and in the steam line, turbine, condenser and feedwater injection system. We present modeling assumptions and their implications to safety analyses, the governing field equations and constitutive relations. We also present appropriate recommendations for improvements at the end of this chapter.

The numerical techniques employed in RAMONA-3B for predicting first the initial steady-state conditions and then the reactor transients are described in Chapter 6. Section 6.4 presents the nodalization scheme for the thermohydraulics and the corresponding sets of ordinary differential and algebraic equations. In Section 6.6 is described the method for predicting steady-state conditions of the coolant and in Section 6.7 can be found the method for integrating the governing equations for the transients.

The thermohydraulics models in RAMONA-3B were developed and programmed by Scandpower, except the models for the steam line dynamics, for the transport of boron, for predicting the critical power ratio, the occurrence of burnout and the heat transfer for transition and stable film boiling. These specific component and process models were developed by BNL. The description here of the models developed by Scandpower is taken or derived from Scandpower documentation and from program listings. The documentation presented here does not account for differences between the actual coding in RAMONA-3B and the model descriptions by the code originators since such a task was beyond the present level of effort and impractical. There is presently no documentation available by which to assess and judge the quality assurance of the FORTRAN programming. The thermohydraulics models, other than that for the steam line dynamics, have not been verified against analytical solutions.

4.1 Scope of Thermohydraulic Modeling in RAMONA-3B

The thermohydraulic models in RAMONA-3B are designed to simulate operational transients between hot standby and full-power conditions and the following abnormal transients: turbine trip with reactor scram (rapid control rod insertion for cessation of fission), Main Steam Isolation Valve closure with reactor scram, Anticipated Transients Without Scram (ATWS) or with partial scram (Partial ATWS) where some control rods fail to enter into the core, further the transients induced by control rod drop and by the failures of the pressure regulator, and finally, feedwater transients.

The models are designed to describe the coolant dynamics and the transport of boron. The models account for two-phase flow of liquid and water vapor mixtures with different phase velocities (nonhomogeneous flow). The models allow for the liquid phase to be subcooled, saturated or superheated, but they restrict the vapor to saturation conditions.

The RAMONA-3B models describe the coolant flows in the pressure vessel of a BWR reactor, in a single recirculation loop, representative of all recirculation loops and in a single steam line, also representative of all steam lines in the BWR power plant. A schematic of the modeled coolant system is given in Figure 4.1. The turbine, condenser and feedwater preheat and injection systems are modeled only to the extent necessary for simulating the control system of the nuclear steam supply system.

The thermohydraulic models are designed to achieve the major mission of the RAMONA-3B code, namely to predict steady-state and transient three-dimensional variations in the core of both fission power, fuel temperatures and coolant flow conditions. The thermohydraulic model for the core computes one-dimensional flow through parallel channels which consist of sets of channel boxes with fuel elements, or of a bypass channel.

The extent to which these code objectives have been achieved is summarized below in Section 4.2. Specific modeling assumptions and their consequences to safety analyses are presented in Section 4.3.

4.2 Code Capabilities and Limitations

This section is the summary of RAMONA-3B code capabilities and limitations related to the thermohydraulics modeling assumptions and associated solution methods. The summary is not complete as the capabilities presented here are further restricted by limitations related to models for neutron kinetics and thermal conduction in structures. The overall summary of RAMONA-3B capabilities and limitations is given in Sections 1.2 and 1.3.

RAMONA-3B is currently the only available systems code for BWR power reactors that offers the capability to predict the local details of three-dimensional distributions of fission power, neutron kinetics and thermohydraulic parameters. The modeling of the thermohydraulics is designed to fully complement the three-dimensional neutron kinetics calculations.

The thermohydraulics modeling enables RAMONA-3B currently to predict:

a) steady-state conditions at rated recirculation pump speed and at power levels between hot standby conditions and full power,

b) operational transients at power levels between hot standby and full power, with the recirculation pump motor at rated generator frequency and rated stator voltage, and with constant feedwater temperature,

c) recirculation pump coast-down transients with zero stator voltage at the pump motor,

d) transients induced by turbine trips (Turbine Stop Valve closure), Main Steam Isolation Valve closures and loss of condenser vacuum, with recirculation pump either at full stator voltage and rated generator frequency, or shut off.

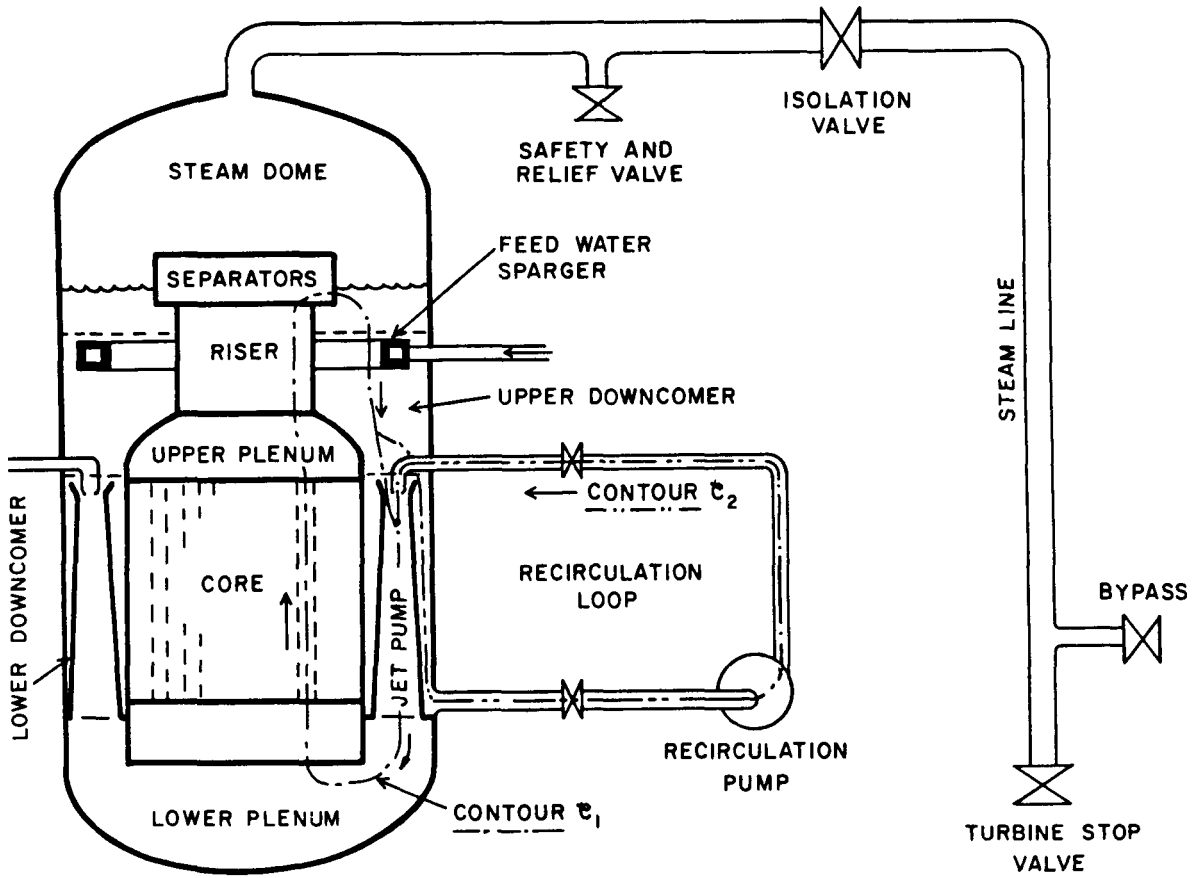

Figure 4.1 Schematic of BWR System and Circulation Loops

e) anticipated transients with scram, partial scram or without scram,

f) thermohydraulic transients caused by control rod motions and control rod failures,

g) transients caused by a failure of the pressure regulator or a steam line break,

h) transients with boron injection.

RAMONA-3B has a simple simulation system for the plant control and protection system to the extent that it is related to the nuclear steam supply system (see Chapter 5). This simple simulation system can be extended by prescribing appropriate boundary conditions as functions of time. Therefore, the above list of simulation capabilities can be widened further, using the currently implemented thermohydraulics models.

RAMONA-3B is currently not capable of simulating BWR transients

a) requiring one to follow variable steam demands by controlling the recirculation pump speed (load-following transients),

b) with large changes in feedwater temperature (50°C or more) or with cold water injection,

c) with conditions of burnout (CHF), producing superheated vapor anywhere for significantly long time periods,

d) with coolant inventory loss or coolant contraction such that the mixture level in the lower part of the steam dome, at the separator discharge elevation, recedes down into the upper plenum,

e) with sudden flashing or intensive boiling such that the coolant level rises above the separators,

f) flow reversal in the reactor vessel beyond the reactor core or the recirculation loop.

Recall that RAMONA-3B is not programmed to simulate loss of coolant accidents, neither large nor small breaks. Reviewing the assumptions and their consequences as presented in the next section, the reader will realize that the elimination of some modeling conflicts would improve the reliability of RAMONA-3B, and a number of relative simple modeling improvements would significantly expand its range of applicability.

4.3 Thermohydraulic Modeling Assumptions and Their Consequences

In this section are presented the thirty-two assumptions implied in the RAMONA-3B models for the thermohydraulics of the coolant in the nuclear steam supply system. The assumptions arising from the numerical solution of the governing thermohydraulics equations are presented in Section 6.4 of Chapter 6. Following the summary of modeling assumptions below is a discussion on their relevance to safety analyses.

4.3.1 Assumptions

Fundamental Balance Equations

Assumption (4-i): Covariances of time and space averaging are ignored in the derivation of two-phase flow balance equations from fundamental local, instantaneous balance equations and interface jump conditions. This means that averages of products are set equal to products of averages, and flow parameters are assumed to be uniform over a cross section.

Assumption (4-ii): The vapor is at saturation, wherever it occurs and at all times.

$$h_v = h_g(p),\ \rho_v = \rho_g(p) \quad \text{and} \quad t_v = t_{sat}(p)\ , \tag{4-ii}$$

where h, ρ, t and p stand for enthalpy, density, centigrade temperature and absolute pressure, respectively, and where the subscripts v, g and sat denote vapor, saturated vapor and saturation, respectively.

Assumption (4-iii): The spatial variation of pressure p is ignored for all thermophysical property calculations and in the mass and energy balances, but in the momentum balance the axial pressure variation is accounted for.

$$\nabla p = 0, \quad \text{properties and mass and energy balances.} \tag{4-iii}$$

Assumption (4-iv): The pressure is uniform in a flow cross section: $\partial p/\partial r = 0$, in the momentum balance.

Assumption (4-v): Longitudinal thermal conduction in a flow channel, kinetic and potential energies and viscous dissipation are ignored in the mixture energy equation.

Assumption (4-vi): Flow channels in core, downcomer and recirculation loop are sectionally of constant cross-section A.

Constitutive Descriptions

Assumption (4-vii): The compressibility and thermal expansion of the liquid phase, whether subcooled, saturated or superheated, can be approximated by that of saturated liquid.

Assumption (4-viii): The isobaric specific heat and the transport properties of liquid water are approximated by saturation properties at the appropriate pressure.

Assumption (4-ix): Onset of nonequilibrium boiling can be approximated by intersecting the single-phase, forced convection, with the nucleate boiling, curves for heat flux versus wall superheat or it can be predicted from the model for vapor generation.

Assumption (4-x): Transition boiling occurs whenever the wall superheat temperature, $t_w - t_{sat}$, lies between the wall superheat temperatures at burnout, $t_{CHF} - t_{sat}$, and the wall superheat temperature at the point of Minimum Stable Film Boiling, $t_{MSFB} - t_{sat}$, even when the wall heat flux q''_w is temporarily either larger than the burnout wall heat flux q''_{CHF}, or smaller than that of Minimum Stable Film Boiling, q''_{MSFB} (see Figure 4.3).*

Assumption (4-xi): Laminar forced and laminar or turbulent free convection flow and heat transfer regimes will not occur in RAMONA-3B applications. A fixed constant serves to describe heat exchange between heated channels and bypass channels.

Assumption (4-xii): The reversible transformation of kinetic energy at abrupt changes of flow cross-sectional area is negligible (see Eqs. 4.4.49 and 4.4.50), and form loss coefficients are independent of flow direction (i.e., the same for contractions as for expansions, under conditions of flow reversal). The flow does not reverse.

Component Modeling

Assumption (4-xiii): The effect of thermal expansion of liquid is ignored in the computation of the time rate of change of system pressure (cf. Eqs. 4.4.90 and 4.4.93).

Assumption (4-xiv): Flow inertia is negligible in the suction intake and the mixing throat of the jet pumps.

Assumption (4-xv): There is only single-phase liquid in the recirculation loops.

Assumption (4-xvi): The liquid in the recirculation loop has uniform density, changing only with time and being equal to the liquid density in the downcomer at the location of the jet pump suction.

Assumption (4-xvii): There is no flow reversal in the recirculation loop. Water flows only from the lower exit of the downcomer through the recirculation pump to the jet pump nozzle.

*This assumption is implied as a consequence of computational procedures and affects the calculations during a neutron kinetics time step, at the end of which the assumption is relaxed in part.

Assumption (4-xviii): The effects of liquid expansion are ignored in the recirculation loop (a conflict with Assumption (4-xvi) above).

Assumption (4-xix): The friction factor and the form loss coefficients for the flow in the recirculation loop are constant, independent of Reynolds number, i.e., flow regime and flow rate.

Assumption (4-xx): The electrical torques of the induction motors driving the recirculation pumps are functions of rotor speed only.

Assumption (4-xxi): The flow quality x_{cu} at the separator discharge toward the downcomer is constant. It is derived to achieve the desired core inlet subcooling temperature under steady-state conditions.

Assumption (4-xxii): An artificial surface mass transfer term is imposed at the separator exit (jump in phasic mass balances and energy balance) to achieve equilibrium conditions ($h_\ell = h_f$ and $h_v = h_g$) at the separator exit. This surface mass transfer term is ignored in the global mass balance for the prediction of the system pressure.

Assumption (4-xxiii): The vapor void fraction is uniform in the low-void region of the downcomer, below the coolant level.

Assumption (4-xxiv): The coolant mixture level remains in the steam dome. The liquid return from the separators discharges always into the steam dome below the mixture level. The mixture level never falls below the separator discharge level nor below the feedwater spargers. There is only pure vapor above the level.

Assumption (4-xxv): The slip ratio S is equal to unity in the low-void regime of the vapor dome.

Assumption (4-xxvi): The steam in the steam line is superheated vapor and behaves like an ideal gas.

Assumption (4-xxvii): Gravity effects and effects of local acceleration are negligible in the steam line dynamics.

Assumption (4-xxviii): Thermal effects of viscosity are unimportant in the steam line; the vapor in the steam line has constant entropy (cf. Assumption (4-v)).

Assumption (4-xxix): Form losses are distributed in the axial direction over steam line pipe sections adjacent to the form loss source location.

Assumption (4-xxx): Injected boron remains in solution in the liquid phase of the coolant.

Assumption (4-xxxi): The liquid water (solvent) injected with the boron is neglected.

Assumption (4-xxxii): Axial diffusion of boron (mixing) is ignored.

4.3.2 Consequences from Modeling Assumptions

In this section we discuss the relevance of the thermohydraulic modeling assumptions in RAMONA-3B to safety analyses. The consequences of the thirty-two assumptions of thermohydraulics modeling in RAMONA-3B are inferred from an estimation of their effects on the governing equations. The assessment is qualitative. The quantitative assessment of RAMONA-3B is presented in Chapter 7.

Fundamental Balance Equations

Assumption (4-i) concerning the neglection of covariances in time and space is of no concern to RAMONA-3B users when analyzing plant transients other than small break loss of coolant accidents. The user is warned to apply RAMONA-3B to transients in which the mixture level falls below the separator discharge elevation, and the steam separators issue a falling liquid film (cf. 4-xxiv).

Assumption (4-ii), restricting the vapor phase to its saturation conditions, is valid for all BWR transients other than those which lead to superheated vapor. This may occur when burnout or dryout conditions are reached in the core sufficiently far below the core exit, and prevailing long enough, to allow the steam to become superheated downstream of the burnout (CHF) location. Such conditions may be reached during ATWS simulations.

Assumption (4-iii) implies uniform pressure in the BWR system for all phasic property calculations. This assumption is highly recommended as it eliminates from the analysis unimportant and computationally expensive acoustic effects. The assumptions permit the integration of the momentum equation separately from mass and energy equations, thereby saving additional computational efforts. The potential limitations from this assumption are that RAMONA-3B cannot be used to predict mechanical interactions between coolant and structures, that the time delay of pressure pulse propagation from the steam line entrance to the core cannot be predicted without additional modeling efforts and that time delay may affect the timing of scram actions relative to reactivity insertion due to vapor void collapse under coolant compression.

Assumption (4-iv) concerning the lateral pressure variation $\partial p/\partial r$ in a flow cross section introduces no restriction in the use of RAMONA-3B, since small-break loss of coolant accidents with flow stratifications in horizontal channels are outside the scope of RAMONA-3B applications.

Assumption (4-v) implies negligible contributions from mechanical energy, viscous effects and longitudinal conduction to the energy balance. These contributions are insignificant and the simplification is recommended for all components in the BWR system. A potential exception is the recirculation loop. The mechanical energy of the recirculation pump affects the thermal expansion, and thereby, the coolant level elevation during the simulation of a transient from cold standby to hot standby.

Assumption (4-vi) about constant flow cross sections is justified by the system geometry, except in the Upper Downcomer and in the jet pump diffuser.

The user must accommodate the temporal acceleration in these flow channel sections by using a mean diameter. Concerning related assumptions about spatial accelerations, the reader is referred to Assumption (4-xii).

Constitutive Descriptions

Assumption (4-vii) implies that subcooled liquid expands like saturated liquid. This assumption leads to the overprediction of thermal expansion in large liquid volumes by a factor of ten (see Eq. 4.4.92) and an appreciable error in the prediction of the system pressure during all transients with significant feedwater temperature or system pressure changes. It is strongly recommended that this error be corrected for future code improvements. See Eq. 4.4.93, last term in denominator, for proper representation of liquid thermal expansion. See Eq. 4.4.94, denominator integral, for the current representation of liquid thermal expansion in RAMONA-3B.

Assumption (4-viii) concerning the approximations of thermophysical and transport properties of liquid is assessed in part in Tables 4.1 and 4.2 of Section 4.4.2.5. The error in specific heat for subcooled liquid ranges between 4% and 19% in the pressure range between 25 and 150 bar and at 20°C liquid subcooling. The error in liquid internal energy ranges between -2% and +44%.

Assumption (4-ix) involves two conflicting criteria by which onset of net vapor formation in the core is predicted by the RAMONA-3B code. This conflict makes it possible that the incorrect heat transfer correlation (forced convection instead of nucleate boiling or vice versa) is used by RAMONA-3B, over some indeterminable axial section of the core.

Assumption (4-x) concerning the departure from, and return to, nucleate boiling affects the RAMONA-3B application for ATWS simulations and for simulations of thermally-induced power and flow oscillations encountering burnout conditions if departure from nucleate boiling occurs.

It is implied as a consequence of coding restrictions in RAMONA-3B that transition boiling conditions exist whenever and wherever the wall superheat temperature lies between the critical wall superheat and the minimum stable film boiling temperature. In reality, however, transition boiling cannot exist unless the conductive heat flux at the cladding surface equals the transition boiling heat flux which corresponds to the wall superheat temperature, as shown in Figure 4.3 of Section 4.4.2.1.1. Instead of following the transition boiling curve, the heat flux vs. wall temperature relation may follow a line from CHF conditions directly to stable film boiling and from minimum stable film boiling directly to nucleate boiling (cf. Figure 4.3).

As these hysteresis effects are not modeled in RAMONA-3B*, the user of the code should expect uncertainties in post-CHF heat transfer and wall temperature

*The correct modeling of hysteresis effects would have required major code modifications to couple computationally hydraulics and thermal conduction calculations in the cladding.

predictions and in predicting the frequency of thermally-induced flow oscillations. The magnitude of these uncertainties needs to be assessed quantitatively to establish their importance.

Assumption (4-xi) implies the absence of laminar flow conditions in RAMONA-3B simulations (laminar flow and flow reversal are accounted for in the steam line dynamics).

Assumption (4-xii) concerns the neglection of the reversible transformation of kinetic energy at sudden expansions and contractions, and the use of the same form loss coefficient for forward and reverse flows. In spite of this assumption, the RAMONA-3B code can be used for simulating transients with normal full flow and near full-flow conditions because the error from this assumption can be compensated for in some range of flow rates by adjusting loss coefficients (cf. Eq. 4.4.49) or flow impedances (cf. Eq. 4.4.133). The code cannot be employed for transients with low flow conditions and flow reversal.

Component Modeling

By Assumption (4-xiii), the effect of thermal expansion in the liquid is ignored in the computation of the system pressure (cf. Eqs. 4.4.90 and 4.4.93). The thermal expansion is expected to be important for feedwater transients when cold water enters the pressure vessel. At a subcooling temperature of 100°C, the thermal expansion of the liquid can be expected to have the same effect on the pressure history as a 24% increase of the feedwater mass flow rate. The error is proportionately less for lower feedwater subcooling temperatures. It is recommended that this assumption be relaxed for future code improvements.

By Assumption (4-xiv), the totally unimportant flow inertia of the flow path from the downcomer to the jet pump intake is ignored. There is no restriction arising from this assumption on the use of RAMONA-3B. To the contrary, the inclusion of this inertia would lead to inordinate computing complexity and computing effort, without any discernible benefit. In fact, the inertia in the entire recirculation loop may be unimportant because the relaxation time of its flow is on the order of 10^{-2} seconds.

Assumption (4-xv) restricts the recirculation loop flows to single-phase flow of liquid. Consequently, RAMONA-3B cannot be used for loss of coolant accident simulations. A pipe break in the recirculation loop leads at once to flashing and two-phase flow in the broken pipe, and to two-phase choked flow out of the pipe.

By Assumption (4-xvi), the density of the liquid in the recirculation loop is imposed to be uniform and equal to the liquid density at the jet pump location. This assumption is entirely acceptable for the momentum balance, as its consequences are negligible on the prediction of flow rates. However, the assumption is in conflict with Assumption (4-xviii) which implies time-invariant liquid density.

Assumption (4-xvii) disallows flow reversal in the recirculation loop but introduces no additional restrictions to the use of the RAMONA-3B code as the code cannot simulate flow reversal for other reasons (cf. Assumptions 4-xii, xv and xix).

Assumption (4-xviii) implies no liquid dilation, i.e., time-invariant liquid density in the recirculation loop. This assumption affects the prediction of the coolant mixture level, particularly in attempts at simulating the transients from cold standby to hot standby conditions and the transients with cold water injection into the downcomer (feedwater transients).

With Assumption (4-xix) RAMONA-3B relies on fixed wall-shear and form loss coefficients for all fluid velocities in the recirculation loop. RAMONA-3B, therefore, cannot compute the low-flow conditions after a recirculation pump trip, nor flow reversal in the recirculation loop.

Assumption (4-xx) implies that the electrical torque of the induction motor, which drives the recirculation pump, is independent of stator voltage magnitude and independent of the voltage frequency. Both quantities are controlled in reality to vary the reactor power from 75% to 100% of full power (via boiling length, void fraction and void reactivity feedback). It is recommended that electrical torque curves be implemented in RAMONA-3B which account for variation of frequency and stator voltage, so that the code can be used for the simulation of pump startup and of power-following transients.

Assumption (4-xxi) regarding the time-invariance of the flow quality at the separator discharge into the downcomer is arbitrary. The calculation of this flow quality even for steady-state conditions, cannot be justified because the flow quality, while physically a measure of steam separator performance, is being misused to adjust the initial core inlet subcooling temperature. It is used to compensate initially for modeling inadequacies (omission of heat transfer, of pumping power dissipation and inaccuracies in specific heat calculations) in downcomer and lower plenum.

The assumption is expected to have no consequences on the use of RAMONA-3B as long as the riser exit void fraction does not depart far from initial conditions. Conflicts with mass and energy balances must be expected when pure liquid or when high-void mixtures enter the separators. This should lead to computational difficulties.

It is strongly recommended that Assumption (4-xxi) be relaxed for future code improvement.

Assumption (4-xxii) introduces an artificial surface evaporation rate at the separator exit to eliminate the unrealistically high liquid superheating temperature produced by the nonmechanistic bulk vapor generation term. There appear to be no adverse consequences from this artifice because the correction is normally small and in the proper direction. However, this assumption should be rendered unnecessary by improving the model for predicting vapor generation rates.

Assumption (4-xxiii) implies a homogeneous mixture of liquid and vapor in the low-void region of the steam dome. Due to vapor upward drift and low

liquid downward flow in the region around the separators, one should expect phase separation: higher vapor concentration just below the liquid level and lower vapor concentration at the downcomer entrance. The assumption has an influence on the prediction of vapor entrainment into the downcomer.

Under normal conditions near full power, the effects of this assumption are compensated for by Assumption (4-xxi). For general conditions, the RAMONA-3B code cannot be expected to predict phase separation reliably unless a new, finer nodalization is employed in the low void region to compute the void distribution. The error on core entrance subcooling from errors in entrainment calculations can be estimated for quasi-static conditions with the aid of Eq. 4.4.161.

Assumption (4-xxiv) introduces some error when the mixture level does not drop below the lower discharge opening of the steam separators. The level motion cannot presently be predicted reliably if the level falls down into the upper downcomer and much less if it falls below the feedwater sparger elevation. The RAMONA-3B code switches its computational logic to inject all vapor-liquid mixtures below the level, regardless of the level position relative to the elevation of injection.

The level tracking model in RAMONA-3B also implies that there is only pure vapor above the level, i.e., that the vapor does not condense appreciably in the dome, during depressurization, nor that there is spray injection above the mixture level.

Assumption (4-xxv) implies that there is stagnant liquid in the dome, below the mixture level. This assumption introduces no restriction in the use of RAMONA-3B for operational plant transient simulations since the vertical velocity component is always negligibly small in the vapor dome. During sharp pressure fluctuations of the system, however, flashing and condensing will cause the mixture level to rise (swelling) or to fall (void collapse). Code predictions become questionable if the level velocity and the liquid velocity reach 0.2 m/s, i.e., a velocity comparable to the vapor drift velocity.

Assumption (4-xxvi) implies that the steam in the steam line is superheated. The steam is saturated in the vapor dome but becomes superheated by adiabatic throttling in the steam line. Estimates have shown that the vapor may condense behind an expansion wave but cannot reach a void fraction below 0.990. Thus, single-phase vapor descriptions are adequate. Comparison of steam table data with ideal gas data have shown that the error from assuming ideal gas conditions is negligible.

Assumption (4-xxvii) concerns the importance of gravity and local inertia effects. These effects have been assessed by order of magnitude comparison with first-order terms. They were found to be negligible (Wulff 1980a).

Assumptions (4-xxviii and xxix) about the thermodynamic process path of the steam in the steam line and about the effects of form losses have been justified by comparison with full-scale experiments (Wulff 1980a).

Assumption (4-xxx), that the injected boron remain in solution, is justified on the basis of boron solubility and coolant temperature.

Assumption (4-xxxi) introduces an error of 0.3% of the feedwater injection through the neglection of the boron solution in the coolant mass balance.

Assumption (4-xxxii): boron diffusion in the axial direction is negligible when compared with convective transport.

This completes the summary of modeling assumptions and the discussion of their consequences. The reader may have noticed that some of the items presented as assumptions are, in fact, modeling conflicts. These have been presented as assumptions in the belief that the modelers had assumed that the consequences from the conflicts are negligible. It should be recognized, however, that modeling conflicts have the tendency to produce computational obstacles. It is therefore recommended that "Assumptions (4-ix, xi, xii and xxiv)" be eliminated first, along with the correction of the $|w|w$ term in the momentum flux term of the mixture momentum balance. It should read w^2 as in Eq. 4.4.6 below.

4.4 Governing Thermohydraulics Equations

This section is the presentation of field equations, constitutive relations, initial and boundary conditions which describe the coolant flow dynamics and the motion of boron. Presented are the equations which apply to the system as a whole, to the closed circulation loops in the system and to the major components in the system. The adaptation of the general equations presented here to particular computational cells involves nodalization and discretization schemes and is therefore presented as part of the discussion on numerical methods in Section 6.4.2 of Chapter 6. The numerical solution techniques for solving and integrating the equations related to the total system, its circulation loops and its individual components are presented in Sections 6.6 and 6.7.

Subject to the assumptions listed above in Section 4.3, the RAMONA-3B code employs a four-equation slip flow model for nonhomogeneous, nonequilibrium two-phase flow. The four equations are the vapor and liquid mass balances, the mixture energy and the mixture momentum balances. With the vapor assumed to be saturated (Assumption 4-ii), the constitutive description for nonequilibrium vapor generation (see Section 4.4.2.3) defines uniquely the degrees of subcooling or superheating in the liquid. The slip correlation (see Section 4.4.2.4) establishes the phasic velocities v_ℓ of the liquid and v_g of the saturated vapor relative to the mixture velocity.

The vapor and liquid mass balances are combined with the phasic equations of state and applied to the total control volume V_{syst} of pressure vessel plus recirculation loop for predicting the time rate of change of the overall system pressure $\langle p \rangle_{syst}$. By using this single pressure for all thermophysical property evaluations, RAMONA-3B achieves large savings in computing time as discussed in Section 4.3 (see Assumption 4-iii).

The one-dimensional momentum balances for mixture or single-phase flows are applied to every closed loop, formed by any core flow channel, together with the upper plenum, the riser, the steam dome, Upper Downcomer, jet pump and lower plenum as shown by the contour $_1$, passing through the core, in Figure 4.1, and as formed by the recirculation loop contour $_2$ shown also in Figure 4.1. This method reduces the stiffness of the system of governing ordinary differential equations by increasing the relaxation time of coolant flow transients and by suppressing acoustic effects. The method leads to only one ordinary differential equation for each closed loop and affords the efficient prediction of a separate coolant mass flow rate in each core channel.

The mixture mass balance is replaced by the equation of volumetric mixture flux divergence, as explained later. This reduces, because of Assumption (4-iii), the task of integrating a partial differential equation in space and time to a simple quadrature in space.

The three important modeling features discussed above leave only two partial differential equations (for vapor mass and mixture energy). These are converted into ordinary differential equations through integration over finite-difference control volumes (see Section 6.4.2).

Special care is given to the modeling of jet pumps, steam separators and the recirculation loop. A separate model for single-phase vapor is used to predict the pressure and flow oscillations in the steam line.

The above modeling features in RAMONA-3B are absolutely necessary for cost-efficient simulations of detailed, transient parameter distributions by three-dimensional neutron kinetics, multiple channel core flow and nonhomogeneous, nonequilibrium two-phase flow modeling in the context of a BWR systems code. The combination of these modeling features provides a unique capability that currently no other systems code can offer.

4.4.1 Field Equations for Thermohydraulics of Coolant

As stated in Section 4.3.1, the field equations of RAMONA-3B thermohydraulics imply six important assumptions. To illustrate clearly their importance, we first present, or derive as necessary, the set of complete field equations, starting with published two-phase flow equations. Then we discuss the omissions or modifications implied in RAMONA-3B, and finally, we present the equations as used in RAMONA-3B.

The thermohydraulics models in RAMONA-3B are based on the following four conservation equations for vapor mass, liquid mass, mixture energy and mixture momentum:

The local, time-averaged phasic mass balances are (Delhaye, Giot and Riethmuller 1981, p. 174), for saturated vapor (subscript g)

$$\frac{\partial}{\partial \tau}(\alpha \rho_g) + \nabla \cdot (\vec{j}_g \rho_g) = \Gamma_v \qquad (4.4.1)$$

and for the liquid phase (subscript ℓ)

$$\frac{\partial}{\partial \tau}\left[(1-\alpha)\ \rho_\ell)\right] + \nabla \cdot (\vec{j}_\ell\, \rho_\ell) = -\Gamma_v \ . \qquad (4.4.2)$$

In Eqs. 4.4.1 and 4.4.2 the symbols α, ρ, j and Γ_v denote, respectively, vapor void fraction, density, volumetric flux and vapor generation rate per unit of volume. The symbol τ stands for time. Note that

$$\vec{j}_g = \alpha \vec{v}_g \qquad \text{and} \qquad \vec{j}_\ell = (1-\alpha)\ \vec{v}_\ell \ , \qquad (4.4.3)$$

where $\vec{v}$ is the local velocity vector.

Notice that Eqs. 4.4.1 and 4.4.2 are written in three-dimensional vector form. This form affords the integration over arbitrarily shaped control volumes (plena, etc.) with three-dimensional flow patterns. The volume integration is needed to derive the equation for the time rate of change of the volume-averaged system pressure $\langle p \rangle_{syst}$. The one-dimensional form of Eq. 4.4.1 as used for channel flow is presented later in Section 6.4.1.3. A one-dimensional form of Eq. 4.4.2 is not required since Eq. 4.4.2 is replaced by a combination of Eqs. 4.4.1 and 4.4.2.

The one-dimensional, instantaneous area-averaged mixture energy equation is (Delhaye, Giot and Riethmuller 1981, Eq. 17, p. 164) by virtue of Assumptions (4-i through iii, v and vi)

$$\frac{\partial}{\partial \tau}\left[\alpha \rho_g u_g + (1-\alpha)\ \rho_\ell u_\ell\right] + \frac{\partial}{\partial z}\left[\alpha \rho_g h_g w_g + (1-\alpha)\ \rho_\ell h_\ell w_\ell\right] = \frac{q'_w}{A} + q'''_\ell\ (1-\alpha) \ , \qquad (4.4.4)$$

where $q'''_\ell\ (1-\alpha)$ is the power density of direct gamma absorption by the liquid phase (only) (cf. Eq. 2.7.17),

$$q'_w = \left(\xi \bar{h}_c\right)_c \left[t_c\,(R_{co}) - t_{f\ell}\right] - (\xi \bar{U})_{lb}\ (t_{f\ell} - t_{lb}) \ , \qquad (4.4.5)$$

and A, ξ, u and h denote cross-sectional area, heated perimeter, specific internal energy and specific enthalpy, respectively. The symbol h_c represents the heat transfer coefficient (see Section 4.4.2.1), while t stands for the centigrade temperature, $t_c\ (R_{co}) = t_w$ is the cladding temperature t_c at the outer cladding surface, $r = R_{co}$, and $t_{f\ell}$ is the fluid temperature. $\bar{U}_{lb}$ is the overall heat transfer coefficient for the heat transfer to the interchannel bypass flow with temperature $t_{\ell b}$ from the heated channel with its fluid temperature $t_{f\ell} = t_\ell$ or $t_{f\ell} = t_{sat}$. In Eq. 4.4.4 w denotes the axial velocity component, and z is the axial coordinate. The void fraction α is an area fraction in Eq. 4.4.4, but a time fraction in Eqs. 4.4.1 and 4.4.2. By virtue of Assumption (4-i) and the commutativity of time and space averaging (Delhaye, Giot and

Riethmuller 1981, p. 181), the void fractions in Eqs. 4.4.1, 4.4.2, 4.4.4 and 4.4.6 through 4.4.8 will be the same, once Eqs. 4.4.1 and 4.4.2 are integrated over a control volume and α appears only in control surface integrals, as shown later.

The one-dimensional, instantaneous area-averaged mixture momentum balance is,* by Assumptions (4-i, ii, iv and vi)

$$\frac{\partial G_m}{\partial \tau} + \frac{\partial}{\partial z}\left[\alpha \rho_g w_g^2 + (1-\alpha)\, \rho_\ell w_\ell^2\right] = -\frac{\partial p}{\partial z} - g_z \rho_m - f_\ell \phi_\ell^2 \frac{G_m |G_m|}{2 \rho_\ell d_h}, \quad (4.4.6)$$

where the mixture momentum G_m in the axial direction is

$$G_m = \alpha \rho_g w_g + (1-\alpha)\, \rho_\ell w_\ell , \quad (4.4.7)$$

and the mixture density ρ_m is given by the thermal equation of state for the two-phase mixture:

$$\rho_m = \alpha \rho_g + (1-\alpha)\, \rho_\ell . \quad (4.4.8)$$

The symbols f_ℓ, ϕ_ℓ^2 and d_h designate, respectively, the single-phase Darcy friction factor, computed as if the mixture were flowing as a liquid, the two-phase flow friction multiplier and the hydraulic diameter of the channel, wetted by the fluid. The symbol g_z is the gravitational acceleration component in the negative z-direction.

Equations 4.4.1, 4.4.2, 4.4.4 and 4.4.6 are the four basic conservation equations in RAMONA-3B. Problem closure requires that flow-regime dependent constitutive relations are provided for the heat transfer coefficient $\overline{h}_c$, the friction factor f_ℓ and its two-phase flow multiplier ϕ_ℓ^2, the vapor generation rate Γ_v and a relation between the phasic velocities w_g and w_ℓ. Also, the one-dimensional momentum balanees will be applied to channel sections of constant flow cross section and then coupled by jump conditions for abrupt changes in cross-sectional area. The dissipation of energy across such area changes must be described by loss coefficients. Moreover, problem closure requires the specification of thermophysical and transport properties. All these constitutive relations are presented in Section 4.4.2, initial and boundary conditions are discussed in Sections 4.5 and 4.6.

*The RAMONA-3B code listing shows that $w|w|$ is used erroneously instead of w^2 in the second term on the left-hand side of Eq. 4.4.6. See Section 4.3.2 for the discussion of this error.

As discussed in the introduction to Chapter 4, Eqs. 4.4.1 and 4.4.2 are combined in RAMONA-3B to yield the equation of mixture volume flux divergence,

$$\nabla \cdot \vec{j}_m = (\rho_\ell - \rho_g)/(\rho_\ell \rho_g)\Gamma_v - \left[\frac{\alpha}{\rho_g}\frac{D_g \rho_g}{D\tau} + \frac{(1-\alpha)}{\rho_\ell}\frac{D_\ell \rho_\ell}{D\tau}\right], \quad (4.4.9)$$

where

$$\vec{j}_m = \vec{j}_g + \vec{j}_\ell = \alpha \vec{v}_g + (1-\alpha)\vec{v}_\ell \quad (4.4.10)$$

and

$$\frac{D_i}{D\tau} = \frac{\partial}{\partial \tau} + v_i \cdot \nabla, \qquad i = g,\ell \quad . \quad (4.4.11)$$

Equation 4.4.9 constitutes the mixture mass balance and replaces in RAMONA-3B the mass balance for the liquid, Eq. 4.4.2 and, as will be seen later, the task of integrating a partial differential equation by the simpler task of integrating over space.

The first term on the right-hand side accounts for volume dilation due to vapor generation, the terms in square brackets represent the phasic compressibilities.

With Assumptions (4-ii and iii) one can reduce the first term in square brackets in Eq. 4.4.9 to

$$\frac{\alpha}{\rho_g}\left(\frac{\partial \rho_g}{\partial \tau} + \vec{v}_g \cdot \nabla \rho_g\right) = \alpha \frac{\rho_g'}{\rho_g}\left[\frac{\partial p}{\partial \tau} + \vec{v}_g \cdot \nabla p\right] = \alpha \frac{\rho_g'}{\rho_g}\frac{d\langle p\rangle_{syst}}{d\tau}, \quad (4.4.12)$$

where the superscripted primes denote differentiation with respect to pressure along the saturation line and $\langle p\rangle_{syst}$ is the system pressure. The compressibility of the liquid is, by Assumption (4-iii)

$$(1-\alpha)\frac{D_\ell \rho_\ell}{D\tau} = (1-\alpha)\left\{\left(\frac{\partial \rho_\ell}{\partial u}\right)_p\left[\frac{\partial u_\ell}{\partial \tau} + \vec{v}_\ell \cdot \nabla u_\ell\right] + \left(\frac{\partial \rho_\ell}{\partial p}\right)_u\left[\frac{d\langle p\rangle_{syst}}{d\tau}\right]\right\} . \quad (4.4.13)$$

By utilizing the phasic energy equation and the interface energy jump condition, subject to Assumptions (4-iii and v) and also the assumption that the thermal conduction in the vapor phase, toward the liquid-vapor interface, is zero, that is, by utilizing

$$(1-\alpha)\ \rho_\ell \left[\frac{\partial u_\ell}{\partial \tau} + \vec{v}_\ell \cdot \nabla u_\ell\right] = -\nabla \cdot \left[(1-\alpha)\ \vec{q}_\ell\right] - \Gamma_v\ (h_g - h_\ell) + q'''_\ell\ (1-\alpha) \tag{4.4.14}$$

one can replace the total derivative in the first square bracket of Eq. 4.4.13 to get

$$(1-\alpha)\ \frac{D_\ell \rho_\ell}{D\tau} = (1-\alpha)\left[\left(\frac{\partial \rho_\ell}{\partial p}\right)_u\right] \frac{d\langle p\rangle_{syst}}{d\tau} + \frac{1}{\rho_\ell} \left\{(1-\alpha)\ q'''_\ell - \nabla \cdot \left[(1-\alpha)\ \vec{q}_\ell\right] - \Gamma_v\ (h_g - h_\ell)\right\} \left(\frac{\partial \rho_\ell}{\partial u}\right)_p \tag{4.4.15}$$

Equation 4.4.15 is valid for general conditions in the liquid. For saturated liquid, $\rho_\ell = \rho_f(p)$ and

$$(1-\alpha)\ \frac{D_\ell \rho_\ell}{D\tau} = (1-\alpha)\ \rho'_f \frac{d\langle p\rangle_{syst}}{D\tau}\ , \text{ saturation}\ . \tag{4.4.16}$$

For the subcooled liquid without vapor (downcomer, lower plenum, recirculation loop under normal operation), Eq. 4.4.15 reduces with $\alpha = 0$ and $\Gamma_v = 0$ to

$$\frac{D_\ell \rho_\ell}{D\tau} = \left(\frac{\partial \rho_\ell}{\partial p}\right)_u \frac{d\langle p\rangle_{syst}}{d\tau} - \frac{1}{\rho_\ell} \left(\frac{\partial \rho_\ell}{\partial u}\right)_p \left[\nabla \cdot \vec{q}_\ell - q'''_\ell\ (1-\alpha)\right]. \tag{4.4.17}$$

With these results we distinguish for later use three forms of Eq. 4.4.9; namely,

<u>for pure liquid</u>, upstream of boiling incipience, in lower plenum, downcomer and recirculation loops

$$\nabla \cdot \vec{j}_\ell = \frac{1}{\rho_\ell^2} \left(\frac{\partial \rho_\ell}{\partial u}\right)_p \left[\nabla \cdot \vec{q}_\ell - q'''_\ell\right] - \frac{\left(\frac{\partial \rho_\ell}{\partial p}\right)_u}{\rho_\ell} \frac{d\langle p\rangle_{syst}}{d\tau}\ , \tag{4.4.18}$$

for the two-phase mixture of saturated vapor and nonequilibrium liquid, in the core downstream of boiling incipience and, during system pressure fluctuations in the upper plenum, riser, separator and steam dome

$$\nabla \cdot \vec{j}_m = \left[\frac{\rho_\ell - \rho_g}{\rho_\ell \rho_g} + \left(\frac{\partial \rho_\ell}{\partial u}\right)_p \frac{h_g - h_\ell}{\rho_\ell^2}\right] \Gamma_v - \left\{\alpha \frac{\rho_g'}{\rho_g} + (1-\alpha) \frac{\left(\frac{\partial \rho_\ell}{\partial p}\right)_u}{\rho_\ell}\right\} \frac{d\langle p\rangle_{syst}}{d\tau}$$

$$+ \frac{1}{\rho_\ell^2} \left(\frac{\partial \rho_\ell}{\partial u}\right)_p \left\{\nabla \cdot \left[(1-\alpha)\, \vec{q}_\ell\right] - (1-\alpha)\, q_\ell'''\right\}, \qquad (4.4.19)$$

and for the two-phase mixture at saturation

$$\nabla \cdot \vec{j}_m = \frac{\rho_\ell - \rho_g}{\rho_\ell \rho_g} \Gamma_g - \left[\alpha \frac{\rho_g'}{\rho_g} + (1-\alpha) \frac{\rho_f'}{\rho_f}\right] \frac{d\langle p\rangle_{syst}}{d\tau} . \qquad (4.4.20)$$

Notice that the equilibrium vapor generation rate Γ_g in Eq. 4.4.20 can be computed from the mixture energy and two phasic mass conservation equations. The result consists of two contributions, one from wall heating and the other from flashing. The latter is proportional to $d\langle p\rangle_{syst}/d\tau$. However, the RAMONA-3B code does not utilize this relation; it therefore cannot achieve and maintain saturation conditions exactly.

This completes the discussion of the four fundamental equations used in this report as a basis for presenting the field equations of RAMONA-3B; namely, Eqs. 4.4.1, 4.4.4, 4.4.6 and 4.4.9 in either of the three forms of Eqs. 4.4.18, 4.4.19 or 4.4.20. Additional simplifying assumptions are used in RAMONA-3B. These will be pointed out as the ordinary differential equations are derived from the above equations in Sections 4.4.3, 4.4.4 and 4.4.5. The governing equations for single-phase vapor in the steam lines are presented in Subsection 4.4.5.5, that for boron transport in Subsection 4.4.6.

4.4.2 Constitutive Equations for Coolant

The integration of Eqs. 4.4.1, 4.4.4, 4.4.6 and 4.4.18 through 4.4.20 requires the specification of constitutive relations for heat transfer ($\bar{h}_c$), wall shear (f_ℓ and ϕ_ℓ^2) and form losses (ζ), vapor generation rate (Γ_v), slip ratio (S) and thermophysical and transport properties for the vapor and liquid phases. These constitutive relations are presented below.

4.4.2.1 Heat Transfer from Cladding Surface to Coolant

The RAMONA-3B code accounts for four heat transfer regimes (cf. Assumption 4-xi), namely

a) turbulent forced convection in single-phase liquid,
b) nucleate boiling,
c) transition boiling and
d) stable film boiling.

We present below first the criteria by which the RAMONA-3B code determines the local, instantaneous heat transfer regime, and then the heat transfer correlations for $\overline{h}_c$ in Eq. 4.4.5, one for each heat transfer regime.

4.4.2.1.1 Transition Criteria Between Heat Transfer Regimes

The Transition from Nonboiling to Nucleate Boiling Heat Transfer Regimes is the boiling incipience (onset of vapor generation). The RAMONA-3B code has two conflicting criteria to predict boiling incipience, none of which is mechanistically related to boiling incipience. The first criterion is embedded in the calculation of the vapor generation rate, Γ_v. In RAMONA-3B, the vapor generation rate Γ_v is predicted to be negative for large liquid subcooling ($t_{sat} - t_\ell$) in single-phase liquid (α=0), as is normally encountered in the lowest core section. As the flow progresses upward, the vapor generation rate Γ_v is computed to increase with decreasing liquid subcooling, until Γ_v passes through zero and becomes positive. Negative values of Γ_v are suppressed in RAMONA-3B, while α=0. Therefore, RAMONA-3B defines, through its first criterion, boiling incipience to occur when and where

$$\Gamma_v = 0 \quad \text{with} \quad \alpha = 0 \quad \text{and} \quad \partial\alpha/\partial z > 0 \ . \tag{4.4.21}$$

As will be shown in Section 4.4.2.3, the condition of Eq. 4.4.21 is dominated by a single, "tunable" parameter, C_{11}, which is involved in the calculation of the bulk evaporation/condensation rate. This parameter depends upon flow channel geometry and operating conditions.

The second criterion in RAMONA-3B, affecting boiling incipience, is associated with the switch from non-boiling to nucleate boiling heat transfer regimes. The RAMONA-3B code computes the outer fuel cladding temperature $t_c(R_{co})$, at radius $r = R_{co}$, twice (according to Eq. 6.3.34 in Section 6.3, using $t_{f\ell} = t_\ell$). The first calculation is performed with the heat transfer coefficient $(\overline{h}_c)_{FC}$ for forced convection in single-phase liquid flow, the second calculation is performed with $(\overline{h}_c)_{NB}$ of nucleate boiling. From the two resultant values for the wall temperature $t_c(R_{co}) = t_w$, the lower one is chosen by RAMONA-3B, as shown on the lower section of the boiling curve in Figure 4.2. Notice that the lower value of the cladding surface temperature t_w is associated with the larger of two values of wall heat flux (cf. Eq. 6.3.17).

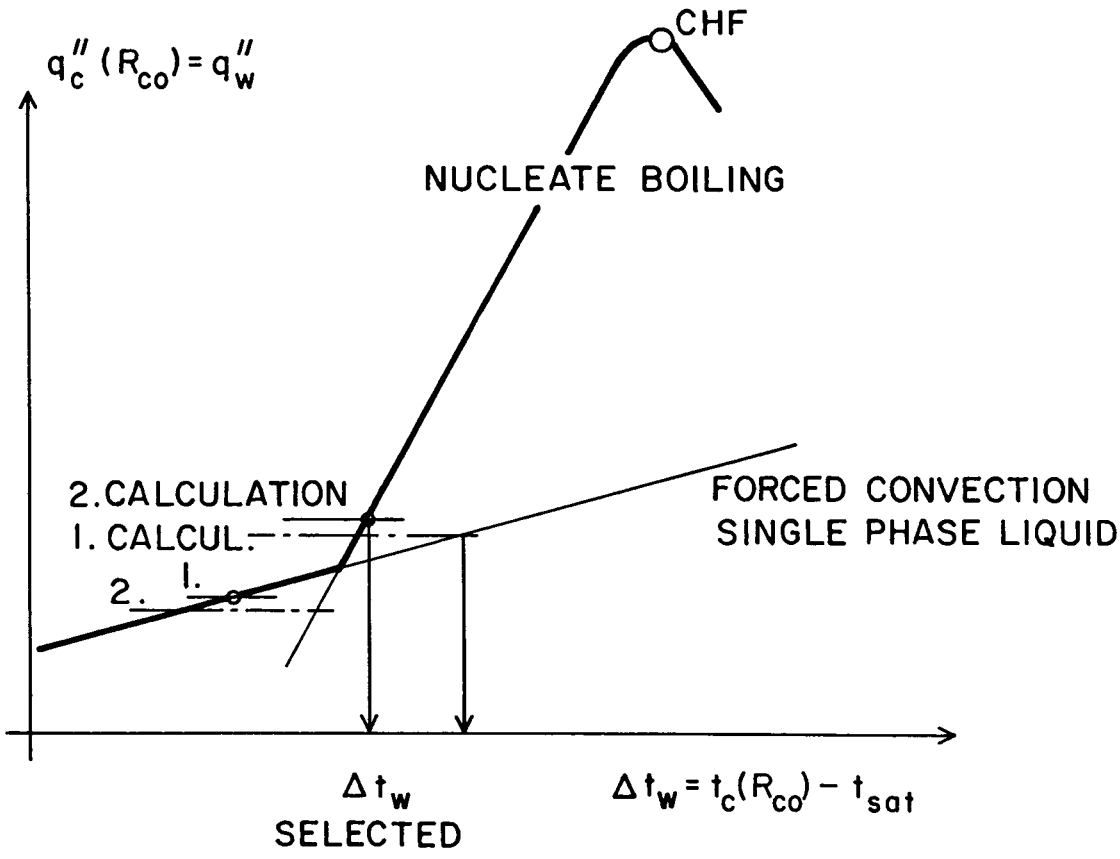

Figure 4.2 Schematic for Criterion of Transition from Nonboiling to Nucleate Boiling Heat Transfer Regimes

Since neither the single-phase, nonboiling, nor the nucleate boiling heat transfer correlations used in RAMONA-3B have been derived to contain information on nonequilibrium boiling incipience, it must be concluded that the intersection of the two lines in Figure 4.2 has no mechanistic relation to boiling incipience. More importantly, there is no mechanism to synchronize the first with the second criterion for boiling incipience. Also, it is possible, in principle, that RAMONA-3B employs nucleate boiling heat transfer correlations when the wall temperature $t_w = t_c(R_{co})$ is below saturation temperature t_{sat}. It is recommended, therefore, to improve the RAMONA-3B code by introducing a single criterion for subcooled boiling incipience (Saha and Zuber 1974) and by subordinating the calculations of vapor generation rate Γ_v, wall heat flux $q''_c(R_{co})$ and cladding surface temperature $t_c(R_{co})$ or heat transfer coefficient $\bar{h}_c$, all to the same criterion.

The Transition from Nucleate to Post-CHF Boiling occurs when and where the wall superheat temperature $\Delta t_w = t_c(R_{co}) - t_{sat}$ reaches Δt_{CHF}, the value associated with the critical heat flux q''_{CHF}.

The wall superheat temperature Δt_w is obtained by subtracting the saturation temperature from the surface temperature $t_c(R_{co})$, computed with the heat transfer coefficient $(\bar{h}_c)_{NB}$ of nucleate boiling (cf. Eqs. 3.4.10 and 6.3.34)

$$\Delta t_w = [t_c(R_{co}) - t_{sat}] \ . \tag{4.4.22}$$

The critical wall superheat temperature is obtained by computing first q''_{CHF} from

$$q''_{CHF} = \left(q''_{CHF}\right)_1^{\tilde{\nu}} \left(q''_{CHF}\right)_2^{1-\tilde{\nu}} , \quad \text{for} \quad 0 \le \tilde{\nu} = \frac{G_m}{100 \ \frac{kg}{m^2 s}} \le 1 \tag{4.4.23}$$

$$q''_{CHF} = \left(q''_{CHF}\right)_1 , \quad \text{for} \quad \tilde{\nu} > 1 \tag{4.4.24}$$

and then by computing

$$\Delta t_{CHF} = \frac{q''_{CHF}}{(\bar{h}_c)_{NB}} \ . \tag{4.4.25}$$

In Eq. 4.4.23, G_m denotes the mixture mass flux, and

$$\left(q''_{CHF}\right)_1 = 4.44 \times 10^8 \ \frac{W}{m^2} \ \frac{\left[7.37 \times 10^{-4} \ \frac{m^2 s}{kg} \cdot G_m\right]^{0.1775 \ \ln(1+x)}}{(1+x)^{3.3906} \left[\frac{p}{N m^{-2}}\right]^{0.3234}} \tag{4.4.26}$$

is the critical heat flux for high mass fluxes, $1 \leq \tilde{v} \leq 40$, according to Condie and Bengston (1978, p. 9). The symbols x and p in Eq. 4.4.26 denote flow quality, $x = G_v/G_m$, and pressure, respectively. Equation 4.4.26 is claimed to hold for $-0.1 < x < 1.0$ and $60 < p < 150$ bar. In Eq. 4.4.23

$$\left(q''_{CHF}\right)_2 = 0.1309\,(1-\alpha)\,h_{fg}\sqrt{\frac{\rho_\ell\,\rho_g}{\rho_\ell+\rho_g}}\sqrt{g\sigma\,(\rho_\ell-\rho_g)} \qquad (4.4.27)$$

is the critical heat flux as derived by Smith and Griffith (1976) from the pool boiling correlation by Zuber (1961), and reported by Delhaye, Giot and Riethmuller (1981, p. 282). The symbols α, ρ_ℓ, ρ_g, σ and h_{fg} stand for vapor void fraction, densities of liquid and vapor, surface tension and latent heat of evaporation, respectively. The heat transfer coefficient $(\bar{h}_c)_{NB}$ is computed from Eq. 4.4.33 below.

Having computed Δt_w from Eq. 4.4.22 and Δt_{CHF} from Eq. 4.4.25, the RAMONA-3B code continues to compute heat transfer in the nucleate boiling regime if $\Delta t_w < \Delta t_{CHF}$, but it advances to the transition boiling regime (cf. Assumption 4-x) if $\Delta t_w \geq \Delta t_{CHF}$. The RAMONA-3B heat transfer model implies also post-CHF conditions, namely transition or stable film boiling conditions, as long as $\Delta t_w \geq \Delta t_{CHF}$.

As the wall superheat temperature increases beyond Δt_{CHF}, the RAMONA code implies that transition boiling prevails until the wall superheat reaches the minimum value Δt_{MSFB} of stable film boiling (cf. Assumption 4-x). In Figure 4.3, this means that the heat flux should decrease along the transition boiling segment of the boiling curve, starting from point CHF and dropping toward the point MSFB. Notice that the cladding temperature rises rapidly by more than 100°C as it approaches the rising fuel pellet outer surface temperature. The thermal cladding response time is approximately fifty milliseconds. Consequently, there may be circumstances under which the heat flux from the cladding surface may be greater after burnout than that corresponding to steady-state transition boiling. After burnout, the relation between wall superheat temperature Δt_w and wall heat flux q''_w may correspond to the path from point CHF to point A (typically) in Figure 4.3, rather than to the path from point CHF to point MSFB. As pointed out in the assessment of Assumption (4-x) (see Section 4.3.2), the heat transfer coefficient $\bar{h}_c$ (Eq. 4.4.5) computed for transition boiling may be too high in RAMONA-3B immediately after burnout and may affect predictions of boiling instability.

The Transition from Transition to Stable Film Boiling occurs when the rising wall superheat temperature $(t_c(R_{co}) - t_{sat} = t_w - t_{sat} = \Delta t_w)$ equals or exceeds the minimum value of wall superheat temperature Δt_{MSFB} for stable film boiling. The minimum stable film boiling wall superheat temperature is computed from the correlation by Henry, Quinn and Spleha (1974):

$$\Delta t_{MSFB} = (t_{HN} - t_{sat}) + \sqrt{\frac{(\rho ck)_\ell}{(\rho ck)_c}}\,(t_{HN} - t_\ell)\,, \qquad (4.4.28)$$

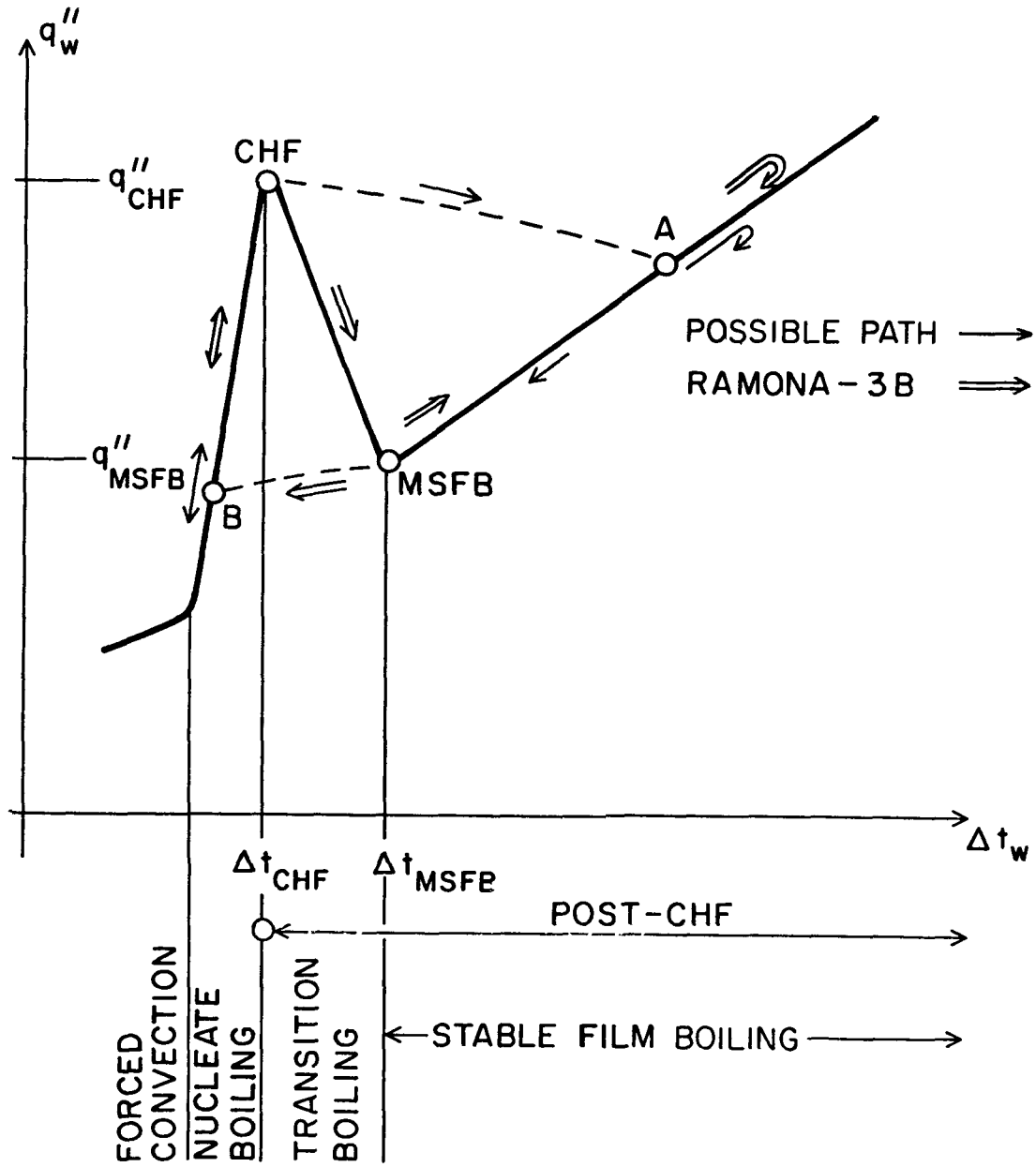

Figure 4.3 Schematic Boiling Curve and Boiling Regimes (Fixed Mass Flux, Quality and Pressure)

where t_{sat}, t_ℓ, c, k and ρ designate saturation and liquid temperatures, specific heat (at constant pressure), thermal conductivity and density, respectively. Subscripts ℓ and c denote liquid and cladding, respectively, and

$$t_{HN} = 312.66\,C + 1.99519 \times 10^{-21}\,C^{-7}\,(t_{sat} + 273.15\,C)^8 \qquad (4.4.29)$$

is the homogeneous nucleation temperature according to Lienhard (1976). All temperatures are centigrade temperatures in Eq. 4.4.29.

Returning to Figure 4.3, the point MSFB of Minimum Stable Film Boiling represents also the minimum possible heat flux q''_{MSFB} for transition boiling. Any decrease in heat flux q''_w below q''_{MSFB} leads to the prompt return to nucleate boiling, along the path from point MSFB to point B. Also, any decrease in wall superheat temperature Δt_w below Δt_{MSFB} leads in general abruptly to nucleate boiling, unless the conductive heat flux in the cladding increases exactly to balance the external convective flux along the curve from point MSFB toward the point CHF. The post-CHF heat transfer models in RAMONA-3B imply the heat transfer coefficients $\bar{h}_c$ (Eq. 4.4.5) for transition boiling whenever $\Delta t_{CHF} < \Delta t_w < \Delta t_{MSFB}$, regardless of heat flux q''_w (cladding temperature gradient at the surface). As pointed out in Section 4.3.2 [cf. Assumption (4-x)], RAMONA-3B may temporarily underpredict the heat transfer coefficient for $q''_w < q''_{MSFB}$ and $\Delta t_{CHF} < \Delta t_w < \Delta t_{MSFB}$.

In summary, it should be pointed out that RAMONA-3B predicts the occurrence of burnout correctly in accordance with the nucleate boiling heat transfer correlation (Jens-Lottes, Eq. 4.33) and the criterion for critical heat flux (Eq. 4.4.23). The RAMONA-3B predictions may not be accurate during some portions of boiling instability simulations, namely during the intervals when post-CHF conditions occur, and when the return occurs from stable film boiling to nucleate boiling.

Any further improvement of post-CHF heat transfer modeling in RAMONA-3B, particularly the modeling of the hysteresis effects between the points CHF and A or MSFB and B in Figure 4.3 requires direct coupling of hydraulics calculations with thermal conduction calculations which is not available in RAMONA-3B at this time (see Sections 6.1 and 6.7.3).

4.4.2.1.2 Heat Transfer Correlations

a) For Forced Convection in Single-Phase Liquid RAMONA-3B employs the Dittus-Boelter (1930) correlation for heating, which is valid ($\approx \pm$ 20%) for turbulent flow, $N_{Re} > 3000$:

$$(\bar{h}_c)_{FC} = \frac{k_\ell}{d_h} \cdot N_{Nu} = \frac{k_\ell}{d_h}\left[0.023\, N_{Re}^{0.8}\, N_{Pr}^{0.4}\right]_\ell , \qquad (4.4.30)$$

where k_ℓ and d_h stand for the thermal conductivity of liquid and for the hydraulic diameter for heat transfer (four times the flow cross-sectional area A, divided by the heated perimeter ξ), respectively. N_{Nu} represents the Nusselt

number and N_{Re} the Reynolds number

$$N_{Re} = \frac{G_m d_h}{\mu} , \qquad (4.4.31)$$

while N_{Pr} denotes the Prandtl number

$$N_{Pr} = \frac{\mu c_p}{k} . \qquad (4.4.32)$$

In Eqs. 4.4.31 and 4.4.32, $G_m = G_\ell$, μ and c_p denote the mass flux, the dynamic viscosity and the specific heat at constant pressure. As Eq. 4.4.30 applies to the pure liquid flow, all properties are those of liquid; they are evaluated at the mean fluid temperature t_ℓ (cf. Eq. 4.4.80).

b) For Nucleate Boiling, RAMONA-3B employs the correlation by Jens and Lottes (1951)*

$$(\bar{h}_c)_{NB} = \frac{q''_{NB}}{\Delta t_w} = 2.555 \frac{W}{m^2 C^4} e^{6.45 \times 10^{-7} m^2/N) p} \Delta t_w^3 , \qquad (4.4.33)$$

where

$$\Delta t_w = [t_c (R_{co}) - t_{sat}] = t_w - t_{sat} \qquad (4.4.34)$$

is the wall superheat temperature, the difference between the cladding surface temperature t_c at the outer cladding radius $r = R_{co}$ and the saturation temperature. Equation 4.4.33 holds for 34 bar $\leq p \leq$ 138 bar. (Tong and Weisman 1970, p. 201).

c) Transition Boiling is computed in RAMONA-3B with the heat transfer coefficient $(\bar{h}_c)_{TB}$

$$(\bar{h}_c)_{TB} = \frac{(q''_w)_{TB}}{\Delta t_w} , \quad \Delta t_{CHF} < \Delta t_w < \Delta t_{MSFB} , \qquad (4.4.35)$$

where $(q''_w)_{TB}$ is interpolated from (Bjornard and Griffith, 1977)

$$(q''_w)_{TB} = \vartheta\, q''_{CHF} + (1-\vartheta)\, q''_{MSFB} , \qquad (4.4.36)$$

*The RAMONA code has 2.567 $Wm^{-2}C^{-4}$ instead of 2.555 $Wm^{-2}C^{-4}$ as obtained from the original correlation.

with the interpolant

$$\vartheta = \left[(\Delta t_{MSFB} - \Delta t_w) \Big/ (\Delta t_{MSFB} - \Delta t_{CHF})\right]^2 . \qquad (4.4.37)$$

In Eq. 4.4.36, q''_{CHF} is as defined by Eq. 4.4.23, while q''_{MSFB} is computed from Eqs. 4.4.28 and 4.4.38 below, namely

$$q''_{MSFB} = (\bar{h}_c)_{FB}\Big|_{\Delta t_{MSFB}} \cdot \Delta t_{MSFB} . \qquad (4.4.38)$$

In Eq. 4.4.37, Δt_{MSFB} and Δt_{CHF} are defined by Eqs. 4.4.28 and 4.4.25, respectively. There is no assessment of the above relation, Eq. 4.4.36, for BWR applications. However the relation is adequate because this regime occurs rarely, if at all in BWRs.

d) For Stable Film Boiling, RAMONA-3B employs the larger of two heat transfer coefficients

$$(\bar{h}_c)_{FB} = \text{Max}\left\{(\bar{h}_c)_{G\,5.9}, (\bar{h}_c)_{MB}\right\} . \qquad (4.4.39)$$

The first one is computed from the Groeneveld 5.9 correlation (Groeneveld 1968):

$$(\bar{h}_c)_{G\,5.9} = 3.27 \times 10^{-3} \frac{k_g}{h_d} (N_{Pr})_g^{1.32} \left\{(N_{Re})_g \left[x+(1-x)\frac{\rho_g}{\rho_f}\right]\right\}^{0.901} Y_M^{-1.5}, \qquad (4.4.40)$$

where

$$Y_M = 1 - 0.1\left[(1-x)\left(\frac{\rho_f}{\rho_g} - 1\right)\right]^{0.4} \qquad (4.4.41)$$

is the Miropolskiy two-phase flow factor, x, ρ, k and d_h denote flow quality, density, thermal conductivity and hydraulic diameter for heating, respectively. The subscripts g and f denote saturated vapor and liquid, respectively. N_{Pr} and N_{Re} are the Prandtl and Reynolds numbers, respectively:

$$N_{Pr} = \frac{\mu\, c_p}{k} \quad \text{and} \quad N_{Re} = \frac{G_m\, d_h}{\mu} . \qquad (4.4.31,32)$$

As before, μ, c_p, and k are dynamic viscosity, specific heat at constant pressure and thermal conductivity, respectively. G_m is the mass flux of the mixture.

The second heat transfer coefficient in Eq. 4.4.39 is computed in accordance with the modified Bromley correlation, using Andersen's analytically derived critical wavelength λ_c, as reported by Delhaye, Giot and Riethmuller (1981, pp. 273-275):

$$(\bar{h}_c)_{MB} = 0.62 \left\{ \frac{g \rho_g (\rho_\ell - \rho_g) h_{fg} k_g^3}{\lambda_c \mu_g \Delta t_w} \right\}^{1/4} , \qquad (4.4.42)$$

where

$$\lambda_c = 16.24 \left\{ \frac{\sigma^4 h_{fg}^3 \mu_g^5}{\rho_g (\rho_\ell - \rho_g) k_g^3 g^5 \Delta t_w^3} \right\}^{1/11} \qquad (4.4.43)$$

and the symbols g, ρ, h_{fg}, k, μ and σ represent, as before, gravitational acceleration, density, latent heat of evaporation, thermal conductivity, dynamic viscosity and surface tension, respectively. The wall superheat temperature Δt_w is computed from $\Delta t_w = t_w - t_{sat}$ and Eqs. 4.4.69 and 6.3.34. An assessment of Eqs. 4.4.40 through 4.4.43 can be found in Delhaye, Giot and Riethmuller (1981, Chap. 14). The data base for Eqs. 4.4.40 and 4.4.41 is

flow quality	$-0.1 < x < 0.9$
pressure	$34 < p < 215$ bar
mass flux	$700 < G_m < 5{,}300$ kg/(m^{2}s).

The data base for Eqs. 4.4.42 and 4.4.43 is

liquid subcooling temperature	$\Delta t_\ell < 77.9$ C
void fraction	$\alpha < 0.4$
mixture velocity	$v_m < 0.3$ m/s
pressure	$1 < p < 7$ bar
heat flux	$30 < q''_w < 130$ kw/m^2.

e) The Overall Heat Transfer Coefficient $\bar{U}_{1b}$ for computing the exchange of heat from the heated channels to the bypass channels (see Eq. 4.4.5) is a user-specified* constant in RAMONA-3B (cf. Assumption xi). Currently, RAMONA-3B has

$$\bar{U}_{1b} = 3100 \text{ W m}^{-2} \text{ C}^{-1} .$$

*HTC on Input Data Card No. 200 015.

4.4.2.2 Wall Shear and Form Losses

The RAMONA-3B code accommodates only turbulent forced convection in the prediction of wall shear in single-phase liquid and two-phase mixtures [cf. Assumption (4-xi)]. The wall shear prediction enters into the thermohydraulics models through the momentum conservation equation, Eq. 4.4.6, via two parameters, the single-phase friction factor f_ℓ and the two-phase multiplier ϕ_ℓ^2 (see Section 4.4.1 for Eq. 4.4.6).

The single-phase flow friction factor is computed in RAMONA-3B from

$$f_\ell = \frac{C_7}{\left(N_{Re}\right)^{C_8}} \qquad 3{,}000 < N_{Re} < 100{,}000 \ , \tag{4.4.44}$$

where C_7 and C_8 are user-specified* constants. Recommended are, according to Blasius (1913), the following two values for C_7 and C_8:

$$C_7 = 0.3164 \tag{4.4.45}$$

$$C_8 = 0.25 \tag{4.4.46}$$

These represent turbulent flows in smooth tubes in the range $3000 < N_{Re} < 100{,}000$. The Reynolds number N_{Re} is defined by Eq. 4.4.31.

The two-phase flow friction multiplier ϕ_ℓ^2 is computed in RAMONA-3B according to the correlation by Becker, Hernborg and Bode (1962).

$$\phi_\ell^2 = 1 + C_9 \left[\frac{x}{1 \frac{m^2}{N} \cdot p} \right]^{0.96} \tag{4.4.47}$$

where

$$C_9 = 1.49 \times 10^8$$

is a user-specified constant,** and x is the flow quality

$$x = \frac{G_g}{G_m} \ . \tag{4.4.48}$$

The correlation in Eq. 4.4.47 has been derived for typical BWR applications.

Form Losses account for the dissipation of kinetic energy in the coolant at locations of abrupt expansions and contractions in cross-sectional area, A.

*G1 and G2 on Data Input Card No. 500 010.

**CRT(1) = 2400 on Input Data Card No. 500 050, used with p converted from atmospheres to N/m^2.

They account indirectly for the forces exerted by the flow channel on the coolant fluid, and play an important role in coupling the momentum balances, Eq. 4.4.6, of two contiguous flow channel segments, each one having a constant but distinct cross-sectional area (cf. Eq. 4.4.102).

The loss coefficient ξ_{12} for the coolant flow from the exit of segment 1 to the entrance of segment 2 (typically) in Figure 4.4 below is normally defined and experimentally obtained through the use of the mechanical energy balance, derived as a jump condition for the interface between the segments. For two-phase flow the definition is

$$p_1 + \frac{1}{2}\left[G_\ell w_\ell + G_g w_g\right]_1 = p_2 + \frac{1}{2}\left[G_\ell w_\ell + G_g w_g\right]_2 + \xi_{12}\frac{1}{2}\left[G_\ell w_\ell + G_g w_g\right]_{A_{min}}, \tag{4.4.49}$$

where p, G, w denote pressure, mass flux and velocity, the subscripts ℓ and v designate liquid and vapor, and the subscript A_{min} indicates that the loss coefficient is defined as the fraction of dissipated kinetic energy relative to the kinetic energy in the narrower cross section (always finite). The loss coefficient depends for single-phase flow upon the direction of the flow, on the geometry of the transition and, most importantly on the area ratio, A_1/A_2, as well as on the Reynolds number. Single-phase flow loss coefficients are collected in handbooks on hydraulics. Idel'chik is recommended for a large number of geometries. Two-phase flow loss coefficients are not available at this time and must be approximated by single-phase loss coefficients.

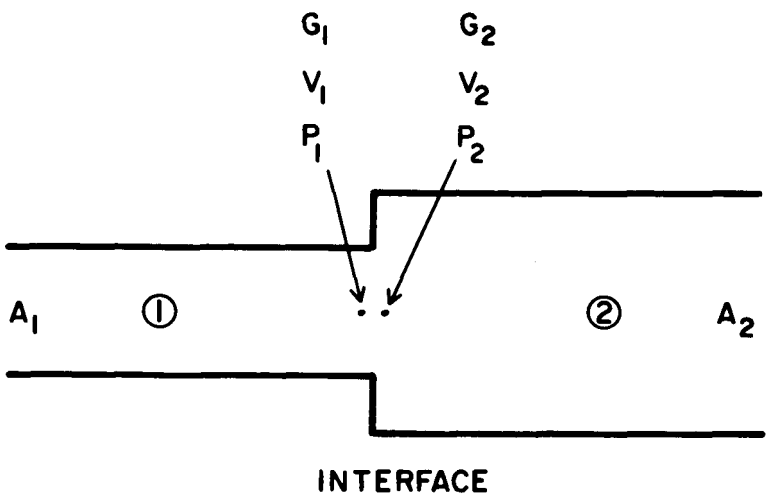

Figure 4.4 Nomenclature for Definition of Form Loss Coefficient

In the RAMONA-3B code, the loss coefficient is defined differently from the standard definition (cf. Assumption (4-xii)), namely, by $C_{10} = \zeta$ through

$$p_1 - p_2 = C_{10}\left[G_\ell|w_\ell| + G_g|w_g|\right]_{A_{min}} . \qquad (4.4.50)$$

The parameter C_{10} is specified by the user,* one parameter for every abrupt change in cross-sectional area. The consequences arising from the nonstandard definition for the loss coefficient are discussed in Section 4.3.2 (cf. Assumption (4-xii)).

4.4.2.3 Vapor Generation Rate

The RAMONA-3B code is designed to account for thermal disequilibrium to the extent that the liquid phase in the two-phase mixture is allowed to be subcooled ($t_\ell < t_{sat}$), saturated ($t_\ell = t_{sat}$) or superheated ($t_\ell > t_{sat}$) while the vapor phase is restricted to saturation conditions ($t_v = t_g = t_{sat}$) (cf. Assumption 4-ii). The temperature, t_ℓ, of the liquid in two-phase mixture is entirely dictated by the calculation for the nonequilibrium vapor generation rate Γ_v. The capability of RAMONA-3B to compute nonequilibrium evaporation and condensation rates Γ_v (under some conditions, see Assumptions (4-ix, x and xi)) is one of its strongest attributes, since Γ_v has a strong and direct impact on the predictions of vapor voids (cf. Eqs. 4.4.1 and 4.4.1.9) and hence of reactivity feedback and fission power generation.

In RAMONA-3B, the vapor generation rate Γ_v is computed in two parts

$$\Gamma_v = \Gamma_w + \Gamma_{ph} . \qquad (4.4.51)$$

The first part, Γ_w, accounts for evaporation due to heat transfer from the wall to the liquid phase, the second part, Γ_{ph}, accounts for mass transfer (evaporation or condensation) due to heat transfer between the phases.

Evaporation from wall heating is predicted in RAMONA-3B on the basis of a model for cyclic ejection of vapor ($\dot{V}_g^+ \delta\tau$) and liquid ($\dot{V}_\ell^+ \delta\tau$) from the boundary layer at the heated wall, followed by the return of cooler liquid ($\dot{V}_\ell^- \delta\tau$) from the bulk of the flow to the boundary layer. This cycle is repeated with the (unimportant) period of $\delta\tau$. The symbol $\dot{V}$ denotes the volumetric exchange rate, averaged over the period $\delta\tau$. The model implies evaporation only and

(i) a steady process on a time-scale larger than the period $\delta\tau$ (no storage of mass or energy),

(ii) imcompressible phases,

(iii) $\dot{V}_g^+ - \dot{V}_\ell^- = 0$, and

*VH(I) on Input Data Card No. 200013 and following cards.

(iv) that the liquid leaving the heated boundary layer has the temperature equal to the arithmetic mean between wall surface and saturation temperatures.

By setting up the mass and energy balances for the boundary layer segment within any axial increment Δz (in bulk flow direction)

$$\rho_g \dot{V}_g^+ + \rho_\ell (\dot{V}_\ell^+ - \dot{V}_\ell^-) = 0 \tag{4.4.52}$$

$$\rho_g h_g \dot{V}_g^+ + \rho_\ell (h_\ell^+ \dot{V}_\ell^+ - h_\ell^- \dot{V}_\ell^-) = \Delta z \, \xi \, q_w'' \, , \tag{4.4.53}$$

and by eliminating $\dot{V}_\ell^-$ from these balance equations, one obtains, using item (iii) above, the evaporation rate $\Gamma_w = \rho_g \dot{V}_g^+/(A \, \Delta z)$:

$$\Gamma_w = \frac{\dfrac{\xi \, q_w''}{A}}{h_g - h_\ell^- + \left(\dfrac{\rho_\ell}{\rho_g} - 1\right)(h_\ell^+ - h_\ell^-)} \, . \tag{4.4.54}$$

Here ξ and A denote the heated perimeter and the cross-sectional area, respectively, of the flow channel. The enthalpy differences in Eq. 4.4.54 are replaced by temperature differences, through

$$h_\ell = h_f + c_{p,\ell} (t_\ell - t_{sat}) \, , \tag{4.4.55}$$

and Assumption (iv) above is introduced to obtain the final result for the vapor generation rate due to wall heating, with $\xi q_w'' = q_w'$

$$\Gamma_w = \frac{q_w'/A}{h_{fg} + c_{p,\ell} \left[(t_\ell - t_{sat}) \dfrac{\rho_\ell}{\rho_g} + \dfrac{1}{2} (t_w - t_{sat}) \left(\dfrac{\rho_\ell}{\rho_g} - 1 \right) \right]} \, . \tag{4.4.56}$$

In Eq. 4.4.56, q_w' is computed as part of the thermal conduction model for the fuel (cf. Eqs. 4.4.5 and 6.3.34); h_{fg}, $c_{p,\ell}$, t_{sat} and ρ_g are the latent heat of evaporation, the specific heat of saturated liquid at constant pressure and the density of saturated vapor, respectively, all being computed as functions of the system pressure $\langle p \rangle_{syst}$. The wall temperature t_w is the cladding surface temperature $t_c(R_{co})$ in Eq. 6.3.34. The liquid temperature t_ℓ is computed from the local internal energy of the mixture, the vapor mass and the thermal equation of state, using Eq. 4.4.80. The liquid density ρ_ℓ is computed from $\langle p \rangle_{syst}$ and t_ℓ according to Eq. 4.4.76.

Equation 4.4.56 accounts for the energy required for evaporation (h_{fg}) and preheating of the subcooled liquid and for the removal of energy by the liquid which returns from the boundary layer to the bulk. Equation 4.4.56 yields correctly the isobaric equilibrium evaporation rate when $t_w = t_{sat}$ and $t_\ell = t_{sat}$. Equation 4.4.56 does not represent the complete separation of energy from wall heating into the net energy entering the liquid phase and the net energy entering the vapor phase, as it does not account for energy transfer between the phases. This is described by the interphase transfer term Γ_{ph} below. Equation 4.4.56 cannot be expected to apply for condensation when the wall temperature $t_w = t_c(R_{co})$ falls below saturation temperature t_{sat}. Then RAMONA-3B sets $\Gamma_w = 0$.

Mass transfer from interphase heat transfer, represented by the second term on the right-hand side of Eq. 4.4.51, is computed in RAMONA-3B from

$$\Gamma_{ph} = \frac{C_{11} + C_{12}\alpha(1-\alpha)}{h_{fg}} \left[(t_\ell - t_{sat}) + C_{13}\,|t_\ell - t_{sat}|\right] , \qquad (4.4.57)$$

where α, t_{sat}, h_{fg} and t_ℓ are the void fraction (cf. Eq. 4.4.1), saturation temperature (cf. Eq. 4.4.69), latent heat of evaporation (cf. Eq. 4.4.72) and liquid temperature (cf. Eq. 4.4.80), respectively. The parameters C_{11}, C_{12} and C_{13} are user-specified input data* and have the recommended values

$$C_{11} = 5 \times 10^6 \ Wm^{-3}C^{-1} \qquad (4.4.58)$$

$$C_{12} = 4 \times 10^7 \ Wm^{-3}C^{-1} \qquad (4.4.59)$$

$$C_{13} = 0.3 . \qquad (4.4.60)$$

Equation 4.4.57 produces condensation for $t_\ell < t_{sat}$ and evaporation for $t_\ell > t_{sat}$. The parameter C_{13}, $0 \leq C_{13} < 1$, measures the hysteresis between evaporation and condensation. As $\alpha(1-\alpha)$ is proportional to the interfacial area density, it has been claimed that C_{12} can control the interfacial mass transfer rate due to interfacial heat transfer. The parameter C_{11} dictates the incipience of boiling (once C_{13} is fixed, of course, but C_{13} has no strong effect on boiling incipience). According to Eq. 4.4.21, boiling starts when

$$\Gamma_w - C_{11}(1 + C_{13})(t_{sat} - t_\ell) = 0 , \qquad (4.4.61)$$

where Γ_w is given by Eq. 4.4.56. Hence the product $C_{11}(1+C_{13})$ is the only "tunable" parameter that defines the liquid subcooling $(t_{sat} - t_\ell)$ at which boiling starts for a given wall superheat temperature $(t_w - t_{sat})$ and a given heating rate q_w.

Equation 4.4.57 is not a mechanistic model for interphase mass transfer due to interphase heat transfer: there exists no universal parameter triplet $\{C_{11}, C_{12}, C_{13}\}$ that can represent all possible conditions in a BWR reactor core. The three parameters C_{11}, C_{12} and C_{13} have, and can be expected, to provide sufficient freedom of adjustment to fit any steady-state experimental

*R_0, R_1 and k, respectively, on Input Data Card No. 500030.

data. The model performs less reliably during pressure fluctuations (flashing and recondensing). The model produces unrealistically high liquid superheating ($\approx$ 1-2°C) under steady-state boiling at high void fractions. It is not possible to produce equilibrium phase change under conditions (adiabatic flow with pressure oscillations of $\sim$1 Hz or less) where equilibrium conditions have been observed.

Rates of vapor generation in the post-CHF regime are computed in RAMONA-3B according to

$$\Gamma_v = \frac{1}{(h_g - h_\ell)} \left[- (1-\alpha)\, \rho_\ell \left(\frac{\partial h_\ell}{\partial \tau} + w_\ell \frac{\partial h_\ell}{\partial z} \right) + \left(\frac{q'_w}{A} + q'''_\ell\, (1-\alpha) \right) \right] \qquad (4.4.62)$$

where q'_w is the wall heating from fuel and channel boxes (see Eq. 4.4.5), and q'''_ℓ is the heat generated due to gamma-ray attenuation and neutron slowdown.

The above expression was derived from the liquid mass conservation equation, Eq. 4.4.2, and the following liquid thermal energy equation:

$$\frac{\partial}{\partial \tau} \left[(1-\alpha)\, \rho_\ell\, h_\ell \right] + \frac{\partial}{\partial z} \left[(1-\alpha)\, \rho_\ell\, w_\ell\, h_\ell \right] = \frac{q'_w}{A} + q'''_\ell\, (1-\alpha) - \Gamma_v h_g \ . \qquad (4.4.63)$$

Assumptions (4-i) through (4-iii, v and vi) discussed in Section 4.3.1 were used to obtain Eq. 4.4.63. In addition, the term $(1-\alpha) \frac{\partial p}{\partial \tau}$ has been neglected since its magnitude is less than 3% of $(1-\alpha)\, \rho_\ell \frac{\partial h_\ell}{\partial \tau}$ at 70 bar. Notice that since the vapor phase in RAMONA-3B is always restricted to be at saturation (Assumption (4-ii)), the vapor enthalpy change is small and the entire wall heat flux is assumed to enter the liquid. In reality, most of the wall heat flux would be transferred through superheated vapor to the liquid while in the post-CHF regime.

The post-CHF vapor generation model, i.e., Eq. 4.4.62, has been implemented such that the superheated liquid reaches saturation in a single calculational time step and thermal equilibrium is maintained thereafter.

4.4.2.4 Slip Correlations

The RAMONA-3B code is designed to account for nonhomogeneous two-phase flow (cf. Assumption (4-xii)): the liquid and the vapor phases are allowed to have different velocities.

The vapor velocity v_g is related in the RAMONA-3B code to the liquid velocity v_ℓ through

$$w_g = S w_\ell + w^o \ . \qquad (4.4.64)$$

The RAMONA-3B code has three options for computing the slip ratio S, the Bankoff-Malnes correlation (Malnes, 1977), the Bankoff-Jones correlation (Jones and Dight, 1962) and the Solberg (1967) correlation. The Bankoff-Malnes correlation is recommended; the Bankoff-Jones correlation overpredicts the slip ratio at void fractions above α=0.5. For the Solberg correlation, there is no adequate data base.

The Bankoff-Malnes correlation as used in RAMONA-3B is

$$S = \frac{1-\alpha}{C_{14} - \alpha} \qquad \text{for } \alpha \leq C_{14} - 0.02 \qquad (4.4.65a)$$

and

$$S = 50 \left[1.02 - C_{14} + 50\,(\alpha - C_{14} + 0.02)(1-C_{14})\right] \qquad \text{for } \alpha > C_{14} - 0.02 \ , \qquad (4.4.65b)$$

where C_{14} is a user-specified* constant. Its recommended value is

$$C_{14} = 0.904 \ . \qquad (4.4.65c)$$

The vapor velocity w^o relative to stagnant liquid is, in conjunction with the Bankoff-Malnes correlation, set** equal to

$$w^o = C_{15} = 0.174 \text{ m/s}. \qquad (4.4.65d)$$

The Bankoff-Jones correlation is

$$S = \frac{1-\alpha}{f(p,\alpha) - \alpha} \ , \qquad (4.4.66a)$$

where

$$f(p,\alpha) = a + (1-a)\,\alpha^b \ , \qquad (4.4.66b)$$

$$a = 0.71 + 1.3119 \times 10^{-8}\ \frac{m^2}{N} \cdot p \qquad (4.4.66c)$$

*CSS(3) on Input Data Card No. 500 020.
**CSS(4) on Input Data Card No. 500 020.

and

$$b = 3.4483 - p\left[2.7194 \times 10^{-8} \frac{m^2}{N} - 1.230 \times 10^{-14} \frac{m^4}{N^2} p\right] . \qquad (4.4.66d)$$

For the Bankoff-Jones correlation, w^o is set equal to zero. Equation 4.4.66 has produced better results than Eq. 4.4.65 in integral, full-scale power plant simulations (turbine trip tests at Peach Bottom 2), but the better agreement is obfuscated by vapor generation and reactivity feedback modeling. An assessment of Eq. 4.4.66 can be found in a paper by Nash (1980). The Bankoff-Jones correlation appears to overpredict the slip ratio at high void fractions ($\alpha > 0.5$); however, the assessment by Nash is affected also by his choice of an evaporation model. Observe that, from Eq. 4.4.66

as

$$\left.\begin{aligned} \frac{1}{a} \le S \le \frac{1}{1-b(1-a)} \\ 0 \le \alpha \le 1 . \end{aligned}\right\} \qquad (4.4.67)$$

The Solberg correlation in RAMONA-3B is

$$\left.\begin{aligned} S &= C_{16} + C_{17}\, \alpha^{C_{18}} \\ w^o &= - C_{19} \frac{\vec{g} \cdot \hat{k}}{g} , \end{aligned}\right\} \qquad (4.4.68)$$

where C_{16}, C_{17}, C_{18} and C_{19} are user-specified* constants, $\vec{g}$ is the gravity vector, g its magnitude and $\hat{k}$ is the unit vector in the direction of the normal flow. We have no recommendations for $C_{16},\ldots,C_{19}$.

4.4.2.5 Thermophysical Properties of Coolant

This subsection presents the thermal and caloric equations of state for liquid and vapor as used in RAMONA-3B. The thermophysical properties as computed with RAMONA-3B have been compared with data (linearly interpolated where necessary) from the VDI Steam Tables (E. Smidt, 1969).** The comparisons are presented in Tables 4.1 and 4.2. The property calculations are deemed to be accurate in the pressure range from 30 to 130 bar and for liquid subcooling of up to 15°C, except the specific heat of liquid (cf. Table 4.1) and the functions depending on specific heat of liquid.

*CSS(I), I=1,...,4 on Input Data Card No. 500 020.

**We could not confirm the 0.1% accuracy for all properties, as claimed by SCANDPOWER.

Table 4.1 RAMONA-3B Computed Saturation Properties, Compared with VDI Steam Table

Pressure (bar)		30	50	70	90	110	130
Saturation Temperature(C)	RAMONA	233.93	263.93	285.77	303.30	318.07	330.87
	VDI	233.84	263.91	285.79	303.31	318.05	330.83
Density of Liquid (kg/m^3)	RAMONA	822.07	777.80	740.19	705.43	671.76	638.04
	VDI	822.17	777.73	740.03	705.27	671.73	638.08
Density of Vapor (kg/m^3)	RAMONA	15.04	25.40	36.55	48.80	62.52	78.23
	VDI	15.01	25.36	36.53	48.79	62.48	78.14
Internal Energy of Liquid*(MJ/kg)	RAMONA	-0.24495	-0.10949	0	0.099619	0.19736	0.29983
	VDI	-0.25315	-0.10983	0	0.093039	0.17632	0.25373
Internal Energy of Vapor*	RAMONA	1.35407	1.33986	1.32304	1.29397	1.29303	1.2846
	VDI	1.33547	1.33011	1.31497	1.29316	1.26625	1.2427
Latent Heat of Evaporation	RAMONA	1.7948	1.6397	1.5060	1.3788	1.2553	1.1306
	VDI	1.7939	1.6397	1.5050	1.3809	1.2587	1.1350
Isobaric Spec. Heat of Liquid ($kJ\ kg^{-1}C^{-1}$)	RAMONA	4.725	5.014	5.326	5.682	6.110	6.648
	VDI	4.732	5.019	5.406	5.850	6.451	7.307
Isobaric Spec. Heat of Vapor† ($kJ\ kg^{-1}C^{-1}$)	RAMONA	3.166	3.615	4.244	5.110	6.314	8.058
	VDI	3.410	4.174	4.601	6.123	7.513	9.597

*Evaluated relative to u_f(70 bar) = 1.2579 MJ/kg.

†Used only for post-CHF heat transfer coefficients.

Table 4.2 RAMONA-3B Computed Properties for Liquid, Compared With VDI Steam Table

		Selected Pressure (bar)			
		25	50	100	150
Saturation Temp (C)		223.94	263.91	310.96	342.13
Selected Temp (C)		200	240	280	320
Density (kg m^{-3})	RAMONA	854.68	797.10	713.52	689.65
	VDI	865.43	815.40	756.37	649.27
Int. Energy* ($MJ\ kg^{-1}$)	RAMONA	-0.39908	-0.22948	-0.03394	0.25253
	VDI	-0.40799	-0.22623	-0.03612	0.17496
Isobaric Spec. Heat ($kJ\ kg^{-1}C^{-1}$)	RAMONA	4.653	5.014	5.885	7.377
	VDI	4.491	4.750	5.196	6.206

*Relative to u_f(70 bar) = 1.2579 MJ kg^{-1} .

a. Saturation temperature is computed in RAMONA-3B by

$$t_{sat}(p) = \sum_{i=0}^{5} a_i p^i \Big/ \sum_{i=0}^{5} b_i p^i \quad , \tag{4.4.69}$$

where p is in N/m^2 and t_{sat} in C and

$a_0 = -3.845\ 764\ 67 \times 10^{2}$, $b_0 = 1.999\ 674\ 70 \times 10^{1}$,
$a_1 = 0.570\ 716\ 464 \times 10^{0}$, $b_1 = 2.094\ 876\ 30 \times 10^{-2}$,
$a_2 = 1.040\ 917\ 92 \times 10^{-4}$, $b_2 = 1.303\ 936\ 69 \times 10^{-6}$,
$a_3 = 1.029\ 493\ 24 \times 10^{-9}$, $b_3 = 6.757\ 168\ 12 \times 10^{-12}$,
$a_4 = 8.520\ 961\ 26 \times 10^{-16}$, $b_4 = 3.174\ 246\ 82 \times 10^{-18}$,
$a_5 = 5.561\ 708\ 47 \times 10^{-23}$, $b_5 = 1.0 \times 10^{-25}$.

b. Density of saturated liquid is computed from

$$\rho_f(p) = \rho_f(t_{sat}) = \sum_{i=0}^{3} a_i t_{sat}^i \Big/ \sum_{i=0}^{3} b_i t_{sat}^i \quad , \tag{4.4.70}$$

where $t_{sat}(p)$ is in C (cf. Eq. 4.4.69), ρ_f is in kg/m^3 and

$a_0 = 2.572\ 043\ 55$, $b_0 = 2.572\ 244\ 87 \times 10^{-3}$,
$a_1 = 3.425\ 101\ 10 \times 10^{-3}$, $b_1 = 3.363\ 883\ 17 \times 10^{-6}$,
$a_2 = -6.203\ 223\ 40 \times 10^{-5}$, $b_2 = -4.535\ 222\ 20 \times 10^{-8}$,
$a_3 = 9.271\ 653\ 24 \times 10^{-8}$, $b_3 = 3.038\ 555\ 54 \times 10^{-11}$,
$b_4 = 5.060\ 341\ 91 \times 10^{-14}$.

c. Density of saturated vapor is computed from

$$\rho_g(p) = \rho_g(t_{sat}) = \sum_{i=0}^{5} a_i t_{sat}^i \Big/ \sum_{i=0}^{3} b_i t_{sat}^i \quad , \tag{4.4.71}$$

where $t_{sat}(p)$ is in C (cf. Eq. 4.4.69), ρ_g is in kg/m^3 and

$a_0 = 8.860\ 267\ 69 \times 10^{-4}$, $b_0 = 1.825\ 181\ 13 \times 10^{-1}$,
$a_1 = 5.577\ 964\ 47 \times 10^{-5}$, $b_1 = -7.496\ 960\ 90 \times 10^{-4}$,
$a_2 = 1.863\ 200\ 39 \times 10^{-6}$, $b_2 = 1.126\ 570\ 20 \times 10^{-6}$,
$a_3 = 1.175\ 296\ 83 \times 10^{-8}$, $b_3 = -9.934\ 695\ 91 \times 10^{-10}$.
$a_4 = 4.447\ 866\ 46 \times 10^{-10}$,
$a_5 = -1.077\ 625\ 69 \times 10^{-12}$,

d. Enthalpy of evaporation is computed from

$$h_{fg}(p) = h_{fg}(t_{sat}) = \sum_{i=0}^{3} a_i t_{sat}^i \Big/ \sum_{i=0}^{4} b_i t_{sat}^i , \qquad (4.4.72)$$

where $t_{sat}(p)$ is in C (see Eq. 4.4.69), h_{fg} is in Ws/kg and

$a_0 = 4.775\ 353\ 76 \times 10^{6}$, $b_0 = 1.909\ 199\ 98$,
$a_1 = 5.617\ 140\ 74 \times 10^{3}$, $b_1 = 4.109\ 092\ 78 \times 10^{-3}$,
$a_2 = -1.165\ 955\ 82 \times 10^{2}$, $b_2 = -4.466\ 649\ 07 \times 10^{-5}$,
$a_3 = 1.806\ 741\ 74 \times 10^{-1}$, $b_3 = 5.432\ 480\ 60 \times 10^{-8}$,
$b_4 = 1.627\ 496\ 41 \times 10^{-12}$.

e. Specific heat at constant pressure for saturated liquid is computed in RAMONA-3B from

$$c_{p,\ell}(p) = c_{p,\ell}(t_{sat}) = \sum_{i=0}^{4} a_i t_{sat}^i \Big/ \sum_{i=0}^{3} b_i t_{sat}^i , \qquad (4.4.73)$$

where $t_{sat}(p)$ is in C (Eq. 4.4.69), $c_{p,\ell}$ is in Ws/(kg C) and

$a_0 = 9.348\ 515\ 89 \times 10^{3}$, $b_0 = 2.219\ 499\ 39$,
$a_1 = 3.377\ 977\ 85 \times 10^{1}$, $b_1 = 8.924\ 479\ 27 \times 10^{-3}$,
$a_2 = -3.185\ 401\ 82 \times 10^{-1}$, $b_2 = -8.638\ 211\ 84 \times 10^{-5}$,
$a_3 = 4.715\ 586\ 12 \times 10^{-4}$, $b_3 = 1.246\ 888\ 42 \times 10^{-7}$.
$a_4 = -9.934\ 252\ 02 \times 10^{-8}$,

The specific heat at constant pressure for subcooled and superheated liquid is approximated by that for saturated liquid, according to Eq. 4.4.73.

f. Specific heat at constant pressure for saturated vapor is computed in RAMONA-3B from (Wulff and Jones 1978, Part 2, Eqs. 2.10.15 and 2.10.16)

$$c_{p,v} = \left(\frac{\partial T_v}{\partial h}\right)_p^{-1} . \qquad (4.4.74)$$

where

$$T_v(h,p) = \sum_{i=0}^{2} \sum_{j=0}^{2} (a_{ij})\, p^j h^j .$$

and

$$
\begin{aligned}
a_{00} &= \ \ 6.565\ 890\ 556 \times 10^{2} \\
a_{01} &= -5.256\ 896\ 914 \times 10^{-4} \\
a_{02} &= \ \ 1.622\ 084\ 838 \times 10^{-10} \\
\\
a_{10} &= \ \ 9.906\ 585\ 925 \times 10^{-5} \\
a_{11} &= -3.440\ 578\ 369 \times 10^{-11} \\
a_{12} &= \ \ 1.867\ 406\ 949 \times 10^{-18} \\
\\
a_{20} &= -2.187\ 860\ 677 \times 10^{-12} \\
a_{21} &= \ \ 7.008\ 133\ 640 \times 10^{-19} \\
a_{22} &= -1.456\ 676\ 437 \times 10^{-26}
\end{aligned}
$$

The specific heat of saturated vapor, $c_{p,g}$, is evaluated by using $h_v = h_g(p)$ in Eq. 4.4.74.

g. Specific internal energy of saturated vapor is approximated in RAMONA-3B by

$$
\begin{aligned}
u_g(p) &= h_{fg} + u_f + p\left(\frac{1}{\rho_f} - \frac{1}{\rho_g}\right) \\
&\cong h_{fg} + p\left(\frac{1}{\rho_f} - \frac{1}{\rho_g}\right) + c_{p,\ell}\,(t_{sat} - t^{o}_{sat}) \quad , \qquad (4.4.75)
\end{aligned}
$$

where $u_g(p)$ is in Ws kg^{-1}, p is in Nm^{-2} and the symbols h_{fg}, ρ_f, ρ_g, $c_{p,\ell}$ and t_{sat} are defined by Eqs. 4.4.72, 4.4.70, 4.4.71, 4.4.73 and 4.4.69), respectively. The symbol t^{o}_{sat} represents the initial, steady-state saturation temperature. Since $c_{p,\ell}$ approximates the specific heat

$$
\left.\frac{\partial u_f}{\partial t_{sat}}\right|_{t^{o}_{sat}}^{t_{sat}} \approx c_{p,\ell}
$$

in Eq. 4.4.75, this equation restricts RAMONA-3B simulations to the pressure range of

$$
\left|\langle p\rangle_{syst} - \langle p\rangle^{o}_{syst}\right| \leq 35 \text{ bar} \ .
$$

Beyond this range, one must expect an uncertainty of approximately 0.5% for the relative error $\Delta u_g/h_{fg}$ of the vapor internal energy, whence 0.5% in static quality, which in turn produces an uncertainty of 0.05 in vapor void fraction. This uncertainty is normally not acceptable because of its strong effect on reactivity feedback and fission power.

h. Density of subcooled and superheated liquid is computed in RAMONA-3B from

$$\rho_\ell(p,t_\ell) = \rho_f(p) + \left(\frac{\partial \rho_\ell}{\partial t}\right)_p (t_\ell - t_{sat}) , \qquad (4.4.76)$$

where

$$\left(\frac{\partial \rho_\ell}{\partial t}\right)_p = \sum_{i=0}^{2} a_i p^i ,$$

and p is in N/m^2, t in C, ρ_f and t_{sat} are given in Eqs. 4.4.69 and 4.4.70.

$$a_0 = -0.8071$$
$$a_1 = -0.1774 \times 10^{-6}$$
$$a_2 = 0.5289 \times 10^{-14}.$$

i. Specific internal energy of liquid is approximated (cf. Approximation 4-viii) in RAMONA-3B by

$$u_\ell(t_\ell,p) = c_{p,\ell}(p) \left[t_\ell - t^o_{sat}\right] , \qquad (4.4.77)$$

where u_ℓ is in Ws kg^{-1}, $c_{p,\ell}$ in Ws $kg^{-1}C^{-1}$ and defined by Eq. 4.4.73, t_ℓ is the liquid temperature in C, and t^o_{sat} is the initial saturation temperature as for Eq. 4.4.76.

j. Interfacial surface tension is computed in RAMONA-3B from Zemanski (1968) according to

$$\sigma(p) = 0.0755 \frac{N}{m} \left(1 - \frac{t_{sat}}{374.15\ C}\right)^{1.2} . \qquad (4.4.78)$$

This completes the description of thermophysical property definitions in RAMONA-3B.

RAMONA-3B uses the mixture internal energy density

$$(\rho_m u_m) = \alpha \rho_g u_g + (1-\alpha) \rho_\ell u_\ell , \qquad (4.4.79)$$

the vapor mass density ($\alpha\rho_g$) and the system pressure $\langle p \rangle_{syst}$ as principal state variables. The previously given definitions of thermophysical properties,

however, require that the liquid temperature t_ℓ is computed first from the principal state variables, before the properties of the liquid phase can be evaluated. By combining Eqs. 4.4.76 and 4.4.77 with Eq. 4.4.79, one finds the liquid temperature from

$$t_\ell = t_{sat} + \frac{\sqrt{b^2 - ac} - b}{a} , \qquad (4.4.80)$$

where

$$a\left(\langle p\rangle_{syst}\right) = \left(\frac{\partial \rho_\ell}{\partial t}\right)_p , \qquad \text{as in Eq. 4.4.76,}$$

$$2b\left(\langle p\rangle_{syst}\right) = \rho_f + a\left(t_{sat} - t^o_{sat}\right)$$

and

$$c\left(\langle p\rangle_{syst}, (\rho_m u_m), \alpha\rho_g\right) = \rho_f\left(t_{sat} - t^o_s\right) - \frac{(\rho_m u_m) - u_g(\alpha\rho_g)}{c_{p,\ell}\left[1 - \frac{(\alpha\rho_g)}{\rho_g}\right]} .$$

Equation 4.4.80 applies for $0 \leq \alpha < 1$, that is for pure liquid and two-phase mixtures, but not for pure vapor, the state that RAMONA-3B cannot achieve in general (cf. Assumption 4-ii). Equation 4.4.80 can be evaluated directly. RAMONA-3B does not use Eq. 4.4.80. Instead it uses previous time step values for the density of liquid. We recommend the use of Eq. 4.4.80 for future improvements.

This completes the descriptions of thermophysical properties used in RAMONA-3B. In general, derivatives of properties, when used in RAMONA-3B, are computed by numerical differentiation (first-order forward differences). Equations 4.4.18, 4.4.19 and 4.4.20 contain liquid density derivatives with respect to pressure and internal energy, and the derivative of saturation densities with respect to pressure along the saturation lines. The derivatives for the liquid are, in terms of properties available in the RAMONA-3B code (cf. Eqs. 4.4.69, 4.4.73, 4.4.76 and 4.4.80):

$$\left(\frac{\partial \rho_\ell}{\partial p}\right)_u = -\left(\frac{\partial \rho_\ell}{\partial t}\right)_p \left(\frac{u_\ell}{c^2_{p,\ell}} \frac{dc_{p,\ell}}{dt_{sat}} + 1\right) t'_{sat} + \rho'_f + (t_\ell - t_{sat}) \frac{d}{dp}\left(\frac{\partial \rho_\ell}{\partial t}\right)_p , \qquad (4.4.81)$$

where superscripted primes denote differentiation with respect to pressure and

$$\left(\frac{\partial \rho_\ell}{\partial u}\right)_p = \frac{1}{c_{p,\ell}}\left(\frac{\partial \rho_\ell}{\partial t}\right)_p , \qquad (4.4.82)$$

but they are not used in the RAMONA-3B code because of Assumption (4-vii). The derivatives of saturation densities, ρ'_g and ρ'_f, are computed by numerical differentiation of Eqs. 4.4.70 and 4.4.71.

4.4.2.6 Transport Properties of Coolant

The original RAMONA models require only the thermal conductivity k_ℓ and the dynamic viscosity μ_ℓ of the liquid phase; RAMONA-3B requires also the same properties for vapor.

a. Thermal conductivity of liquid is computed in RAMONA-3B from

$$k_\ell(p) = k_\ell(t_{sat}) = \sum_{i=0}^{4} a_i t_{sat}^i \Big/ \sum_{i=0}^{3} b_i t_{sat}^i , \qquad (4.4.83)$$

where $t_{sat}(p)$ is in C and defined by Eq. 4.4.69, k_ℓ is in $Wm^{-1}C^{-1}$ and

$$\begin{aligned} a_0 &= 6.099\ 370\ 00 \times 10^{-1}, & b_0 &= 1.0, \\ a_1 &= -2.056\ 114\ 90 \times 10^{-3}, & b_1 &= -5.388\ 780\ 00 \times 10^{-3}, \\ a_2 &= -9.675\ 658\ 00 \times 10^{-6}, & b_2 &= 3.641\ 552\ 90 \times 10^{-6}, \\ a_3 &= 3.946\ 890\ 00 \times 10^{-8}, & b_3 &= 5.998\ 070\ 00 \times 10^{-9}. \\ a_4 &= -3.170\ 096\ 00 \times 10^{-11}, \end{aligned}$$

The thermal conductivity k_ℓ according to Eq. 4.4.83 is used for all liquid states, whether subcooled, saturated or superheated.

b. Thermal conductivity of vapor is computed in RAMONA-3B from (Wulff and Jones 1978)

$$k_g(h,p) = x_1 + \rho_g \left(x_2 + pct_{sat}^{-4.2} \right), \qquad (4.4.84)$$

where t_{sat} is computed from $p = \langle p \rangle_{syst}$ and

$$x_1 = \sum_{i=0}^{3} a_i t_{sat}^i$$

$$x_2 = \sum_{i=0}^{2} b_i t_{sat}^i$$

and

$$a_0 = 1.76 \times 10^{-2} \qquad b_0 = 1.0351 \times 10^{-4}$$
$$a_1 = 5.87 \times 10^{-5} \qquad b_1 = 4.198 \times 10^{-7}$$
$$a_2 = 1.04 \times 10^{-7} \qquad b_2 = -2.771 \times 10^{-11}$$
$$a_3 = 4.51 \times 10^{-11} \qquad c = 2.1482 \times 10^{5}.$$

In Eq. 4.4.84, k_g is in $Wm^{-1}C^{-1}$, t_{sat} is in C and p is in N/m^2. An accuracy assessment of Eq. 4.4.84 is given in the reference by Wulff and Jones (1978).

c. Dynamic viscosity of liquid is computed from

$$\mu_\ell(p) = \mu_\ell(t_{sat}) = \sum_{i=0}^{4} a_i t_{sat}^i \Big/ \sum_{i=0}^{3} b_i t_{sat}^i , \qquad (4.4.85)$$

where $t_{sat}(p)$ in C is given by Eq. 4.4.69 and μ_ℓ is in kg $s^{-1}m^{-1}$. In Eq. 4.4.85, the coefficients are

$$a_0 = -7.378\ 281\ 37 \times 10^{-5}, \qquad b_0 = -4.098\ 097\ 60 \times 10^{-2},$$
$$a_1 = 6.515\ 214\ 74 \times 10^{-7}, \qquad b_1 = -1.035\ 654\ 16 \times 10^{-3},$$
$$a_2 = -1.775\ 192\ 64 \times 10^{-9}, \qquad b_2 = 9.450\ 251\ 34 \times 10^{-7},$$
$$a_3 = 1.199\ 574\ 82 \times 10^{-11}, \qquad b_3 = 7.941\ 315\ 16 \times 10^{-8}.$$
$$a_4 = -1.440\ 476\ 22 \times 10^{-14},$$

The dynamic viscosity μ_ℓ as computed from Eq. 4.4.85 is applied for subcooled, saturated and superheated liquid.

d. Dynamic viscosity of vapor is computed in RAMONA-3B from the following two relations (Wulff and Jones 1978):

for $t_{sat} \leq 300°C$

$$\mu_g = \mu_o - \rho_g \left[1.858 \times 10^{-7} - 5.90 \times 10^{-10}\ t_{sat}\right], \qquad (4.4.86a)$$

for $300°C < t_{sat} < 375°C$

$$\mu_g = \mu_o + p\left[\sum_{i=0}^{3} f_i t_{sat}^i + \left(\sum_{i=0}^{3} g_i t_{sat}^i\right)\left(\sum_{i=0}^{2} a_i p^i\right)\right]. \qquad (4.4.86b)$$

Here μ_g and μ_o are in kg $m^{-1}s^{-1}$, t_{sat} in C, ρ in kg m^{-3} and p in N m^{-2}. The constants in Eq. 4.4.86 are

$$\mu_o = 0.407 \times 10^{-7} t_{sat} + 8.04 \times 10^{-6}$$

and

$a_0 = 3.53 \times 10^{-8}$
$a_1 = 6.765 \times 10^{-11}$
$a_2 = 1.021 \times 10^{-14}$

$f_0 = -2.885 \times 10^{-6}$
$f_1 = 2.427 \times 10^{-8}$
$f_2 = -6.7893 \times 10^{-10}$
$f_3 = 6.317\ 037 \times 10^{-13}$

$d = 1.858 \times 10^{-7}$
$e = 5.90 \times 10^{-10}$

$g_0 = 176.0$
$g_1 = -1.60$
$g_2 = 4.8 \times 10^{-3}$
$g_3 = -4.7407 \times 10^{-6}$

An accuracy assessment of Eq. 4.4.86 is given in the reference by Wulff and Jones (1978).

4.4.3 The System Pressure

4.4.3.1 General Derivation

Using the four conservation equations, Eqs. 4.4.1, 4.4.4, 4.4.6 and 4.4.9 (in the form of Eqs. 4.4.18, 4.4.19 and/or 4.4.20), of RAMONA-3B and its constitutive descriptions presented in Section 4.4.2, we present now the system modeling equations. First, we present the equation that defines the system pressure, $\langle p \rangle_{syst}$, because it involves the entire pressure vessel and the recirculation loops as control volume. Later, we present the equations describing the coolant flows, as these equations involve flow contours through parts of the pressure vessel and through the recirculation loops. Finally, the governing equations for individual computational cells are presented in Chapter 6, Section 6.4.2.3, because they involve a nodalization scheme of numerical solution.

The use of a single system pressure $\langle p \rangle_{syst}$ in RAMONA-3B achieves computing efficiency and speed, by suppressing acoustical effects and by "effectively" decoupling the momentum from the mass and energy balances through the elimination of phasic density variations with local pressure variations. The momentum equation can be integrated separately once the void and temperature distributions are computed. It remains coupled in time and space through the effects of gravity which is important for the simulation of natural circulation. The single pressure concept (cf. Assumption (4-iii)) is very powerful for all BWR transient simulations, except for the simulation of dynamic interactions between coolant and structures during rapid pressure oscillations. Such transients are outside the scope of RAMONA-3B. A possible limitation of the single pressure concept lies in its inability to predict the delays of

pressure pulses due to their finite propagation speeds, should such delays be important relative to the response time of reactivity controls. An example is a turbine trip transient. However, the single pressure concept should not be compromised because of this possible limitation. Instead, it is recommended for future code improvements, that a time delay be computed separately, based on the sound propagation speed and the distance between the core center and the source of the pressure pulse (steam line entrance, for example), and then introduced into the reactivity feedback or the reactivity control.

The system pressure is defined by

$$\langle p \rangle_{syst} = \frac{1}{V_1 + V_2} \int_{V_1+V_2} p \, dV \tag{4.4.87}$$

as the pressure, averaged over the volume V_1 of liquid and the volume V_2 of two-phase mixture and pure vapor, as shown in Figure 4.5. The time rate of change of $\langle p \rangle_{syst}$ is computed by integrating Eq. 4.4.18 over V_1 and Eq. 4.4.19 over V_2. In the resultant equations, one replaces the volume integrals of $\nabla \cdot \vec{j}_m$ by surface integrals and recognizes the continuity of the volumetric flux j at all locations of flow discontinuity (cf. Assumption iii) and at moving interfaces (Wulff 1981). By adding up the two equations and solving for the time-derivative $d\langle p \rangle_{syst}/d\tau$, one arrives at

$$\frac{d\langle p \rangle_{syst}}{d\tau} = \left\{ (Aj)_{FW} + \sum (Aj)_{ECC} - (Aj)_{SL} + \int_{V_2} \left[\frac{\rho_\ell - \rho_g}{\rho_\ell \rho_g} + \left(\frac{\partial \rho_\ell}{\partial u} \right)_p \frac{h_g - h_\ell}{\rho_\ell^2} \right] \Gamma_v \, dV \right.$$

$$- \int_{V_1} \frac{1}{\rho_\ell^2} \left(\frac{\partial \rho_\ell}{\partial u} \right)_p \left[\nabla \cdot \vec{q}_\ell - q_\ell''' \right] dV - \int_{V_2} \frac{1}{\rho_\ell^2} \left(\frac{\partial \rho_\ell}{\partial u} \right)_p \left\{ \nabla \cdot \left[(1-\alpha) \, \vec{q}_\ell \right] \right.$$

$$\left. \left. - (1-\alpha) \, q_\ell''' \right\} dV \right\} \Bigg/ \left\{ \int_{V_2} \left[\alpha \frac{\rho_g'}{\rho_g} + (1-\alpha) \frac{1}{\rho_\ell} \left(\frac{\partial \rho_\ell}{\partial p} \right)_u \right] dV + \int_{V_1} \frac{1}{\rho_\ell} \left(\frac{\partial \rho_\ell}{\partial p} \right)_u dV \right\}. \tag{4.4.88}$$

The symbols in Eq. 4.4.88 have the previously defined meanings. The first two terms of the numerator (first curled brackets) are the contributions to pressure rise from injected flows: $(Aj)_{FW}$ and $(Aj)_{ECC}$ are the volumetric flow rates of feedwater and emergency core cooling. The third term, $(Aj)_{SL}$ is the vapor volumetric flow rate entering the steam line, tending thereby to reduce the pressure change rate. The fourth term accounts for the effects of phase change; the first term of the integrand is the change in specific volume during phase change, the second one accounts for thermal contraction in the liquid as

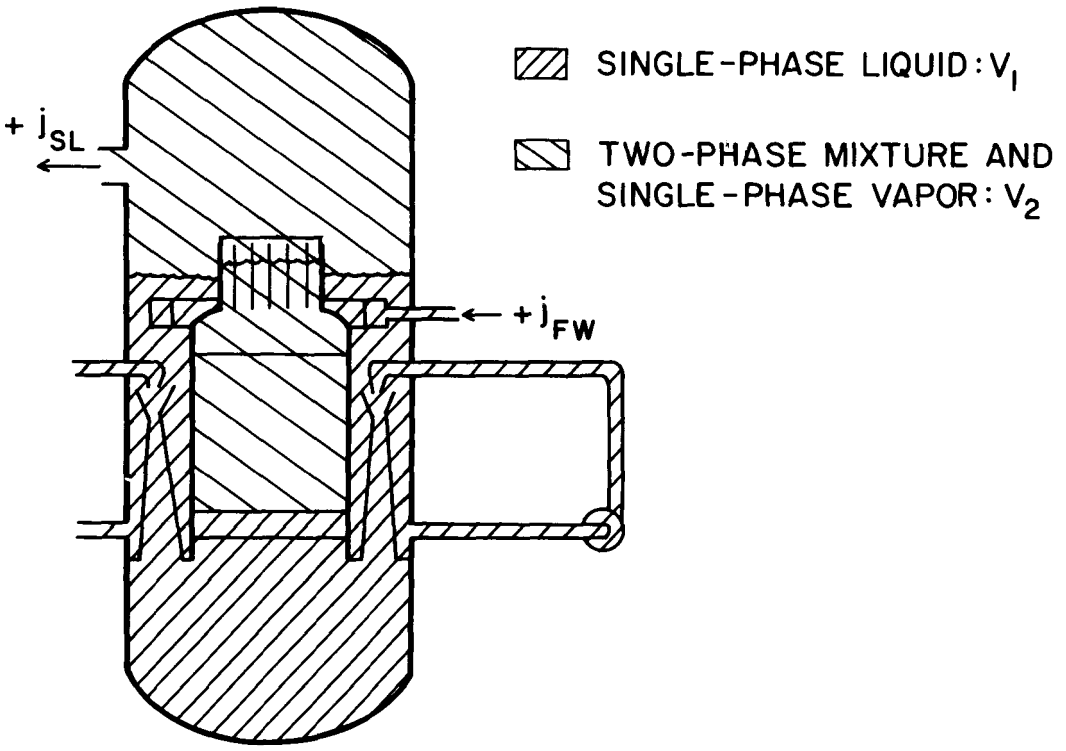

Figure 4.5 Typical Control System for System Pressure Calculation

it gives up the total heat for evaporation, $h_g - h_\ell$. This thermal contraction is only ~4% (at p = 70 bar) of the change in specific volume and can be ignored, i.e.,

$$\frac{\rho_\ell - \rho_g}{\rho_\ell \rho_g} \gg \left| \left(\frac{\partial \rho_\ell}{\partial u}\right)_p \frac{h_g - h_\ell}{\rho_\ell^2} \right| . \qquad (4.4.89)$$

The fifth term of the numerator accounts for the thermal expansion or contraction in the large liquid volume, volume V_1 in Figure 4.5. It cannot be ignored since it affects strongly the pressure and the coolant level during feedwater transients.* Using the mean-value theorem of integral calculus (for the entire volume V_1 or for appropriate subdivisions) and then Green's divergence theorem, one obtains (for the global application)

$$-\int_{V_1} \frac{1}{\rho_\ell^2}\left(\frac{\partial \rho_\ell}{\partial u}\right)_p \nabla \cdot \vec{q}_\ell \, dV = \overline{\left\{\frac{1}{\rho_\ell^2}\left(\frac{\partial \rho_\ell}{\partial u}\right)_p\right\}}_{V_1} \int_{(A_h)_1} q''_w \, dA_h , \qquad (4.4.90)$$

where $(A_h)_1$ is the total heat transfer area contacted by the liquid in volume V_1. The last term in the numerator of Eq. 4.4.88 accounts for the thermal expansion and contraction of the liquid in the nonequilibrium mixture. The term is small (approximately 1-2% of the displacement by feedwater) and should be ignored:

$$\overline{\left\{\frac{1}{\rho_\ell^2}\left(\frac{\partial \rho_\ell}{\partial u}\right)_p\right\}}_{V_2} \left\{\int_{(A_h)_2} (1-\alpha)\, q''_{w,\ell} \, dA_h + \int_{V_2} (1-\alpha)\, q'''_\ell \, dV\right\} \ll (Aj)_{FW} . \qquad (4.4.91)$$

The denominator of Eq. 4.4.88 is the measure of system compressibility. At p=70 bar, one finds (cf. Eqs. 4.4.70, 4.4.71 and 4.4.81):

$$\left.\begin{aligned} \frac{1}{\rho_\ell}\left(\frac{\partial \rho_\ell}{\partial p}\right)_u &\approx 10^{-3} \frac{\rho'_g}{\rho_g} \\ &\approx 10^{-1} \frac{\rho'_f}{\rho_f} \end{aligned}\right\} \qquad (4.4.92)$$

*The contribution to Eq. 4.4.88 is 50% of feedwater injection effects $(Aj)_{FW}$ if the feedwater subcooling temperature is 200°C.

This estimate suggests that the second term of the first integrand in the denominator should be ignored unless the void fraction in Volume 2 approaches zero (as for a low-void mixture filling the steam dome). The second term in the denominator represents the compressibility of all single-phase liquid. It should be retained only for the cases when $V_1 >> V_2$ (pressure vessel flooded with liquid; the third term is normally less than 2% of the first term in the denominator).

Substitution of Eqs. 4.4.89 through 4.4.92 into Eq. 4.4.88 yields this final result:

$$\frac{d\langle p\rangle_{syst}}{d\tau} = \left\{ (Aj)_{FW} + \sum (Aj)_{ECC} - (Aj)_{SL} + \int_{V_2} \frac{\rho_\ell - \rho_g}{\rho_\ell \rho_g} \Gamma_v \, dV \right.$$

$$\left. - \left[\frac{1}{\rho_\ell^2}\left(\frac{\partial \rho_\ell}{\partial u}\right)_p\right]_{V_1} \left[\int_{(A_h)_1} q''_w \, dA_h + \int_{V_1} q'''_\ell \, dV\right] \right\} \Bigg/$$

$$\left\{ \int_{V_2} \alpha \frac{\rho'_g}{\rho_g} \, dV + \int_{V_1} \frac{1}{\rho_\ell}\left(\frac{\partial \rho_\ell}{\partial p}\right)_u dV \right\} . \qquad (4.4.93)$$

In Eq. 4.4.93, the volumetric flow rates $(Aj)_{FW}$ and $(Aj)_{ECC}$ are prescribed as functions of time by tabulated input data. The flow rate $(Aj)_{SL}$ of steam entering the steam line is computed from the steam line dynamics model presented in Section 4.4.5.5. The vapor generation rate Γ_v is computed as discussed in Section 4.4.2.3. The vapor void fraction α is computed from the vapor mass balance, Eq. 4.4.1, having the product $(\rho_g \alpha)$ as its principal variable, and the vapor density ρ_g, Eq. 4.4.71. All the other properties are computed in accordance with Section 4.4.2.5.

4.4.3.2 Pressure Prediction in RAMONA-3B

The wall heat flux q''_w from the walls wetted by the single-phase liquid in Volume 1 is computed in RAMONA-3B only for the nonboiling section of the core (cf. Eq. 6.3.14), but ignored elsewhere (cf. Assumption (3-ii)). Also, the RAMONA-3B code ignores completely the last term of the numerator in Eq. 4.4.93, thereby producing an error equivalent to a 24%-error in feedwater flow rate for every 100°C of feedwater subcooling or of cold water injection subcooling (cf. Assumption 4-xiii).

Finally, the last term in the denominator of Eq. 4.4.93 is approximated in RAMONA-3B by the relative compressibility of saturated liquid (cf. Approximation (4-vii)), corresponding to the last term in Eq. 4.4.20. As shown earlier in Eq. 4.4.92, by this approximation RAMONA-3B overpredicts the liquid compressibility in Volume 1 of Figure 4.5 by a factor of ten. Both this approximation

and the omission of the effects of thermal expansion (last term in numerator of Eq. 4.4.93) reduce the predicted time rate of pressure change. The equation used in RAMONA-3B is

$$\frac{d\langle p\rangle_{syst}}{d\tau} = \frac{(Aj)_{FW} + (Aj)_{ECC} - (Aj)_{SL} + \int_{V_2} \frac{\rho_\ell - \rho_g}{\rho_\ell \rho_g} \Gamma_v \, dV}{\int_{V_1+V_2} \left[\alpha \frac{\rho_g'}{\rho_g} + (1-\alpha) \frac{\rho_f'}{\rho_f} \right] dV} \quad . \qquad (4.4.94)$$

It is recommended that Eq. 4.4.93 be used instead of Eq. 4.4.94 for future improvements of RAMONA-3B.

4.4.4 Coolant Circulation

This section presents the methods used in RAMONA-3B for the prediction of coolant flow velocities. The flow is first described for the circulation through the core and then for the recirculation loops.

Figure 4.1 shows as contour $\mathcal{C}_1$ one of N_c flow circuits through the core, having N_c parallel flow channels. Figure 4.1 shows also contour $\mathcal{C}_2$, a typical recirculation loop. The core flows and the recirculation flows are coupled dynamically at two common points of their respective contours: once at the point of divergence above the jet pump suction inlet and once at the point of convergence in the jet pump mixing throat. The flows are coupled through the inertia of the suction flow and through the momentum exchange in the jet pump mixing throat. Since this unimportant flow inertia is ignored in RAMONA-3B (cf. Assumption 4-xiv), the flows through core and recirculation loop remain coupled only through quasi-steady momentum exchange in the jet pump. The flows are therefore described by separate explicit ordinary differential equations, one set of N_c equations for the core, and one equation for the recirculation loop.

At the present time RAMONA-3B represents both recirculation loops by a single representative loop and all the jet pumps by a single representative jet pump.

The prediction of coolant flows is based on two conservation equations and four constitutive equations for wall shear and form losses (Section 4.4.2.2), vapor generation rate (Section 4.4.2.3) and slip (Section 4.4.2.4), along with equations for thermophysical and transport properties. The first conservation equation is the mixture momentum balance, Eq. 4.4.6. It determines the time-dependence of the closed-contour momentum. The second conservation equation is the mixture mass balance, Eq. 4.4.9 (in the form of Eq. 4.4.18 for the liquid, Eq. 4.4.19 for the two-phase mixture or Eq. 4.4.20 for saturated mixtures). The mixture mass balance is integrated to yield firstly the relation between the total momentum of the coolant along the contour and the volumetric flow rate of the mixture at some reference point (inlet to upper downcomer for core flows),

and then secondly, the relation between the local mixture volumetric flow rate and the reference flow rate.

The prediction of the coolant flow velocity on the basis of the closed-contour momentum balance is one of the outstanding modeling features in RAMONA-3B. It produces efficiently computing accuracy with a far smaller computing effort than that of conventional finite difference techniques for integrating partial differential equations. It achieves computing efficiency at the expense of only the insignificant loss from not simulating unimportant acoustic effects. The method is possible on account of Assumption (4-ii), by ignoring phasic density dependence on local pressure variations. The important density variations due to thermal expansion and phase change are fully accounted for. The method has been used successfully in the past (Wulff 1979), notably also in commercial training simulators for nuclear power plant operators (Wulff 1980b). In RAMONA-3B, the method supports fully the need of simulating the flow through many parallel flow channels in the core for multi-dimensional neutron kinetics predictions.

4.4.4.1 Vessel Circulation (Core Flow)

4.4.4.1.1 Derivation of Contour Momentum Balance

To obtain the closed contour momentum balance for a typical contour $\mathcal{C}_1$ in Figure 4.1 through the j-th core flow channel, we divide the contour into N_s straight segments of constant flow cross section. A typical segment is shown in Figure 4.6 below. We denote the segment average of the i-th segment by

$$\langle \cdot \rangle_i = \frac{1}{L_i} \int_0^{L_i} \cdot \, dz \, . \qquad (4.4.95)$$

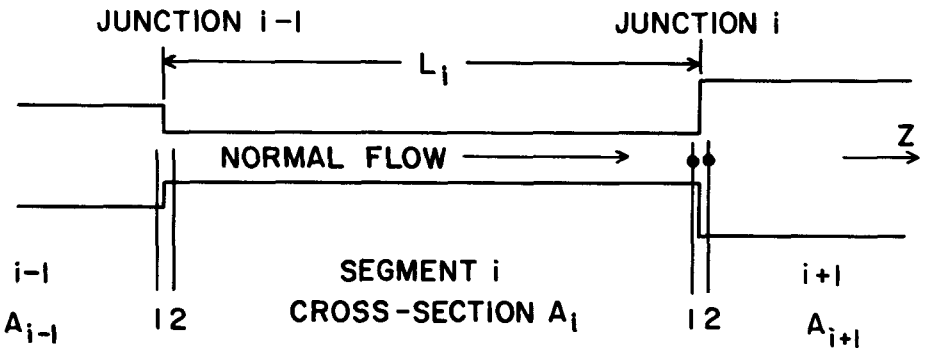

Figure 4.6 Notations for Contour Integration of Momentum Balance

Adjacent segments (with indices i-1, i, i+1) need not have the same orientation relative to the gravity vector. Adjacent segments are connected by abrupt cross-sectional area transitions, orifice restrictions or elbows.

By integrating the momentum balance, (Eq. 4.4.6), separately for each one of the N_s segments in the j-th contour through the j-th core channel (set of channel boxes), one obtains first N_s segment-averaged momentum balances:

$$\left\{p + \left[\alpha\rho_g w_g^2 + (1-\alpha)\,\rho_\ell w_\ell^2\right]\right\}_{(i-1),2} - \left\{p + \left[\alpha\rho_g w_g^2 + (1-\alpha)\,\rho_\ell w_\ell^2\right]\right\}_{i,1}$$

$$= L_i \frac{d\langle G_m\rangle_i}{d\tau} + g_{z,i} L_i \langle\rho_m\rangle_i + \frac{1}{2d_{h,i}} \int_o^{L_i} \frac{f_\ell \phi_\ell^2}{\rho_\ell} G_m |G_m| dz$$

$$i=1,\ldots,N_s, \qquad (4.4.96)$$

where

$$\langle G_m\rangle_i = \langle\alpha\rho_g w_g + (1-\alpha)\,\rho_\ell w_\ell\rangle_i \ . \qquad (4.4.97)$$

In Eqs. 4.4.96, the junction with $i=N_s$ is the entrance to the segment with i=1. Next, one adds up the N_s equations for the j-th flow contour to obtain a single, ordinary differential equation for the time rate of change of momentum along the closed contour with index j.

$$\frac{d\mathcal{M}_j}{d\tau} = \sum_{i=1}^{N_s} \Delta \left\{p + w_g G_g + w_\ell G_\ell\right\}_j$$

$$- \left\{\sum_{i=1}^{N_s} g_{z,i} L_i \langle\rho_m\rangle_i + \frac{1}{2}\sum_{i=1}^{N_s} \frac{1}{d_{h,i}} \int_o^{L_i} \frac{f_\ell \phi_\ell^2}{\rho_\ell} G_m |G_m|\, dz\right\}_j$$

$$j=1,\ldots,N_c \qquad (4.4.98)$$

In Eq. 4.4.98, we have used these four abbreviations:

$$\mathcal{M}_j = \left(\sum_{i=1}^{N_s} L_i \langle G_m\rangle_i\right)_j = \left(\sum_{i=1}^{N_s} \int_o^{L_i} G_m\, dz\right)_j \ , \quad j=1,\ldots,N_c \ , \qquad (4.4.99)$$

for the closed-contour momentum, $G_\ell = (1-\alpha)\rho_\ell w_\ell$, $G_g = \alpha\rho_g w_g$ and

$$\Delta\left\{p + w_g G_g + w_\ell G_\ell\right\}_i = p_{i,2} - p_{i,1} + \left\{\alpha\rho_g w_g^2 + (1-\alpha)\rho_\ell w_\ell^2\right\}_{i,2} - \left\{\alpha\rho_g w_g^2 + (1-\alpha)\rho_\ell w_\ell^2\right\}_{i,1} .$$

The pressure differences across the junction with index i are eliminated with the aid of the jump condition given by Eq. 4.4.49 in Section 4.4.2.2. The result is

$$\Delta\left\{p + w_g G_g + w_\ell G_\ell\right\}_i = \frac{1}{2}\left\{\left[w_g G_g + w_\ell G_\ell\right]_2 - \left[w_g G_g + w_\ell G_\ell\right]_1 - \zeta_{12}\left[w_g G_g + w_\ell G_\ell\right]_{A_{min}}\right\}_i, \quad i=1,\ldots,N_s;\ i\neq i_{JT} \tag{4.4.100}$$

and applies to all junctions, except across the mixing throat in the jet pump, designated by i=JT. Here

$$\Delta\left\{p + w_g G_g + w_\ell G_\ell\right\}_{JT} = \Delta p_{JT} \tag{4.4.101}$$

applies and Δp_{JT} is given by Eq. 4.4.138 later. By substituting Eqs. 4.4.101 and 4.4.102 into Eq. 4.4.98, one finds for the N_s closed-contour momentum equations

$$\frac{d\mathcal{M}_j}{d\tau} = \Delta p_{JT} - \left\{\sum_{i=1}^{N_s} g_{z,i}\,\langle\rho_m\rangle_i\,L_i + \frac{1}{2}\sum_{i=1}^{N_s}\frac{1}{d_{h,i}}\int_0^{L_i}\frac{f_\ell\phi_\ell^2}{\rho_\ell}\,G_m|G_m|\,dz\right\}_j + \frac{1}{2}\sum_{\substack{i=1\\ i\neq i_{JT}}}^{N_s}\left\{\left[w_g G_g + w_\ell G_\ell\right]_2 - \left[w_g G_g + w_\ell G_\ell\right]_1\left[1 + \left(\frac{A_1}{A_{min}}\right)^2\zeta_{12}\right]\right\}_j$$

$$j=1,\ldots,N_c . \tag{4.4.102}$$

In Eq. 4.4.102, ζ_{12} applies to the normal flow direction in Figure 4.6, arbitrarily chosen as the direction of normal operation, upward through the core.

Should the flow reverse, ζ_{12} would have to change as a contraction becomes an expansion upon flow reversal. Also,

$$A_{min} = \text{Min } (A_1, A_2) \tag{4.4.103}$$

appears in Eq. 4.4.102 because of the standard definition of (single-phase) loss coefficients. Equation 4.4.102 is the closed-contour momentum balance which can be integrated, provided ρ_m, G_m, G_g, G_ℓ, w_g and w_ℓ can be computed in terms of and local thermodynamic conditions. The density is computed from $(\alpha\rho_g)$, resulting from the integration of the vapor mass balance, Eq. 4.4.1, from $\langle p\rangle_{syst}$, resulting from the integration of Eq. 4.4.94 and being used to compute ρ_g, then t_ℓ according to Eq. 4.4.80 and finally ρ_ℓ according to Eq. 4.4.76. With α, ρ_g and ρ_ℓ known, one evaluates ρ_m according to Eq. 4.4.8 (see diagram below). The relation between and G_m, G_g, G_ℓ, w_g and w_ℓ is given below. But first we point out the differences between Eq. 4.4.102 and the closed-contour momentum equation actually used in RAMONA-3B.

4.4.4.1.2 The Loop Momentum Balances in RAMONA-3B

The user should be aware that RAMONA-3B employs loop momentum balances which differ in two important aspects from Eq. 4.4.102 and which imply three limitations regarding the modeling of form losses.

a) RAMONA-3B does not employ the standard definition of loss coefficients (cf. Eq. 4.4.49). Instead it employs Eq. 4.4.50 thereby neglecting the reversible transformation of kinetic energy. The result is the disappearance of the factor 1/2 in the last summation of Eq. 4.4.102, except on the loss term (proportional to ζ_{12}) and a change of sign on the momentum flux terms $[w_g G_g + w_\ell G_\ell]$. The consequence from the nonconventional definition of loss coefficients is discussed in Section 4.3.2 (cf. Assumption xii).

b) RAMONA-3B has consistently $|w|G$ in the momentum flux terms instead of wG. This is done, apparently, to achieve flow retardation for all flow directions, without switching the loss coefficients from forward to reverse flow values. As a consequence, RAMONA-3B can be used only for normal, forward flow conditions, i.e., with upward core flow.

Thus, the closed-contour momentum balance in RAMONA-3B is

$$\frac{d\mathcal{M}_j}{d\tau} = \Delta p_{JT} - \sum_{i=1}^{N_s} \left\{ g_z \langle\rho\rangle_m L + \frac{1}{2d_h} \int_o^{L_i} \frac{f_\ell \phi_\ell^2}{\rho_\ell} G_m |G_m| dz \right\}_{ij}$$

$$+ \sum_{\substack{i=1 \\ i\neq JT}}^{N_s} \left\{ \left[|w_g| G_g + |w_\ell| G_\ell \right]_1 \left[1 + \frac{1}{2} \left\{ -\zeta \left(\frac{A_1}{A_{min}} \right)^2 \right\} \right] - \left[|w_g| G_g + |w_\ell| G_\ell \right]_2 \right\}_{ij} ,$$

$$j = 1, \ldots, N_c \ . \tag{4.4.104}$$

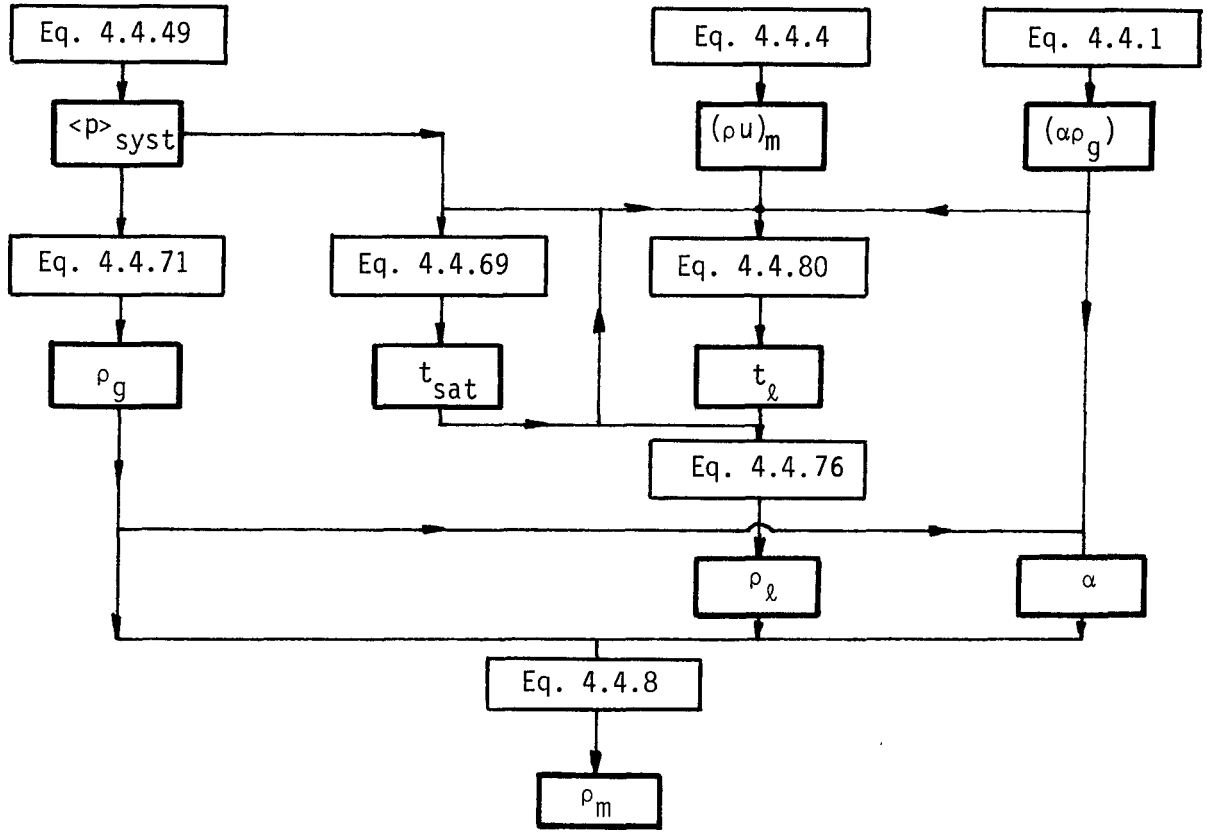

Computing Sequence for Nonequilibrium Mixture Density

It should be pointed out, that the number N_S of cross-sectional area changes is fixed in RAMONA-3B to be $N_S=7$, while the number N_C of parallel core channels can be specified by the user. The seven junctions with form losses connect Upper Downcomer, Lower Downcomer, two lower plenum sections, core, upper plenum and riser, in that order. Moreover, the code user should be aware that:

a) The effect of cross-sectional area change in the jet pump diffuser on inertia is not accounted for in Eqs. 4.4.6, 4.4.102 or 4.4.104. An average cross-sectional area must be used for the jet pump diffuser.

b) Contrary to general conventions on loss coefficients, the negative value $-\zeta(A_1/A_{min})^2$ is to be specified for each junction ($i=1,\ldots,N_S$; $i \neq JT$).

c) Flow reversal cannot be simulated with RAMONA-3B because it has at every junction only one value for the loss coefficient, and because it uses $|w|G$ in the momentum flux instead of wG.

4.4.4.1.3 Derivation of Flow Distribution Model

Next we relate the key parameters in Eqs. 4.4.102 and 4.4.104; namely, the mass flux G_m, the phasic mass fluxes G_g and G_ℓ, and the phasic velocities w_g and w_ℓ first to the local volumetric flux of liquid or mixture, j_ℓ or j_m and then to the closed-contour momentum . These relationships are required to integrate Eqs. 4.4.102 or 4.4.104, as well as the vapor mass and mixture energy balances, Eqs. 4.4.1 and 4.4.4, respectively.

Using the relation between phasic velocities w_ℓ and w_g, as given by Eq. 4.4.64 in Section 4.4.24, and the definition for the mixture volumetric flux j_m, Eq. 4.4.10 in Section 4.4.1, one finds for the phasic velocities

$$w_\ell = \frac{j_m - \alpha w^o}{1+\alpha(S-1)} , \qquad 0 \leq \alpha < 1 \qquad (4.4.105)$$

and

$$w_g = \frac{S j_m + (1-\alpha) w^o}{1+\alpha(S-1)} , \qquad 0 \leq \alpha < 1 . \qquad (4.4.106)$$

After substituting these results into Eq. 4.4.7, one arrives at the mixture mass flux

$$G_m = (A j_m) \chi + \psi , \qquad (4.4.107)$$

where

$$\chi = \frac{1}{A}\left[\rho_\ell - \alpha \frac{S(\rho_\ell - \rho_g)}{1+\alpha(S-1)}\right] \tag{4.4.108}$$

$$\psi = w^o\alpha(\rho_\ell - \rho_g)\left[1 - \frac{\alpha S}{1+\alpha(S-1)}\right] . \tag{4.4.109}$$

The phasic mass fluxes, G_ℓ and G_g can be evaluated with the results of Eqs. 4.4.105 and 4.4.106, respectively

$$G_\ell = (1-\alpha)\,\rho_\ell\, w_\ell \tag{4.4.110}$$

$$G_g = \alpha\rho_g\, w_g \quad . \tag{4.4.111}$$

Thus, all important fluxes and velocities are given in terms of the mixture volumetric flux $j_m(z)$. The volumetric flow rate (Aj_m) (which reduces, of course, to Aj_ℓ in the regions of subcooled liquid) is computed by integrating Eq. 4.4.9 in its appropriate form (cf. Eqs. 4.4.18, 4.4.19 or 4.4.20), starting from one arbitrarily chosen* flow cross section at z=0, continuing along the contour of a particular core channel, upward through the core, and returning to the starting point. The integration is carried out over the coolant volume in the flow channel between the starting cross section at z=0 and a cross section at position z.

We need to recognize the core inlet position z_{CI} and the core exit position z_{CE} as important locations of flow branching and convergence.** Because of Assumption (4-ii), we have $\nabla p=0$ implied in the volume flux divergence equation, i.e., neither flashing or condensing, nor phasic density changes are accounted for. Therefore, the volumetric flow remains continuous across the core entrance

$$A(z_{CI}^-)\, j_m(z_{CI}^-) = \sum_{j=1}^{N_c} Aj(z_{CI}^+)\, j_{m,j}(z_{CI}^+) \quad ; \tag{4.4.112}$$

where N_c denotes the number of parallel flow channels in the core and

$$z_{CI}^- = \lim_{\varepsilon\to 0}(z_{CI} - \varepsilon), \quad z_{CI}^+ = \lim_{\varepsilon\to 0}(z_{CI} + \varepsilon), \quad \varepsilon > 0 \ .$$

*The upper downcomer entrance in RAMONA-3B.

**The flow into and out of the recirculation loops is modeled to cancel at one and the same position.

Similarly, for the core exit

$$\sum_{j=1}^{N_c} A_j(z_{CE}^-)\, j_{m,j}(z_{CE}^-) = A(z_{CE}^+)\, j_m(z_{CE}^+) . \qquad (4.4.113)$$

Equations 4.4.112 and 4.4.113 constitute mass conservation across core inlet and exit, subject to Assumption (4-ii).

The integral of Eq. 4.4.9 over the coolant volume in the vessel, between the fixed reference cross section at z=0 and any cross section at position $z < z_{CI}$ (CI is core inlet) yields

$$A(z) \cdot j_m(z) = (Aj_m)_o + \phi_I(z) , \quad 0 \le z < z_{CI} \qquad (4.4.114)$$

where

$$\phi_I(z) = \int_o^z \left\{ A\left[\frac{\rho_\ell - \rho_g}{\rho_\ell \rho_g} \Gamma_v - \frac{\alpha}{\rho_g} \frac{D_g \rho_g}{D\tau} - \frac{1-\alpha}{\rho_\ell} \frac{D_\ell \rho_\ell}{D\tau} \right] + \xi_{INJ}\, j_{INJ}(z) \right\} dz. \qquad (4.4.115)$$

The expression in square brackets is evaluated for liquid to be equal to the right-hand side of Eq. 4.4.18, for mixture to be equal to that of Eq. 4.4.19 or 4.4.20. The last term in the curly bracket of the above integrand represents the net volume injection at location z, entering across the injection perimeter ζ_{INT}. This accounts for feedwater injection. Discharge into, and return from, the recirculation loop are modeled to cancel each other at one and the same position (cf. Assumption (4-xviii)).

For the core, one obtains similarly (z_{CE} is the core exit location)

$$A_j(z)\, j_{m,j}(z) = A(z_{CI}^+)\, j_{m,j}(z_{CI}^+) + \phi_j(z) , \quad z_{CI} < z < z_{CE} \qquad (4.4.116)$$

with

$$\phi_j(z) = \int_{z_{CI}}^z A_j \left[\frac{\rho_\ell - \rho_g}{\rho_\ell \rho_g} \Gamma_v - \frac{\alpha}{\rho_g} \frac{D_g \rho_g}{D\tau} - \frac{(1-\alpha)}{\rho_\ell} \frac{D_\ell \rho_\ell}{D\tau} \right]_j dz . \qquad (4.4.117)$$

For the flow above the core, through upper plenum and riser, one obtains, with the aid of Eq. 4.4.113

$$A(z)\, j_m(z) = \sum_{j=1}^{N_c} \left\{ A(z_{CI}^+)\, j_{m,j}(z_{CI}^+) + \phi_j(z_{CE}) \right\} + \phi_{II}(z)$$
$$z_{CE} < z < z_{RSE} \qquad (4.4.118)$$

where

$$\phi_{II}(z) = \int_{z_{CE}}^{z} \left\{ A \left[\frac{\rho_\ell - \rho_g}{\rho_\ell \rho_g} \Gamma_v - \frac{\alpha}{\rho_g} \frac{D_g \rho_g}{D\tau} - \frac{(1-\alpha)}{\rho_\ell} \frac{D_\ell \rho_\ell}{D\tau} \right] + \xi_{INJ} j_{INJ}(z) \right\} dz \tag{4.4.119}$$

and $j_{INJ} > 0$ accounts for emergency coolant injection above the core, $j_{INJ} < 0$ for removal of coolant, such as steam into the steam dome.

Equations 4.4.114, 4.4.116 and 4.4.118 define the volumetric flow rates completely in the vessel, but still in terms of $(N_c + 1)$ unknown reference flow rates: $(Aj_m)_o$ and $(Aj_m)_j$ at each core flow channel entrance. These unknowns are computed with the aid of Eqs. 4.4.99 and 4.4.112.

First we substitute Eq. 4.4.107 into Eq. 4.4.99:

$$\mathcal{M}_j = \oint_{\mathcal{C}_j} G_m dz = \oint_{\mathcal{C}_j} \left[(Aj_m)\chi + \psi \right]_j dz \ , \tag{4.4.120}$$

where the closed-contour integration replaces the summation over segment integrals in Eq. 4.4.99. After replacing (Aj_m) in Eq. 4.4.120 from Eqs. 4.4.114, 4.4.116 and 4.4.118, we find, with Eq. 4.4.113 that

$$\begin{aligned} \mathcal{M}_j = & \oint_{\mathcal{C}_j} \psi_j dz + \int_o^{z_{CI}} \chi \left[(Aj_m)_o + \phi_I(z) \right] dz \\ & + \int_{z_{CI}}^{z_{CE}} \chi_j \left\{ \left[A_j(z_{CI}^+)\, j_{m,j}(z_{CI}^+) \right] + \phi_j(z) \right\} dz \\ & + \int_{z_{CE}}^{z_{RSE}} \chi \left\{ (Aj_m)_o + \phi_I(z_{CI}) + \sum_{j=1}^{N_c} \phi_j(z_{CE}) + \phi_{II}(z) \right\} dz \ . \end{aligned}$$

Notice that there is no momentum contribution from the radial flow between riser and downcomer. Next, we solve the above equation for the j-th core inlet volume flow rate:

$$\begin{aligned} A_j(z_{CI}^+)\, j_{m,j}(z_{CI}^+) = & \left\{ \mathcal{M}_j - \oint_{\mathcal{C}_j} \psi_j dz - \int_{z_{CI}}^{z_{CE}} \chi \phi_j dz - (Aj_m)_o \left[\int_o^{z_{CI}} \chi dz + \int_{z_{CE}}^{z_{RSE}} \chi dz \right] \right. \\ & \left. - \left[\int_o^{z_{CI}} \chi \phi_I dz + \int_{z_{CE}}^{z_{RSE}} \chi \phi_{II} dz + \left\{ \phi_I(z_{CI}) + \sum_{j=1}^{N_c} \phi_j(z_{CE}) \right\} \int_{z_{CE}}^{z_{RSE}} \chi dz \right] \right\} \Bigg/ \int_{z_{CI}}^{z_{CE}} \chi_j dz. \end{aligned} \tag{4.4.121}$$

Finally, we sum both sides of Eq. 4.4.121 over all core channels, j=1,...N_c, use Eq. 4.4.112 and recognize from Eq. 4.4.114 that

$$A(z_{CI}^-)\, j_m(z_{CI}^-) = (Aj_m)_o + \phi_I(z_{CI}) = \sum_{j=1}^{N_c} Aj(z_{CI}^+)\, j_{m,j}(z_{CI}^+) .$$

Solving the result for the unknown reference flow rate $(Aj_m)_o$ at the entrance to the upper downcomer, we arrive at

$$(Aj_m)_o = \left\{ \sum_{j=1}^{N_c} \frac{\mathcal{M}_j - \oint_{\ell_j} \psi_j dz - \int_{z_{CI}}^{z_{CE}} \chi\phi_j\, dz}{\int_{z_{CI}}^{z_{CE}} \chi_j dz} \right.$$

$$\left. - \left\{ \int_o^{z_{CI}} \chi\phi_I dz + \int_{z_{CE}}^{z_{RSE}} \chi\phi_{II}\, dz + \left[\phi_I(z_{CI}) + \sum_{j=1}^{N_c} \phi_j(z_{CE}) \right] \int_{z_{CE}}^{z_{RSE}} \chi dz \right\} * \right.$$

$$\left. \sum_{j=1}^{N_c} \frac{1}{\int_{z_{CI}}^{z_{CE}} \chi dz} \right\} \Bigg/ \left\{ 1 + \left[\int_o^{z_{CI}} \chi dz + \int_{z_{CE}}^{z_{RSE}} \chi dz \right] \sum_{j=1}^{N_c} \frac{1}{\int_{z_{CI}}^{z_{CE}} \chi dz} \right\} . \tag{4.4.123}$$

This completes the prediction of the flow fields in the vessel with its N_s parallel flow channels through the core.

Equation 4.4.123 yields the reference volumetric flow rate at the entrance to the upper downcomer, $(Aj_m)_o$, in terms of principal state variables $\langle p \rangle_{syst}$ (Eq. 4.4.93), $\mathcal{M}_j$,j=1,...,N_c (Eq. 4.4.104), of local variations of vapor generation rate Γ_v (Section 4.4.2.3) and thermophysical properties (Section 4.4.2.5). The functions χ, ψ and ϕ in Eq. 4.4.123 are specified by Eqs. 4.4.108, 4.4.109, 4.4.115, 4.4.117 and 4.4.119. Specifically, for flow channel sections filled with pure liquid, these equations read

$$\chi = \frac{\rho_\ell}{A} , \tag{4.4.108a}$$

$$\psi = 0, \text{ and} \tag{4.4.109a}$$

$$\phi = \int_o^{z \le z_\lambda} \left\{ -\frac{1}{\rho_\ell^2} \left(\frac{\partial \rho_\ell}{\partial u} \right)_p \left(q_w' + q_\ell''' A \right) - \frac{A}{\rho_\ell} \left(\frac{\partial \rho_\ell}{\partial p} \right)_u \frac{d\langle p \rangle_{syst}}{d\tau} + \xi_{INJ}\, j_{INJ} \right\} dz , \tag{4.4.124}$$

where q'_w is defined by Eq. 4.4.5 and q'''_ℓ by Eq. 2.7.17. For sections filled with two-phase mixture, X and ψ are given by Eqs. 4.4.108 and 4.4.109, while

$$\phi = \int_{z_\lambda}^{z} \left\{ A \left[\frac{\rho_\ell - \rho_g}{\rho_\ell \rho_g} \Gamma_v - \alpha \frac{\rho'_g}{\rho_g} \frac{d\langle p \rangle_{syst}}{d\tau} \right] + \xi_{INJ} j_{INJ} \right\} dz \ . \qquad (4.4.125)$$

The appropriate integration limits of Eqs. 4.4.124 and 4.4.125 are those given in Eqs. 4.4.115, 4.4.117 and 4.4.119. Equations 4.4.124 and 4.4.125 are consistent with Eq. 4.4.93 for $d\langle p \rangle_{syst}/d\tau$.

4.4.4.1.4 Flow Calculations in RAMONA-3B

The RAMONA-3B code does not employ Eqs. 4.4.124 or 4.4.125 for $\phi(z)$. Instead, in RAMONA, the liquid is assumed to expand as if it were saturated, whence

$$\phi = \int_{0}^{z} \left\{ A \left[\frac{\rho_\ell - \rho_g}{\rho_\ell \rho_g} \Gamma_v - \left[\alpha \frac{\rho'_g}{\rho_g} + (1-\alpha) \frac{\rho'_f}{\rho_f} \right] \frac{d\langle p \rangle_{syst}}{d\tau} \right] + \xi_{INJ} j_{INJ} \right\} dz \ . \qquad (4.4.126)$$

Equation 4.4.126 is used everywhere in the vessel (with $\Gamma_v = 0$ when $\alpha = 0$). The equation corresponds to Eq. 4.4.20 for the flux divergence; it is also consistent with Eq. 4.4.94 used in RAMONA-3B for the system pressure, but it overpredicts the liquid expansion during pressure transients and underpredicts liquid expansion during feedwater temperature variations, as discussed in Section 4.4.3.2.

Once the volumetric flow rate $(Aj_m)_0$ at the upper downcomer entrance is computed, one finds each core inlet flow $Aj(z_{CI}^+) j_{m,j}(z_{CI}^+)$, $j=1,\ldots,N_c$ from Eq. 4.4.121 and the volumetric flow rates anywhere in the vessel from Eqs. 4.4.114, 4.4.116 and 4.4.118. With these flow rates, one computes the mass fluxes G_m, G_ℓ and G_v in accordance with Eqs. 4.4.107, 4.4.110 and 4.4.111 and the phasic velocities w_ℓ and w_g from Eqs. 4.4.105 and 4.4.106.

Note that this procedure satisfies mixture mass and momentum balances. Only one momentum balance per core flow channel is integrated in time, via an ordinary differential equation, Eq. 4.4.104. The integration of the mass balance is reduced to quadratures in space (cf. Eqs. 4.4.114, 4.4.116 and 4.4.118), which require only simple summations in the computer solution. This outstanding modeling feature in RAMONA-3B contributes to its exceptional computing speed, this the more the greater the number N_c is of parallel channels in the core.

The driving potentials for the core flow are gravity forces, the second term on the right-hand side of Eq. 4.4.104, and the jet pump-induced pressure rise, Δp_{JT}, the first term in Eq. 4.4.104. The effects of gravity are directly

computed from the distributions of void fraction, phasic densities and channel orientation. The pressure rise induced by the jet pump, Δp_{JT}, is computed from the recirculation flow, as discussed in the next section.

4.4.4.2 Recirculation Flow

This section presents the method by which the recirculation flow through the recirculation loops, each with its recirculation pump, and into the jet pump is predicted. See Figure 4.1 for this flow path, indicated by contour $\mathcal{C}_2$.

The model for the recirculation flow implies the nine assumptions summarized in Section 4.3.1 as Assumptions (4-iv), (4-vi), (4-vii), and (4-xiv) through (4-xix). The assumption of single-phase flow reduces the number of balance equations from four in the reactor vessel to three in the recirculation loop. The assumption of quasi*-incompressible flow replaces also the mass and energy conservation equations, leaving only the momentum equation which governs the recirculation flow rate.

The basis for predicting the recirculation flow is, as in Section 4.4.4.1 for the vessel flow, a closed-loop momentum equation. A single loop around contour $\mathcal{C}_2$ in Figure 4.1, with a single jet pump represents in RAMONA-3B all recirculation loops with all their jet pumps.

The closed contour momentum equation has been derived in Section 4.4.4.1. The result is Eq. 4.4.102 and can be used here with appropriate simplifications which reflect the assumptions implied in the RAMONA-3B recirculation model.

Assumptions (4-xv and xviii) reduce Eq. 4.4.102 to the closed-contour momentum equation for single-phase flow of an incompressible liquid:

$$\frac{d\mathcal{M}_{RCL}}{d\tau} = \Delta p_{RCP} - \sum_{i=1}^{N_s} \left(\frac{f_\ell L}{2 d_h} \frac{W_\ell |W_\ell|}{\rho_\ell A_1^2} \right)_i + \sum_{i=1}^{N_s} \left\{ \left(\frac{W_\ell^2}{2 \rho_\ell A^2} \right)_2 - \left(\frac{W_\ell^2}{2 \rho_\ell A^2} \right)_1 \left[1 + \left(\frac{A_1}{A_{min}} \right)^2 \zeta_{12} \right] \right\}_i \qquad (4.4.127)$$

where $W_\ell = AG$ is the mass flow rate of the liquid, and Δp_{RCP} is the pressure rise across the recirculation pump. See Figure 4.4 for the meaning of subscripts 1 and 2. Notice that the gravity effects are neglected on account of the uniform density (cf. Assumption (4-xvi)).

*Compare Assumptions (4-xvi and xviii) to recognize the conflict between the assumptions of time-dependent density and incompressible flow.

In the RAMONA-3B code, the recirculation loop consists of four segments ($N_S = 4$): firstly, of the flow path from the branch point in the upper downcomer (see Figure 4.1) down to the exit of the downcomer; secondly, of the suction line of the recirculation pump; thirdly, of the discharge line of the recirculation pump, up to the jet pump nozzle where recirculation flow and jet pump suction flow converge (Figure 4.1); and fourthly, of the path between this point of convergence and the branch point in the upper downcomer. Call W_{RCL} the mass flow rate in one of the N_{RCL} recirculation loops. Then we can evaluate Eq. 4.4.127 term by term. In the first three segments, we have

$$(W_\ell)_i = W_{RCL} , \quad i=1,2,3 \tag{4.4.128}$$

because the liquid expansion is ignored (cf. Assumption (4-xviii). In the fourth section we have, with $\rho_\ell (Aj_\ell)_{JT} = \{\rho_\ell Aj_\ell\}(z_{JT})$

$$(W_\ell)_4 = W_{SCT} = \frac{1}{N_{RCL}} \left(\rho_\ell Aj_\ell\right)_{JT} - W_{RCL} , \tag{4.4.129}$$

i.e., the mass flow rate in the suction path $(W_\ell)_4 = W_{SCT}$ is equal to the difference between the downcomer mass flow rate at the suction location and the mass flow rate through the recirculation loop (mass balance for branch point). Thus, Eq. 4.4.127 reads for normal forward flow (cf. Assumption (4-xvii))

$$\frac{d\mathcal{M}_{RCL}}{d\tau} = \Delta p_{RCP} - W_{RCL}^2 \sum_{i=1}^{3} \left\{ \frac{1}{2 A_1^2 \rho_\ell} \left[f_\ell \frac{L}{d_h} + \zeta_{12} \left(\frac{A_1}{A_{min}}\right)^2 + \left\{ 1 - \left(\frac{A_1}{A_2}\right)^2 \right\} \right] \right\}_i - \frac{W_{SCT}^2}{2 A_{SCT}^2 \rho_\ell} (\zeta_{SCT} - 1) . \tag{4.4.130}$$

The area ratio is zero in the last term for the suction flow, because the kinetic energy in the free stream outside the suction intake of the jet pump is very small and ignored. The wall shear and form loss coefficients in the summation of Eq. 4.4.130 are taken to be fixed (cf. Assumption (4-xix)) and lumped together in RAMONA-3B with the coefficient $1/(2A_1^2\rho_\ell)$. Also, the reversible conversion of kinetic energy is ignored in RAMONA-3B (cf. Assumption (4-xii)) which is equivalent to setting $A_1/A_2 = 1$ in Eq. 4.4.130.

Finally, we express $\mathcal{M}_{RCL}$ in terms of mass flow rates. Since there is no inertia contribution from the suction path (cf. Assumption (4-xiv)), we have

$$\mathcal{M}_{RCL} = W_{RCL} \sum_{i=1}^{3} \frac{L_i}{A_i} . \tag{4.4.131}$$

The substitution of Eqs. 4.4.129 and 4.4.131 into Eq. 4.4.130, the above combination of wall shear and form losses and the neglection of kinetic energy in Eq. 4.4.130 yields

$$\frac{dW_{RCL}}{d\tau} = \frac{1}{\sum_{i=1}^{3} \frac{L_i}{A_i}} \left\{ \Delta p_{RCP} - W_{RCL}^2 \left(Z_{RCL} + Z_{DC} + Z_{NZZ} - \frac{1}{2\rho_\ell A_{NZZ}^2} \right) - \left[\frac{\rho_\ell (Aj_\ell)_{JT}}{N_{RCL}} - W_{RCL} \right]^2 \left(Z_{SCT} - \frac{1}{2\rho_\ell A_{SCT}^2} \right) \right\} . \quad (4.4.132)$$

In Eq. 4.4.132 the flow impedances Z are defined from Eq. 4.4.130 to be

$$\begin{aligned} Z_{RCL} &= \frac{1}{2\rho_\ell} \left[\frac{1}{A^2} \left(f \frac{L}{d_h} + \zeta \right) \right]_{RCL} \\ Z_{DC} &= \frac{1}{2\rho_\ell} \left[\frac{1}{A^2} \left(f \frac{L}{d} + \zeta \right) \right]_{DC} \\ Z_{NZZ} &= \left(\frac{\zeta}{2\rho_\ell A^2} \right)_{NZZ} \\ Z_{SCT} &= \left(\frac{\zeta}{2\rho_\ell A^2} \right)_{SCT} \end{aligned} \quad (4.4.133)$$

where the subscripts RCL, DC, NZZ and SCT denote, respectively, the recirculation loop piping, the downcomer, the jet pump nozzle and the jet pump suction. Notice that the kinetic energy is accounted for in the suction intake and the drive nozzle exit of the jet pump, as can be seen in Eq. 4.4.132, in that the flow impedances Z_{NZZ} and Z_{SCT} are reduced by $1/(2\rho_\ell A^2)$.

In RAMONA-3B, the flow impedances Z are fixed, user-specified* input parameters and must have the dimensions of $kg^{-1}m^{-1}$.

Equation 4.4.132 describes the flow rate through the recirculation loop and can be integrated if the mass flow rate $\rho_\ell(Aj_\ell)_{JT}$ in the lower downcomer, at the location of the jet pump suction, and the pressure rise across the recirculation pump, Δp_{RCP}, are specified. The mass flow rate $\rho\ (Aj_\ell)_{JT}$ is computed from Eq. 4.4.114 and the local density of the liquid. The prediction of the pressure rise Δp_{RCP} is given in Section 4.4.4.4.

4.4.4.3 Jet Pump Model

This subsection presents the method for the prediction of Δp_{JT} in the closed contour momentum equations, Eqs. 4.4.104.

The pressure rise Δp_{JT} induced by the jet pump is the pressure between the upper branch point in Figure 4.1 and the diffuser exit, but it is imposed in RAMONA-3B at the location of the jet pump suction intake cross section. The pressure rise Δp_{JT} is computed without inertia and gravity effects, it is computed as a momentum jump condition and imposed at a horizontal interface (without mass) in the downcomer. The jet pump model is subject to the same assumptions as the model for the recirculation loop (cf. Assumptions (4-iv, vi, vii and xiv through xix)).

The pressure rise Δp_{JT} across the jet pump consists of three parts: the pressure change Δp_{SCT} between the upper branch point in Figure 4.1, i.e., the free-stream conditions in the downcomer, and the nozzle exit plane, Plane a in Figure 4.7, then the pressure change Δp_{TRT} in the jet pump mixing throat, between Planes a and b in Figure 4.7, and thirdly, the pressure change in the diffuser, Δp_{DIF}.

The suction intake pressure drop has already been computed in Section 4.4.4.2. It is

$$\Delta p_{SCT} = \left[\rho_\ell \frac{(Aj_\ell)_{JT}}{N_{RCL}} - W_{RCL}\right]^2 \left(\frac{1}{2\,\rho_\ell\, A_{SCT}^2} - Z_{SCT}\right) . \qquad (4.4.134)$$

The momentum balance for the fluid between Planes a and b in Figure 4.7 yields the pressure change in the throat:

$$\Delta p_{TRT} = \frac{1}{A_{TRT}}\left[\frac{\rho_\ell\left(\frac{Aj_\ell}{N_{RCL}}\right)^2_{JT}}{A_{TRT}} - \frac{W_{RCL}^2}{\rho_\ell A_{NZZ}} - \frac{\left[\left(\rho_\ell Aj_\ell\right)_{JT} / N_{RCL} - W_{RCL}\right]^2}{\rho_\ell\,(A_{TRT} - A_{NZZ})}\right] . \qquad (4.4.135)$$

*Actually, the user specifies W_{RCL} instead of Z_{RCL} and the computer returns Z_{RCL}.

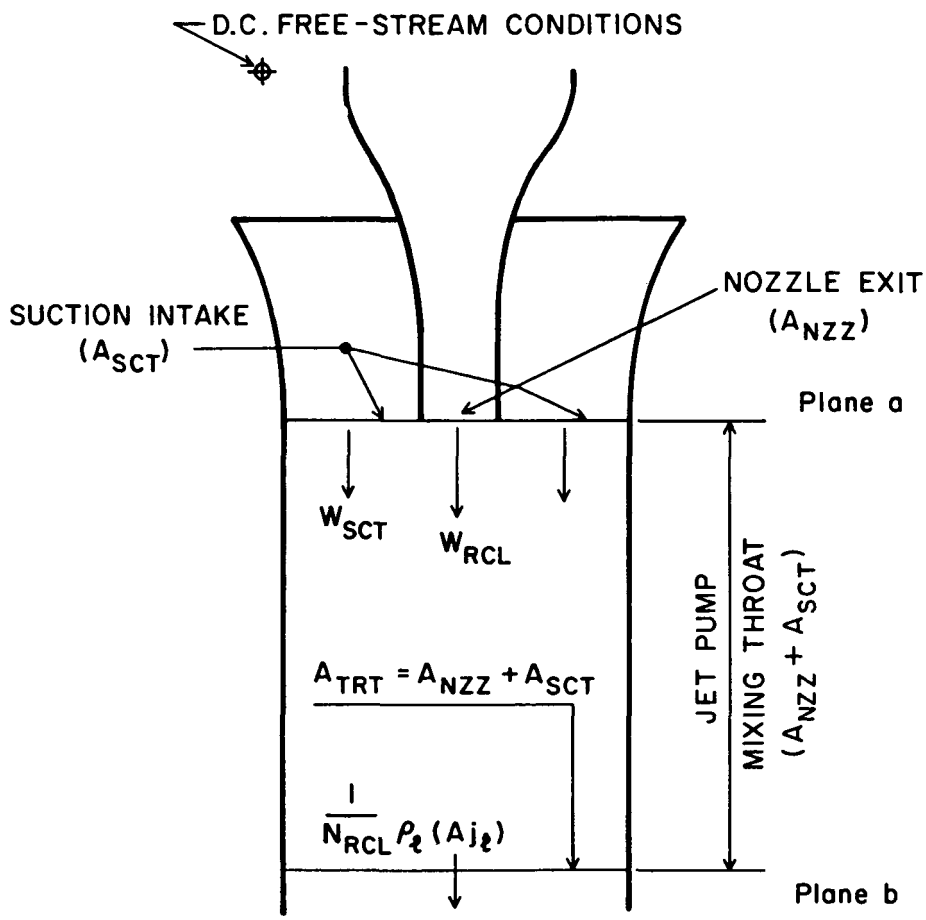

Figure 4.7 Schematic of Jet Pump Mixing Region and Notations for Jet Pump Model

See Figure 4.7 for the meaning of subscripts and for geometry. The pressure recovery in the diffuser is computed from Bernoulli's equation. It is

$$\Delta p_{DIF} = \frac{\left\{\rho_\ell \left(A j_\ell\right)\right\}^2_{JT}}{N^2_{RCL}} \left[\frac{-1 + \left(\frac{A_{TRT}}{A_{DIF}}\right)^2 + \zeta_{DIF}}{2\,\rho_\ell\, A^2_{TRT}}\right] .$$

The square of the area ratio is approximately 0.03 and is ignored. Thus

$$\Delta p_{DIF} = \frac{\left\{\rho_\ell \left(A j_\ell\right)\right\}^2_{JT}}{N^2_{RCL}} \left[-\frac{1}{2\,\rho_\ell\, A^2_{TRT}} + Z_{DIF}\right] , \qquad (4.4.136)$$

where

$$Z_{DIF} = \frac{\zeta_{DIF}}{2\,\rho_\ell\, A^2_{TRT}} \qquad (4.4.137)$$

is a (user-specified*) constant in RAMONA-3B. Since the mass flow rates $\{\rho_\ell(A j_\ell)\}_{JT}$ and W_{RCL} are known from Eqs. 4.4.114 and 4.4.132, respectively, one can compute the total pressure rise Δp_{JT} across the jet pump from Eqs. 4.4.134, 4.4.135 and 4.4.136:

$$\Delta p_{JT} = -\left(\Delta p_{SCT} + \Delta p_{TRT} + \Delta p_{DIF}\right) . \qquad (4.4.138)$$

This pressure rise Δp_{JT} is used in Eqs. 4.4.102 and 4.4.104.

4.4.4.4 Recirculation Pump Model

The recirculation pumps, one in each recirculation loop, drive the recirculation flow through the recirculation loops into the jet pumps. Through momentum exchange in the jet pumps, the recirculation pumps drive indirectly the coolant through the core. Their pumping action is enhanced by buoyancy effects due to the low density in the boiling two-phase mixture of the core and the high density of liquid in the downcomer. The recirculation pumps are used to control the core flow, consequently the inlet subcooling temperature, the nonboiling height, and thereby, the vapor void fraction, moderator density and fission power.

*RAMONA-3B accepts the initial liquid coolant flow $\rho_\ell(A j_\ell)_{JT}$ at the jet pump intake (equal to core inlet flow rate) and returns Z_{DIF}.

The purpose of the recirculation pump model is to predict the pressure rise Δp_{RCP} in Eq. 4.4.132. This pressure rise depends not only upon the recirculation flow rate W_{RCL} but also on the angular speed ω_{RCP} of the recirculation pump. The angular speed, ω_{RCP} is computed from the equation of motion for the pump, the motion being governed by the balance between the electrical torque and the pump torque. The pump torque consists of the hydraulic torque and the frictional torque.

The pressure rise across the recirculation pump and its torque are normally determined from experiments which render homologous maps of normalized pressure rise and torque as functions of reduced pump speed.

In RAMONA-3B the pressure rise across the recirculation pump is predicted from

$$\Delta p_{RCP} = C\,\omega_{RCP}^2 - C_{21}\,W_{RCL} - C_{22}\,(W_{RCL} + C_{23})\,|W_{RCL} + C_{23}|\,, \qquad (4.4.139)$$

where ω_{RCP} is computed from Eq. 4.4.141 below, W_{RCL} is the mass flow rate in a loop, computed from Eq. 4.4.132 and C, C_{21}, C_{22}, C_{23} are constants. The first constant, C, is computed from the user-specified, initial steady-state recirculation loop mass flow rate $(W_{RCL})_o$ and the corresponding normal pump speed, $(\omega_{RCL})_{rated}$, by substituting Eq. 4.4.139 into Eq. 4.4.132. The constants C_{21}, C_{22} and C_{23} are specified by the user.* We have used**

$$\left.\begin{aligned} C_{21} &= 32.67 && m^{-1}\,s^{-2} \\ C_{22} &= 0.1080 && m^{-1}\,kg^{-1} \\ C_{23} &= 0 && kg\,s^{-1} \end{aligned}\right\} \qquad (4.4.140)$$

The constant C has the dimensions of $N/(m\ s)^2$. The pressure rise Δp_{RCP} from Eq. 4.4.139 is used in Eq. 4.4.132.

The angular velocity ω_{RCP} in Eq. 4.4.139 is computed from the equation of angular motion of pump rotor and motor rotor, namely

$$I_{PM}\,\frac{d\omega_{RCP}}{d\tau} = T_{EL} - T_{RCP} \qquad (4.4.141)$$

*Input Data Card No. 500 040; C_{21} and C_{22} are specified with signs opposite to those in Eqs. 4.4.139 and 4.4.140.

**Data obtained from G.E. by private communication.

where I_{PM} is the moment of inertia of motor and pump rotor assembly and

$$T_{EL} = (T_{EL})_{ref} \text{ fct. } (\omega/\omega_{rated}) \qquad (4.4.142)$$

is the electrical torque of the recirculation pump drive motor. This drive motor is normally an induction motor, the rotational speed of which is controlled by voltage and frequency to vary the reactor power between 75 and 100% of full power (without control rod actions). The electrical torque simulated in RAMONA-3B according to Eq. 4.4.142, with the user-specified, fixed reference torque $(T_{EL})_{ref}$, is valid only for fixed stator voltage and generator frequency (cf. Assumption (4-xx)). The rotor speed-dependent function, fct.(ω/ω_{rated}), is the relative torque variation. It can be constructed from the Heyland diagram (Nuernberg 1952), using electrical measurements at idle speed and blocked rotor conditions. The function is entered into RAMONA-3B as a table, as shown below, covering the speed range from $\omega=0$ up to 1.20 times the synchronous speed. At the present time, the RAMONA-3B code has the following specification for the reference electrical torque and reference motor speed:

$$(T_{EL})_{ref} = 38{,}935 \text{ Nm}$$
$$\omega_{rated} = 172.8 \text{ s}^{-1} \quad . \qquad (4.4.143)$$

Table 4.3 Relative Electrical Torque for Recirculation Pump (cf. Eq. 4.4.142)

ω/ω_{rated}	fct.(ω/ω_{rated})
0.00	0.80
0.20	0.82
0.40	0.92
0.60	1.12
0.80	1.60
0.90	2.22
1.00	1.00
1.04	0.00
1.20	-5.00

The pump torque, T_{RCP} in Eq. 4.4.141 consists of the hydraulic torque (Euler) and the bearing torque in the recirculation pump. It is predicted in RAMONA-3B from

$$T_{RCP} = C_{24}\,\omega_{RCP}^2 + C_{25}\,\omega_{CRP}\,W_{RCL} + C_{26}\,(W_{RCL} + C_{27}\,\omega_{RCP})\,|W_{RCL} + C_{27}\,\omega_{RCP}|\,, \qquad (4.4.144)$$

where C_{24} through C_{27} are user-specified* constants. RAMONA-3B uses presently

$$\left.\begin{aligned} C_{24} &= 0.8506 \text{ J s}^2 \\ C_{25} &= 0.0408 \text{ J s}^2 \text{ kg}^{-1} \\ C_{26} &= -4.567 \times 10^{-3} \text{ J s}^2 \text{ kg}^{-2} \\ C_{27} &= -8.966 \text{ kg} \end{aligned}\right\} \quad (4.4.145)$$

Finally, the moment of inertia of the pump impeller and motor rotor assembly, I_{PM} in Eq. 4.4.141, must also be specified by the code user.** RAMONA-3B has currently

$$I_{PM} = 1.013 \times 10^3 \text{ kg m}^2 . \quad (4.4.146)$$

This completes the description of the recirculation pump model in RAMONA-3B, and thereby, the descriptions of the models for predicting the coolant circulations in the pressure vessel and the recirculation loops.

4.4.5 Reactor Component Modeling

This section describes the thermohydraulic models for particular components and processes in the reactor vessel and the model for the steam line dynamics.

The thermohydraulics models for the reactor vessel are based in RAMONA-3B on

a) the vapor mass balance, Eq. 4.4.1,

b) the mixture mass balance, in the form of Eqs. 4.4.123, 4.4.121 and then 4.4.114, 4.4.116 and 4.4.118,

c) the mixture momentum balance, Eq. 4.4.104,

d) the mixture energy equation, Eq. 4.4.4,

and on the constitutive relations presented in Section 4.4.2.

*TP1 through TP4 on Input Data Card No. 500 054.
**RJJP on Input Data Card No. 500 053.

We present in this section particular modeling supplements to the above equations, supplements which have been implemented in RAMONA-3B to account for specific component features. These modeling supplements distinguish the RAMONA-3B code from general systems codes and render it suitable for a wide range of applications to transients in BWR power plants of U.S. designs.

The steam line dynamics model is not based on any of the above equations since its purpose is to predict acoustical effects in the steam lines and these effects are not modeled elsewhere.

4.4.5.1 The Reactor Core Model

The reactor core is divided into N_c-1 heated flow channels, each containing a number of channel boxes, and one "unheated" bypass channel which contains all the coolant flowing between the channel boxes (but not the stagnant water at the periphery of the core*).

All N_c flow channels have the same terminal pressures imposed at the lower and upper plena for computing the individual flow rates from their individual closed-contour momentum equations, Eqs. 4.4.104. Each individual, heated channel exchanges thermal energy with the single bypass channel according to Eq. 4.4.5. The "unheated" bypass channel receives heat indirectly from all directly heated channels, by setting

$$q'_w = \sum_{j=1}^{N_c-1} (\xi\bar{U})_{lb} (t_{f\ell} - t_{lb}) \qquad (4.4.5a)$$

instead of Eq. 4.4.5.

The initial steady-state flow distribution between heated and bypass channels is controlled by the orifice design in the fuel support plate which, in turn, is reflected by the proper selection of loss coefficients $\zeta(A_1/A_{min})^2$ in Eq. 4.4.104.

An important safety criterion for BWRs is the Critical Power Ratio (CPR), which is a measure for assessing the safety margin from burnout conditions under steady-state operations. The Critical Power Ratio is the core-wide minimum ratio of thermal power required to produce critical heat flux conditions (cf. Eq. 4.4.23), to the thermal power actually transferred to the coolant in a particular channel. The Critical Power Ratio can be computed as a function of axial position for core elevations above boiling incipience; it reaches its minimum value at the core exit, and it should reach unity when and where the wall heat flux q''_w equals the critical heat flux during (quasi-) steady

*We recommend that the water of the reflector be accounted for in a separate channel of stagnant liquid that is allowed to flash and to expand into the riser. Its energy content is important in long-term transients.

operation. The larger the Critical Power Ratio is, the further the reactor is from burnout conditions.

RAMONA-3B is programmed to compute CPR, using the empirical correlation from General Electric (1977) for the critical flow quality X_{CHF} at burnout. This correlation is proprietary at this time and, therefore, not documented in this report.

From the definition of CPR, the steady-state energy balance (Section 4.4.1, Eq. 4.4.4) and the definition of flow quality, G_v/G_m (cf. Eq. 4.4.48), one finds

$$CPR = \frac{(1-x_{CHF})(h_\ell)_{CHF} + x_{CHF} h_g - (h_\ell)_{CI}}{(1-x)\, h_\ell + x\, h_g - (h_\ell)_{CI}} , \qquad (4.4.147)$$

where h denotes enthalpy, the subscripts f and g indicate saturation enthalpies of liquid and vapor, respectively, and the subscript CI indicates core inlet conditions. By neglecting the subcooling $\Delta h = h_f - h_\ell$ at the point of burnout, relative to the enthalpy of evaporation, h_{fg}, one can simplify Eq. 4.4.147 to read

$$CPR = 1 + \frac{x_{CHF} - x}{x + \frac{\Delta h_{CI}}{h_{fg}}} . \qquad (4.4.148)$$

The flow quality x is computed from Eqs. 4.4.48, 4.4.111 and 4.4.107; the critical flow quality x_{CHF} is computed from the proprietary reference by G.E. (1977). The latent heat of evaporation, h_{fg}, is computed from the system pressure, (Eq. 4.4.49), and from Eq. 4.4.72, while the inlet subcooling enthalpy, Δh_{CI} is computed from liquid temperature $(t_\ell)_{CI}$ (cf. Eq. 4.4.80) at the core entrance and from

$$\Delta h_{CI} = c_{p,\ell} \left[(t_\ell)_{CI} - t_{sat}\right] + \langle p \rangle_{syst} \left(\frac{1}{\rho_f} - \frac{1}{\rho_\ell}\right) \qquad (4.4.149)$$

and the appropriate correlations for t_{sat}, ρ_f and ρ_ℓ (Eqs. 4.4.69, 4.4.70 and 4.4.76).

There are no other special modeling features for the core hydraulics in RAMONA-3B.

4.4.5.2 Upper Plenum and Riser

The upper plenum and riser sections are modeled with the standard balance equations of RAMONA-3B as listed at the beginning of Section 4.4.5. The upper plenum and riser sections are taken to be adiabatic flow channels (cf. Assumptions 3-i and ii). This implies $q'_w = 0$ and $q'''_\ell = 0$ in the energy equation, Eq. 4.4.4, and in the equation for vapor generation rate Γ_w from wall heating, Eq. 4.4.56.

The steam separators are modeled to be part of the riser section. Their modeling supplements are discussed in the next section.

4.4.5.3 Steam Separators

The purpose of the particular modeling for the steam separators is to account for (a) the flow inertia in the spiral paths of the separators, (b) for the form losses in the separator and (c) to predict the volumetric flow rate $(Aj_g)_{SPE}$ of saturated vapor leaving the vessel circulation loops (cf. last term in integrand of Eq. 4.4.119) and entering the steam dome above the coolant level as shown in Figure 4.8 (entrainment of vapor or carry-under).

The supplementary modeling in RAMONA-3B has been developed by Scandpower (Rasmussen 1979). The documentation of the separator model is not complete because

1. the control volume of the separator analysis is not uniquely defined,

2. the separator analysis involves control volumes of steam dome, downcomer and lower plenum to describe processes in the separator, and

3. the separator analysis employs the conservation equations already used, to predict new unknowns.

The separator model presently in RAMONA-3B should therefore be used with caution in predicting the amount of carry-under vapor which enters the vapor dome control volume below the coolant level $(Aj_g)_{CU}$ (see Figure 4.8) whenever core exit conditions deviate significantly from steady-state conditions. The carry-under is used in the prediction of the volumetric flow rate of the steam entering the dome above the mixture level. More importantly, the contradictions of the model developed for the low-void region in the steam dome could render the level predictions unreliable and may lead to computational difficulties, particularly with high void fractions in the riser and as the coolant level falls into the upper downcomer. Since the precise prediction of carry-under vapor is not important for many operational transients, RAMONA-3B can be expected to simulate transients during which the coolant level remains near its normal elevation, and while the riser entrance void fraction does not exceed its normal, full-power value (~ 0.6).

In addition to the stated objectives for the separator model, the RAMONA-3B separator model is also used to impose saturation conditions on the liquid

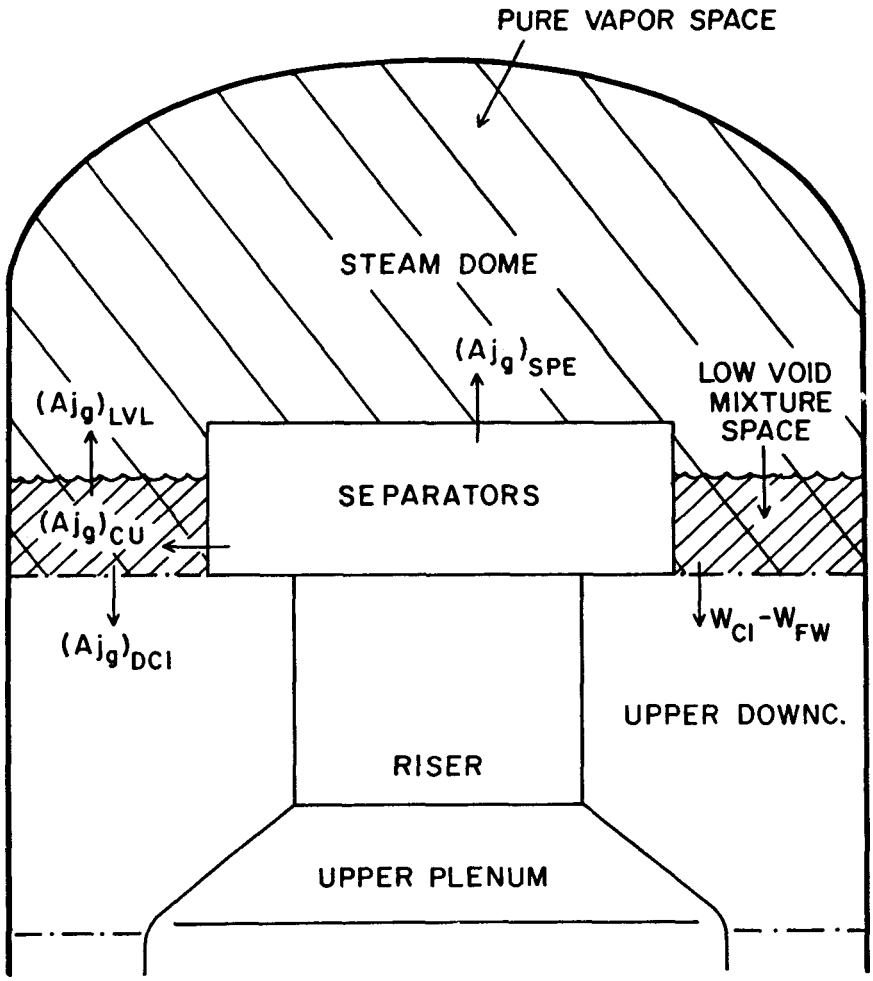

Figure 4.8 Schematic for Separator and Steam Dome Analysis

phase at the separator exit (cf. Assumption (4-xxii)). This is necessary to compensate for the appearance of unrealistically high liquid superheat temperatures, produced by the nonphysical vapor generation model (Eq. 4.4.57 for Γ_{ph}). The saturation conditions are achieved by imposing at the separator exit interface a jump condition with an evaporation source Γ_a (kg $m^{-2}s^{-1}$).

Let W designate mass flow rates and superscripted (-) and (+) signs denote up and downstream conditions at the interface. Then the mass jump condition for the liquid is

$$W_\ell^- = W_f^+ + A\Gamma_a \quad , \tag{4.4.150}$$

the mixture mass jump condition is

$$W_\ell^- + W_g^- = W_m = W_f^+ + W_g^+ \, , \tag{4.4.151}$$

and the mixture energy jump condition is

$$W_\ell^- h_\ell^- + W_g^- h_g = (Wh)_m = W_f^+ h_f + W_g^+ h_g \quad . \tag{4.4.152}$$

Since W_ℓ^-, W_m and $(Wh)_m$ are known, one can compute from Eqs. 4.4.150 through 4.4.152, with given h_f and h_g:

$$A\Gamma_a = W_\ell^- + \frac{(Wh)_m - h_g W_m}{h_{fg}} \quad , \tag{4.4.153}$$

and

$$W_g^+ = \frac{(Wh)_m - h_f W_m}{h_{fg}} \tag{4.4.154}$$

and

$$W_\ell^+ = W_m - W_g^+ \quad . \tag{4.4.155}$$

The term $(A_{exit}/V)_{RSR}\,\Gamma_a$ is added to Γ_{ph} of Eq. 4.4.57 when applied to the riser. The vapor mass flow rate $(W_g^+)_{RSR}$ is discharged into the steam dome, primarily above the coolant level, but also in part below this level as carry-under vapor, $\rho_g(Aj_g)_{CU}$ in Figure 4.8.

We now proceed to present the models with which to achieve the three stated objectives for the steam separator models in RAMONA-3B.

(a) The flow inertia is accounted for in RAMONA-3B by multiplying the riser segment length L in the momentum balance (cf. Eq. 4.4.99) with an empirically obtained coefficient (Linford 1973, p. 2-30). The coefficient is currently represented in RAMONA-3B by L_{RSR},

$$\iota_{RSR} = \frac{A_{RSR}}{L_{RSR}\, N_{SEP}} (1-x_{RSR}) \left\{ \left(\frac{L}{A}\right)_o + x_{RSR}\, (1{,}357 + 6{,}561\ x_{RSR})\, (m^{-1}) \right\} . \quad (4.4.156)$$

The segment length L of the riser is multiplied by multiplying χ of the riser in Eq. 4.4.108 by ι_{RSR}. In Eq. 4.4.150 A_{RSR} and L_{RSR} are the riser flow cross section and height, respectively, N_{SEP} is the number of separators, x_{RSR} is the flow quality (defined as in Eq. 4.4.8) at the entrance to the riser and $(L/A)_o$ is the measured effective L/A ratio for single-phase liquid flow. Currently used in RAMONA-3B is

$$\left(\frac{L}{A}\right)_o = (L/A)_{liquid} \quad (4.4.157)$$

$$= 120.0\ m^{-1} . \quad (4.4.158)$$

Equation 4.4.156 is based on the observation (Linford 1973, p. 2-28) that the water film is not affected by the mass flow rate in the range of 25.3 kg/s $\leq W_{RSR} \leq$ 101.1 kg/s, that the water film thickness is dependent only upon the flow quality at the separator entrance and that the water film dominates the inertia. Equation (4.4.156) is based on experiments in the range of $0 \leq X_{RSR} \leq$ 0.16. The pressure is not reported for the experimental data base.

(b) The loss coefficient $\{-\zeta(A_1/A_{min})^2\}_{SRS}$ for the riser section, modeled to contain the separator, is user-specified* in RAMONA-3B to be -30.0 (dimensionless).

(c) The description of carry-under flow in RAMONA-3B is arbitrary and nonphysical. The carry-under flow is defined in terms of the flow quality X_{CU} of the discharge flow from the separator toward the downcomer (see Figure 4.8)

$$x_{CU} = \frac{\rho_g\, (Aj_g)_{CU}}{(A\, G_m)_{RSR,CU}} . \quad (4.4.159)$$

*VHRO on Input Data Card No. 200 013.

The flow quality, X_{CU}, is used to impose, for prescribed feedwater conditions, the desired initial liquid subcooling temperature at the core inlet. Then the value of X_{CU} is retained during the transient. It is obvious that the separator performance model is being used to compensate for modeling inadequacies in the downcomer and recirculation loop (omission of heat transfer from core to downcomer, of heat addition from recirculation pumps, etc., from the energy equations), rather than to describe the vapor branching in the separator (cf. Assumption (4-xxi)).

The total vapor flow rate $(W_g^+)_{RSR}$ from Eq. 4.4.156 is split into the mass flow rate $(Wg)_{SPE} = \rho_g(Ajg)_{SPE}$ of the vapor entering the dome (and leaving through the steam lines) and the mass flow rate $\rho_g(Ajg)_{CU}$ of the vapor, also entering the dome, but below the coolant level. This carry-under vapor mass flow rate is further split

$$\rho_g(Aj_g)_{CU} = \rho_g(Aj_g)_{DCI} + \rho_g(Aj_g)_{LVL} \tag{4.4.160}$$

i.e., into the vapor leaving from the steam dome into the downcomer and the vapor passing through the stationary coolant level. This split constitutes the steady-state vapor balance for the control volume in the dome and below the coolant level, namely, a region entirely outside the separator for which this analysis has been developed.

Next, the mass flow rate $\rho_g(Aj_g)_{DCI}$ of the vapor entering the downcomer is chosen to produce the desired core inlet subcooling enthalpy Δh_{CI} $[h_f - (h_\ell)_{CI}]$. From the steady-state energy balance for the control volume which contains the downcomer and the lower plenum up to the core entrance yields, if one ignores heat addition from the hot vessel walls, the core barrel and the recirculation pumps,

$$\rho_g(Aj_g)_{DCI} = \frac{W_{FW}\Delta h_{FW} - W_{CI}\Delta h_{CI}}{h_{fg}} , \tag{4.4.161}$$

where $\Delta h_{FW} = h_f - (h_\ell)_{FW}$ is the feedwater subcooling enthalpy and h_{fg} is the heat of evaporation. The symbols W_{FW} and W_{CI} are feedwater and core inlet mass flow rates. Equation 4.4.161 gives the first term in Eq. 4.4.160. To compute the second term, we need to compute the void fraction first. Specifically, we need the void fraction just below the mixture level. By Assumption (4-xxiii), however, the vapor void fraction is taken to be uniform in the vapor dome below the mixture level. Rather than compute the average vapor void fraction for the low-void region in the dome from the steady-state vapor mass balance, Eq. 4.4.1, RAMONA-3B computes the vapor void fraction from a slip correlation, Eq. 4.4.64 and the known vapor mass flux $\rho_g(Aj_g)_{DCI}$ at the downcomer entrance. This is accomplished as follows:

Since one knows the steady-state mass flow rates in core, W_{CI}, and feedwater sparger W_{FW}, one can write, for steady-state conditions, the total mass flux at the dome exit or downcomer entrance (above feedwater sparger)

$$W_{CI} - W_{FW} = A_{DCI} \left[\alpha \rho_g w_g + (1-\alpha) \rho_\ell w_\ell\right] \quad . \tag{4.4.162}$$

From Eq. 4.4.161, one obtains

$$\rho_g (Aj_g)_{DCI} = A_{DCI} \alpha \rho_g w_g \tag{4.4.163}$$

and from Eq. 4.4.64

$$w_g = S w_\ell + v^o \quad . \tag{4.4.64}$$

Equations 4.4.162, 4.4.163 and 4.4.164 are solved for the void fraction

$$\alpha = 1 - \frac{1}{2} \left[\sqrt{A^2 - 4B} - A\right] \quad , \tag{4.4.165}$$

where

$$A = 1 + \frac{S(W_{CI} + W_{FW}) - (S+1) \rho_g (Aj_g)_{DCI}}{A_{DCI} \rho_\ell v^o} \tag{4.4.166a}$$

and

$$B = S \frac{\rho_g}{\rho_\ell} \frac{(jg)_{DCI}}{v^o} \quad . \tag{4.4.166b}$$

Observe that the void fraction computed from Eq. 4.4.165 need not agree with the void fraction already computed from the vapor mass balance, Eq. 4.4.1, applied to the low-void region of the dome as discussed in Section 4.4.5.4.

Having evaluated the void fraction α from Eq. 4.4.165, the RAMONA-3B model continues on to compute the last term in Eq. 4.4.160, namely, the vapor flow penetrating the (stationary) coolant mixture level (v_ℓ=0), using Eq. 4.4.64:

$$(j_g)_{LVL} = \alpha v^o \tag{4.4.167}$$

Thus, the carry-under vapor leaving the separator is computed from Eq. 4.4.160, and Eq. 4.4.159 can be evaluated since $(G_m A)_{CU} = W_\ell^+ + \rho_g (A j_g)_{CU}$ and W_ℓ^+ is given from Eq. 4.4.155.

In summary, the carry-under vapor flow rate which should be computed from the separator characteristics is computed to adjust the core inlet subcooling enthalpy, thereby relying on a slip correlation to compute a vapor void fraction rather than using the vapor void fraction computed from the vapor mass balance.

4.4.5.4 Steam Dome

The steam dome is not modeled by the mixture mass and momentum equations for flow channels as itemized at the beginning of Section 4.4.5. Instead, the steam dome is modeled as a reservoir with stagnant saturated vapor above a stagnant, low-void two-phase mixture as shown in Figure 4.8.

RAMONA-3B is the only systems code that has a correct model for tracking the two-phase mixture level in the steam dome. However, the level motion is restricted (cf. Assumption (4-xxiv)) to the steam separator elevation such that the liquid return drainage from the separator discharges below the mixture level. The level is further restricted such that the low-void mixture in the dome does not cover the vapor discharge ports at the top of the steam separator. The level tracking model in RAMONA-3B implies that there is only pure vapor above the level, hence no falling liquid films or sprays.

The RAMONA-3B model for the steam dome consists of two parts. One part deals with the entire dome volume (see Figure 4.8), the other with the low-void regime below the mixture level.

The vapor mass $(M_g)_{DOM}$ and mixture energy $(\overline{uM})_{DOM}$ of all the coolant in the steam dome is obtained by subtracting from the total system vapor mass $(M_g)_{syst}$ and total system energy $(\overline{uM})_{syst}$, respectively, the vapor mass and mixture energy of all segments in the system, except those of the dome.

The system vapor mass balance

$$\frac{d(M_g)_{syst}}{d\tau} = \iiint_V \Gamma_v \, dV - W_{SL} \tag{4.4.168}$$

and the overall energy balance

$$\frac{d(\overline{uM})_{syst}}{d\tau} = (hW)_{FW} - (hW)_{SL} + (hW_{ECC}) + \iint_{A_h} q''_w \, dA + \iiint_V (1-\alpha) \, q'''_\ell \, dV \qquad (4.4.169)$$

are integrated. Subscripts FW, SL and ECC denote feedwater, steam line and emergency coolant injection flows, respectively, A_h is the entire heated area and V is the entire coolant volume. Since the local void fraction and energies are known (cf. Eqs.4.4.1 and 4.4.4) in all components (with total volume $V^* = V_{syst} - V_{DOM}$), except in the dome, one can compute

$$(M_g)_{DOM} = (M_g)_{syst} - \rho_g \iiint_{V^*} \alpha \, dV \qquad (4.4.170)$$

and

$$(\overline{uM})_{DOM} = (\overline{uM})_{syst} - \iiint_{V^*} \left[\rho_g \alpha u_g + (1-\alpha) \rho_\ell u_\ell\right] dV \quad . \qquad (4.4.171)$$

With $(\overline{uM})$ and M_g known, the temperature t_ℓ and density ρ_ℓ of the liquid are computed from Eqs. 4.4.80 and 4.4.76. The thermal equation of state then yields the liquid mass in the dome

$$(M_\ell)_{DOM} = (\rho_\ell)_{DOM} \left[V_{DOM} - \frac{(M_g)_{DOM}}{\rho_g}\right] , \qquad (4.4.172)$$

which, by Assumption (4-xxiv), is all below the liquid level.

The second part of the steam dome model of RAMONA-3B deals with the low-void two-phase mixture below the mixture level in the steam dome (see Figure 4.8). The objective of the analysis for this regime is to predict (a) its void fraction, (b) its volume and thereby the mixture level elevation and (c) the entrance conditions at the upper downcomer.

The void fraction α is computed from the vapor mass balance. Let the subscript LVD denote the low-void regime in the vapor dome. Then the vapor mass balance in RAMONA-3B reads*

$$\frac{1}{\rho_g}\frac{d(M_g)_{LVD}}{d\tau} = (Aj_g)_{CU} - (Aj_g)_{DCI} - \left[A\alpha(w_g - w_i)\right]_{LVL} + \frac{(V\Gamma_v)_{LVD}}{\rho_g}, \quad (4.4.173)$$

where the subscripts CU, DCI and LVL denote, respectively, riser exit, downcomer entrance and liquid level.

In Eq. 4.4.173, the interface velocity w_i of the mixture level is equal to the liquid velocity because of Assumption (4-xxiv)

$$w_i = w_\ell \qquad \text{at } z = z_{LVL} . \quad (4.4.174)$$

Since the slip ratio is assumed to be unity (cf. Assumption (4-xxv)), one gets for the relative vapor velocity

$$(w_g - w_i)_{LVL} = w^o , \quad (4.4.175)$$

the vapor velocity relative to stagnant liquid. The vapor volumetric fluxes $(Ajg)_{RSE}$ and $(Ajg)_{DCI}$ are computed from Eqs. 4.4.118 and 4.4.161 (the latter being derived originally for steady-state conditions and then used for the transient). The vapor generation rate in Eq. 4.4.173 is computed from Eq. 4.4.57.

With the mass of the vapor below the mixture level given by Eq. 4.4.173 and with the liquid mass and liquid density computed according to Eqs. 4.4.172 and 4.4.76, one finds the vapor void fraction α below the mixture level in the steam dome from

$$\alpha = \frac{(M_g)_{LVD}/\rho_g}{\frac{(M_\ell)_{DOM}}{\rho_\ell} + \frac{(M_g)_{LVD}}{\rho_g}} . \quad (4.4.176)$$

*The first term on the right-hand side is presented here as found in the FORTRAN listing and differs from the corresponding term in the original Scandpower documentation.

Notice that this void fraction is most likely in conflict with the same void fraction computed from Eq. 4.4.165, even under conditions of steady state.

(b) The liquid level in the vapor dome is computed from the cross-sectional area A_{LVL} of the steam dome at the separator elevation (see Figure 4.8)

$$L_{LVL} = \frac{1}{A_{LVL}} \left[\frac{(M_\ell)_{DOM}}{\rho_\ell} + \frac{(M_g)_{LVD}}{\rho_g} \right] . \qquad (4.4.177)$$

(c) The mixture volumetric flow rate $(Aj_m)_o$ at the downcomer entrance is given by Eq. 4.4.123, that of the vapor by Eq. 4.4.161. Therefore, the liquid volumetric flow rate is

$$(Aj_\ell)_{DCI} = (Aj_m)_o - (Aj_g)_{DCI} . \qquad (4.4.178)$$

The density ρ_g and internal energy u_g of the vapor are functions of the system pressure $\langle p \rangle_{syst}$. The density ρ_ℓ and internal energy u_ℓ of the liquid entering the downcomer are taken to equal those of the liquid in the low-void mixture below the level in the vapor dome, i.e., the same as computed in item (a) above.

4.4.5.5 Steam Line Dynamics

The purpose of the steam line dynamics model in RAMONA-3B is to simulate the acoustic effects in the steam lines induced by abrupt valve closures which lead to traveling and reflecting compression and expansion waves. The pressure pulses in turn propagate through the steam dome into the reactor core, cause there the collapse of vapor voids, thusly insert reactivity and cause the fission power to rise sharply. The acoustic phenomena of pressure pulses and flow oscillations must be resolved on a time scale of approximately 0.05 seconds.

The model description summarized here has been documented earlier (Wulff 1980a), together with the model assessment by comparison with an anlytical solution, with other computer code results and with full-scale reactor experiments. Below we present the steam line geometry and the modeling equations for the transient. The steady-state description of the steam line flow is included in Section 4.5. The numerical solution techniques for the steam line dynamics are described in Section 6.4.2.3.

4.4.5.5.1 Steam Line Geometry

The steam line system as modeled consists of a single pipe with specified length and diameter (which may change at branch positions), connecting the steam dome with the turbine valve and having two branches at freely specified axial positions. One branch leads to the pressure relief and safety valves, the other branch leads into the bypass line and to the bypass valve. Thus, the steam line system terminates at the steam dome exit, at the turbine valve, at the relief and safety valves and at the bypass valve.

Two or more steam lines in parallel are modeled by a single line with its length equal to the arithmetic mean length of the parallel lines and with its internal diameter equal to the actual diameter of an individual pipe. The computed mass and enthalpy flow rates at the steam dome exit are then multiplied by the number of parallel steam lines.

A Main Steam Isolation Valve (MSIV) closure is modeled with a steam line segment leading from the reactor vessel to the isolation valve, including the safety and relief valves but without the line sections downstream of the isolation valve.

4.4.5.5.2 Governing Equations for Steam Line Dynamics

The steam line dynamics model in RAMONA-3B is subject to Assumptions (4-i, v, and xxvi through xxix) listed in Section 4.3. The assumptions have been justified on the basis of an order of magnitude estimation of their effects and on the basis of a comparison between analytical solutions and experimental data (Wulff 1980b). The model limits the application of RAMONA-3B to transients in which the low-void, two-phase mixture level in the reactor vessel does not reach the entrance to the steam line (cf. Assumption (4-xxiv)).

The general one-dimensional conservation equations for the steam flow in the steam lines are

the mass balance

$$A \frac{\partial \rho}{\partial \tau} + \frac{\partial W}{\partial z} = 0 \qquad (4.4.179)$$

where

$$W = \int_A \rho w dA \ ,$$

the momentum balance

$$\frac{\partial W}{\partial \tau} + \frac{1}{A} \frac{\partial}{\partial z} \left(\widetilde{\beta} \frac{W^2}{\rho} \right) = - A g_z \rho - A \frac{\partial p}{\partial z} - \frac{f + \zeta \frac{d}{L}}{2dA} \frac{|W|}{\rho} W \ , \qquad (4.4.180)$$

where

$$\tilde{\beta} = \frac{\rho A}{W^2} \int_A \rho w^2 dA ,$$

and f designates the Darcy friction factor, ζ designates the form loss coefficient, and L is the length of a pipe segment with constant cross-sectional area A,

the energy balance

$$\frac{\partial h}{\partial \tau} - \frac{1}{\rho}\frac{\partial p}{\partial \tau} + \frac{W}{A\rho}\left(\frac{\partial h}{\partial z} - \frac{1}{\rho}\frac{\partial p}{\partial z}\right) = \frac{1}{\rho}\left[\frac{4q''_w}{d} + q''_z + \phi_\mu\right] , \qquad (4.4.181)$$

where q''_z designates axial conduction and ϕ_μ designates viscous dissipation. The symnbols A, d, ρ, p, h, g_z and q''_w in Eqs. 4.4.179 through 4.4.181 denote cross-sectional area, pipe diameter, density, pressure, enthalpy, gravitational constant and wall heat flux, respectively.

Assumptions (4-xxvi and xxviii) imply isentropic processes in an ideal gas. Combining the equation of state

$$\rho = \frac{\kappa}{\kappa-1}\frac{p}{h} \qquad (4.4.182)$$

and Assumptions (4-xxvi and xviii) with Eq. 4.4.181 yields, since $TDs/D\tau = 0 = Dh/D\tau - (1/\rho)Dp/D\tau$,

$$\kappa \frac{d\rho}{\rho} = \frac{dp}{p} \qquad (4.4.183)$$

and

$$\rho(\tau,z) = \rho_o \left[p(\tau,z)/\langle p\rangle^o_{syst}\right]^{1/\kappa} \qquad (4.4.184)$$

where $\langle p\rangle^o_{syst}$ is the initial steam dome pressure, $\rho_o = \rho_g(\langle p\rangle^o_{syst})$ is the initial saturation density of the steam in the dome.

Assumption (4-xxvii) and Eq. 4.4.184 reduce Eq. 4.4.180 to this final form of the momentum balance

$$\frac{\partial W}{\partial \tau} = -A\frac{\partial p}{\partial z} - \frac{f+\zeta\, d/L}{2\,dA\,\rho_o}\left[\langle p\rangle^o_{syst}/p\right]^{1/\kappa} |W|W . \qquad (4.4.185)$$

Substitute Eq. 4.4.184 into the mass balance, Eq. 4.4.179 and find the final form for the mass balance

$$\frac{\partial p}{\partial \tau} = - \frac{\kappa \langle p \rangle^{o}_{syst}}{A \rho_o} \left[p / \langle p \rangle^{o}_{syst} \right]^{\frac{\kappa-1}{\kappa}} \frac{\partial W}{\partial z} \quad . \tag{4.4.186}$$

As the energy balance is already implied in Eq. 4.4.183 (prescription of thermodynamic path), Eqs. 4.4.185 and 4.4.186 describe the flow between branch points.

Pipe branches at the safety and relief valves and at the bypass branch are modeled with the global balances for the steam volume V in the branch section. The mass balance for a branch is

$$\dot{\bar{p}} = - \frac{\kappa \langle p \rangle^{o}_{syst}}{V \rho_o} \left[p / \langle p \rangle^{o}_{syst} \right]^{\frac{\kappa-1}{\kappa}} \sum_j W_{j,out} \tag{4.4.187}$$

where $\bar{p}$ is the mean pressure in the branch section and the superscripted dot designates a time derivative. Notice that mass flows W_j toward the branch are counted negatively in the sum on the right-hand side of Eq. 4.4.187. For the momentum balance, the pressure p is taken to occur at the intersection of pipe axes in the branch section. Equation 4.4.185 is integrated in two parts across the terminal cross sections of the branch and up to the first node in each pipe leading to the branch section. Since this involves nodalization, the result is shown later in Section 6.4.2.3.

The constitutive equations are required for form loss coefficients ζ, the friction factor f and the isentropic expansion coefficient κ.

Form loss coefficients are specified from hydraulic resistance handbooks, such as that by Idel'chik (1960), and defined as input data.* The dependence of form losses on Reynolds number is ignored. Form losses in branch points are represented by one loss coefficient for each of the two flow paths.

The Darcy friction factor f is computed for turbulent flow with $N_{Re} \geq (N_{Re})_{lim}$ from $f = f_t$, where

$$\frac{1}{\sqrt{f_t}} = 2 \log_{10} \frac{N_{Re} \sqrt{f_t}}{1 + 0.1\varepsilon N_{Re} \sqrt{f_t}} - 0.8 \tag{4.4.188}$$

*Input Data Card No. 800 001 and 800 006. Standard definition of ζ (nondimensional).

and for laminar flow with $N_{Re} \leq (N_{Re})_{lim}$ from $f = f_\ell$, where

$$f_\ell = 64/N_{Re} \quad . \tag{4.4.189}$$

Here $N_{Re} = 4|W|/(\pi d \mu_o)$ is the Reynolds number, ε is the user-specified* relative pipe roughness, normalized by the pipe diameter d and $\mu_o = \mu(p_o, \rho_o)$ is the dynamic viscosity of steam at initial steam dome conditions. The limiting Reynolds number is computed such that

$$f_t\left\{(N_{RE})_{lim}\right\} = f_\ell\left\{(N_{Re})_{lim}\right\} \tag{4.4.190}$$

that is, the friction factor f itself is a continuous function of Reynolds number N_{Re} for every roughness parameter ε. Equation 4.4.188 represents the Moody diagram (Hansen 1967) for $N_{Re} \geq 2{,}400$, but it overpredicts the friction factor f in the narrow range of $1{,}000 < (N_{Re})_{lim} \leq N_{Re} < 2{,}400$. The effect of overprediction, however, is too small to be detected in the comparison of final results with experimental data. Equation 4.4.189 has a pole for $N_{Re} = 0$ and therefore, the friction factor f_ℓ and the absolute value of mass flow rate $|W|$, in Eq. 4.4.185 are multiplied and evaluated as the fixed, finite product

$$f_\ell |W| = 16 \pi \mu_o d \quad . \tag{4.4.189a}$$

The isentropic expansion coefficient κ is computed from this identity, valid at initial steam dome conditions:

$$\kappa = \rho_o \Big/ \left\{ <p>^o_{syst} \left[(\partial\rho/\partial p)_h + (1/\rho)(\partial\rho/\partial h)_p \right]_o \right\} \quad . \tag{4.4.191}$$

The thermodynamic and transport properties ρ_o, κ and μ_o are computed with steam-water property subprograms published earlier by Wulff and Jones (1978). Initial conditions are described in Section 4.5. The boundary conditions for Eqs. 4.4.181 and 4.4.182 are (a) the pressure at the steam dome exit or entrance (z=0) to the steam line

$$p(o,\tau) = <p>_{syst} - \frac{1 + \zeta_c}{4 \rho_o A^2} |W|(W + |W|) \tag{4.4.192}$$

and (b) the prescribed mass flow rates W_{TSV}, W_{BYP} and W_{SRV} at the turbine stop or control valve, at the bypass valve and at the safety and relief valves, respectively.

*Input Data Card No. 800 002.

In Eq. 4.4.192, $\langle p \rangle_{syst}$ is the system pressure in the pressure vessel, ζ_c is the entrance contraction loss and ρ_o the initial steam density in the dome. Equation 4.4.192 implies inertia free acceleration from stagnation conditions in the steam dome to the velocity in the steam line entrance, while steam enters the steam line. Equation 4.4.192 also implies subsonic discharge from the steam line into the dome, with the steam line to dome interface pressure being equal to the system pressure.

The mass flow rates W_{TSV}, W_{BYP} and W_{SRV} are imposed by the plant control system as discussed in Chapter 5.

4.4.5.6 Downcomer and Lower Plenum

The particular modeling for the downcomer, divided into the Upper and Lower Downcomers, has been described as part of the discussion on the mixture mass balance (cf. feedwater injection, Eq. 4.4.119) and the closed contour momentum equation (cf. jet pump models, Section 4.4.4.3). The vapor mass and mixture energy equations, Eqs. 4.4.1 and 4.4.4, are applied to the downcomers and the lower plenum without additional assumptions (recall that the flow is assumed to be adiabatic).

There remains to be specified only the particular slip correlation used especially in the downcomers and in the lower plenum (for the general slip correlations, see Section 4.4.2.4):

$$S = 1 - 0.3\,(1-\alpha)^2 \qquad (4.4.193)$$

$$v^o = -\,0.35\,\hat{k}\,\vec{g}/g\ , \qquad (4.4.194)$$

where α is the local void fraction, $\hat{k}$ the unit vector in the direction of the flow, $\vec{g}$ is the gravity vector and g its magnitude.

4.4.6 Transport of Boron

The boron injection capability in a BWR power plant is part of the plant protection system and serves to shut down the fission process in the event of a control rod malfunction or failure.

This section presents the governing equation for the transport of boron, namely the boron mass balance in the form of a partial differential equation. The numerical method employed in RAMONA-3B for the integration of the partial differential equation consists of transforming the partial into a set of ordinary differential equations and of integrating the latter with a first-order Euler scheme. The transformation involves an arbitrary nodalization scheme for the core and is, therefore, presented as part of the numerical scheme in Section 6.4.2.3.

The boron transport model is subject to Assumptions (4-i and xxx through xxxii). Also, the boron concentration is small enough (less than 0.1% in the vessel) so that one can ignore its volume fraction in the liquid. The boron

concentration c_B is defined as the mass fraction of boron in the liquid phase.

The transient boron concentration c_B is computed from the boron mass balance (cf. Assumption (4-xxxii))

$$\frac{\partial[\rho_\ell(1-\alpha)\,c_B]}{\partial\tau} + \nabla\cdot(\rho_\ell\, c_B\, \vec{j}_\ell) = B \qquad (4.4.195)$$

and from the mass balance for the liquid, Eq. 4.4.2. In Eq. 4.4.195, α, ρ_ℓ and j_ℓ denote the void fraction, liquid density and liquid volumetric flux, while B is the source of boron. Equation 4.4.195 is applied to vessel components, arranged contiguously along the closed contours $\mathcal{C}$.

Boron is injected during the transient, at a constant rate B, into the Upper Downcomer, at the jet pump nozzle elevation. The injection is represented as a distributed source B along a contour segment. Equation 4.4.195 is integrated for periodic boundary conditions

$$c_B(z_{JT}^+) = c_B(z_{JT}^-) \qquad (4.4.196)$$

to conform to the closed circuit.

RAMONA-3B is also programmed to compute a hypothetical steady-state boron concentration for the purpose of estimating the boron reactivity worth.

The steady-state concentration is computed with a prescribed entrance concentration $c_B(z_{JT}^+)$ and by integrating the steady-state forms of Eqs. 4.4.195 and 4.4.2.

4.5 Steady State and Initial Conditions

The RAMONA-3B code computes transients by starting out from steady-state initial conditions.

Steady-state initial conditions are uniquely defined by one of several sets of boundary conditions. The number of parameters in the permissible sets of boundary conditions is limited, or else the initial conditions are overspecified. RAMONA-3B is designed to work with overspecified boundary conditions to accommodate desirable design specifications. The RAMONA-3B code is therefore programmed to adjust constitutive parameters (from loss coefficients, jet pump diffuser efficiency, etc.) and process descriptions (carry-under at the separator discharge), in order to produce internal parameters such as core mass flow rate, recirculation mass flow rate, core inlet subcooling temperature, etc. at initial steady-state conditions. All of the internal parameters

are, strictly speaking, determined by fission power, system pressure, feedwater injection conditions, recirculation pump voltage and frequency of generator voltage. The user of RAMONA 3-B must verify, that the parameters derived by RAMONA-3B through adjustments agree with experimental data from separate effect tests. The derived parameters are: the flow impedance Z_{DIF} (Eq. 4.4.137) of the jet pump diffuser, the flow impedance of the recirculation loop, Z_{RCL} (Eq. 4.4.132), the coefficient C (characterizing the ideal pump performance after Euler!) in the recirculation pump pressure rise prediction (Eq. 4.4.139) and the flow quality x_{cu} of the separator discharge flow (Eq. 4.4.159).

The steady state is, in principle, computed from the conservation equations for the transients, specialized for the steady state by setting the time-derivatives equal to zero. These conservation equations are for the steady state:

a) the vapor mass balance, Eq. 4.4.1, with $\partial(\alpha\rho_g)/\partial\tau = 0$

b) the mixture mass balance in the form of Eqs. 4.4.114, 4.4.116, 4.4.118, 4.4.121, and 4.4.123, with $d\langle p\rangle_{syst}/d\tau = 0$ in the ϕ-terms (cf. Eqs. 4.4.19 and 4.4.20),

c) the momentum balance for vessel flow, Eq. 4.4.104, with $d_j/d\tau = 0$,

d) the mixture energy equation, Eq. 4.4.4, with $\partial[(1-\alpha)\rho_\ell u_\ell + \alpha\rho_g u_g]/\partial\tau$ set equal to zero,

e) the momentum balance, for recirculation flow, Eq. 4.4.132, with $dW_{RCL}/d\tau$ set equal to zero, and

f) Equation 4.4.169 with $d(\overline{uM})_{syst}/d\tau$ and W_{ECC} (emergency injection mass flow rate) set equal to zero,

g) Equations 4.4.185 and 4.4.186 with $\partial W/\partial\tau$ and $\partial p/\partial z$ set equal to zero.

The equations listed as Items (a) through (d) determine the steady-state conditions in the reactor vessel. Observe that the steady-state form of Eq. 4.4.173 is not included in this list, since the steady-state vapor void fraction in the low void regime of the steam dome is computed in RAMONA-3B in accordance with Eq. 4.4.165. This gives rise to the first discrepancy between steady-state calculations in RAMONA-3B and subsequent simulations of a transient. The simulation of a transient, starting from steady-state initial conditions and carried out with the boundary conditions fixed at their initial values, ought to yield the initial conditions indefinitely. The above discrepancy, however, will introduce a temporary perturbation at the start of a transient simulation.

The fifth equation, Item (e) in the above list, determines the steady recirculation flow. The sixth equation, Item (f), is combined with the overall steady-state mass balance, equating feedwater and steam line mass flow rates

$$W_{FW} = W_{SL} \tag{4.5.1}$$

and with the caloric equations of state for saturated vapor and for the liquid, to yield the steam mass flow rate W_{SL} in the steam line, in terms of the total initial fission power $Q_o = \int_{A_h} q''_w dA + \int_V q'''_\ell dV$ and the feedwater temperature t_{FW}

$$W_{SL} = \frac{Q_o}{e_g - c_{p,\ell}(t_{FW} - t^o_{sat}) + \langle p \rangle^o_{syst} \left(\frac{1}{\rho_g} - \frac{1}{\rho_{\ell,FW}} \right)} \quad . \qquad (4.5.2)$$

Equation 4.5.2 gives rise to the second discrepancy between steady-state calculations and subsequent transient simulations in RAMONA-3B. The mass flow rates W_{SL} and W_{FW} as computed from Eqs. 4.5.2 and 4.5.1, respectively, cannot render the right-hand side of Eq. 4.4.94 for the rate of pressure change exactly equal to zero, not only because of approximations inherent in the quadrature of the integral in the numerator of Eq. 4.4.94, but also because Eq. 4.4.94 implies approximations (4-vii and xiii) while Eq. 4.5.2 does not. It is obvious that some temporary perturbations must be expected at the start of a transient simulation, no matter how tight the selected convergence criteria are for computing the steady state from the nonlinear equations listed above.

As will be explained later in Chapter 6, RAMONA-3B compensates for these discrepancies between steady-state and transient simulations by starting out from a negative time, chosen such that at time zero these perturbations have dissipated.

Finally, the last set of equations (Item (g)) establishes steady-state conditions in the steam line and bypass line. Observe that there is no boron present in the reactor at initial conditions. No steady-state boron concentrations are required for initial steady-state conditions.

All the transient field equations are solved numerically with reference to a mesh of computational cells. The quadratures in Eqs. 4.4.114, 4.4.116, 4.4.118, 4.4.121, and 4.4.123 are carried out numerically. In order to minimize the discrepancies as described above, appearing at the transition from initial steady-state to transient calculations, the RAMONA-3B code does not solve directly the nonlinear equations itemized above. Instead, the finite difference analogues of these transient equations are solved, with their time-derivatives set equal to zero. This is explained in Section 6.6, after the presentation of the finite difference equations in Section 6.5.

4.6 Boundary Conditions for System Hydraulics

The boundary conditions for the thermohydraulics of the coolant are specified by

a) the cladding surface temperature,

b) the feedwater flow rate and feedwater temperature,

c) the mass flow rates at the turbine control or stop valves, at the bypass valve and at the safety and relief valves, and

d) the mass flow rates of emergency coolant injection.

The cladding surface temperature is computed in RAMONA-3B as described in Chapter 3. The other boundary conditions can be specified as time-dependent functions through tabulated data; they are normally computed from valve characteristics and control functions as discussed in Chapter 5. The feedwater conditions are an exception, since they must be prescribed by the user.

4.7 Summary and Recommendations for Improvements

RAMONA-3B has advanced thermohydraulics models for the efficient simulation of nonhomogeneous, nonequilibrium, two-phase flow in a BWR reactor vessel. RAMONA-3B has the capability to predict detailed coolant flow conditions in a large number of core channels. This enables RAMONA-3B to predict the three-dimensional neutron flux and fission power distribution in large BWR power reactors.

RAMONA-3B's outstanding modeling features are its elimination of acoustic effects from the thermohydraulics model* for the vessel and recirculation loops, its reduction of the partial differential equation for the mixture mass balance to a simple quadrature in space and its replacement of the standard discrete-parameter representation of the momentum balance by closed contour momentum equations, one for each core flow channel (set of channel boxes). RAMONA-3B has individual component models, accounts for the recirculation flow dynamics and simulates the acoustical effects from valve closures in the steam lines. RAMONA-3B also simulates the spread of boron in the reactor vessel.

RAMONA-3B has a number of weaknesses in its thermohydraulic models which affect its ability to predict reliably operational and selected off-normal transients, such as feedwater transients, cold water injection and load following maneuvers. Below is a summary of recommendations for improvements which have been prompted from the assessment of modeling assumptions and modeling conflicts. The summary of proposed improvements is inherently not

*This method has been employed successfully for almost thirty years in stability analyses of two-phase flows (Serov 1953 and Boure 1966).

all-inclusive, as there are no code modifications listed which would serve to extend the applicability of RAMONA-3B (to small-break LOCAs, for example), but also because the process of code improving is inherently open-ended.

(a) First, we recommend that the momentum equations be corrected with regard to the momentum flux representation: $w|w|$ should be replaced by w^2 in Eq. 4.4.6 and all equations derived from it.

(b) Standard definitions for loss coefficients should be employed to correct the momentum jump conditions at component interfaces (cf. Eqs. 4.4.49 and 4.4.50), to allow the use of experimentally obtained and published loss coefficients and to account properly for flow reversal.

(c) The compressibility (thermal expansion) of subcooled liquid should be used for subcooled liquid and not the compressibility of saturated liquid (refer to assumption (4-vii), use Eq. 4.4.93 instead of Eq. 4.4.94 and correct the equations in RAMONA-3B for the volumetric flow rate, Eqs. 4.4.115, 4.4.117 and 4.4.119.

(d) Account for the thermal expansion of subcooled liquid (Eq. 4.4.93), so that overcooling and feedwater transients can be simulated.

(e) Revise the separator model to predict carry-under, rather than to adjust the initial core inlet subcooling temperature.

(f) Change the steam dome model such that the void fraction for the low-void regime is computed consistently from the vapor mass balance, both for steady-state and transient simulations, further, that the vapor discharge from the top of the separators is not introduced into the low-void regime below the coolant level, and finally, that the coolant level motion and the vapor mass in the steam dome are properly computed even if the mixture level rises or falls beyond its normal range.

(g) Eliminate the conflict between two opposing criteria for boiling incipience (assumption 4-ix).

(h) Change the recirculation pump model such that friction in the pump is properly accounted for (see footnote regarding Eq. 4.4.144) and such that the electric torque can be computed as a function of generator frequency and of stator voltage.

These first eight recommendations in thermohydraulics modeling improvements are necessary for RAMONA-3B's intended objectives of simulating operational plant transients. The following six recommendations would improve its accuracy and reliability.

(i) Improve the caloric equations of state for subcooled liquid (see Table 4.2).

(j) Revise the post-CHF heat transfer models to account for hysteresis effects (see Section 4.4.2.1.1); this requires direct coupling between

conduction and thermal hydraulics presently not possible within RAMONA-3B.

(k) Introduce homologous maps for recirculation pump performance.

(l) Extend friction factor and heat transfer calculations to accommodate natural circulation.

(m) Account for superheated vapor. This will involve major code modifications but may be necessary to account for extended dryout or burnout periods.

No attempt has been made to set priorities for the implementation of the above recommendations, except that the first eight improvements, or corrections are required.

5. MODELING OF PLANT CONTROL AND PROTECTION SYSTEMS

This chapter presents the models for simulating the plant control and protection systems which affect the nuclear steam supply system. These models have been developed by BNL and implemented in the RAMONA-3B code.

RAMONA-3B has the models for pressure regulation, safety and relief valve operation, feedwater control, Main Steam Isolation and Bypass Valve operations, Turbine Stop Valve Closure, Reactor Scram, Reactor Core Isolation Cooling and Recirculation Pump trips (not speed control).

We present here the description of control objectives, control functions and mathematical formulae used in RAMONA-3B for plant control simulation. The numerical solution of the mathematical formulation is presented in Chapter 6.

5.1 Scope

The dynamic simulation of operational, incidental and accidental transients in boiling water reactors, using computer codes such as RAMONA-3B, requires mathematical models to represent the plant control and plant protection systems. To this end a set of digital computer models have been developed and implemented into RAMONA-3B for the key systems. However, the modeling to date is not complete but should be adequate for most of the transients for which RAMONA-3B is intended. Current limitations of control models are listed in Section 5.3. For those controls not yet implemented, simulation can still be achieved through user-specified boundary conditions such as flow rates as a function of time.

The models developed and implemented to date are: the manual and automatic pressure control system consisting of the turbine control and bypass valve subsystem and the safety and relief valves (SRV); the plant protection systems (PPS) which include the high pressure coolant injection subsystem (HPCI), control rod, Main Steam Isolation Valve and Recirculation Pump trips; and the reactor core isolation cooling system (RCIC). Modeling to simulate feedwater control and the recirculation pumps speed control are planned for future work.

5.2 Plant Control and Protection Systems

5.2.1 System Pressure Regulation

5.2.1.1 Objectives

In a BWR, an increase in vessel steam pressure results in an increase in steam flow through the steam line and the collapse of steam voids in the reactor. The latter means that the water density increases and hence there is an

increase in neutron moderation. This in turn leads to an increase in power which has the effect of increasing pressure. In order to deal with this positive feedback a pressure regulator is provided. It is designed to maintain the pressure about some design value during normal (or anticipated) transients. To maintain an approximately constant system pressure, turbine control valves are provided. The bypass valves also direct excess steam flow to the primary heat sink (main condenser) during start-up or load rejection events.

Since the turbine and bypass flow controllers will influence the system response during many system transients it is important to have them properly represented with RAMONA-3B. A model based on available documentation (Linford 1973) has been derived and implemented into the code as an additional part of the steam line model. The control system is shown schematically in Fig. 5.1 and has two basic components. One component is the pressure regulator control system which senses the pressure p_{HDR} at the steam line header and controls the valve positions S_{CV} and S_{BY} for the control and bypass valves. The other component of the model is the turbine system. The valve position determines the flow rates to the turbine (W_{TRB}) and bypass (W_{BY}) systems. These flow rates determine the steam line header pressure and affect indirectly the reactor pressure.

5.2.1.2 Pressure Regulator

The pressure regulator shown schematically in the block diagram of Fig. 5.2 is composed of a sensor-transmitter, comparator, proportional-integral-derivative (PID) element, a time lag element and the valve actuator.

This model is a simplified representation of the actual plant controllers and is a first step towards a more detailed representation of the turbine and bypass pressure regulators.

In the next section we present at first the turbine control valve dynamics. The bypass valve is discussed in Section 5.2.1.4, the turbine and bypass flow dynamics is presented in Section 5.2.1.5.

5.2.1.3 Control Valve Dynamics

Pressure Sensor and Transmitter

In order to account for the time lags associated with pressure measurement and transmission, the combined pressure sensor and transmitter is modelled using a first order system as shown below. The symbols are defined in the nomenclature.

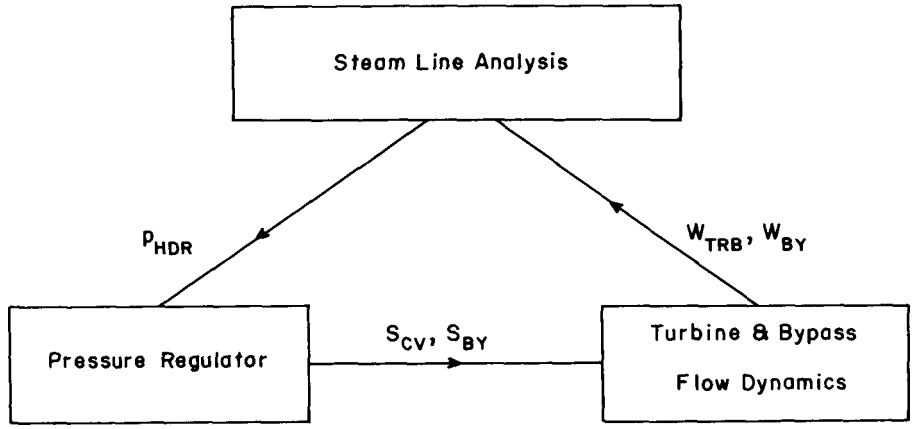

Figure 5.1 Interaction of Pressure Regulator and System Dynamics

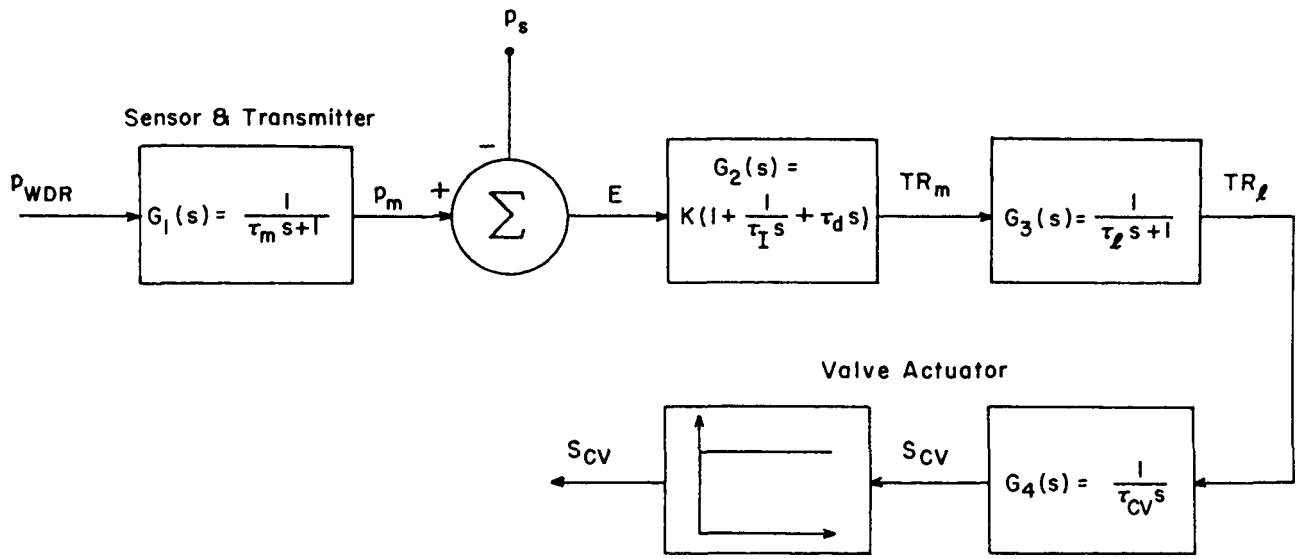

Figure 5.2 Block Diagram Representation of the Simplified Pressure Regulator

Equation: $$\tau_m \frac{dp_m}{d\tau} = p_{HDR} - p_m \ ,$$

Numerical Approximation: $$p_m^{k+1} = p_m^k \left(1 - \frac{\Delta\tau}{\tau_m}\right) + \frac{\Delta\tau}{\tau_m} p_{HDR}^k \ , \qquad (5.2.1)$$

Initial Condition: $$p_m(\tau=0) = p_{HDR}\ (\tau=0) .$$

Comparator

The output of the pressure sensor is fed to a comparator where the measured pressure p_m is compared to the desired setpoint pressure p_s. That is:

Equation: $$E = (p_m - p_s)/p_s \ ,$$

Numerical Approximation: $$E^{k+1} = (p_m^{k+1} - p_s)/p_s \ . \qquad (5.2.2)$$

Proportional-Integral-Derivative Controller (PID)

The error signal is fed to a proportional-integral-derivative controller, which in turn generates a trim signal as follows:

Equation: $$TR_m = \bar{K}\left(E + \frac{1}{\tau_I}\int_0^\tau E\, d\tau + \tau_d \frac{dE}{d\tau}\right) \ ,$$

Numerical Approximation: $$TR_m^{k+1} = \bar{K}\left(E^{k+1} + \frac{1}{\tau} I^{k+1} + \tau_d \frac{E^{k+1} - E^k}{\Delta\tau}\right) , \qquad (5.2.3)$$

$$I^{k+1} = I^k + \Delta\tau\, E^k ,$$

Initial Condition: $$I(\tau=0) = 0.$$

Lag Element

The trim signal is lagged according to the following first order system:

Equation: $$\tau_\ell \frac{d\, TR_\ell}{d\tau} = TR_\ell^k \left(1 - \frac{\Delta\tau}{\tau_\ell}\right) + \frac{\Delta\tau}{\tau_\ell} TR_m^k \ ,$$

Numerical Approximation: $$TR_\ell^{k+1} = TR_\ell^k \left(1 - \frac{\Delta\tau}{\tau_\ell}\right) + \frac{\Delta\tau}{\tau_\ell} TR_m^k \ , \qquad (5.2.4)$$

Initial Condition: $$TR_\ell(\tau=0) = TR_m\ (\tau=0) = 0.$$

Valve Actuator and Limiter

The valve actuator dynamics are approximated by

Equation:
$$\tau_{CV} \frac{d\, S_{CV}}{d\tau} = TR_{\ell} \ ,$$

Numerical Approximation:
$$S_{CV}^{k+1} = S_{CV}^{k} + \frac{\Delta\tau}{\tau_{CV}} TR_{\ell}^{k} \ , \qquad (5.2.5)$$

Initial Condition: $S_{CV}\ (\tau=0) = S_{CVi}$.

In order to prevent unrealistic valve positions, the actuator output is limited according to:

$$S_{CV} = \begin{cases} S_{max} & S_{CV} \geq S_{max} \\ S_{min} & S_{CV} \leq S_{min} \end{cases} \qquad (5.2.6)$$

Equations 5.2.1 through 5.2.6 illustrate that any increase in steam header pressure beyond the setpoint pressure causes the valve to open, similarly any decrease in steam header pressure below the setpoint leads to valve closure. Therefore, the control valve adjusts its position in order to maintain the desired setpoint pressure.

5.2.1.4 Turbine Bypass Valve

The turbine bypass valve is not operative during normal plant operation. It opens to bypass (dump) the excess steam to the condenser during abnormal transients such as turbine trip, load rejection, and high power ascension.

In the present model, the turbine bypass valve regulator is assumed to be identical to the turbine control valve regulator as shown in Fig. 5.2. However, the operational characteristics of the bypass valve can be quite different than the turbine control valve.

5.2.1.5 Turbine and Bypass Flow Dynamics

The purpose of the models for turbine and bypass flow dynamics is to predict the mass flow rates W_{TRB} and W_{BY} through the turbine control and bypass valves, as a function of their respective valve fractional positions; namely S_{CV}, and S_{BY}. These mass flow rates are boundary conditions for the steam line analysis.

The turbine system consists of the turbine control valve, turbine bypass valve, and the turbine, as shown schematically in Fig. 5.3. The hydraulics of the system can be adequately represented using a quasi-static flow model.

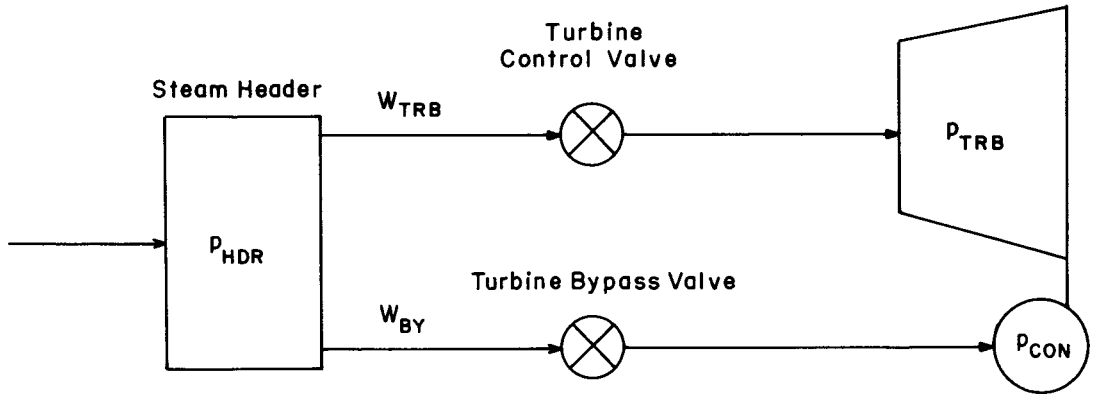

Figure 5.3 Schematic of Turbine and Bypass System

This model is deemed valid because the fluid in this system is single phase vapor of negligible inertia.

The pressure drop along the turbine leg consists of two parts:

$$(P_{HDR} - P_{CON}) = \Delta P_{CV} + \Delta P_{TRB}, \tag{5.2.7}$$

where P_{HDR} is the steam header pressure, P_{CON} is the condenser pressure, ΔP_{CV} is the pressure drop in the control valve, and ΔP_{TRB} is the pressure drop in the turbine and associated piping system.

The pressure drop in the turbine and piping system can be modelled by

$$\Delta P_{TRB} = C_{TRB} W_{TRB}^2, \tag{5.2.8}$$

where C_{TRB} is the mass flux impedance, and W_{TRB} is the mass flow rate through the turbine leg.

The relationship between the pressure drop across the valve, the pressure at the valve inlet and the flow through the valve is given by a unified valve capacity equation for saturated steam (Considine 1974).

$$W_{TRB} = S_{CV}^n K_{CV} P_{HDR} (Y - 0.148Y^3) \tag{5.2.9}$$

and

$$Y = \frac{1.63}{C_{crit}} \sqrt{\frac{\Delta P_{CV}}{P_{HDR}}} \tag{5.2.10}$$

with a maximum value of $Y = 1.5$. At this value $(Y - 0.148Y^3) = 1.0$, leading to choked flow where $\Delta P_{CV} = 0.847\ C_{crit}^2\ P_{HDR}$. Here C_{crit} is the critical flow factor, n is the constant characterizing the valve (n=1 linear valve, n=2 parabolic valve), and K_{CV} is the valve coefficient at fully open position.

Combining Eqs. 5.2.7 through 5.2.10 and rearranging, we obtain a transcendental equation for the turbine flow in terms of the turbine valve capacity, the header pressure, the condenser pressure, and the turbine control valve fractional steam position:

$$W_{TRB} = S_{CV}^n K_{CV} P_{HDR} (Y - 0.148Y^3) \tag{5.2.11}$$

and

$$Y = \frac{1.63}{C_{crit}} \sqrt{\frac{P_{HDR} - P_{CON} - C_{TRB} W_{TRB}^2}{P_{HDR}}} \tag{5.2.12}$$

The turbine and valve coefficients can be determined from user specified rated conditions as:

$$K_{CV} = \frac{W_{TRB}\ (\tau=0)}{S^{n}_{CV}\ (\tau=0)\ p_{HDR}\ (\tau=0)\left[Y(\tau=0) - 0.148Y^{3}(\tau=0)\right]} \qquad (5.2.13)$$

and,

$$Y(\tau=0) = \frac{1.63}{C_{crit}} \sqrt{\frac{p_{HDR}\ (\tau=0) - p_{CON}\ (\tau=0) - C_{TRB}\ W^{2}_{TRB}\ (\tau=0)}{p_{HDR}\ (\tau=0)}} \cdot \qquad (5.2.14)$$

A similar analysis for the bypass leg yields:

$$W_{BY} = S^{n}_{BY}\ K_{BY}\ p_{HDR}\ (Y - 0.148Y^{3}) \qquad (5.2.15)$$

and

$$Y = \frac{1.63}{C_{crit}} \sqrt{\frac{p_{HDR} - p_{CON}}{p_{HDR}}} \qquad (5.2.16)$$

where subscript BY refers to the bypass leg.

The pressure in the condenser is very low ($p_{CON} \sim 300\text{-}500$ pa $<<$ p_{HDR}) and can be neglected; hence Eqs. 5.2.15 and 5.2.16 become,

$$W_{BY} \simeq S^{n}_{BY}\ K_{BY}\ p_{HDR} \cdot \qquad (5.2.17)$$

Note, in arriving at Eq. 5.2.17 it was further assumed that the pressure drop in the bypass leg is dominated by the pressure drop across the bypass valve.

Equations 5.2.11 and 5.2.17 provide the mass flow rate boundary conditions for the steam line analysis.

It must be noted that, in addition to the automatic pressure regulator system, an overriding manual feature is also included, which enables the user to activate the turbine control and bypass valves at any desired time into the transient, by supplying a table of steam flow vs. time values.

5.2.1.6 Typical Controller Data

Table 5.1 gives a set of data applicable to the Peach Bottom - 2 type power plant (Linford 1973 and Hornyik 1981).

Table 5.1 Typical Data

τ_m, s	0.10
τ_I, s	0.02
τ_d*, s	2.00
τ_ℓ*, s	5.00
τ_{CV}, s	0.10
τ_{BY}, s	0.10
S_{min} -	0.00
S_{max} -	1.00
$S_{CV,i}$ -	1.00
$S_{BY,i}$ -	0.00
n -	0.04
K -	0.033
p_s, bars	65.65
C_{crit} -	0.85

*Actual plant regulator settings as reported in (Linford, 1977) are τ_d = 1.0 and τ_ℓ = 10.0.

5.2.2 Safety and Relief Valves (SRVs)

5.2.2.1 Objectives

In a BWR there are typically 10 to 16 valves in the steam lines which serve as safety and relief valves to maintain the system pressure below prescribed limits. RAMONA-3B has been programmed to represent up to five different banks; each bank representing one or more safety or relief valves. Each bank can be activated: 1) at a user specified time in order to represent an operator action on an electrically operated relief valve or an accident condition; or 2) when the pressure at the location of the safety or relief valve (a single location in the steam line model) reaches a specified setpoint. The signal for valve closure can be either time or pressure.

5.2.2.2 Modeling Equations

The flow rate through a bank W (kg/s) is limited by choking. The critical flow rate W_{crit} is calculated using the critical velocity for an ideal gas, i.e.,

$$v_{crit} = \sqrt{\kappa p/\rho}, \tag{5.2.18}$$

where κ is the polytropic expansion coefficient and ρ is the density of the vapor. The critical mass flux is then ρv_{crit} or:

$$G_{crit}(p) = \sqrt{\kappa \rho p}. \tag{5.2.19}$$

The critical flow rate for a bank is obtained by defining an effective area which includes all valves in a bank:

$$A_c = W_{cap}/G_{crit}(p_{set}) , \tag{5.2.20}$$

where W_{cap} is the rated capacity of all the valves in the bank and $G_{crit}(p_{set})$ is the critical mass flux at the opening pressure setpoint p_{set}. Equations 5.2.18, 5.2.19 and 5.2.20 give

$$W_{crit} = A_c\, G_{crit}(p) = W_{cap} \left(\frac{p}{p_{set}}\right)^{\frac{1+\kappa}{2\kappa}} . \tag{5.2.21}$$

If the flow rate at a valve bank is being changed (opened or closed) on time (operator action), then the flow rate can be represented as

$$W = W_{crit}\, f(\tau) \tag{5.2.22}$$

with the user providing the (f_i, τ_i) table to represent $f(\tau)$.

If a valve bank is being opened on a pressure signal, an additional tabular function, g(p) is required, where g(p) represents the fractional valve opening as a function of pressure. Figure 5.4 shows a typical valve lift characteristic (fractional opening (lift) vs. pressure) for opening and closing of valves.

A delay time between the activation of a SRV signal and the beginning of flow through the valve is user specified. For activation on pressure, the pressure must remain above the setpoint during this period (typically 0.4 s) in order for the valve to open.

The flow rate out of the valve bank can then be represented as $W = \min(W_1, W_{crit})$ where

$$W_1 = W_{cap} \frac{p}{p_o} g_o(p)\, f_o(\tau) \tag{5.2.23}$$

Equation 5.2.23 is based on information from General Electric. The term p_o is the pressure at rated conditions. The lift characteristics represented by $g_o(p)$ $(0 \leq g_o \leq 1)$ is an input table which in general is

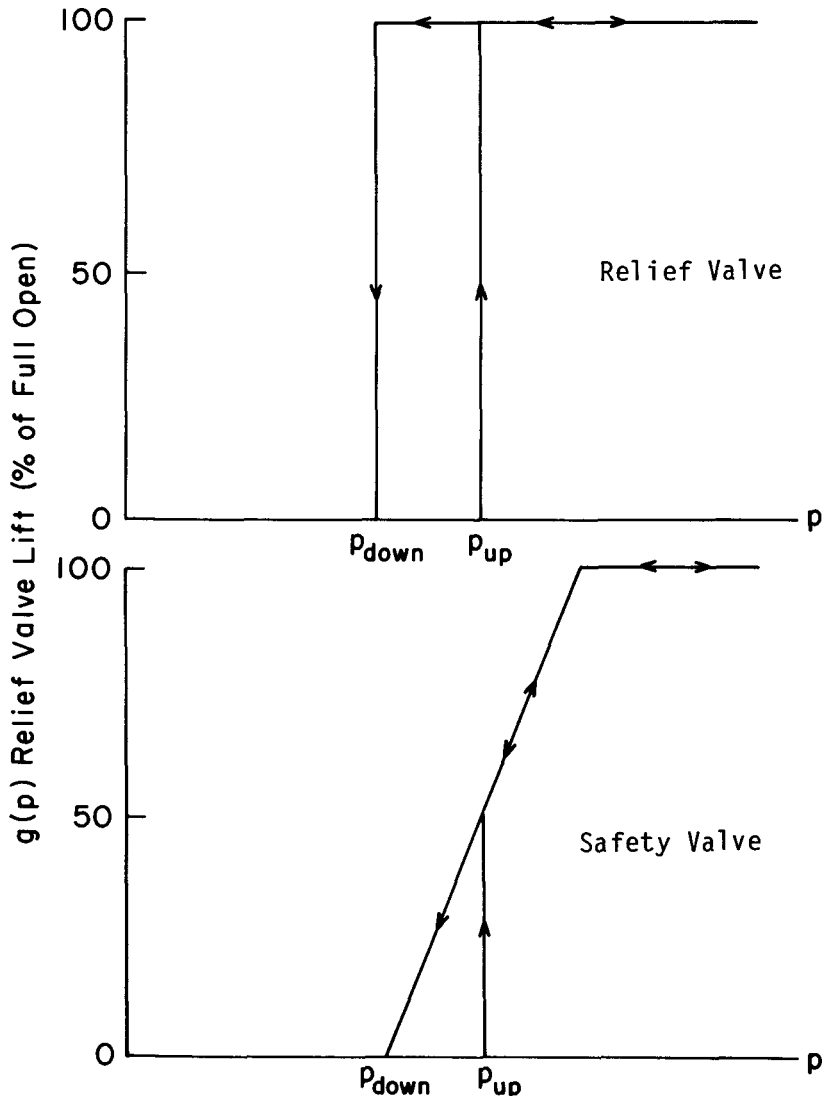

Figure 5.4 Typical Safety and Relief Valve Characteristics (p_{up} and p_{down} are the opening and closing pressure setpoints)

different for safety and relief valves. The time behavior of the valve $f_o(\tau)$ $(0 \leq f_o \leq 1)$ is also input. Typically $f_o(\tau) = (1 - e^{-\tau/\tau_v})$ where τ_v is the valve time constant ($\sim$0.1s), and τ is measured from the time of starting the valve action.

If a valve bank is being closed on a pressure signal, the user provides the two functions $g_c(p)$ and $f_c(\tau)$ that characterize the closing of a valve (usually different from the $g_o(p)$ and $f_o(\tau)$ that characterize the opening of a valve). The flow rate out the valve is then given by

$$W = W_o \, g_c(p) \, f_c(\tau) \tag{5.2.24}$$

where W_o was the flow rate out the valve just before it started closing.

The flow rate is calculated for each valve and then summed. This information is fed to subroutine DRV which calculates the derivatives needed by the steam line algorithm. The logic takes into account that the code may backstep in time in the integration of either the steam line, hydraulics, or neutronics equations (all of which use a different time step).

5.2.3 Main Steam Isolation Valve (MSIV)

5.2.3.1 Objectives

The purpose of the Main Steam Isolation Valve model is to predict the mass flow rate of steam through the MSIV during its closure.

5.2.3.2 Modeling Description

The steam flow rate through the valve is determined using a user supplied table of flow fractions (relative to the initial flow rate) vs. time after actuation. Once this table is used the location of the MSIV becomes a boundary of the steam line with the flow rate as the boundary condition. At this time the steam line segment downstream of the MSIV is no longer part of the calculation , i.e., only the steam line segment within the primary containment is simulated.

MSIV closure can be initiated in the code on signals due to: 1) time (to simulate operator action), 2) low vessel water level, 3) high steam line flow (at the location of the MSIV) and 4) low steam line pressure (at the location of the MSIV).

A user supplied time delay must be reached following MSIV actuation signal for MSIV flow rate to change according to the prescribed values.

5.2.4 Plant Protection System (PPS)

5.2.4.1 Objectives

The BWR Plant Protection System (PPS) is to assure that the consequences of all postulated conditions do not exceed the specified safety limits in the

reactor system. It should provide the required protection by sensing the necessity and implementation of reactor scrams, pump trips, turbine-generator set trips and subsequent isolation.

Safety limits are imposed on important process variables required to reasonably protect the integrity of each of the physical barriers which guard against the uncontrolled release of radioactivity. The maximum safety settings for automatic protective devices are related to variables on which safety limits have been placed. A maximum safety setting should be selected such that automatic protective action will correct even the most abnormal situation before the safety limit is exceeded. Thus, the safety limit on reactor power would be the power level at which operation is deemed to become unsafe, while the maximum safety setting would be the power level at which a scram is initiated. The maximum safety setting must take into account measurement and instrumentation uncertainties associated with the process variables.

The PPS can be viewed as a control system, which, in routine operation, acts as an observer and which is activated only when the plant system reaches the limit of permissible operation (maximum safety setting). The PPS includes the Shutdown System(s) and the Engineering Safety Features.

The PPS does not directly include the reactor operator implementation of protective function. However, manual shutdown devices are considered part of the PPS.

5.2.4.2 Method of Simulation

In RAMONA-3B, the PPS functions include both manual and automatic modes.

In the manual mode, the operator's action is simulated through a user specified "trip time", at which the desired shutdown system is activated as depicted schematically in Fig. 5.5.

In the automatic mode, important system variables are processed through appropriate PPS subsystem trip functions for possible protective action in response to selected instrumentation signals. Following the PPS signal, a user supplied trip time delay must be exceeded before PPS action is initiated as shown in Fig. 5.5.

Table 5.2 sets forth the PPS subsystem trip functions for reactor scram, turbine and Recirculation Pump trips which are currently simulated by RAMONA-3B.

In addition, a rudimentary feedwater flow control system is also included, which can be activated either through a user supplied time or a high reactor vessel water level signal. If this system is called upon, a table of feedwater flow rate (as a fraction of the flow rate just before the change) and enthalpy versus time must be provided as input.

It must be noted that, if a reactor scram is possible, the user must provide the desired control rod insertion speed.

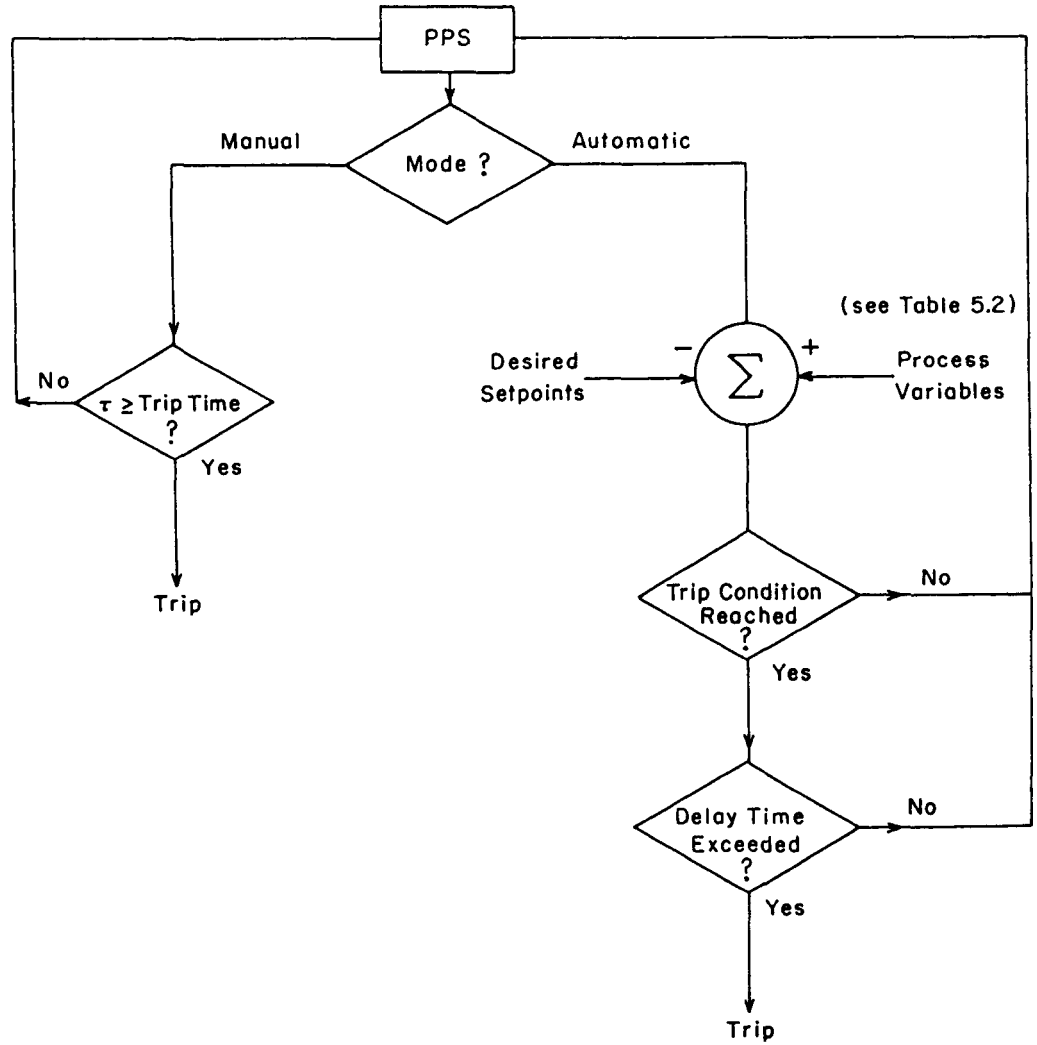

Figure 5.5 Manual and Automatic Features of PPS

Table 5.2 Plant Protection System

System	PPS Trip Function
Reactor	1. Manual (time) 2. Turbine Inlet Valve Closure 3. High Neutron Flux 4. Low Reactor Vessel* Water Level 5. High Reactor Vessel* Water Level 6. High System Pressure 7. MSIV Closure
Turbine	1. Manual (time) 2. Turbine Inlet Valve Closure 3. High System Pressure 4. Low Reactor Vessel* Water Level
Recirculation Pump	1. Manual (time) 2. Turbine Inlet Valve Closure 3. High System Pressure 4. Low Reactor Vessel* Water Level

5.2.5 High Pressure Coolant Injection (HPCI) System

5.2.5.1 System Description

The HPCI System is designed to assure adequate coolant inventory in the reactor vessel for a spectrum of design basis LOCA conditions that do not result in a rapid depressurization of the reactor vessel (small breaks). It is also important in other transients, such as ATWS and LOFW, in which the vessel water level drops below the low level setpoint due to an imbalance in the feedwater flow relative to the flow out the steam line. The HPCI system causes the reactor to be depressurized through the addition of cold water and makes up for inventory lost through either a break or an open valve. It continues to operate until the vessel pressure is below that at which the low pressure coolant injection and core spray systems can be operated or until the vessel water level reaches the high level setpoint.

The injection system has a steam turbine driven pump. Two sources of water are available. Water is supplied initially from a condensate storage tank. When the water in the condensate storage tank has fallen to a predetermined level or the water in the suppression pool is above a predetermined level, the pump suction supply is automatically transferred to the suppression pool. The water is pumped into one of the reactor feedwater system lines and distributed within the reactor vessel through the feedwater spargers for mixing with the hot water in the vessel.

*As sensed in the Upper Downcomer.

HPCI system operation is automatically initiated upon detection of either low reactor vessel water level or high drywell pressure. The HPCI system can also be manually initiated by the control room operator.

Because the steam supply line to the HPCI system turbine is part of the main steam line reactor coolant pressure boundary, certain signals automatically isolate this steam line causing shutdown of the HPCI system turbine. These signals are HPCI system steam line high flow, high turbine exhaust pressure, steam leak detection system initiation, and low steam supply pressure.

The HPCI system turbine also can be shut down directly by the following signals. These signals are high turbine exhaust pressure, low pump suction pressure, high reactor vessel water level, turbine overspeed, any of the steam supply line isolation signals given above, and a manual operator controlled signal. The HPCI system has an automatic reset after it trips off on high vessel water level.

5.2.5.2 Modeling Equations

In RAMONA-3B the HPCI flow is added to the feedwater (FW) and RCIC flows if any. The HPCI flow rate is specified through as a tabulated function of time after initiation. A tabulated flow vs. time table is also input of the shutoff sequence, where the flow in this case is a fraction of the flow that existed at the time of shutoff. The temperature of the HPCI water is specified as a constant.

Complete mixing is assumed between the feedwater, HPCI and RCIC flows. A simple energy balance allows the temperature of the three-component mixture to be calculated as a mass flow weighted average of the component temperatures:

$$t_{avg}(\tau) = \sum_i W_i\ (\tau)\ t_i / \sum_i W_i(\tau), \quad i = \text{FW, HPCI, RCIC,}$$

where W_i is the mass flow rate of system i, and t_i is the temperature of injectant of system i.

The actuation signals incorporated into the code were designed to represent the essential system actions without becoming too complex. In the code, HPCI system can be actuated by either time or low vessel water level signals. A delay time between signal actuation and the use of the flow vs. time table must be specified by the user.

The HPCI system is shut off by a high vessel water level signal and, again, a delay time is accounted for before the shutdown flow table is used. The system can also be indirectly shut off on a time signal by making the input start-up flow rate terminate after a certain time interval. After being shut off, the trigger is reset (as in the actual reactor) so that the system may be actuated again on the low vessel water level signal.

The coding to accomplish the above takes into account the time back-stepping that takes place in RAMONA-3B. For example, if HPCI is in the "on" mode the code can handle a back-step into the "off" mode and vice versa. If in the extremely unlikely case where the back-step occurs from an "on" mode to the previous "on" mode, the HPCI flow is set to zero and a message is printed.

At the beginning of a run all the trip specifications for that run are printed. During a run, whenever a trip is activated, a message appears.

5.2.6 Reactor Core Isolation Cooling (RCIC) System

5.2.6.1 System Description

The RCIC system provides sufficient water to the reactor vessel to cool the core and to maintain the reactor in a standby condition if the vessel becomes isolated from the main condenser and experiences a loss of feedwater flow. The system is also designed to permit complete plant shutdown under conditions of loss of normal feedwater flow by maintaining the necessary reactor water inventory until the vessel is depressurized to the point where the Residual Heat Removal (RHR) system can function in the shutdown cooling mode. RCIC is not a safety-grade system. Its capacity (flow rate) is about 10% of that of HPCI. In situations where HPCI is required, RCIC will also be actuated.

The RCIC system is not automatically reset after it trips off on high vessel water level.

5.2.6.2 Modeling Description

In RAMONA-3B the RCIC flow is added to the feedwater flow together with any HPCI flow. The flow rates after system activation and after system trip, and the temperature of the injected water are input. The activation and shut-off signals are of the same kind as the for HPCI system but may differ quantitatively. The RCIC system can not be turned on again after it has been shut off, and the temperature of the injected water is input. The activation and shutoff signals are of the same kind as the HPCI system but may differ quantitatively. The RCIC system can not be turned on again after it has been shut off on high vessel water level.

5.3 Summary, Limitations and Recommendations

Models and numerical techniques for simulation of BWR plant control and protection systems were described. The models include system pressure regulations, safety and isolation valves, plant protection system functions, high pressure injection system, and reactor core isolation cooling systems.

These models provide a considerable simulation capability for RAMONA-3B. However, the following limits must be recognized:

(1) The lack of automatic master and reactor flux level controller prevents the simulation of transient conditions where automatic reactor power level control is needed.

(2) The pressure regulator model is a simplified six-element controller which can represent the overall dynamics, excluding the interactions with the turbine-generator system.

(3) The feedwater flow control can only simulate an on-off normal action, with feedwater flow rate supplied as a boundary condition.

It is recommended that improved models be developed and added in the future. These improvements should include:

(1) detailed plant control system model including reactor power control feedwater, pump drive and control system.

(2) detailed dynamic representation of the safety and relief valves including simulation of pressure sensor and the actuator dynamics.

(3) detailed representation of controller elements including, lead, lag, delay and relay along with weighted summer elements.

Incorporation of these improvements in RAMONA-3B will enable the user to extend the capability of the code for simulation of various operational transients including load changes and control system-initiated transients.

Finally, these models must be exercised extensively and compared to data, as more plant data become available.

6. SOLUTION METHODS

All the physical models in the RAMONA-3B code have been described previously in this report. The models for neutron kinetics and thermal power generation are presented in Chapter 2. The models for predicting the transient fuel temperatures are found in Chapter 3. The models for predicting the transient thermohydraulics of the coolant are described in Chapter 4, while the mathematical formulations of the plant control and protection models are given in Chapter 5.

This chapter presents the numerical methods of solution which are used in RAMONA-3B to implement the above models on a digital computer for predicting steady-state and transient conditions. Presented are the schemes of discretization, the iterative methods for solving the nonlinear finite difference equations, as they arise in predicting the steady-state conditions and the transients of neutron kinetics and thermal conduction, and the method for integrating the ordinary differential equations of coolant dynamics.

The first section in this chapter is an overview of the computing schemes in RAMONA-3B. The following three sections contain the finite difference and ordinary differential equations for neutron kinetics, thermal conduction, and coolant thermohydraulics, respectively. After having summarized in Section 6.5 all the sets of algebraic, finite difference and ordinary differential equations to be solved and integrated, we present in Section 6.6 and 6.7 the details of solving and integrating these equations. In Section 6.8 the reader can find the descriptions for accuracy and integration step size control. Section 6.9 concludes this chapter with some recommendations for improving the solution methods in RAMONA-3B.

6.1 General Solution Strategy

RAMONA-3B is programmed to seek first an approximation to the initial steady state by a nested sequence of successive substitutions; then to compute a pseudo-transient with fixed boundary conditions to achieve an accurate initial steady state. This two-fold procedure is necessary because of minor discrepancies between the equation sets for steady-state and transient conditions.

The transient neutron kinetics calculations provide the master timing of the transient calculations. The calculations of transient temperature distributions in fuel pellets and fuel cladding are synchronized with the neutron kinetics calculations.

Within the master integration step for neutron kinetics and conduction calculations are carried out several integration steps for the thermohydraulics equations, describing the coolant dynamics in the vessel and recirculation loops. Each of these substeps is controlled by separate accuracy and stability criteria. Each substep is carried out with interpolated boundary conditions, i.e. heat flux and cladding wall temperatures, from the first conduction calculations.

Within the substep for thermohydraulics integration there are carried out several minor substeps each for the steam line dynamics and for the transport of boron.

After all calculations for coolant dynamics, vapor dynamics in the steam lines and boron transport have been advanced to the end of the master step for neutron kinetics, the neutron kinetics calculations are repeated with the thermohydraulics parameters obtained from the several substeps. The results of this calculation are compared with the predictions from the first neutron kinetics calculations. Depending on the agreement between the fast-neutron fluxes from the first and last neutron kinetics calculations, the results of the entire procedure are either accepted, and the integration is continued, or they are rejected and the entire step is repeated with a smaller master step size.

6.2 Neutron Kinetics and Power Generation

This section presents the numerical algorithms and methods used in RAMONA-3B to obtain the numerical solutions to the governing equations of the neutron kinetics and power generation described in Chapter 2.

6.2.1 System of Governing Equations

The system of governing equations for neutron kinetics and power generation have been discussed in Chapter 2. Specifically, Eqs. 2.3.1a, 2.3.31 and 2.3.1c are the governing equations for neutron kinetics, Eq. 2.4.1 or 2.4.2 is the governing equation for thermohydraulic feedback, and Eqs. 2.7.16, 2.7.17 and 2.7.18 are the governing equations for the power generation. For the convenience of the reader, we summarize them here as follows:

Neutron Kinetics:

$$\frac{1}{v_1}\frac{\partial \varphi_1}{\partial \tau} = \nabla\cdot D_1\nabla\varphi_1 - \Sigma_1\varphi_1 + (1-\beta)\left(\nu_1\Sigma_{f_1}\varphi_1 + \nu_2\Sigma_{f_2}\varphi_2\right) + \sum_{m=1}^{I}\lambda_m c_m \qquad (6.2.1)$$

$$\frac{1}{v_2}\frac{\partial \varphi_2}{\partial \tau} = \Lambda_2 - \Sigma_2\varphi_2 + \Sigma_{21}\varphi_1 + \delta_B S_B\varphi_1 \qquad (6.2.2)$$

$$\frac{\partial c_m}{\partial \tau} = \beta_m\left(\nu_1\Sigma_{f_1}\varphi_1 + \nu_2\Sigma_{f_2}\varphi_2\right) - \lambda_m c_m\,; \qquad m = 1,2,\ldots,I. \qquad (6.2.3)$$

Here we have used a new index m for the delayed neutron data to avoid confusion with the spatial index (i,j,k) to be used later.

Power Generation:

$$q''' = q'''_f + q'''_\ell + q'''_{\ell b} \tag{6.2.4}$$

$$q'''_f = \frac{(1-\eta_{pw})\int_V q'''_p \, d\underline{r} + (1-\eta_{dw})\int_V q'''_d \, d\underline{r}}{\pi r_f^2 h_z N_r} \tag{6.2.5}$$

$$q'''_\ell = \frac{\eta_c}{A_c h_z}\left(\eta_{pw}\int_V q'''_p \, d\underline{r} + \eta_{dw}\int_V q'''_d \, d\underline{r}\right) \tag{6.2.6}$$

$$q'''_{\ell b} = \frac{(1-\eta_c)}{A_b h_z}\left(\eta_{pw}\int_{core} q'''_p \, d\underline{r} + \eta_{dw}\int_{core} q'''_d \, d\underline{r}\right) \tag{6.2.7}$$

$$q'''_p = K\,(1-H_o)\left(\Sigma_{f_1}\varphi_1 + \Sigma_{f_2}\varphi_2\right) \tag{6.2.8}$$

$$\begin{aligned} q'''_d = {} & q'''_\tau\,[H(\tau,\infty) - H(\tau+\tau^*,\infty)] \\ & + KY\left(\Sigma_{f_1}\varphi_1 + \Sigma_{f_2}\varphi_2\right)[H(o,\infty) - H(\tau,\infty)] \end{aligned} \tag{6.2.9}$$

Thermohydraulic Feedback:

$$\Sigma = \Sigma\,(\alpha, T_\ell, T_f, f, c_B, x_e) \tag{6.2.10}$$

For ease of writing, we have dropped here the argument $(\underline{r},\tau)$ in the above equations, keeping in mind that they are both space- and time-dependent.

Note that the single equation (6.2.10) actually consists of nine equations for the nine two-group parameters (D_1, D_2, Σ_1, Σ_2, Σ_{21}, $\nu_1\Sigma_{f1}$, $\nu_2\Sigma_{f2}$, ν_1, ν_2). The thermohydraulic state variables (α, T_ℓ, T_f) are determined from the volumetric heat generation rates (q'''_ℓ, $q'''_{\ell b}$, q'''_f) by means of the thermohydraulics

models described in Chapters 3 and 4. Thus, the two-group parameters are actually functions of these volumetric heat generation rates. Hence, the system of governing equations forms a set of nonlinear equations. The tandem strategy (as discussed in Section 2.2.1), is usually employed to solve the set of nonlinear equations.

The governing equations for the neutron kinetics are subject to the boundary conditions described in Section 2.3.3 and the initial conditions discussed in Section 2.3.4. They are summarized as follows.

Boundary Conditions:

For fast neutron flux,

$$-D_1 \nabla \varphi_1 \Big|_{\underline{r} = \underline{r}_s} = \frac{D_1 \varphi_1 (\underline{r}_s - \underline{\xi}/2)}{\lambda_{eff}} \tag{6.2.11}$$

where $\underline{r}_s$ denotes the boundary surfaces, $\underline{\xi} = (h_x, h_y, h_z)$, and $\varphi_1(\underline{r}_s - \underline{\xi}/2)$ is the center fast flux of the boundary nodes. Note that λ_{eff} is actually λ^T_{eff} for the top boundaries, λ^B_{eff} for the bottom boundaries, and λ^S_{eff} for the side boundaries:

$$\lambda^T_{eff} = \lambda^T_1 + \frac{h_z}{2} \tag{6.2.12}$$

$$\lambda^B_{eff} = \lambda^B_1 + \frac{h_z}{2} \tag{6.2.13}$$

$$1/\lambda^S_{eff} = 1\Big/\left(\lambda^S_1 + \frac{h_x}{2}\right)_{ref} + C_{ref}\left(D^S_1 - D^{ref}_1\right) \tag{6.2.14}$$

Recall that $h_y = h_x$ is assumed in RAMONA-3B, and the λ_1's are the linear extrapolation lengths discussed in Section 2.5.1.

For thermal neutron flux,

$$\delta_B S_B = \delta^B_B \frac{D^B_1 \theta_B}{\lambda^B_{eff} h_z} + \delta^T_B \frac{D^T_1 \theta_T}{\lambda^T_{eff} h_z} + \delta^S_B \frac{D^S_1 n \theta_s}{\lambda^S_{eff} h_x} \tag{6.2.15}$$

where n is the number of reflector-facing surfaces for the side (radial) boundary nodes, the θ's are the thermal-to-fast current ratios discussed in Section 2.5.2, and the δ's are Kronecker deltas defined to be unity at the boundary node of interest and zero elsewhere.

Initial Conditions:

$$- \nabla \cdot D_1 \nabla \varphi_1 + \Sigma_1 \varphi_1 = \frac{1}{k_{eff}} \left(\nu_1 \Sigma_{f_1} \varphi_1 + \nu_2 \Sigma_{f_2} \varphi_2 \right) \tag{6.2.16}$$

$$- \Lambda_2 + \Sigma_2 \varphi_2 = \Sigma_{21} \varphi_1 + \delta_B S_B \varphi_1 \tag{6.2.17}$$

$$c_m = \frac{\beta_m}{\lambda_m} \left(\nu_1 \Sigma_{f_1} \varphi_1 + \nu_2 \Sigma_{f_2} \varphi_2 \right) ; \tag{6.2.18}$$

$$m = 1,2,\ldots,I.$$

6.2.2 Finite Difference Approximation

The system of governing equations summarized in the previous section is solved numerically by means of the standard finite difference approximation in space and time.

For space differencing, we partition the reactor core into a number of identical, non-overlapping, coarse-mesh regions, called "nodes," with a three-dimensional mesh spacing of (h_x, h_y, h_z) subject to the restriction that $h_x = h_y \neq h_z$. A typical node is shown in Figure 6.1. The (x,y,z) mesh is described by (i,j,k) nomenclature, respectively. Here we have used the symbol ψ to represent the fast group flux and we shall use another symbol, Φ, to denote the thermal group flux to avoid confusion. The core consists of a number of such nodes at the centers of which the fluxes are to be calculated. Thus, vertically, the first point (k=1) is $h_z/2$ away from the bottom of the core and the last point (k=KMAX) is $h_z/2$ from the top. Horizontally, all the boundary points are $h_x/2$ from the side core-reflector interfaces. In the x-direction, the mesh points range from i=1 to i=IMAX. In the y-direction, the mesh points start at j=1 and end at j=JMAX. In summary, the finite difference approximation in space is based on a seven-point, center-meshed, differencing scheme.

For time differencing, we discretize the time scale of interest into a number of contiguous discrete time points: $\tau_0, \tau_1, \ldots, \tau_n, \tau_{n+1}, \ldots$ such that $\tau_{n+1} = \tau_n + \Delta\tau_n$ where $\Delta\tau_n$ is the time step size at the time step n. Since only the neutron kinetics equations carry the time derivatives, the time differencing will be applied only to the neutron kinetics equations using backward differences. Thus, the finite difference approximation in time is based on an implicit time differencing.

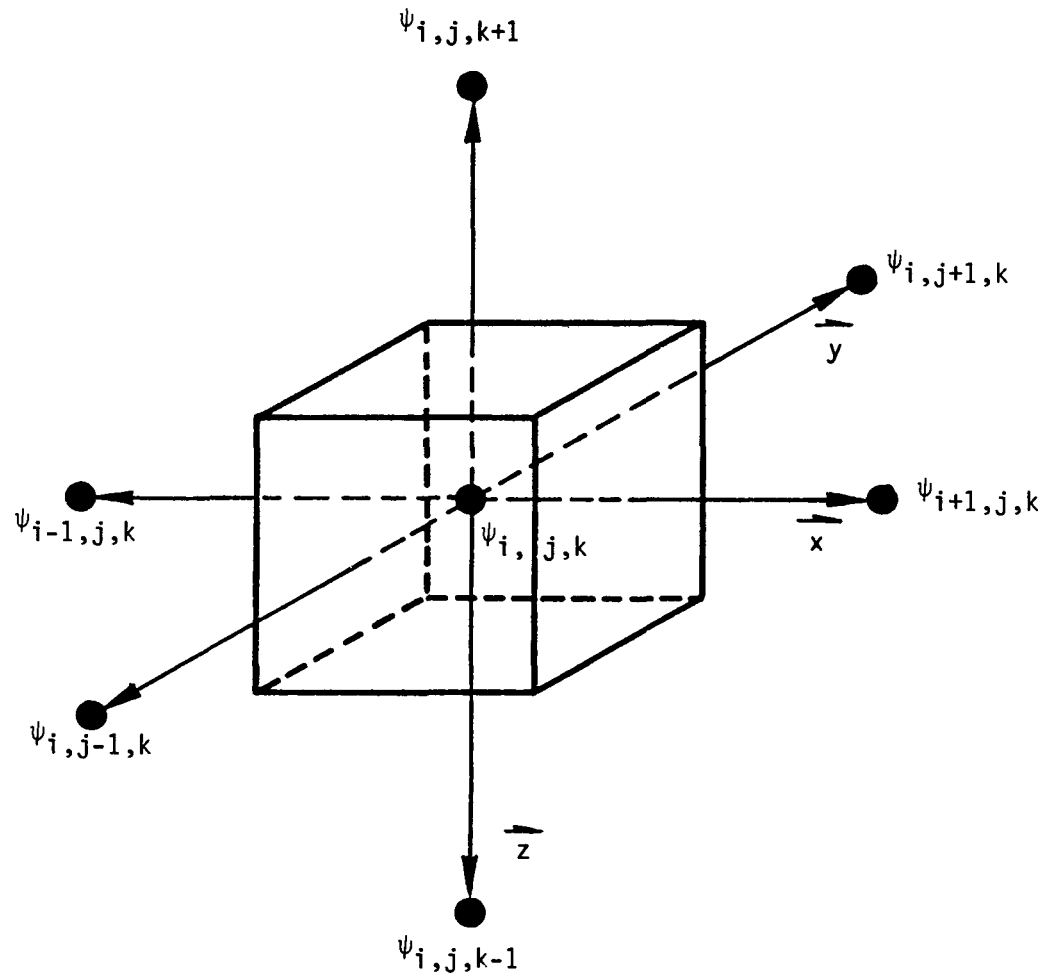

Figure 6.1 Core Spatial Mesh

If we apply the finite difference approximation in both space and time simultaneously to the neutron kinetics equations, we will obtain a system of simultaneous (algebraic) equations, which can be solved by any standard method such as the Gauss-Seidel iteration technique. We shall defer the discussion of the solution methods until Sections 6.6 and 6.7.

In order to see more clearly the underlining assumptions or approximations involved, we shall derive first the ordinary differential equations for neutron kinetics by applying the finite difference approximation in space only, then obtain the finite difference equations for neutron kinetics by implicit time differencing.

6.2.3 Ordinary Differential Equations for Neutron Kinetics

We shall apply the finite difference approximation in space, as outlined in the preceding section, to the neutron kinetics equations to obtain a set of ordinary differential equations in time only for neutron kinetics. Since the fast flux equation is the only one which carries the divergence term, we shall derive first the ordinary differential equation (ODE) for the fast flux. The ODEs for the thermal flux and delayed neutron precursor concentrations can then be readily deduced.

Consider a coarse-mesh volume $V_{i,j,k} = h_x^2 h_z$ as depicted in Figure 6.1. Define the following average quantities for the volume $V_{i,j,k}$:

$$\bar{\varphi}_{1_{i,j,k}} = \frac{1}{V_{i,j,k}} \int_{V_{i,j,k}} \varphi_1 \, d\underline{r} \tag{6.2.19}$$

$$\bar{\varphi}_{2_{i,j,k}} = \frac{1}{V_{i,j,k}} \int_{V_{i,j,k}} \varphi_2 \, d\underline{r} \tag{6.2.20}$$

$$\bar{c}_{m_{i,j,k}} = \frac{1}{V_{i,j,k}} \int_{V_{i,j,k}} c_m \, d\underline{r} \tag{6.2.21}$$

Here we have suppressed the argument $(\underline{r},\tau)$ for the sake of simplicity.

We now integrate the fast flux equation (6.2.1) over the volume $V_{i,j,k}$ and make use of the definitions (6.2.19), (6.2.20) and (6.2.21) to obtain

$$\frac{1}{v_1}\frac{d}{d\tau}\bar{\varphi}_{1_{i,j,k}} = \frac{1}{V_{i,j,k}}\int_{V_{i,j,k}} \nabla\cdot D_1\nabla\varphi_1 d\underline{r} - \Sigma_1\bar{\varphi}_{1_{i,j,k}}$$

$$+ (1-\beta)\left(\nu_1\Sigma_{f_1}\bar{\varphi}_{1_{i,j,k}} + \nu_2\Sigma_{f_2}\bar{\varphi}_{2_{i,j,k}}\right) + \sum_m \lambda_m \bar{c}_{m_{i,j,k}} \quad . \qquad (6.2.22)$$

Here the two-group parameters are flux-weighted averages of the cell volume, $V_{i,j,k}$, evaluated from cell-averaged state variables (void fraction, temperature, etc.) as discussed in Section 2.2.2. However, they are, in general, different in different thermohydraulic nodes because of the feedback effects as well as their dependence on fuel type. For ease of writing, we have suppressed their spatial indices. Fortunately, this does not cause any ambiguity since they always appear together with the neutron fluxes which are clearly indexed.

The integral term in Eq. 6.2.22 is what requires the finite difference approximation for its evaluation. By means of the divergence theorem, we can rewrite the volume integral as a surface integral:

$$\frac{1}{V_{i,j,k}}\int_{V_{i,j,k}} \nabla\cdot D_1\nabla\varphi_1 d\underline{r} = \frac{1}{V_{i,j,k}}\int_{A_{i,j,k}} D_1\nabla\varphi_1\cdot d\underline{A} \qquad (6.2.23)$$

where $A_{i,j,k}$ is the surface area of the coarse-mesh volume $V_{i,j,k}$.

For convenience, let us use J to denote the fast neutron current ($J = -D_1\nabla\phi_1$) and use the indices ($i\pm1/2$, $j\pm1/2$, $k\pm1/2$) to represent the interfaces of the volume $V_{i,j,k}$ in (x,y,z) directions, respectively. Furthermore, we wish to include the boundary currents (J_T, J_B, J_S) at the top, bottom and side boundary surfaces so that the boundary conditions discussed in Section 2.3.3 can be applied if $V_{i,j,k}$ happens to be a boundary node. With all these, we can now express the volume integral as

$$\frac{1}{V_{i,j,k}}\int_{V_{i,j,k}} \nabla\cdot D_1\nabla\varphi_1 d\underline{r} = -\left[\frac{1}{h_x}\left(\sum_{\substack{\ell'=1\\ \ell'\neq s}}^{2} J_{\ell',j,k} + \delta_{s\ell'} J_s\right)\right.$$

$$\left. + \frac{1}{h_x}\left(\sum_{\substack{\ell'=1\\ \ell'\neq s}}^{2} J_{i,\ell',k} + \delta_{s\ell'} J_s\right) + \frac{1}{h_z}\left(\sum_{\substack{\ell'=1\\ \ell'\neq b,t}}^{2} J_{i,j,\ell'} + \delta_{t\ell'} J_T + \delta_{b\ell'} J_B\right)\right] \qquad (6.2.24)$$

where the δ's are the Kronecker deltas defined to be unity at the boundary surfaces of interest and zero elsewhere, and the index ℓ' takes on:

$$\ell' = i + \frac{1}{2},\ j + \frac{1}{2},\ \text{or}\ k + \frac{1}{2} \qquad \text{for } \ell' = 1 \ ;$$

$$\ell' = i - \frac{1}{2},\ j - \frac{1}{2},\ \text{or}\ k - \frac{1}{2} \qquad \text{for } \ell' = 2 \ .$$

For ease of writing, from now on, we shall use D to denote the fast diffusion coefficient D_1 and use $\mathcal{D}$ to denote the thermal diffusion coefficient D_2. In addition, we shall use the symbol φ to represent the fast flux φ_1 and use the symbol Φ to denote the thermal flux φ_2.

We wish to express the interface currents in Eq. 6.2.24 in terms of the center (midpoint) fluxes of the volume $V_{i,j,k}$ and its six neighbors. To this end, we apply the finite difference approximation to the interface current at, say, $\ell' = i+1/2$:

$$J_{\ell',j,k} = - D_{i,j,k} \frac{\varphi_{\ell',j,k} - \varphi_{i,j,k}}{(h_x/2)} \tag{6.2.25}$$

This same current can also be expressed in terms of the center and surface fluxes of the right neighbor node of $V_{i,j,k}$:

$$J_{\ell',j,k} = - D_{i+1,j,k} \frac{\varphi_{i+1,j,k} - \varphi_{\ell',j,k}}{(h_x/2)} \tag{6.2.26}$$

Equating the above two equations and solving for the surface flux, we obtain

$$\varphi_{\ell',j,k} = \frac{D_{i,j,k}\,\varphi_{i,j,k} + D_{i+1,j,k}\,\varphi_{i+1,j,k}}{D_{i,j,k} + D_{i+1,j,k}} \tag{6.2.27}$$

We now substitute Eq. 6.2.27 into Eq. 6.2.25 to obtain the interface current:

$$J_{\ell',j,k} = d_{i,i+1} \frac{\varphi_{i,j,k} - \varphi_{i+1,j,k}}{h_x} \tag{6.2.28}$$

where

$$d_{i,i+1} = \frac{2\,D_{i,j,k}\,D_{i+1,j,k}}{D_{i,j,k} + D_{i+1,j,k}} \quad . \tag{6.2.29}$$

Likewise, we can derive similar expressions for the other five interface currents. We summarize them as follows:

$$J_{\ell',j,k} = d_{i,\ell}\,\frac{\varphi_{i,j,k} - \varphi_{\ell,j,k}}{h_x} \quad ; \qquad \ell = i \pm 1 \quad , \tag{6.2.30}$$

$$J_{i,\ell',k} = d_{j,\ell}\,\frac{\varphi_{i,j,k} - \varphi_{i,\ell,k}}{h_x} \quad ; \qquad \ell = j \pm 1 \quad , \tag{6.2.31}$$

$$J_{i,j,\ell'} = d_{k,\ell}\,\frac{\varphi_{i,j,k} - \varphi_{i,j,\ell}}{h_z} \quad ; \qquad \ell = k \pm 1 \quad . \tag{6.2.32}$$

where

$$d_{i,\ell} = \frac{2\,D_{i,j,k}\,D_{\ell,j,k}}{D_{i,j,k} + D_{\ell,j,k}} \quad ; \qquad \ell = i \pm 1 \quad , \tag{6.2.33}$$

$$d_{j,\ell} = \frac{2\,D_{i,j,k}\,D_{i,\ell,k}}{D_{i,j,k} + D_{i,\ell,k}} \quad ; \qquad \ell = j \pm 1 \quad , \tag{6.2.34}$$

$$d_{k,\ell} = \frac{2\,D_{i,j,k}\,D_{i,j,\ell}}{D_{i,j,k} + D_{i,j,\ell}} \quad ; \qquad \ell = k \pm 1 \quad . \tag{6.2.35}$$

Note that we have introduced a new index ℓ to denote the adjacent nodes of $V_{i,j,k}$; whereas, ℓ' denotes the interfaces:

$$\ell = i+1,\ j+1,\ \text{or}\ k+1 \qquad \text{for } \ell=1,$$
$$\ell = i-1,\ j-1,\ \text{or}\ k-1 \qquad \text{for } \ell=2.$$

The boundary currents can be expressed in terms of the center fluxes of the boundary nodes as discussed in Section 2.3.3:

$$\delta_{t\ell'} J_T = \delta_{t\ell} \frac{D_{i,j,t} \varphi_{i,j,t}}{\lambda^T_{eff}} \tag{6.2.36}$$

$$\delta_{b\ell'} J_B = \delta_{b\ell} \frac{D_{i,j,b} \varphi_{i,j,b}}{\lambda^B_{eff}} \tag{6.2.37}$$

$$\delta_{x\ell'} J_S = \delta_{x\ell} \frac{D_{x,j,k} \varphi_{x,j,k}}{\lambda^S_{eff}} \tag{6.2.38}$$

$$\delta_{y\ell'} J_S = \delta_{y\ell} \frac{D_{i,y,k} \varphi_{i,y,k}}{\lambda^S_{eff}} \tag{6.2.39}$$

Here we have used the subscripts (t, b, x, y) to denote the top, bottom, x-side, y-side boundary nodes, respectively.

Using these boundary currents and the interface currents, Eqs. 6.2.30 through 6.2.32, we obtain the following expression for the volume integral, Eq. 6.2.24:

$$\begin{aligned}
\frac{1}{V_{i,j,k}} \int_{V_{i,j,k}} \nabla \cdot D_1 \nabla \varphi_1 \, d\underline{r} = & - \frac{1}{h_x^2} \left[\left(\sum_{\ell=1}^{2} d_{i,\ell} + \sum_{\ell=1}^{2} d_{j,\ell} + R \sum_{\ell=1}^{2} d_{k,\ell} \right) \varphi_{i,j,k} \right. \\
& + \delta_{x\ell} \frac{h_x D_{x,j,k} \varphi_{x,j,k}}{\lambda^S_{eff}} \Bigg] + \frac{1}{h_x^2} \left[\left(\sum_{\ell=1}^{2} d_{i,\ell} \varphi_{\ell,j,k} + \sum_{\ell=1}^{2} d_{j,\ell} \varphi_{i,\ell,k} \right) \right. \\
& - \delta_{y\ell} \frac{h_x D_{i,y,k} \varphi_{i,y,k}}{\lambda^S_{eff}} \Bigg] + \frac{R}{h_x^2} \left[\sum_{\ell=1}^{2} d_{k,\ell} \varphi_{i,j,\ell} - \delta_{t\ell} \frac{h_z D_{i,j,t} \varphi_{i,j,t}}{\lambda^T_{eff}} \right. \\
& \left. - \delta_{b\ell} \frac{h_z D_{i,j,b} \varphi_{i,j,b}}{\lambda^B_{eff}} \right]
\end{aligned} \tag{6.2.40}$$

where R is defined as

$$R = \left(\frac{h_x}{h_z}\right)^2 \quad . \tag{6.2.41}$$

Using Eq. 6.2.40 in Eq. 6.2.22 and rearranging, we obtain the ordinary differential equation for the fast flux:

$$\frac{1}{v_1}\frac{d}{d\tau}\bar{\varphi}_{i,j,k} = \left[(1-\beta)\nu_1\Sigma f_1 - \Sigma_1\right]\bar{\varphi}_{i,j,k} + (1-\beta)\nu_2\Sigma f_2\,\bar{\phi}_{i,j,k} + \sum_m \lambda_m \bar{c}_{m\,i,j,k}$$

$$- \zeta_{i,j,k}\,\varphi_{i,j,k} + \frac{1}{h_x^2}\left(\sum_{\ell=1}^{2} d_{i,\ell}\,\varphi_{\ell,j,k} + \sum_{\ell=1}^{2} d_{j,\ell}\,\varphi_{i,\ell,k}\right) + \frac{R}{h_x^2}\sum_{\ell=1}^{2} d_{k,\ell}\,\varphi_{i,j,\ell} \tag{6.2.42}$$

where

$$\zeta_{i,j,k} = \frac{1}{h_x^2}\left(\sum_{\ell=1}^{2} d_{i,\ell} + \sum_{\ell=1}^{2} d_{j,\ell} + R\sum_{\ell=1}^{2} d_{k,\ell} + \delta_{x\ell}\,\frac{h_x D_{x,j,k}}{\lambda^S_{eff}}\right.$$

$$\left. + \delta_{y\ell}\,\frac{h_x D_{i,y,k}}{\lambda^S_{eff}} + \delta_{t\ell}\,\frac{R h_z D_{i,j,t}}{\lambda^T_{eff}} + \delta_{b\ell}\,\frac{R h_z D_{i,j,b}}{\lambda^B_{eff}}\right) . \tag{6.2.43}$$

It is important to point out that the ODE (6.2.42) contains both the average fluxes and the center fluxes. The difference between the average and center fluxes is the key to the success of any coarse-mesh diffusion theory. We shall defer the treatment of the average fluxes until Section 6.2.4.

The spatial integration procedure used to derive the ODE (6.2.42) is called "box integration." Using the same box integration procedure, we can derive the ODEs for the thermal flux and the delayed neutron precursor concentrations from Eqs. 6.2.2 and 6.2.3, respectively:

$$\frac{1}{v_2}\frac{d}{d\tau}\bar{\phi}_{i,j,k} = \bar{\Lambda}_{i,j,k} - \Sigma_2\bar{\phi}_{i,j,k} + (\Sigma_{21} + \delta_B S_B)\,\bar{\varphi}_{i,j,k} \qquad (6.2.44)$$

$$\frac{d}{d\tau}\bar{c}_{m_{i,j,k}} = \beta_m \nu_1 \Sigma_{f_1}\bar{\varphi}_{i,j,k} + \beta_m \nu_2 \Sigma_{f_2}\bar{\phi}_{i,j,k} - \lambda_m \bar{c}_{m_{i,j,k}} \quad ; \qquad (6.2.45)$$

$$m = 1,2,\ldots,I.$$

where

$$\bar{\Lambda}_{i,j,k} = \frac{1}{V_{i,j,k}}\int_{V_{i,j,k}} \Lambda_2\, d\underline{r} \equiv \Sigma_L\bar{\phi}_{i,j,k} \quad . \qquad (6.2.46)$$

In practice Σ_L can be determined from the above definition if Λ_2 is available. A simple treatment of Λ_2 has been discussed in Section 2.3.2. For now we shall assume that Σ_L is known in the following discussion.

RAMONA-3B introduces an approximate factorization (Borresen 1971) to simplify the coefficients, d's, as follows:

$$d_{i,\ell} = \frac{2D_{i,j,k}D_{\ell,j,k}}{D_{i,j,k}+D_{\ell,j,k}} \approx \sqrt{D_{i,j,k}}\sqrt{D_{\ell,j,k}} \quad ; \quad \ell = i+1 \text{ or } i-1, \qquad (6.2.47)$$

$$d_{j,\ell} \approx \sqrt{D_{i,j,k}}\sqrt{D_{i,\ell,k}} \quad ; \quad \ell = j+1 \text{ or } j-1, \qquad (6.2.48)$$

$$d_{k,\ell} \approx \sqrt{D_{i,j,k}}\sqrt{D_{i,j,\ell}} \quad ; \quad \ell = k+1 \text{ or } k-1. \qquad (6.2.49)$$

The relative error of these approximations depends on how much the diffusion coefficients of the two adjacent nodes differ from each other. The error is only 0.11% with 10% mismatch in the diffusion coefficient, about 0.42% with 20% mismatch, and increases to 2.1% with 50% mismatch. The fast diffusion coefficient in a BWR is fairly uniform in the radial direction and varies gradually from node to node in the axial direction (due to the void distribution). Thus, the error is expected to be well within 1% in most situations for a BWR.

To take advantage of the above approximations, we redefine the neutron fluxes and precursor concentrations as follows:

$$\varphi_{i,j,k} = \frac{\psi_{i,j,k}}{\sqrt{D_{i,j,k}}} \tag{6.2.50}$$

$$\bar{\varphi}_{i,j,k} = \frac{\bar{\psi}_{i,j,k}}{\sqrt{D_{i,j,k}}} \tag{6.2.51}$$

$$\bar{\phi}_{i,j,k} = \frac{\bar{\Phi}_{i,j,k}}{\sqrt{D_{i,j,k}}} \tag{6.2.52}$$

$$\bar{c}_{m_{i,j,k}} = \frac{\bar{\xi}_{m_{i,j,k}}}{\sqrt{D_{i,j,k}}} \tag{6.2.53}$$

With these definitions and the factorization approximations, the ordinary differential equations (6.2.42), (6.2.44) and (6.2.45) reduce to

$$\left\{ \begin{aligned} \frac{d}{dt}\bar{\psi}_{i,j,k} &= b_{11}\bar{\psi}_{i,j,k} + b_{12}\bar{\Phi}_{i,j,k} + \sum_m b_{1m}\bar{\xi}_{m_{i,j,k}} - \mu\psi_{i,j,k} \\ &\quad + \eta\left(\sum_{\ell=1}^{2}\psi_{\ell,j,k} + \sum_{\ell=1}^{2}\psi_{i,\ell,k} + R\sum_{\ell=1}^{2}\psi_{i,j,\ell}\right), \qquad (6.2.54) \\ \frac{d}{dt}\bar{\Phi}_{i,j,k} &= b_{21}\bar{\psi}_{i,j,k} - b_{22}\bar{\Phi}_{i,j,k}, \qquad (6.2.55) \\ \frac{d}{dt}\bar{\xi}_{m_{i,j,k}} &= b_{m1}\bar{\psi}_{i,j,k} + b_{m2}\bar{\Phi}_{i,j,k} - \lambda_m\bar{\xi}_{m_{i,j,k}}, \qquad (6.2.56) \end{aligned} \right.$$

where

$$b_{11} = v_1 \left[(1-\beta)\nu_1 \Sigma_{f_1} - \Sigma_1\right] \quad , \tag{6.2.57}$$

$$b_{12} = v_1 (1-\beta)\nu_2 \Sigma_{f_2} \quad , \tag{6.2.58}$$

$$b_{1m} = v_1 \lambda_m \quad , \tag{6.2.59}$$

$$b_{21} = v_2 (\Sigma_{21} + \delta_B S_B) \quad , \tag{6.2.60}$$

$$b_{22} = v_2 (\Sigma_2 + \Sigma_L) \quad , \tag{6.2.61}$$

$$b_{m1} = \beta_m \nu_1 \Sigma_{f_1} \quad , \tag{6.2.62}$$

$$b_{m2} = \beta_m \nu_2 \Sigma_{f_2} \quad , \tag{6.2.63}$$

$$\mu = v_1 \zeta_{i,j,k} \tag{6.2.64}$$

$$\eta = v_1 \frac{D_{i,j,k}}{h_x^2} \quad . \tag{6.2.65}$$

In summary, Eqs. 6.2.54, 6.2.55 and 6.2.56 form the set of ordinary differential equations for neutron kinetics to be solved for a three-dimensional core. We shall apply an implicit time differencing scheme to these ODEs to obtain the finite difference equations for neutron kinetics in Section 6.2.5. Before we can do this, we must develop a relationship between the average fast fluxes and the center fast fluxes. Note that such a relationship for the thermal fluxes is not necessary so long as the average fast fluxes are available.

6.2.4 Average Nodal Fluxes

The ordinary differential equations derived in the previous section call for the average nodal fluxes and average precursor concentrations as well as the midpoint fast fluxes. The simplest approximation is to set the average values equal to the corresponding midpoint values. While this is adequate for fine-mesh diffusion calculations, it may introduce significant errors for coarse-mesh calculations.

How to obtain an accurate estimate for the average flux in terms of the midpoint fluxes is the heart of the problem for the development of modern nodal methods for coarse-mesh diffusion calculations. Generally speaking, if the detailed flux profile in a coarse-mesh volume is known, one can readily determine

the average flux from its definition (6.2.19). Unfortunately, such a profile is not known a priori, and one must resort to some approximate way of obtaining such a profile. For instance, the analytical nodal method (Smith and Henry 1979) obtains the flux profile from the analytical solutions of separate one-dimensional problems. The German code, CUBOX, (Langenbuch 1977) employs a cubic polynomial expansion to represent the flux profile.

RAMONA-3B uses a scheme which expresses the average fast flux in a node as a weighted average of the midpoint flux in that node and its six adjacent nodes (Borressen 1971). This scheme can be derived by means of a Taylor series expansion about the midpoint flux:

$$\varphi(x,y,z) = \varphi_{i,j,k} + \sum_{n=1}^{\infty} \frac{1}{n!} \left[(x-x_i) \frac{\partial}{\partial x} + (y-y_j) \frac{\partial}{\partial y} + (z-z_k) \frac{\partial}{\partial z} \right]^n \varphi|_{x_i,y_j,z_k} \tag{6.2.66}$$

If we retain only the terms up to the second order and use it in Eq. 6.2.19, we will obtain an expression for the average fast flux consisting of the center flux and three second-order derivatives with respect to x, y, and z, respectively. We then apply the finite difference approximation to the derivative terms and introduce a weighting factor (a free parameter to allow for better accuracy, if precisely known). This will lead to a relationship between the average flux and the midpoint fluxes of the coarse-mesh volume $V_{i,j,k}$ and its six neighbors. Converting it to the ψ's, we will obtain the expression for the average $\overline{\psi}$. The derivation is tedious. We omit the details here and present only the final result (Borressen 1971) below:

$$\overline{\psi}_{i,j,k} = (b + cr_{i,j,k}) \psi_{i,j,k} + c \left(\sum_{\ell=1}^{2} \psi_{\ell,j,k} + \sum_{\ell=1}^{2} \psi_{i,\ell,k} + R \sum_{\ell=1}^{2} \psi_{i,j,\ell} \right) \tag{6.2.67}$$

where

$$b = \frac{3a}{3a + (1-a)(R+2)} , \tag{6.2.68}$$

$$c = \left(\frac{1-a}{4} \right) \frac{1}{3a + (1-a)(R+2)} , \tag{6.2.69}$$

$$r_{i,j,k} = \sqrt{D_{i,j,k}}\left(\sum_{\ell=1}^{2}\frac{1}{\sqrt{D_{\ell,j,k}}}+\sum_{\ell=1}^{2}\frac{1}{\sqrt{D_{i,\ell,k}}}+R\sum_{\ell=1}^{2}\frac{1}{\sqrt{D_{i,j,\ell}}}\right), \tag{6.2.70}$$

and a is the weighting factor for the fast flux, a required input for RAMONA-3B. Experience indicated that a = 0.3 is near optimum, and hence recommended (Borressen 1971).

For the thermal flux, such a formula for its average is not necessary as we have discussed in the previous section. However, RAMONA-3B employs the following formula for the average thermal flux in a node (only in the case of Λ_2=0):

$$\bar{\Phi}_{i,j,k} = (b_t + c_t r_t)\,\Phi_{i,j,k} + c_t\left(\sum_{\ell=1}^{2}\Phi_{\ell,j,k}+\sum_{\ell=1}^{2}\Phi_{i,\ell,k}+R\sum_{\ell=1}^{2}\Phi_{i,j,\ell}\right) \tag{6.2.71}$$

where b_t, c_t and r_t are similarly defined as in Eqs. 6.2.68, 6.2.69, and 6.2.70 except that a is replaced by a_t, the weighting factor for the thermal flux, again a required input for RAMONA-3B, and the D's are replaced by the corresponding thermal diffusion coefficients. The typical value for the parameter a_t is 0.7 (Borressen 1971).

6.2.5 Finite Difference Equations for Neutron Kinetics

6,2.5.1 Transient Finite Difference Equations

We now apply the implicit time differencing scheme discussed in Section 6.2.2 to the ODEs (6.2.54), (6.2.55) and (6.2.56) to obtain the following difference equations:

$$\frac{1}{\Delta\tau_n}\left(\bar{\psi}^{n+1}_{i,j,k}-\bar{\psi}^{n}_{i,j,k}\right) = b_{11}^{n+1}\,\bar{\psi}^{n+1}_{i,j,k}+b_{12}^{n+1}\,\bar{\Phi}^{n+1}_{i,j,k}+\sum_{m}b_{1m}^{n+1}\,\bar{\xi}^{n+1}_{m\,i,j,k}$$

$$-\mu^{n+1}\,\psi^{n+1}_{i,j,k}+\eta^{n+1}\left(\sum_{\ell=1}^{2}\psi^{n+1}_{\ell,j,k}+\sum_{\ell=1}^{2}\psi^{n+1}_{i,\ell,k}+R\sum_{\ell=1}^{2}\psi^{n+1}_{i,j,\ell}\right), \tag{6.2.72}$$

$$\frac{1}{\Delta\tau_n}\left(\bar{\Phi}^{n+1}_{i,j,k} - \bar{\Phi}^{n}_{i,j,k}\right) = b^{n+1}_{21}\,\bar{\psi}^{n+1}_{i,j,k} - b^{n+1}_{22}\,\bar{\Phi}^{n+1}_{i,j,k} \quad , \tag{6.2.73}$$

$$\frac{1}{\Delta\tau_n}\left(\bar{\xi}^{n+1}_{m_{i,j,k}} - \bar{\xi}^{n}_{m_{i,j,k}}\right) = b^{n+1}_{m1}\,\bar{\psi}^{n+1}_{i,j,k} + b^{n+1}_{m2}\,\bar{\Phi}^{n+1}_{i,j,k} - \lambda_m\,\bar{\xi}^{n+1}_{i,j,k} \quad . \tag{6.2.74}$$

First, we solve Eq. 6.2.73 for the average thermal flux at time step n+1:

$$\bar{\Phi}^{n+1}_{i,j,k} = \frac{\bar{\Phi}^{n}_{i,j,k} + \Delta\tau_n\, b^{n+1}_{21}\,\bar{\psi}^{n+1}_{i,j,k}}{\left(1 + \Delta\tau_n\, b^{n+1}_{22}\right)} \tag{6.2.75}$$

where

$$b^{n+1}_{21} = v_2\left(\Sigma^{n+1}_{21} + \delta_B\, S^{n+1}_{B}\right) \quad , \tag{6.2.76}$$

$$b^{n+1}_{22} = v_2\left(\Sigma^{n+1}_{2} + \Sigma^{n+1}_{L}\right) \quad . \tag{6.2.77}$$

Next we solve Eq. 6.2.74 for the average delayed neutron precursor concentrations at time step n+1:

$$\bar{\xi}^{n+1}_{m_{i,j,k}} = \frac{\bar{\xi}^{n}_{m_{i,j,k}} + \Delta\tau_n\, b^{n+1}_{m1}\,\bar{\psi}^{n+1}_{i,j,k} + \Delta\tau_n\, b^{n+1}_{m2}\,\bar{\Phi}^{n+1}_{i,j,k}}{\left(1 + \Delta\tau_n\,\lambda_m\right)} \quad ; \tag{6.2.78}$$

$$m = 1,2,\ldots,I.$$

where

$$b_{m1}^{n+1} = \beta_m \nu_1^{n+1} \Sigma_{f_1}^{n+1} \quad , \tag{6.2.79}$$

$$b_{m2}^{n+1} = \beta_m \nu_2^{n+1} \Sigma_{f_2}^{n+1} \quad . \tag{6.2.80}$$

We now use Eqs. 6.2.75 and 6.2.78 in 6.2.72, solve for the average fast flux at step n+1 to obtain, after some manipulation:

$$\bar{\psi}_{i,j,k}^{n+1} = \frac{1}{g_1^{n+1}} \bar{\psi}_{i,j,k}^{n} + \frac{g_2^{n+1}}{g_1^{n+1}} \Phi_{i,j,k}^{n} + \frac{1}{g_1^{n+1}} \sum_m \pi_m^{n+1} \bar{\xi}_{m_{i,j,k}}^{n} - \frac{\Delta\tau_n \mu^{n+1}}{g_1^{n+1}} \psi_{i,j,k}^{n+1}$$

$$+ \frac{\Delta\tau_n \eta^{n+1}}{g_1^{n+1}} \left(\sum_{\ell=1}^{2} \psi_{\ell,j,k}^{n+1} + \sum_{\ell=1}^{2} \psi_{i,\ell,k}^{n+1} + R \sum_{\ell=1}^{2} \psi_{i,j,\ell}^{n+1} \right) \quad , \tag{6.2.81}$$

where

$$g_1^{n+1} = 1 - \Delta\tau_n \left[b_{11}^{n+1} - \sum_m \pi_m^{n+1} b_{m1}^{n+1} - \kappa_{21}^{n+1} \left(b_{12}^{n+1} + \sum_m \pi_m^{n+1} b_{m2}^{n+1} \right) \right] \quad , \tag{6.2.82}$$

$$\pi_m^{n+1} = \frac{\Delta\tau_n b_{1m}^{n+1}}{1 + \Delta\tau_n \lambda_m} \quad , \tag{6.2.83}$$

$$\kappa_{21}^{n+1} = \frac{\Delta\tau_n b_{21}^{n+1}}{1 + \Delta\tau_n b_{22}^{n+1}} \quad , \tag{6.2.84}$$

$$g_2^{n+1} = \kappa_{12}^{n+1} \left(1 + \frac{\Delta\tau_n}{b_{12}^{n+1}} \sum_m \pi_m^{n+1} b_{m2}^{n+1} \right) \quad , \tag{6.2.85}$$

$$\kappa_{12}^{n+1} = \frac{\Delta\tau_n b_{12}^{n+1}}{1 + \Delta\tau_n b_{22}^{n+1}} \quad , \tag{6.2.86}$$

$$\mu^{n+1} = \frac{v_1}{h_x^2}\left(\sum_{\ell=1}^{2} d_{i,\ell}^{n+1} + \sum_{\ell=1}^{2} d_{j,\ell}^{n+1} + R\sum_{\ell=1}^{2} d_{k,\ell}^{n+1} + \delta_{x\ell}\frac{h_x D_{x,j,k}^{n+1}}{\lambda_{eff}^{S}}\right.$$

$$\left. + \delta_{y\ell}\frac{h_x D_{i,y,k}^{n+1}}{\lambda_{eff}^{S}} + \delta_{t\ell}\frac{h_z D_{i,j,t}^{n+1}}{\lambda_{eff}^{T}} + \delta_{b\ell}\frac{h_z D_{i,j,b}^{n+1}}{\lambda_{eff}^{B}}\right) , \qquad (6.2.87)$$

$$\eta^{n+1} = \frac{v_1 D_{i,j,k}^{n+1}}{h_x^2} . \qquad (6.2.88)$$

We now apply the formula (6.2.67) for the average fast fluxes at time steps n+1 and n in Eq. 6.2.81 to obtain the transient algorithm for the fast flux:

$$\psi_{i,j,k}^{n+1} = p_{i,j,k}^{n+1}\left(\sum_{\ell=1}^{2} \psi_{\ell,j,k}^{n+1} + \sum_{\ell=1}^{2} \psi_{i,\ell,k}^{n+1} + R\sum_{\ell=1}^{2} \psi_{i,j,\ell}^{n+1}\right) + S_{i,j,k}^{n} \qquad (6.2.89)$$

where

$$p_{i,j,k}^{n+1} = \frac{\Delta\tau_n \eta^{n+1} - g_1^{n+1} c}{g_1^{n+1}\left(b + cr_{i,j,k}^{n+1}\right) + \Delta\tau_n \mu^{n+1}} , \qquad (6.2.90)$$

$$S_{i,j,k}^{n} = \frac{\bar{\psi}_{i,j,k}^{n} + g_2^{n+1}\bar{\Phi}_{i,j,k}^{n} + \sum_m \pi_m^{n+1}\bar{\xi}_{m\,i,j,k}^{n}}{g_1^{n+1}\left(b + cr_{i,j,k}^{n+1}\right) + \Delta\tau_n \mu^{n+1}} , \qquad (6.2.91)$$

$$\bar{\psi}_{i,j,k}^{n} = \left(b + cr_{i,j,k}^{n}\right)\psi_{i,j,k}^{n} + c\left(\sum_{\ell=1}^{2} \psi_{\ell,j,k}^{n} + \sum_{\ell=1}^{2} \psi_{i,\ell,k}^{n} + R\sum_{\ell=1}^{2} \psi_{i,j,\ell}^{n}\right) . \qquad (6.2.92)$$

In summary, the transient finite difference equations for neutron kinetics are Eq. 6.2.89 for the midpoint fast flux, Eq. 6.2.75 for the average thermal flux, and Eqs. 6.2.78 for the average delayed neutron precursor concentrations (m=1,2,...,I). The forms of these equations suggest the following computing sequence:

(1) Compute the midpoint fast flux at the time step n+1 by solving Eq. 6.2.89 with an iterative procedure such as the Gauss-Seidel method.

(2) Compute the average fast flux at the time step n+1 from the midpoint fast fluxes by Eq. 6.2.92 but with n replaced by n+1.

(3) Compute the average thermal flux at time step n+1 from its previous value at time step n and the average fast flux at the time step n+1 by Eq. 6.2.75.

(4) Compute the average delayed neutron precursor concentrations (m=1,2, ...,I) from their previous values at time step n, and the average fast and thermal fluxes at time step n+1 by Eq. 6.2.78.

The details of the solution methods will be discussed later in Section 6.7.

6.2.5.2 Steady-State Finite Difference Equations

The steady-state finite difference equations are obtained from the ODEs (6.2.54), (6.2.55), and (6.2.56) by setting the time derivatives to zero:

$$\mu\psi_{i,j,k} = b_{11}\,\bar{\psi}_{i,j,k} + b_{12}\,\bar{\Phi}_{i,j,k} + \sum_m b_{1m}\,\bar{\xi}_{m_{i,j,k}} + \eta\left(\sum_{\ell=1}^{2}\psi_{\ell,j,k} + \sum_{\ell=1}^{2}\psi_{i,\ell,k} + R\sum_{\ell=1}^{2}\psi_{i,j,\ell}\right), \tag{6.2.93}$$

$$\bar{\Phi}_{i,j,k} = \left(\frac{\Sigma_{21} + \delta_B S_B}{\Sigma_2 + \Sigma_L}\right)\bar{\psi}_{i,j,k}, \tag{6.2.94}$$

$$\bar{\xi}_{m_{i,j,k}} = \frac{\beta_m}{\lambda_m}\left(\nu_1\Sigma_{f_1}\bar{\psi}_{i,j,k} + \nu_2\Sigma_{f_2}\bar{\Phi}_{i,j,k}\right); \tag{6.2.95}$$

$$m = 1,2,\ldots,I.$$

We substitute Eqs. 6.2.94 and 6.2.95 into Eq. 6.2.93 and combine like terms to obtain

$$\zeta_{i,j,k}\,\psi_{i,j,k} = \Sigma_1\left(\frac{k_\infty}{k_{eff}} - 1\right)\overline{\psi}_{i,j,k} + \frac{D_{i,j,k}}{h_x^2}\left(\sum_{\ell=1}^{2}\psi_{\ell,j,k} + \sum_{\ell=1}^{2}\psi_{i,\ell,k} + R\sum_{\ell=1}^{2}\psi_{i,j,\ell}\right) , \qquad (6.2.96)$$

where

$$\frac{k_\infty}{k_{eff}} = \frac{\nu_1\Sigma_{f_1}}{\Sigma_1} + \frac{\Sigma_{21} + \delta_B S_B}{\Sigma_2 + \Sigma_L}\left(\frac{\nu_2\Sigma_{f_2}}{\Sigma_1}\right) . \qquad (6.2.97)$$

Here k_{eff} is the eigenvalue or the effective multiplication factor of the core, and k_∞ is often referred to as the infinite multiplication factor.

We now make use of Eq. 6.2.67 for the average fast flux in Eq. 6.2.96. After some manipulation, we obtain the steady-state algorithm for the midpoint fast flux:

$$Q_{i,j,k}\,\psi_{i,j,k} = \sum_{\ell=1}^{2}\psi_{\ell,j,k} + \sum_{\ell=1}^{2}\psi_{i,\ell,k} + R\sum_{\ell=1}^{2}\psi_{i,j,\ell} \qquad (6.2.98)$$

where

$$Q_{i,j,k} = \frac{p_{i,j,k} + q_{i,j,k}\left(b + cr_{i,j,k}\right)}{1 - cq_{i,j,k}} , \qquad (6.2.99)$$

$$p_{i,j,k} = \frac{1}{\sqrt{D_{i,j,k}}}\left(\sum_{\ell=1}^{2}\sqrt{D_{\ell,j,k}} + \sum_{\ell=1}^{2}\sqrt{D_{i,\ell,k}} + R\sum_{\ell=1}^{2}\sqrt{D_{i,j,\ell}}\right) , \qquad (6.2.100)$$

$$q_{i,j,k} = -\frac{h_x^2}{M^2_{i,j,k}} \left(\frac{k_{\infty_{i,j,k}}}{k_{eff}} - 1 \right) , \qquad (6.2.101)$$

$$M^2_{i,j,k} = \frac{D_{i,j,k}}{\Sigma 1_{i,j,k}} . \qquad (6.2.102)$$

Note that we have attached the spatial indices (i,j,k) to the infinite multiplication factor, k_∞, since it is a function of the two-group parameters which depend on (i,j,k). The quantity, $M^2_{i,j,k}$, is known as the migration area for fast neutrons in reactor physics.

In summary, the steady-state finite difference equations are Eq. 6.2.98 for the midpoint fast flux, Eq. 6.2.94 for the average thermal flux, and Eq. 6.2.95 for the average delayed neutron precursor concentrations. The forms of these equations suggest the following sequence of solutions:

(1) First, compute the midpoint fast flux by solving Eq. 6.2.98 with an iterative technique such as the Gauss-Seidel method.

(2) Compute the average fast flux from the midpoint fluxes by Eq. 6.2.67.

(3) Compute the average thermal flux from the average fast flux by Eq. 6.2.94.

(4) Finally, compute the average precursor concentrations (m=1,2,...,I) from the average fast and thermal fluxes by Eq. 6.2.95.

The details of the solution methods will be discussed later in Section 6.6.

6.2.6 Finite Difference Equations for Power Generation

The power generation equations were derived in Section 6.2. In this section, we derive the finite difference equations for power generation using the box integration procedure. We shall use the time step index n+1 to represent the time of interest in the following discussion.

We first determine the average fission density, as defined by Eq. 2.7.3, from the average fluxes discussed in Section 6.2.5 for the node indexed by (i,j,k):

$$\bar{F}^{n+1}_{i,j,k} = \frac{\Sigma^{n+1}_{f1_{i,j,k}}}{\sqrt{D^{n+1}_{i,j,k}}} \bar{\psi}^{n+1}_{i,j,k} + \frac{\Sigma^{n+1}_{f2_{i,j,k}}}{\sqrt{D^{n+1}_{i,j,k}}} \bar{\Phi}^{n+1}_{i,j,k} \qquad (6.2.103)$$

Define the average prompt and delayed volumetric heat generation rates at time step n+1 as

$$\bar{q}'''^{n+1}_{p_{i,j,k}} = \frac{1}{V_{i,j,k}} \int_{V_{i,j,k}} q'''^{n+1}_{p} \, d\underline{r} \quad , \tag{6.2.104}$$

$$\bar{q}'''^{n+1}_{d_{i,j,k}} = \frac{1}{V_{i,j,k}} \int_{V_{i,j,k}} q'''^{n+1}_{d} \, d\underline{r} \quad . \tag{6.2.105}$$

Using Eqs. 6.2.8, 6.2.9 and 6.2.103, we obtain

$$\bar{q}'''^{n+1}_{p_{i,j,k}} = K(1-H_o)\, \bar{F}^{n+1}_{i,j,k} \quad , \tag{6.2.106}$$

$$\bar{q}'''^{n+1}_{d_{i,j,k}} = \bar{q}'''^{o}_{i,j,k} \left(H^{n+1}_{\infty} - H^{n+1+\tau}_{\infty}\right) + K\gamma^{n+1}\, \bar{F}^{n+1}_{i,j,k} \left(H^{o}_{\infty} - H^{n+1}_{\infty}\right) \tag{6.2.107}$$

where $q'''^{o}_{i,j,k}$ is the initial average (total) volumetric heat generation rate at $\tau=0$, and γ^{n+1} is defined by Eq. 2.7.9. Here we have used the notation: $H^{n+1} = H(t,\infty)$ and the other H's are similarly defined.

We now use Eqs. 6.2.106 and 6.2.107 in Eqs. 6.2.5, 6.2.6 and 6.2.7 to obtain the average nodal values of the volumetric heat generation rates in the fuel, coolant, and bypass channel, respectively:

$$\bar{q}'''^{n+1}_{f_{i,j,k}} = \left(\frac{h_x^2}{\pi r_f^2 N_r}\right) \left[(1-\eta_{pw})\, \bar{q}'''^{n+1}_{p_{i,j,k}} + (1-\eta_{dw})\, \bar{q}'''^{n+1}_{d_{i,j,k}}\right] \quad , \tag{6.2.108}$$

$$\bar{q}'''^{n+1}_{\ell_{i,j,k}} = \left(\frac{\eta_c h_x^2}{A_c}\right) \left(\eta_{pw}\, \bar{q}'''^{n+1}_{p_{i,j,k}} + \eta_{dw}\, \bar{q}'''^{n+1}_{d_{i,j,k}}\right) \quad , \tag{6.2.109}$$

$$\bar{q}'''^{n+1}_{\ell b_{i,j,k}} = \frac{h_x^2}{A_c}(1-\eta_c)\left(\eta_{pw}\,\bar{q}_p'''^{n+1} + \eta_{dw}\,\bar{q}_d'''^{n+1}\right) \qquad (6.2.110)$$

where $\bar{q}_p'''^{n+1}$ and $\bar{q}_d'''^{n+1}$ are the sums over the core:

$$\bar{q}_p'''^{n+1} = \sum_{i,j,k} \bar{q}_{p_{i,j,k}}'''^{n+1} \quad , \qquad (6.2.111)$$

$$\bar{q}_d'''^{n+1} = \sum_{i,j,k} \bar{q}_{d_{i,j,k}}'''^{n+1} \quad . \qquad (6.2.112)$$

The average total volumetric heating rate is then given by

$$\bar{q}'''^{n+1}_{i,j,k} = \bar{q}_{p_{i,j,k}}'''^{n+1} + \bar{q}_{d_{i,j,k}}'''^{n+1} \quad . \qquad (6.2.113)$$

The numerical algorithms above are developed for transient power generations. However, they are also applicable to steady-state power generations. All that needs to be done is to remove the time step index or to assign "o" to them.

6.2.7 Summary and Recommendations

We have developed the transient and steady-state numerical algorithms for neutron kinetics and power generation. A box integration procedure was used to treat the space variables and an implicit time differencing scheme was employed to treat the time variable. The derived numerical algorithms are in finite difference forms. The logical computing sequences suggested by these algorithms were discussed. The numerical methods of solutions to these algorithms were not discussed as they will be discussed later in Sections 6.6 and 6.7.

Currently, RAMONA-3B computes not only the midpoint fast fluxes but also the midpoint thermal fluxes, then computes the average thermal flux from the midpoint thermal fluxes by means of a weighting factor, a_t, required as an input. As we have discussed in Section 6.2.4, this is unnecessary and, in fact, may introduce an additional uncertainty. We recommend that the average thermal fluxes be calculated directly from its balance equation using the average fast fluxes.

6.3 Finite-Difference Formulations for Thermal Conduction

In this section are presented the finite-difference analogues of the partial differential equations presented in Chapter 3 for predicting the thermal response in fuel pins. The finite difference equations presented here are solved on the computer with the methods described later in Section 6.6 for the steady-state initial conditions and in Section 6.7 for the transients.

Transient thermal conduction in fuel pins is computed in RAMONA-3B by first-order implicit Euler integration with respect to time of the ordinary differential equations derived from Eqs. 3.4.2 and 4, by integrating these partial differential equations in space over a discrete control volume. The steady-state temperature distributions in fuel pins are computed by solving iteratively the nonlinear set of finite-difference equations, which represent Eqs. 3.4.22 and 23.

6.3.1 System of Governing Equations for Transient Conduction

The system of partial and ordinary differential equations and of algebraic expressions comprising the conduction model are presented in Section 3.4. Finite difference analogues are needed for the time-dependent field equations, Eqs. 3.4.22 and 23 (which are special forms of the former equations) and for the boundary conditions involving spatial derivatives, namely Eqs. 3.4.5, 10, 11 and 12. The algebraic expressions for constitutive relations are evaluated as part of the solution process presented in Section 6.6, and do not affect the transformation from differential to finite-difference equations presented here.

Summarizing from Section 3.4, the equations to be converted to finite-difference form are:

for the fuel pellet (Eqs. 3.4.2, 5 and 11)

$$(\rho c)_f \frac{\partial t_f}{\partial \tau} = \frac{1}{r}\frac{\partial}{\partial r}\left(r k_f \frac{\partial t_f}{\partial r}\right) + q_f''' \quad ,0 \le r < R_f \ , \ \tau > o \tag{6.3.1}$$

$$\frac{\partial t_f}{\partial r} = 0 \quad ,r = 0, \text{ all } \tau \tag{6.3.2}$$

$$k_f \frac{\partial t_f}{\partial r} = \frac{k_{gp}}{\delta}\left[t_c(R_{ci}) - t_f(R_f)\right] ,r = R_f, \text{ all } \tau, \tag{6.3.3}$$

and for the fuel cladding (Eqs. 3.4.4, 12 and 10)

$$(\rho c)_c \frac{\partial t_c}{\partial \tau} = \frac{\partial}{\partial r}\left(k_c \frac{\partial t_c}{\partial r}\right) \qquad ,R_{ci} < r < R_{co},\ \tau > 0 \tag{6.3.4}$$

$$k_c \frac{\partial t_c}{\partial r} = \frac{k_{gp}}{\delta}\left[t_c(R_{ci}) - t_f(R_f)\right],\ r = R_{ci},\ \text{all } \tau \tag{6.3.5}$$

$$-k_c \frac{\partial t_c}{\partial r} = \bar{h}_c \left[t_c(R_{co}) - t_{fl}\right] \quad ,\ r = R_{co},\ \text{all } \tau \tag{6.3.6}$$

Equations 6.3.1 through 6 describe transient conduction. Steady-state conditions are computed by setting equal to zero the left-hand sides of Eqs. 6.3.1 and 6.3.4.

6.3.2 Nodalization Scheme for Conduction

The nodalization scheme for the fuel pin is shown in Figure 6.2. The fuel pellet is subdivided into M_f concentric zones with equal cross-sectional areas. Let i be the zone index and r_i the inner radius of Zone (i) in the fuel pellet. Then

$$r_i = R_f \sqrt{\frac{i-1}{M_f}}, \quad i = 1, \ldots, M. \tag{6.3.7}$$

The fuel cladding is subdivided into N_{cl} concentric zones with equal thicknesses Δr_c. Therefore

$$\Delta r_c = (R_{co} - R_{ci})/N_c = s_c/N_{cl} \ . \tag{6.3.8}$$

and

$$r_j = R_{ci} + j\Delta r_c,\ j = 0, 1, \ldots, N_{cl} \tag{6.3.9}$$

are the radii of zone boundaries in the fuel cladding.

The numbers M_f and N_{cl} are specified by the code user*. They are restricted to the ranges $2 < M_f < 4$ and $2 < N_{cl} < 3$.

*MM and MC on input data card No. 380 000.

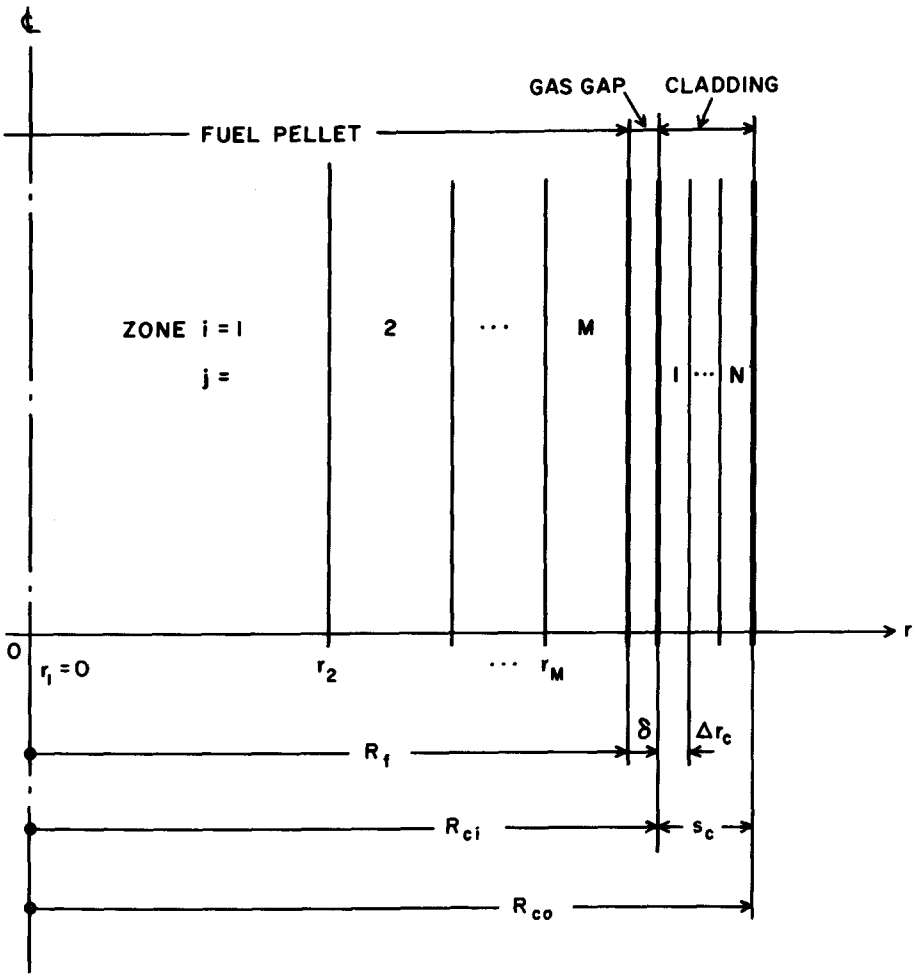

Figure 6.2 Nodalization for Fuel Pins

The nodalization scheme for the fuel pellet domain is used to discretize Eqs. 6.3.1 through 3, while Eqs. 6.3.4 through 6 are discretized over the fuel cladding domain.

6.3.3 The Finite Difference Equations for Thermal Conduction

The transformation from Eqs. 6.3.1 and 4 to their finite difference forms is carried out for RAMONA-3B in two steps. First, these equations are

averaged over the cross-sectional areas between radii r_i and r_{i+1}, i=1,...,M_f for the fuel pellet and between $R_{ci} + j\,\Delta r_c$ and $R_{ci} + (j+1)\,\Delta r_c$, j=0,1,..., N_{cl}-1 for the fuel cladding. Temperature gradients remaining after this averaging and arising from Eqs. 6.3.2, 3, 5 and 6 are approximated to obtain ordinary differential equations with respect to time, without any spatial derivatives. Secondly, the time-derivatives in the ordinary differential equations are replaced by first-order, backward difference quotients. The result is a nonlinear system of equations in unknown temperatures t^{k+1} at time level (k+1).

6.3.3.1 Assumptions and Approximations for Finite Difference Equations of Thermal Conduction

The discretization in the RAMONA-3B code of the field equations for thermal conduction implies that:

(i) one axial fuel pin segment represents all the fuel pin segments within a control volume for neutron kinetics calculations.

(ii) for the purposes of recording computed temperatures and estimating temperature gradients, the area-averaged zone temperatures $\bar{t}_{f,i}$, i=1,..., M_f, and $\bar{t}_{c,j}$, j=1,...,N_{cl} are taken to occur at the arithmetic mean of the radii at the zone boundaries, i.e.

$$r_{i,m} = \frac{R_f}{2\sqrt{M_f}} \left(\sqrt{i-1} + \sqrt{i}\right), \; i = 1, \ldots, M_f \tag{6.3.10}$$

for the pellet and

$$r_{j,m} = R_{ci} + \frac{2j+1}{2}\,\Delta r_c \;, \; j = 0, \ldots, N_{cl}-1 \tag{6.3.11}$$

for the cladding.

(iii) the heat fluxes in radial outward direction, $q_f = -k_f \frac{\partial t_f}{\partial r}$, are approximated at zone boundaries r_i (Eq. 6.3.7) in the fuel pellet by

$$q''_{f,1} = 0 \qquad \text{(exact)} \tag{6.3.12}$$

$$q''_{f,i} \cong \frac{2\sqrt{M_f}\; k_f(t_{f,i})}{R_f} \; \frac{(\bar{t}_{i-1} - \bar{t}_i)_f}{\sqrt{i+1} - \sqrt{i-1}} \;, \; i = 2, \ldots, M_f \tag{6.3.13}$$

$$q''_f\,(R_f) \cong \frac{2k_f\left\{t_f(R_f)\right\}}{R_f} \; \frac{\bar{t}_{f,M} - \bar{t}_f\,(R_f)}{1 - \sqrt{1 - 1/M_f}} \tag{6.3.14}$$

and at zone boundaries r_j (Eq. 6.3.9) in the fuel cladding by

$$q''_{c,o} = q''_c\,(R_{ci}) \cong \frac{2k_c}{\Delta r_c}\left[t_c(R_{ci}) - \overline{t}_{c,1}\right] \tag{6.3.15}$$

$$q''_{c,j} \cong \frac{k_c}{\Delta r_c}\left[\overline{t}_{c,j+1} - \overline{t}_{c,j}\right], \quad j = 1, \ldots, N_{c1}-1 \tag{6.3.16}$$

$$q''_{c,N} = q''_c\,(R_{co}) \cong \frac{2k_c}{\Delta r_c}\left[\overline{t}_{c,N} - t_c(R_{co})\right] . \tag{6.3.17}$$

In Eqs. 6.3.13 and 14, the superscripted bar over t_f and t_c denotes zone-average temperatures in pellet and cladding, respectively

$$\overline{t}_{f,i} = \frac{2}{r_{i+1}^2 - r_1^2}\int_{r_i}^{r_{i+1}} t_f\, r dr , \quad i = 1, \ldots, M_f , \tag{6.3.18}$$

$$\overline{t}_{c,j} = \frac{1}{\Delta r_c}\int_{r_{j-1}}^{r_j} t_c dr , \quad j = 1, \ldots, N_{c1} . \tag{6.3.19}$$

Notice that $r_{M+1} = R_f$ in Eq. 6.3.18, $r_o = R_{ci}$ and $r_N = R_{co}$ in Eq. 6.3.19. The thermal conductivity $k_f\,(t_{f,i})$ in Eq. 6.3.13 is evaluated at the temperature $t_{f,i}$ of the position $r_{f,i}$ by interpolating t_f from

$$t_{f,i} = \frac{\sqrt{i+1} - \sqrt{i-1}}{\sqrt{i+1} - \sqrt{i-2}}\,\overline{t}_{f,i-1} + \frac{\sqrt{i-1} - \sqrt{i-2}}{\sqrt{i+1} - \sqrt{i-2}}\,\overline{t}_{f,i} , \quad i = 2, \ldots, M_f \tag{6.3.20}$$

The above three assumptions and approximations have the following implications:

(i) The representation of all fuel pin segments by a single fuel pin segment in a computational cell of neutron kinetics calculations is adequate and consistent with the detail of neutron kinetics parameter representations in that cell. The code user can achieve, at cost, any desired accuracy by

increasing the number of computational cells for neutron kinetics calculations.

(ii) The association of zone-averaged temperatures with zone center positions is inaccurate near the fuel pellet center, even under steady-state conditions. This is shown in Table 6.1 for $M_f = 4$ (the highest accuracy currently attainable in RAMONA-3B). The error is less near the pellet periphery where the zone boundaries are more evenly spaced than near the center. The error affects the interpretation of computed temperatures and their locations in the pellet and it affects the computation of temperature-dependent properties.

Table 6.1 Errors in Magnitude and Location of Fuel Pellet Temperatures t_f, Due to Assumption (ii)

Pellet Zone Index	1	2	3	4
Position of $\bar{t}_{f,i}$	0.354 R_f	0.612 R_f	0.791 R_f	0.935 R_f
Zone Center $r_{i,m}$	0.250 R_f	0.604 R_f	0.787 R_f	0.933 R_f
Rel. Position Error*	-21%	-4%	-3%	-1%
$\dfrac{\bar{t}_{f,i} - t_f(R_f)}{t_f(0) - t_f(R_f)}$	0.875	0.625	0.375	0.127
$\dfrac{t_f(r_{i,m}) - t_f(R_f)}{t_f(0) - t_f(R_f)}$	0.938	0.636	0.381	0.129
Rel. Temp. Error†	+7%	+2%	+2%	+2%

* $\left[r_{i,m} - r(\bar{t}_{f,i})\right] / \left[r_{i+1} - r_i\right]$,

† $\left[t_f(r_{i,m}) - \bar{t}_{f,i}\right] / \left[t_f(0) - t_f(R_f)\right]$.

(iii) The assumption concerning temperature gradients at zone boundaries has been justified by Scandpower on the basis of Assumption (ii) above and on the assumption that the spatial temperature derivative at the zone interface be equal to the slope of the line segment through neighboring zone mean temperatures $\bar{t}_i$, occurring at zone centers $r_{i,m}$. This approximation introduces an error of 42% at the innermost zone and 2% at the outermost zone, in the calculation of heat fluxes. Thus, the finite differences formulation introduces inaccuracies in RAMONA-3B which render predicted fuel temperature distributions questionable. Standard differencing schemes (Lahey and Moody 1977, p. 275, Dusinberre 1961, p. 64) are recommended to remove Assumptions (ii) and (iii).

6.3.3.2 Ordinary Differential Equations of Transient Conduction

With this assessment of the simplifications used in RAMONA-3B for the finite difference formulation of the conduction equations, one can carry out the first step in transforming Eqs. 6.3.1 and 4 into their finite difference forms. Multiply Eq. 6.3.1 by (rdr), integrate from r_i to r_{i+1} and obtain by virtue of the constant volumetric heat capacity $(\rho c)_f$ in the fuel pellet (Assumption (3-vii) in Section 3.3.2.1) for the principal temperatures $\bar{t}_{f,i}$, $i = 1, \ldots, M_f$ in the fuel pellet

$$(\rho c)_f \frac{d\bar{t}_{f,i}}{d\tau} = \bar{q}'''_{f,i} + \frac{2\sqrt{M_f}}{R_f}\left[\sqrt{i-1}\, q''_{f,i} - \sqrt{i}\, q''_{f,i+1}\right],$$

$$i = 1, \ldots, M_f - 1 \qquad (6.3.21)$$

and

$$(\rho c)_f \frac{d\bar{t}_{f,M}}{d\tau} = \bar{q}'''_{f,M} + \frac{2\sqrt{M_f}}{R_f}\left[\sqrt{M_f - 1}\, q_{f,M} - \sqrt{M_f}\, q''_f(R_f)\right] . \qquad (6.3.22)$$

Because of Assumption (3-v) in Section 3.3.2.1, the nodal power generation rates $\bar{q}'''_{f,i}$, $i = 1, \ldots, M_f$ in Eqs. 6.3.21 and 22 are all equal:

$$\bar{q}'''_{f,i} = \frac{2}{r_{i+1}^2 - r_1^2} \int_{t_i}^{t_{i+1}} q'''_f(r)\, r\, dr = \bar{q}'''_f , \qquad i=1,\ldots,M_f. \qquad (6.3.23)$$

The heat fluxes $q''_{f,i}$, $i = 1, \ldots, M_f$ in Eqs. 6.3.21 and 22 are already given in terms of principal fuel pellet temperatures $\bar{t}_{f,i}$, $i = 1, \ldots, M_f$ by Eqs. 6.3.12 and 13. The heat flux $q''_f(R_f)$ at the fuel pellet surface is computed from Eqs. 6.3.3, 5, 14 and 15 in terms of principal fuel pellet and fuel cladding temperatures

$$q''_f(R_f) = q''_c(R_{ci}) = \frac{\bar{t}_{f,M} - \bar{t}_{c,1}}{\frac{R_f(1 - \sqrt{1-1/M_f})}{2k_f[t_f(R_f)]} + \frac{\delta}{k_{gp}} + \frac{\Delta r_c}{2k_c}} . \qquad (6.3.24)$$

The same equations yield also the fuel pellet surface temperature $t_f(R_f)$, which is required to evaluate $k_f\{t_f(R_f)\}$, also in terms of principal temperatures, namely

$$t_f(R_f) = \frac{\dfrac{R_f(1-\sqrt{1-1/M_f})}{k_f[t_f(R_f)]}(\bar{t}_{c,1} - \bar{t}_{f,M})}{\dfrac{R_f(1-\sqrt{1-1/M_f})}{k_f[t_f(R_f)]} + \dfrac{2\delta}{k_{gp}} + \dfrac{\Delta r_c}{k_c}} + \bar{t}_{f,M} \qquad (6.3.25)$$

The gap conductance (k_{gp}/δ) of which occurs the reciprocal in Eqs. 6.3.24 and 25, is to be evaluated, according to Assumption (3-xi) in Section 3.3.2.1, with the fuel pellet mean temperature*

$$\bar{t}_f = \frac{1}{M_f} \sum_{i=1}^{M_f} \bar{t}_{f,i} \qquad (6.3.26)$$

Substitution of Eqs. 6.3.12, 13, 23 and 24 into Eqs. 6.3.21 and 22 yields these M_f explicit, first-order ordinary differential equations for the M_f principal fuel pellet temperatures $\bar{t}_{f,i}$, $i = 1, \ldots, M_f$:†

$$\frac{d\bar{t}_{f,1}}{d\tau} = \frac{4 \cdot M_f}{\sqrt{3}-1} \frac{k_f(t_{f,2})}{R_f^2(\rho c)_f}(\bar{t}_{f,2} - \bar{t}_{f,1}) + \frac{\bar{q}_f'''}{(\rho c)_f} \qquad (6.3.27)$$

$$\frac{d\bar{t}_{f,i}}{d\tau} = \frac{4 \cdot M_f}{R_f^2(\rho c)_f}\left\{k_f(t_{f,i})\frac{\bar{t}_{f,i-1} - \bar{t}_{f,i}}{\sqrt{\frac{i+1}{i-1}} - 1} - k_f(t_{f,i+1})\frac{\bar{t}_{f,i} - \bar{t}_{f,i+1}}{\sqrt{1+\frac{2}{i}} - 1}\right\}$$

$$+ \frac{\bar{q}_f'''}{(\rho c)_f}, \quad i = 2, \ldots, M_f - 1 \qquad (6.3.28)$$

$$\frac{d\bar{t}_{f,M}}{d\tau} = \frac{4 \cdot M_f}{R_f^2(\rho c)_f}\left\{k(t_{f,M})\frac{\bar{t}_{f,M-1} - \bar{t}_{f,M}}{\sqrt{\frac{M_f+1}{M_f-1}} - 1} - \frac{R_f(\bar{t}_{f,M} - \bar{t}_{c,1})}{\frac{R_f(1-\sqrt{1-1/M_f})}{k_f\{t_f(R_f)\}} + \frac{2\delta}{k_{gp}} + \frac{\Delta r_c}{k_c}}\right\}$$

$$+ \frac{\bar{q}_f'''}{(\rho c)_f} \qquad (6.3.29)$$

---

*RAMONA-3B uses instead $\bar{t}_{f,M}$, the result of integrating Eq. 6.3.33.

†These equations are derived by the author. The original RAMONA documentation presented these equations in terms of individual radii r_i instead of the position indices i.

Equations 6.3.27, 28 and 29 determine the transient temperature distribution in the fuel pellet in terms of M_f principal state variables which are the area-averaged temperatures $\bar{t}_{f,i}$ of the M_f zones. The zone interface temperatures $t_{f,i}$, $i=2,\ldots,M_f$, and $t_f(R_f)$ needed to evaluate the thermal conductivity $k_f(t_{f,i})$ and $k_f\{t_f(R_f)\}$ are defined in terms of principal state variables $\bar{t}_{f,i}$ by Eqs. 6.3.20 and 25. The gas gap conductance (k_{gp}/δ) is defined, also in terms of principal state variables, via Eqs. 3.4.19 and 6.3.26. Equation 6.3.29 couples the thermal responses of pellet and cladding and also accounts for the thermal resistance of the gas gap.

Turning to the fuel cladding, we integrate Eq. 6.3.4 from r_{j-1} to r_j, $j = 1,\ldots,N_{cl}$ and obtain N_{cl} ordinary differential equations for the area-averaged temperatures $\bar{t}_{c,i}$ of the cladding zone j

$$\bar{t}_{c,j} = \frac{1}{\Delta r_c} \int_{r_{j-1}}^{r_j} t_c(r)\, dr \quad , \qquad j = 1, \ldots, N_{cl} . \tag{6.3.30}$$

(as 6.3.19)

The differential equations are, after utilizing Eqs. 6.3.6, 15, 16, 17 and 24:

$$\frac{d\bar{t}_{c,1}}{d\tau} = \frac{k_c[\bar{t}_{c,2}-\bar{t}_{c,1}]}{(\Delta r_c)^2(\rho c)_c} - \frac{\dfrac{\bar{t}_{f,M} - \bar{t}_{c,1}}{\Delta r_c(\rho c)_c}}{\dfrac{R_f(1-\sqrt{1-1/M_f})}{2k_f\{t_f(R_f)\}} + \dfrac{\delta}{k_{gp}} + \dfrac{\Delta r_c}{2k_c}} \tag{6.3.31}$$

$$\frac{d\bar{t}_{c,j}}{d\tau} = \frac{k_c[\bar{t}_{c,j+1} - 2\bar{t}_{c,j} + \bar{t}_{c,j-1}]}{(\Delta r_c)^2(\rho c)_c} , \quad j = 2, \ldots, N_{cl}-1 \tag{6.3.32}$$

$$\frac{d\bar{t}_{c,N}}{d\tau} = \frac{\bar{t}_{c,N} - t_{f\ell}}{\Delta r_c(\rho c)_c\left[\dfrac{\Delta r_c}{2k_c} + \dfrac{1}{\bar{h}_c}\right]} - \frac{k_c[\bar{t}_{c,N} - \bar{t}_{c,N-1}]}{(\Delta r_c)^2(\rho c)_c} \tag{6.3.33}$$

Since $2 \leq N_{cl} \leq 3$ at the present time in RAMONA-3B, Eq 6.3.32 appears now only if $\bar{N}=3$, and then with $j=2$. Equation 6.3.31 couples the cladding temperature field t_c to that of the pellet, via the term $\bar{t}_{f,M}$, while the fluid temperature $t_{f\ell}$ in Eq. 6.3.33 couples the thermal response of the cladding to the coolant. The convective film coefficient $\bar{h}_c$ in Eq. 6.3.33 depends on the outer cladding surface temperature $t_c(R_{co})$ when boiling occurs. This temperature is, from Eqs. 6.3.6 and 17

$$t_c(R_{co}) = t_{f\ell} + \frac{\bar{t}_{c,N} - t_{f\ell}}{1 + \frac{h_c \Delta r_c}{2k_c}} \qquad (6.3.34)$$

The computation of the convective film coefficient is discussed in Section 4.4.2.1.

RAMONA-3B has two similar inconsistencies affecting the surface heat fluxes $q''_f(R_f)$ and $q''_c(R_{co})$ in Eqs. 6.3.14 and 17 and the thermal impedances in Eqs. 6.3.24 and 34, respectively. We present these discrepancies here to inform the code user about the actual formulations in RAMONA-3B's conduction model. The first inconsistency arises from the incorrect assertion that the rate of heat transfer, i.e., heat flux q" times area $2\pi r\Delta z$, at the pellet surface $r=R_f$, is equal to that at the location $r = R_f[3+\sqrt{1-1/M_f}]/4$, i.e., at the midpoint between the assumed location where the zone averaged temperature $\bar{t}_{f,M}$ occurs, and the outer radius of the pellet. While it is true that the heat flux represented by Eq. 6.3.14 approximates the actual heat flux better at this midpoint than at the pellet surface, it must be recognized that fuel pellet and gas gap are coupled by the surface heat flux, not by some interior heat transfer rate, and that with this assertion one ignores the storage of energy between R_f and $R_f(3+\sqrt{1-1/M_f})/4$. If one seeks a second-order approximation for $q''_f(R_f)$, one should use the derivative of a second-order polynomial through $\bar{t}_{f,M}$ $\bar{t}_{f,M-1}$ and $\bar{t}_{f,M_f-2}$ at their true locations, rather than a second-order approximation for the wrong heat flux. The same is true for the identical inconsistency regarding the outer cladding heat flux. While these formulations in RAMONA-3B produce the insignificant difference of only 3% in the surface heat flux calculation, when compared to the first-order approximation used everywhere else, the additional computational effort required by them should be avoided in future code improvements (see also Sect. 6.3.5).

This completes the first step in the process of transforming the partial differential equations, Eqs. 6.3.1 and 4, and their boundary conditions, Eqs. 6.3.2,3,5 and 6 into finite difference form. The first step produces the ordinary differential equations, Eqs. 6.3.27 through 29 and Eqs. 6.3.31 through 6.3.33. Even though RAMONA-3B employs an explicit integration scheme for the integration of the thermohydraulic equations, which could be employed directly to integrate also the above equations of thermal conduction, RAMONA-3B uses instead implicit time integration with iterations for the transient conduction equations. This affords greater computational stability than explicit integration. The second step, therefore, consists of developing the implicit finite difference equations for the ordinary differential equations, Eqs. 6.3.27 through 29 and Eqs. 6.3.31 through 33.

6.3.3.3 Finite Difference Equations for Transient and Steady Conduction

In order to present this second step conveniently, we introduce first the (M_f+N_{c1})-dimensional column vector of principal temperatures $\underset{\sim}{t}$

$$\underset{\sim}{\bar{t}} = \begin{bmatrix} \bar{t}_{f,1} \\ \bar{t}_{f,2} \\ \vdots \\ \bar{t}_{f,M} \\ \bar{t}_{c,1} \\ \vdots \\ \bar{t}_{c,N} \end{bmatrix} \tag{6.3.35}$$

and the vector function $\underset{\sim}{F}$ whose (M_f+N_{cl}) components are the right-hand sides of Eqs. 6.3.27, 28, 29, 31, 32, and 33, in that order. Next we combine these (M_f+N_{cl}) ordinary differential equations into a single vector equation

$$\frac{d\underset{\sim}{\bar{t}}}{d\tau} = \underset{\sim}{F}\left\{\bar{t},\ \bar{q}_f'''\ ,\ t_{f\ell},\ \bar{h}_c\right\} \ . \tag{6.3.36}$$

The finite difference form for Eq. 6.3.36 is obtained by replacing the time derivative at the time level k+1 by its first-order, backward time difference quotient, namely by

$$\frac{d\underset{\sim}{\bar{t}}}{d\tau}(\tau^{k+1}) \cong \frac{\underset{\sim}{\bar{t}}^{k+1} - \underset{\sim}{\bar{t}}^{k}}{\Delta\tau} \ . \tag{6.3.37}$$

Substitution of Eq. 6.3.37 into Eq. 6.3.36 yields the set of $(M+N_{cl})$ implicit finite difference equations for the temperature of fuel pellet and cladding in a computational cell of neutron kinetics nodalization:

$$\underset{\sim}{\bar{t}}^{k+1} - \underset{\sim}{\bar{t}}^{k} = \Delta\tau\ \underset{\sim}{F}\left\{\underset{\sim}{\bar{t}}^{k+1},\ (\bar{q}_f''')^{k+1},\ t_{fl}^{k+1},\ \bar{h}_c^{k+1}\right\}. \tag{6.3.38}$$

Equations 6.3.38 are nonlinear in the unknown, zone-averaged temperatures $\bar{t}^{k+1}$ because of the nonlinear dependencies of constitutive parameters k_f, (k_{gp}/δ), $\bar{h}_c$ and $\bar{q}_f'''$ on $\underset{\sim}{\bar{t}}$. These nonlinear relationships are summarized in Section 6.3.4 below.

Equations 6.3.38 are solved iteratively, in step with the iterations for the solution of neutron kinetics equations, but in two separate iterations, one for the fuel pellet and the other for the cladding. This iteration scheme, along with the methods of coupling Eqs. 6.3.38 with the neutron kinetics calculations via fuel temperatures $\underset{\sim}{\bar{t}}_f$ and heat generation rate $\bar{q}_f'''$ and with the thermohydraulics via coolant temperature $t_{f\ell}$ and convective heat transfer coefficient $\bar{h}_c$, are described in Section 6.7. This section

presents also the simplifications imposed on Eqs. 6.3.38 for their iterative solution.

6.3.4 Problem Closure for Conduction

Equation 6.3.38 contain constitutive parameters for thermal conductivities, volumetric heat capacities, gas gap conductance and convective heat transfer coefficient. These parameters depend on the principal state variables, namely the zone-averaged temperatures $\underset{\sim}{\bar{t}}$.

The thermal conductivity $k_f(t_f)$ of the fuel is computed in accordance with Eqs. 3.4.15 through 17 in Section 3.4.1.3, using the temperatures $t_{f,i}$ defined by Eq. 6.3.20.

The thermal conductivity k_c of the cladding is fixed by user input in accordance with Eq. 3.4.18 in Section 3.4.1.3, but should be a function of cladding temperature.

The volumetric heat capacities $(\rho c)_f$ and $(\rho c)_c$ of fuel pellet and cladding, respectively, are fixed also by user input in accordance with Eqs. 3.4.13 and 14. These parameters should be computed as functions of temperatures.

The gas gap conductance (k_{gp}/δ) should be computed, according to Eq. 3.4.19, with the mean fuel temperature (to account for all the thermal expansion in the fuel) defined by Eq. 6.3.26, but is computed with $\bar{t}_{f,M}$, the zone-averaged temperature of the outermost fuel pellet zone.

The calculation of the convective film coefficient is given in Section 4.4.2.1.

Problem closure requires also the specification of the nuclear power generation rate $\bar{q}'''_f$. Its computation is presented in Section 2.7.3 (see Eq. 2,7.16) as part of neutron kinetics calculations. The timing for calculating $(q'''_f)^{k+1}$ relative to calculating fuel temperatures $\underset{\sim}{\bar{t}}^{k+1}$ and the associated Doppler feedback is presented in Section 6.7.

Finally, the formulation of transient conduction problems requires the specification of initial conditions. Steady-state initial conditions must be computed from Eqs. 3.4.22 and 23 in Section 3.4.2. Their finite difference form is

$$F^o[\underset{\sim}{\bar{t}}^o, (\bar{q}_f)^o, t^o_{f\ell}, \bar{h}^o_c] = 0, \tau = 0 \qquad (6.3.39)$$

where the components of $\underset{\sim}{F}^o$ are the same as for $\underset{\sim}{F}$ in Eq. 6.3.36, but the first M_f components multiplied by $(\rho c)_f$ and the remaining components multiplied by $(\rho c)_c$. The iteration scheme for solving Eqs. 6.3.39 is explained in Section 6.6.

6.3.5 Recommendations for Improvements

The discretization errors shown in Table 3.1 and the error of estimating interior heat fluxes in the fuel pellet should be reduced by using standard differencing schemes (Lahey and Moody 1977, p. 275 or Dusinberre 1961, p. 64).

A discrete model as now employed in RAMONA-3B is efficient only for fast thermal responses in the fuel with characteristic response times less than 0.5 seconds. For most operational transients, a lumped-parameter model with a single ordinary differential equation for fuel pellet and cladding is more efficient and at least as accurate as the currently used discrete-parameter model (see Wulff 1981). We recommend to provide an option for a lumped-parameter conduction model as part of future code improvements.

It is strongly recommended to compute transient conduction in step with the thermohydraulics calculations, rather than in step with the neutron kinetics calculations, because the physical coupling is tighter between conduction and hydraulics (changes in heat transfer regimes) than between conduction and neutron kinetics. The thermal inertia of the fuel pellet retards its response to fission power changes, while the cladding responds quickly to changes in heat transfer (CHF).

It is also recommended to solve Eqs. 6.3.38 and 39 together as one system of nonlinear equations, instead of in two parts, using two nested iterations. This would save computing time and it would produce simpler, more transparent programming than is currently implemented in RAMONA-3B.

Finally, we recommend that the conduction model be validated by comparison with exact analytical solutions.

6.4 Numerical Quadratures and Ordinary Differential Equations for Coolant Thermohydraulics

The thermohydraulic transients of the reactor coolant are computed in RAMONA-3B by integrating numerically a set of ordinary differential equations of the form

$$\frac{d\underset{\sim}{y}}{d\tau} = \underset{\sim}{F}(\underset{\sim}{y},\tau) \quad , \tag{6.4.1}$$

subject to the steady-state initial conditions

$$\underset{\sim}{F}(\underset{\sim}{y}_0,0) = 0 \quad . \tag{6.4.2}$$

In Eq. 6.4.1 $\underset{\sim}{y}$ is the state-variable vector, whose components are the system-averaged pressure $\langle p \rangle_{syst}$ (Eq. 4.4.87), the closed-contour momenta Γ_j (Eq. 4.4.99), $j=1,\ldots,N_c$, one of which is associated with each one of N_c core flow channels, further the mass flow rate through the recirculation loop, W_{RCL} (Eq. 4.4.132), the angular velocity ω_{RCP} of the recirculation pump, the

vapor mass $(M_g)_{syst}$ in the entire system (Eq. 4.4.169), the internal energy $(\overline{uM})_{syst}$ in the entire system (Eq. 4.4.169), the vapor mass $(M_g)_{LVD}$ in the low-void regime of the vapor dome (Eq. 4.4.173) and, finally the vapor mass $(m_g)_k$ and the internal energy $(\overline{um})_k$, $k=1,\ldots,N_{CEL}$, in each one of N_{CEL} computational cells (see Eqs. 6.4 and below). The vector $\underset{\sim}{y}_o$ in Eq. 6.4.2 is the initial steady-state vector $\underset{\sim}{y}(o)$ at time zero. The vector function $\underset{\sim}{F}$ has the same dimension as the vectors $\underset{\sim}{y}$ and $\underset{\sim}{y}_o$. It can be seen from the inspection of the equations referenced above, that this vector function $\underset{\sim}{F}$ is not specified explicitly in terms of only principal state variables $\underset{\sim}{y}$ but also in terms of secondary variables $\underset{\sim}{x}$, which are specified by a set of equations $\underset{\sim}{G}$, that is:

$$\underset{\sim}{F}(\underset{\sim}{y},\tau) = \underset{\sim}{F}\left\{\underset{\sim}{y},\underset{\sim}{x}(\underset{\sim}{y}),\tau\right\} \tag{6.4.3}$$

$$0 = \underset{\sim}{G}(\underset{\sim}{y},\underset{\sim}{x},\tau) \tag{6.4.4}$$

The secondary variables are thermophysical properties of the coolant, other than those which are principal variables, transport properties, heat transfer coefficients, friction factors, vapor generation rate, slip ratio, local velocities and boundary conditions, as discussed in Chapter 4.

We have not included the state variables of the steam line dynamics

$$\left.\begin{aligned}\left(\frac{d\underset{\sim}{y}}{d\tau}\right)_{SL} &= \underset{\sim}{F}_{SL}\left\{\underset{\sim}{y}_{SL},\ \tau,\ \langle p\rangle_{syst}\right\}\\ 0 &= \underset{\sim}{F}_{SL}\left\{\underset{\sim}{y}_{SL,o},\ 0,\ \langle p\rangle^{o}_{syst}\right\}\end{aligned}\right\} \tag{6.4.5}$$

and of boron concentration

$$\left.\begin{aligned}\frac{d\underset{\sim}{c}_B}{d\tau} &= \underset{\sim}{F}_B\ (\underset{\sim}{c}_B,\ \tau)\\ \underset{\sim}{c}_B &= 0 \qquad \text{for } \tau \leq \tau_{B,injection}\end{aligned}\right\} \tag{6.4.6}$$

even though their equations have the same form as Eqs. 6.4.1 and 2. The same could be said in principle for the control equations. We have separated the steam line dynamics simulation and the boron transport simulation from Eqs. 6.4.1 and 2 because Eqs. 6.4.5 and 6 are integrated separately. We have excluded the simulation of controls since their numerical representation has been presented for convenience already in Chapter 5.

With this brief overview it can be established that there are two principal tasks of numerical analysis arising in RAMONA-3B from the thermohydraulics simulation: the task of solving nonlinear equations and the tasks of integrating explicit first-order ordinary differential equations. The first task arises in the search for initial conditions (Eqs. 6.4.2). Both the first and second tasks arise in computing the transient (cf. Eq. 6.4.4 for the first task,

Eq. 6.4.1 for the second task). A third, but minor, procedure is involved in the task of solving nonlinear equations, that is the numerical quadratures of the integrals over space appearing in several of the equations presented in Chapter 4.

In this section, Section 6.4, we recollect first the governing equations of thermohydraulics in pressure vessel and recirculation loop, introduce the nodalization scheme of RAMONA-3B as it is applied to the solution of the only two partial differential equations remaining in the vessel coolant dynamics model, Eqs. 4.4.1 and 4, which are to be converted to ordinary differential equations, and then we proceed with this conversion. Following that, we repeat the same three steps, first for the two partial differential equations of the steam line dynamics model, Eqs. 4.4.185 and 186, and then for the partial differential equation of boron transport, Eq. 4.4.195.

6.4.1 Coolant Dynamics in Reactor Vessel and Recirculation Loop

This section serves to present the detailed definitions of the vector function F in Eq. 6.4.1 and those parts of the vector function G in Eq. 6.4.4 which are related to the conservation equations for the coolant dynamics in the vessel and recirculation loop. These equations are integrated and solved, respectively, under one separate time step control.

6.4.1.1 Governing Equations

For the reader's convenience, we present below a summary of the governing equations for the principal state variables of the thermohydraulics models in RAMONA-3B. These equations have been established in Chapter 4, and they are* for the coolant in the vessel:

two partial differential equations of vapor mass† and mixture mass conservation (cf. Eqs. 4.4.1 and 4)

$$\partial(\alpha\rho_g)/\partial\tau + \nabla\cdot(\rho_g \vec{i}_g) = \Gamma_v \tag{6.4.7}$$

$$\partial[\alpha\rho_g u_g + (1-\alpha)\rho_\ell u_\ell]/\partial\tau + \partial[\rho_g h_g j_g + \rho_\ell h_\ell j_\ell]/\partial z = \frac{q'_\omega}{A} + (1-\alpha)q'''_\ell , \tag{6.4.8}$$

six ordinary differential equations, one for the volume-averaged pressure $\langle p\rangle_{syst}$ (Eq. 4.4.94)

*The notation is here the same as in Chapter 4.
†See comment in second paragraph after Eq. 6.4.27 below.

$$\frac{d\langle p\rangle_{syst}}{d\tau} = \frac{(Aj_\ell)_{FW} + (Aj_\ell)_{ECC} - (Aj_g)_{SL} + \int_{V_2} \frac{\rho_\ell - \rho_g}{\rho_\ell \rho_g} \Gamma_v \, dV}{\int_{V_1+V_2} \left[\alpha \frac{\rho'_g}{\rho_g} + (1-\alpha) \frac{\rho'_f}{\rho_f} \right] dV} , \qquad (6.4.9)$$

one for the total vapor mass $(M_G)_{syst}$ in the system (reactor vessel) (Eq. 4.4.168)

$$\frac{d(M_g)_{syst}}{d\tau} = \int_{V_1+V_2} \Gamma_v \, dV - W_{SL}, \qquad (6.4.10)$$

one for the total internal energy $(\overline{uM})_{syst}$ in the system (reactor vessel) (Eq. 4.4.169)

$$\frac{d(\overline{uM})_{syst}}{d\tau} = (hW)_{FW} + (hW)_{ECC} - h_g W_{SL} + \int_{A_h} q''_w \, dA + \int_{V_1+V_2} (1-\alpha) q'''_\ell \, dV, \qquad (6.4.11)$$

one for the vapor mass $(M_g)_{LVD}$ in the low-void regime, below the mixture level, in the steam dome (Eqs. 4.4.173 and 175)

$$\frac{d(M_g)_{LVD}}{d\tau} = \rho_g \left\{ (Aj_g)_{CU} - (Aj_g)_{DCI} - (A\alpha W^o)_{LVD} \right\} + (V\langle \Gamma_v \rangle)_{LVD} , \qquad (6.4.12)$$

further, one equation for the mass flow rate W_{RCL} in the recirculation loop (Eq. 4.4.132)

$$\frac{dW_{RCL}}{d\tau} = \frac{1}{\sum_{i=1}^{3} \frac{L_i}{A_i}} \left\{ \Delta p_{RCP} - W_{RCL}^2 \left(Z_{RCL} + Z_{DC} + Z_{NZZ} - \frac{1}{2\rho_\ell A_{NZZ}^2} \right) \right.$$

$$\left. + \left[\frac{\rho_\ell (Aj_\ell)_{JT}}{N_{RCL}} - W_{RCL} \right]^2 \left(Z_{SCT} - \frac{1}{2\rho_\ell A_{SCT}^2} \right) \right\}, \qquad (6.4.13)$$

one equation for the angular velocity ω_{RCP} of the recirculation pump (Eq. 4.4)

$$\frac{d\omega}{d\tau} = \frac{1}{I_{PM}} (T_{EL} - T_{RCP}), \qquad (6.4.14)$$

and, finally the set of N_C ordinary differential equations for the closed-contour momenta $\mathcal{M}_j$, $j=1,\ldots,N_C$ (Eq. 4.4.104), one for each of the N_C core flow channels,

$$\frac{d\mathcal{M}_j}{d\tau} = \Delta p_{JT} - \sum_{i=1}^{N_S} \left\{ g_z \langle \rho_m \rangle L + \frac{1}{2d_h} \int_o^L \frac{f_\ell \phi_\ell^2}{\rho_\ell} G_m |G_m| dz \right\}_{ij} + \sum_{\substack{i=1 \\ i \neq JT}}^{N_S} \left\{ \left[|W_g| G_g + |w_\ell| G_\ell \right], \right.$$

$$\left. \left[1 + \frac{1}{2} \left\{ - \zeta \left(\frac{A_1}{A_{mm}} \right)^2 \right\} \right] - \left[|W_g| G_g + |W_\ell| G_\ell \right] \right\}_{ij} \quad j = 1, \ldots, N_c. \qquad (6.4.15)$$

The above two partial and $(N_C + 6)$ ordinary differential equations are supplemented by the mixture mass balance which is used to compute first the volumetric flow rate $(Aj_m)_o$ at the downcomer entrance (Eq. 4.4.123)

$$(Aj_m)_o = \left\{ \sum_{j=1}^{N_c} \frac{\mathcal{M}_j - \oint_{C_j} \psi_j \, dz - \int_{z_{CI}}^{z_{CE}} (\chi\phi)_j \, dz}{\int_{z_{CI}}^{z_{CE}} \chi_j dz} - \right.$$

$$\left. \frac{\left\{ \int_o^{z_{CI}} (\chi\phi_I) dz + \int_{z_{CE}}^{z_{RSE}} (\chi\phi_{II}) dz + \left[\phi_I(z_{CI}) + \sum_{j=1}^{N_c} \phi_j(z_{CE}) \right] \int_{z_{CE}}^{z_{RSE}} \chi dz \right\} \sum_{j=1}^{N_c} \left(\int_{z_{CI}}^{z_{CE}} \chi dz \right)^{-1}}{1 + \left[\int_o^{z_{CI}} \chi dz + \int_{z_{CE}}^{z_{RSE}} \chi dz \right] \sum_{j=1}^{N_c} \left(\int_{z_{CI}}^{z_{CE}} \chi dz \right)^{-1}} \right\}$$

(6.4.16)

then the volumetric flow rate $(Aj_m)_{CI,j}$ at the entrance of the j-th core flow channel (Eq. 4.4.121)

$$(Aj_m)_{CI,j} = \left\{ \mathcal{M}_j - \oint_{C_j} \psi_j dz - \int_{z_{CI}}^{z_{CE}} \chi\phi_j dz - (Aj_m)_o \left[\int_o^{z_{CI}} \chi dz + \int_{z_{CE}}^{z_{RSE}} \chi dz \right] \right.$$

$$\left. - \left[\int_o^{z_{CI}} \chi\phi_I dz + \int_{z_{CE}}^{z_{RSE}} \chi\phi_{II} dz + \left\{ \phi_I(z_{CE}) + \sum_{j=1}^{N_c} \phi_j(z_{CE}) \right\} \int_{z_{CE}}^{z_{RSE}} \chi dz \right] \right\}$$

$$\Big/ \int_{z_{CI}}^{z_{CE}} \chi_j dz, \qquad (6.4.17)$$

and finally the volumetric flow rates anywhere in the vessel (Eqs. 4.114, 116 and 118):

$$A(z) \cdot j_m(z) = (Aj_m)_o + \phi_I(z) \, , \quad 0 = z < z_{CI} \qquad (6.4.18)$$

$$A_j \cdot j_{m,j}(z) = (Aj_m)_{CI,j} + \phi_j(z) \, , \quad z_{CI} < z < z_{CE} \qquad (6.4.19)$$

$$A(z) \cdot j_m(z) = \sum_{j=1}^{N_c} \left[(Aj_m)_{CI,j} + \phi_j(z_{CE}) \right] + \phi_{II}(z),$$

$$z_{CE} < z < z_{RSE} \, . \qquad (6.4.20)$$

The functions X,ψ and ϕ in Eqs. 6.4.16 through 20 are defined in Chapter 4 by Eqs. 4.4.108, 109 and 126, respectively. The volumetric flow rates Aj_m as computed from Eqs. 6.4.18 through 20 serve to compute all the phasic velocities (cf. Eqs. 4.4.105 and 106) and the mixture and phasic mass fluxes (cf. Eqs. 4.4.107, 110 and 111).

Equations 6.4.7 through 17 constitute the conservation equations of the coolant thermohydraulics model in RAMONA-3B for the coolant in the pressure vessel and in the recirculation loops. These equations are supplemented by the constitutive equations presented in Section 4.4.2 and by the algebraic equations of component modeling which are presented in Sections 4.4.4.3, 4.4.4.4, and 4.4.5. The constitutive equations, the component modeling equations and the algebraic equations from the mixture mass conservation equation, Eqs. 6.4.16 through 20, form the vector function $\underset{\sim}{G}$ in Eq. 6.4.4. On the other hand, Eqs. 6.4.9 through 15 are already in the form of Eq. 6.4.1. We transform in the next two sections Eqs. 6.4.7 and 8 also to the form of Eq. 6.4.1.

6.4.1.2 Nodalization Scheme for Coolant Dynamics in Reactor Vessel

The reactor vessel of the BWR power plant is subdivided into computational cells or control volumes with fixed boundaries as shown in Fig. 6.3. The nodalization scheme is applied only to Eqs. 6.4.7 and 8, the only partial differential equations of thermohydraulic modeling for coolant dynamics in the vessel.

The numbers of computational cells are chosen by the user* for each major component. With $(n_{CI}-1)$ cells in steam dome (Index 1), Upper Downcomer, Lower Downcomer and lower plenum, $(n_{CE} - n_{CI})$ cells in each of N_C parallel core channels and $(n_{RSE}-n_{CE}+1)$ cells above the core in upper plenum, riser and separators, the total number of computational cells in the vessel is

$$N_{CEL} = (n_{CE} - b_{CI})N_C + n_{CI} + n_{RSE} - n_{CE}, \qquad (6.4.21)$$

where n_{CI}, n_{CE} and n_{RSE} are the cardinal indices of the cells at core entrance, core exit and riser exit, respectively, as shown in Fig. 6.3.

The index k in Fig. 6.3 labels computational cells outside the core. The double index kj indicates the k-th axial core node in the j-th core flow channel.

The discretization in space of the partial differential equations of vapor mass and mixture energy, Eqs. 6.4.7 and 8, implies the assumption that volume-averaged fluid properties in a computational cell be equal to the area-averaged fluid properties at the downstream cell boundary. Therefore, we use the index k to denote not only the cell but also its downstream boundary.

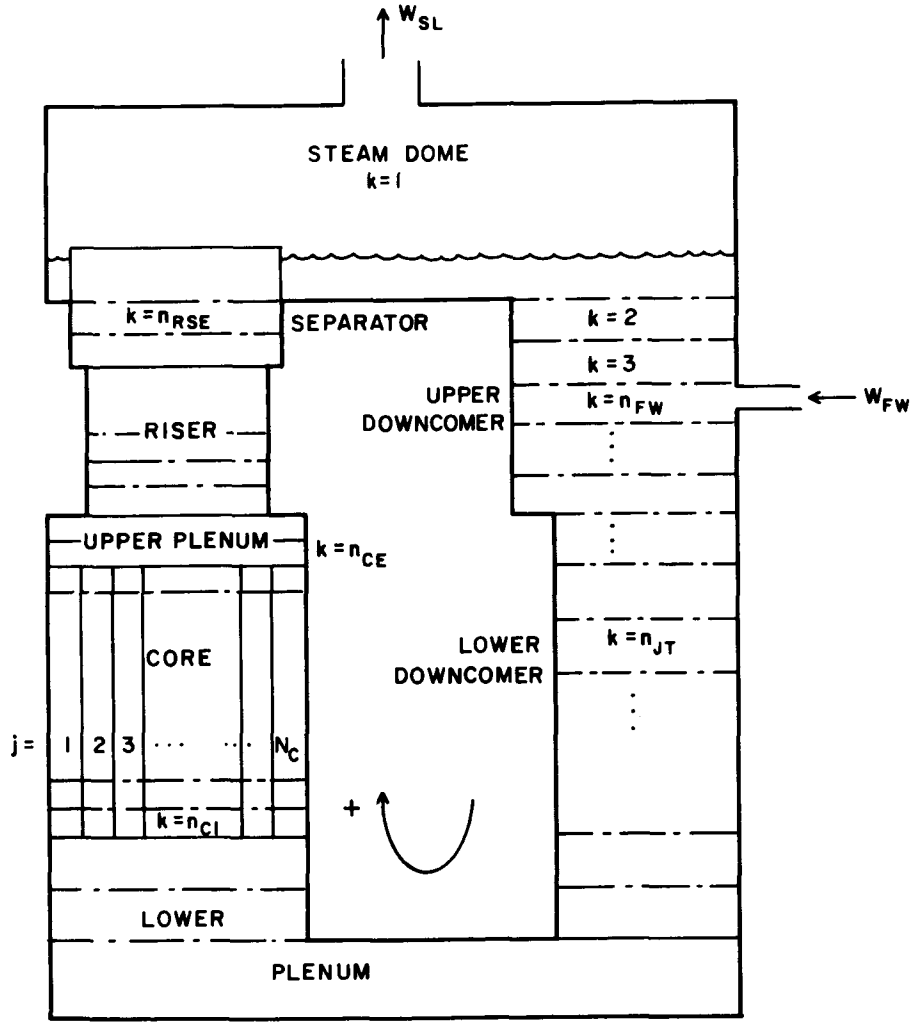

Figure 6.3 Nodalization Scheme for Coolant Dynamics, Eqs. 6.4.7 and 8.

6.4.1.3 Space Discretization for Vapor Mass and Mixture Energy Conservation Equations

By integrating first Eq. 6.4.7 over the computational cell with index k and fixed volume Δ

$$\int_{\Delta V_k} \frac{\partial(\alpha\rho_g)}{\partial\tau}\, dV + \int_{\Delta V_k} \nabla\cdot(\rho_g \vec{j}_g)\, dV = \int_{\Delta V_k} \Gamma_v\, dV,\ k = 2,\ldots,\ N_{CEL}$$

then interchanging the order of integration and time differentiation and finally, by using the divergence theorem, one obtains

*With some restrictions as explained in the Users Manual.

$$\frac{d}{d\tau}\int_{\Delta V_k}(\alpha\rho_g)dV + (A\rho_g j_g)_k - (A\rho_g j_g)_{k-1} = \int_{\Delta V_k}\Gamma_v dV.$$

$$k = 2,\ldots,N_{CEL} \qquad (6.4.22)$$

The vapor density is uniform throughout the system [cf. Assumptions (4-ii and iii)]. Call

$$(m_g)_k = \int_{\Delta V_k}\alpha\rho_g dV = \rho_g \langle\alpha\rangle_k \Delta V_k\ ,\quad k = 2,\ldots,\ N_{CEL} \qquad (6.4.23)$$

$$(W_g)_k = (A\rho_g j_g)_k = (A\rho_g w_g \alpha)_k\ ,\quad k = 2,\ldots,\ N_{CELL} \qquad (6.4.24)$$

and rewrite Eq. 6.4.22 to read

$$\frac{d(m_g)_k}{d\tau} = \langle\Gamma_v\rangle_k \Delta V + (W_g)_{k-1} - (W_g)_k\ ,$$

$$k = 2,\ldots,\ N_{CEL}. \qquad (6.4.25)$$

The vapor mass in a computational cell, other than the steam dome (k=1), is a principal state variable. Equations 6.4.25 are part of the system of Eqs. 6.4.1.

The steam dome (k=1) is omitted from Eqs. 6.4.25 since the vapor mass of the steam is computed indirectly from Eq. 6.4.10 as explained in Section 4.4.5.4 (cf. Eq. 4.4.170).

Finally, it should be pointed out that in RAMONA-3B the vapor void fraction α_k at k-th interface between computational cells is computed with the approximation

$$\langle\alpha\rangle_k \cong \alpha_k \qquad (6.4.26)$$

from

$$\alpha_k = \frac{(m_g)_k}{\rho_g(<p>_{syst})\Delta V_k} \quad , \tag{6.4.27}$$

where $(m_g)k$ and $<p>_{syst}$ are principal state variables.

The vapor generation rate $<\Gamma_v>$ in Eq. 6.4.25 is computed from Eq. 4.4.51 in Chapter 4. The vapor mas flow rate $W_g = AG_g$ is computed from the known cross-section A and the vapor mass flux G_g according to Eq. 4.4.111 and Eq. 4.4.106 for the vapor velocity. This calculation involves Eqs. 6.4.16 through 20 for the calculation of the mixture volumetric flux j_m.

It should be pointed out to the reader who may wish to consult the original RAMONA documentation (Scandpower 1977), that even though this reference claims that RAMONA-3B integrates the mixture mass balance for each computational cell (cf. Eq. 3.133 on p. 29 of Section C-103, Scandpower 1977) instead of the vapor mass balance, in fact RAMONA-3B contains Eq. 6.4.25 above in SUBROUTINE HYDRO2 on FORTRAN listing Line HRAM3-606. There is no mixture mass balance of the documented from integrated in RAMONA-3B. The mixture mass balance is already contained in Eq. 4.4.9, as evaluated in Eqs. 6.4.16 through 20.

Turning next to the second partial differential equation, Eq. 6.4.8 for the mixture energy conservation, we introduce first, as for Eq. 4.4.80,

$$u_m\rho_m \equiv (1-\alpha)\rho_\ell u_\ell + \alpha\rho_g u_g \tag{6.4.28}$$

into Eq. 6.4.8 and integrate it over the cell volume $V_k = A_k \Delta z_k$

$$\int_{\Delta V_k} \frac{\partial(u_m\rho_m)}{\partial\tau}\, dV + (h_g W_g + h_\ell W_\ell)_k - (h_g W_g + h_\ell W_\ell)_{k-1}$$

$$= <q'_w>_k \Delta z_k + <A(1-\alpha)q'''_\ell>_k \Delta z_k \quad ,$$

$$k = 2,\ldots, N_{CEL} \quad . \tag{6.4.29}$$

The integral

$$\int_{\Delta V_k} \rho_m u_m dV = \langle \rho_m u_m \rangle_k \, \Delta V_k = \langle u_m m_m \rangle_k \tag{6.4.30}$$

is a principal state variable in RAMONA-3B and computed from Eq. 6.4.29 as follows:

$$\frac{d\langle u_m m_m \rangle_k}{d\tau} = (h_g W_g + h_\ell W_\ell)_{k-1} - (h_g W_g + h_\ell W_\ell)_k$$

$$+ \left[\langle q'_w \rangle_k + \langle A(1-\alpha) q'''_\ell \rangle_k \right] \Delta z_k$$

$$k = 2, \ldots, N_{CEL} \, .^* \tag{6.4.31}$$

The mass flows W_ℓ and W_g are computed from the mass fluxes G_ℓ and G_g, respectively (cf. Eqs. 4.4.110 and 111) and from the known cross-sectional area A by using $W = AG$. The vapor enthalpy $h_g = u_g + \langle p \rangle_{syst}/\rho_g$ is computed from the known system pressure $\langle p \rangle_{syst}$ and from Eqs. 4.4.75 and 71. The liquid enthalpy $h = u_\ell + \langle p \rangle_{syst}/\rho_\ell$ is computed from Eqs. 4.4.77 and 72 via the liquid temperature t_ℓ from Eq. 4.4.80. Equation 4.4.80 contains the product (cf. Eq. 6.4.30).

$$(\rho_m u_m)_k \approx \langle \rho_m u_m \rangle_k = \frac{\langle u_m m_m \rangle_k}{\Delta V_k} \, ,$$

$$k = 2, \ldots N_{CEL} \tag{6.4.32}$$

which is evaluated with the assumption that cell-averages are equal to downstream cell boundary values. The linear wall heating rate $\langle q'_w \rangle_k$ is computed from Eq. 4.4.5, using cladding wall, coolant and bypass coolant temperatures and heat transfer coefficients $\bar{h}_c$ as discussed in Section

*For $k=n_{FW}$ see Eq. 6.4.33 below.

4.4.2.1.1. The rate of direct gamma heat absorption $\langle AK(1-\alpha)q_{\ell}'''\rangle_k \Delta z_k$ is defined by Eq. 2.7.17 for heated core channels and by Eq. 2.7.18 for the bypass channel.

The system of Eqs. 6.4.3 is also part of Eq. 6.4.1. The vapor dome is not represented because Eq. 6.4.11 is used to compute indirectly the energy content in the dome (see Section 4.4.5.4, Eq. 4.4.171). Moreover, for the computational cell with index $k = n_{FW}$, one must account for the energy addition from feedwater by adding the term

$$(W_{FW}\, h_{FW}) = (Wh)_{FW} \tag{6.4.33}$$

to the right-hand side of Eq. 6.4.31.

Equations 6.4.25 and 31 imply upwind-differencing and are stable only for flows in normal direction, $G_g < 0$ and $G > 0$. Even though RAMONA-3B is restricted to normal flow directions by virtue of Assumptions (4-xi, xii and xvii) and because of an error in the momentum flux formulation (see Item b above Eq. 4.4.104), RAMONA-3B has an index switching logic to account for flow reversal. The logic is equivalent to replacing the right-hand side of Eq. 6.4.25 by

$$\langle \Gamma_v \rangle_k \Delta V + \frac{1}{2}\left[(W_g)_{k-1}\left(\frac{W_g}{|W_g|}+1\right)_k - (W_g)_{k+1}\left(\frac{W_g}{|W_g|}-1\right)\right] - (W_g)_k \tag{6.4.34}$$

and the first term on the right-hand side of Eq. 6.4.31 by

$$\frac{1}{2}\left[(W_g h_g)_{k-1}\left(\frac{W_g}{|W_g|}+1\right)_k - (W_g h_g)_{k+1}\left(\frac{W_g}{|W_g|}-1\right)_k + (W_\ell h_\ell)_{k-1}\left(\frac{W_\ell}{|W_\ell|}+1\right)_k - (W_\ell h_\ell)_{k-1}\left(\frac{W_\ell}{|W_\ell|}-1\right)_k\right]. \tag{6.4.35}$$

In addition, $(W_g)_k$ and $(W_\ell)_k$ themselves are recomputed when the velocity $(w_\ell)_k$ of the <u>liquid</u> is found to be negative according to Eq. 4.4.105. If

$(w_\ell)_k$ is negative when computed first with α_k then both $(w_\ell)_k$ and $(w_g)_k$ are recomputed by Eqs. 4.4.105 and 106, using α_{k+1}. The switching coefficients $(W_i/|W_i|+1)$, i=g,ℓ, are also recomputed. The switch from α_k to α_{k+1} is justified by the claim that the void fraction is convected in the direction of the flow.

This claim is not correct. The vapor void fraction disturbances are convected with the vapor void propagation-velocity which differs from the velocity w_ℓ of the liquid and the velocity w_g of the vapor, but which is closer to w_g than to w_ℓ, the velocity used in RAMONA-3B as the switching criterion. Therefore, since computational stability is guaranteed already with Expressions 6.4.34 and 35, since no accuracy improvement is achieved by the switch from α_k to α_{k+1} and since this switch violates the requirement of Lipschitz continuity for integration, it is recommended that this switch be eliminated from the RAMONA-3B code for future improvements and for its extension to simulating flow reversal.

6.4.1.4 Numerical Quadratures

Equations 6.4.9, 10, 11 and 15 through 20 contain integrals over coolant volume and along the coolant stream lines. Their evaluations by numerical integration are carried out in RAMONA-3B with the assumption that the mean value of the integrand in a computational cell (Figure 6.3) is equal to the value of the integrand at the downstream cell interface

$$\int_{z_{k-1}}^{z_k} f\,A\,dz = \langle fA\rangle_k\,\Delta z_k \approx f_k\,\langle A\rangle_k\,\Delta z_k = f_k\,\Delta V_k\,. \qquad (6.4.36)$$

In Eq. 6.4.9, the integral in the numerator is approximated by

$$\int_{V_2} \frac{\rho_\ell - \rho_\ell}{\rho_\ell\,\rho_g}\,\Gamma_v\,dV \approx \sum_{k=1}^{n_{RSE}} \left(\frac{\rho_\ell - \rho_\ell}{\rho_\ell\,\rho_g}\,\Gamma_v\right)_k \Delta V_k\,. \qquad (6.4.37)$$

Here the integration is carried out over the entire volume $V_1 + V_2$ of the pressure vessel, since $\Gamma_v = 0$ in V_1. The integral in the denominator of Eq. 6.4.9 is approximated by

$$\int_{V_1+V_2} \left[\alpha\,\frac{\rho'_g}{\rho_g} + (1-\alpha)\,\frac{\rho'_f}{\rho_f}\right] dV = -\sum_{k=1}^{n_{RSE}} \left[\left(\frac{1}{\rho_f}\right)'\Delta m_\ell + \left(\frac{1}{\rho_g}\right)'\Delta m_g\right]_k\,, \qquad (6.4.38)$$

where $(\Delta m_\ell)_k = (1-\alpha_k)(\rho_\ell)_k \Delta V_k$ and $(\Delta m_g)_k$ is computed from Eq. 6.4.25. The prime denotes differentiation with respect to pressure along the saturation lines.

In Eq. 6.4.11, the first integral is approximated by

$$\int_{A_n} q''_w \, dA = \int_{z_{CI}}^{z_{CE}} q''_w \, \xi \, dz \approx \sum_{j=1}^{N_c} \sum_{k=n_{CI}}^{n_{CE}-1} (q'_w)_{kj} \Delta z_{kj} \, , \qquad (6.4.39)$$

where $q'_w = \xi q''_w$ is the linear heating rate. The second integral is approximated by

$$\int_{V_1+V_2} (1-\alpha) \, q'''_\ell \, dV \approx \sum_{j=1}^{N_c-1} \sum_{k=n_{CI}}^{n_{CE}-1} (q'''_c)_{kj} A_{kj} \Delta z_k + \sum_{k=n_{CI}}^{n_{CE}-1} (q'''_b)_k \, A_{N_c k} \, \Delta z_k \, ,$$

(6.4.40)

where q'''_c and q'''_b are the direct absorption rates in the heated core channel (Eq. 2.7.17) and in the bypass (Eq. 2.7.18), respectively.

The friction integral in Eq. 6.4.15 is computed as follows:

$$\sum_{i=1}^{N_s} \int_0^{L_i} \left\{ \frac{f_\ell \, \phi_\ell^2}{2\rho_\ell d_n} G_m |G_m| \right\}_{ij} dz \approx \sum_{k=2}^{n_{CI}-1} \left\{ \frac{f_\ell \, \phi_\ell^2}{2\rho_\ell d_h} G_m |G_m| \Delta z \right\}_k$$

$$+ \sum_{k=n_{CI}}^{n_{CE}-1} \left\{ \frac{f_\ell \, \phi_\ell^2}{2\rho_\ell d_n} G_m |G_m| \Delta Z \right\}_{jk} + \sum_{k=n_{CE}}^{n_{RSE}} \left\{ \frac{f_\ell \, \phi_\ell^2}{2\rho_\ell d_n} G_m |G_m| \Delta z \right\}_k \, .$$

(6.4.41)

The first and the last terms are common to all contours $_j$, $j=1,\ldots,N_c$ while the second term is to be computed separately for each core flow channel.

The integrals in the expressions for the volumetric flow rate, namely in Eqs. 6.4.16 through 20, are also evaluated by the rule given in Eq. 6.4.36. In particular

$$\phi(z_k) \approx \sum_{i=2}^{k} \left\{ \left(\frac{\rho_\ell - \rho_g}{\rho_\ell \, \rho_g} \Gamma_v \right)_i + \left[\left(\frac{1}{\rho_f} \right)' \Delta m_\ell + \left(\frac{1}{\rho_g} \right)' \Delta m_g \right]_i \frac{d\langle p \rangle_{syst}}{d\tau} \right\} A_i \, \Delta Z_i$$

$$+ \delta_{in_{FW}} (Aj_\ell)_{FW} , \quad k = 2,\ldots, n_{RSE} , \tag{6.4.42}$$

where δ_{inFW} is the Kronecker delta, equal to unity when $i=n_{FW}$ and zero otherwise (see Fig. 6.3). Next, the contour integral

$$\oint_{\mathcal{C}_j} \psi_j \, dz \approx \sum_{k=2}^{n_{CI}-1} \psi_k \, \Delta z_k + \sum_{k=n_{CI}}^{n_{CE}-1} \psi_{kj} \, \Delta z_k + \sum_{k=n_{CE}}^{n_{RSE}} \psi_k \, \Delta z_k , \tag{6.4.43}$$

contains the three segments, the segment from downcomer entrance to core entrance

$$\int_0^{z_{CI}} f \, dz \approx \sum_{k=2}^{n_{CI}-1} f_k \, \Delta z_k , \tag{6.4.44}$$

the segments in the core

$$\int_{z_{CI}}^{z_{CE}} f \, dz \approx \sum_{k=n_{CI}}^{n_{CE}-1} f_k \, \Delta z_k , \tag{6.4.45}$$

and the segment above the core

$$\int_{z_{CE}}^{z_{RSE}} f \, dz \approx \sum_{k=n_{CE}}^{n_{RSE}} f_k \, \Delta z_k . \tag{6.4.46}$$

The rules given by Eqs. 6.4.44 through 46 apply to all the definite integrals in Eqs. 6.4.16 and 17.

This completes the description of all the ordinary differential equations in system of Eqs. 6.4.1 for the coolant thermohydraulics in the reactor vessel and in the recirculation loops.

6.4.2 Steam Line Dynamics

This section is a presentation of the vector functions F_{SL} in Eqs. 6.4.5 which describe the transient flow in the steam lines. The system of Eqs. 6.4.5 represents the partial differential equations given earlier as Eqs. 4.4.185 and 186 and the ordinary differential equations, Eqs. 4.4.187, for the pressure in branch points along the steam line. Recall Eqs. 4.4.185 and 186 from Chapter 4

$$\frac{\partial W}{\partial \tau} = - A \frac{\partial p}{\partial Z} + \frac{f + \zeta d/L}{2dA\rho_o} \left[<p_{syst}>^o / p \right]^{1/\kappa} W|W| \quad . \tag{6.4.47}$$

$$\frac{\partial p}{\partial \tau} = - \frac{<p>^o_{syst}}{A\rho_o} \left[p/<p>^o_{syst} \right]^{\frac{\kappa-1}{\kappa}} \frac{\partial W}{\partial Z} \quad . \tag{6.4.48}$$

The notation is the same as in Chapter 4 (Section 4.4.5.5).

6.4.2.1 Nodalization Scheme for Steam Line

Equations 6.4.47 and 48 are converted into ordinary differential equations by discretization with respect to the axial coordinate z on a staggered mesh such that

(a) pressure nodes are cell-centered.

(b) branch points of safety and relief valves and of the bypass line coincide with pressure nodes.

(c) mass flow rate nodes lie on cell boundaries, particularly the exit mass flow rates W_{TSV} and W_{BY} at the Turbine Stop Valve and the Bypass Valve, respectively, are associated with the corresponding pipe ends.

(d) the node spacings ΔL_{M1}, and ΔL_{CB} are uniform between steam line entrance and bypass branch, between bypass branch and Turbine Stop Valve and between bypass branch and Bypass Valve, respectively.

We designate with M_0 and M_1 the cardinal numbers of the safety and relief valve and of the bypass branch nodes, with M_2 the total number of nodes in the main steam line and with N_{CB} the number of nodes in the bypass line. As shown in Figure 6.4. the node positions z_j, $j=1,\ldots,M_2+N_{CB}$ are given by

$$\begin{aligned} Z &= [0.5 + (j-1)]\Delta L_{M1} && \text{for} \quad 1 \le j \le M_1 \\ Z &= L + (j-M_1)\Delta L_{M2} && \text{for} \quad (M_1+1) \le j \le M_2 \\ Z &= (j-M_2)\Delta L_{CB} && \text{for} \quad (M_2+1) \le j \le (M_2+N_{CB}). \end{aligned} \tag{6.4.49}$$

In Eqs. 6.4.49 the individual pipe segments of a cell are

$$\begin{aligned} \Delta L_{M1} &= 2L_1/(2M_1-1) && = \Delta L_j, \; j = 1,\ldots, M_1 \\ \Delta L_{M2} &= 2L_2/[2(M_2-M_1)+1] && = \Delta L_j, \; j = (M_1+1),\ldots, M_2 \\ \Delta L_{CB} &= 2L_{CB}/(2N_{CB}+1) && = \Delta L_j, \; j = (M_2+1),\ldots, (M_2+N_{CB}) \; . \end{aligned} \tag{6.4.50}$$

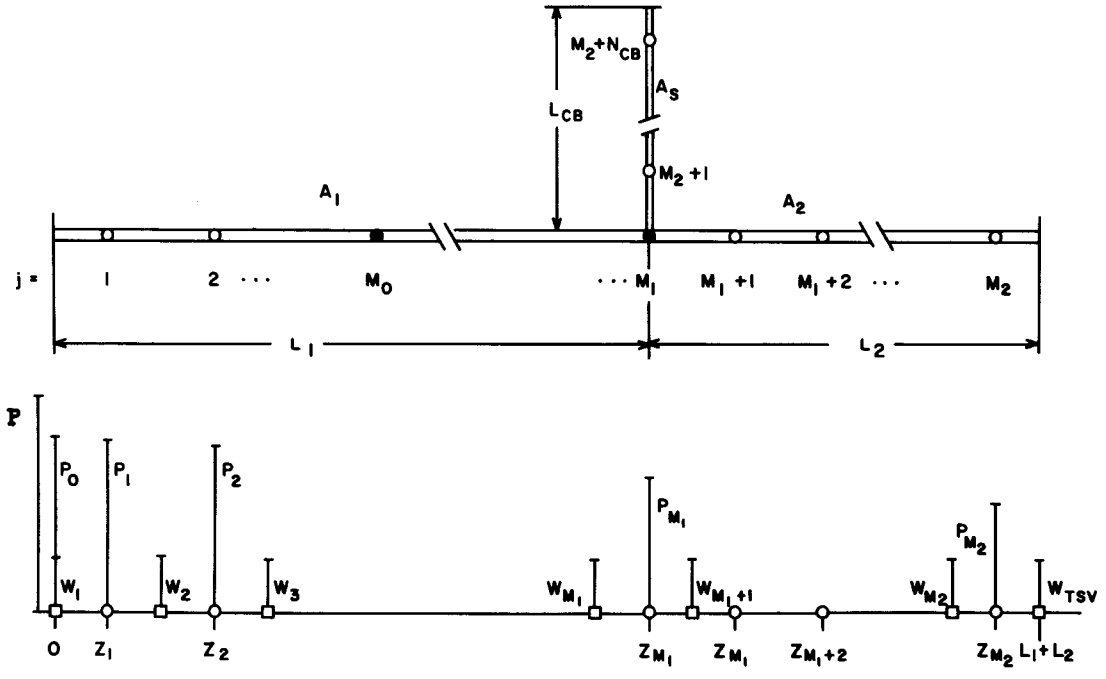

Fig. 6.4 Nodalization Scheme for Steam Lines.

where L_1, L_2 and L_{CB} are the lengths of the pipe sections as measured from the bypass branch point z_{M1} to the main steam line entrance (z=0), to the main steam line exit ($z=L_1+L_2$) and to the bypass line exit, as shown in Fig. 6.4. The positions z_j in Eqs. 4.4.49 are centers of the computational cells for the mass balance, Eq. 6.4.48, and the mesh nodes for the pressure calculations. In the staggered mesh scheme, the centers of the computational cells for the momentum equation are the mesh nodes for the mass flow rate W_i and lie between the pressure nodes:

$$\begin{aligned} z_i &= (i-1)\Delta L_{M1} && \text{for} && 2 \le i \le M_1 \\ z_i &= L_1 + (i-M_1-0.5)\Delta L_{M2} && \text{for} && (M_1+1) \le i \le M_2 \\ z_i &= (i-M_2-0.5)\Delta L_{CB} && \text{for} && (M_2+1) \le i \le (M_2+N_{CB}). \end{aligned} \tag{6.4.51}$$

and $z_1 = \Delta L_{M1}/2$. The nodalization scheme assures that the mass flow rate boundary conditions are imposed exactly at the pipe ends.

6.4.2.2 Ordinary Differential Equations for Steam Line Dynamics

The partial differential equations of steam line dynamics, Eqs. 6.4.47 and 48, are converted to ordinary differential equations by replacing the space derivatives with difference analogues. Combining Eqs. 4.4.192 with Eq. 6.4.47 yields

$$\frac{dW_1}{d\tau} = (A/\Delta L)_1 \left[\langle p \rangle_{syst} - p_1 - (RW)_1 W_1 \right] \tag{6.4.52}$$

where the impedance $(RW)_1$ is given by

$$(RW)_1 = \frac{\Delta L_1}{4 d_1 A_1^2 \rho_o} \left(\frac{\langle p \rangle^o_{syst}}{p_1} \right)^{1/\kappa} \left\{ f_1 |W_1| + \frac{2 d_1}{\Delta L_1} \left[\zeta_1 W_1 + \frac{1+\zeta_c}{2} (W_1 + |W_1|) \right] \right\}. \tag{6.4.53}$$

Equation 6.4.47 yields for interior mass flow rate nodes $z=z_1$ (cf. Eq. 6.4.51)

$$\frac{dW_i}{d\tau} = (A/\Delta L)_i \left[p_{i-1} - p_i - (RW)_i W_i \right]$$

$$i = 2, \ldots, M_2, (M_2+1), \ldots, (M_2+N_{CB}), \tag{6.4.54}$$

with the impedances $(RW)_i$ for interior nodes

$$(RW)_i = \frac{\Delta L_i}{2d_i A_i^2 \rho_o} \left(\frac{<p>^o_{syst}}{p_i} \right)^{1/\kappa} \left\{ f_i + \zeta \frac{d}{\Delta L}_i \right\} |W_i| \quad . \tag{6.4.55}$$

Equation 6.4.48 yields, after discretization, the pressures at cell centers z_j (cf. Eq. 6.4.49) other than branch points

$$\left(\frac{dp}{d\tau} \right)_j = \frac{W_j - W_{j+1}}{c_j}$$

i.e., for $j=1,\ldots,(M_o-1),(M_o+1),\ldots,(M_1-1),(M_1+1),\ldots,(M_2-1)$

$$(M_2+1),\ldots,(N_{CB}-1), \tag{6.4.56}$$

and

$$\left(\frac{dp}{d\tau} \right)_{M_2} = \frac{W_{M_2} - W_{TSV}(\tau)}{C_{M_2}} \quad . \tag{6.4.57}$$

$$\left(\frac{dp}{d\tau} \right)_{N_c} = \frac{W_{N_c} - W_B(\tau)}{C_{N_c}} \quad . \tag{6.4.58}$$

The symbols W_{TSV} and W_{BY} designate mass flow rates at the turbine stop valve and the bypass valve, respectively. These mass flow rates are prescribed boundary conditions and determined by the models for the plant control system (see Chapter 5). For branch points we use Eq. 4.4.187 directly:

$$\left(\frac{dp}{d\tau} \right)_{M_o} = \frac{W_{M_o} - W_{M_o+1} - W_{SR}(\tau)}{C_{M_o}} \tag{6.4.59}$$

$$\left(\frac{dp}{d\tau} \right)_{M_1} = \frac{W_{M_1} - W_{M_1+1} - W_{M_2+1}}{C_{M_1}} \tag{6.4.60}$$

The capacitances C_j in Eqs. 6.4.56 through 60 are given by

$$C_j = \frac{(A\Delta L)_i \rho_o}{\kappa <p>^o_{syst}} \left(\frac{<p>^o_{syst}}{p_j} \right)^{\frac{\kappa-1}{\kappa}} \qquad (6.4.61)$$

for $j=1,\ldots,(M_1-1),(M_1+1),\ldots,M_2\ldots,(M_2+N_{CB})$

and by

$$C_{M_1} = \left[(A\Delta L)_{M_1} + (A\Delta L)_{M_2+1} \right] \frac{\rho_o}{2\kappa <p>^o_{syst}} \left(\frac{<p>^o_{syst}}{p_{M_1}} \right)^{\frac{\kappa-1}{\kappa}} . \qquad (6.4.62)$$

Equations 6.4.52, 54 and 56 through 60 constitute the system of ordinary differential equations, Eqs. 6.4.5, which govern the steam line dynamics. Their integration requires the solution to a transcendental equation, Eq. 4.4.188, for the friction factor, which is presented next.

6.4.2.3 Iterative Procedure for Friction Factor Calculation

The limiting Reynolds number between laminar and turbulent flows in the steam line must be computed once for every steam line geometry (roughness). After substituting Eqs. 4.4.188 and 189 into Eq. 4.4.190 one gets

$$X - e_1 + e_2 \ln [(1+X)/X] = 0, \qquad (6.4.63)$$

where

$$e_1 = 0.8 \ (9.6-16\log_{10}\varepsilon)\varepsilon$$

and

$$e_2 = 12.8\varepsilon / \ln 10$$

are constants, and X is related to the unknown transition Reynolds number $(N_{Re})_{lim}$ by

$$(N_{Re})_{lim} = [X/0.8\varepsilon]^2 \qquad (6.4.64)$$

The symbol ε designates the relative pipe roughness.

Equation 6.4.63 is solved iteratively with

$$X^{\circ} = 39.19$$

$$X^{k+1} = \frac{X^k \left\{ (1+X^k)\left[e_1 - e_2 \ln \frac{1+X^k}{X^k} \right] - e_2 \right\}}{X^k(1+X^k) - e_2}$$

$$k = 0, \ldots, k_e \, . \qquad (6.4.65)$$

This Newton-Raphon iteration is terminated when

$$\left| \frac{X^{k_e} - X^{k_e-1}}{X^{k_e}} \right| < 10^{-12}$$

and the transition Reynolds number is then computed from Eq. 6.4.64. Iteration 6.4.65 has always been completed with $k_e \leq 9$.

Finally, one has to solve Eq. 4.4.188 for the turbulent friction factor f_t. We set

$$\tilde{\Phi} = 0.1 \quad N_{Re} \sqrt{f_t} \qquad (6.4.66)$$

and define the two constants

$$e_3 = \frac{12\text{-}20 \log_{10} \varepsilon}{\varepsilon N_{Re}} \quad \text{and} \quad e_4 = \frac{20}{\varepsilon N_{Re} \ln 0}$$

to convert Eq. 4.4.188 into

$$\frac{1}{\tilde{\Phi}} - e_3 + e_4 \ln \frac{1 + \tilde{\Phi}}{\tilde{\Phi}} = 0 \, . \qquad (6.4.67)$$

This equation is solved by the following algorithm:

$$\tilde{\Phi}^{o} = \frac{1}{e_3}$$

$$\tilde{\Phi}^{k+1} = \frac{\tilde{\Phi}^{k}\left\{e_4\tilde{\Phi}^{k} + (1+\tilde{\Phi}^{k})\left[2+\tilde{\Phi}^{k}\left(e_4 \ln \frac{1+\tilde{\Phi}^{k}}{\tilde{\Phi}^{k}} - e_3\right)\right]\right\}}{1 + (1+e_4)\tilde{\Phi}^{k}}$$

$$k = 0, \ldots, k_e \,, \tag{6.4.68}$$

where k_e is determined from

$$\left| \frac{\tilde{\Phi}^{k_e} - \tilde{\Phi}^{k_e-1}}{\tilde{\Phi}^{k_e}} \right| < 10^{-6} \quad . \tag{6.4.69}$$

When (6.4.69) is satisfied then f_t is found from Eq. 6.4.66, namely

$$f_t = \left(\frac{10\tilde{\Phi}^{k_e}}{N_{Re}}\right)^2 \tag{6.4.70}$$

This completes the procedures for computing the right-hand sides of the vector equations in the system of Eqs. 6.4.5 for the transient vapor flow in the steam lines.

6.4.3 The Transport of Boron

In this section is presented the conversion of the partial differential equation of boron transport, Eq. 4.4.195, to the form of Eqs. 6.4.6, the ordinary differential equations which are integrated in RAMONA-3B by the first-order explicit Euler integration method with a special integration step size. For the reader's convenience, we repeat the governing equations, Eqs. 4.4.195 and 4.4.2:

$$\frac{\partial\left[\rho_\ell(1-\alpha)c_B\right]}{\partial\tau} + \nabla\cdot(\rho_\ell c_B \vec{j}_\ell) = B \tag{6.4.71}$$

$$\frac{\partial\left[\rho_\ell(1-\alpha)\right]}{\partial\tau} + \nabla\cdot(\rho_\ell \vec{j}_\ell) = -\Gamma_v \tag{6.4.72}$$

The first equation represents the boron mass conservation, the second one the liquid mass conservation. The equations are integrated over the control volume of a computational cell and combined into a single ordinary differential equation for c_B.

6.4.3.1 Nodalization Scheme for Boron Transport

The coolant in the entire reactor vessel is divided into up to ten control volumes, two for the downcomer, two for the lower plenum, one for the bypass channel, up to three equally long axial segments in the active core, one for upper plenum plus riser and steam separators, and one for the steam dome. The two downcomer volumes meet at the jet pump elevation, where boron is injected. One of the two volumes in the lower plenum is below the core shroud, the other inside the shroud, below the active core.

It is quite clear that these control volumes are much larger than those used for the discretization of the vapor mass and mixture energy conservation equations and shown in Figure 6.3. The size of the computational cells for boron transport have been chosen to minimize the number of ordinary differential equations and whence the computational effort of integrating them. However, the coarse control volume division requires a compensation for the intolerable numerical diffusion. As will be explained later, this is achieved by time delay calculations which, however, not only introduce discontinuities (thereby compromising the Lipschitz continuity required for numerical integration) but also impose repeatedly drastic reductions in integration step size. This is accompanied by the need for complicated branching in the computational procedure and may not reduce the computational effort after all. It is therefore recommended that for future code improvements the standard RAMONA-3B nodalization scheme (see Figure 6.3) be adopted to determine whether it produces better accuracy at lower computing cost.

6.4.3.2 Boron Transport Equation

By integrating Eqs. 6.4.71 and 72 over the volume ΔV_k of the k-th computational cell, one obtains these two ordinary differential equations:

$$\frac{d\left[\langle\rho_\ell(1-\alpha)c_B\rangle_k \Delta V_k\right]}{d\tau} = \Delta V_k \langle B\rangle_k - \int_{A_k} c_B \rho_\ell \vec{j}_\ell \cdot \vec{dA} \qquad (6.4.73)$$

$$\frac{d\left[\langle\rho_\ell(1-\alpha)\rangle_k dV_k\right]}{d\tau} = -\Delta V_k \langle\Gamma_v\rangle_k - \int_{A_k} \rho_\ell \vec{j}_\ell \cdot \vec{dA} \; . \qquad (6.4.74)$$

Call

$$(\bar{c}_B)_k = \frac{\langle \rho_\ell c_B (1-\alpha)\rangle_k}{\langle \rho_\ell (1-\alpha)\rangle_k}$$

and

$$(\tilde{c}_B)_k = \frac{\int_{A_k} c_B \rho_\ell \vec{j}_\ell \cdot d\vec{A}}{\int_{A_k} \rho_\ell \vec{j}_\ell \cdot d\vec{A}} \qquad (6.4.75)$$

Since $(m_\ell)_k = \Delta V_k \langle \rho_\ell (1-\alpha)\rangle_k$ and $W_\ell)_k = \int_{Ak} c_B \rho_\ell \vec{j}_\ell \cdot d\vec{A}$, where k denotes the cell and its exit cross-sectional area, we can rewrite Eqs. 6.4.73 and 74 as follows:

$$(\bar{c}_B)_k \frac{d(m_\ell)_k}{d\tau} + (m_\ell)_k \frac{d(\bar{c}_B)_k}{d\tau} = \Delta V_k \langle B\rangle_k + (\tilde{c}_B W_\ell)_{k-1} - (\tilde{c}_B W_\ell)_k \qquad \ldots \quad (6.4.76)$$

$$\frac{d(m_\ell)_k}{d\tau} = -\Delta V_k \langle \Gamma_v \rangle_k + (W_\ell)_{k-1} - (W_\ell)_k \qquad (6.4.77)$$

After multiplying Eq. 6.4.77 by $(c_B)_k$ and subtracting from Eq. 6.4.76 we obtain the ordinary differential equation for boron transport:

$$\frac{d(\bar{c}_B)_k}{d\tau} = \frac{1}{(m_\ell)_k} \Big\{ \Delta V (\langle B\rangle + \bar{c}_B \langle \Gamma_v \rangle)_k + (W_\ell)_{k-1} \left[(\tilde{c}_B)_{k-1} - (\bar{c}_B)_k\right] - (W_\ell)_k \left[(\tilde{c}_B)_k - (\bar{c}_B)_k\right] \Big\}$$

$$k = 1, \ldots, N_B \leq 10. \qquad (6.4.78)$$

Equation 6.4.78 can be integrated, subject to $(c_B)_k = 0$, all k, at $\tau = 0$ and the boundary condition, Eq. 4.4.196, provided a relation is given between $(\tilde{c}_B)_k$ and $(\bar{c}_B)_k$ in Eq. 6.4.78.

In the control volume of the steam dome and in the control volume containing the boron injection ($\langle B\rangle_k \neq 0$) nozzle, RAMONA-3B implies

$$(\tilde{c}_B)_k (\tau) = (\bar{c}_B)_k (\tau), \text{ dome \& injection volume} \qquad (6.4.79a)$$

on the assumption that perfect mixing is achieved in these cells. For all other cells the time delay of $m_\ell/(2W_\ell)$ is introduced, such that

$$(\tilde{c}_B)_k(\tau) = (c_B)_k\ (\tau - \frac{m_\ell}{2W_\ell}_k), \tag{6.4.79b}$$

subject to the following constraints: if in cell k

$$\left.\begin{aligned} &(\bar{c}_B)_k(\tau) > (\tilde{c}_B)_k(\tau) \text{ and } \frac{d(\bar{c}_B)_k}{d\tau} > 0 \\ &\text{then} \\ &(\tilde{c}_B)_k(\tau) = (\bar{c}_B)_k(\tau). \end{aligned}\right\} \tag{6.4.79c}$$

The constraint in Eq. 6.4.79c is introduced to avoid an insignificant (2%) overshoot of boron concentration which would otherwise result from a (hypothetical) step change in upstream boron concentration. The constraint introduces, however, an instantaneous jump in cell exit concentration (30% of step change) which compromises continuity requirements for both the numerical integration and for the application of stability criteria. It is therefore recommended that the constraint in Eq. 6.4.79c be eliminated for future code improvements.

Equation 6.4.78 and 79 constitute the system of state equations, Eqs. 6.4.6. Thus all the ordinary differential and algebraic equations for coolant hydraulics, steam line dynamics and boron transport are established. The constitutive relations required also for problem closure are given in Section 4.4.2 of Chapter 4. Finally, the algebraic equations arising from component modeling are found in Sections 4.4.4.3, 4.4.4.4 and 4.4.5.

6.5 Summary of RAMONA-3B State Equations

This section contains the tabulation of all state equations in RAMONA-3B. State equations are the transient field (conservation) equations which determine the transient values of the principal state variables. The state equations are integrated with respect to time. The coolant mixture mass balance is the only conservation equation in RAMONA-3B which is not integrated with respect to time but instead with respect to axial distance (space quadrature). It is therefore not part of the system of state equations.

The principal state variables define at any instant the conditions of the entire system. All other state variables and time dependent parameters can be computed from the principal state variables.

The state equations in RAMONA-3B are given in Sections 6.2.3 and 4. They are in one of the following three forms, namely either in the form of explicit first-order ordinary differential equations.

$$\frac{d\underset{\sim}{y}}{d\tau} = \underset{\sim}{F}(\underset{\sim}{y},\tau)$$
$$0 = \underset{\sim}{F}(\underset{\sim}{y}_0,0), \qquad (6.5.1)$$

or in the form of implicit systems of nonlinear equations

$$\underset{\approx}{A}^{n+1}\ \underset{\sim}{Y}^{n+1} = \underset{\sim}{B}^{n}$$
$$\underset{\approx}{C}^{0}\ \underset{\sim}{Y}^{0} = \underset{\sim}{D}^{0} \qquad (6.5.2)$$

which are derived from conservation equations in the form of Eqs. 6.5.1 (see Sections 6.2 and 3) by first-order backward differencing of their time-derivatives, or, thirdly, in the form of explicit systems of nonlinear equations

$$\underset{\sim}{Z}^{n+1} = \underset{\sim}{E}(Y^{n+1})$$
$$\underset{\sim}{Z}^{0} = \underset{\sim}{E}(Y^{0}) \quad . \qquad (6.5.3)$$

The following table lists the state equations, first for the neutron kinetics models, then the thermal conduction models and finally the coolant hydraulics models, including the steam line dynamics and boron transport models. The state equations are classified by types (cf. Eqs. 6.5.1, 2 and 3), and they are referenced by the equation number in this report. Also listed are state variables defined by each one of the state equations.

The equations listed in Categories (a) and (b) are integrated with a common integration step, the equations in Categories (c) through (e) each have their own integration steps. This is explained in Section 6.7. Before that, we present the methods for computing the steady-state initial conditions.

6.6 Solution Techniques for Initial Steady-State Conditions

Before describing the particular details of the search for initial steady-state conditions, we present here the general concepts first.

The originally stated approach to computing initial conditions in RAMONA-3B is:

Table 6.2 Summary of State Equations

Type of Equation	Equation Number	State Variable(s) Symbol	Definition
		a) NEUTRON KINETICS	
6.5.2	6.2.89	$\psi_{i,j,k}$	Fast Neutron Flux (midpoint)
6.5.3	6.3.75	$\Phi_{i,j,k}$	Cell-Avg. Thermal Neutron Flux
6.5.3	6.2.78	$\xi_{i,j,k}$	Cell-Avg. Delayed Neutron Precursor Concentration
		b) THERMAL CONDUCTION	
6.5.2	6.3.38	$t_{f,i}, t_{c,j}$	Fuel and Cladding Temperature
		c) COOLANT HYDRAULICS	
6.5.1	6.4.9	$\langle p \rangle_{syst}$	Overall System Pressure
6.5.1	6.4.10	$(M_g)_{syst}$	Vapor Mass in System
6.5.1	6.4.11	$(u^M)_{syst}$	Internal Energy in System
6.5.1	6.4.12	$(M_g)_{LVD}$	Vapor Mass in Low-Void Region of Vapor Loop
6.5.1	6.4.13	W_{RCL}	Mass Flow Rate in Recirculation Loop
6.5.1	6.4.14	ω_{RCP}	Angular Speed of Recirculation Pump
6.5.1	6.4.15	$\mathcal{M}_j$	Closed Contour Momentum
6.5.1	6.4.25	$(\bar{m}_g)_k$	Vapor Mass in Cell k
6.5.1	6.4.31	$(\rho_m u_m)_k$	Mixture Internal Energy in Cell k
		d) STEAM LINE DYNAMICS	
6.5.1	6.4.52 6.4.53	W_j	Vapor Mass Flow Rate in Steam Line
6.5.1	6.4.56 6.4.57 6.4.58 6.4.59 6.4.60	p_j	Local Pressure in Steam Line
		e) BORON TRANSPORT	
6.5.1	6.4.78	$(c_B)_k$	Boron Mass Concentration in Liquid

(a) to impose a set of desirable operating conditions, (rather than a set of boundary conditions which define uniquely the steady state of the system),

(b) to set the time-derivatives in all system state equations (see Section 6.5) equal to zero, combine the resulting nonlinear equations with all other modeling equations and solve the coupled set of these nonlinear equations iteratively, thereby adjusting selected parameters (loss coefficients) to compensate for the redundant boundary conditions (see (a) above), until finally all equations are satisfied within prescribed convergence criteria.

The capability to specify more operating conditions than necessary for a unique definition of the steady state allows the user to substitute well known or desirable parameters for poorly known constitutive parameters such as form loss coefficients for complicated geometries or efficiencies for diffusers or pumps. For example, the user of RAMONA-3B is permitted to specify the recirculation pump speed, the recirculation mass flow rate and the core flow rate, even though the latter two are dictated by the former. Consequently, at least two constitutive parameters can be computed by the code.

The danger from computing redundant parameters is the attendant tendency to overlook an unknown number of modeling weaknesses collectively at one condition and to hope that the compensation remains valid under all conditions of a transient. It is recommended that all constitutive parameters computed by the code be carefully validated by the code user. The computed constitutive parameters known to the author are the jet pump diffuser impedance, Eq. 4.4.137, the recirculation loop impedance, Eq. 4.4.133, the leading coefficient for the recirculation pump characteristic, Eq. 4.4.139, and the vapor carry-under at the steam dome-to-downcomer interface, Eq. 4.4.159. It should be clear that the latter cannot have general validity during the transient.

RAMONA-3B deviates from Item (b) above since

(a) different equations are used for steady-state and transient calculations and

(b) different assumptions are used for steady-state and transient conditions.

As has been discussed in Section 4.5 of Chapter 4, the steady-state vapor void fraction in the low-void regime of the steam dome is not computed from the steady-state vapor mass balance but from an energy balance for downcomer and lower plenum. The computation of the steady-state steam mass flow rate at the steam line is computed without the corresponding assumptions used for computing the transient system pressure (cf. Eq. 4.4.198). Finally, the velocity of the liquid is computed for steady-state calculations first from the kinematic relation, Eq. 4.4.105, and then corrected with the aid of the steady-state mass balance for the liquid phase, Eq. 4.4.2, with $d/d\tau=0$ and integrated over cell volume ΔV_k). However, the transient liquid mass balance is not used at all for the transient simulation because is is replaced by the volume flux divergence equation, Eq. 4.4.9.

To compensate for these (and possibly other) discrepancies, RAMONA-3B starts out from its initial steady state but uses it only as an initial guess. With this initial guess and a user-specified negative time, RAMONA-3B computes first a "transient" with a fixed set of operating conditions until it reaches the time τ=0. The user then assures himself that he has indeed a steady state.

The steady state is governed by several sets of nonlinear equations as indicated symbolically in Section 6.5. For prompt neutron kinetics and thermal conduction in the fuel, the equations have the form

$$\underset{\approx}{C}^{o}\underset{\sim}{Y}^{o} = \underset{\sim}{D}^{o}. \tag{6.6.1}$$

For thermal and delayed neutron kinetics, the equations are explicit in terms of $\underset{\sim}{Y}^{o}$

$$\underset{\sim}{Z}^{o} = \underset{\sim}{E}(\underset{\sim}{Y}^{o}). \tag{6.6.2}$$

For coolant thermohydraulics we have

$$\underset{\sim}{F}(\underset{\sim}{y}_{o}) = 0. \tag{6.6.3}$$

All of the above equations are coupled. The overall solution scheme for the steady state is successive substitution. Starting with an initial guess for the solution to Eqs. 6.6.1 and 6.6.2 (uniform power distribution) and with specified "boundary" conditions* (total fission power, feedwater conditions, system pressure, steam mass flow rate and control rod positions) a solution is found for Eq. 6.6.3 and substituted into Eqs. 6.6.1 and 6.6.2. Solutions are then sought for Eq. 6.6.1 and substituted into Eq. 6.6.2. With the solutions of Eqs. 6.6.1 and 6.6.2, the cycle is repeated until convergence is obtained (or the procedure is discontinued because it does not converge).

The individual solutions for each of the systems of Eqs. 6.6.1, 6.6.2 and 6.6.3, and their subsystems are found by accelerated Gauss-Seidel iterations, by successive update techniques and by successive substitution, as discussed in Section 6.6.1, 6.6.2 and 6.6.3 below. The successive substitution procedure for solving Eq. 6.6.3 for the coolant dynamics involves itself nested successive substitution schemes. Each elementary procedure in RAMONA-3B has its own convergence criterion.

Since successive substitution is the overall computing method for seeking steady-state conditions and since it is also used for solving several subsets of nonlinear equations in RAMONA-3B, the conditions should be established which must be met by the equations and the initial guesses so that successive substitution can work. These conditions can be found, for example, in Analysis of

*Recall the comments regarding overspecification of boundary conditions, presented at the beginning of this section.

Numerical Methods (Isaacson and Keller 1966, p. 109). Successive substitution is represented formally by

$$\underset{\sim}{x}^{k+1} = \underset{\sim}{g}(\underset{\sim}{x}^{k}), \qquad k=0,1,... \tag{6.6.4}$$

where a new value of the solution $\underset{\sim}{x}$ is computed from the vector equation $\underset{\sim}{g}$ at the previous iteration level k, to find the solution to the general system of nonlinear equations

$$\underset{\sim}{x} - \underset{\sim}{g}(\underset{\sim}{x}) = 0. \tag{6.6.5}$$

Here $\underset{\sim}{x}$ and $\underset{\sim}{g}$ have the same dimension. The least restrictive criteria for Eq. 6.6.4 to converge to a unique solution $\underset{\sim}{x}^*$ within the neighborhood $||\underset{\sim}{x}^*-\underset{\sim}{x}|| \leq \rho_s$ of the initial guess, i.e.,

$$\lim_{k\to\infty} \underset{\sim}{x}^{k} = \underset{\sim}{x}^* \tag{6.6.6}$$

are, that the function $\underset{\sim}{g}(\underset{\sim}{x})$ must be Lipschitz-continuous

$$||\underset{\sim}{g}(\underset{\sim}{x}_1) - \underset{\sim}{g}(\underset{\sim}{x}_2)|| \leq \lambda\, ||\underset{\sim}{x}_1 - \underset{\sim}{x}_2|| \tag{6.6.7}$$

for all vectors $\underset{\sim}{x}_1$ and $\underset{\sim}{x}_2$ within the radius ρ_s from the initial guess

$$||\underset{\sim}{x}_1 - \underset{\sim}{x}^0|| \leq \rho \quad \text{and} \quad ||\underset{\sim}{x}_2 - \underset{\sim}{x}^0|| \leq \rho_s, \tag{6.6.8}$$

that the Lipschitz constant λ satisfies

$$0 \leq \lambda < 1, \tag{6.6.9}$$

and that the initial guess satisfies

$$||\underset{\sim}{g}(\underset{\sim}{x}^0) - \underset{\sim}{x}^0|| \leq \rho_s(1-\lambda). \tag{6.6.10}$$

For the vector norms $||\cdot||$ appearing in Eqs. 6.6.7, 6.6.8 and 6.6.10, one may use the Euclidean norm, the maximum norm or, simply $||\cdot||_1 = \sum_j |\cdot|_j$, summing over all components.

The above convergence criteria imply that there should be no branching from one expression to another in $\underset{\approx}{C}^0$, $\underset{\approx}{D}^0$, $\underset{\approx}{E}$ and $\underset{\approx}{F}$ of Eqs. 6.6.1, 6.6.2 and 6.6.3, unless the transition preserves continuity Eq. 6.6.7. The criteria also

imply that the decomposition of $\underset{\sim}{F}$ for the coolant dynamics into $\underset{\sim}{q}$ has to be such that Eq. 6.6.9 can be satisfied by all equations. For further details and more convenient but also more restrictive criteria, we refer the reader to standard texts on numerical analysis.

The user should know that the above continuity criteria are not systematically met in RAMONA-3B, primarily because of the switching logic in the computational procedures. There is also no built-in test to check initial guesses (Eq. 6.6.10). However, most violations of the above criteria lead normally to involuntary termination of a computer run. The user, who intends to modify the code, should make certain that his modifications do not violate the above criteria.

The next sections describe briefly the individual techniques used to seek the solutions in each subtask, first for neutron kinetics, then for thermal conduction and finally for coolant dynamics.

6.6.1 Solution Techniques for Neutron Kinetics

The steady-state finite difference equations for neutron kinetics, given by Eqs. 6.2.98 and 6.2.94, constitute an eigenvalue problem with k_{eff} being the fundamental eigenvalue. RAMONA-3B employs the standard solution technique for the eigenvalue problem, which consists of an inner iteration to get at the neutron fluxes and an outer iteration to obtain the eigenvalue. Furthermore, since the thermohydraulic feedback influences strongly the neutron kinetics, a third iteration loop, called "power-void iteration", is necessary to take into account the influence of thermohydraulic feedback.

6.6.1.1 Inner Iteration

The inner iteration is required to solve the fast flux Eq. 6.2.98 because the fast flux at a point depends on its six neighbors. For the inner iteration, RAMONA-3B uses the Gauss-Seidel iteration augmented by a method of relaxation. The Gauss-Seidel scheme uses the most recent iterates of the flux surrounding a node to compute the flux at the node:

$$\psi^{(n)}_{i,j,k} = \frac{1}{Q^{(n-1)}_{i,j,k}} \left[\psi^{(n)}_{i-1,j,k} + \psi^{(n-1)}_{i+1,j,k} + \psi^{(n)}_{i,j-1,k} + \psi^{(n-1)}_{i,j+1,k} + R\left(\psi^{(n)}_{i,j,k-1} + \psi^{(n-1)}_{i,j,k+1} \right) \right]. \qquad (6.6.11)$$

Here we have used the supercript (n) to denote the inner iteration index in order to avoid confusion with the time step index n.

To apply the Gauss-Seidel scheme, we sweep the mesh grid from (i=1, j=1) to (i=IMAX, j=JMAX) for each vertical plane k from k=1 to k=KMAX. To start the iteration, we need an initial guess for all ψ's. This is done in RAMONA-3B by setting them equal to unity.

The inner iteration is terminated if either the number of iterations exceeds a maximum value called NSMAX (an input parameter on Card 800000) or the following convergence test is met for all nodes:

$$\left| \psi_{i,j,k}^{(n)} - \psi_{i,j,k}^{(n-1)} \right| < \varepsilon_1 \, \bar{\psi}^{(n-1)} \quad , \tag{6.6.12}$$

where ε_1 is the convergence criterion required as an input (called DLS) and $\bar{\psi}^{(n-1)}$ is the core-average ψ at the previous iteration defined as

$$\bar{\psi}^{(n-1)} = \frac{1}{NEND} \sum_{i,j,k} \psi_{i,j,k}^{(n-1)} \tag{6.6.13}$$

with NEND being the total number of neutronic nodes in the core.

After each Gauss-Seidel iteration, the following relaxation scheme is applied to the fast fluxes in order to accelerate the convergence of the Gauss-Seidel iteration:

$$\tilde{\psi}_{i,j,k}^{(n)} = (1-\Omega)\, \psi_{i,j,k}^{(n)} + \Omega \, \psi_{i,j,k}^{(n-1)} \quad , \tag{6.6.14}$$

where the tilde indicates the relaxed fluxes and Ω is a relaxation parameter required as an input (called A3). The relaxation scheme in the above form is a under-relaxation ($0 \leq \Omega \leq 1$). Typical values of Ω are $0.1 \sim 0.2$.

In summary, the solution technique for the steady-state fast flux is based on the Gauss-Seidel iteration (a method of successive displacements) followed by a successive under-relaxation.

The convergence property of the inner iteration depends on the convergence properties of the Gauss-Seidel method and the successive relaxation method. The convergence is guaranteed if the absolute values of all the eigenvalues associated with the iteration matrices, implied in Eqs. 6.6.11 and 6.6.12, are less than unity. This is equivalent to saying that the largest eigenvalue (called "spectral radius") of the iteration matrices is less than unity. That this is indeed the case for neutron diffusion problems is well established (Clark and Hansen 1964).

In the present case, we can demonstrate the convergence as follows. Define a vector $\underline{\psi}$ with its elements representing all the ψ's in space:

$$\underline{\psi} = \left[\psi_{1,1,1}\ \psi_{2,1,1}\cdots\psi_{IMAX,JMAX,KMAX}\right]^T . \qquad (6.6.15)$$

The problem at hand is to seek the solution of the following matrix equation:

$$\underline{\underline{A}}\,\underline{\psi} = 0 , \qquad (6.6.16)$$

where $\underline{\underline{A}}$ is a tri-diagonal coefficient matrix with its diagonal elements being $Q_{i,j,k}$ and its off-diagonal elements being -1 for all (i,j) indices and -R for all k indices. [This can be readily seen from Eq. 6.6.11.]

We can now observe the convergence property by examining the properties of the coefficient matrix $\underline{\underline{A}}$. First of all, $\underline{\underline{A}}$ is a real symmetric matrix. Secondly, it is also diagonally dominant. This can be seen by examining Eqs. 6.2.99, 6.2.100, and 6.2.101. Note that, typically, $b \approx 0.3$, $c \approx 0.06$, $q_{i,j,k} < 1$, and $p_{i,j,k} \approx 6$, $r_{i,j,k} \approx 6$, hence $Q_{i,j,k} >> 1$.

It has been shown that the method of successive displacements (Gauss-Seidel) and successive relaxation always converges for a real symmetric coefficient matrix with diagonal dominance (Clark and Hansen 1964, also Varga 1962).

6.6.1.2 Eigenvalue Iteration

There are two methods that can be used to estimate the fundamental eigenvalue, k_{eff}. One method is based on the power method of iteration for the solution of an eigenvalue equation. Recall that the eigenvalue, k_{eff}, appears in $q_{i,j,k}$ of Eq. 6.2.98, which can be cast as an eigenvalue equation:

$$\underline{\underline{B}}\,\underline{\psi} = \frac{1}{k_{eff}}\,\underline{\underline{F}}\,\underline{\psi} , \qquad (6.6.17)$$

where the matrices, $\underline{\underline{B}}$ and $\underline{\underline{F}}$, can be derived from Eq. 6.2.98. We shall not present their derivations here since they are not essential for the following discussion.

The eigenvalue iteration may be expressed formally by the following iteration algorithm:

$$\underline{\psi}^{(m)} = \frac{1}{k_{eff}^{(m-1)}}\,\underline{\underline{B}}^{-1}\,\underline{\underline{F}}\,\underline{\psi}^{(m-1)} , \qquad (6.6.18)$$

where the superscript (m) denotes the eigenvalue iteration index.

The fundamental eigenvalue can be estimated by a successive update procedure based on the Rayleigh quotients (Wachspress 1966 and Varga 1962):

$$k_{eff}^{(m)} = k_{eff}^{(m-1)} \frac{\sum_{i,j,k} \left(\psi_{i,j,k}^{(m)}\right)^2}{\sum_{i,j,k} \left(\psi_{i,j,k}^{(m)} \psi_{i,j,k}^{(m-1)}\right)} \quad . \tag{6.6.19}$$

An initial guess on k_{eff} is necessary to start off the iteration. This is usually done by setting $k_{eff}^{(o)} = 1$.

The other method is based on the physical definition of the fundamental eigenvalue, k_{eff}:

$$k_{eff} = \frac{\text{Total Neutron Production}}{\text{Total Neutron Absorption + Total Neutron Leakage}} , \tag{6.6.20}$$

where

Total neutron production =

$$\sum_{i,j,k} \left(\frac{\nu_1 \Sigma_{f_1}}{\sqrt{D_{i,j,k}}} \bar{\psi}_{i,j,k} + \frac{\nu_2 \Sigma_{f_2}}{\sqrt{D_{i,j,k}}} \bar{\Phi}_{i,j,k} \right) V_{i,j,k} , \tag{6.6.21}$$

Total neutron absorption =

$$\sum_{i,j,k} \frac{\Sigma_1}{\sqrt{D_{i,j,k}}} \bar{\psi}_{i,j,k} V_{i,j,k} , \tag{6.6.22}$$

Total neutron leakage = $T + B + S$, (6.6.23)

with

$$T = \frac{1}{h_z} \sum_{\substack{(i,j) \\ k=KMAX}} \frac{\sqrt{D_{i,j,k}}}{\lambda_{eff}^{T}} \psi_{i,j,k} V_{i,j,k} \quad , \tag{6.6.24}$$

$$B = \frac{1}{h_z} \sum_{\substack{(i,j) \\ k=1}} \frac{\sqrt{D_{i,j,k}}}{\lambda_{eff}^{B}} \psi_{i,j,k} V_{i,j,k} \quad , \tag{6.6.25}$$

$$S = \frac{1}{h_z} \sum_{k} \left(\frac{1}{\lambda_{eff}^{S}} \right) \sqrt{D_{i,j,k}} \psi_{i,j,k} V_{i,j,k} \, . \tag{6.6.26}$$

(i,j) = side boundary nodes

Here $1/\lambda_{eff}^{S}$ is given by Eq. 6.2.24.

RAMONA-3B uses this second method to estimate the eigenvalue. It is calculated only after the inner iteration has converged or exceeded its maximum iteration number (NSMAX) specified in the input. The eigenvalue k_{eff} as defined by Eq. 6.6.20 should carry the index (m) to indicate that it is also being iterated on. The eigenvalue iteration is terminated if the following convergence test is satisfied:

$$\left| 1 - \frac{k_{eff}^{(m-1)}}{k_{eff}^{(m)}} \right| < \varepsilon_2 \quad , \tag{6.6.27}$$

where ε_2 is the convergence criterion for the eigenvalue required as an input (called DLK). The eigenvalue iteration is also subject to a maximum number of iterations (called MEIT) which is also required as an input. This parameter can be used to combine the eigenvalue iteration with the power-void iteration (to be discussed in the next section) by setting MEIT = 1.

It should be pointed out that, at convergence, the two methods of eigenvalue calculations should yield the same value for the fundamental eigenvalue, k_{eff}.

6.6.1.3 Power-Void Iteration

The power-void iteration is used to compute the power (fission density) distribution which is consistent with the thermohydraulic feedback. After the fluxes and the fundamental eigenvalue have been obtained by the inner and eigenvalue iterations, the fission density is computed at each power-void iteration as follows:

$$F^{(p)}_{i,j,k} = \frac{\Sigma_{f1}}{\sqrt{D_{i,j,k}}} \bar{\psi}^{(p)}_{i,j,k} + \frac{\Sigma_{f2}}{\sqrt{D_{i,j,k}}} \bar{\Phi}^{(p)}_{i,j,k} \qquad (6.6.28)$$

where the superscript (p) denotes the power-void iteration index.

Note that RAMONA-3B actually computes the second term at the righthand side of Eq. 6.6.18 as $(\Sigma_{f2}/\sqrt{D_2})\ \psi_2$ where $\bar{\psi}_2$ is calculated from the midpoint thermal fluxes.

We have pointed out, in Section 6.2, that this is unnecessary and that it is better to compute $\bar{\Phi}_{i,j,k}$ directly from its balance equation using the average flux, $\bar{\psi}_{i,j,k}$. In this approach, the fission density should be computed as Eq. 6.6.28. We recommend this for future refinement.

The method of successive relaxation, as applied to the fast flux in the inner iteration, is also used to refine the fission density before the next power-void iteration:

$$\tilde{F}^{(p)}_{i,j,k} = (1-\Omega_p)\ F^{(p)}_{i,j,k} + \Omega_p\ F^{(p-1)}_{i,j,k} \qquad (6.6.29)$$

where Ω_p is a relaxation factor for the fission density, which is also required as an input quantity (RELF) for RAMONA-3B. In this form, Ω_p is meant to be an under-relaxation factor ($0 \leq \Omega_p \leq 1$). Typical values of Ω_p are 0.4 $\sim$ 0.5.

We wish to point out that the power-void iteration is necessary because of the thermohydraulic feedback alters the two-group parameters which, in turn, change the neutron fluxes, and hence the fission density distribution must be updated each time a new set of thermohydraulic variables is obtained from solving the thermohydraulics equations described in Chapters 3 and 4. The updated power distribution is then used to recompute the thermohydraulic variables. This process is repeated until the power distribution is converged. We see that the power iteration, Eq. 6.6.29, is inherently related to the void iteration (recalculation of thermohydraulics). They are, therefore, collectively called the "power-void iteration". The name "void iteration" is used because void feedback is the most dominant among all thermohydraulic feedback mechanisms.

The power-void iteration is terminated if either the number of iterations exceeds a maximum value called NCMAX (an input parameter on Card 800000) or the following convergence test is satisfied for all nodes:

$$\frac{\left| F_{i,j,k}^{(p)} - F_{i,j,k}^{(p-1)} \right|}{\bar{F}^{(p)}} < \varepsilon_3 \qquad (6.6.30)$$

where ε_3 is the convergence criterion for the local power density required as an input (called DPINP), and $\bar{F}^{(p)}$ is the core average power density at p-th iteration:

$$\bar{F}^{(p)} = \frac{1}{NEND} \sum_{i,j,k} F_{i,j,k} \quad . \qquad (6.6.31)$$

Here NEND is the total number of neutronic nodes in the core.

It is worth noting that the relaxation scheme (6.6.29) is not the most efficient method in use. A very powerful method, called "Chebyshev extrapolation," has been developed to accelerate the power iteration (Hagemen and Kellog 1966). This Chebyshev extrapolation technique is very efficient, widely used, and can be used for future improvement, if necessary.

6.6.2 Steady-State Fuel and Cladding Temperatures

It has been shown earlier that Eq. 6.3.39 defines the intial steady-state temperatures in the fuel and in the cladding. RAMONA-3B is programmed to solve this set of equations, which is coupled with those of neutron kinetics and coolant dynamics, separately during one step of the overall system iteration. For this purpose the initial guesses or current iterates for heat generation $(\bar{q}_f''')_k^o$ and fluid temperature $(t_{f\ell})_k$ and bypass coolant temperature $(t_{\ell b})_k$ at positions z_k are used and kept fixed while seeking the solution to Eq. 6.3.39.

Since during steady state

$$(q_w')_k^o = (\xi \bar{q}'')_k^o = \pi R_f^2 (\bar{q}_f''')_k^o \quad , \tag{6.6.32}$$

Equation 4.4.5 yields the outer cladding surface temperature $(t_w)_k^o = \{t_c(R_{co})\}_k^o$. Equation 4.4.5 is solved twice, once with the assumption of single-phase forced convection in liquid and once with the assumption of nucleate boiling. The lower result is retained (cf. Fig. 4.2 and Eqs. 4.4.30 and 4.4.33).

Once the wall temperature $(t_w)_k^o$ is known, a marching procedure yields successively the interior cladding temperature $(\bar{t}_{c,j})_k^o$ and the inner fuel temperature $(\bar{t}_{f,i})_k^o$. The marching procedures start by solving Eq. 6.3.34 for the outermost interior cladding temperature $(\bar{t}_{c,N})_k^o$ and continue by solving successively Eqs. 6.3.33 and 6.3.32, with $d/d\tau = 0$, for $(\bar{t}_{c,N-1})_k^o$, $(\bar{t}_{c,N-2})_k^o, \ldots, (\bar{t}_{c,1})_k^o$ and then Eqs. 6.3.31, 6.3.29 and 6.3.28, also with $d/d\tau = 0$ for $(\bar{t}_{f,M})_k^o$, $(\bar{t}_{f,M-1})_k^o, \ldots, (\bar{t}_{f,1})_k^o$. Equations 6.3.31, 6.3.29 and 6.3.28 should be solved iteratively because the thermal conductivity and the gas gap conductance depend on unknown temperatures. However, RAMONA-3B iterates only to account for the temperature dependence of the gas gap conductance, not for that of the thermal conductivity. The iteration for the outer-most interior fuel temperature* is discontinued when two successive iterates are within 0.1°C.

It should be pointed out that the initial cladding surface temperatures are computed in two subroutines, namely in SUBROUTINE TEPLO, FORTRAN listing Lines CLADD 71 through 79 and in SUBROUTINE FUNCSS, FORTRAN listing Lines DRAM3 954 through 956 and 964 through 966. It is recommended that for future code improvements an unambiguous computation of the cladding surface temperature is assured.

6.6.3 Steady-State Coolant Hydraulics

Listed in Section 4.5 are the equations which govern the steady-state flow-conditions in the vessel, in the recirculation loops and in the steam

*Actually, RAMONA-3B computes the initial fuel surface temperature which is not needed since it is not a state variable.

lines. These equations are of the form of Eq. 6.6.3, the most general form of nonlinear equations.

Within the overall systems calculation of steady-state conditions, the steady-state coolant conditions are computed from the specified total mass flow rate W^o_{CI} through the core,* from the specified recirculation mass flow rate W^o_{RCL}, from specified feedwater temperature t^o_{FW}, from the specified system pressure $\langle P \rangle^o_{syst}$, from the specified core inlet subcooling temperature $(\Delta t_\ell)^o_{CI}$, from the specified mixture level L^o_{LVD} and from the current iterate (or initially guess) of the axial heating rate $[q'_w(z)]^o$.

The vapor mass flow rate in the steam line is computed from Eq. 4.4.198, as the total thermal power is also known. The feedwater mass flow rate W^o_{FW} is then computed from Eqs. 4.4.197.

For the computation of steady-state coolant conditions in the reactor vessel, one must distinguish between the methods used for the core with its parallel flow channels and the methods used elsewhere in the vessel. The computations are started by seeking the conditions at the downcomer entrance and by computing the flow parameters along the flow path, up to the core entrance.

Next, the flow parameters in the core are computed such that all parallel flow channels have the same pressure difference between upper and lower plenum. Finally, the flow parameters are computed above the core.

Outside the core, the mixture mass flow rate W^o_m and the mixture enthalpy flow rates $(hW)^o_m$ are known and constant. Upstream of the feedwater injection elevation the mixture mass flow rate is

$$(W_m)^o_k = W^o_{CI} - W^o_{FW} \qquad 2 \le k < \eta = \omega \tag{6.6.33}$$

Downstream of this elevation it is

$$(W_m)^o_k = W^o_{CI} . \qquad \eta_{FW} \le k < \eta_{CI} \tag{6.6.34}$$

The vapor mass flow rate $(W_g)^o_{DCI}$ at the downcomer entrance is computed from Eq. 4.4.161, the vapor void fraction α^o_{DCI} at the same location from Eq. 4.4.165. By virtue of Assumption (4-xxii), the liquid is at saturation when entering the downcomer. Whence

*If the jet pump and recirculation loop models are not used, an alternate option permits to specify instead the jet pump pressure difference.

$$(W_f)^o_{DCI} = W^o_{CI} - W^o_{FW} - (W_g)^o_{DCI} \qquad (6.6.35)$$

and

$$(hW_m)_k = h_f(W_f)^o_{DCI} + h_g(W_g)^o_{DCI} \quad , \qquad \text{for } 2 \le k < n_{FW} \qquad (6.6.36)$$

$$(hW_m)_k = h_f(W_f)^o_{DCI} + h_{FW}\, W^o_{FW} + h_g(W_g)^o_{DCI}, \quad \text{for } n_{FW} \le k < n_{CI} \; . \qquad (6.6.37)$$

A marching procedure is used, starting with k=2 at the downcomer entrance and proceeding with increasing index k, to compute ten flow parameters from ten coupled equations. The ten parameters are the phasic mass flow rates $(W_g)^o_k$ and $(W_\ell)^o_k$, the phasic velocities $(w_g)^o_k$ and $(w_\ell)^o_k$, the temperature $(t_\ell)^o_k$, density $(\rho_\ell)^o_k$ and enthalpy $(h_\ell)^o_k$ of the liquid, the vapor void fraction α^o_k, the slip ratio S^o_k and the vapor generation rate $(\Gamma_v)^o_k = (\Gamma_{ph})^o_k$. The ten equations are

$$(W_g)^o_k + (W_\ell)^o_k = (W_m)^o_k \quad , \qquad k = 2,\ldots,n_{CI} - 1 \qquad (6.6.38)$$

$$(W_g)^o_k = \rho_g(\alpha w_g A)^o_k \qquad (6.6.39)$$

$$(W_\ell)^o_k = \left[(1-\alpha)\rho_\ell\, w_\ell\, A\right]^o_k \qquad (6.6.40)$$

$$(w_g)^o_k = (Sw_\ell)^o_k + (w^o)_k \qquad (6.6.41)$$

$$(W_g)^o_k = (W_g)^o_{k-1} + \Delta V_k \langle\Gamma_v\rangle_k, \quad (W_g)^o_1 = (W_g)^o_{DCI} \qquad (6.6.42)$$

$$\left[(hW)_m\right]^o_k = h_g(W_g)^o_k + (h_\ell W_\ell)^o_k \qquad (6.6.43)$$

plus the constitutive equations for slip $S(\alpha,\langle p\rangle^o_{syst}$ (see Section 4.4.2.4), for vapor generation rate Γ_{ph} $(\alpha,\langle p\rangle^o_{syst}$, $t_\ell)$, Eq. 4.4.57, and for properties of the liquid phase, Eqs. 4.4.76 and 4.4.77 with the relation $h_\ell = u_\ell + \langle p\rangle_{syst}/\rho_\ell$. Notice that ρ_g and h_g are computed from the specified system pressure $\langle p\rangle^o_{syst}$, Eqs 4.4.71 and 4.4.75 and the relation $h_g = u_g + \langle p\rangle_{syst}/\rho_g$. Also w^o in Eq. 6.3.41 denotes not only a steady-state velocity but the user-specified, fixed vapor velocity relative to stagnant liquid (see Section 4.4.2.4).

RAMONA-3B computes α^o_k, S^o_k, $(w_g)^o_k$, $(w_\ell)^o_k$ and $(W_\ell)^o$ in an inner iteration of successive substitutions on Eqs. (6.6.38), (6.6.39), (6.6.40), (6.6.41) and the slip correlation $S(\alpha,\langle p\rangle^o_{syst})$. The remaining five unknown parameters are computed in an outer iteration, involving the other five equations, except Eq. (4.4.76) since the variation of liquid density with temperature is ignored. The outer iteration involves a linear extrapolation relative to liquid temperature for the vapor generation rate Γ_{ph} from Eq. (4.4.57). The iteration at each location z_k is started from upstream values as initial guesses.

To compute the flow parameters for steady-state conditions in each of the parallel core flow channels, the total mass flow rate W^o_{CI} is at first divided into the channel flows (W^o_j), proportionately to the respective flow cross-sectional areas A_j. Then the same ten flow parameters are computed as for the flow upstream of the core, by a slightly modified procedure to account for the heating effects. This is explained below. After the flow parameters are established, RAMONA-3B computes the pressure difference across the core, in accordance with Eq. 4.4.97 where $d\langle G_m\rangle_i/d\tau$ is set equal to zero. Once the pressure differences $\Delta p^o_j = (p^o_{CE} - p^o_{CI})_j, j=1,\ldots,N_c$ are computed, RAMONA-3B corrects iteratively all mass flow rates until all pressure differences are equal and $\Sigma(W^o_j) = W^o_{CI}$. This is achieved in the primary iteration loop:

$$\left.\begin{aligned} (W^o_j)^{n+1}_p &= (W^o_j)^n + \frac{\partial W^o_j}{\partial \Delta p^o_j}\left[\frac{\sum_{j=1}^{N_c}(\Delta p^o_j)^n}{N_c} - (\Delta p^o_j)^n\right] \\ (W^o_j)^{n+1} &= (W^o_j)^{n+1}_p \frac{N_c\, W^o_{CI}}{\sum_{j=1}^{N_c}(W^o_j)_p}, \\ & n = 0,1,\ldots \end{aligned}\right\} \qquad (6.6.44)$$

The partial derivative in the first of Eqs. 6.6.44 is obtained by numerical differentiation of Eq. 4.4.97 with $d\langle G_m\rangle_i/d\tau = 0$.

Nested into the primary iteration loop is the secondary iteration loop to compute in each channel and in each axial subdivision the temperature $(t_\ell)^o_{kj}$ of the liquid and the evaporation rate $(\Gamma_v)^o_{kj}$. This is done with the procedure as used outside of the core, except that the right-hand side of Eq. 6.4.31, set equal to zero, replaces Eq. 6.6.43 and that Γ_v is computed from Eqs. 4.4.51, 4.4.56 and 4.4.57. The iterations are started with values from upstream cells; they are carried out by starting from the core entrance and marching toward the core exit.

Nested within the secondary iteration loop is the tertiary iteration loop to compute void fraction α°, phasic velocities $(w_g)^o_{kj}$, $(w_\ell)^o_{kj}$, phasic mass flow rates $(W_g)^o_{kj}$ and $(W_\ell)^o_{kj}$ and slip S° through the same equation set as listed above for the flow upstream of the core.

All the iterations on void fraction, coolant temperature and vapor generation rate are terminated when their new iterant is within 0.1% of the previous iterant. The iteration for the core channel flows is terminated when the square bracket in the first of Eqs. 6.6.44 is within 0.1% of the mean pressure drop across the core.

After having computed the flow parameters in all core channels, RAMONA-3B proceeds to obtain the steady-state conditions in the upper plenum, riser

and steam separators, using the same procedure as for the flow upstream of the core. The user-specified mixture level L_{LVD} of the low-void mixture in the steam dome and the vapor void fraction $\alpha^{\circ}_{LVD} = \alpha^{\circ}_{DCI}$ (cf. Assumption [(4-xxiii)] according to Eq. 4.4.165 determine the conditions in the steam dome since the liquid is assumed to be at saturation conditions [cf. Assumption (4-xxii)].

With the flow conditions established in the vessel, the pressure drops are computed outside the core and added to the core pressure drop to obtain the pressure rise across the jet pump. The pressure drops are computed from Eq. 4.4.97 with $d\langle G_m\rangle_i/d\tau = 0$. The computed pressure rise across the jet pump is used to find the jet pump diffuser impedance Z_{DIF} (Eq. 4.4.136). The initial steady-state calculations for the vessel are completed, after all the convergence criteria of the overall systems iterations are met, by computing the initial primary state variables from their definitions:

$$(m_g)^{\circ}_k = \Delta V_L \rho^{\circ}_g \alpha^{\circ}_k \qquad k = 2,\ldots, N_{CEL} \tag{6.6.45}$$

$$(u_m\rho_m)^{\circ}_k = \Delta V_L \left\{\rho_g u_g \alpha_k + [\rho_\ell u_\ell (1-\alpha)]_k\right\}^{\circ} \tag{6.6.46}$$

$$(M_g)^{\circ}_{syst} = \sum_{k=2}^{N_{CEL}} (m_g)^{\circ}_k + (M_g)^{\circ}_{LVD} + \rho^{\circ}_g \left[\Delta V_1 - (AL)_{LVD}\right] \tag{6.6.47}$$

$$(\overline{uM})^{\circ}_{syst} = \sum_{k=1}^{N_{CEL}} (u_m\rho_m)^{\circ}_k \Delta V_k \tag{6.6.48}$$

$$(M_g)^{\circ}_{LVD} = A_{LVD} L_{LVD} \alpha^{\circ}_{LVD} \rho^{\circ}_g \tag{6.6.49}$$

and $\mathcal{M}^{\circ}_j$, j=1,...,N, from Eq. 4.4.99. As $\langle p\rangle^{\circ}_{syst}$, the initial system pressure is user-specified, all vessel-related primary fluid state variables are herewith initialized.

For the recirculation flow the initial mass flow rate W°_{RCL}, the initial recirculation pump pressure rise Δp_{RCP} and the initial pump speed ω°_{RCP} are specified by the user. RAMONA-3B computes the recirculation loop impedance Z_{RCL} from Eq. 4.4.132 and the recirculation pump characteristic C in Eq. 4.4.139.

The initial steady-state conditions in the steam line are computed from the specified system pressure $\langle p\rangle^{\circ}_{syst}$ in the steam dome and from the mass flow rate, W°_{SL}/N_{SL}, where N_{SL} is the number of parallel steam lines. Since the bypass and safety and relief valves are closed, the mass flow rate is constant along the steam line and zero elsewhere. The initial pressure distribution is defined from Eqs. 6.4.52 and 6.4.54 by setting $dW_j/d\tau = 0, j=1,\ldots, M_2$. Setting equal to zero the right-hand sides of these equations yields

$$X_j + \gamma_j X_j^{-1/\kappa} - X_{j-1} = 0$$

$$j = 1,\ldots, M_2 \qquad (6.6.50)$$

where

$$X_j = \frac{(p_j)^o}{<p>^o_{syst}} \quad , \quad X_o = 1, \qquad (6.6.51)$$

and

$$\gamma_1 = \frac{\Delta L_1 (W^o_{SL})^2 \left[f_1 + \frac{2d_1}{\Delta L_1}(1+\zeta_c+\zeta_1)\right]}{2d_1 (N_{SL}A_1)^2 \rho_o <p>^o_{syst}} \qquad (6.6.52)$$

$$\gamma_j = \frac{\Delta L_j (W^o_{SL})^2 \left[f_1 + \frac{d_j}{\Delta L_j}\zeta_j\right]}{2d_j (N_{SL}A_j)^2 \rho_o <p>^o_{syst}} \quad j = 2,\ldots, M_2 \qquad (6.6.53)$$

are constants. The unknown $X_j, j=2,\ldots,M_2$, is computed from the following Newton-Raphson iteration scheme, starting with j=1 and X_o from Eq. 6.6.51.

$$X_j^o = X_{j-1}$$

$$X_j^{k+1} = X_j^k + \frac{X_{j-1} - X_j^k - \gamma_j (X_j^k)^{-1/\kappa}}{1 - (\gamma_j/\kappa)(X_j^k)^{-(\kappa+1)/\kappa}}$$

$$k = 1,2,\ldots, k_e. \qquad (6.6.54)$$

The iteration for node j is terminated, when $k=k_e$ for

$$|X_j^{k_e} - X_j^{k_e-1}| < 10^{-10}$$

Since $X_j<1$ always. Then $X_j = X_j^k e$ and the procedure is applied to the next node j+1. After all the $X_j, j=1^J,\ldots,M_2$, are computed, the initial pressures are given by (see Fig.6.4)

$$\left.\begin{aligned} p_j^o &= \langle p\rangle_{syst}^o X_j \quad , \; j = 1,\ldots, M_2 \\ p_j^o &= p_{M1}^o \quad , \; j = M_2 + 1,\ldots, (M_2+N_c) \end{aligned}\right\} \tag{6.6.55}$$

since the pressure in the bypass line is uniform and equal to the pressure in the pipe branch to the bypass. Thus, all the initial conditions are established for the steam lines.

The initial conditions for the boron concentration are

$$(\bar{c}_B)_k = 0 \quad , \quad k = 1,\ldots, N_B \tag{6.6.56}$$

This completes the presentation of the methods for computing the steady-state initial conditions. Recall that the initial conditions as obtained from the overall systems iteration, involving neutron kinetics calculations, thermal conduction calculations and thermohydraulics calculations, are used for starting a transient calculation with fixed operating conditions. This pseudo-transient is started with a negative time and continued until time zero. Its purpose is to relax numerically the differences between the governing equations for steady state and for transient calculations.

6.7 Integration Techniques for Transients

In this section we present first the different methods used in RAMONA-3B for computing the transients, namely the methods for integrating the systems of Eqs. 6.5.1 and 6.5.2. After having described the individual integration methods in Section 6.7.1 for neutron kinetics, in Section 6.7.2 for thermal conduction Eqs. 6.5.2 and in Section 6.7.3 for the ordinary differential equations of coolant dynamics Eqs. 6.5.1, we explain in Section 6.7.4 the synchronization of these techniques for the overall systems integration.

6.7.1 Solution Techniques for Neutron Kinetics

The transient finite difference equations for neutron kinetics have been derived by means of a box integration procedure in space and an implicit differencing in time. They are summarized in Section 6.5.1. The solutions of these equations at a given time step also require a double iteration loop: an inner iteration to solve the fast flux Eq. 6.2.89 and an outer iteration to account for the thermohydraulic feedback.

6.7.1.1 Inner Iteration

For the inner iteration, RAMONA-3B employs the Gauss-Seidel iteration scheme, augmented by an acceleration technique of relaxation, to solve Eq. 6.2.89. The Gauss-Seidel method uses the most recent iterates of the fast flux surrounding a node to compute the fast flux at the node (i,k,j):

$$\psi_{i,j,k}^{(n)} = p_{i,j,k}\left[\psi_{i-1,j,k}^{(n)} + \psi_{i+1,j,k}^{(n-1)} + \psi_{i,j-1,k}^{(n)} + \psi_{i,j+1,k}^{(n-1)}\right.$$

$$\left. + R\left(\psi_{i,j,k-1}^{(n)} + \psi_{i,j,k+1}^{(n-1)}\right)\right] + S_{i,j,k} \qquad (6.7.1)$$

where the superscript (n) denotes the inner iteration index, and we have dropped the time step indices n and n+1 to avoid confusion. Since the inner iteration is done at every time step, there is no loss of validity in suppressing the time step index here.

The Gauss-Seidel iteration scheme is applied to all nodes in a double loop, an outer loop that sweeps all the radial nodes (channels) and an inner loop that sweeps axially along each radial channel.

The inner iteration is terminated if the following convergence test is satisfied for all nodes:

$$\left|\psi_{i,j,k}^{(n)} - \psi_{i,j,k}^{(n-1)}\right| < \varepsilon_4 \bar{\psi}^{(n-1)} \qquad (6.7.2)$$

where ε_4 is the convergence criterion required as an input (called DPJ) and $\bar{\psi}(n-1)$ is the core-average ψ at the previous iteration defined as

$$\bar{\psi}^{(n)} = \frac{1}{NEND} \sum_{i,j,k} \psi_{i,j,k}^{(n-1)} \qquad (6.7.3)$$

with NEND = IMAX * JMAX * KMAX, the total number of neutronic nodes in the core.

In Section 6.6.1 we have shown that the Gauss-Seidel iteration scheme at the steady-state has good convergence properties. In the transient case, the matrix equation to be solved takes the form:

$$\underline{\underline{A}}\,\underline{\psi} = \underline{S} \tag{6.7.4}$$

where $\underline{\underline{A}}$ is also a tri-diagonal coefficient matrix with its diagonal elements now depending on the time step size. Thus, the convergence properties for transients are generally not as good as those at the steady state, depending upon the time step size chosen. Clearly, there is a need for a powerful acceleration technique to speed up the Gauss-Seidel iteration.

Two methods are available in RAMONA-3B for speeding up the inner iteration. The first method attempts to adjust only the flux level via a renormalization factor, $\Omega^{(n)}$ (Fadeeva 1959):

$$\tilde{\psi}^{(n)}_{i,j,k} = \psi^{(n)}_{i,j,k}\,(1+\Omega^{(n)}) \tag{6.7.5}$$

where

$$\Omega^{(n)} = \left(\frac{E'_n}{1 - E'_n}\right) \cdot \frac{\bar{\psi}^{(n)} - \bar{\psi}^{(n-1)}}{\bar{\psi}^{(n-2)}}\,, \tag{6.7.6}$$

with

$$E'_n = \frac{E_n}{|E_n|} \min\,(|E_n|,\ 0.96), \tag{6.7.7}$$

and

$$E_n = \frac{\bar{\psi}^{(n)} - \bar{\psi}^{(n-1)}}{\bar{\psi}^{(n-1)} - \bar{\psi}^{(n-2)}}\,. \tag{6.7.8}$$

Here all the average $\bar{\psi}$'s are defined similarly as Eq. 6.7.3.

The second method attempts to not only adjust the flux level but also correct the flux residual, and hence is more efficient than the first method. In this method, two iteration algorithms are used:

$$\tilde{\psi}^{(n)}_{i,j,k} = \psi^{(n)}_{i,j,k} + \omega \left(\psi^{(n)}_{i,j,k} - \psi^{(n-1)}_{i,j,k} \right) \tag{6.7.8}$$

$$\tilde{\psi}^{(n)}_{i,j,k} = \omega_1 \, \psi^{(n)}_{i,j,k} + \omega_2 \left(\psi^{(n)}_{i,j,k} - \psi^{(n-1)}_{i,j,k} \right) , \tag{6.7.9}$$

where ω, ω_1 and ω_2 are the relaxation parameters. Note that the two iteration algorithms are not used at the same time. Typically, the simple relaxation 6.7.8 is applied first for a few iterations, then the second algorithm 6.7.9 is applied once, and the cycle repeats again until the convergence test is met.

The relaxation parameters are determined in RAMONA-3B by minimizing, in a least square sense, the function $J^{(n)}$:

$$J^{(n)} = \left(\underline{\underline{A}} \, \underline{\psi}^{(n)} - \underline{S} \right)^T \left(\underline{\underline{A}} \, \underline{\psi}^{(n)} - \underline{S} \right) . \tag{6.7.10}$$

This leads to the following formulas for the relaxation parameters:

$$\omega = (b_2 - a_{12})/a_{22} , \tag{6.7.11}$$

$$\omega_1 = (b_1 \, a_{22} - b_2 \, a_{12})/(a_{11} \, a_{22} - a_{21} \, a_{12}) , \tag{6.7.12}$$

$$\omega_2 = (b_1 \, a_{21} - b_2 \, a_{11})/(a_{12} \, a_{21} - a_{22} \, a_{11}) , \tag{6.7.13}$$

where

$$a_{11} = \left(\underline{\psi}^{(n)} \right)^T \underline{\underline{A}}^T \, \underline{\underline{A}} \, \underline{\psi}^{(n)} , \tag{6.7.14}$$

$$a_{12} = \left(\underline{\psi}^{(n)} - \underline{\psi}^{(n-2)}\right)^T \underline{\underline{A}}^T \underline{\underline{A}}\, \underline{\psi}^{(n)} \quad , \tag{6.7.15}$$

$$a_{21} = \left(\underline{\psi}^{(n)}\right)^T \underline{\underline{A}}^T \underline{\underline{A}} \left(\underline{\psi}^{(n)} - \underline{\psi}^{(n-2}\right) = a_{12} \quad , \tag{6.7.16}$$

$$a_{22} = \left(\underline{\psi}^{(n)} - \underline{\psi}^{(n-2)}\right)^T \underline{\underline{A}}^T \underline{\underline{A}} \left(\underline{\psi}^{(n)} - \underline{\psi}^{(n-2)}\right) , \tag{6.7.17}$$

$$b_1 = \underline{S}^T \underline{\underline{A}}\, \underline{\psi}^{(n)} \quad , \tag{6.7.18}$$

$$b_2 = \underline{S}^T \underline{\underline{A}} \left(\underline{\psi}^{(n)} - \underline{\psi}^{(n-2)}\right) \quad . \tag{6.7.19}$$

We see that, in order to compute these relaxation parameters, it is neceesary to do two Gauss-Seidel iterations. One iteration starts at the top of the matrix Eq. 6.7.3 and goes to the bottom. The second iteration starts at the bottom and goes to the top.

The choice between the two acceleration methods is made through the input parameter called IOPT(10). If IOPT(10) = 0, the old method as given by Eq. 6.7.4 is used. If IOPT(10) = 1, the new method as described by Eqs. 6.7.8 and 6.7.9 is employed. The number of Gauss-Seidel iterations to be applied per the relaxation scheme (6.7.8) is also specified by an input quantity called IOPT(9).

6.7.1.2 Outer Iteration (Time Step Control)

The outer iteration attempts to account for the effects of thermohydraulic feedback on neutron kinetics not strictly in an iterative sense. Rather, the transient neutron kinetics equations are resolved only if the changes in the neutron fluxes due to the thermohydraulic feedback are significant enough with respect to some accuracy criterion. In this sense, the outer iteration is intimately related to the time step control logics for neutron kinetics in RAMONA-3B. In fact the outer iteration (or the time step control) is designed to establish a proper coupling between neutron kinetics and thermohydraulics during a transient.

As stated in Section 2.1 of Chapter 2, a tandem strategy is usually used to establish such a coupling. The tandem strategy is based on a predictor-corrector procedure as follows.

(1) Assuming that all the neutron kinetic and thermohydraulic variables have been determined and accepted at time step n, we first predict to the next time step n+1:

   (a) the fast flux (ψ's) from the subroutine F1DYN,

   (b) the average thermal flux from the subroutine F2DYN,

   (c) the fuel temperature and heat transfer to the coolant from the subroutine TFDYN, and

   (d) the fission rate and the average volumetric heat generation rates in the coolant.

(2) We now linearly allocate the power to coolant for each hydraulic (time) step between the neutron kinetic steps n and n+1. (This is necessary because the hydraulic step is, in general, smaller than the neutron kinetic step due to the explicit time differencing used for hydraulics.) Using the linearly interpolated volumetric heat generation rates, we then solve the hydraulic equations at each hydraulic step until it catches up with the neutron kinetic step at n+1.

(3) Using the new hydraulic properties at the step n+1, we determine the new two-group parameters (including the control rod movement, if any) and correct the fast flux (ψ's) by resolving the fast flux equation using the subroutine F1DYN.

(4) Check if the corrected fast flux vector $\underline{\psi}^{corr}$ satisfies the following acceptance (accuracy) criterion with respect to the predicted fast flux vector $\underline{\psi}^{pred}$:

$$\left| \frac{\bar{\psi}^{pred}}{\bar{\psi}^{corr}} - 1 \right| < \varepsilon_5 \quad , \tag{6.7.20}$$

where

$$\bar{\psi}^{pred} = \frac{1}{NEND} \sum_{i,j,k} \psi^{pred}_{i,j,k} = AVGP \quad , \tag{6.7.21}$$

$$\bar{\psi}^{corr} = \frac{1}{NEND} \sum_{i,j,k} \psi^{corr}_{i,j,k} = AVGF \quad , \tag{6.7.22}$$

with NEMD being the total number of neutronic nodes.

The parameter ε_5 is related to an input quantity called ACCF. It should be pointed out that the accuracy test (6.7.20) is an oversimplification of the more complicated tests actually implemented in RAMONA-3B (see Fig. 6.1) where the average difference $\Delta\overline{\psi}$ is also used:

$$\Delta\overline{\psi} = \frac{1}{NEND} \sum_{i,j,k} \left| \psi^{corr}_{i,j,k} - \psi^{pred}_{i,j,k} \right| = SUMDF \quad . \qquad (6.7.23)$$

If the accuracy test is not satisfied, go to step (6); otherwise, go to step (5).

(5) Accept the predicted and corrected results and march to the next neutron kinetic step n+2, and so on.

(6) Reduce the neutron kinetic time step size and repeat the steps (1) through (4) until the accuracy test is passed.

Figure 6.5 illustrates the flow diagram of the neutron kinetic time step control procedure used in RAMONA-3B. In this flow chart H and HT are the present and previous time step sizes, respectively, NS is the inner iteration counter, ACCF is the (input) convergence criterion and IPMAX is the (input) maximum number of inner iterations. Upon a close examination we can see that this time step control procedure is very cautious in advancing time and too hasty in cutting back the time step. This is probably conservative for very severe power excursions such as a rod drop accident. It may be too inefficient for most anticipated transients of interest to RAMONA-3B. We have revised the original time step control logic so as to advance the transient time more rapidly, especially for relatively slow transients. This is illustrated in Fig. 6.6. Limited experience to date has shown that it does indeed speed up the time advancing and hence reduce the computer time.

6.7.2 Solution Techniques for Transient Thermal Conduction in Fuel and Cladding

The transient conduction equations for the temperature distribution in fuel pellet and fuel cladding are presented in Section 6.3 as Eqs. 6.3.38. The dimension of the vector $\underset{\sim}{t}$ of mean cell temperatures varies between four and seven. Equations 6.3.38 are implicit nonlinear (because of the temperature dependencies of thermal conductivity and gap conductance) equations of the form of Eqs. 6.5.3.

RAMONA-3B is programmed to solve the (at most) seven equations in two nested procedures, one for the four fuel pellet equations, the other for the three cladding equations.

The procedure for the fuel pellet temperature is a predictor-corrector iteration, during which the inner-most cladding temperature remains fixed. The predictor $\underset{\sim}{t}_p$ is computed directly from Eq. 6.3.83

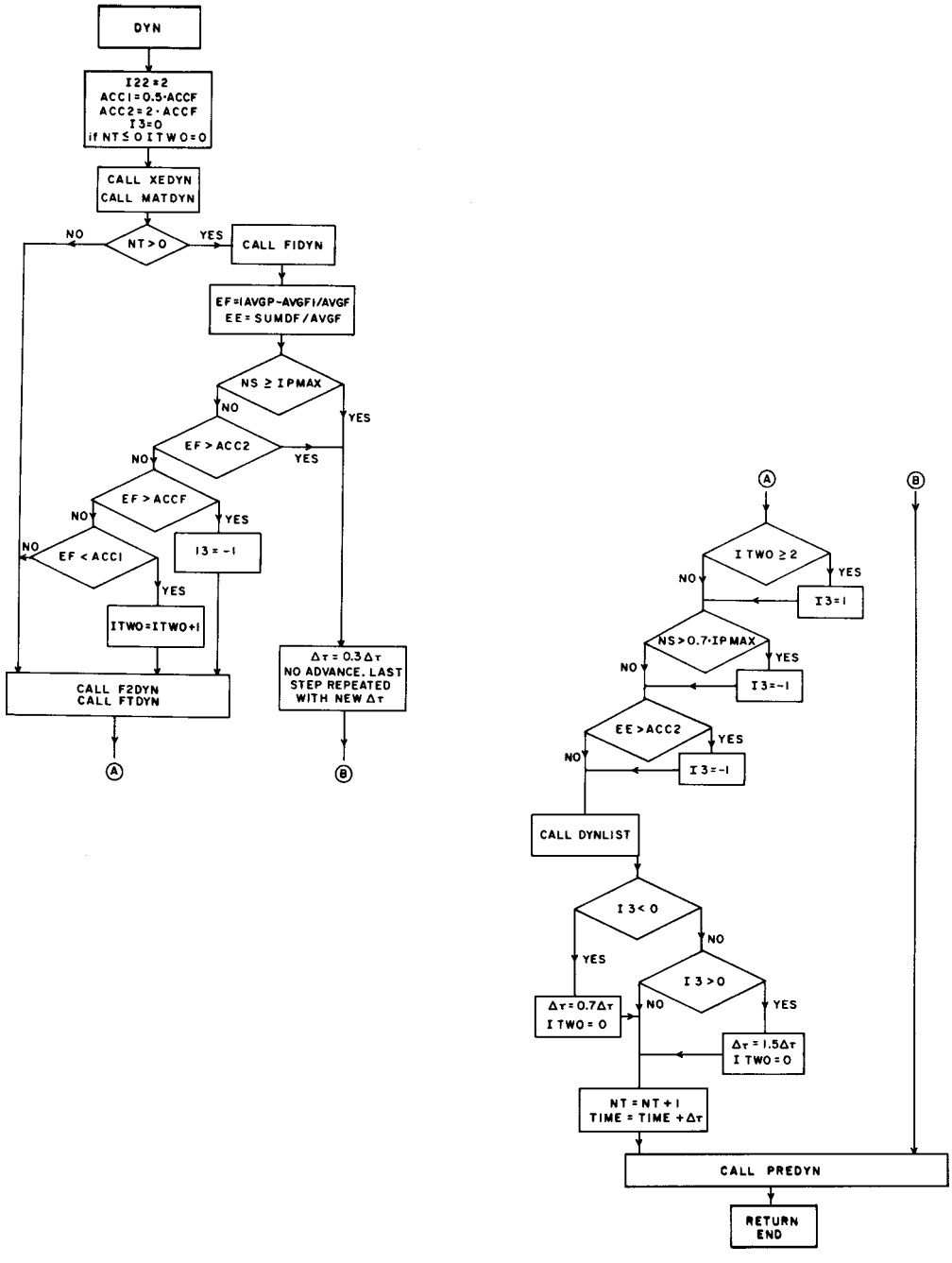

Fig. 6.5 RAMONA-3B Time Step Control Diagram for Neutron Kinetics.

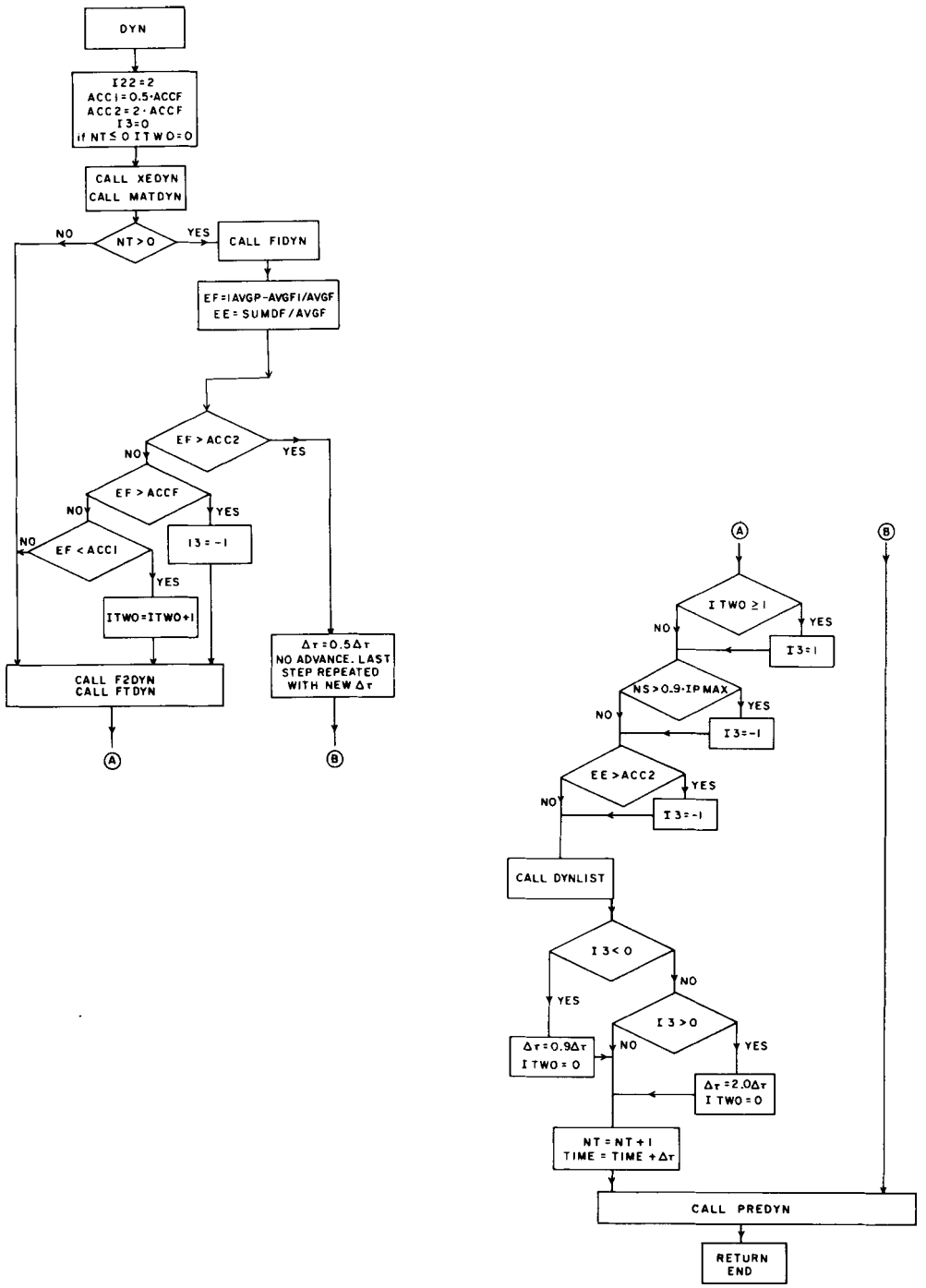

Fig. 6.6 Diagram for Revised Time Step Control of Neutron Kinetics.

$$\left(\bar{t}_{f,i}^{k+1}\right)_p = \left(\bar{t}_{f,i}^{k}\right)_p + \Delta\tau\, F_{f,i}^{k}$$

$$k = 0.1,\ldots,j, \quad i = 1,\ldots,M \tag{6.7.24}$$

The predictor is used to compute the properties k_f and k_{gp} and to compute the corrector $\underset{\sim}{\bar{t}}_f$. By inspection of Eqs. 6.3.27, 28 and 29 one can observe the vector function $\underset{\sim}{F}$ in Eqs. 6.3.38 is a linear combination of neighboring temperatures $\bar{t}_{f,i-1}$, $\bar{t}_{f,i}$ and $\bar{t}_{f,i+1}$, where $\bar{t}_{f,M+1}$ is replaced by $t_{c,i}$. The linear combination is of this form:

$$F_i = a_i + b_i\, \bar{t}_{f,i-1} + c_i\, \bar{t}_{f,i} + d_i\, \bar{t}_{f,i+1}, \quad i = 1,\ldots,M . \tag{6.7.25}$$

After substituting predictor temperatures $(\bar{t}_{f,i-1})_p$ and $(\bar{t}_{f,i+1})_p$ into Eqs. 6.7.25 after evaluating the coefficients $a_i,\ldots,d_i$ with the predictor temperatures $(t_f)_p$ and then substituting the result in to Eqs. 6.3.38 one can solve Eqs. 6.3.38 for the corrector temperature

$$\bar{t}_i^{k+1} = \frac{\Delta\tau\left[a_i + b_i\, \bar{t}_{f,i-1} + d_i\, \bar{t}_{f,i+1}\right]_p^{k+1}}{\left[1 + \Delta\tau\left(c_i^{k+1}\right)_p\right]}, \quad i = 1,\ldots,M . \tag{6.7.26}$$

The coefficients $a_i,\ldots,d_i$ can be identified by inspection from Eqs. 6.3.27, 28 and 29. The corrector values are substituted into Eq. 6.7.24 to repeat the cycle. The cycle is discontinued for $k=k_e$ when

$$\left| \bar{t}_{f,M}^{k_e} - \bar{t}_{f,M}^{k_e-1} \right| < 10^{-4}\, \bar{t}_{f,M}^{k_e} . \tag{6.7.27}$$

Nested within the above procedure for computing the fuel pellet temperature is the iterative procedure for solving the nonlinear system of three equations for the fuel cladding temperature. The system of equations is not linear even though the heat capacity and the thermal conductivity of the cladding material are assumed in RAMONA-3B to be constant and the gas gap conductance is kept fixed during this procedure. The temperature dependence of the convective heat transfer coefficient $\bar{h}_c$ in Eq. 6.3.33 renders the system of equations nonlinear. The fluid temperature t_{f_ℓ} (cf. Eq. 6.3.33) is kept constant during the conduction calculations.

The three equations, Eqs. 6.3.31, 32, and 33 are solved iteratively by successive substitution (cf. Eqs. 3.3.38). Because of the non-linear dependence

of the convective heat transfer $\bar{h}_c$ on the surface temperature $t_c(R_{co}) = t_w$, a linear extrapolation estimate for t_w is used to reduce the number of necessary iterations. The estimate is computed from a set of equations in RAMONA-3B, equivalent* to Eqs. 6.3.34 and the correlations for $\bar{h}_c$ given in Section 4.4.2.1.2. The successive substitution procedure is terminated when

$$\left| \bar{t}^{k}_{c,N} - t^{k-1}_{c,N} \right| < 10^{-6}\, \bar{t}^{k}_{c,N} \quad . \tag{6.7.28}$$

The procedure of Eq. 6.7.24 is conditionally stable, the procedure of Eq. 6.7.26 is stable. Whether the overall-procedure (Eqs. 6.7.24 and 26) for the pellet temperature and the combination of pellet and cladding temperature calculations is unconditionally stable, cannot be said with certainty as there is no known stability criterion for this procedure.

For future code improvements, it is recommended to use a single procedure for fuel pellet and cladding temperature calculations, to assess the need for three computational zones in the fuel cladding, to simplify the entire formulation algebraically before programming and, specifically, to solve the two linear equations for fuel cladding temperatures $\bar{t}_{c,1}$ and $\bar{t}_{c,2}$, analytically in terms of $\bar{t}_{c,3}$ and $t_{f,M}$.

6.7.3 Solution Techniques for Transient Thermohydraulics in Coolant System and Steam Line

The summary in Table 6.2 shows that the state equations for coolant dynamics, steam line dynamics and boron transport are of the form of Eqs. 6.5.1:

$$\left.\begin{aligned} \frac{d\underset{\sim}{y}}{d\tau} &= \underset{\sim}{F}\,(\underset{\sim}{y},\tau) \\ 0 &= \underset{\sim}{F}\,(\underset{\sim}{y}_0,0) \end{aligned}\right\} \quad . \tag{6.5.1}$$

The specific equations have been summarized in Section 6.4.1.1 Eqs. 6.4.9, 10, 11, 12, 13, 14 and 15, in Section 6.4.1.3, Eqs. 6.4.25 and 31, in Section 6.4.2.2, Eqs. 6.4.52, 53 and 56 through 60 and in Section 6.4.3.2, Eqs. 6.4.78.

*The actual procedure in RAMONA-3B involves several equations because they have not been simplified to the form of Eq. 6.3.34.

The first-order, explicit Euler method is used to integrate the equations of Sections 6.4.1.1, 6.4.1.3 and 6.4.3.2. The fourth-order explicit Runge-Kutta method is used for simulating the steam line dynamics (equations in Section 6.4.2.2). The Euler integration is carried out in two distinct procedures, one for all the coolant dynamics (equations in Sections 6.4.1.1 and 6.4.1.3), the other for the transport of boron Eqs. 6.4.78, using a separate time step control.

6.7.3.1 The Explicit First-Order Euler Method

The explicit first-order Euler method* is the primary integration method in RAMONA-3B for simulating coolant thermohydraulics.

6.7.3.1.1 General Features of Euler Integration

The method is used to integrate Eqs. 6.5.1 and consists of

$$\underset{\sim}{y}^{n+1} = \underset{\sim}{y}^{n} + \Delta\tau\, \underset{\sim}{F}\,(\underset{\sim}{y}^{n},\tau^{n}), \qquad n = 0,1,\ldots, \tag{6.7.29}$$

where $\Delta\tau$ is the integration step size and $\underset{\sim}{y}^{n}$ is the approximation to $\underset{\sim}{y}(\tau^{n})$. The first-order Euler method has the advantage of requiring the least computational effort per integration step and the least amount of memory when compared to any other numerical integration method. The method, has, however, the lowest boundary for induced instability, the instability caused by the integration algorithm, rather than by Eqs. 6.5.1, as the integration step $\Delta\tau$ is increased. It has the lowest computing accuracy and it need not have the least requirement of overall computing efforts.

Stability. The eigenvalues $\tilde{\lambda}_i, i=1,\ldots,I$, of the algorithm defined by Eqs. 6.7.29 for I-dimensional vectors $\underset{\sim}{y}$ and $\underset{\sim}{f}$ are related to the eigenvalues $\tilde{\sigma}_i, i=1,\ldots,I$, of the Jacobian J_{ij} of $\underset{\sim}{F}$ in Eqs. 6.5.1, namely to

$$J_{ij} = \frac{\partial F_i}{\partial y_j}, \qquad i,j = 1,\ldots,I \tag{6.7.30}$$

by

$$\tilde{\lambda}_i = 1 + (\Delta\tau)\,\tilde{\sigma}_i\ . \tag{6.7.31}$$

Stability of the algorithm, Eq. 6.7.29, requires (Lomax 1968, p. 8) that

*Also called the Euler-Cauchy Method.

$$\max_i |\tilde{\lambda}_i| = \max_i |1 + (\Delta\tau)\tilde{\sigma}_i| < 1 \qquad (6.7.32)$$

or, if there are no multiple eigenvalues $\lambda_i \neq \lambda_j$, $i \neq j$, that $\max|\lambda_i| \leq 1$. Since the eigenvalues σ_i are in general complex

$$\tilde{\sigma}_i = \bar{\sigma}_i e^{\sqrt{-1}\,\theta_i}, \quad 0 \leq \theta_i \leq \pi/2 \qquad (6.7.33)$$

and must have nonpositive real parts, $\bar{\sigma}_i < 0$, for physical reasons, it is clear that the Euler method has a real induced stability boundary of

$$|(\Delta\tau) \cdot \max_i \bar{\sigma}_i| < 2 , \qquad (6.7.34a)$$

while its imaginary induced instability boundary is zero. The complete induced instability boundary is

$$(\Delta\tau)\,|\bar{\sigma}_i| < 2 \cos\theta_i, \quad i = 1,\ldots,J. \qquad (6.7.34b)$$

This means that the Euler method is unstable for all $\Delta\tau$ if one of the eigenvalues of J_{ij} in Eq. 6.7.30 is purely imaginary.

Observe that the Jacobian J_{ij} must exist* in the entire integration interval, $0 < \tau^n < \tau_e$, that is, there must not be any discontinuities in state variables or constitutive equations. Discontinuities are permitted only in time-dependent boundary conditions.

Stability for $\Delta\tau \to 0$ implies consistency and convergence. An integration scheme for the ordinary differential equations in Eqs. 6.5.1 is consistent if its truncation errors $\underset{\sim}{e}_T$

$$\underset{\sim}{e}_T^n = \frac{\underset{\sim}{y}^{n+1} - \underset{\sim}{y}^n}{\Delta\tau} - \underset{\sim}{F}(\underset{\sim}{y}^n, \tau^n) , \quad n = 0,1,\ldots \qquad (6.7.35)$$

tend toward zero as $\Delta\tau \to 0$. The Euler scheme is consistent provided $\underset{\sim}{F}$ is evaluated with $\underset{\sim}{y}^n$ only, but without any components $\underset{\sim}{y}^{n-1}$ of y at the time level τ^{n-1}, i.e. without time-lagged variables. An integration scheme converges if its computational errors $\underset{\sim}{e}_C$

$$\underset{\sim}{e}_C^n = \underset{\sim}{y}^n - \underset{\sim}{y}(\tau^n) , \quad n = 0,1,\ldots \qquad (6.7.36)$$

*Actually, uniform Lipschitz continuity with respect to y is sufficient. The Euler-Cauchy scheme is not a two-step integration scheme involving y and F at two time levels.

tend toward zero as $\Delta\tau \to 0$. The Euler scheme converges, if

a) all variables in $\underset{\sim}{F}$ are evaluated from $\underset{\sim}{y}^n$ at time level τ^n and $\underset{\sim}{F}$ is Lipschitz continuous in $\underset{\sim}{y}$,

b) the initial error $\underset{\sim}{e}_C = \underset{\sim}{y} - \underset{\sim}{y}(o) \to 0$ as $\Delta\tau \to 0$, and

c) the round-off error $\underset{\sim}{e}_R \to 0$ as $\Delta\tau \to 0$

Items (b) and (c) are never satisfied with fixed word lengths in digital computers. However, the computational error $\underset{\sim}{e}_C$ does not increase with decreasing $\Delta\tau$ until

$$\Delta\tau < \Delta\tau_{min} = \sqrt{\frac{2\,\rho_c}{M_f}} \quad , \tag{6.7.37}$$

where ρ_c is the round-off error and M_F is the maximum magnitude of the second derivative of $\underset{\sim}{y}$ with respect to τ, namely

$$M_F = \underset{\tau^n}{\text{Max}} \left| \frac{\partial F_i}{\partial \tau} + \sum_{j=1}^{I} \frac{\partial F_i}{\partial y_j} F_j \right| . \tag{6.7.38}$$

The lower limit for $\Delta\tau$ in Eq. 6.7.37 is extremely low for the CDC 7600 computer ($\sim 10^{-8}$ seconds or less) and imposes no practical limits on the application of the Euler-Cauchy method. Item (a) is not safisfied in RAMONA-3B as will be discussed below.

Accuracy: The computational error is essentially proportional to the time step size $\Delta\tau$, if that $\Delta\tau$ is larger than $\Delta\tau_{min}$ in Eq. 6.7.37 and if Item (a) above is satisfied. The computational error has three parts. The first part stems from the errors in the initial data, $\underset{\sim}{e}_C$, the second from the truncation errors $\underset{\sim}{e}_T$ and third part stems from the round-off error. The condition $\overline{\sigma}_i < 0$, $i=1,2,\ldots,I$, guarantees that the initial error cannot grow. The contribution from the truncation errors $\underset{\sim}{e}_T$ is proportional to $\Delta\tau$, and that from the (unimportant) round-off error is proportional to $1/\Delta\tau$. An error estimate of the truncation error of a particular integration step is obtained from the Taylor series expansion, provided J_{ij} is continuous:

$$y_i^{n+1} = y_i^n + \Delta\tau\, F_i^n + \frac{(\Delta\tau)^2}{2} \left[\frac{\partial F_i}{\partial \tau} + \sum_{j=1}^{I} \frac{\partial F_i}{\partial y_j} F_j \right]^n + O(\Delta\tau)^3 . \tag{6.7.39}$$

The first two terms on the right-hand side are accounted for in Eqs. 6.7.29. The series is truncated after the second term. Thus the third term is the estimate of the truncation error contribution per integration step.

$$(\Delta\tau^n)(e_T^n)_i = \left[y(\tau^{n+1}) - y(\tau^n)\right] - F_i\left\{y_i(\tau^n),\tau^n\right\}(\Delta\tau^n)$$

$$\cong \frac{(\Delta\tau^n)^2}{2}\left[\frac{\partial F_i}{\partial\tau} + \sum_{j=1}^{I}\frac{\partial F_i}{\partial y_j}F_j\right]^n . \qquad (6.7.40)$$

6.7.3.1.2 Implementation of the Euler-Cauchy Method in RAMONA-3B for Coolant Hydraulics

After having established the general features of the Euler-Cauchy method, we proceed now to discuss its implementation in RAMONA-3B. The method is employed to integrate Eqs. 6.4.9 through 15, 6.4.25 and 31 for coolant dynamics and Eq. 6.4.78 for boron transport.

The implementation of the Euler-Cauchy method in RAMONA-3B does not satisfy the requirements of consistency, since at least the following variables are taken at time level τ^{n-1} instead of at time level τ^n as called for by Eqs. 6.7.29 (time-lagged variables):

density of the liquid, ρ_ℓ phasic velocities, W_f, W_g volumetric flow rates, Aj_m, Aj_g, Aj_ℓ	:	almost everywhere. heat transfer calculation, level tracking.

Thermodynamic properties, namely temperature and void fraction, at the riser inlet are estimated (for unknown reasons) by spatial extrapolations from upstream variables.

The error $y_i^n - y_i^{n-1}$ introduced by a time-lagged state variable y_i or a correlation is proportional to the integration step size $\Delta\tau$. The number of such errors produced during the integration from $\tau=0$ to $\tau=\tau_e$, with average $\overline{\Delta\tau}$ is $\tau_e/\overline{\Delta\tau}$. As a consequence, the accumulated effects from the truncation error* arising from these time-lagged variables does not decrease with decreasing time step $\Delta\tau$. Two successive calculations, carried out with different-size integration steps $\Delta\tau_1$, $\Delta\tau_2$, below some (unknown) step size, may produce the same result even though the numerical solution did not converge to the solution of Eqs. 6.5.1.

In most calculations with RAMONA-3B, the sensitivity of the results to the effects from time-lagged variables can be expected to be insignificant. However, the code user should be aware of the potential for computational

*The truncation error is a systematic error. Unlike the stochastic round-off error, the truncation error must be expected to accumulate and to increase with the number of integration steps in a calculation.

difficulties (involuntary stops) and inaccuracies, particularly when there are drastic changes expected (e.g., in flow rates during flashing or void collapse).

Consistency of Eqs. 6.7.29 is also compromised in RAMONA-3B by a large number of discontinuities in $\underset{\sim}{F}$ of Eqs. 6.5.1, caused by logical branches in the computer code, since not all of such branches have been programmed to maintain continuity. The total number of these discontinuities is not documented at this time. Any discontinuity in either a state variable y_i or in a correlation depending on state variables renders the Jacobian of Eqs. 6.5.1 (cf. Eqs. 6.7.30) non-existent at the discontinuity. As the time-step control in RAMONA-3B depends, both for accuracy and stability criteria, on the existence of the Jacobian J_{ij}, there may be time steps in the integration procedure where the time-step control fails.

The integration step size (time step size) $\Delta\tau$ is controlled in RAMONA-3B with the aim to assure stability and accuracy by setting

$$\Delta\tau^{n+1} = \text{Min } (\Delta\tau_S, \Delta\tau_A)^n, \tag{6.7.41}$$

where $\Delta\tau_S$ and $\Delta\tau_A$ satisfy, respectively, the stability and accuracy criteria.

Stability Criterion in RAMONA-3B. Equation 6.7.35a is used instead of Eq. 6.7.35 to compute $(\Delta\tau)_S$. As J_{ij} in Eq. 6.7.30 is nonsymmetric, at least some eigenvalues σ_i are complex. RAMONA-3B ignores the imaginary parts of all eigenvalues. This means that even though the dominant eigenvalue, say $\tilde{\sigma}_1$, is real* and larger in magnitude than the real parts of all the other eigenvalues, some the real parts of other pairs of complex conjugate eigenvalues $\tilde{\sigma}_i$, $\tilde{\sigma}_j$; i,j=2,...,I may fail Eq. 6.7.35 with the integration step computed from Eq. 6.7.35a by using $\tilde{\sigma}_1$.

Moreover, the dominant eigenvalue is not computed from the complete Jacobian J_{ij} (cf. Eq. 6.7.30) of the system of Eqs. 6.7.29, because of prohibitive computing costs. Instead, the Jacobian is first reduced by judiciously setting equal to zero all its off-diagonal terms which are deemed to be small. This reduction eliminates imaginary parts of eigenvalues and permits the decomposition of J_{ij} into two square matrices S_{ij} and L_{ij}, both centered on the diagonal, two diagonal terms and blocks or rows and columns of zeroes everywhere else. The reader must be warned that this decomposition, documented in a proprietary report by Bech (1970), is based to a large extend on unsupported beliefs by Bech and on two special test cases, which were carried out in a code version of 1970 and produced one not fully understood result.

The square matrix S_{ij} represents the subsystem of momentum balances, Eqs. 6.4.15, of the total system, Eqs. 6.5.1. Its dominant eigenvalue (σ) is computed by the power method (see Isaacson and Keller 1966, p. 147).

*This is true because the elements of J_{ij} are real.

The second square matrix, L_{ij}, represents the sets of Eqs. 6.4.25 and 6.4.31 for vapor mass* and mixture energy in each computational cell, except in the vapor dome. Of this system, the equations of two computational cells in the core are selected, all others are ignored. For each of the selected cells, a separate square matrix of rank 2 is formed from the respective vapor mass and mixture energy balance equations. The corresponding four eigenvalues $(\sigma_i)_{VM}$, $(\sigma_i)_{ME}$, i=1,2 are computed from two quadratic equations. The chosen computational cells are the cell (1) with the largest diagonal element in the row corresponding to its mixture energy balance and the cell (2) which has also the largest diagonal element in the row corresponding to its mixture energy balance but which does not lie in the same channel as cell 1.

The two single diagonal elements left in the reduced matrix are for the pressure equation, Eq. 6.4.9, and for the mass balance of the vapor in the low-void regime of the steam dome, Eq. 6.4.12. The diagonal element of J_{ij} in the row corresponding to Eq. 6.4.9 is computed by numerical differentiation of the right-hand side of Eq. 6.4.9, with respect to $\langle p \rangle_{syst}$. The result is set equal to the eigenvalue $(\sigma)_{\langle p \rangle}$. The eigenvalue of Eq. 6.4.12 for the vapor mass below the mixture level in the steam dome is ignored, as are the effects of Eqs. 6.4.10, 11, 13 and 14 on stability. These equations were not included in the original (unreduced) Jacobian.

The largest of the five eigenvalues $(\sigma)_{\mathcal{M}}$, $(\sigma_1)_{VM}$, $(\sigma_1)_{ME}$, $(\sigma_2)_{VM}$, $(\sigma_2)_{ME}$ and $(\sigma)_{\langle p \rangle}$ is used to evaluate the stability limit $(\Delta\tau)_S$ of the integration step by Eq. 6.7.34. The above eigenvalues are not computed for every integration step, instead they are multiplied by the ratio of corresponding diagonal elements $(J_{jj})^n/(J_{jj})^{n-1}$ as long as successive diagonal elements $(J_{jj})^{n-1}$, $(J_{jj})^n$ change less than 5% in magnitude for one step.

It can be said that the stability criterion implemented in RAMONA-3B for integrating the hydraulics equations works most of the time, but that it cannot be expected to work every time. Every code modification introduces new uncertainties even when such modifications satisfy the requirements of consistency, convergence and stability.

Accuracy Criterion in RAMONA-3B. The second time increment, $(\Delta\tau)_A$, in Eq. 6.7.41 is computed to produce the desirable accuracy of the numerical solution. $(2N_c+3)$ elements of the state variable vector, namely

$\langle p \rangle_{syst}$,	the system pressure,
$(m_g)_{FW}$,	the vapor mass in the computational cell with feedwater injection,
$(\rho_m u_m)_{FW}$,	the internal energy density in the cell with feedwater injection,
$\mathcal{M}_j, j=1,\ldots N_c$,	the loop momentum for all the N_c core flow channels, and
$(\rho_m u_m)_{nCE,j}$, $j=1,\ldots,N_c$	the internal energy densities in all core exit cells,

*The report by N. Bech shows mixture mass instead of vapor mass, as is used in RAMONA-3B.

are selected in RAMONA-3B to control the effect of the local (single time-step) truncation error, defined earlier in Eq. 6.7.40. RAMONA-3B is programmed to approximate the square bracket in Eq. 6.7.40 by

$$\frac{\partial F_i}{\partial \tau} + \sum_{j=1}^{I} \frac{\partial F_i}{\partial y_j} F_j = \frac{dF_i}{d\tau} \approx \frac{F_i^n - F_i^{n-1}}{(\Delta\tau)^n} . \tag{6.7.42}$$

Substituting this approximation into Eq. 6.7.40 yields the local truncation error contribution

$$(\Delta\tau^n)(e_T^n)_i \approx \frac{\Delta\tau}{2} (F_i^n - F_i^{n-1}) . \tag{6.7.43}$$

This error for the computation of the variable y^{n+1} from its previous value y_i^n is normalized by y_i^{n+1} to yield the relative error

$$\varepsilon_i^n = \left| \frac{\Delta\tau(F_i^n - F^{n-1})}{2y_i^{n+1}} \right| . \tag{6.7.44}$$

The accuracy-related integration step $\Delta\tau_A$ is computed from

$$\Delta\tau_A^n = 0.8\ (\Delta\tau^n)\sqrt{\frac{\bar{\varepsilon}}{\varepsilon_i^n}} \tag{6.7.45}$$

and used, along with $\Delta\tau_S^n$ from the stability criterion, to compute the next time step $\Delta\tau^{n+1}$ according to Eq. 6.7.41. The integration is continued if

$$\varepsilon_i^n \leq \bar{\varepsilon} \tag{6.7.46}$$

or else, the last integration step is repeated with the rejected step size used in Eq. 6.7.45. (This step size reduction appears to have no relation to the accuracy improvement expected from the step size reduction.) The symbol $\bar{\varepsilon}$ in Eq. 6.7.46 is a user-specified* error limit which applies to all the $(2N_c+3)$ variables listed above.

Notice that the error definition in Eqs. 6.7.43 and 44 relates to the control of the growth rate of the variable rather than to the control of the truncation error (cf. Isaacson and Keller 1966, Eq. 16 on p. 372). While it is possible to control and reduce the effects from truncation errors by means of Eq. 6.7.45, it is not possible to relate the error of the computed variable y_i^n at τ^n to the magnitude of the user-specified limit $\bar{\varepsilon}$*, since the evaluation of $dF_i/d\tau$ from Eq. 6.7.42 is itself affected by the truncation $(\varepsilon_T^{n-1})_i$.

*RAMONA-3B is being executed with $\bar{\varepsilon} = 10^{-3}$.

For future code improvements it appears desirable to have separate error limits for key variables. Specifically, an error of 0.1% in system pressure may be 5% of the total change in pressure during a transient and may have far greater consequences than a 0.1%-error in loop momentum $\mathcal{M}_j$ or vapor mass in a computational cell. It is also recommended that available standard, well established integration packages for stiff systems of ordinary differential equations be considered for replacing the first-order Euler method in RAMONA-3B, particularly since experience has shown that during transients the low accuracy limitation of this method predominantly dictates the integration step size. Special attention should be paid to efficient rational error controls.

6.7.3.1.3 Euler-Cauchy Integration for Boron Transport

The integration step size for the boron transport simulation is an integer fraction of the step size for the coolant dynamics simulation, $\Delta\tau_B = \Delta\tau_H/N$, where subscripts B and H denote boron and hydraulics calculations, respectively.

To maintain computational stability, the dominant eigenvalue λ_i of Eqs. 6.7.29*, ignoring the effects of time delay (cf. Eq. 6.4.79b, time delays have only stabilizing effects), is computed by the power method (Isaacson and Keller 1966, p. 147). Then the criterion of Eq. 6.7.34a is applied to correct the step size $\Delta\tau_B$ if necessary. Notice that this method does not guarantee stability since stability requires the condition of Eq. 6.7.35. This method may work most of the time but cannot be expected to assure stability all the time. Incidentally, the stability check is applied only at selected integration steps to save computing time.

To control computing errors for the boron transport equation, RAMONA-3B is programmed to compute the relative truncation error estimate

$$\left| \frac{(e_T^n)_i}{F_i^n} \right| = \left| \frac{F_i^n - F_i^{n-1}}{N \cdot F_i^n} \right|_B = (\varepsilon_B^n)_i \qquad (6.7.47)$$

where n indicates time levels of the hydraulics integration prior to the integration of boron transport calculation.

If $|F_i^n|_B > 1$ and $(\varepsilon_B^n)_i > 0.05$ then $\Delta\tau_B^{n+1} = \frac{1}{2}\Delta\tau_B^n$.

If $|F_i^n|_B > 1$ and $0.004 < \varepsilon_B^n \leq 0.05$ then $\Delta\tau_B^{n+1} = \frac{2}{3}\Delta\tau_B^n$.

*The matrix $\underset{\approx}{A}$ in $\underset{\sim}{c}^{n+1} = \underset{\approx}{A}\underset{\sim}{c}_B^n$ is not symmetric but real. Its dominant eigenvalue is real.

$$\text{If} \quad |F_i^n|_B > 1 \quad \text{and} \quad 0.001 < \varepsilon_B^n \leq 0.004 \quad \text{then} \quad \Delta\tau_B^{n+1} = \frac{\Delta\tau_B^n}{0.7} .$$

IF $|F_i^n|_B < 1$ then ε_B^n in Eq. 6.7.47 is replaced by $(\varepsilon_B^n)_i F_i^n$ and the above three criteria are used to continue the integration. This last procedure implies that the absolute value of the truncation error is used as long as the rate of concentration change is less than one per second (probably most of the time), and the relative error of the concentration is very high near steady state conditions.

It is recommended that standard methods be implied in future improved code versions for integrating the boron transport equation (Roache 1972, Chapter 3).

6.7.3.2 The Explicit Fourth-Order Runge-Kutta Integration Method

The Runge-Kutta method with Simpson-Integration for automatic integration step size control via user-specified relative and absolute integration error limits is used in RAMONA-3B to integrate the acoustics equations, Eqs. 6.4.52, 54, and 56 through 60 for the steam in the steam lines.

6.7.3.2.1 General Features of the Runge-Kutta Method

The fourth-order Runge-Kutta integration method employed in RAMONA-3B is (see Isaacson and Keller 1966, p. 402, fourth entry of Table 2)

$$\left.\begin{aligned} y^{n+1} &= y + \frac{1}{6}(K_1 + 2K_2 + 2K_3 + K_4) \\ \text{where} \\ K_1 &= \Delta\tau\, F\{y^n, \tau^n\} \\ K_2 &= \Delta\tau\, F\{y^n + \tfrac{1}{2}K_1, \tau^n + \tfrac{1}{2}\Delta\tau\} \\ K_3 &= \Delta\tau\, F\{y^n + \tfrac{1}{2}K_2, \tau^n + \tfrac{1}{2}\Delta\tau\} \\ K_4 &= \Delta\tau\, F\{y^n + K_3, \tau^n + \Delta\tau\}, \end{aligned}\right\} \qquad (6.7.48)$$

and $\underset{\sim}{F}$ is defined by Eqs. 6.5.1, the equations to be integrated. This method requires four evaluations of $\underset{\sim}{F}$ for every integration step and it requires at least five memory cells in the computer for every differential equation. However, the method is stable for

$$\Delta\tau|\bar{\sigma}_j| \lesssim 2.8, \tag{6.7.49}$$

and this induced instability boundary is essentially constant for all the complex parts (phase angles θ) of the eigenvalues σ_j of the Jacobian J_{ij} in Eqs. 6.7.30.

The method in Eqs. 6.7.48 requires Lipschitz continuity of the vector function $\underset{\sim}{F}$ in Eqs. 6.5.1, with respect to $\underset{\sim}{y}$, in the infinite strip $0 \leq \tau \leq \tau_e$ and $|y| < \infty$, to ascertain consistency, convergence and stability*. Consequently, there must not be any discontinuities in state variables or correlations for the simulation of the steam line dynamics, except for the discontinuities from boundary conditions (valve actions etc.)

The overall computing accuracy for the algorithm in Eqs. 6.7.39 increases with the fourth power of the decreasing time step $\Delta\tau$ [the error per time step is proportional to $(\Delta\tau)^5$], if $\underset{\sim}{F}$ has continuous fifth-order derivatives. The method is of first-order accuracy at selected instances τ^n, where $\underset{\sim}{F}$ is only Lipschitz-continuous as a result of discontinuities in the first derivatives, for example, for transition from laminar to turbulent flows, cf. Eqs. 4.4.188 and 189. The algorithm used in RAMONA-3B is in principle capable of integrating discontinuous $\underset{\sim}{F}$-functions but this option is not required for the steam line dynamics, since all valve actions are controlled to be continuous.

6.7.3.2.2 Implementation of Runge-Kutta Method in RAMONA-3B

Since acoustical effects in coolant dynamics are eliminated by selective thermohydraulic modeling in RAMONA-3B, but included in the modeling of the steam line dynamics, it appeared necessary to integrate the equations of steam line dynamics with much smaller integration steps than the equations of vessel coolant dynamics. The established fourth-order Runge-Kutta-Simpson algorithm (Fendall 1961) implemented in RAMONA-3B has these four capabilities:

(a) The number I of differential equations is free, it requires twelve storage locations for each equation in order to afford (i) error control, (ii) restart capability at discrete arguments τ, where any f_j is discontinuous, and (iii) repetition of integration steps so that any selected argument τ_i, i=1,..., or any properly selected value for any of the solutions y_j (trip criterion) can be reached exactly during integration.

(b) The time step can be selected and fixed or it can be controlled by error criteria (see Item c below). The time step can also be controlled to reach any trip condition or any selected time for output listing.

*This requirement is necessary also to establish a unique solution to Eq. 6.5.1.

(c) The integration error per integration step can be maintained for every variable below the sum of a preselected absolute error limit, plus the product of the magnitude of the instantaneous solution times a preselected relative error limit. The integration step size is increased or decreased to meet the error criterion with the largest possible step size, provided the computing mode with variable step size is selected. The integration step control also affords numerical stability.

(d) The integrating algorithm can be restarted at every discontinuity in $\underset{\sim}{F}$ of Eqs. 6.5.1 with a single control parameter (this capability was not required in the RAMONA-3B application).

These features guarantee that the numerical solution satisfies the Eqs. 6.5.1 with any desirable accuracy. It must be pointed out, however, that all subsidiary computations in $\underset{\sim}{F}$, including iterations (Eqs. 6.4.65 and 68) must have greater precision than the desired overall accuracy of Eqs. 6.7.48. The user must also realize that the error control for Eqs. 6.7.48 is used to assure its stability. Extremely lax error controls may lead to instability before they reduce the integration step size. However, in the steam line simulation the step size has to be controlled by computing accuracy. This has been established as part of RAMONA-3B applications: stability criteria are overruled by accuracy requirements.

Computing Accuracy and Integration Step Size Control

The time step is controlled within the integration algorithm itself (subroutine RKS) to meet the computing accuracy and stability criteria and also in the BNL steam line code section which controls output listing and terminates the integration (subroutine CNTRL).

The accuracy and stability criteria are satisfied by performing every integration step in two half-steps, using the conventional Runge-Kutta method, to obtain mid-point values of the derivatives. These are used, along with the derivatives at the initial and end points, to execute Simpson's rule over the full step. The magnitude $|d_j|$ of the difference between Runge-Kutta integration over two half-steps and the Simpson integration over the full step is used as the basis for controlling the integration step.

Let a_j and r_j represent the user-specified absolute and relative error bounds of the variable $y_j, j=1,\ldots,I$. After completion of an integration step, the ratios

$$R_j = \left| \frac{d_j}{a_j + r_j |y_j|} \right| \quad ; \; j = 1, \ldots, I \tag{6.7.50}$$

are formed and their maximum R_m is determined. Then, the integration step $\Delta\tau$ is reduced, left unchanged or increased according to the following table:

If $1 \leq R_m$ then $\Delta\tau$ is divided by $(\sqrt[5]{10R_m})$,

if $0.75 \leq R_m < 1.0$, then $\Delta\tau$ is divided by $\sqrt[5]{10}$,

if $0.0075 \leq R_m < 0.075$, then $\Delta\tau$ is left unaltered ,

if $R_m < 0.075$, then $\Delta\tau$ is multiplied by $\sqrt[5]{10}$.

The integration is continued after modification of the step size, except when $R \geq 1$ in which case the last step is repeated. The integration is terminated prematurely whenever $R_m > 10^9$, and the equation with the largest discrepancy R_m is identified.

The steam line module in RAMONA-3B has been satisfactorily executed (three reliable digits in mass flow rate) with

	relative error limit	absolute error limit
pressure	10^{-3}	1000 N/m^2
mass flow rate	10^{-3}	10^{-3} kg/s

The computing time increases with the fifth root of the number of reliable digits. The computing time per step with fixed step size is half of the computing time with automatic control. For a given accuracy requirement, however, the computing time is generally less with variable step size than with fixed step size, unless one knows beforehand the optimum variation of step sizes in the entire range $0 \leq \tau \leq \tau_e$ of integration.

It may be possible to select a more efficient integration algorithm [predictor corrector methods, Gear method (Gear 1966, etc.)] for future code improvements, i.e. an algorithm which requires less computing effort, tolerable storage requirements, but which has also a rational error control.

6.7.4 Coupling of Integration Schemes in RAMONA-3B

In this section we describe the interphasing of the five autonomous integration schemes for

(1) neutron kinetics
(2) thermal conduction in fuel elements
(3) thermohydraulics of coolant in vessel and recirculation loops
(4) steam line dynamics
(5) transport of boron

which have been presented in Sections 6.7.1, 2 and 3. Even though the procedures for Items (3) and (5) are the same in principle, they are programmed separately in RAMONA-3B, they differ in stability and error control criteria

and they employ different integration step sizes. Therefore they are considered separately.

Figure 6.7 is the schematic of the integration cycle. Entering from steady-state calculations at the top of the diagram, the computations continue through this cycle until the simulation is completed (or some cut-off condition is encountered) at the time $\tau = \tau_e$, and the computations terminate as shown at the right bottom corner of Figure 6.7.

At first, the neutron kinetics variables are predicted for the time level $\tau^n + \Delta\tau$, n=0,1,..., with all thermohydraulic parameters and fuel temperatures at time level τ^n. Here, $\Delta\tau$ is the master integration step size. The neutron kinetics calculations embody the master clock [Procedure (1)].

Secondly, the fuel pellet and cladding temperatures are advanced from time level τ^n to the level $\tau^n + \Delta\tau$, in one step, by using all thermohydraulic parameters at time level τ^n and the heat generation rates at time level τ^{n+1}, as predicted in the first step. This calculation yields an estimate of temperatures and wall heat fluxes in the time interval $\tau^n < \tau < \tau^n + \Delta\tau$, by linear interpolation with respect to time [Procedure (2)].

Thirdly, the thermohydraulics parameters for the coolant in the pressure vessel and in the recirculation loop are advanced from time level τ^n ,n=0,..., to the time level $\tau^n + \Delta\tau_H$, where the step size $\Delta\tau_H < \Delta\tau$ is determined by stability and accuracy criteria of Procedure (3).

Fourthly, the steam line dynamics variables are advanced to the time level $(\tau^n + \Delta\tau_H)$, using the system pressure $\langle p \rangle_{syst}$ at time level $(\tau^n + \Delta\tau_H)$. This advancement is carried with as many integration substeps as are required by the error criteria in the Runge-Kutta-Simpson procedure (cf. Section 6.7.3.2.2). The time level $(\tau^n + \Delta\tau_H)$ is reached precisely by adjusting the last substep size. The integration is performed with the steam line boundary conditions computed at every substep. The integration produces the vapor mass flow rate at the steam line entrance, a boundary condition for the pressure vessel, at the time level $(\tau^n + \Delta\tau_H)$ [Procedure (4)].

Fifthly, the boron concentration is computed for the time level $(\tau^n + \Delta\tau_H)$, using either a single integration step or several steps as required by the accuracy and stability criteria in the boron transport Procedure (5).

The third, fourth and fifth steps are repeated until the time level $\tau^{n+1} = \tau^n + \Delta\tau$ is reached precisely by adjusting the last time step size $\Delta\tau_H$. Now, all variables in RAMONA-3B are at the same time level τ^n. The neutron kinetics calculations are repeated with the hydraulics parameters and fuel temperatures taken at the time level τ^{n+1}. The result is the corrector of neutron kinetics variables.

The entire procedure above, starting from the first step, is rejected if the corrector mean fast flux differs from the predictor mean fast flux by more than a specified limit, or if the mean difference of corrector and predictor fast fluxes exceeds a specified limit (see Figure 6.5 for details). If the procedure is rejected then it is repeated with $0.3\ \Delta\tau$. Otherwise, the

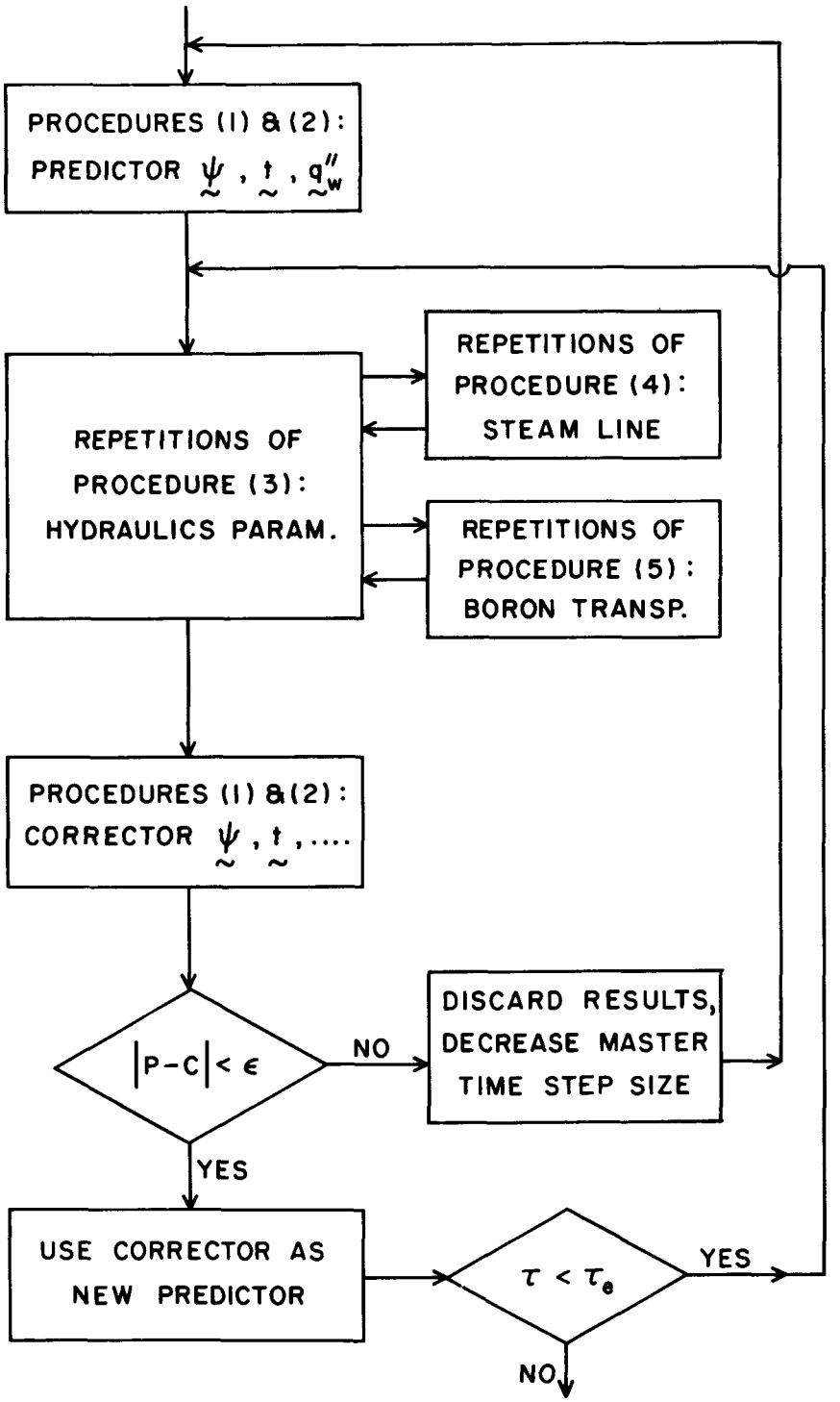

Fig. 6.7 Computational Cycle for Transients.

integration is continued by redefining the last corrector as the new predictor and starting at the second step above.

The integration terminates when the time τ exceeds the terminal time τ_e.

For future code improvements, it is recommended, that Procedure (2) be synchronized with Procedure (3) via a common time step. Thermal conduction in the fuel is always less tightly coupled to neutron kinetics than it is to the coolant hydraulics because the response time of the fuel pellet (receiving fission power) is much larger (≈ 10 s) than the response time of the fuel cladding (≈ 0.05 s) which reacts promptly to changes in coolant conditions (burnout, for example).

6.8 Relation Between Nodalization, Error Control and Computing Time

6.8.1 Scope

For a detailed system code with three-dimensional neutron kinetics capability such as RAMONA-3B, computing time and cost are of primary concern to the user in applications to realistic problems. The computing time depends, to a large extent, on the nodalization structure selected and the acceptance criteria used for the error control. Thus, a judicious choice of the nodalization structure and the error control criteria is essential for the economical and efficient applications of RAMONA-3B. In this section we shall discuss our limited experience to date in this regard which, we hope, would be useful for the potential user.

We have conducted a nodalization study for a three-dimensional problem of the Anticipated Transient With Half Scram (ATWHS) as well as a timing study for a one-dimensional problem of the Licensing Basis Transient (LBT). These studies are by no means sufficiently comprehensive to be of general applicability for the nodalization and timing studies which are generally problem-dependent. Nevertheless, they should serve as a useful guide for the user to apply to his specific problem of interest.

6.8.2 Nodalization Studies

The nodalization study was undertaken to find a simplified coarse-mesh representation for the three-dimensional core so that the ATWHS can be calculated by RAMONA-3B for ~ 15 min with a reasonable computing time (and cost) without undue sacrifice on the accuracy of the results. The nodalization study took advantage of the fact that the ATWHS is a half-core symmetric problem. The discussion in the following, therefore, assumes the half-core symmetry.

Typically, the 1 1/2-group, coarse-mesh, diffusion model employs a 6-in cube as the coarse-mesh node for neutron kinetics. This means one node per fuel bundle in the horizontal plane and 24 nodes in the axial directions. Such a core representation for neutron kinetics produces accurate results for BWRs using the 1 1/2-group diffusion model and serves as the reference case for the nodalization study. The thermohydraulic variables vary less drastically than the neutron flux in the core. Consequently, the nodalization structure for thermohydraulics is simpler than that for neutron kinetics. Typically, a thermohydraulic node may consist of a number of neutronic nodes. To avoid confusion, we shall use the word "channel" to denote the coarse-mesh nodes in the horizontal plane and use the word "node" or "plane" to designate the coarse-mesh nodes in the axial direction. Furthermore, we shall assume that the number of axial nodes is the same for both neutron kinetics and thermohydraulics. This assumption is also implied for the simplified cases to be discussed later.

For the reference case, we used 24 axial nodes for both neutron kinetics and thermohydraulics, and used 382 neutronic channels (fuel bundles), 49 hydraulic channels and one bypass channel for the half core of the Peach Bottom II BWR. Thus, there are a total of 432 channels for the reference case, which we may refer to as the 432-channel case.

Two cases of simplified nodalizations for neutron kinetics and thermohydraulics were considered. One case used 44 neutronic channels, 14 hydraulic channels, and one bypass channel for the half core. The other case used 16 neutronic channels, 6 hydraulic channels, and one bypass channel. Both cases used 12 axial nodes for both neutron kinetics and thermohydraulics. For ease of reference, we may refer to the two cases as the 59-channel and 23-channel cases, respectively. Table 6.3 summarizes the three cases calculated in the nodalization study.

Table 6.3 Cases of Nodalization Studies

	Number of Channels			Number of
	Neutronics	Hydraulics	Bypass	Axial Nodes
Reference Case	382	49	1	24
59 - Channel Case	44	14	1	12
23 - Channel Case	16	6	1	12

The ATWHS is initiated from an all-rod-out, full power, condition by a turbine trip without bypass with half of the control rods failing to scram on closure of the turbine inlet valve. We shall not dwell on the detail of the transient as it is described in detail in Chapter 7. Since the nodalization study was done only for the initial condition here. The essential initial conditions are summarized in Table 6.4.

Table 6.4 Initial Conditions for Nodalization Studies

Core Thermal Power (MWt)	3,440
Core Inlet Temperature (°C)	276
Total Core Inlet Flow Rate (Kg/s)	11,708
Core Bypass Flow Rate (Kg/s)	1,280
System Pressure (MPa)	7,246
Steam Flow Rate (Kg/s)	1,734
Feedwater Flow Rate (Kg/s)	1,734
Feedwater Temperature (°C)	196

Steady-state calculations were done with RAMONA-3B for the three cases of different nodalization structures. As discussed in Section 2.5, the boundary condition parameters for neutron kinetics depend on the nodal size. They were, therefore, determined separately for the three cases in accordance with their nodalization structures.

The adequacy of the simplified cases was judged with respect to the reference case in the effective multiplication factor (fundamental eigenvalue) and the power distributions for neutron kinetics and in the void profiles for thermohydraulics. The results are shown in Figs. 6.8 through 6.11. On the basis of these comparisons, we conclude that the 23-channel case is acceptable for the ATWHS analysis. It is recommended that the transient calculations be done for 2 seconds for both the reference and 23-channel cases to further confirm the acceptability of the simplified nodalization.

6.8.3 Timing Studies

The primary objective of the simplified nodalizations discussed in the previous section is to reduce the computing time for the ATWHS. Even for the 23-channel case, the computing time was estimated to be still eighty times the real time. This means that it would take roughly 20-hour CPU time of the CDC

114 111.9	113 111.0	111 109.3	104 109.9	89 88.7
113 111.0	112 110.2	110 108.0	105 107.7	84 84.6
111 109.3	110 108.0	106 104.9	111 98.6	66 66.8
104 109.9	105 107.9	111 98.8	74 75.0	
89 88.7	84 84.6	66 66.8	59 CHANNELS 432 CHANNELS	

K_{EFF} = 1.0053 59 CHANNELS

K_{EFF} = 0.9998 432 CHANNELS

Figure 6.8 Anticipated Transient with Half Scram Normalized Initial Radial Power Distribution, 59 Channels

114 111.3	111 108.9	100 97.3
111 108.9	101 105.4	80 80.4
100 97.4	80 80.4	23 CHANNELS 432 CHANNELS

K_{EFF} = 1.0082 23 CHANNELS

K_{EFF} = 0.9998 432 CHANNELS

Figure 6.9 Anticipated Transient with Half Scram Normalized Radial Power Distribution, 23 Channels

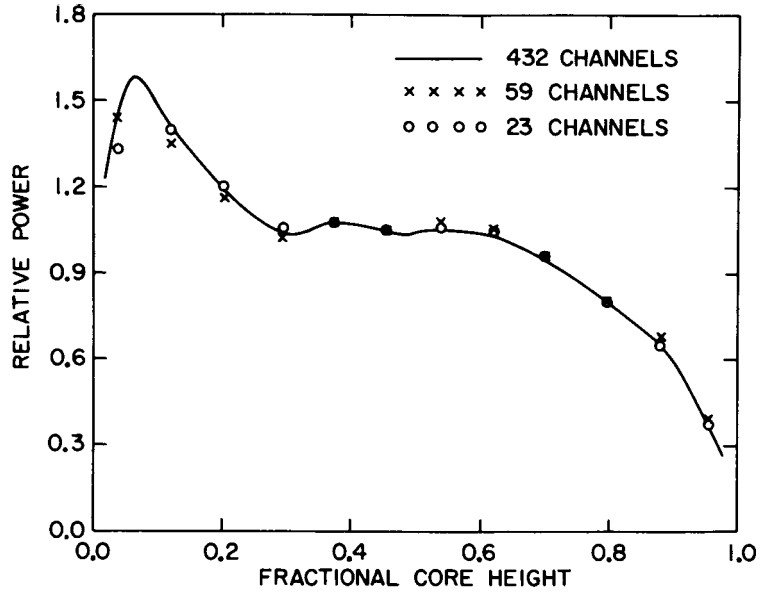

Figure 6.10 Axial Power Distributions

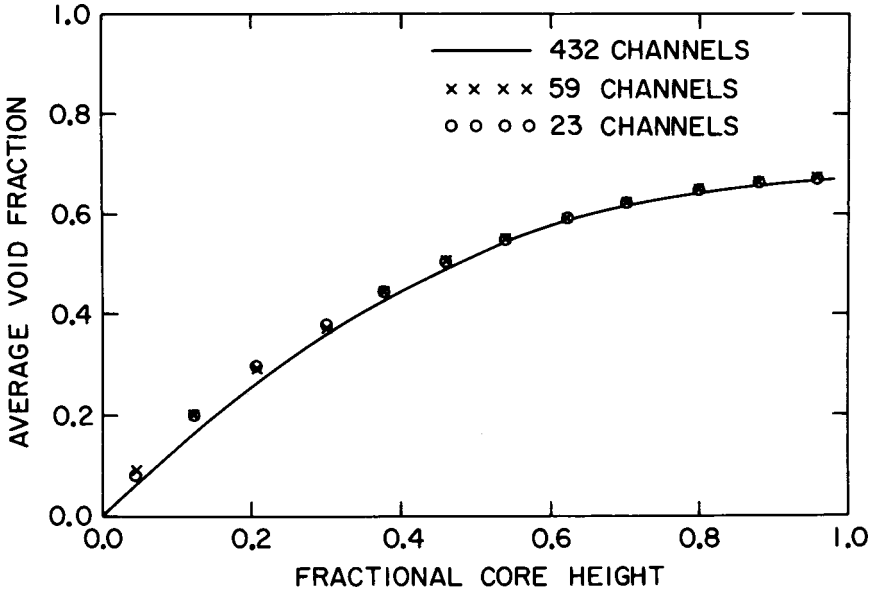

Figure 6.11 Average Void Profiles

7600 computer for the 15-min ATWHS. To further reduce the computing time for this transient, we made various timing studies regarding the neutron kinetics, vessel hydraulics, and steam line dynamics.

For the timing studies we selected the one-dimensional representation of the Licensing Basis Transient (LBT) in order to minimize the computing cost. This was thought justified because the findings would most likely be applicable to the more realistic three-dimensional representation of the transient. The LBT is a turbine trip event without steam bypass accompanied by a reactor scram on the turbine stop valve closure with a 0.27 s delay. It is, therefore, similar to the ATWHS except for the scram condition (i.e., full scram vs. half scram). The reactor is assumed to operate initially at 104.5% of the rated power and 100% of the rated flow at the end of cycle (EOC) with all control rods fully withdrawn. The initial conditions of the LBT are similar to those listed in Table 6.4.

All the calculations done in the timing studies used 24 axial nodes (for both neutron kinetics and thermohydraulics), a single neutronic channel, a single hydraulic channel, and a bypass channel. Feedwater flow and temperature were prescribed as the boundary condition. Steam lines were attached to the pressure vessel to couple the steam line dynamics to the vessel hydraulics. Thus, the steam flow and pressure were calculated rather than prescribed.

6.8.3.1 Steam Line Dynamics

The timing study regarding the steam line dynamics investigated the effect of steam line nodalization and error criteria on the computing time of RAMONA-3B. For the steam line nodalization, we used a 77-node representation (67 nodes in the main steam line and 10 nodes in the bypass line) as the reference case for comparison. A simplified nodalization (8 nodes in the main steam line and 2 nodes in the bypass line) was then tried as a potential candidate for reducing the computing time in steam line dynamics. The two cases were computed for 2 seconds with the original tight error control criteria (Wulff 1980) so that we can estimate the saving in the computing time due to the simplified steam line nodalization alone. The results are shown in Figs. 6.12 through 6.19. The close agreement between the two cases clearly demonstrates the adequacy of the simplified 10-node representation. The saving in the computing time by the 10-node representation is substantial as shown in Table 6.5. We recommend that the 10-node representation be used for the steam line dynamics calculation in RAMONA-3B.

For the timing study regarding the error criteria, we used the original built-in criteria as the standard for comparison because they are extra-ordinarily tight. The error control is concerned with both the absolute and relative errors of the pressure (p) and flow (W). As a first try, we relaxed the error criteria by a factor of 100 for both the pressure and flow (a relative error of 10^{-4} for p and 10^{-3} for W), and ran the 77- and 10-node cases, respectively. The results indicated that the relaxation of the error criteria reduces the computing time for the steam line dynamics by a factor of 2 for the 77-node case and 2.9 for the 10-node case. Yet, in both cases, a four-digit accuracy in steam line pressure and flow as well as the vessel

Figure 6.12

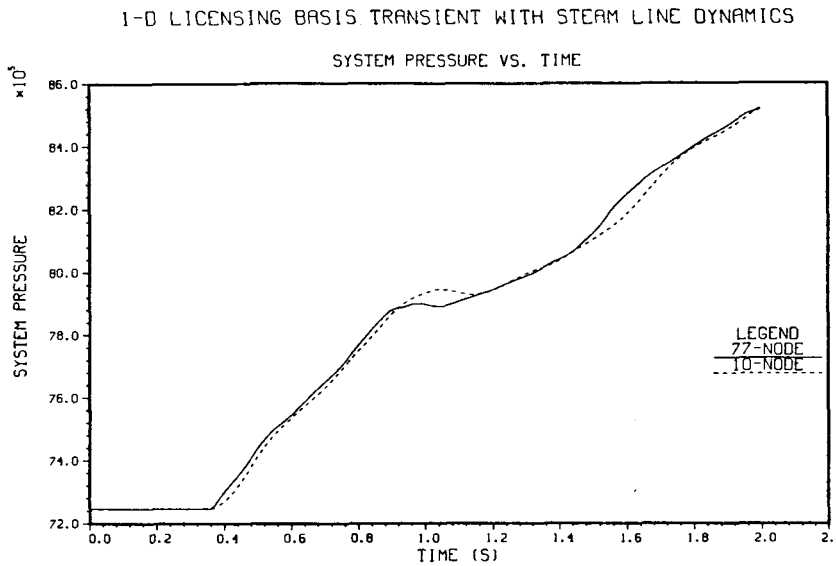

Figure 6.13

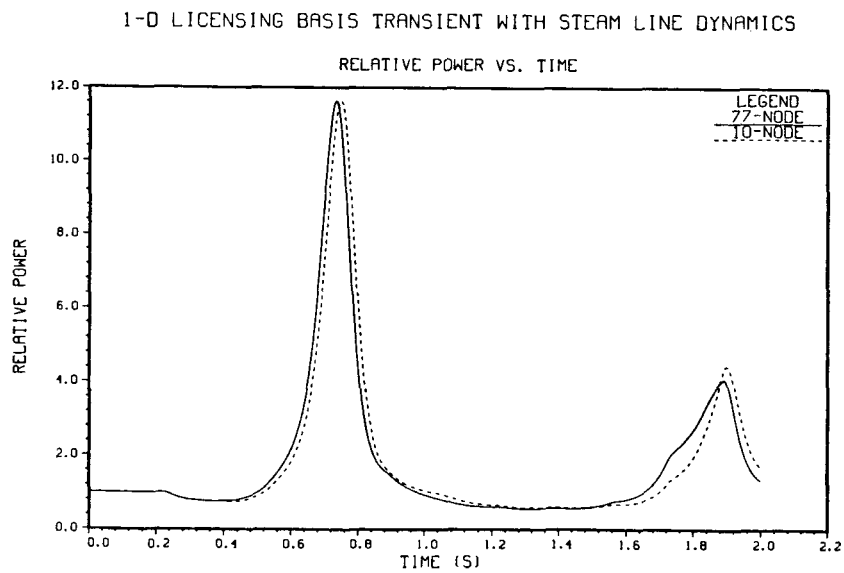

Figure 6.14

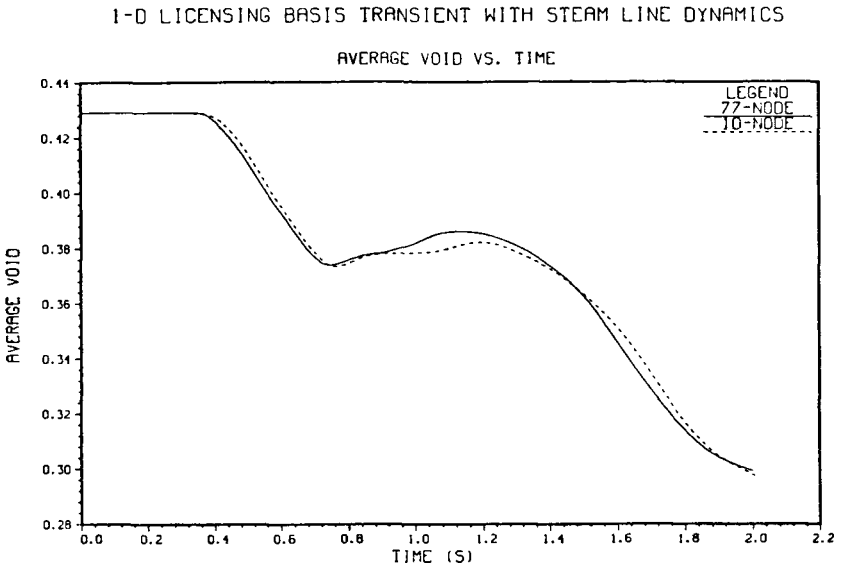

Figure 6.15

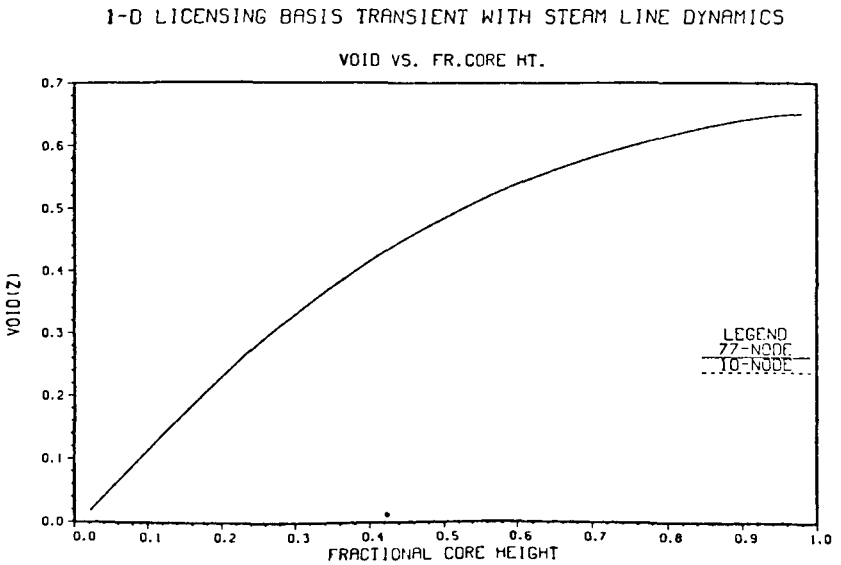

Figure 6.16

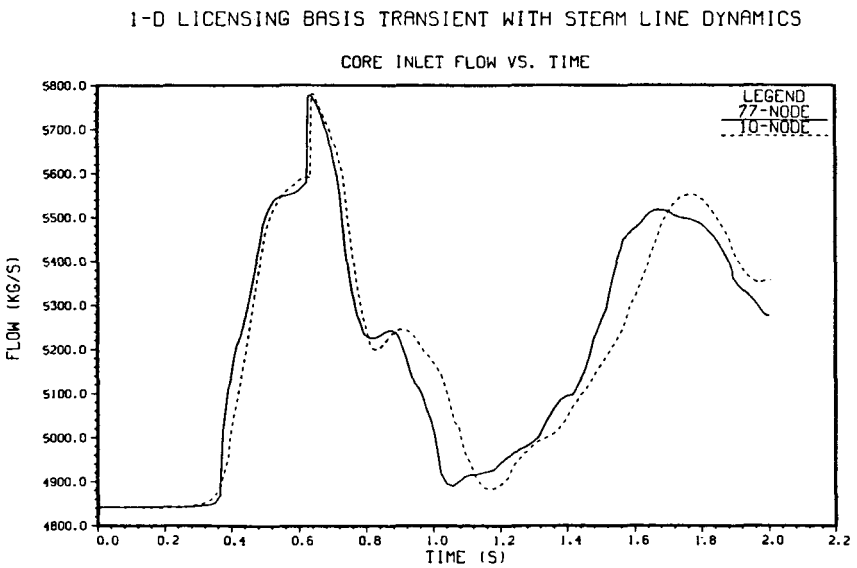

Figure 6.17

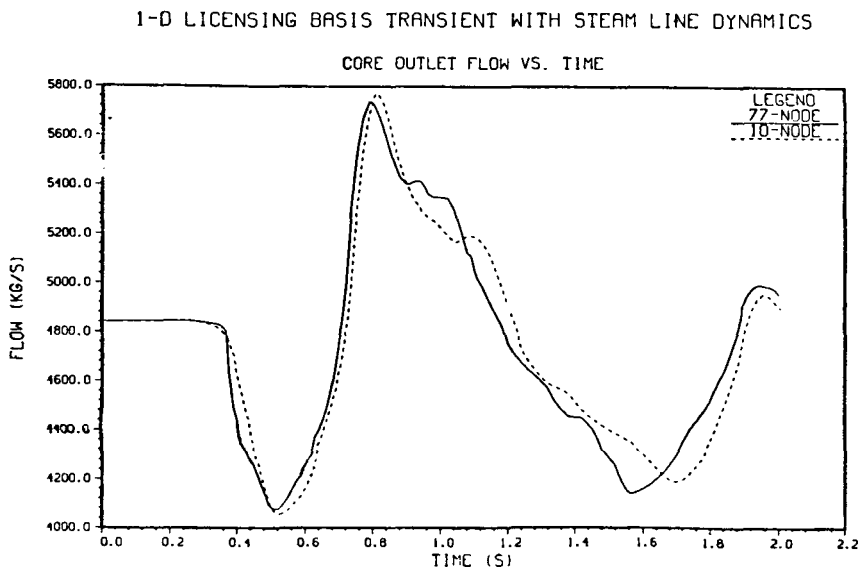

Figure 6.18

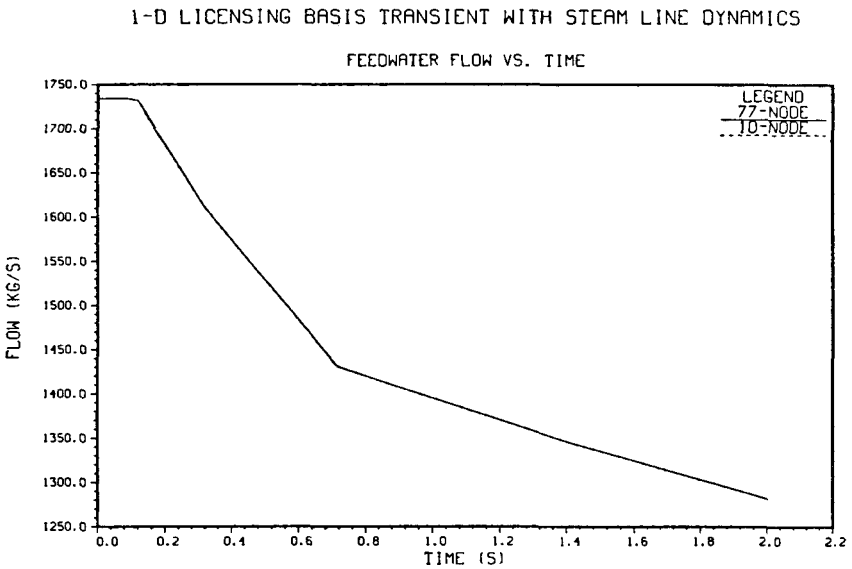

Figure 6.19

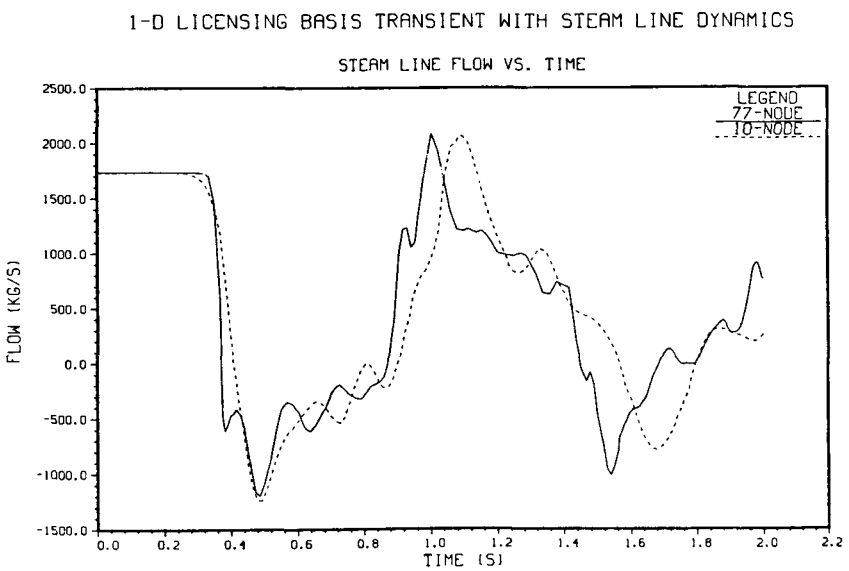

Table 6.5 Computing Times and Steam Line Nodalizations

	77 Nodes	10 Nodes
Total CPU(s)	146.54	74.84
Steam Line Dynamics*		
CPU(s)	76.46	4.65
% of Total	52%	6%
Vessel Hydraulics		
CPU(s)	25.03	25.00
% of Total	17%	34%
Neutron Kinetics		
CPU(s)	45.05	45.19
% of Total	31%	60%

*The Comparison is based on these error limits for time integration:

Absolute error for pressures - 1 N/m^2
Absolute error for mass flow rates - 10^{-4} kg/s
Relative error for pressures - 10^{-6}
Relative error for mass flow rates - 10^{-5}

hydraulic variables was preserved. This favorable experience prompted us to try a further relaxation of the pressure error criteria by a factor of 10, resulting in a relative error of 10^{-3} for p. (The relative flow error of 10^{-3} was retained). For this set of error criteria (10^{-3} for both p and W), we only ran the 77-node case. The results showed a reduction in the computing time for the steam line dynamics by a factor of 3 relative to the standard case, yet still maintaining a 3-digit accuracy in the important thermohydraulic variables. Table 6.6 summarizes the results of the timing study regarding the error criteria. The error criteria used for the three cases in Table 6.6 are summarized as follows.

	Absolute Errors		Relative Errors	
	p (bar)	W(kg/s)	p	W
Standard Case	10^{-5}	10^{-4}	10^{-6}	10^{-5}
Trial 1	10^{-3}	10^{-2}	10^{-4}	10^{-3}
Trial 2	10^{-2}	10^{-2}	10^{-3}	10^{-3}

We recommend that the error criteria for the Trial 2 case be used for the steam line dynamics calculation in RAMONA-3B.

Table 6.6 Computing Times and Error Criteria for Steam Line Dynamics

	Standard	Trial 1	Trial 2
Total CPU(s)	146.54	106.49	96.80
Steam line Dynamics*			
CPU(s)	76.46	36.27	25.59
% of Total	52%	34%	26%
Vessel Hydraulics			
CPU(s)	25.03	25.00	25.00
% of Total	17%	23%	26%
Neutron Kinetics			
CPU(s)	45.04	45.22	46.21
% of Total	31%	43%	48%

*The 77-node steam line representation was used for all three cases.

6.8.3.2 Vessel Hydraulics

The timing study regarding the vessel hydraulics was concerned with the stability and accuracy criteria for the hydraulic time step control. For the one-dimensional LBT problem, the stability limit dictated the hydraulic time step. Consequently, the accuracy criterion did not come into play in the study.

In RAMONA-3B the stability limit for the hydraulic time step is estimated by a subroutine called "LAMBDA" from time to time during the transient. The computing speed for the vessel hydraulics cannot go beyond the "true" stability limit of the problem at hand. However, the true stability limit is hardly known and one can only hope to estimate it as accurately as possible. If the estimate is way off on the conservative side, it can have a great impact on the computing time for the vessel hydraulics. Any endeavor to make the LAMBDA routine more accurate and reliable is quite worthwhile. We recommend this for future improvement.

For the LBT problem, it was found that the stability limit determined the hydraulic time step throughout the 2-s transient and that the integrated momentum equation in the bypass channel dictated the stability limit, resulting in a very small time step size ($\sim$ 5 ms). An examination of the bypass channel data used for the LBT revealed that the loss coefficient (K), flow area (A_f) and hydraulic diameter (D_h) for the bypass channel were unrealistically large. They were re-computed using the actual geometric data of a typical fuel bundle with the control blade in place (to simulate scram). The following values were obtained:

$$K = -542.9,\ A_f = 2.362\ m^2,\ D_h = 0.0155\ m$$

The use of these data for the bypass channel gave rise to an average stability limit of 20 ms, a factor of four larger than the previous value. This means that the computing time for the vessel hydraulics was reduced by roughly a factor of four by using the more realistic bypass channel data.

6.8.3.3 Neutron Kinetics

The timing study regarding the neutron kinetics concentrated on the error criteria and the automatic time step control logics. We found that the error criteria had a greater impact on the computing time for neutron kinetics than the time step control logics for the one-dimensional LBT problem.

The essential neutron kinetic error criteria are the convergence criterion (called DPJ) for the inner iteration and the accuracy criterion (called ACCP) for the outer iteration (time step control) employed for the transient solution of neutron kinetics. (These error criteria are required input data on Card 720 000). For computing efficiency a judicious choice of the two error criteria is important. Our experience indicated that DPJ = 0.0005 and ACCF = 0.02 are a good choice for the LBT problem as shown in Table 6.7. We did not observe any appreciable difference in the accuracy of the transient solutions among the four sets of the error criteria that were tested.

Table 6.7 Computing Times and Error Criteria for Neutron Kinetics

Error Criteria	Neutron Kinetics CPU(s) (Revised Time Step Control)	Neutron Kinetics CPU(s) (Original Time Step Control)
DPJ = 0.0005 ACCF = 0.02	26.54	33.23
DPJ = 0.0001 ACCF = 0.01	40.26	45.20
DPJ = 0.00005 ACCF = 0.01	41.68	---
DPJ = 0.001 ACCF = 0.01	---	56.61

Also shown in Table 6.7 are the results obtained with the revised neutronic time step control logics as described in Fig. 6.7.2 of Chapter 6. It appears to save the neutron kinetics computing time by 10-20% relative to the original time step control algorithm; whereas, the good choice of the error criteria saved the computing time by 34%.

6.8.4 Summary and Recommendations for Nodalization and Error Controls

Nodalization and timing studies were performed to seek ways of reducing the computing time without too much sacrifice on the solution accuracy. Although the scope of the studies is limited, the results support the following recommendations:

1. The 10-node representation should be used for the steamline dynamics calculation with the relaxed error criteria.

2. The more realistic bypass channel data should be used for the vessel hydraulics calculation. The LAMBDA routine for computing the stability limit should be examined to see if its accuracy can be improved.

3. The optimum error criteria along with the revised neutronic time step control algorithm should be used for the neutron kinetics calculation.

4. The 23-channel case should be used for the ATWHS calculation along with the recommendations above so that the 15-min. transient can be computed with a reasonable computing time and cost. As a further assurance, the adequacy of the 23-channel case for the transient calculation be checked against the reference case for say 2 seconds.

6.9 Summary and Recommendations

RAMONA-3B employs ordinary differential equations and finite difference formulations to integrate the partial differential equations of neutron balances, coolant mass, momentum and energy balances of boron transport.

The transient calculations are started from an initial steady-state condition which is computed by successive substitutions, involving nested procedures with Gauss-Seidel eliminations, successive substitutions and linear extrapolations for improving the rate of convergence. The steady-state calculations are completed by executing a pseudo-transient with fixed boundary conditions. The pseudo-transient is computed to eliminate minor discrepancies between the steady-state and transient state conditions.

The transient is computed by five separate integration procedures, with the master clock in the procedure for neutron kinetics calculations. Each procedure has its own accuracy and stability criterion. The four procedures for thermal conduction, thermohydraulics, steam line dynamics and boron transport are subordinated to the neutron kinetics calculational procedure with its master criterion on fast neutron flux.

The programming of mathematical procedures in RAMONA-3B is not structured in modular form, except for the steam line module. The code appears to have undergone a long sequence of modifications upon modifications, arising from modeling changes and subsequent needs to remedy program failures. As mathematical procedures are intimately intertwined with program sections for state equations and related logic controls, the coding of these procedures has become difficult. It is impossible to assure absolute correctness of the programming in RAMONA-3B on the basis of its code listing and its documentation.

RAMONA-3B has successfully executed a large number of simulations for BWR plant transients as described in Chapter 7. It is, however recommended to validate the mathematical procedures in RAMONA-3B by comparison with relevant exact solutions to transient problems. This should be carried out as part of a code assessment program.

For future code improvements we recommend the following:

1. the average thermal neutron flux be calculated directly from its balance equation by using the average fast flux (cf. Section 6.2.7).

2. standard finite difference schemes or finite-element collocation methods be used to reduce the current discretization errors in the RAMONA-3B code for calculating thermal conduction in fuel pellets.

3. a lumped-parameter option be introduced into RAMONA-3B to compute the temperature variations in fuel and pellet by a single ordinary differential equation, whenever plant transients are simulated.

4. standard donor cell differencing for flow reversal be used to replace the current switching logic in RAMONA-3B, as this logic produces discontinuities (cf. Section 6.4.1.3).

5. standard differencing schemes with the current RAMONA-3B nodalization scheme (Figure 6.4.1) be compared with the currently used differencing scheme for boron transport, to find a more reliable method and improve computing speed.

6. currently used time delay concepts for boron transport be replaced by standard (continuous) first-order time delay approximations.

7. the Chebychev extrapolation technique be used to replace the less efficient relaxation scheme currently used in RAMONA-3B steady-state neutron kinetics calculations.

8. the seven discrete temperatures in fuel pellet and cladding be computed by a single iteration procedure, rather than by two separate ones and that the cladding surface temperature be computed only in one place in the code (cf. Section 6.6.2).

9. all convergence criteria for steady-state calculations be reviewed to assure that innermost iterations produce greater accuracy than outer iterations.

10. the newly introduced convergence criteria for the transient neutron kinetics calculations be assessed further to eliminate previously used convergence criteria whenever they are more restrictive than necessary.

11. a well established, efficient numerical procedure be selected for integrating the ordinary differential equations of coolant dynamics and that this procedure be introduced into RAMONA-3B as a module (see end of Section 6.7.3.1.2).

12. the boron transport equation be integrated by standard procedures with valid stability and accuracy criteria, possibly with the procedure selected by recommendation (11) above.

13. a procedure, less expensive in computing effort than the Runge-Kutta method, but equally effective in error control, may be found for integrating the equations of steam line dynamics.

14. the program sections for computing thermohydraulics and thermal conduction should be carefully checked for coding inconsistencies, undocumented code modifications (patches) and overriding instructions. Coding inconsistencies should be removed. Undocumented modifications and instructions which do not reflect the documented modeling should be justified and documented or removed.

15. an independent global energy balance should be performed to assure that internal fluxes of energy cancel properly and that energy is not lost due to truncation errors.

7. DEVELOPMENTAL CODE ASSESSMENT

7.1 General Scope and Need for Additional Assessment

The ultimate objective of the RAMONA-3B code assessment is to determine the accuracy with which the code can predict BWR transients. Toward this end, code assessment at BNL has proceeded in three areas:

i) Evaluation of modeling to determine whether or not it is pertinent to the physical processes experienced during a transient

ii) Verification of the code to assure that the solution techniques and coding are correct

iii) Qualification of the code by comparison with relevant data from separate-effects tests and plant transients.

In this section we summarize what has been done in each of these areas and recommend additional assessment activities. More details of some of the developmental code assessment are given in Sections 7.2-7.4. Experience with the use of RAMONA-3B for calculating a transient with partial scram and a rod drop accident are given in Sections 7.5 and 7.6, respectively.

The evaluation of modeling to determine whether or not it is pertinent to the physical processes experienced during a transient is given in Chapters 2, 3 and 4 for the neutron kinetics, thermal conduction and thermohydraulics, respectively. In each chapter the assumptions which enter into the models are given and their consequences explained. The impact of these consequences on the ability of the code to calculate specific BWR transients is summarized in Sections 1.2 and 1.3 on RAMONA-3B capabilities and limitations, respectively.

There has been a limited amount of verification of the code to assure that the code is producing numbers consistent with the modeling. Models introduced at BNL (namely, the steam line dynamics, plant control and protection system, post-CHF thermohydraulics, boron transport, decay heat, Bankoff-Jones slip and BNL cross-section feedback) have been subjected to a degree of quality control by having more than one person looking at the programming and by doing "hand" calculations to check certain aspects of the calculation. The most thorough example of such verification (and the only one for which documentation exists) is the comparison of the results of a steam line calculation as a stand-alone code with an analytical solution for a specific problem (see Section 7.3.3).

There has been limited verification of the coding written by Scandpower. One exception to this is the core coolant thermohydraulics for steady state, which has been verified (see Section 7.2.2) by comparing hand calculations with RAMONA-3B results. It is recommended that this approach to verification should be pursued for key components of the RAMONA-3B calculation (specifically, the level tracking and thermal neutron diffusion models).

Since analytical solutions exist for certain heat conduction and space-independent neutron kinetics problems, consideration should be given to using these for code verification. Furthermore, three-dimensional, two-group neutron flux benchmark problems (Computational Benchmark Problems Committee 1977, Source Situation 11 for steady state and Source Situation 14 for dynamics) are available and suitable for code verification.

The qualification of RAMONA-3B has primarily involved the comparison of code results with data from separate-effects tests and plant transients. It has also involved the calculation of certain BWR transients for which no data are available. The separate-effects tests were heated channel experiments which were used to assess the steady-state core coolant thermohydraulics (see Section 7.2). The plant transients were turbine trip tests performed at an operating reactor, which were used to assess the steam line dynamics (both as a stand-alone code and within RAMONA-3B), and the modeling of reactor response to an overpressurization situation. The additional BWR transient calculations were for a situation initiated by a main steam line isolation valve closure with only one-half the control rods inserted after reactor trip and for a control rod drop accident.

Based on four comparisons of calculated vs. measured void fraction along a heated channel (Section 7.2), it was concluded that RAMONA-3B predicts the onset of net vapor too far downstream in the channel and that the Bankoff-Jones correlation should not be the recommended slip option. Additional comparisons are recommended in order to further substantiate the latter conclusion and provide more qualification of the ability of the code to predict the steady-state void distribution.

Comparisons should be made using the Bankoff-Malnes slip correlation since that is the recommended slip option (Section 7.2.3). These comparisons should be extended beyond the four tests used to date. Sources of measured data for void fraction along heated channel include not only Eklund, Gelius and Nylund (1965) and Nylund et al. (1968) used in the study reported in Section 7.2, but also, Nylund et al. (1969) and Nylund et al. (1970). The first of these references uses a 6-rod bundle, whereas the latter three use 36-rod bundles and both uniform and nonuniform axial and radial heat flux distributions.

No qualification of the post-CHF heat transfer and void generation model has yet been carried out. It is recommended that suitable data from both steady state and transient heated channel experiments be used to compare with computed results using the RAMONA-3B modeling. Experiments which may be candidates for this work include those of Nahavandi et al. (1981) and Shiralker et al. (1972) on 16-rod bundles and Muralidharan et al. (1976) on 49-rod bundles. These experiments all used flow decay and nonuniform power profiles to reach CHF.

Another aspect of code qualification is the comparison of data from operating plant transients with computed results. This has been done with RAMONA-3B for the turbine trip tests carried out at the Peach Bottom-2 reactor. Comparisons of pressure data from steam line measurements at two locations with results computed using the steam line model as a stand-alone code are given in Section 7.3.4. RAMONA-3B calculations of initial, core-average axial power

distribution and transient core power and steam dome pressure are compared with data and discussed in Sections 7.4.4 and 7.4.5. The results provide an assessment of the steam line model and demonstrate the adequacy of the code for overpressurization transients. However, it is strongly recommended (cf. Section 7.4.5) that more extensive comparisons be made using the Peach Bottom-2 tests.

It is recommended that this type of assessment be extended using data from other operating plant transients. Table 7.1 [compiled using Bailey (1981) and Fabic and Andersen (1981)] lists several candidates (and for completeness, the Peach Bottom-2 turbine trip tests) along with the corresponding reference, the event which initiated the transient and how the transient is characterized. Although each of these events has been analyzed with other codes and a reference is given, it is not clear whether sufficient documentation exists for use with RAMONA-3B.

Additional sources of information on BWR transients are listed in Table 7.2 (from Bailey 1981). No analyses with any code have been performed for these transients. Since the source of information for these transients is either a Startup Test Report or a Licensee Event Report, it is again not clear whether sufficient documentation exists for use with RAMONA-3B. The last set of tests listed in Table 7.2 are yet to be done, but may prove very useful due to the fact that the Grand Gulf Plant will be using a sophisticated data acquisition and recording system not used at other plants.

The last form of code assessment in this chapter is the calculation of BWR accidents for which no data exist. There is a discussion in Section 7.5 of a transient initiated by the closure of a main steam line isolation valve wherein the control rods in half the reactor do not insert after reactor trip. There are no other known calculations of this accident in which three dimensional neutron kinetics in the core are modelled concurrently with the thermohydraulics of the steam supply system. In Section 7.6 the calculation of a center control rod drop accident is discussed. In both sections the results are judged to be reasonable based on general experience with these types of accidents. It is recommended that calculations of other transients discussed in Section 1.2 be made in order to "exercise" parts of the code that have not yet been used in a realistic transient (e.g. the pressure regulator) and to see how different sequences of events affect the operation of the code.

Table 7.1

BWR Transients for which Analyses Have Been Performed

Plant	Reference	Transient Initiator	Transient Characteristic
Peach Bottom-2	Carmichael and Neimi (1978)	Turbine trip test with delayed scram	Overpressurization
Browns Ferry	Forkner, Bell and Winkler (1978)	Generator load rejection Feedwater pump trip Recirculation pump trip	Overpressurization Overpressurization Decrease in coolant flow
KRB	General Electric (1977)	Pressure setpoint oscillation	Pressure variation
Dresden-3	General Electric (1977)	Oscillator test	Pressure variation
Peach Bottom-2	McFadden et al. (1978)	Safety and relief valve test	Decrease in coolant inventory
Vermont Yankee	McFadden et al. (1978)	Generator load rejection Recirculation pump trip	Overpressurization Decrease in coolant flow
Oyster Creek	Linford (1973)	Recirculation pump trip tests	Decrease in coolant flow

Table 7.2

BWR Transients for which No Analyses Have Been Performed

Plant	Reference	Transient Initiator	Transient Characteristic
Pilgrim 1	Licensee Event Report	Stuck relief valve	Decrease in coolant inventory
Dresden 2&3 Quad Cities 1&2	Startup Test Reports	MSIV closure Recirculation pump trip Turbine trip Generator trip Feedwater pump trip Loss of generator & offsite power	Overpressurization Decrease in coolant flow Overpressurization Overpressurization Decrease in coolant inventory Overpressurization
Quad Cities 1&2	Startup Test Reports	Loss of feedwater heater	Decrease in coolant temperature
Oyster Creek	Licensee Event Report	Feedwater pump trip due to inadvertent scram	Overpressurization
Hatch 2	Licensee Event Report	Loss of feedwater MSIV closure Turbine & feedwater trip	Overpressurization Overpressurization
Peach Bottom-2	Startup Test Reports	Pump trip Turbine trip Pressure regulator setpoint change Feedwater controller startup	Decrease in coolant flow Overpressurization Decrease in coolant temperature Decrease in coolant temperature
Grand Gulf	Proposed Startup Tests	RCIC vessel injection Loss of offsite power Generator load rejection Recirculation pump trip Turbine trip Feedwater pump trip Loss of feedwater heater MSIV closure	Decrease in coolant temperature Overpressurization Overpressurization Decrease in coolant flow Overpressurization Decrease in coolant inventory Decrease in coolant temperature Overpressurization

7.2 Assessment of Core Coolant Thermohydraulics

7.2.1 Scope

A limited assessment of the model for core coolant thermohydraulics in RAMONA-3B was performed by applying the model to steady-state heated-channel experiments. The objectives of this work were to see how well the code predicts the steady-state void distribution along the channel and the location of the onset of net vapor formation.

For this purpose, the following specific hydraulics models which affect the void distribution in the core were used:

a) the Bankoff-Jones correlation for slip ratio, Eq. 4.4.66,

b) the vapor generation rate correlation, Eqs. 4.4.51 and 4.4.56-60,

c) the heat transfer correlations for single-phase liquid flow (Dittus-Boelter), Eqs. 4.4.30-32, and for two-phase flow with boiling (Jens-Lottes), Eqs. 4.4.33-34, and

d) the criterion for onset of net vapor formation, Eq. 4.4.21.

The Bankoff-Malnes and Solberg slip correlations which are present as options in the code (cf. Section 4.4.2.4) were not used in this analysis.

The experimental data with which the calculations were compared are from four tests. Three tests involved a six-rod bundle (Eklund et al. 1965). One test result was taken from the FRIGG-2 test series on a 36-rod bundle (Nylund et al. 1968). The test conditions covered the range of liquid inlet subcooling from 5.7°C to 27.2°C and the range of system pressures from 3.16 to 5.14 MPa.

The result of these comparisons is that the predicted void fraction is everywhere lower than the measured void fraction. This is a consequence, in part, of the predicted onset of net vapor formation being too far downstream in the channel. The shape of the predicted void distribution agrees in two out of four tests with the measured void distribution.

7.2.2 Calculations of Heated Channel Experiments

The calculations were done using the void model specified in Section 7.2.1, the appropriate balance equations and certain simplifying assumptions. The balance equations are the steady-state forms (i.e., $\partial/\partial\tau$ is set to zero) of Eqs. 4.4.1 and 4.4.2 for vapor mass and liquid mass, respectively, and Eq. 4.4.4 for mixture energy. The simplifying assumptions are that the pressure is uniform in the heated channel (as in the RAMONA-3B code) and that the specific heat and density of liquid are constant.

The solution to the equations which constitute this model was obtained outside of RAMONA-3B (using a programmable hand-calculator) using a numerical

integration scheme different from that found in the code. Selected results from RAMONA-3B for the same heated-channel conditions were compared with the "hand" calculations and found to be in agreement. This exercise confirmed that the model had been programmed correctly in RAMONA-3B.

The test specifications for the four experiments used in this study are given in Table 7.3. The comparisons between the test results for void fraction along the channel and the corresponding calculations are given in Figs. 7.1-7.4.

7.2.3 Conclusions and Recommendations

The comparison of computed with measured void fraction (Figs. 7.1-7.4) shows for all the test conditions involved that the predicted onset of net vapor formation is too far downstream in the channel. For given liquid subcooling and pressure, the onset of vapor formation predicted by RAMONA-3B is dictated by the product C_{11} $(1+C_{13})$ (cf. Section 4.4.2.3). The larger this product, the farther downstream the point of onset will occur. The comparison shown here indicates that this product as recommended for RAMONA-3B (Eqs. 4.4.58 and 4.4.60) is too large, approximately by the factor of two. Note that the parameters involved (C_{11} and C_{13}) are contained in the expression describing nonequilibrium bulk boiling, Γ_{ph} (Eq. 4.4.57). This expression is not founded on physics and cannot universally predict steady-state void distributions without careful tuning.

The comparison of computed with measured void fraction also shows that the predicted void fraction is everywhere lower than the measured void fraction. This is, in part, a consequence of the predicted onset of boiling being too far downstream. The shape of the predicted void distribution agrees in two out of four tests with the measured void distribution. More comparisons would have to be carried out to determine if the void distribution calculated with the Bankoff-Jones slip correlation does in general agree with the measured distribution in so far as shape is concerned. Good agreement was not found by Nash (1980); his results show that the Bankoff-Jones slip correlation overpredicts the slip ratio at void fractions greater than 0.5.

This difficulty with the Bankoff-Jones slip correlation leads us to recommend the use of the Bankoff-Malnes slip option in RAMONA-3B. The Bankoff-Malnes slip correlation was qualified (Malnes 1980) in conjunction with the RAMONA-3B vapor generation rate model, by comparisons with an extensive set of heated-channel steady-state measurements. The test data covered a wide range of conditions and were from tests at the FRIGG facility that are available in the open literature (e.g. Nylund et al. 1968), and also, from proprietary tests on 8x8 rod bundles which simulate a BWR fuel bundle.

No calculations of heated-channel experiments have been done using the Bankoff-Malnes slip correlation option in RAMONA-3B that are in the open literature. Therefore, it is strongly recommended that this be carried out in order to verify that this option is indeed the best choice. In the meantime, there is evidence that the use of the Bankoff-Malnes slip option would improve the agreement between calculated and measured void distributions. RAMONA-3B

Table 7.3

Specifications for Heated-Channel Tests

Test Number (Reference)	13026 (Eklund 1965)	13027 (Eklund 1965)	13028 (Eklund 1965)	313020 (Nylund 1968)
Number of Rods in Bundle	6	6	6	36
Pressure, MPa	3.16	5.16	5.14	4.97
Heat Flux, kW m	467.	645.	645.	646.
Mass Flux, kg m s	1345.	1597.	1607.	1159.
Inlet Subcooling, K	5.7	13.2	27.2	22.4
Flow Channel Area, m^2	0.00305	0.00305	0.00305	0.01310
Flow Channel Perimeter, m	0.262	0.262	0.262	1.561
Hydraulic Diameter, m	0.0251	0.0251	0.0251	0.02689 0.03660
Channel Heated Length, m	4.00	4.00	4.00	4.375

(a) For wall shear.

(b) For heat transfer.

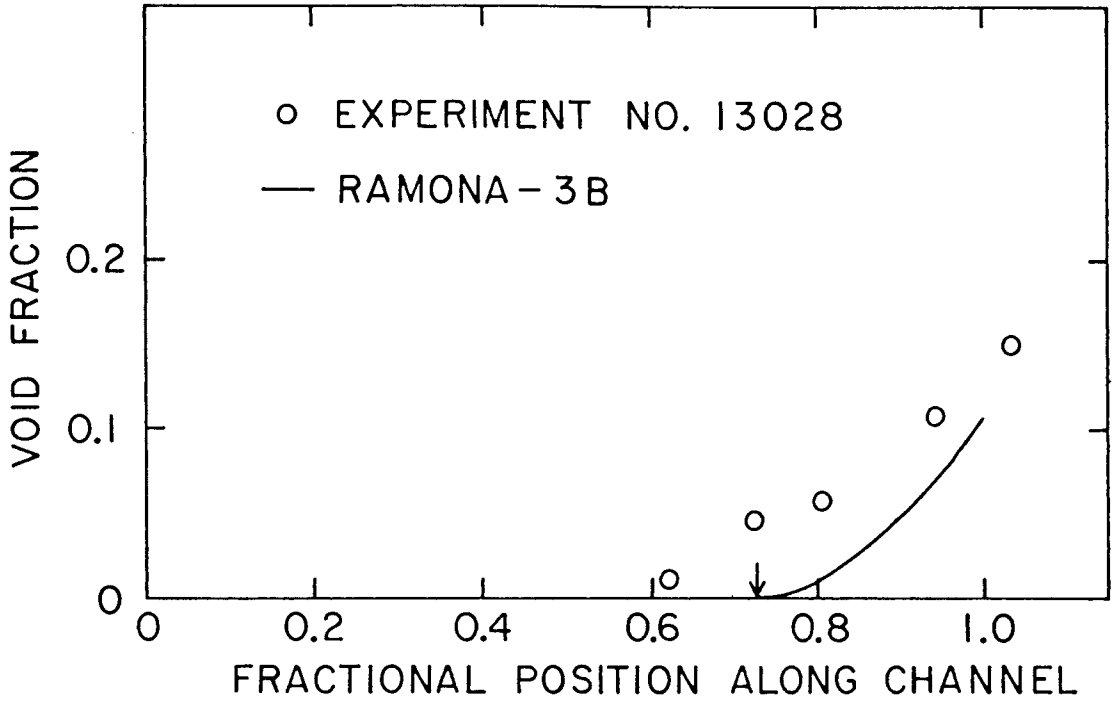

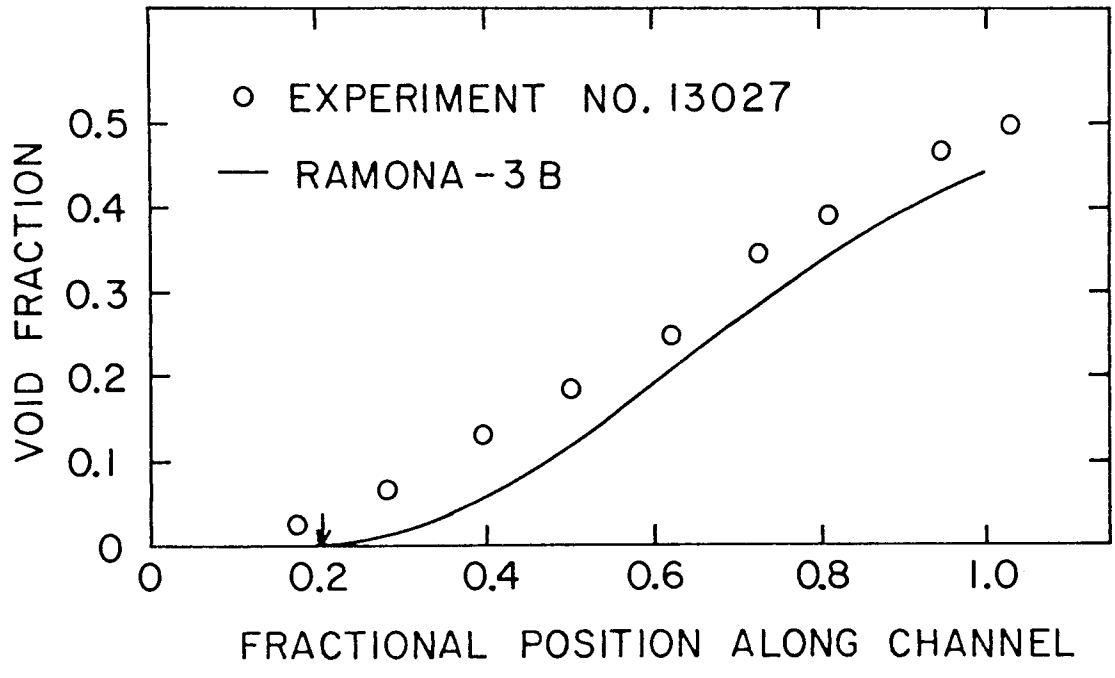

Figures 7.1,7.2 Comparison of RAMONA-3B Models with Measurements in a 6-Rod Cluster (Eklund et al. 1965)

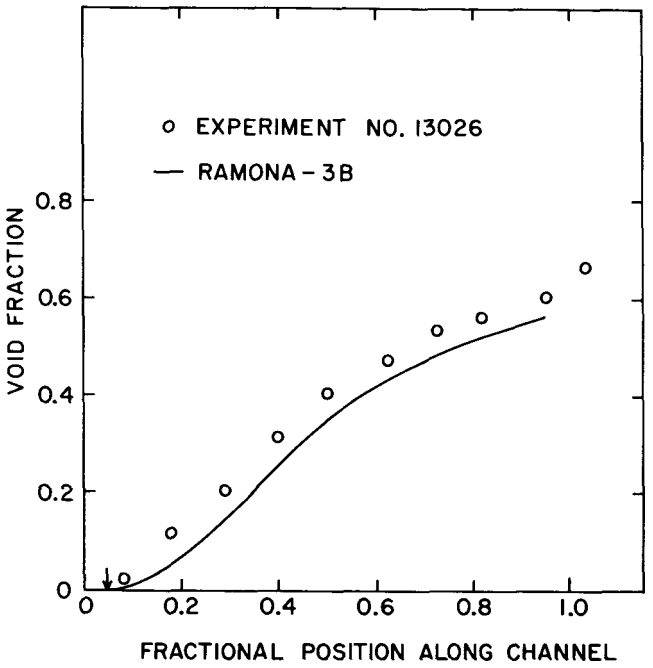

Figure 7.3 Comparison of RAMONA-3B Models with Measurements in a 6-Rod Bundle (Eklund et al. 1965)

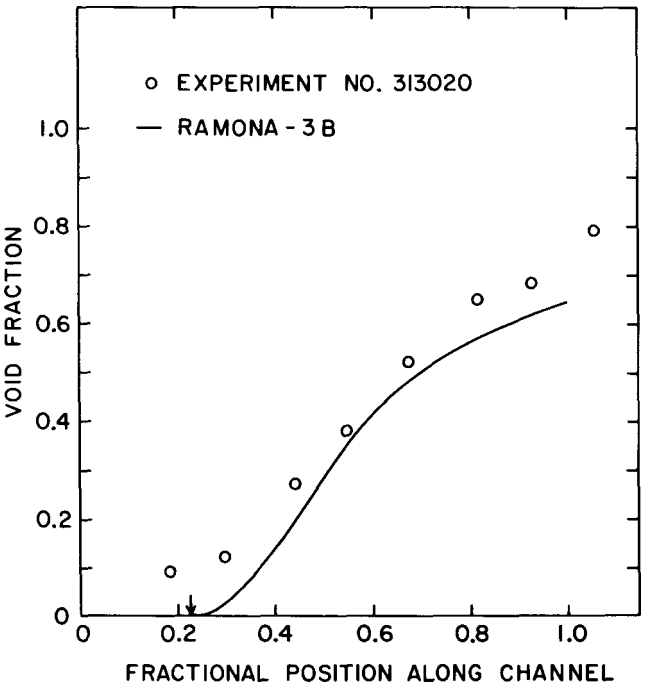

Figure 7.4 Comparison of RAMONA-3B Models with Measurements in a 36-Rod Bundle (Nylund et al. 1968)

steady-state calculations for the Peach Bottom-2 reactor (cf. Section 7.4) and for a generic BWR/4 (cf. Section 7.5) resulted in a core average void fraction using the Bankoff-Malnes slip option that was 0.05-0.07 higher than with the Bankoff-Jones slip option. If we translate this to the heated-channel data shown in Figs. 7.1-7.4, we would expect to see close agreement between the data and calculations with the Bankoff-Malnes slip option although the onset of boiling would still be at the same location.

7.3 Assessment of Steam Line Hydrodynamics

7.3.1 Scope

The steam line model (Section 4.4.5.5) was assessed as a stand-alone code before being made a part of RAMONA-3B. Calculations of steam line pressure were compared with: 1) computer results from General Electric's (GE) ODYN code (General Electric 1978); 2) analytical results, and 3) experimental results from the Peach Bottom-2 Turbine Trip Tests (Carmichael and Neimi 1978). The details of these comparisons are given in the original documentation of the steam line model (Wulff 1980, Chapter 5). The following sections summarize the assessment.

7.3.2 Comparison with ODYN Code Results

The comparison between computer results was carried out because the BNL steam line model and the steam line model of the ODYN code imply similar assumptions. Specifically, the ODYN code reference specifies the same equations as Eqs. 6.4.54, 6.4.56, 6.4.59 and 6.4.60.

The steam line test conditions for comparing computer results were selected by GE and consist of a straight pipe with constant inlet pressure and a flow rate at the exit which decreases linearly with respect to time in order to represent a turbine stop valve closure. The pressure history at the outlet (turbine stop valve) was calculated by both codes. The results show good agreement only for the phase of the pressure pulses. The first pressure peak as computed by the ODYN code is 21% below the corresponding point computed by the BNL code. This discrepancy was resolved by the comparison with analytical results discussed in Section 7.3.3. That comparison showed that the BNL steam line code computes pressure amplitudes correctly in accordance with the governing equations 4.4.185 and 4.4.186.

7.3.3 Comparison With Analysis

An analytical solution was derived to predict the pressure at the turbine stop valve under the conditions used for the comparison of the ODYN and BNL steam line models (Section 7.3.2). By selecting these particular conditions it was possible to assess, not only the numerical integration procedure in the BNL steam line code, but also to decide which of the two codes computes the correct pressure amplitude.

The BNL code was modified to not only suppress inlet pressure drop, inlet contraction losses and turbulent friction as needed for the calculations described in Section 7.3.2, but also to allow for the linearization of pipe friction which was necessary to obtain an analytical solution. The problem is further simplified with assumptions that imply that the density is independent of enthalpy, that the ratio of density to pressure is a constant and that there is laminar flow without form losses. The details of the problem definition and the derivation of the solution are given in Wulff 1980, Section 5.2.1.

The pressure rise at the turbine stop valve calculated with the BNL steam line code was compared with the pressure rise obtained from the analytical solution. The results are given in Fig. 7.5 and show that the BNL steam line code computes the pressure amplitude correctly in accordance with the governing equations, Eqs. 4.4.185 and 4.4.186, with the simplifying assumptions used to define the test problem. Since those assumptions do not alter the general solution algorithm, it is claimed that the BNL steam line code computes the pressure amplitude and phase correctly and that the pressure amplitude as computed by the ODYN code for the test problem is too low.

An analytical solution was also obtained for inviscid flow. The calculated pressure rise for the analytical and finite-difference solutions are in agreement as can be seen in Fig. 7.6. This is further evidence that the spatial differencing scheme in particular, and the numerical integration method, in general, produce the correct solution for the original partial differential equations.

7.3.4 Comparison With Experiments

The comparison of BNL steam line code results with measurements taken at the three Peach Bottom-2 Turbine Trip Tests assesses the overall code and in particular Assumptions 4-xxvi, 4-xxvii and 4-xxix in Section 4.3.1. The assessment consists of imposing the measured steam dome pressure as inlet boundary condition, the measured valve stem actions at the turbine stop valve and at the bypass valve as exit boundary conditions, and then of comparing the two measured pressure histories at the main steam isolation valve and at the turbine stop valve with computed pressure histories.

The three turbine trip tests are described in detail in Carmichael and Neimi 1978. A summary of the plant conditions at the time of the test is given in Section 7.4.2. The specific input data for geometry, initial conditions, control of computations, and boundary conditions are given in Wulff 1980, Section 5.3.

The resulting calculations of pressure rise were compared with the corresponding data from the two locations in the steam line. The results at the location of the main steam line isolation valves are shown in Figs. 7.7, 7.8 and 7.9 for test numbers 1, 2 and 3, respectively. The experimental results have high-frequency oscillations which were caused by the sensor connecting lines. At both locations the computed pressures agree well with the measured mean pressures, i.e., discounting the oscillations, although they have slightly less damping of pressure pulse amplitudes at the location of the turbine stop valve. These results, therefore, provide further qualification of the steam line model.

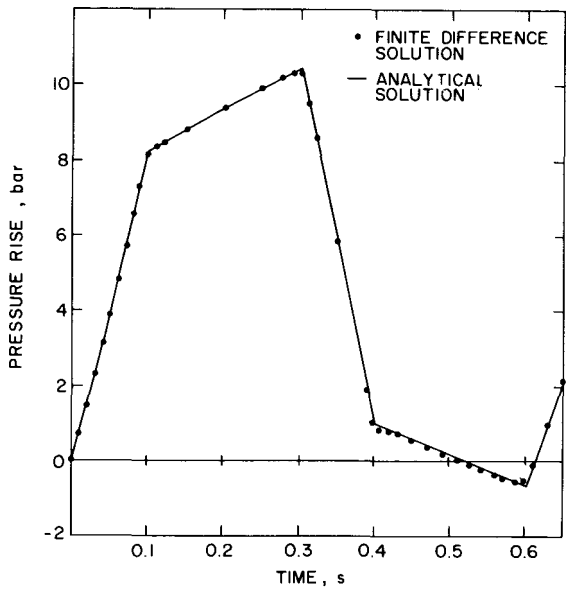

Figure 7.5 Comparison of Analytical Solution with Solution Based on the RAMONA-3B Steam Line Model; General Case with Friction (Wulff 1980, Fig. 4, p. 40)

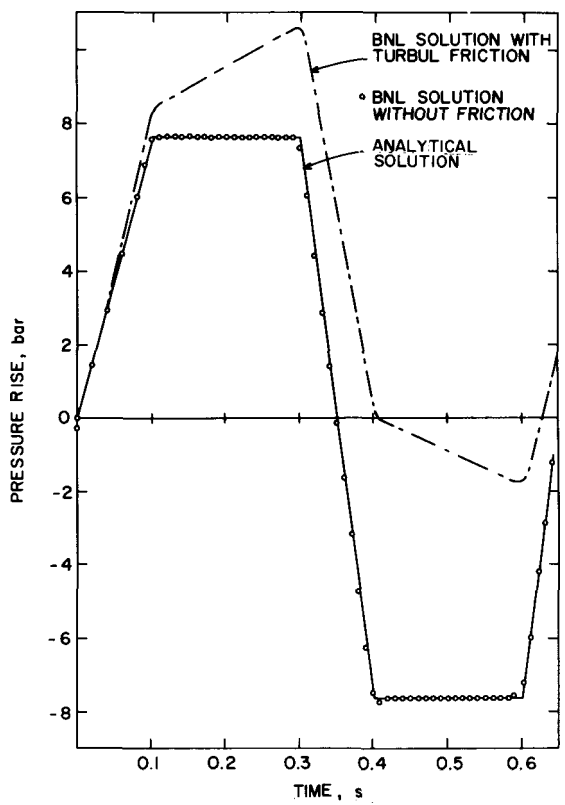

Figure 7.6 Effect of Friction and Comparison of Analytical Solution for Inviscid Flow with Solution Based on the RAMONA-3B Steam Line Model (Wulff 1980, Fig. 5, p. 40)

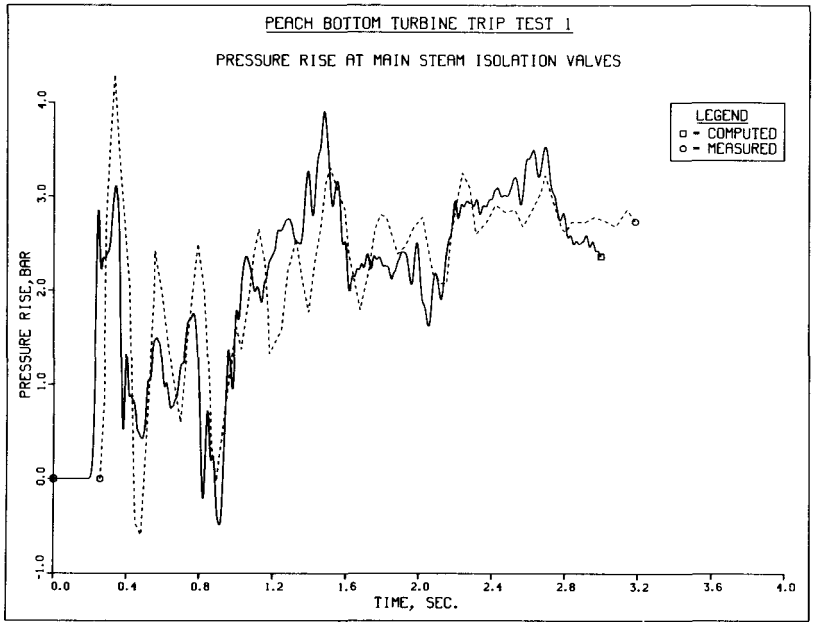

Figure 7.7 Comparison of Computed with Experimental Pressure Rise Histories at the Main Steam Isolation Valve for Turbine Trip Test No. 1 (Wulff 1980, Fig. 13, p. 51)

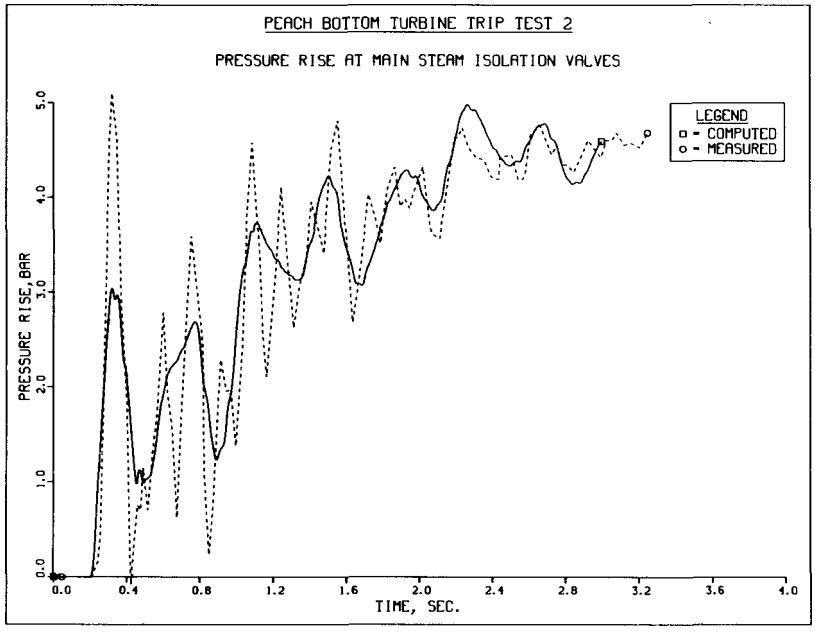

Figure 7.8 Comparison of Computed with Experimental Pressure Rise Histories at the Main Steam Isolation Valve for Turbine Trip Test No. 2 (Wulff 1980, Fig. 14, p. 52)

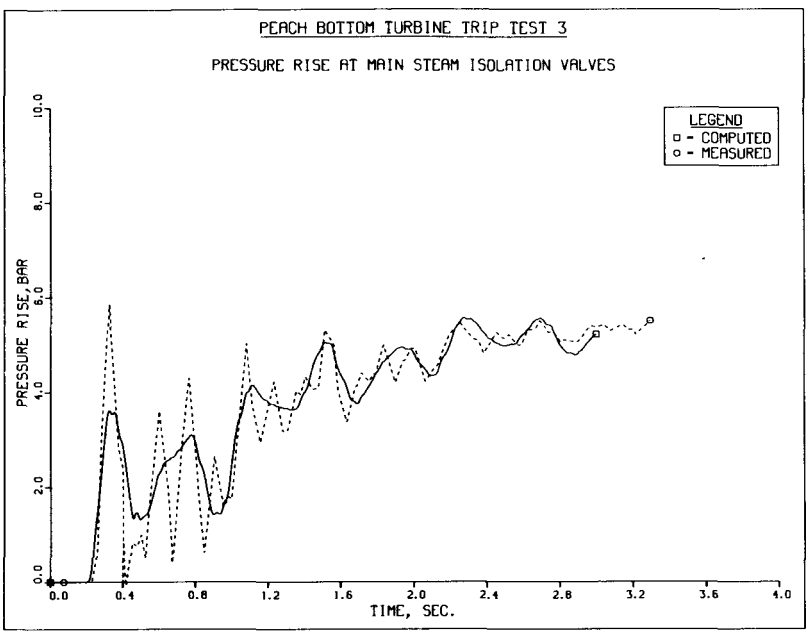

Figure 7.9 Comparison of Computed with Experimental Pressure Rise Histories at the Main Steam Isolation Valve for Turbine Trip Test No. 3 (Wulff 1980, Fig. 15, p. 52)

7.4 Simulation of Peach Bottom-2 Turbine Trip Tests

7.4.1 Scope of Measurements and Calculations

Three turbine trip tests were performed at the Peach Bottom-2 (PB2) BWR (Carmichael and Neimi 1978). These tests provide the only openly available and well-documented plant data which can be used in the assessment of BWR transient codes. In particular, the tests provide an assessment of the adequacy of codes, like RAMONA-3B, to calculate overpressurization events.

The PB2 tests were initiated by the closure of the turbine stop valve (TSV) which causes the propagation of an acoustic wave through the steam line to the reactor vessel. The pressure pulse in the vessel results in a reduction in steam void volume which increases the reactivity of the reactor. In normal operation, the trip of the TSV would cause a control rod scram signal. In these tests this scram trip was bypassed, and hence, a significant power transient occurred. This transient is terminated by a decrease in reactivity due to the (delayed) insertion of control rods and an increase in vapor generation which is caused by the increase in power.

The measurements taken during these transients can qualify the modeling of steam line dynamics and vessel thermohydraulics in conjunction with the neutron kinetics. Since there is very tight coupling between the pressure, void fraction and neutron flux, it is difficult to use these tests for the qualification of specific parts of the modeling, e.g., for the neutron kinetics alone.

A limited assessment of RAMONA-3B was performed using the PB2 tests. Comparisons between calculated values and measurements of the initial axial power distribution and the power and steam dome pressure during the transient showed generally good agreement. As a result of this comparison, it is clear that the code is well-suited for analyzing overpressurization transients. Nevertheless, it is recognized that the RAMONA-3B simulations of the turbine trip tests reflect the code as constituted in September 1980, prior to many improvements and were of a limited nature. As discussed in Sections 7.1 and 7.4.5, a complete assessment of RAMONA-3B using the PB2 data is recommended.

7.4.2 Test Conditions

Thorough descriptions of the PB2 reactor and the turbine trip tests are available in Larsen 1978 and Carmichael 1978, respectively. The following is a summary of the most relevant information.

Peach Bottom-2 is a BWR/4 design with a rated thermal power output of 3293 MW, a rated core flow of 1.29×10^4 kg/s, and a rated steam flow of 1.68×10^3 kg/s at a turbine inlet pressure of 6.65 MPa. Each of the four main steam lines is equipped with a flow-limiting nozzle, main steam line isolation valve, safety and relief valves and a turbine stop valve (TSV). The steam bypass system consists of nine bypass valves (BPVs) mounted on a common header which is connected to each of the four steam lines. The valves, in turn, are connected to the main steam condensers through individually orificed pipes.

The core consists of 764 fuel bundles with an active length of 3.66 m. The tests were conducted at the end of the second fuel cycle with 576 of the original fuel bundles containing a 7x7 array of fuel rods. The remaining bundles contained an 8x8 array and were loaded at the beginning of cycle-2. Reactivity control is maintained with 185 cruciform control blades located in the bypass region between fuel bundles.

Pressure measurements are available at the core exit plenum (through taps on the core spray piping near the entrance to the reactor pressure vessel), in the steam dome, in the steam lines (before and after the flow limiters), and at the entrance of the TSVs. The water level in the upper downcomer is measured by a Δp transducer which compares the static head at a tap below the level to the static head in a reference riser pipe which is vented to the steam dome.

Reactor power is monitored by 43 vertical strings of stationary in-core probes distributed throughout the core. Each string holds four miniature fission chambers which serve as local power range monitors (LPRMs) at four elevations. The amplified signals of the LPRMs are read out individually as well as combined and averaged over suitably selected groups of 20 to provide six independent channels for the average power range monitor (APRM). In addition, each of the 43 tubes containing LPRMs can be entered by one of five traversing in-core probes (TIPs) to obtain a more accurate vertical power profile in the steady state.

All three turbine trip tests were initiated from steady-state conditions. For each test the control rod pattern was different in order to achieve a critical reactor with a satisfactory power distribution at the desired operating state point. The state point as defined by core power level, nominal, flow rate, inlet temperature and pressure is given in Table 7.4 for each test. In anticipation of a significant level drop during the test, the water level was raised to its maximum value (based on a high-level alarm) at the beginning of each test. Prior to closing the TSV, nuclear and thermohydraulic edits were obtained from the plant process computer.

In order to enhance the pressure-void-power feedback effect, the scram signal due to TSV closure was delayed during these tests. In order to limit the power surge that this would cause, the flux level at which scram is actuated was lowered. The set-points for each test are given in Table 7.4. These actions were meant to keep the fuel linear heat generation rate within the preconditioning envelope and to guarantee a satisfactory minimum critical power ratio at all times during the transients while still obtaining a significant power increase due to void feedback.

7.4.3 RAMONA-3B Modeling of the Plant

The boundary conditions and perturbations that must be represented in RAMONA-3B in order to model the plant during the tests relate to the turbine and bypass valves, the feedwater and recirculation flow, and the control rod motion.

Table 7.4

Peach Bottom-2 Turbine Trip Tests
Initial Conditions

Test	Power % Rated	Scram Setting % Rated	Core Flow % Rated	Core Pressure MPa	Inlet Temperature K
1	47.4	85	100.3	6.97	552
2	61.6	95	82.1	6.85	548
3	69.1	77	100.9	6.95	549

Table 7.5

Peach Bottom-2 Turbine Trip Tests
Valve Characteristics

	Test Number		
	1	2	3
TSV Steady State Flow Rate (kg/s)	191	256	288
TSV Closing Time (ms)	75	95	95
BPV Delay Time (ms)	300	30	49
BPV Closing Time (ms)	588	595	667

In all three tests the flow rate at the turbine stop valve was assumed to decrease linearly. Table 7.5 gives the initial (steady-state) flow rate and the time required to close the TSV (Carmichael and Neimi 1978). Note that the time to TSV closure was not measured for Test Number 1 and had to be estimated.

The delay time between initiation of TSV closure and the initiation of bypass valve opening, and the BPV closing time are given in Table 7.5. These times were derived from the data given in Carmichael and Neimi 1978. The delay times take into account signal delays and valve hysteresis. The mass flow rate at the BPV was specified to reach 26.2% of the steam flow rate at rated power under eventual steady-state flow conditions. This maximum flow capacity is exceeded during the initial surge of steam into the lines downstream of the BPV, which are at condenser vacuum conditions. This surge has been analyzed using the RETRAN code (Hornyik and Naser 1978) and an approximation to the resulting flow rate (Wulff 1980, pp. 46,48) has been used in the present study.

During the first 3 seconds in each test, neither the feedwater nor the recirculation system showed any appreciable change in flow rate or temperature (Carmichael and Neimi 1978). Hence, constant conditions were assumed in the RAMONA-3B calculation for both these systems.

The initial control rod pattern was different for each test. For all three tests the average rod motion begins approximately 0.19 s after the scram signal is received. It takes 3 s (from the time the motion begins) to insert the rods fully into the core (Carmichael and Neimi 1978).

The nodalization used in RAMONA-3B for the thermohydraulic calculations in the vessel and steam line is given in Table 7.6 (cf. Fig. 6.4.1). For the neutron kinetics calculation each fuel bundle was represented as a separate node. For the core thermohydraulics calculation, the fuel bundles in an octant of the core were lumped together into 30 hydraulic channels, as shown in Fig. 7.10. (The core had octant symmetry.) In addition, there was a hydraulic channel for the bypass water. For the fuel rods, four nodes were used in the pellet and two in the clad.

The cross sections that were used in the PB2 calculations were originally derived for use with a two-dimensional (R,Z) coupled neutron kinetics and core thermohydraulics code (BNL-TWIGL). The method used to obtain the data (Cheng and Diamond 1978, p. 17) did not include core burnup calculations. Beginning-of-life data were systematically varied until the core-average axial power distribution gave agreement with the measured distribution for one of the PB2 tests. No further adjustment was made for the other tests. This procedure was used for BNL-TWIGL since cross sections were needed within a certain amount of time, precluding the use of the recommended procedure (Sections 2.2.2 and 2.4). The resulting data were qualified via the successful application of BNL-TWIGL to the Peach Bottom-2 tests (Cheng and Diamond 1978). Because the data had been used successfully in the past and were immediately available, they were used in the RAMONA-3B analysis of the PB2 tests.

The use of these data results in a core description with eight axial and two radial material (or exposure) zones. There are eleven cross-section sets

Table 7.6

Nodalization for Turbine Trip Test Calculations

Region	Number of Nodes
Upper downcomer	6
Lower downcomer	6
Lower plenum	5
Upper plenum, riser, separator	5
Steam line	
Vessel to junction for BPV	65
Junction for BPV to TSV	2
Junction for BPV to BPV	10
Core	
Axial	24
Planar	
Neutron Kinetics (core quadrant)	191
Thermohydraulics	32

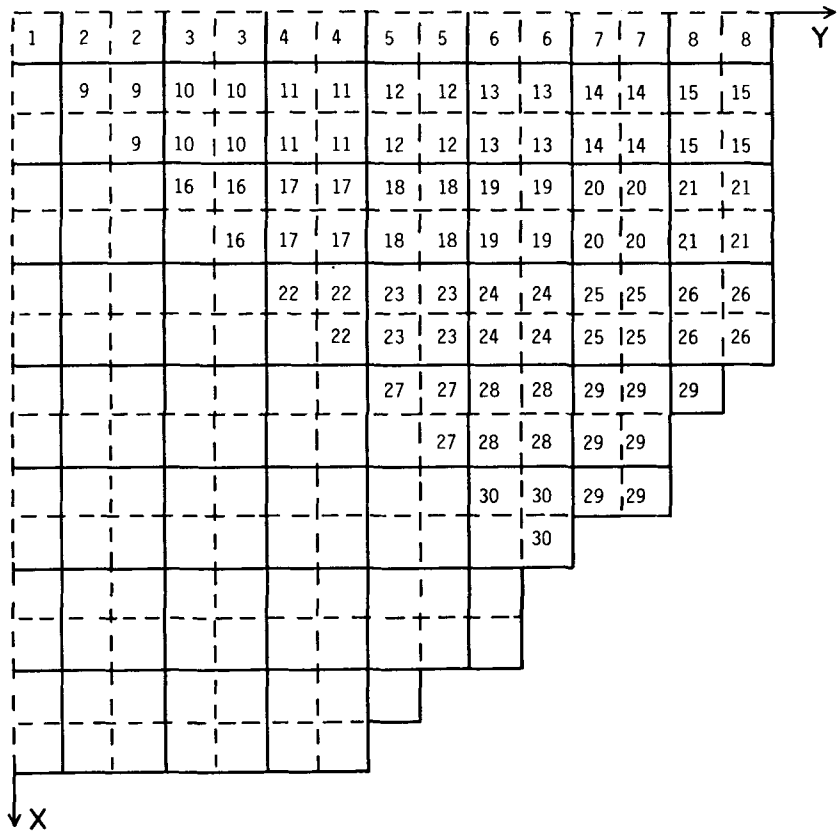

Figure 7.10 Hydraulic Channel Number at Each Fuel Bundle in a Core Octant

to describe these 16 zones. Hence, although each bundle is represented explicitly in terms of obtaining the spatial solution to the neutron kinetics equations, the bundles are actually homogenized over large regions of the core with respect to the cross-section data.

The recommended option in RAMONA-3B for slip is the Bankoff-Malnes model (Section 4.4.2.4). However, the Bankoff-Jones slip correlation was used in the PB2 calculations because it yielded an initial power distribution which was in reasonable agreement with data. The Bankoff-Jones slip, in conjunction with the RAMONA-3B vapor generation rate model, underpredicts the void fraction (Section 7.2) which can compensate for a high void-neutron feedback. Therefore, good agreement between calculated and measured steady-state power distributions is not a sufficient test for either the void dependence of the two-group cross sections or for the void model.

Additional details of the RAMONA-3B Peach Bottom-2 model can be obtained from the input listing for Turbine Trip Test 3 found in the Appendix.

7.4.4 Comparison of Calculations with Measurements

Figures 7.11, 7.12 and 7.13 give the initial axial (radially-averaged) power distributions for Turbine Trip Tests 1, 2 and 3 (TT1, TT2, and TT3), respectively. The agreement between calculation and measurement is in general good for all three tests. Specifically, the code overpredicts the test data in the bottom of the core for TT2 by about 15% but is closer elsewhere. The results for TT1 overpredict the power at the center of the core by about 14% and somewhat underpredict it elsewhere. The results for TT3 are similar to TT2 but somewhat less pronounced. No error is quoted for the measurements.

The power distribution is sensitive to the location of control rods and the void distribution. Therefore, the general agreement noted above helps validate the cross-sectional dependence on void and control rods in conjunction with the ability of the code to calculate the void distribution. As noted in Section 7.4.3, the void model (specifically the slip correlation) being used in RAMONA-3B for these calculations is not the recommended option and the cross sections were not obtained in the recommended manner. Nevertheless, the combination works reasonably well for the steady state and, as shall be shown below, for the transient.

Figures 7.14, 7.15 and 7.16 show measured and calculated system (steam dome) pressures for TT1, TT2 and TT3, respectively. The zero-time for all curves is the instant when the flow through the TSV begins to change. The graphs show qualitative agreement out to 2 seconds where the calculation was stopped. Quantitatively, the differences between calculated and measured curves are 5-20% of the total change in pressure. The interpretation of these results is complicated by the fact that RAMONA-3B overpredicts the pressure in TT1 and underpredicts it in TT2 and TT3.

Only the initial rise of the pressure is important in determining the core power because control rods and a negative component of void feedback rapidly shut down the reactor. During this early period, the calculations are in good

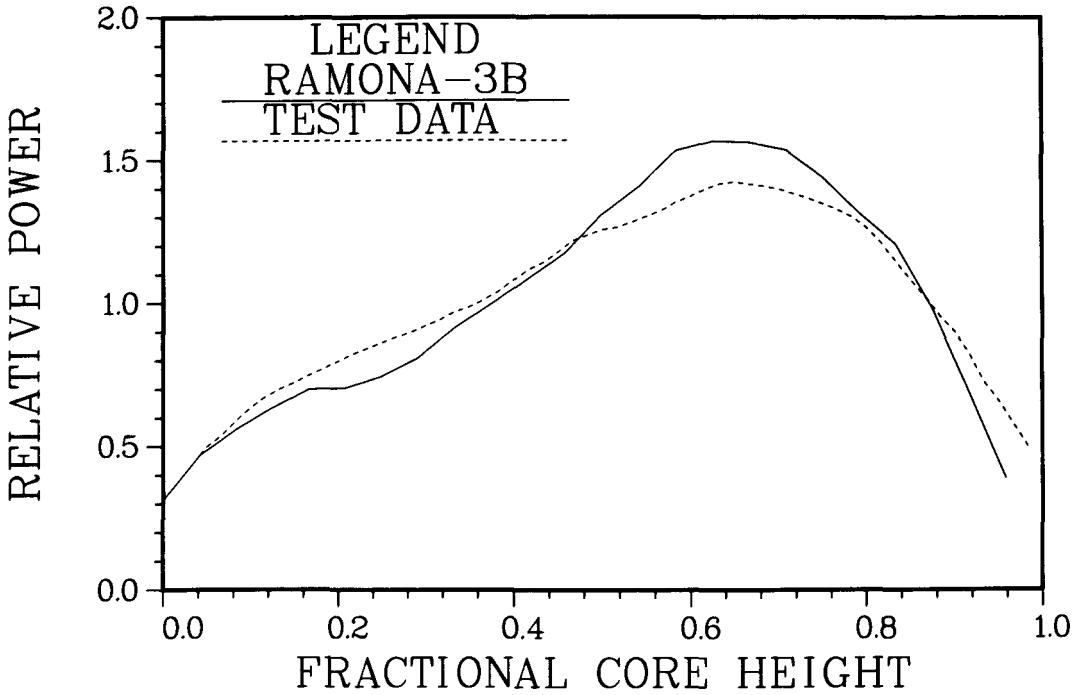

Figure 7.11 Steady-State Axial Power Distribution for Turbine Trip Test No. 1

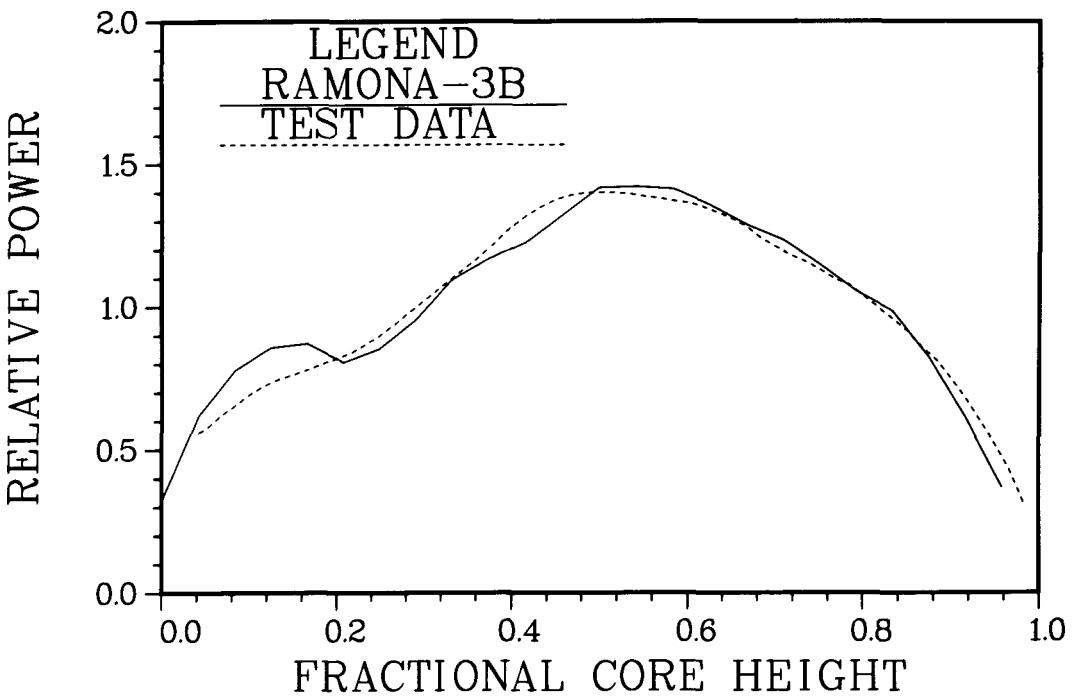

Figure 7.12 Steady-State Axial Power Distribution for Turbine Trip Test No. 2

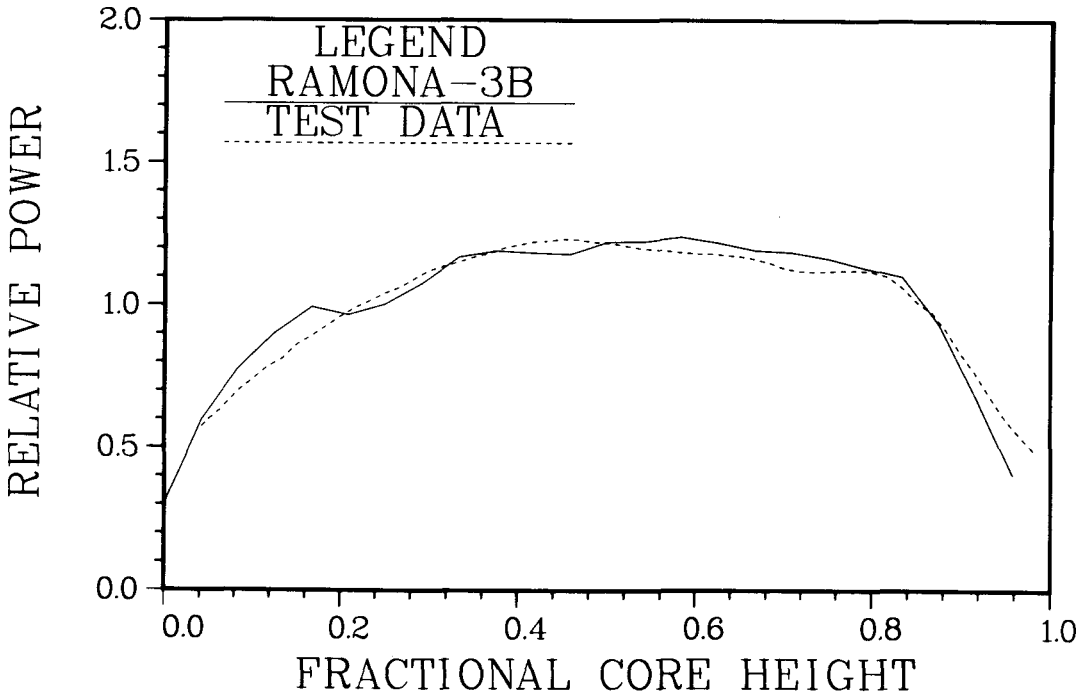

Figure 7.13 Steady-State Axial Power Distribution for Turbine Trip Test No. 3

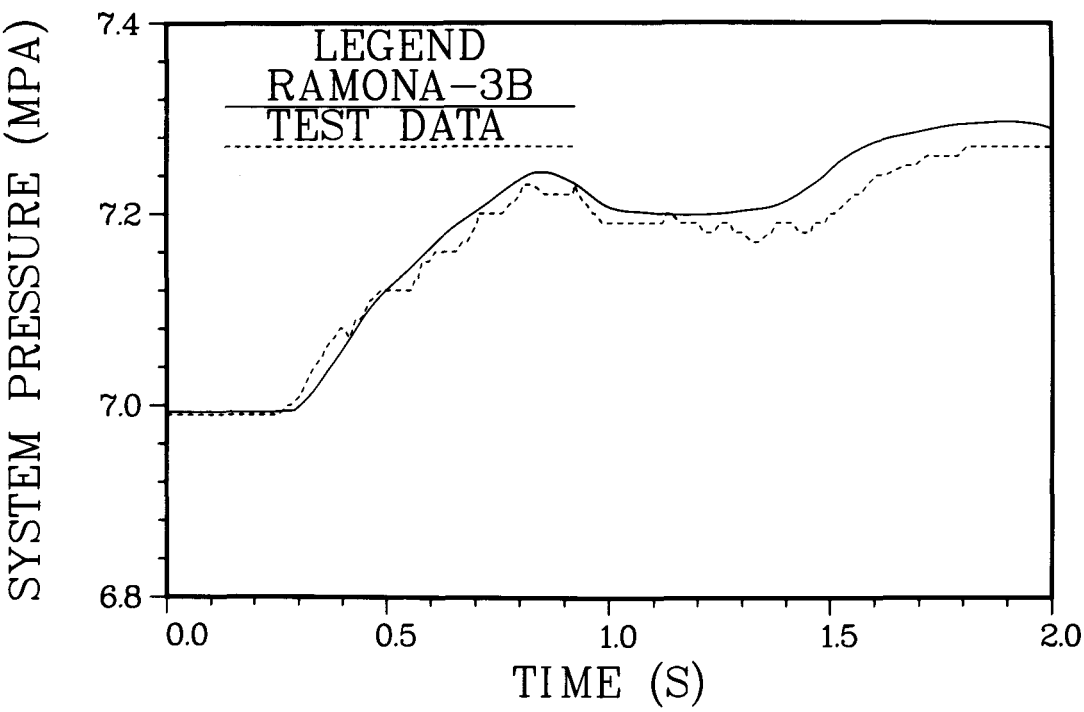

Figure 7.14 Transient System Pressure for Turbine Trip Test No. 1

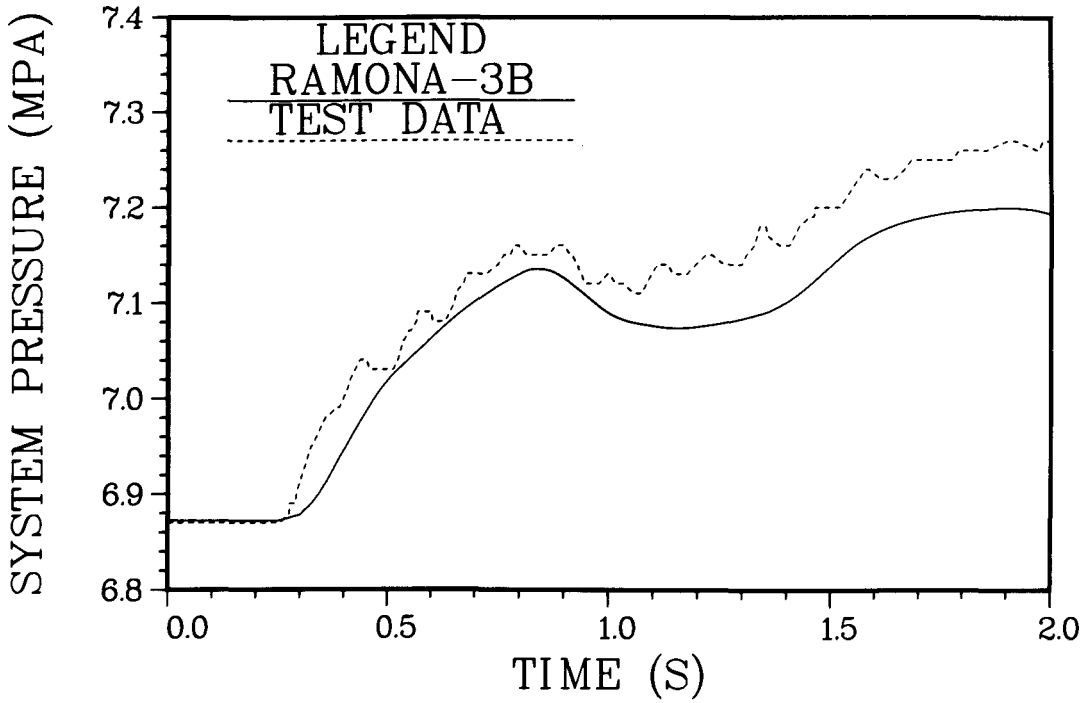

Figure 7.15 Transient System Pressure for Turbine Trip Test No. 2

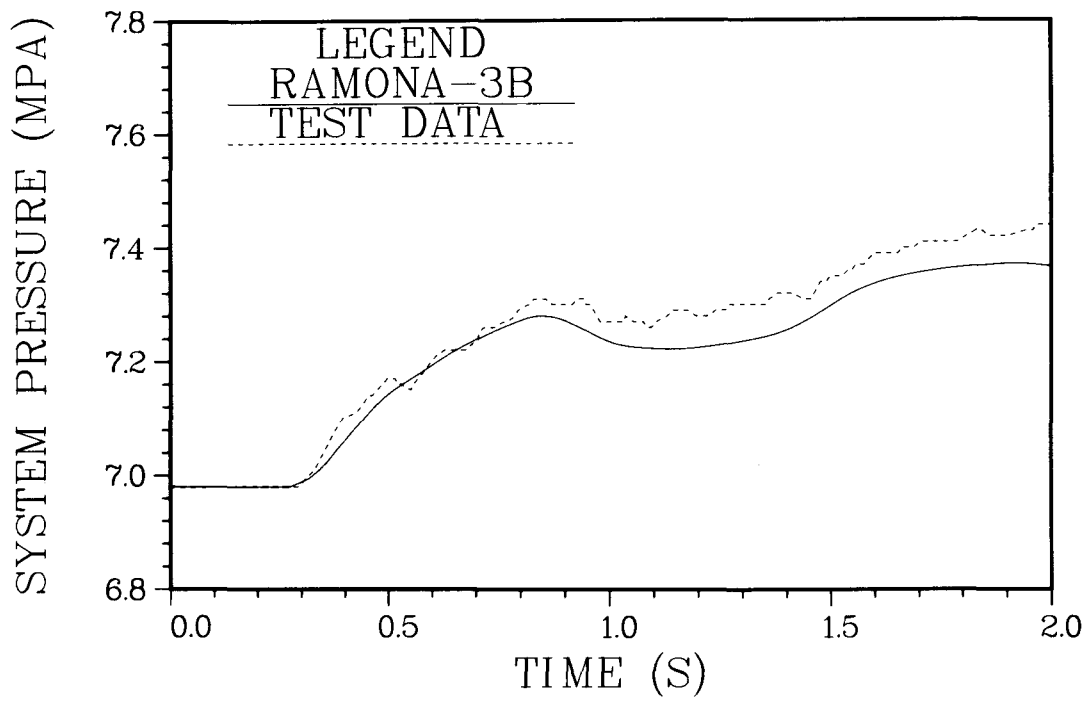

Figure 7.16 Transient System Pressure for Turbine Trip Test No. 3

agreement with the data. The longer term behavior of the system pressure will, of course, be important in other transient scenarios.

These pressure comparisons are a good test of the steam line dynamics and its interaction with the rest of the code. They complement the comparisons done with the steam line model in a stand-alone code (cf. Sect. 7.3). If the steam dome pressure is predicted well, then the pressures at the TSV and the isolation valves should also be accurate (Wulff 1980, p.41).

This calculation is influenced by the flow rates through the TSV and BPV which must be supplied, i.e., they are not calculated in the code. The TSV closes rapidly and the linear assumption for flow rate versus time should be good. On the other hand, the TSV closing time was not measured for one test and the delay time and flow characteristics for the BPV are not well defined (cf. Section 7.4.3).

Figures 7.17, 7.18 and 7.19 compare the calculated and measured relative power during the transient for TT1, TT2 and TT3, respectively. The agreement between measured and calculated core power is in general good for all three tests. This is true for peak power, time to peak and total energy released. These results are particularly good since the core reactivity approaches prompt-critical, and hence, the results are very sensitive to small changes in input assumptions.

The rising part of the power curves depends strongly on void feedback, and hence, it tests the ability of the code to calculate: 1) the pressure wave from the TSV to the core; 2) the effect of pressure on the steam voids; and 3) the reactivity effect of a change in void content. As discussed above, the steam line dynamics is predicted well. Item 2 relates to the core thermohydraulic model. The third item is a strong function of cross section input.

The descending portion of the power traces depends on the change in void content and the effect of control rod insertion. Since the transient is not severe -- in magnitude and duration -- the fuel temperature rise is moderate and the Doppler effect plays an unimportant role.

The change in vapor generation rate which limits the transient power is due to heat addition and flow variations. The heat deposited in the coolant comes primarily from neutron slowing-down and gamma-ray interactions in the water, and secondarily, from heat conducted through the cladding. The heat flux from the clad to the coolant is a secondary contribution since the fuel rod time constant for conduction is larger than the time span (full width at half maximum is 0.2 s) of the transient.

The effect of control rod motion depends on the reactivity worth of the rods (and hence the cross sections), the rod speed and the time delay between the high flux signal and rod movement. The delay time obtained from plant data is not precisely defined.

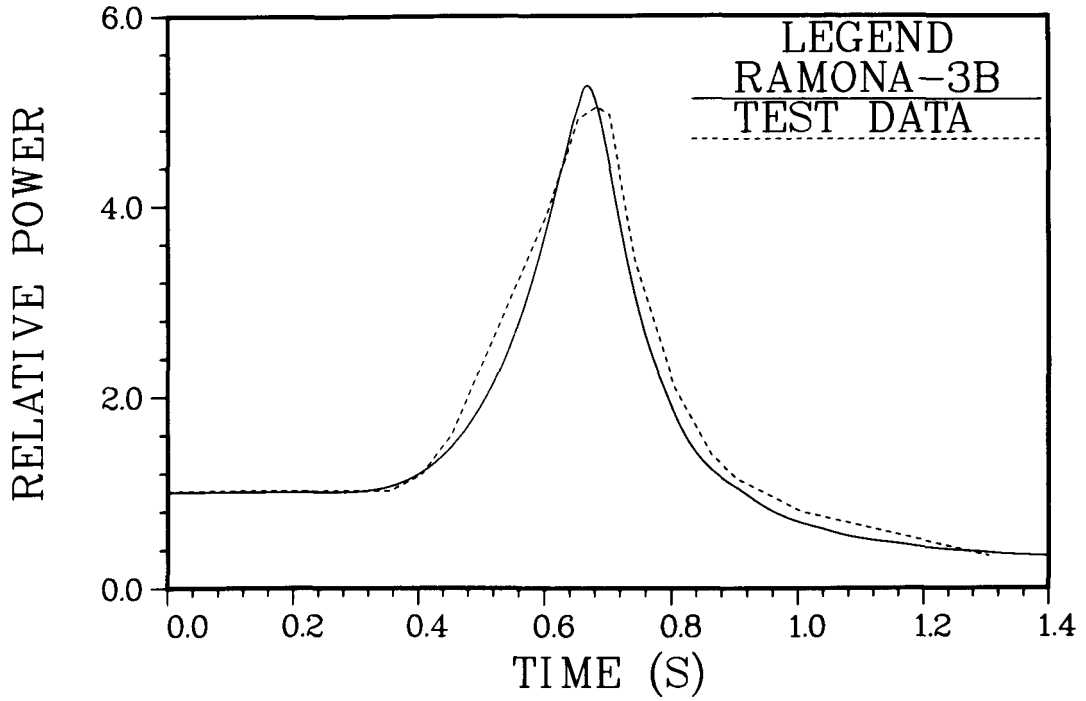

Figure 7.17 Transient Relative Core Power for Turbine Trip Test No. 1

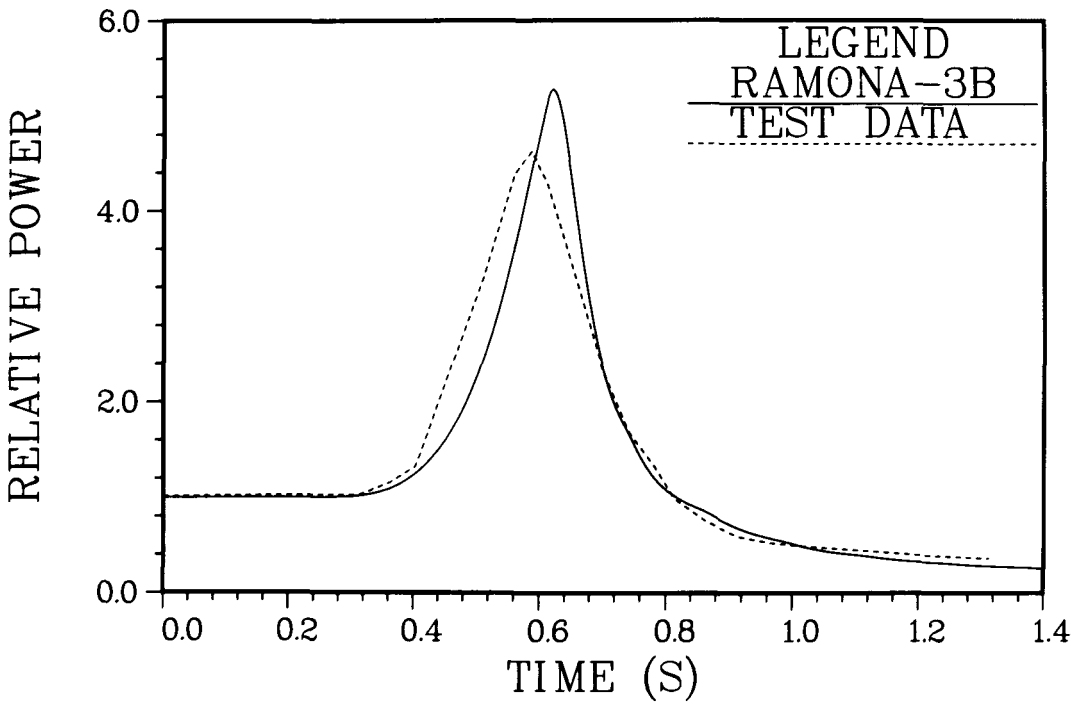

Figure 7.18 Transient Relative Core Power for Turbine Trip Test No. 2

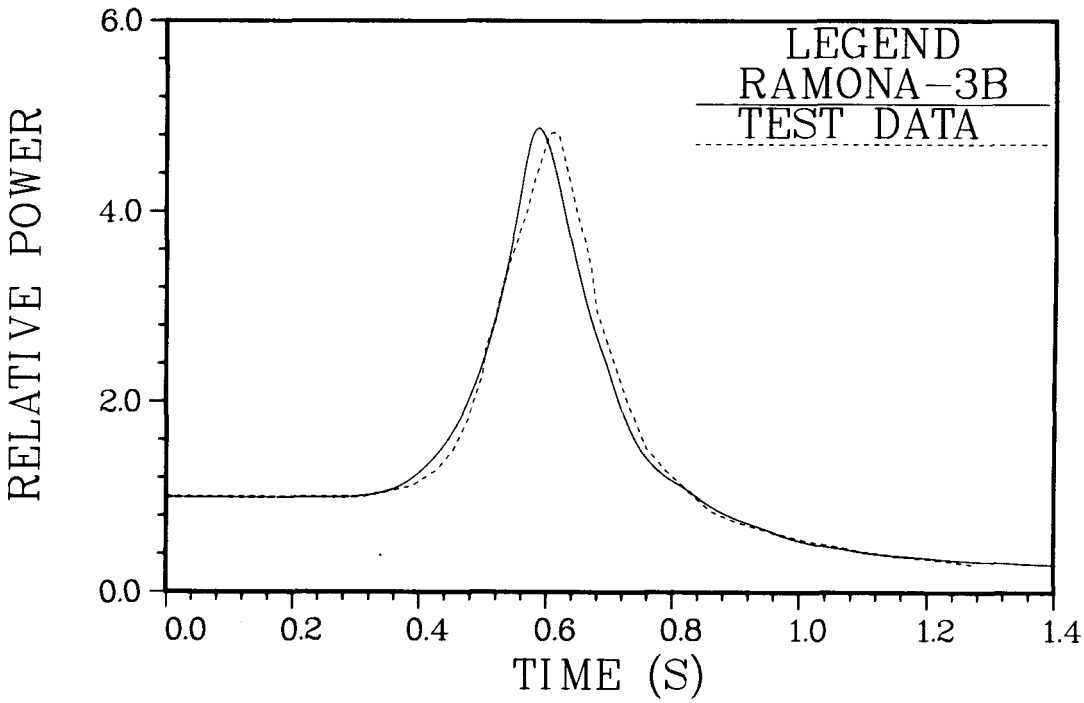

Figure 7.19 Transient Relative Core Power for Turbine Trip Test No. 3

7.4.5 Conclusions and Recommendations

Comparisons between RAMONA-3B calculations and the data for initial axial power distribution and steam dome pressure and core power during three turbine trip tests show general agreement. They demonstrate that the code could be used successfully for overpressurization transients such as those caused by turbine trip, MSIV closure, generator load rejection, loss of condenser vacuum and pressure regulator malfunction. Any future calculations with the cross-section set used in this analysis of the PB2 tests must be made with the Bankoff-Jones slip model option.

The PB2 tests can, and should, be used to provide a larger degree of qualification of RAMONA-3B than has been presented here. This is borne out by the many applications of other codes to those tests (Congdon and Linford 1978, Hornyik and Naser 1979, Hsu et al. 1978 and Moberg et al. 1981*). An expanded code assessment using the Peach Bottom tests would be very beneficial, not only in providing confidence in the code, but also in pointing out areas where improvements should be made.

A complete code assessment using the PB2 measurements must include the following elements which were lacking in the limited assessment described in the preceding sections:

i) Comparison with all data available

ii) An accurate plant input model

iii) The use of recommended constitutive descriptions

iv) Sensitivity studies

Regarding Item i); the results shown in Section 7.4.4 are for total core power and steam dome pressure during the early part of the transient. Data are available for longer times and for other variables that have not been extracted from the calculations; namely, downcomer water level, steam line pressure (at the main steam line isolation valve), pressure at the turbine stop valve and fission rate at 172 locations in the core. For the initial steady state, comparisons between calculations of the radially-averaged, axial power distribution and the corresponding data have been made. Measurements of axial power distributions in 43 locations are also available and should be utilized.

Regarding Item ii); the original calculations were done with an input model of the plant which was based on limited information and contained some inaccuracies. Each of the improvements that can be made are expected to have a small effect on the results of the calculations. Nevertheless, without making these changes it is not clear what the aggregate effect might be.

*A part of this study used the Scandpower version of RAMONA-3B for the calculation of TT3. It should be noted that sufficient differences exist between the BNL and ScP versions of the code so that that study does not constitute a part of the RAMONA-3B code assessment effort.

The specific data which must be changed (and which have been changed in subsequent calculations, such as those for transients with partial scram, Section 7.5) include the coefficients for the calculation of the drive pump head and torque, the drive pump moment of inertia and the jet pump loss coefficients. The loss coefficients used in the multichannel core representation have been refined since the turbine trip test calculations were done, as has the representation of the geometry for the flow outside the fuel bundle channel boxes. Our understanding of the neutron kinetics parameters has also improved and more accurate boundary conditions (see Section 2.5) and coupling coefficients (see Section 6.2.4) can be applied.

Regarding Item iii); the calculations should be done using the Bankoff-Malnes slip correlation, as recommended in Section 7.2.3, and a cross-section set derived, as explained in Sections 2.2.2 and 2.4, rather than the slip option and cross-section data used in the original calculation (cf. Section 7.4.3). Furthermore, minor changes in the fuel rod material properties described by input data should be made to be consistent with the recommendations given in Section 3.4.1.3.

Regarding Item iv); no sensitivity studies were carried out with respect to the PB2 calculations. This is a basic element of any code assessment effort (Fabic and Andersen 1981, p. 50) and is necessary in order to determine the uncertainty in a calculated key result as well as to indicate which input choices are the most important.

For the sensitivity studies one must consider physical data as well as user options which relate to code usage. Since other BWR codes have been assessed using these tests (Congdon and Linford 1978, Hornyik and Naser 1979, Hsu et al. 1978 and Moberg et al. 1981), it is already clear which physical parameters may lead to the greatest uncertainty. These include the scram delay time, direct energy deposition fraction for coolant, turbine stop valve closure rate, bypass valve delay time and flow characteristics, and effective delayed neutron fraction. The user options which must be tested relate to the time step control and nodalization.

7.5 Calculation of an Anticipated Transient with Partial Scram

7.5.1 Scope

Anticipated BWR transients in which there is no reactor trip (i.e., no scram) continue to be an unresolved licensing issue. Since the reactor does not shut down immediately, it is particularly important to adequately analyze the core neutronics and thermohydraulics during the transient. For those transients in which only part of the reactor is scrammed, as occurred in the Browns Ferry Plant, a multidimensional treatment of the spatial effects occurring in the core is essential. RAMONA-3B offers the unique capability to dynamically represent the spatial neutron kinetics coupled explicitly with the thermohydraulics of the entire system. For this reason, a transient accompanied by partial scram failure was simulated to provide a test of the overall code capability to perform such analyses. The results do not represent the

actual situation as it occurred at Browns Ferry, but rather, they demonstrate the code's ability to simulate similar transients.

The accident analyzed with RAMONA-3B is initiated by the (inadvertent) closure of the main steam line isolation valves (MSIVs) from (approximately) rated core power and flow conditions. It is assumed that all control rods in one-half the core fail to scram after the reactor trip signal is received. Other safety systems are assumed operable; the recirculation pumps trip, pressure relief valves operate, and the high pressure coolant injection system, the reactor core isolation cooling system and the standby liquid control system all actuate when required.

The MSIV closure event is one of the most limiting for peak vessel pressure and suppression pool temperature considerations. Although RAMONA-3B does not calculate the pool temperature, it does provide the steam flow through the safety and relief valves which is required for the pool temperature calculation.

Analyses of this accident have been performed at General Electric (Buchholz 1980) and at BNL (Lu et al. 1982). Both of these analyses used auxiliary steady-state core calculations to help determine the core power and used assumptions slightly different than those used with RAMONA-3B. Nevertheless, the results reported herein are consistent with the previous work.

7.5.2 Modeling of Accident Conditions

The reactor modeled for this calculation was a BWR/4 at end-of-cycle conditions similar to those used by Lu et al. (1982). The initial reactor state corresponded to operation at 104.5% of rated power and 100% of rated flow. All rods were initially withdrawn. Table 7.7 lists some of the initial conditions. The input listing given in the Appendix provides additional information.

The nodalization is given in Table 7.8. A coarse mesh was used in both the steam line and the core. This mesh was found to be acceptable based on comparisons with calculations using a finer mesh (see Section 6.8). The core model used had 32 nodes in the x-y plane for the neutron kinetics calculation, but took advantage of half-core symmetry. Figure 7.20 shows the half-core configuration and the numbering for the neutron kinetics nodes and thermohydraulic channels. When the rods in half the core are inserted, it is the left side (i.e., nodes 1-3, 7-9, 13 and 14) that becomes rodded. It is recognized that there are control blades at the boundaries between nodes 3 and 4, 9 and 10 and 14 and 15, and that this representation "splits" them in half. Although this might lead to an error in the power in these nodes, this error is expected to be small and have a negligible effect on the total core power and on the thermohydraulic calculation. This is due to the fact that the thermohydraulic channels include neutron kinetics nodes away from the rodded-unrodded interface.

The cross sections used were originally derived for use with a two-dimensional (R,Z) coupled neutron kinetics and core thermohydraulics code (BNL-TWIGL). The method used to obtain the data (Lu et al 1979, p. 19) did not

Table 7.7

Initial Conditions for the ATWS/2

Thermal power, MW	3440.
System pressure, MPa	7.03
Core (including bypass) inlet flow rate, kg s^{-1}	1.28×10^4
Drive loop flow rate, kg s^{-1}	4.34×10^3
Feedwater flow rate, kg s^{-1}	1.73×10^3
Core inlet subcooling, K	12.2
Control rod pattern	All Out

Table 7.8

Nodalization for MSIV Closure Transient

Region	Number of Nodes
Upper downcomer	6
Lower downcomer	6
Lower plenum	5
Upper plenum, riser, separator	5
Steam line (4 lines modeled as 1 line)	
Vessel to MSIV	3
MSIV to junction for BPV	4
Junction for BPV to TSV	1
Junction for BPV to BPV	2
Core	
Axial	12
Planar	
Neutron kinetics (half-core)	16
Thermohydraulics	7

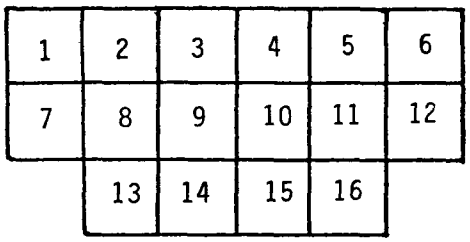

a) Neutron Kinetics Nodes

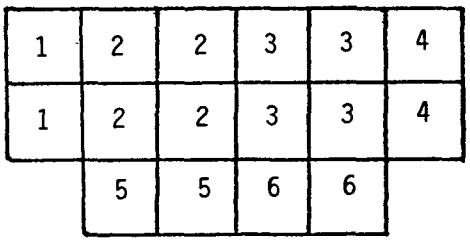

b) Thermohydraulic Channels

Figure 7.20 Core Configuration for Partial Scram Calculation

include core burnup calculations. Beginning-of-life data were systematically varied until the core-average axial power distribution gave agreement with the expected end-of-life (Haling) power distribution. This procedure resulted in eleven cross-section sets which are distributed to 16 material (or exposure) zones based on eight axial and two radial divisions.

In transforming the actual core geometry (cf. Figure 7.10) into the configuration shown in Figure 7.20, no attempt was made to homogenize fuel bundles with reflector water for the nodes at the core periphery. The good agreement in radial power distribution with a more detailed calculation (see Section 6.8) justifies this approach.

The reactor protection and control system as assumed for this calculation (based on Lu et al. 1982) is summarized in Table 7.9. Reactor trip would normally occur due to the signal for MSIV closure. That signal is ignored and the assumption is that the trip signal will be due to high power. The control rods in half the core move at a speed of 0.91 m s^{-1}. The low level signal for both the high pressure coolant injection (HPCI) and the reactor core isolation cooling (RCIC) systems is -1.77 m relative to the initial water level outside the steam separator skirts. The HPCI and RCIC systems are assumed to take 3 s to reach their full flow rate.

The two trip signals given for the safety and relief valves (S/RVs) in Table 7.9 are the closing and opening pressures, respectively. The opening and closing flow rates are assumed to be exponential with a time constant of 0.1 s (see Section 5.2.2). The feedwater control system is represented by an input boundary condition. The flow rate was obtained from GE (Buchholz 1980) where it was calculated for a similar accident situation. Figure 7.21 is a plot of the flow rate from the feedwater sparger. The early flow (< 200 s) is due to the feedwater system (water at 196°C) and the latter flow (> 300 s) is due to the HPCI and RCIC systems (water at 48.9°C). The standby liquid control system was initiated on a time signal to represent operator action at 255 s coupled with a delay time of 45 s. The rate of boron addition to the vessel at the location of the jet pump instrumentation lines (cf. Table 7.9) corresponds to an injectant flow rate of 2.7 kg s^{-1} (43 gpm) with a boron concentration of 23,000 ppm.

7.5.3 Results

The transient calculated with RAMONA-3B was initiated by an MSIV closure and then calculated for 400 s. During this period, control rods were inserted, the recirculation pumps tripped, pressure relief valves opened and closed, the amount of feedwater changed and the HPCI/RCIC and SLCS systems were actuated. The effect of these actions and the interaction of the different feedback mechanisms makes the local and global system behavior very complex. The major events and trends during the transient as calculated by RAMONA-3B are given in Table 7.10. The following discussion is separated into five parts in order to explain certain features of the calculation.

Figure 7.21

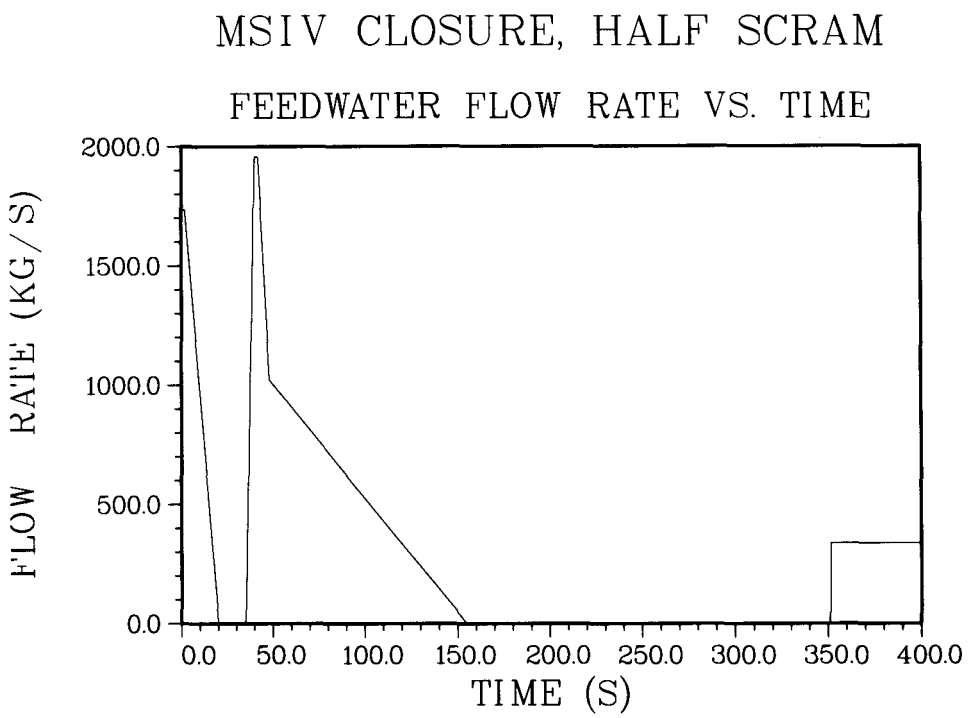
MSIV CLOSURE, HALF SCRAM
FEEDWATER FLOW RATE VS. TIME
FLOW RATE (KG/S)
2000.0
1500.0
1000.0
500.0
0.0
0.0
50.0
100.0
150.0
200.0
250.0
300.0
350.0
400.0
TIME (S)

Table 7.9

Reactor Protection and Control System

	Trip Signal	Delay Time s	Capacity kg s^{-1}
MSIV closure	Time zero	4 s for closure	Not applicable(N.A.)
Reactor trip	120% rated power	0.3	N.A.
Recirculation pump trip	System pressure 8.03 MPa	0.53	N.A.
HPCI/RCIC	Low level	27	337
S/RV			
Bank 1 (4R)*	7.48, 7.62 MPa	0.4	395
Bank 2 (4R)	7.55, 7.69 MPa	0.4	395
Bank 3 (3R)	7.62, 7.76 MPa	0.4	297
Bank 4 (2S)	8.53, 8.67 MPa	0.4	235
Feedwater	Automatic system simulated (cf. Figure 7.21)		
SLCS	255 s (Operator)	45	.062 (boron)

*Number of relief (R) or safety (s) valves in bank

Table 7.10

Transient Chronology

Time (s)	Event/Comment
0	MSIV begins to close initiating the transient. It closes completely in 4 s causing system pressure to rise. This in turn causes void collapse and hence a reactor power increase.
2	Feedwater trip. Feedwater reduced to zero in 18 s.
2.2	Power reaches 120% of rated power. After a 0.3 s delay, half the control rods are inserted in 4 s.
3.8-4.0	System pressure reaches the setpoints of relief valve banks 1-3. All valves stay open until approximately 15 s.
4.1	Overall reactor power peaks at a power of 2.9 relative to the steady-state power. Unscrammed side of reactor peaks at a relative power of 3.5.
4.5	System pressure reaches 8.03 MPa. After 0.53 s delay, recirculation pump trips.
5-6	Power in scrammed half of reactor reaches decay heat levels and remains so for duration of transient.
6-7	Average fuel temperature for hottest node peaks at 1300°C.
8	System pressure peaks at approximately 8.3 MPa.
15	Liquid velocity in downcomer below bubble rise velocity setting up potential for countercurrent flow.
20	Feedwater shut off completely.
30-400	Relief valve bank 1 opening and closing drives the system pressure in an oscillatory manner. Other system variables including reactivity follow.
35	Downcomer water level at temporary low. Feedwater turned on to simulate control system response.
35-120	Water level rises above steam separator skirt.
60	Recirculation pump coastdown completed.
155	Feedwater flow rate reduced to zero.

Table 7.10 (continued)

Transient Chronology

Time (s)	Event/Comment
140-350	Water level decreases.
180-220	Liquid in vessel approaches saturation temperature following removal of subcooled feedwater. Average void fraction in core increases from 0.23 to 0.30. In response to system pressure oscillations, liquid in vessel goes from being superheated to subcooled and vapor generation rate changes accordingly.
300	Boron injection is initated.
320	Boron enters core.
350	HPCI flow initiated.
360	Water level stabilized. HPCI flow approximates the steam line flow.
375	Subcooled water from HPCI injection reaches core entrance.
400	End of demonstration run.

a) Initial Overpressurization Transient

The MSIV closure causes an increase in pressure in the vessel (cf. Figure 7.22). This pressure pulse is less severe than that caused by a turbine stop valve closure due to the relatively long time (4 s) it takes for the MSIV to close. The increase in pressure collapses steam voids (cf. Figure 7.23) which has the effect of increasing core power (cf. Figure 7.24). This tends to be self-limiting because an increase in power increases the void fraction. However, the insertion of control rods due to an overpower (120% of rated power) signal, the decrease in flow due to the RPT and the decrease in pressure due to the opening of relief valves combine to terminate the early phase of the transient.

Figure 7.25 shows the fission rate during this early phase for (neutron kinetics) channel 5 (cf. Figure 7.20) in which all control rods are inserted and channel 2 in which no control rods move. Reactor trip occurs at 2.5 s and by 10 s only the decay heat level is significant in channel 5. Note that the ability to monitor behavior such as in Figure 7.25 requires a code with spatial neutron kinetics. The changes in fission rate that are most pronounced on Figure 7.25 (and not seen on Figure 7.24 because of the different scale) occur after 2.8 s with a frequency of 3 Hz. These are due to the insertion of control rods and the coarseness of the axial mesh. The rods move at a speed of 3 nodes per second. As soon as a control rod enters a node, the cross section is modified for the entire node (.30 m long). This artificial perturbation can be eliminated with a finer noding or with a control density function for the node that is not proportional to the fractional insertion as is currently found in RAMONA-3B. However, this effect should not change the behavior of the fission rate averaged over several periods ($\sim$ 1 s).

b) Effect of Recirculation Pump Trip (RPT)

The RPT occurs due to the pressure exceeding 8.03 MPa at 5 s. The resulting drive loop flow rate is shown in Figure 7.26. (This flow rate and the pump speed after a RPT with only a feedwater trip and no control rod insertion have been compared with GE results for up to 12 s (Philadelphia Electric 1972, Fig. 14.4.12b) and found to be within 3%.) The flow rates for (thermohydraulic) channels 2 and 3 (cf. Figure 7.20) are shown in Figure 7.27 for the core inlet and for the core exit in Figure 7.28. Channel 3 contains control rods after the reactor trip and channel 2 is unrodded. Because the power is higher in channel 2 than in channel 3, the flow rate is also higher. Figures 7.27 and 7.28 show that the natural circulation flow rate in this transient is 25-30% of the steady-state flow rate.

By reducing the flow rate to natural circulation, the void fraction is maintained reasonably high (cf. Figure 7.23). Because of void feedback the reactor power is kept lower than might have been attained otherwise. (Note that the pressure is approximately 7.6 MPa during the transient which is higher than the initial value of 7.0 MPa, and this by itself would decrease the void fraction.) This is an important strategy for dealing with this type of accident. Figure 7.24 shows that the time-average relative power is $\sim$20% up to 150 s and $\sim$15% during the latter part of the transient.

Figure 7.22

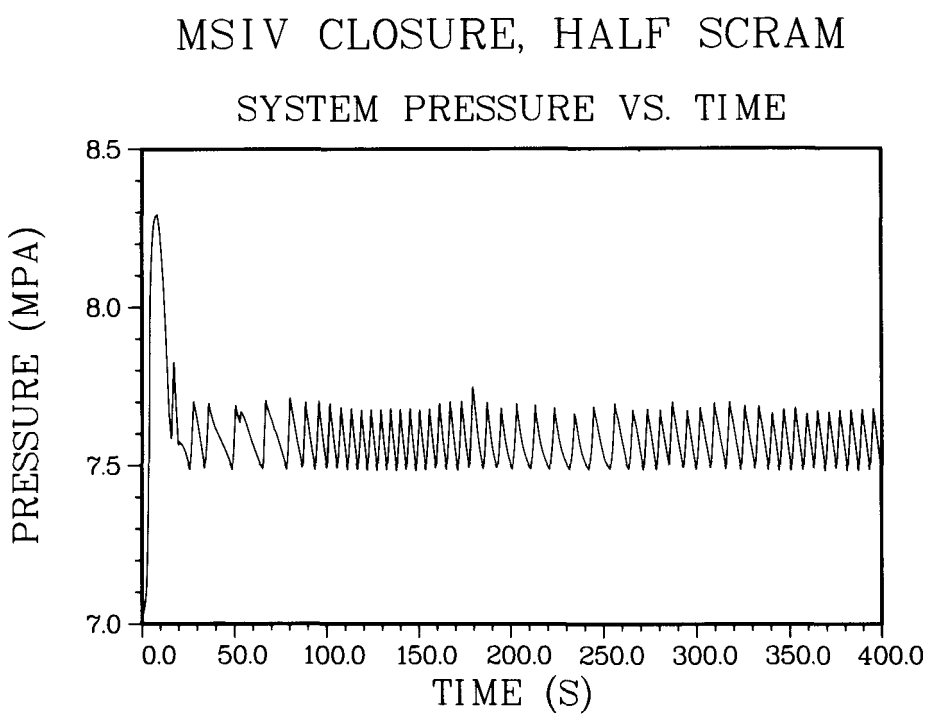

Figure 7.23

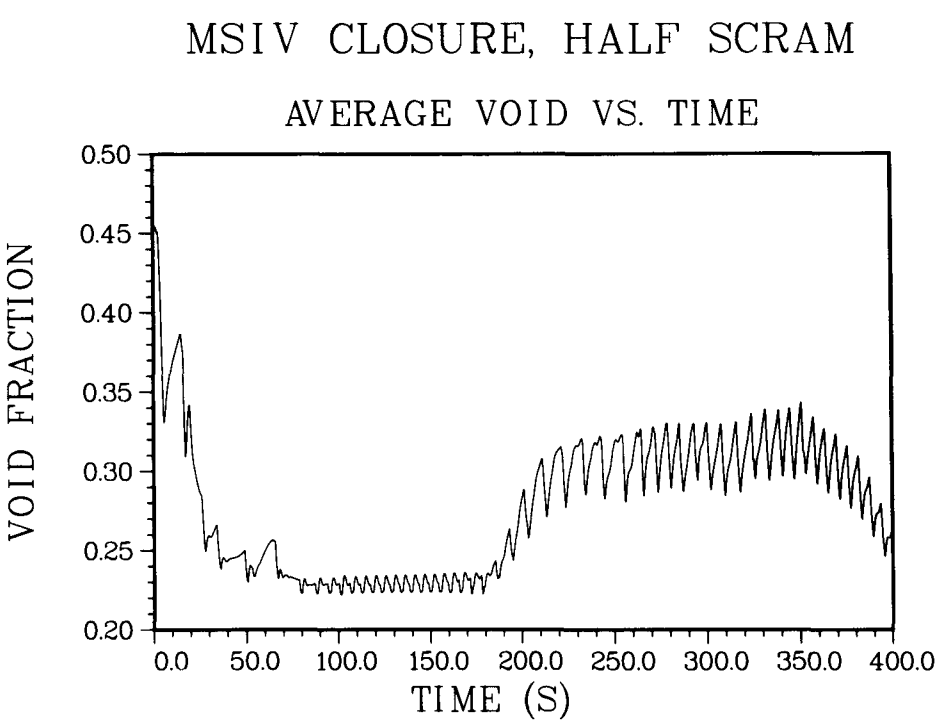

Figure 7.24

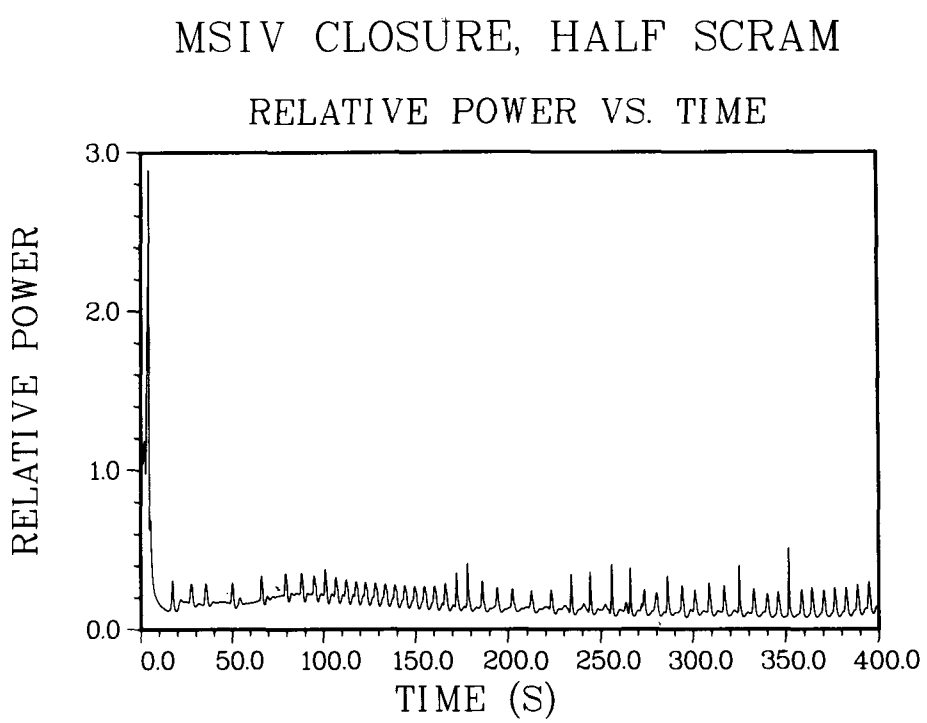

Figure 7.25

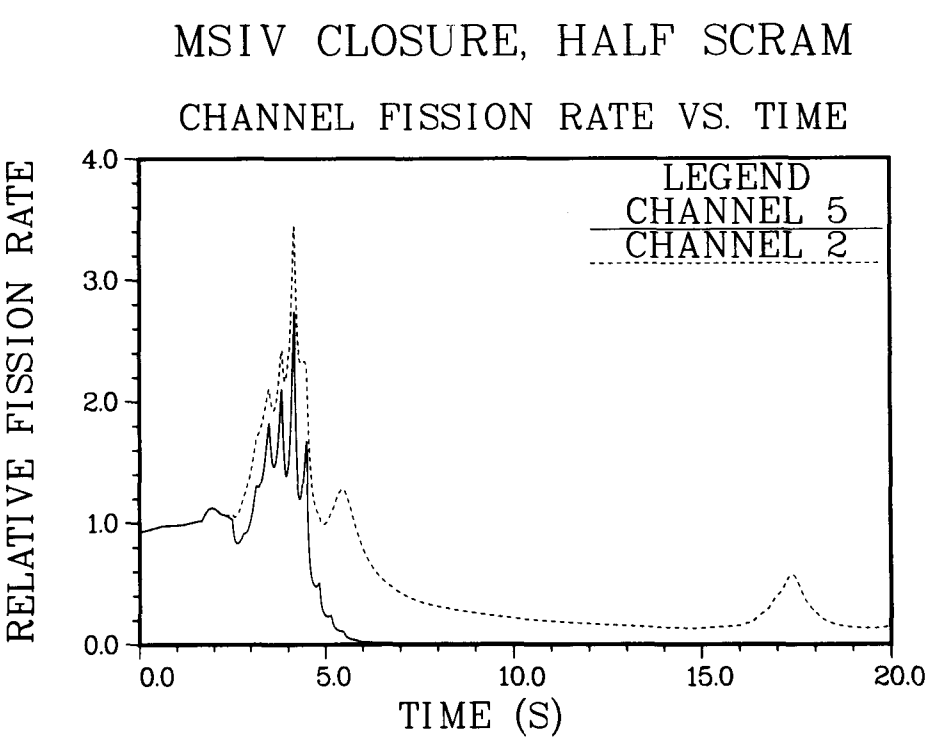

Figure 7.26

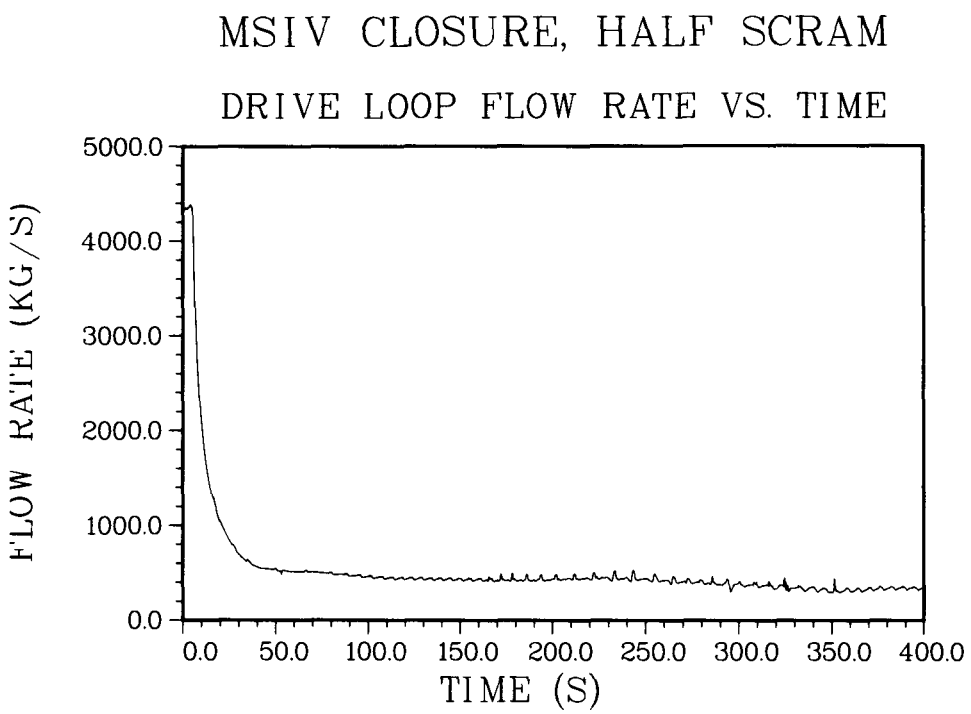

Figure 7.27

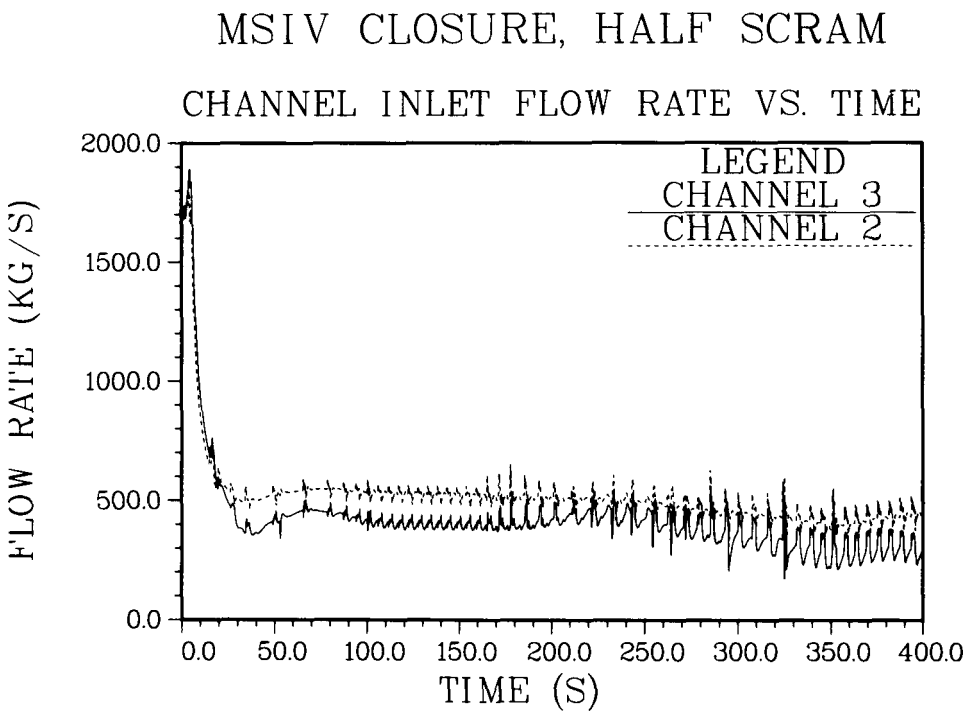

Figure 7.28

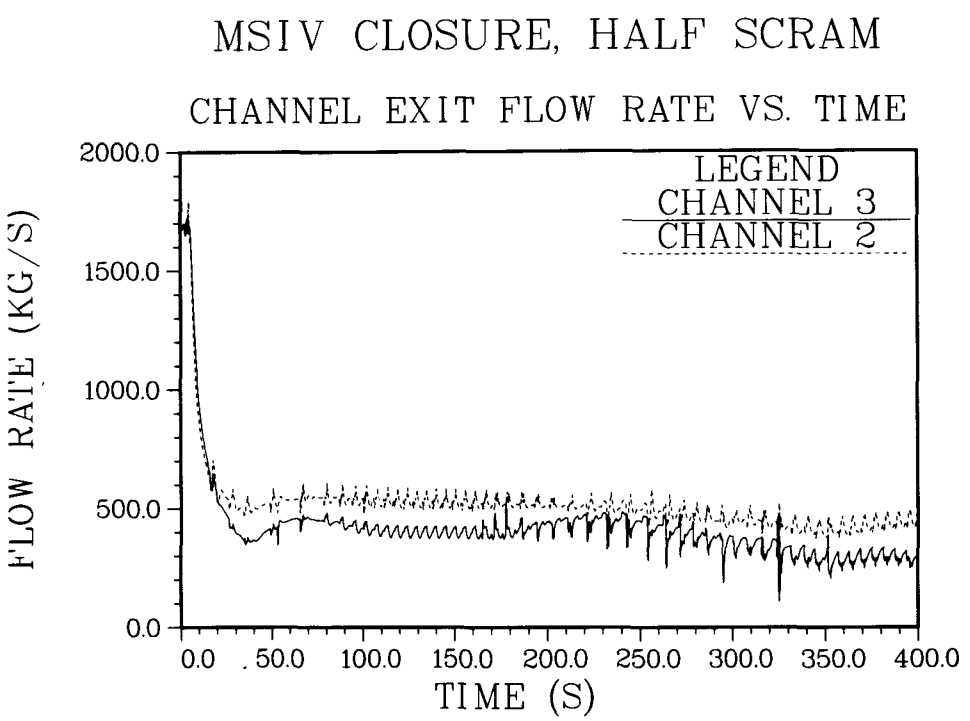
MSIV CLOSURE, HALF SCRAM
CHANNEL EXIT FLOW RATE VS. TIME
LEGEND
CHANNEL 3
CHANNEL 2
FLOW RATE (KG/S)
2000.0
1500.0
1000.0
500.0
0.0
0.0
50.0
100.0
150.0
200.0
250.0
300.0
350.0
400.0
TIME (S)

c) Effect of Relief Valve Cycling

The initial overpressurization (cf. Figures 7.22 and 7.29) is sufficient to open all three banks of relief valves. However, after a 10 s period of venting and a reduction in core power, the pressure is only sufficient to actuate one bank of valves. Since the MSIVs have closed, the vapor generated in the core exhausts through this bank. The opening of valves reduces pressure, and hence, the valves open and close in a fairly regular cycle. The flow rate through all the valves is given in Figure 7.30. The period of the valve cycling shown ranges from 5-15 s. Hand calculations at two different time intervals ($\sim$ 70 s and 130 s) confirmed the periods calculated by the code. The variation of this time period is expected since the rate of pressure drop when the valve is open is primarily governed by the difference between the steam flow rate out of the vessel (cf. Figure 7.31) and the total vapor generation rate in the vessel, i.e., a small difference between two large numbers.

The cycling of the relief valves affects the system pressure (cf. Figures 7.22 and 7.29) and this in turn causes the oscillation in power during the transient (cf. Figures 7.24 and 7.25). These oscillations can also be seen in the flow rates shown in Figures 7.27 and 7.28 and the core-average void fraction in Figure 7.23.

The flow rates at the core exit shown in Figure 7.28 for a channel in which the power is relatively high and for a channel with only decay heat are not in phase. During the latter half of the transient they are close to 180° out-of-phase with the flow rate increasing in one channel when it is decreasing in the other and vice-versa.

The flow rate through the valves (cf. Figure 7.30) is one of the key parameters in this transient since it will determine the temperature of the suppression pool. Since the pool temperature is such an important parameter, it is recommended that a simple calculation based on a pool-average mass and energy balance be added to RAMONA-3B.

d) Water Level in the Vessel

Figure 7.32 shows the water level in the downcomer region. The water inventory in the vessel and the level in the downcomer are closely related to the feedwater flow, as can be seen by comparing Figure 7.21 with Figure 7.32. The water level calculation in RAMONA-3B takes into account that steam voids are present in the downcomer; the measurement in a BWR uses an instrumentation line in which the void condition may be different. Hence, care must be exercised in interpreting the calculated water level.

e) Other Features of the Core Conditions

Figure 7.33 shows the core-average fuel temperature which in general follows the core-average power (cf. Figure 7.24). RAMONA-3B also identifies the location and magnitude of the peak nodal-average temperature.

Figure 7.34 shows the core inlet subcooling which is a strong function of the feedwater flow rate (cf. Figure 7.21). The inlet subcooling (along with

Figure 7.29

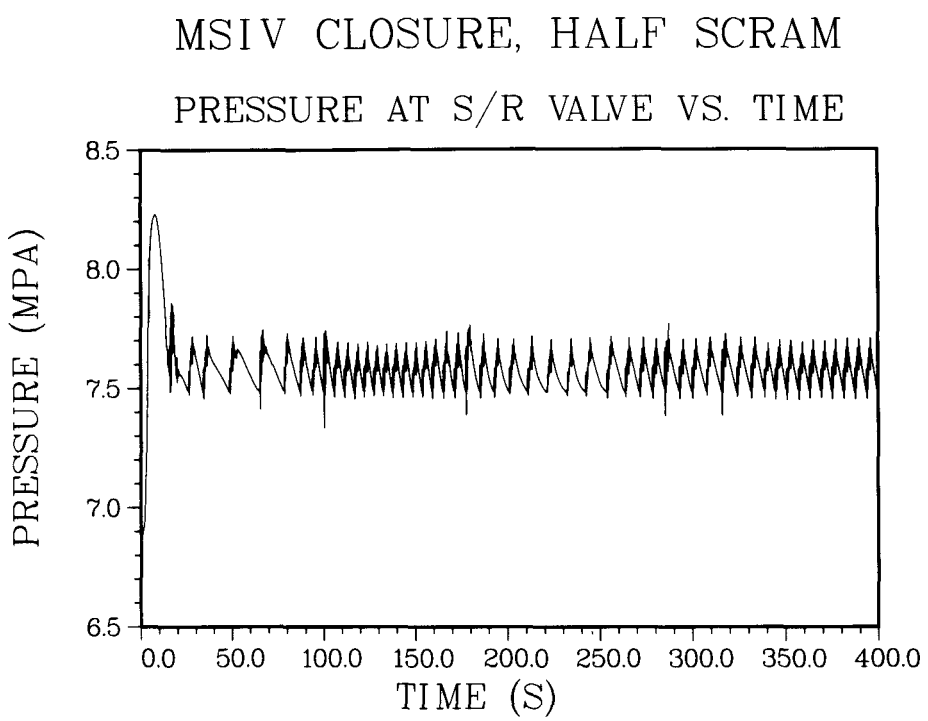

Figure 7.30

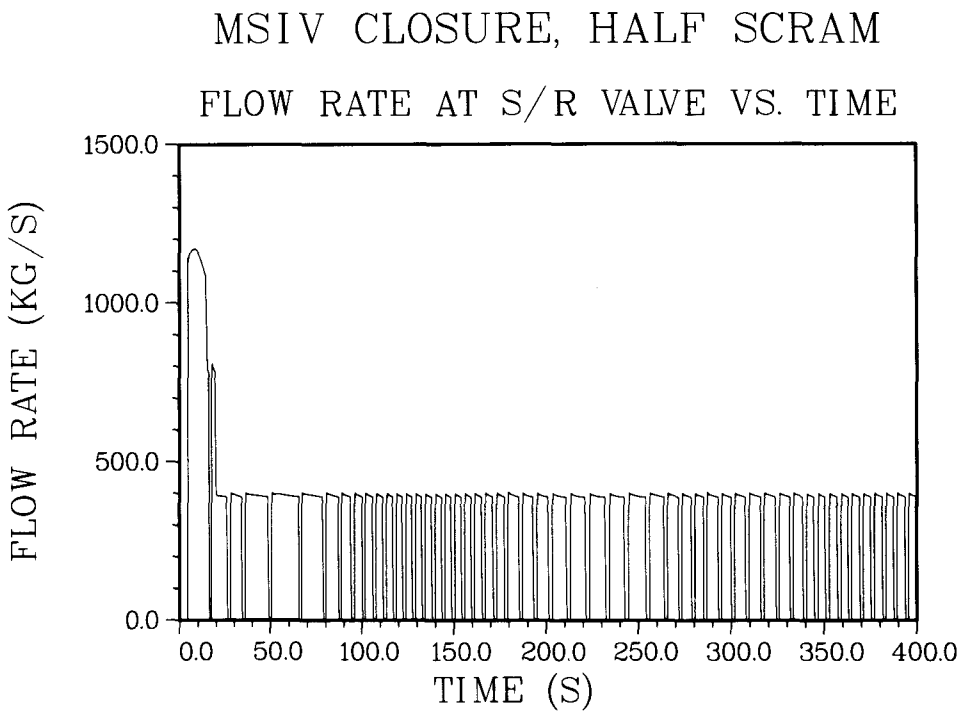

Figure 7.31

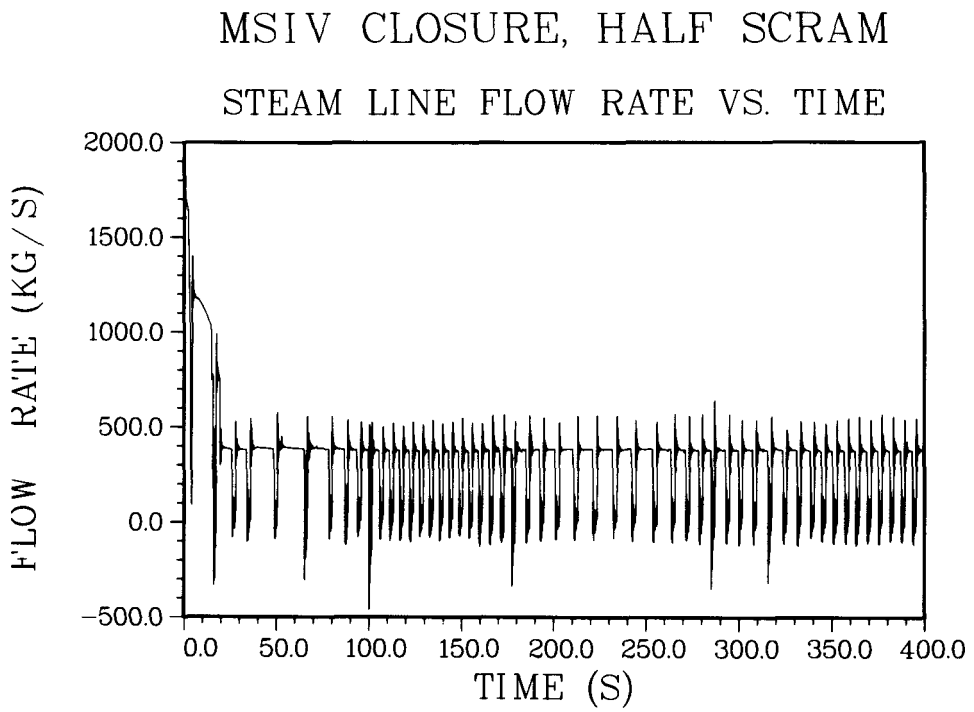

Figure 7.32

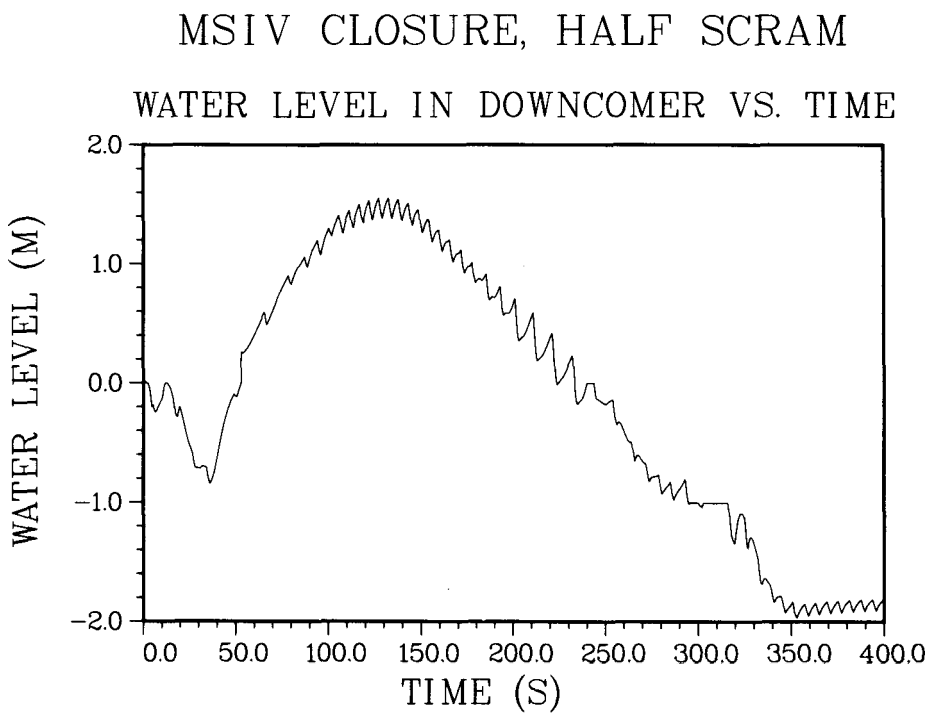

Figure 7.33

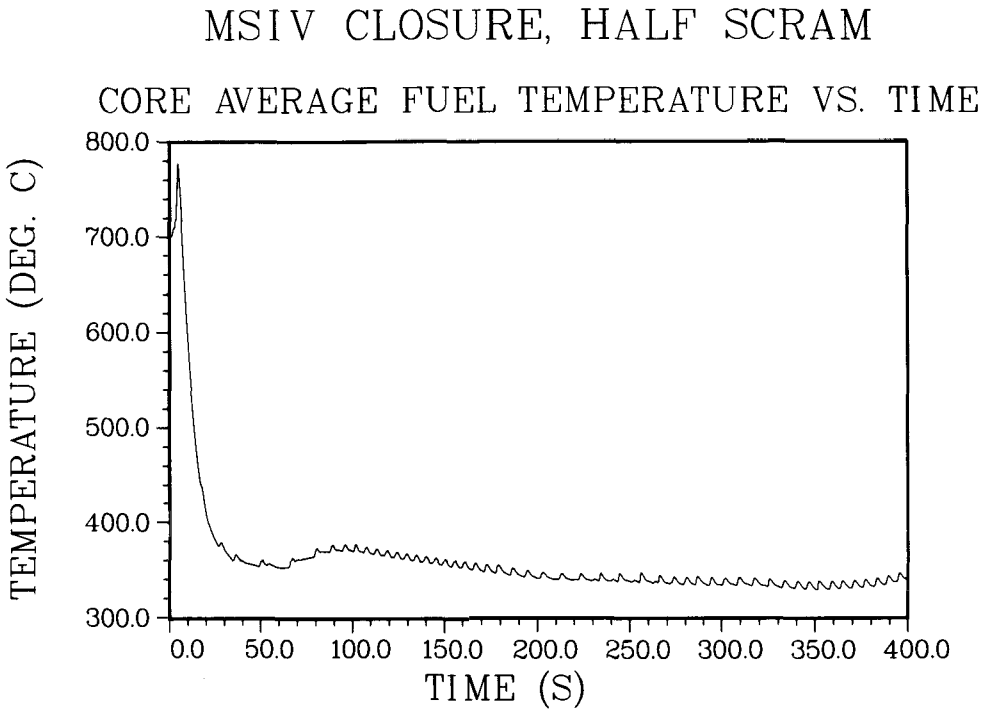

Figure 7.34

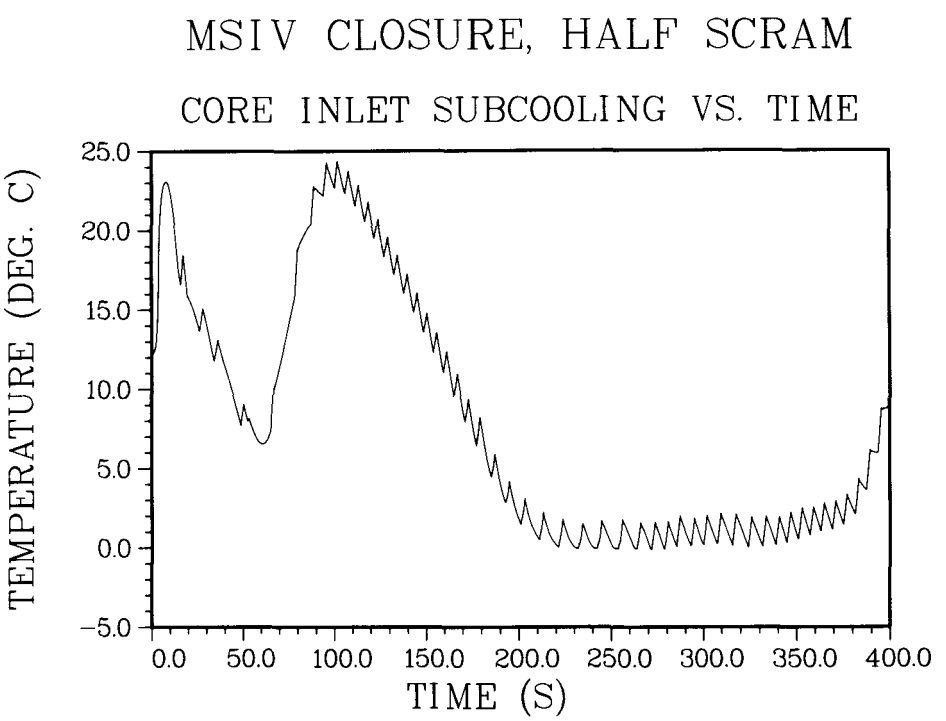

the flow rate and power) helps determine the void fraction in the core. When the inlet subcooling is close to zero at times greater than 200 s, the void fraction significantly increases (cf. Figure 7.23). This reduction in inlet subcooling corresponds to a reduction in subcooling throughout the vessel. When this occurs, the pressure oscillations cause the vessel liquid state to oscillate between subcooled and superheated and flashing and condensation can take place.

Figure 7.35 shows the inlet and outlet flow rates in the bypass channel. The flow rate in the entire system is decreasing, and since there is little void created in the bypass channel (and hence no corresponding buoyancy), the flow rate approaches zero. The flow rate at the top of the bypass channel is slightly negative several times at $\sim$300 s due to the collapse of voids. There may be other transients (e.g., those with no control rod insertion) where the void fraction in the bypass region becomes relatively large (> 0.10). The corresponding loss of neutron moderation at the top of the core where in-channel void fractions are usually high may be important in changing reactivity. It is recommended that the cross sections be made a function of the bypass void fraction to take this into account.

Figures 7.36 and 7.37 show the average axial distribution of void and power at different times during the transient. No excessive power peaking or voiding occurs. No node reached critical heat flux (CHF) during this calculation. The CHF calculation is based on nodal-average properties. A more conservative approach would be to apply some correction factor (in the form perhaps of a power peaking factor) in order to have the CHF calculation apply to the most limiting fuel bundle within a thermohyraulic node. The power distributions in Figure 7.37 change dramatically during the transient; another demonstration of the importance of using spatial neutron kinetics.

f) The Effect of Boron

Boron enters the vessel at the location of the jet pump at 300 s (cf. Table 7.9). It starts to enter the core approximately 20 s later and increases to a concentration of $\sim$20 ppm by the time the calculation is terminated at 400 s. This is insufficient to shut down the reactor. It is expected to take $\sim$400 ppm of boron before the fission rate is reduced to a negligible level and this will take approximately 2000 s.

Since it was not practical to calculate this test run for such a long time, an artificial problem was set up to demonstrate the effect of boron. The latter part of the calculation was rerun with a boron injection rate ten times the (correct) rate used originally. The resulting boron concentration in the lower downcomer region and in the bottom third of the core is shown in Figure 7.38. The boron concentration will increase in steps determined by the transit time of the recirculating water which is approximately 100 s for the conditions experienced in this transient. Figure 7.38 shows the first step for both regions modified by flow oscillations.

The relative power during this time interval is shown in Figure 7.39. Although the power is a function of several things that are changing in the reactor (e.g., flow rate and inlet subcooling) the clear trend toward lower

Figure 7.35

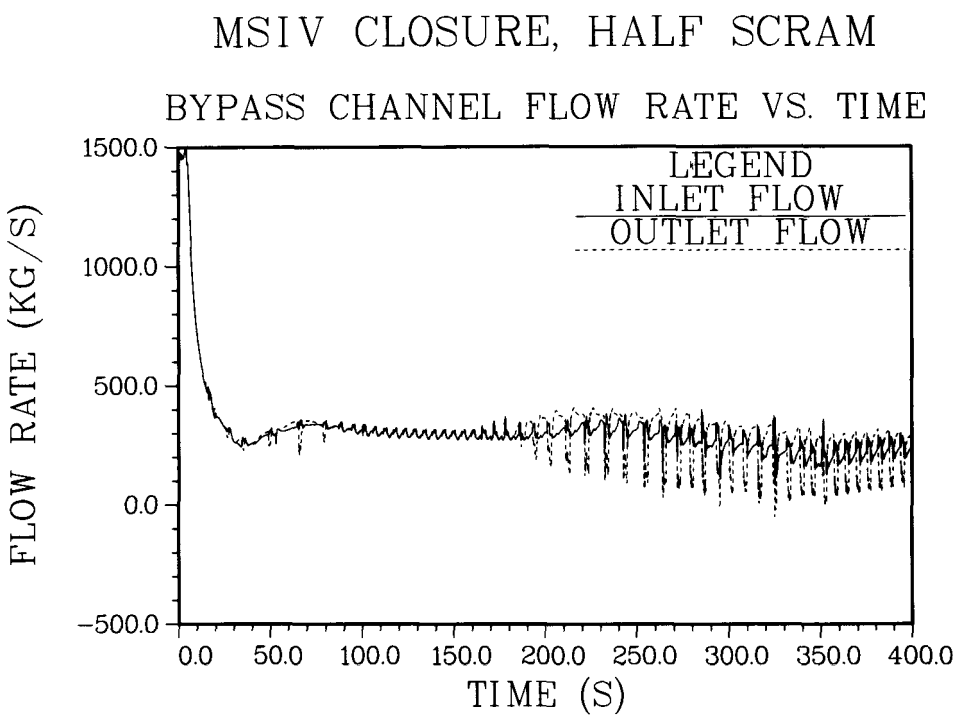
MSIV CLOSURE, HALF SCRAM
BYPASS CHANNEL FLOW RATE VS. TIME
LEGEND
INLET FLOW
OUTLET FLOW
FLOW RATE (KG/S)
1500.0
1000.0
500.0
0.0
-500.0
0.0
50.0
100.0
150.0
200.0
250.0
300.0
350.0
400.0
TIME (S)

Figure 7.36a

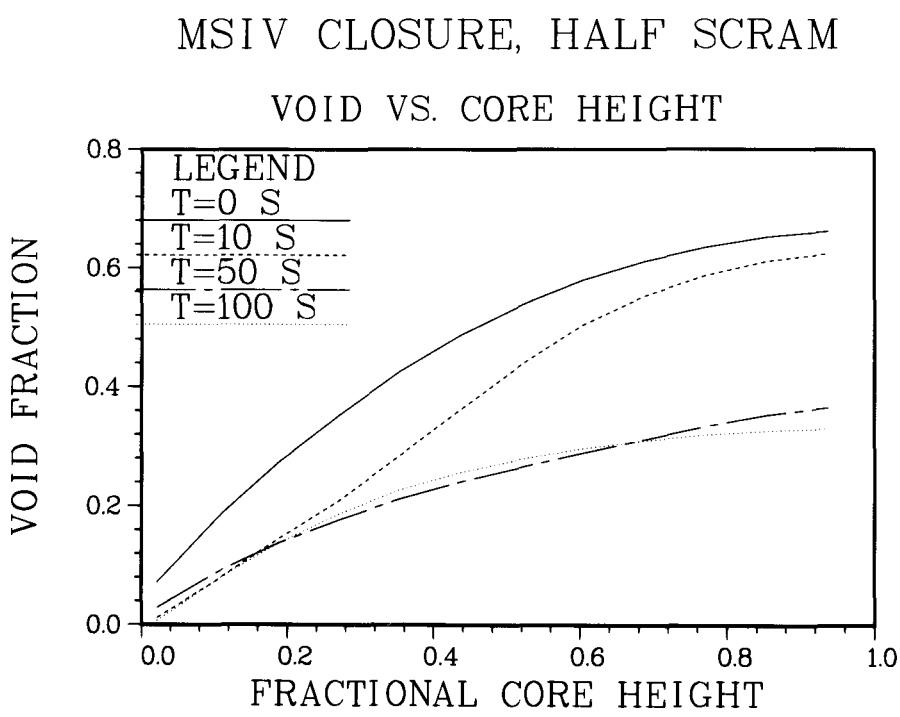

Figure 7.36b

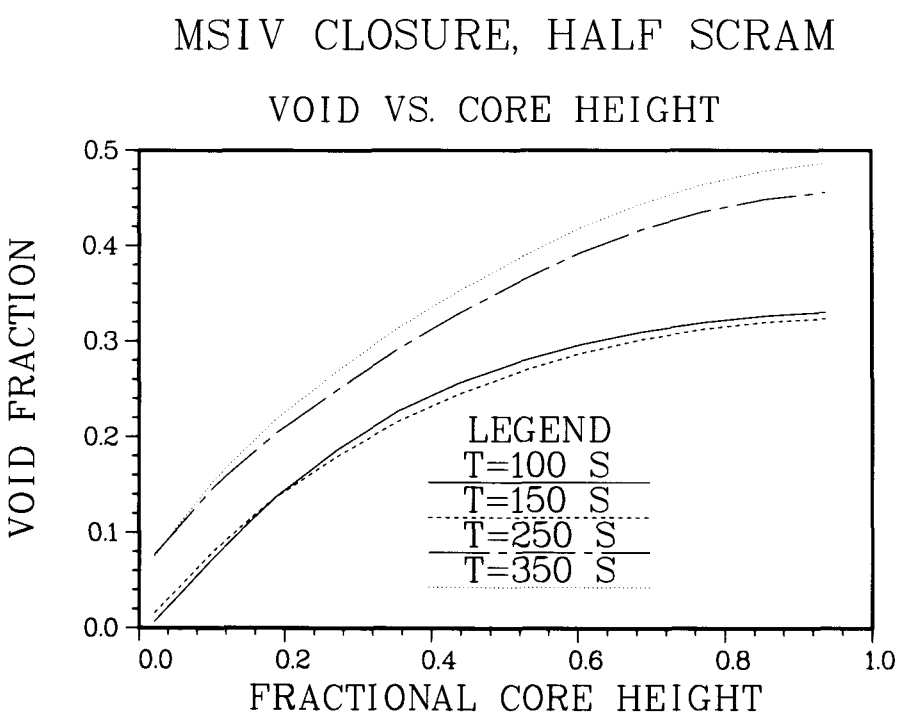

Figure 7.37a

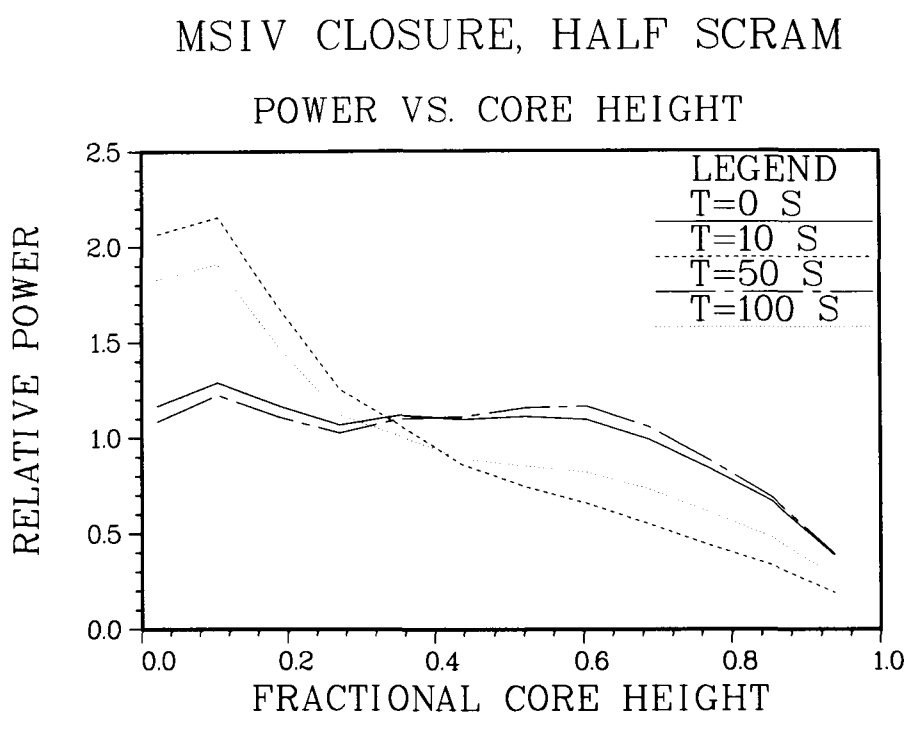

Figure 7.37b

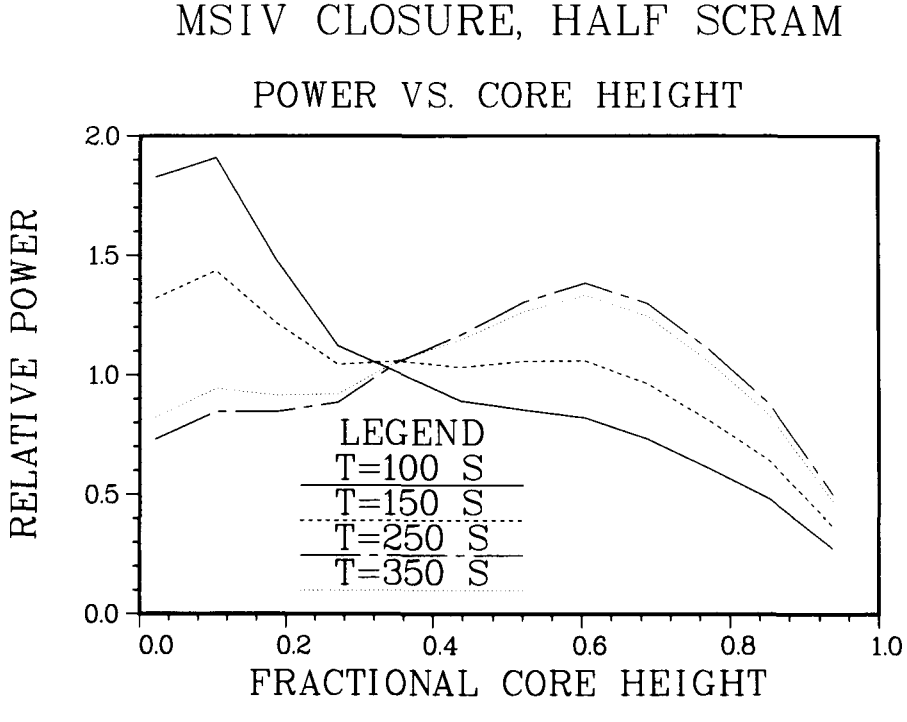

Figure 7.38

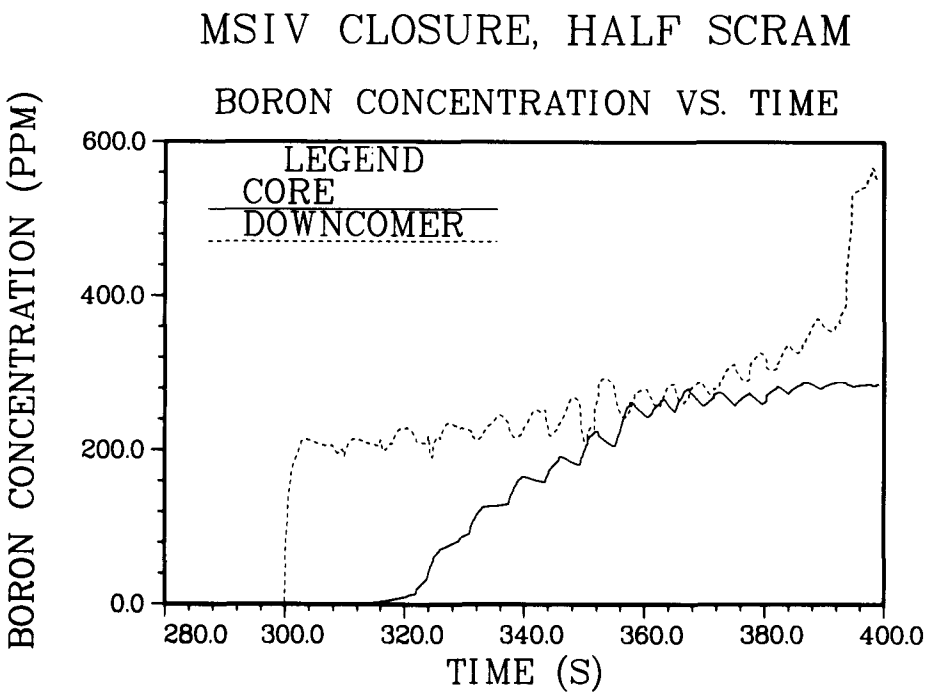

Figure 7.39

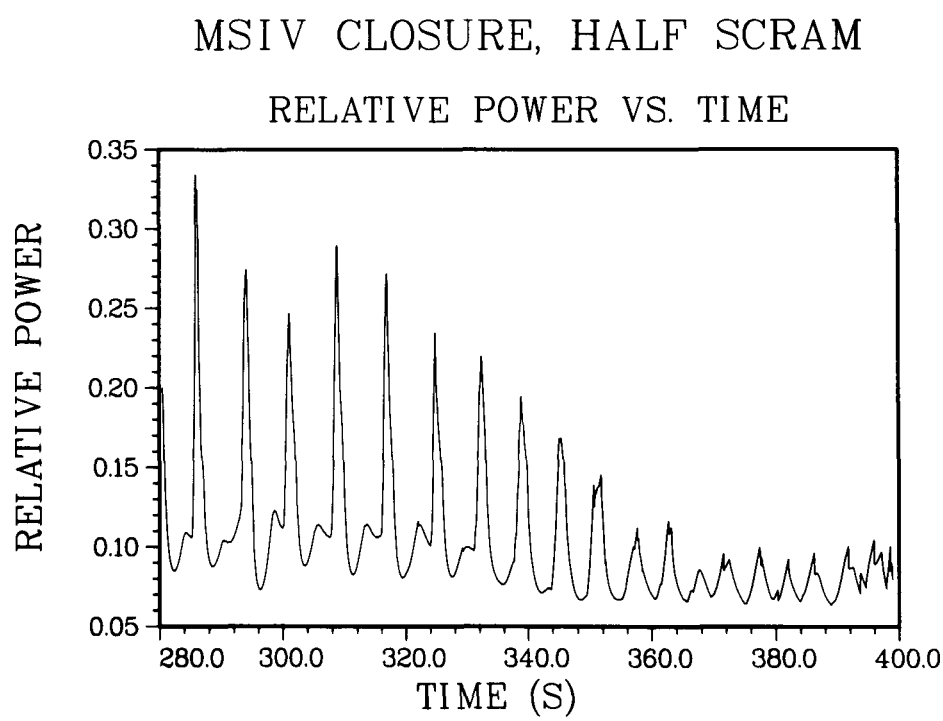

peaks in the power oscillations is due to the presence of boron and demonstrates that the effect of boron is being accounted for by RAMONA-3B.

7.5.4 Conclusions and Recommendations

RAMONA-3B has been successfully applied to a transient initiated by MSIV closure in which only the control rods in half of the core are inserted after reactor trip. This accident is an excellent example of a situation in which it is important to model the steam supply system with a core component that includes three-dimensional neutron kinetics. RAMONA-3B is unique in its ability to satisfy this requirement. This calculation has involved not only the basic vessel and steam line thermohydraulic models and the neutron kinetics model, but also the activation of different parts of the control and protection system model. Specifically, the calculation involves reactor trip, recirculation pump trip, S/RV and MSIV actuation, feedwater, HPCI/RCIC and SLCS.

The code calculated over a range of conditions encountered in 400 s of reactor time with a (reasonable) computing time on BNL's CDC-7600 equipment that averaged $\sim$15 times reactor time. The results are in qualitative agreement with those reported by Lu et al. (1982), i.e., there is an initial overpressurization phase followed by a long period of operation with natural circulation characterized by oscillations with a frequency of $\sim$0.1 Hz. This oscillatory behavior is reflected in power, pressure, flow and other system variables. Quantitative comparisons with other calculations (Lu et al. 1982 and Buchholz 1981) are not possible because of differences in the assumptions used in each calculation.

It is recommended that a systematic comparison be made with other available calculations. This would best be accomplished for transients in which there is no control rod insertion at all since there is an extensive set of such GE calculations. These calculations could be done using a one-dimensional core model in RAMONA-3B since that is sufficient in terms of core modeling and more efficient than a three-dimensional core model. Further calculations should also address the sensitivity of results to uncertainties in various input parameters and to different input options in order to obtain estimates of the overall uncertainty.

Future work should also be directed toward developing greater confidence in some existing models and improving upon others. In order to further test the coarse mesh core representation (cf. Section 6.8), transient results should be compared with those obtained with a finer mesh. The flow characteristics during natural circulation should be further tested by comparisons with data expected during 1982 from the Two Loop Test Apparatus Facility. Modeling which needs to be improved includes: 1) the adding of a limiting-bundle correction for CHF calculations with large thermohydraulic channels; 2) taking into account nonequilibrium effects when cold HPCI/RCIC water enters the vessel; 3) correcting the water level calculation to correspond to instrument reading; 4) improving the carry-under model by allowing for the carry-under to vary during the transient and 5) making the cross sections a function of bypass void fraction.

7.6 Calculation of a Control Rod Drop Accident

7.6.1 Scope

The control rod drop accident (CRDA) is one of the important design-basis accidents for boiling water reactors. The accident is defined by the accidental drop (out of the core) of a control rod in a reactor configuration such that the reactivity worth of the rod is maximized. This occurs with control rod insertion patterns such as are possible for cold startup to ∿10% of rated power.

Analysis of this accident in the past (e.g., Cheng and Diamond 1982) has demonstrated the importance of a multidimensional representation as well as the importance of properly calculating the time-varying thermohydraulic parameters and the corresponding neutron kinetics feedback. These previous results suggest that RAMONA-3B should be ideally suited for calculating the CRDA.

The RAMONA-3B calculation that is described in Sections 7.6.2 and 7.6.3 was performed as part of a study (Neogy 1981) of the CRDA being funded by the USNRC's Office of Nuclear Reactor Regulation. It serves as a demonstration of the ability of the code to calculate some of the important parameters of the CRDA.

7.6.2 Modeling of Accident Conditions

The reactor chosen for these calculations was a BWR/4 at beginning-of-life. The initial reactor state corresponded to operation at 10% of rated power with 33% of rated flow. Table 7.11 lists some of the initial conditions. The control rod pattern prior to the rod drop is given in Figure 7.40. In this diagram 48 represents the number of notches for complete insertion of a particular control rod. No number at a control rod position implies completely withdrawn. Because of the symmetry of the core, only a quadrant is shown.

Table 7.11

Initial Conditions for the CRDA

Thermal power, MW	329.3
System pressure, MPa	6.897
Core inlet flow, kg s^{-1}	4262
Feedwater flow, kg s^{-1}	163.9
Core inlet subcooling, °C	3.6

The RAMONA-3B modeling of this reactor was similar to that used for the analysis of the Peach Bottom-2 turbine trip tests (cf. Section 7.4) except for

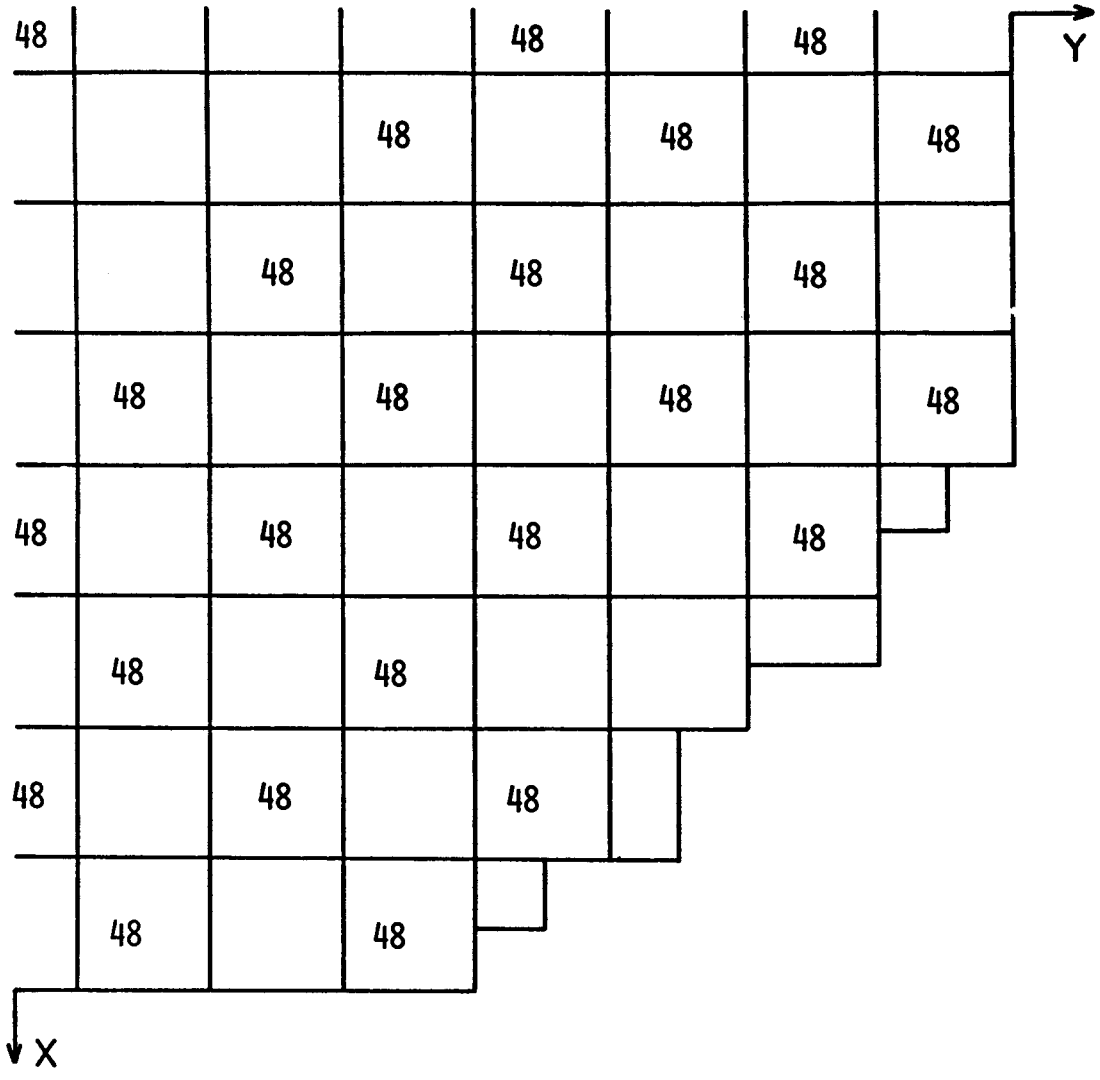

Figure 7.40 Control Rod Position (Notches Inserted) Prior to the CRDA.

the steam line representation and the cross sections for the neutron kinetics. All input specifications are listed in the Appendix. The neutron kinetics employed one planar node for each fuel bundle. The corresponding thermohydraulic channels are shown in Figure 7.10. The nodalization along the flow path within the vessel is given in Table 7.6. Since the steam line dynamics does not affect this accident, no steam line was represented. The steam load during the transient is calculated as a direct function of system pressure (see Diamond et al. 1981, Input Data Card No. 500 081). The cross sections representing beginning-of-life conditions were taken from a previous BNL study (Cheng and Diamond 1982) which utilized two-group neutron cross sections.

The accident was represented by withdrawing the central control rod at a speed of 1.52 m s^{-1}. By performing steady-state calculations with the rod fully inserted and fully removed, its reactivity worth was determined to be 0.0074. During the accident feedwater flow and recirculation pump speed were kept constant. In a BWR a reactor trip would occur due to the increase in power during the transient. However, in the present study no control rods were inserted during the transient in order to observe core behavior in their absence.

7.6.3 Results

The transient that results when the center rod drops out of the core under the conditions described in Section 6.2 is not a severe one relative to other CRDA situations (see Cheng and Diamond 1982). The relative core power is shown in Figure 7.41. Power increases to almost 40% of the rated value at which point negative feedback due to an increase in fuel temperature and an increase in void fraction causes the termination of the first surge. The core average fuel temperature and void fraction are shown in Figures 7.42 and 7.43, respectively. The increase in void fraction is slightly delayed relative to the increase in fuel temperature, since it is in part due to the conduction of heat into the coolant which occurs with a time constant on the order of one second. Since 2% of the power is generated directly in the coolant due to gamma ray absorption and neutron slowing-down, the delay in vapor generation is less than the time constant for conduction.

The reduction in power after the first surge decreases the rate of vapor generation and the increase in fuel temperature. The second peak in the power (see Figure 7.41) is due to a reduction in voids caused not only by the reduced power, but also by the increase in pressure (see Figure 7.44) and the increase in core inlet flow rate (see Figure 7.45). Had there been a reactor trip due to the first power surge, the influence of control rod insertion would have probably eliminated the second peak.

On a core-average basis, the void fraction does not decrease (see Figure 7.43). However, locally the void fraction will decrease. Figure 7.46 shows the radially averaged void fraction at a height of approximately 0.7 m. In order to see the net (properly weighted) effect of void fraction, it would be advantageous if RAMONA-3B edited the reactivity effect of void (and indeed for all variables which affect reactivity). A comparison of Figures 7.43 and 7.44 not only helps explain the second power peak, but also vividly demonstrates the importance of using spatial neutron kinetics for calculating the CRDA.

Figure 7.41

ROD DROP AT 10% POWER
RELATIVE POWER VS. TIME

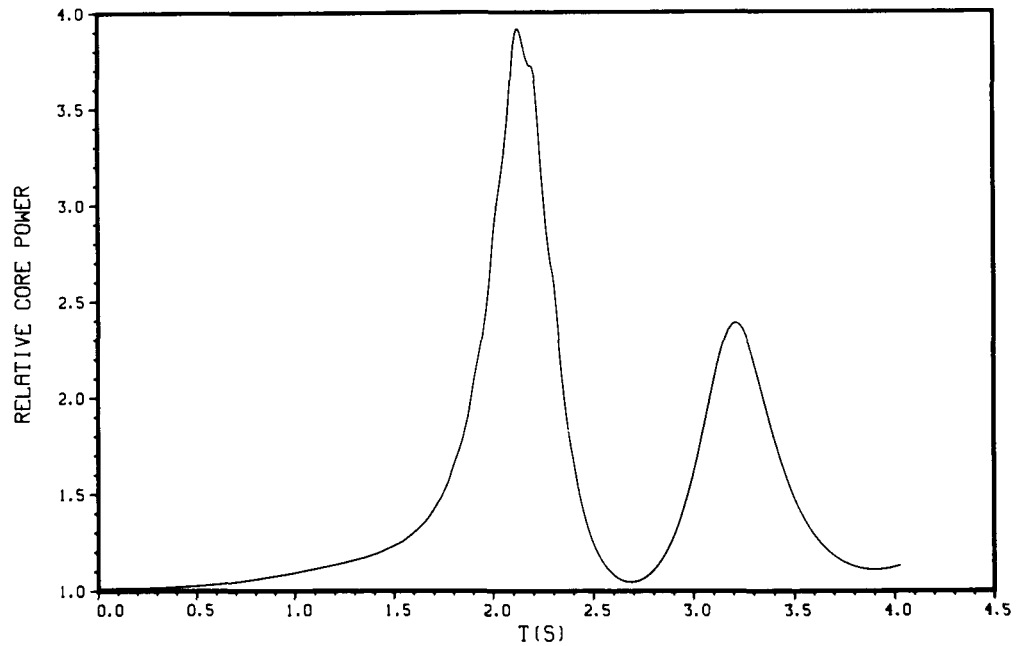

Figure 7.42

ROD DROP AT 10% POWER
AVERAGE FUEL TEMPERATURE VS.TIME

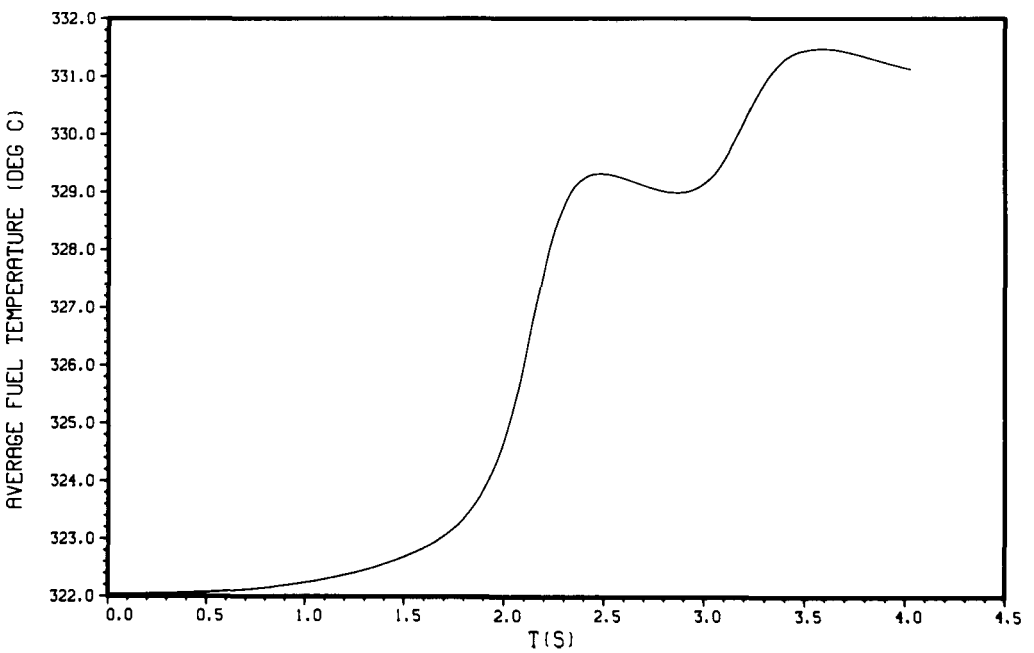

Figure 7.43

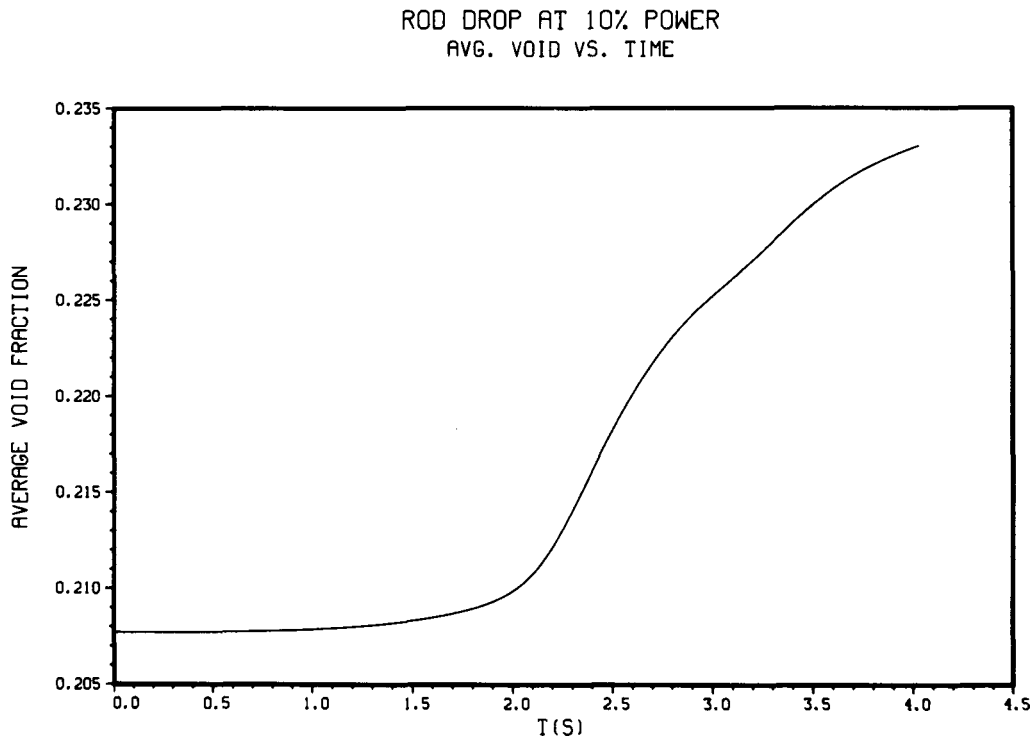

Figure 7.44

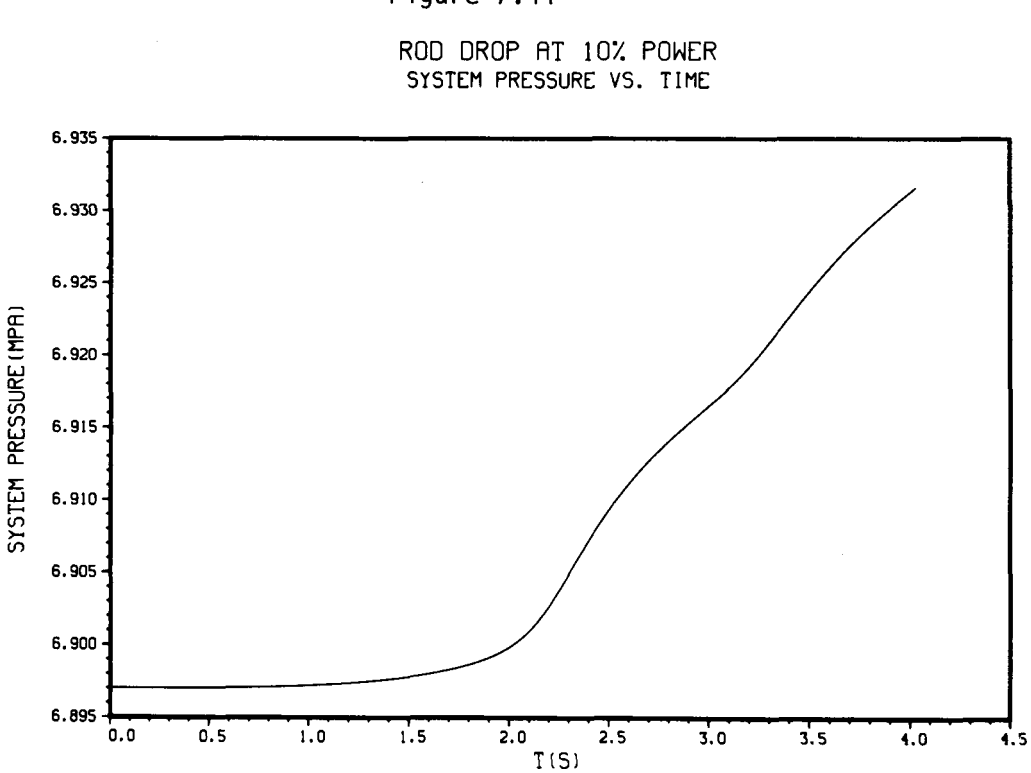

Figure 7.45

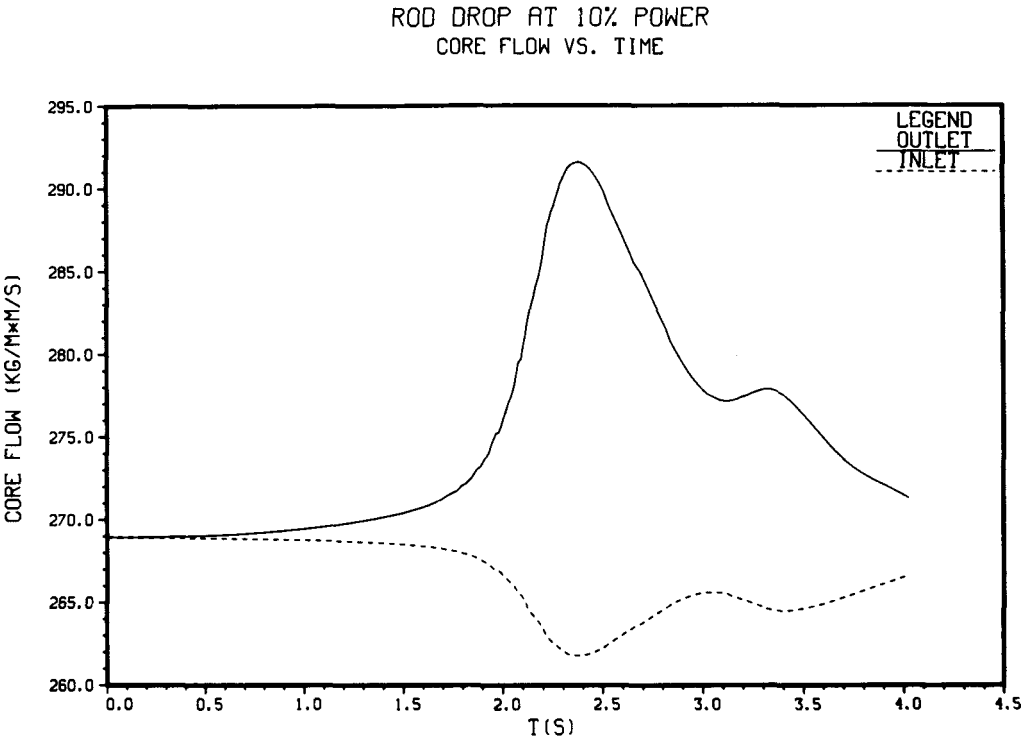

Figure 7.46

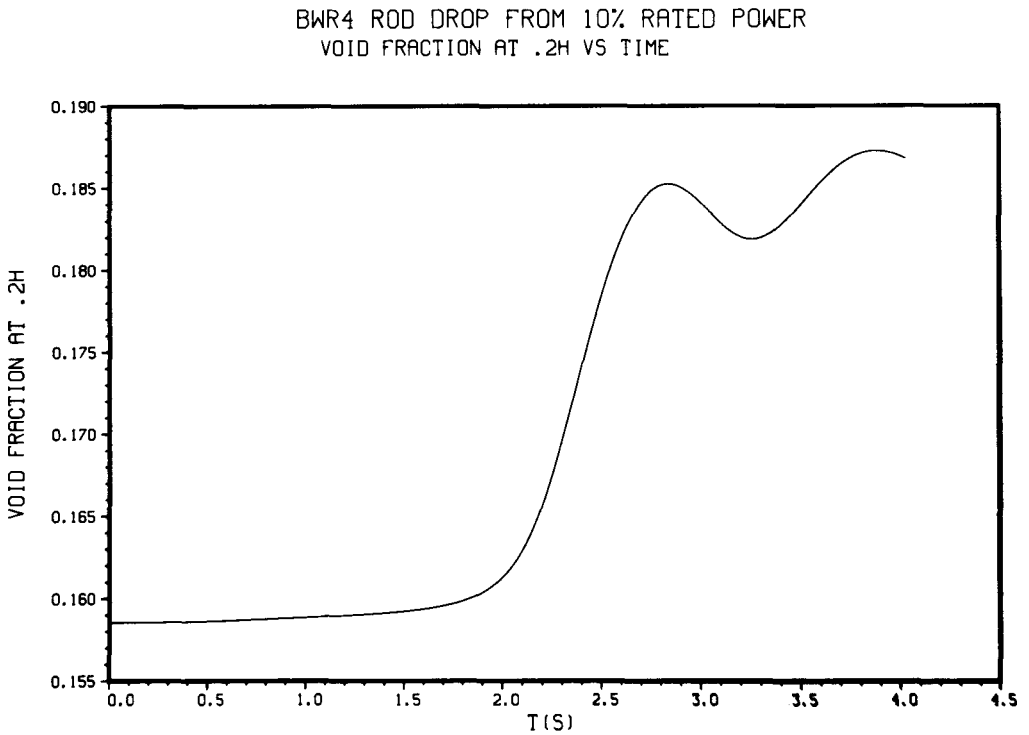

Figure 7.47

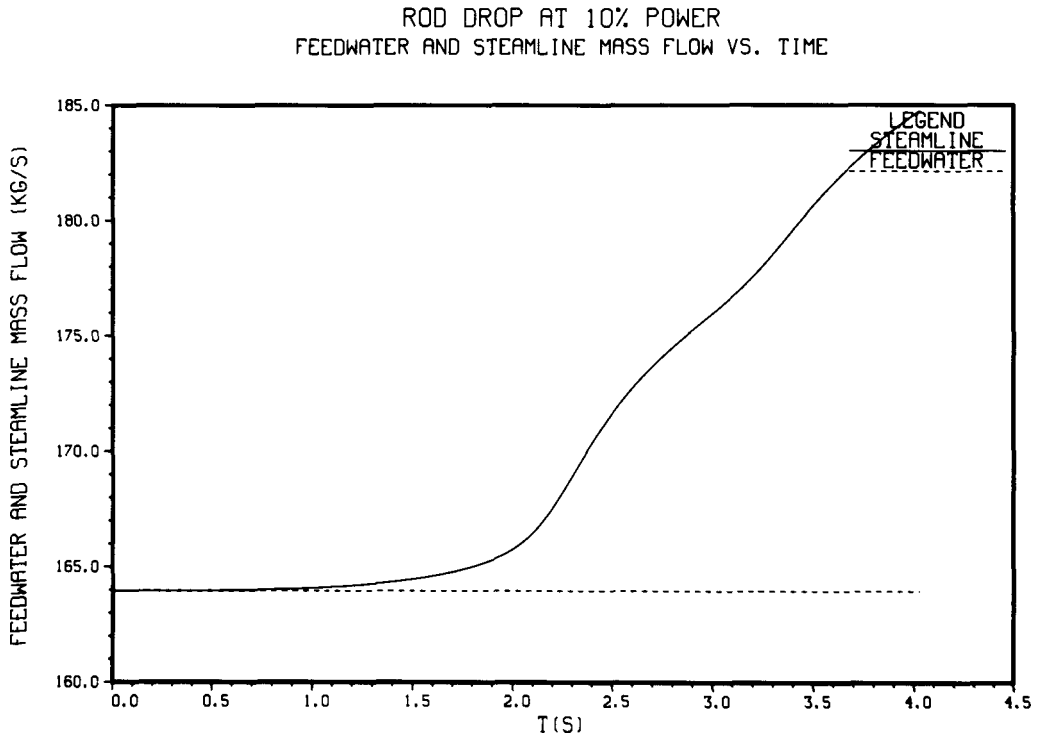

Figure 7.48

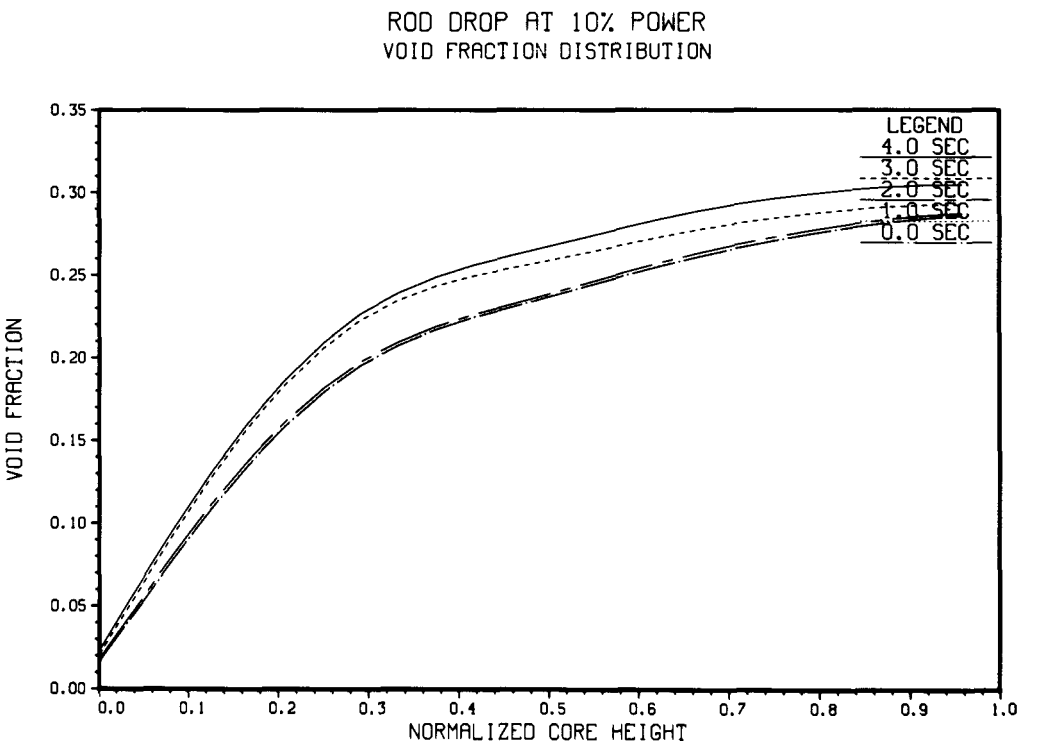

The core inlet and outlet flow rates are shown in Figure 7.45. An increase in void generation tends to increase the core exit flow rate and decrease the core inlet flow rate. Of course, these flow rates have a feedback effect on the rate of vapor generation. The steam line flow rate is shown in Figure 7.47 and reflects the increase in power during the transient.

The axial distribution of void fraction and power on a core-average basis is given in Figures 7.48 and 7.49, respectively. The axial power distribution is influenced by the void distribution and the axial distribution of gadolinia in the fuel. Since control rods are either fully inserted or withdrawn, they do not influence the axial power shape.

7.6.4 Conclusions and Recommendations

The results discussed in Section 7.6.3 exhibit the behavior usually seen in the analysis of the control rod drop accident (Cheng and Diamond 1982). RAMONA-3B therefore seems capable of calculating such transients. It should be noted that these calculations were done prior to the installation of the post-critical heat flux (CHF) modeling in RAMONA-3B. Since local conditions in the fuel bundles surrounding the dropped control rod might be severe enough to reach CHF, it is recommended that the calculations be repeated with the current version of the code.

It is recommended that code assessment activities be pursued in order to further qualify the ability of RAMONA-3B for the CRDA. This can be done by modeling a CRDA which is as close as possible to a calculation done with a different code (Cheng and Diamond 1982) and comparing results. Consideration should also be given to using experimental results obtained from a reactivity insertion test performed with a small oxide-fueled pressurized water reactor (McCardell et al. 1969).

Two improvements to the code would facilitate the analysis of the CRDA and are recommended. One is the addition of edits of the reactivity effect of void fraction, fuel temperature, and control rod movement. The other is the addition of a calculation of peak pellet-average enthalpy, the parameter of most interest during the CRDA. Currently a pellet-average fuel temperature is calculated at every neutron kinetics node. This temperature can be converted into enthalpy, the node with the peak valve located, and a peaking factor applied to relate this node average value to the enthalpy expected at the hottest fuel rod within the node.

Figure 7.49

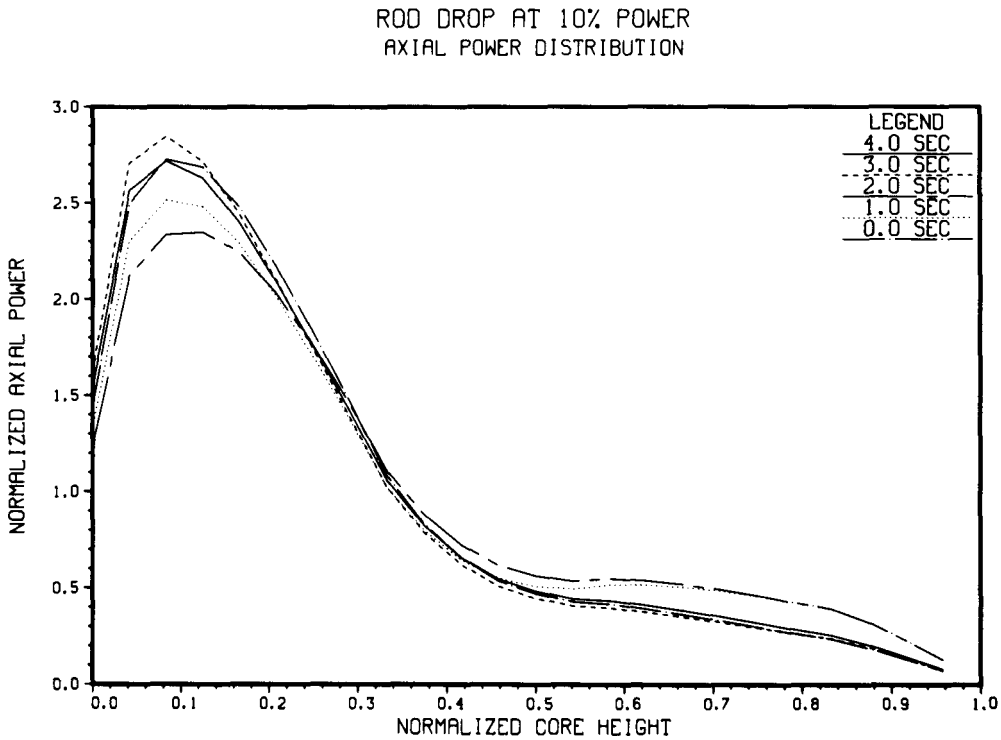
ROD DROP AT 10% POWER
AXIAL POWER DISTRIBUTION
LEGEND
4.0 SEC
3.0 SEC
2.0 SEC
1.0 SEC
0.0 SEC
NORMALIZED AXIAL POWER
NORMALIZED CORE HEIGHT
3.0
2.5
2.0
1.5
1.0
0.5
0.0
0.0
0.1
0.2
0.3
0.4
0.5
0.6
0.7
0.8
0.9
1.0

8. SUMMARY OF CONCLUSIONS AND RECOMMENDATIONS

This chapter presents the summary of conclusions and of recommendations for future improvement made earlier in the chapters on neutron kinetic models, heat conduction and thermohydraulic models, on numerical techniques and on future code assessment.

8.1 Conclusions

The RAMONA-3B code is a unique BWR systems code for the efficient and accurate prediction of three-dimensional* neutron kinetics and of nonequilibrium, nonhomogeneous two-phase flow conditions. RAMONA-3B's current capabilities and limitations are summarized in Chapter 1, Sections 1.2 and 1.3. As pointed out in Chapter 7, RAMONA-3B has been assessed for seven separate effects and for one integral system transient. RAMONA-3B has also been demonstrated to execute a transient induced by a partial scam of the reactor core, followed by a Main Steam Isolation Valve closure. However, independent code assessment is still required by comparing code results with experimental data from both separate effects tests and full-size plant tests. The user of RAMONA-3B must be cautioned to expect computational difficulties in systems simulations with RAMONA-3B which have not yet been executed by RAMONA-3B, as is the case with most newly developed or modified large systems codes.

8.2 Recommendations for Future Code Improvements

Recommendations for future code improvements are summarized below, first for neutron kinetics, then for modeling of heat conduction and thermohydraulics and finally for numerical techniques. Considerable improvement can be achieved with selected minor modifications. Modifications which are deemed to be necessary are listed first where appropriate in each category. No attempt has been made to set priorities for nonmandatory modifications since such priorities depend on unknown user objectives. Finally, we point out that code improvement is open-ended, and the summary of recommendations given below is therefore not all-inclusive.

Detailed descriptions and justifications for the recommendations are found in the appropriate chapters of this report.

8.2.1 Recommendations for Improvement of Neutron Kinetics

a) The new ScP feedback model should be implemented in RAMONA-3B for future applications. The BNL1 option should be deleted, but the BNL2 option should be retained.

*As well as one-dimensional neutron kinetics.

b) A higher order term (e.g., cubic term) should be included for the void feedback for the case of $\alpha > 0.75$ (post-CHF applications).

(c) The void dependence and control-state dependence of the Doppler feedback coefficients should be included to treat the Doppler feedback effect more accurately.

(d) A linear void dependence of the direct heating fractions should be considered.

(e) An edit of various reactivity components (void reactivity, Doppler reactivity, control reactivity, etc.) is highly desirable for it will provide legitimate reactivity input for point kinetics that is still widely used in many system codes. Moreover, it is extremely helpful for understanding the characteristics of a transient. It is, however, not a trivial task. A similar capability has been implemented in the BNL version of the 3-D neutron kinetics code, MEKIN-B (Aronson et al. 1980), and can be used as a guide to the installation in RAMONA-3B.

(f) Because of the importance of thermal neutron diffusion in certain situations, a better treatment of the thermal neutron diffusion would be desirable and is recommended.

(g) The microscopic absorption cross sections, σ_{a1} and σ_{a2}, of Boron-10 required for the boron reactivity calculation should be obtained with a hardened neutron spectrum in the water of a typical fuel cell. Since the hardness of the neutron spectrum depends on the boron concentration in the water, the cross sections (σ_{a1} and σ_{a2}) are, in general, functions of the boron concentration, C_B.

8.2.2 Recommendations for Improvements of Heat Conduction Models

(a) Conduction models must be implemented to account for energy storage in, and release from, structural components such as vessel walls, core barrel etc. The simulation of environmental temperature variations is also needed.

(b) The temperature dependence of thermophysical properties and of the gas gap conductance in the fuel element should be accounted for. The modeling of heat transfer in the fuel element should be consistent with the accommodation of local detail in the three-dimensional neutron kinetics calculations.

(c) Lumped-parameter conduction models should be considered for improving the computational efficiency in heat transfer calculations.

(d) Computed temperature distributions obtained from any nonstandard computing scheme should be compared with analytical or standard numerical solutions of known accuracy, before the implementation of such nonstandard conduction model.

8.2.3 Recommended Improvements for Thermohydraulics Models

The first eight recommendations below address thermohydraulics modeling conflicts and weaknesses which impact RAMONA-3B's intended objectives of simulating operational plant transients.* The following six recommendations would improve its accuracy and reliability.

(a) First, we recommend that the momentum equations be corrected with regard to the momentum flux representation: $w|w|$ should be replaced by w^2 in Eq. 4.4.6 and all equations derived from it.

(b) Standard definitions for loss coefficients should be employed to correct the momentum jump conditions at component interfaces (cf. Eqs. 4.4.49 and 4.4.50), to allow the use of experimentally obtained and published loss coefficients and to account properly for flow reversal.

(c) The compressibility (thermal expansion) of subcooled liquid should be used for subcooled liquid and not the compressibility of saturated liquid (refer to Assumption (4-vii), use Eq. 4.4.93 instead of Eq. 4.4.94 and correct the equations in RAMONA-3B for the volumetric flow rate, Eqs. 4.4.115, 4.4.117 and 4.4.119). The total amount of liquid in the vessel must be included.

(d) Account for the thermal expansion of subcooled liquid (Eq. 4.4.93), so that overcooling and feedwater transients can be simulated.

(e) Revise the separator model to predict carry-under, rather than to adjust the initial core inlet subcooling temperature.

(f) Correct the steam dome model such that the void fraction for the low-void regime is computed consistently from the vapor mass balance, both for steady-state and transient simulations, further, that the vapor discharge from the top of the separators is not introduced into the low-void regime below the coolant level, and finally, that the coolant level motion and the vapor mass in the steam dome are properly computed even if the mixture level rises or falls beyond its normal range.

(g) Eliminate the conflict between two opposing criteria for boiling incipience (Assumption 4-ix).

(h) Correct the recirculation pump model such that the electric torque can be computed as a function of generator frequency and of stator voltage.

The less important recommendations are:

---

*The magnitude of the impact on RAMONA-3B from the modeling weaknesses is to be determined through developmental assessment and sensitivity studies.

(i) Improve the caloric equations of state for subcooled liquid (see Table 4.2).

(j) Revise the post-CHF heat transfer models to account for hysteresis effects (see Section 4.4.2.1.1).

(k) Revise the vapor generation rate prediction to yield the limit of equilibrium evaporation.

(l) Introduce homologous maps for recirculation pump performance.

(m) Extend friction factor and heat transfer calculations to accommodate natural circulation and flow reversal.

(n) Account for superheated vapor. This will involve major code modifications but may be necessary to account for extended dryout or burnout periods.

8.2.4 Recommendations for Improving the Simulation of Reactor Controls

The RAMONA-3B code should have the following plant control models for simulating the proper time sequence of disturbances (boundary conditions) on the nuclear steam supply system:

a) Reactor power control system.

b) Feedwater control system.

c) Motor-generator control system for recirculation pump drive.

d) Dynamic safety and relief valve models and valve control system simulation models.

To implement these control systems it is necessary to develop and implement dynamic models for these balance-of-plant systems:

e) Turbines for load generation and feedwater drives.

f) Condensers.

g) Feedwater preheaters and pumps.

h) Motor-generator set for recirculation pump drive.

i) Suppression pool.

8.2.5 Recommendations for Improving the Numerical Solution Techniques in RAMONA-3B

Concerning the transformation from partial to ordinary differential equations and their numerical integration we recommend that:

a) The average thermal neutron flux be calculated directly from its balance equation by using the average fast flux (cf. Section 6.2.7).

b) Standard finite difference schemes or finite-element collocation methods be used to reduce the current discretization errors in the RAMONA-3B code for calculating thermal conduction in fuel pellets.

c) A lumped-parameter option be introduced into RAMONA-3B to compute the temperature variations in fuel and pellet by a single ordinary differential equation, whenever plant transients are simulated.

d) Standard donor cell differencing for flow reversal be used to replace the current switching logic in RAMONA-3B, as this logic produces discontinuities (cf. Section 6.4.1.3).

e) Standard differencing schemes with the current RAMONA-3B nodalization scheme (Fig. 6.4.1) be compared with the currently used differencing scheme for boron transport, to find a more reliable method and improve computing speed.

f) Currently used time delay concepts for boron transport be replaced by standard (continuous) first-order time delay approximations.

g) The Chebychev extrapolation technique be used to replace the less efficient relaxation scheme currently used in RAMONA-3B steady-state neutron kinetics calculations.

h) The seven discrete temperatures in fuel pellet and cladding be computed by a single iteration procedure, rather than by two separate ones and that the cladding surface temperature be computed only in one place in the code (cf. Section 6.6.2).

i) All convergence criteria for steady-state calculations be reviewed to assure that innermost iterations produce greater accuracy than outer iterations.

j) The newly introduced convergence criteria for the transient neutron kinetics calculations be assessed further to eliminate previously used convergence criteria whenever they are more restrictive than necessary.

k) A well established, efficient numerical procedure be selected for integrating the ordinary differential equations of coolant dynamics and that this procedure be introduced into RAMONA-3B as a module (see end of Section 6.7.3.1.2).

l) The boron transport equation be integrated by standard procedures with valid stability and accuracy criteria, possibly with the procedure selected by recommendation (11) above.

m) A procedure, less expensive in computing effort than the Runge-Kutta method, but equally effective in error control, may be found for integrating the equations of steam line dynamics.

n) The program sections for computing thermohydraulics and thermal conduction should be carefully checked for coding inconsistencies, undocumented code modifications (patches) and overriding instructions. Coding inconsistencies should be removed. Undocumented modifications and instructions which do not reflect the documented modeling should be justified and documented or removed.

o) Independent global mass and energy balances should be performed to assure that internal fluxes of mass and energy cancel properly and that neither mass nor energy are lost due to truncation errors.

8.3 Recommendations for Code Documentation

The RAMONA-3B Users Manual should be revised to satisfy the requirements of existing standards ANS-10.3/N413-1974. Specifically, the objectives and interface variables of all subroutines should be defined. The documentation should contain not only the complete specification of input parameters but also the detailed description of all options of output listings.

8.4 Recommendations for Future Independent Code Assessment

a) Analytical results and reference computer calculations with known, documented accuracy should be used to assess neutron kinetics, heat conduction and coolant flow calculations in RAMONA-3B.

b) Constitutive relations for slip should be assessed separately with results from air-water tests or from tests on equilibrium liquid-vapor mixtures in adiabatic flow channels with rod bundles.

c) Having established an acceptable slip model, the nonequilibrium evaporation rate model should be assessed with results from experiments in electrically heated rod bundles. The tests should include post-CHF conditions.

d) The void feedback correlation should be assessed by using only verified slip and vapor generation rate models.

Section 7.1 contains references for available test data to assess slip and vapor generation rate models.

e) Friction and form losses should be assessed separately with the use of steady-state data from full-scale plant experiments.

f) Integrated systems tests, start-up and load-following transient tests should be used to assess the code as a whole. See Section 7.2 for references on available test data. The Peach Bottom Turbine Trip tests should be used further to assess long-term capabilities of the code.

REFERENCES

American Nuclear Society, 1978, "Decay Heat Power in Light Water Reactors," Proposed ANS Standard 5.1.

Ancona, A., 1980, "SIMULATE: BWR Radial Albedo Boundary Condition and Spectrum Correction Factor Verifications," Trans. Am. Nucl. Soc., 34, p. 825.

Aronson, A.L., Cheng, H.S., Diamond, D.J. and Lu, M.S., 1980, "MEKIN-B: The BNL Version of the LWR Core Dynamics Code MEKIN," BNL-NUREG-28071, Brookhaven National Laboratory.

Bailey, P., 1981, Private Communication, Electric Power Research Institute.

Bakstad, P.F. and Solberg, K.O. 1968, "RABCON A-I, A FORTRAN Code for Transient Analysis of Boiling Water Reactors and Boiling Loops," KR-135, Institutt for Atomenergi.

Bech, N., 1970, "Numerical Integration on the Stability Limit," Scandpower A/S, Proprietary Information.

Becker, K., Hernborg and Bode, M., 1962, "An Experimental Study of Pressure Gradients for Flow of Boiling Water in a Vertical Round Duct," Parts 1,2 and 3, AE 69, 70 and 85, AB Atomenergi, Studsvik.

Bjornard, T.A. and Griffith, P., 1977, "PWR Blowdown Heat Transfer," Symposium on the Thermal and Hydraulic Aspects of Nuclear Reactor Safety, Light Water Reactors, Vol. 1 (edited by O.C. Jones, Jr. and S.G. Bankoff).

Blasius, H., 1913, "Das Aehnlichkeitsgesetz bei Reibungsvorgaengen in Fluessigkeiten," Forschung. Ing.-Wes., No. 131.

Boley, B.A. and Weiner, J.H., 1960, "Theory of Thermal Stresses," John Wiley & Sons, Inc.

Borresen, S., 1971, "A Simplified, Coarse-Mesh, Three-Dimensional Diffusion Scheme for Calculating the Gross Power Distribution in a Boiling Water Reactor," Nucl. Sci. & Eng., 44, p. 37.

Borresen, S., Skardhamar, T. and Wennemohanssen, S., 1979, "Application of FMSR RECORD/PRESTO for Analysis and Simulation of Operating LWR Cores," NEACRP Specialists Meeting on Calculation of Three-Dimensional Rating Distribution in Operating Reactors, Paris.

Boure, J., 1966, "The Oscillatory Behavior of Heated Channels, An Analysis of Density Effects," C.E.A.R. 3049, Centre d'Etudes Nucleaires de Grenoble, France.

Buckholz, R.H., 1980, Letter to P.S. Check, USNRC, August 29, 1980, General Electric Company.

Carmichael, L.A. and Neimi, R.O., 1978, "Transient and Stability Tests at Peach Bottom Atomic Power Station Unit 2 at End of Fuel Cycle 2," EPRI NP-564, Electric Power Research Institute.

Cheng, H.S. and Diamond, D.J., 1978a, "BWR Doppler Feedback: Effect of Voids, Control Blades, Gadolinia and Exposure," BNL-NUREG-24433, Brookhaven National Laboratory.

Cheng, H.S. and Diamond, D.J., 1978b, "Core Analysis of Peach Bottom-2 Turbine Trip Tests," BNL-NUREG-24903, Brookhaven National Laboratory.

Cheng, H.S. and Diamond, D.J., 1982, "Analyzing the Rod Drop Accident in a Boiling Water Reactor," Nucl. Tech. 56, p. 40.

Cheng, H.S., Diamond, D.J. and Lu, M.S., 1978, "Boiling Water Reactor Scram Reactivity Characteristics," Nucl. Tech., 37, p. 246.

Clark, M., Jr. and Hansen, K.F., 1964, Numerical Methods of Reactor Analysis, Academic Press, New York and London.

Cokinos, D., Kohut, P., Lai, J. and Diamond, D., 1980, "Simulation of Quad Cities 1 Cycle Operation with the ARMP Code System," BNL-NUREG-29019, Brookhaven National Laboratory.

Computational Benchmark Problems Committee, 1977, "Argonne Code Center: Benchmark Problem Book," ANL-7416, Supp. 2, Argonne National Laboratory.

Condie, K.G. and Bengston, S.G., 1978, "Development of the Mod 7 Correlation," EG&G Report, Attachment PN-181-78.

Connell, H.R., Neymotin, L., Saha, P. and Slovik, G., 1984, "User's Manual for RAMONA-3B: A Computer Code with Three-Dimensional Neutron Kinetics for BWR Systems Transients," to be published.

Congdon, S.P. and Linford, R.B., 1978, "Peach Bottom Turbine Trip Simulation with a One-Dimensional Transient Model," Trans. Am. Nucl. Soc. 30, 217.

Considine, D.M., 1974, Process Instruments and Control Handbook, McGraw-Hill Book Co., p. 19-48.

Crowther, R.L., 1981, "Light Water Reactor Physics - A Critical Review," Trans. Am. Nucl. Soc., 38, p. 11.

Delhaye, J.M., Giot, M. and Riethmuller, M.L., 1981, Thermohydraulics of Two-Phase Systems for Industrial Design and Nuclear Engineering, McGraw-Hill Book Company.

Diamond, D.J., Ed., 1976, "BNL-TWIGL, A Program for Calculating Rapid LWR Core Transients," BNL-NUREG-21925, Brookhaven National Laboratory.

Diamond, D.J. and Cheng, H.S., "Higher Order Effects in Calculating Boiling Water Reactor Doppler and Void Reactivity Feedback," Nucl. Tech., 46, p. 493.

Dittus, F.W. and Boelter, L.M.K., 1930, "Heat Transfer in Automobile Radiators of Tubular Type," Publications in Engineering, University of California, Berkeley, p. 443.

Dusinberre, G. M., 1961, Heat Transfer Calculations by Finite Differences, International Textbook Company.

Eisenhart, L.O. and Diamond, D.J., 1980, "Automatic Generation of Cross-Section Input for BWR Spatial Dynamics Calculations," BNL-NUREG-28796, Brookhaven National Laboratory.

Eklund, R., Gelius, O. and Nylund, O., 1965, "Froja, FT-6 Preliminary Results of Experiments," ASEA-PM-KAB-65-8, ASEA Atom, Vasteras (1965)

Fabic, S. and Andersen, P.S., 1981, "Plans for Assessment of Best Estimate LWR Systems Codes," NUREG-0676, U.S. Nuclear Regulatory Commission.

Fendall, C.K., 1961, "SHARE Program AT RKS3", Aeronutronic, Newport, California. Code documentation by D. Schermerhorn, Aerospace Corporation, San Bernadino Operations (1964).

Forkner, S.L., Bell, D.L. and Winkler, E.N., 1978, Internal Document, Tennessee Valley Authority.

Gear, C.W., 1965, "Hybrid Methods for Initial Value Problems in Ordinary Differential Equations," J. Soc. Industrial Applications of Mathematics, Ser. B, Numerical Analysis, Vol. 2(1), pp. 69-86.

General Electric Company, 1978, "Qualification of the One-Dimensional Core Transient Model for Boiling Water Reactors," Vol. 1, a Licensing Topical Report, NEDO-24154, 78 NED 290.

General Electric Staff, 1977a, "GE BWR Thermal Analysis Basis (GETAB), NEDO-10958-A, General Electric San Jose, California.

General Electric Company, 1977b, "Stability and Dynamic Performance of the General Electric Boiling Water Reactor," NEDO-21506, General Electric Company.

Glasstone, S. and Edlund, M.C., 1956, The Elements of Nuclear Reactor Theory, D. Van Nostrand Co., Inc., Princeton, N.J.

Groeneveld, D.C., 1968, "An Investigation of Heat Transfer in the Liquid-Deficient Regime," Report No. AECL-3281, revised August 1969.

Hageman, L.A. and Kellog, R.B., 1966, "Estimating Optimum Acceleration Parameters for Use in the Successive Over-Relaxation and the Chebyshev Polynomial Methods of Iteration," WAPD-TM-592, Bettis Atomic Power Laboratory.

Hagrman, D.L., Reymann, G.A. and Masen, R.E., 1980, "MATPRO-Version II (Revision I), A Handbook of Materials Properties for Use in the Analysis of Light Water Reactor Fuel Bed Behavior," TREE-NUREG 1280, Rev. 1 NUREG/CR-0497.

Hansen, A.G., 1967, Fluid Mechanics, John Wiley & Sons, Inc., New York, London, Sydney, p. 420.

Henry, A.F., 1975, Nuclear Reactor Analysis, The MIT Press, Cambridge, Mass.

Henry, R.E., Quinn, D.J. and Spleha, E.A., 1974, "An Experimental Study of the Minimum Film Boiling Point for Liquid-Liquid Systems," Fifth Int. Heat Transfer Conference, Tokyo, Japan.

Holt, R. and Rasmessew, J., 1968, "RAMONA-II, A FORTRAN Code for Transient Analysis of Boiling Water Reactors," KR-147, Instititt for Atomenergi.

Hornyik, K., 1981, "Special RETRAN Modeling Studies Performed in Conjunction with the Peach Bottom-2 Transient Test Analysis," EPRI-NP-1842, Electric Power Research Institute.

Hornyik, K. and Naser, J., 1978, "Effects of Transient Modeling of Bypass Steam Line on BWR Pressurization," Trans. Am. Nucl. Soc. 30, p. 231.

Hornyik, K. and Naser, J., 1979, "RETRAN Analysis of the Turbine Trip Tests at Peach Bottom Atomic Power Station Unit 2 at the End of Cycle 2," EPRI NP-1076-SR, Electric Power Research Institute.

Hsu, C.J., Lu, M.S., Cheng, H.S., Diamond, D.J., Shier, W.G. and Odar, F., 1978, "Analysis of a BWR Turbine Trip Experiment," Trans. Am. Nucl. Soc. 30, p. 223.

Idel'chik, I.E., 1960, Handbook of Hydraulic Resistance, translated from Russian, available from the U.S. Department of Commerce Clearinghouse for Federal Scientific Information, Springfield, Va. AEC-tr-6630.

Isaakson, E. and Keller, H.B., 1966, Analysis of Numerical Methods, John Wiley & Sons, Inc., New York, London, Sydney.

Jens, W.H. and Lottes, P.A., 1951, "Analysis of Heat Transfer, Burnout, Pressure Drop and Density Data for High-Pressure Water," USAEC Report ANL-4627, Argonne National Laboratory.

Jones, A.B. and Dight, D.G., 1962, "Hydrodynamic Stability of a Boiling Channel," KAPL-2208, Knolls Atomic Power Laboratory.

Khalid, Z.M., Becker, M. and Harris, D.R., 1980, "Influence of Axial Node Size on Modified Coarse-Mesh Nodal Methods," Trans. Am. Nucl. Soc. 34, p. 827.

Khatib-Rahbar, M., 1980, "Modeling of Plant Protection and Control Systems for SSC," BNL-NUREG-51241, Brookhaven National Laboratory.

Kohut, P., Cokinos, D. and Carew, J., 1981, "Simulation of Quad Cities 1 Cycle 2 Operation, BNL-NUREG-29639, Brookhaven National Laboratory.

Lahey, R.T., Jr. and Moody, F.J., 1977, "The Thermal-Hydraulics of a Boiling Water Nuclear Reactor," American Nuclear Society.

Langenbuch, S., Maurer, W. and Werner, W., 1977, "Coarse-Mesh Nodal Diffusion Method for the Analysis of Space-Time Effects in Large Light Water Reactors," Nucl. Sci. & Eng., 63, p. 437.

Larsen, N.H., 1978, "Core Design and Operating Data for Cycles 1 and 2 of Peach Bottom 2," EPRI NP-563, Electric Power Research Institute.

Lathrop, K.D. and Brinkley, F.W., 1973, "TWOTRAN-II: An Interfaced, Exportable Version of TWOTRAN Program for Two-Dimensional Transport," LA-4848-MS, Los Alamos Scientific Laboratory.

Lienhard, J.M., 1976, "Correlations for the Limiting Liquid Superheat," Chemical Engineering Science, Vol. 31, pp. 847-849.

Linford, R.B., 1973, "Analytical Methods of Plant Transient Evaluations for General Electric Boiling Water Reactors," NEDO-10802, General Electric Company.

Lourax, H., 1968, "On the Construction of Highly Stable, Explicit Numerical Methods for Integrating Coupled Ordinary Differential Equations with Parasitic Eigenvalues," Ames Research Center, Moffett Field, Calif., NASA TN D-4547.

Lu, M.S. and Cheng, H.S., 1976, "Data Generation for BWR Scram Reactivity Function Study: Monthly Progress Report for February of 1976 to R.E. Heineman of the Office of Nuclear Reactor Regulation, U.S. Nuclear Regulatory Commission.

Lu, M.S., Cheng, H.S., Shier, W.G., Diamond, D.J. and Levine, M.M., 1979, "Analysis of Licensing Basis Transients for a BWR/4," BNL-NUREG-26684, Brookhaven National Laboratory.

Lu, M.S., Shier, W.G., Levine, M.M., Cerbone, R.J. and Diamond, D.J., 1982, "Analysis of a Partial scram Event in a Typical BWR/4," BNL-NUREG report in press, Brookhaven National Laboratory.

Nuernberg, W., 1952, Die Asynchronmaschine, (The Inductions Motor) Springer Verlag, Berlin.

Nylund, O., Becker, K.M., Eklund, R., Gelius, O., Haga, I., Hernborg, G., Rouhani, Z. and Akerhielm, F., 1968, "Hydrodynamic and Heat Transfer Measurements on a Full-Scale Simulated 36-Rod Marviken Fuel Element with Uniform Heat Distribution," FRIGG-2, R4-447/RTL-1007, AB Atomenergi, Stockholm.

Nylund, O., Becker, K.M., Eklund, R., Gelius, O., Haga, I., Jensen, A., Malnes, D., Olsen, A., Rouhani, Z., Skaug, J. and Akerhielm, F., 1969, "Hydrodynamic and Heat Transfer Measurements on a Full-Scale Simulated 36-Rod Marviken Fuel Element with Non-Uniform Radial Heat Flux Distribution," FRIGG-3, R4-494/RL-1154, AB Atomenergi, Stockholm.

Nylund, O., Becker, K.M., Eklund, R., Gelius, O., Jensen, A., Malnes, D., Olsen, A., Rouhani, Z. and Akerhielm, F., 1970, "Hydrodynamic and Heat Transfer Measurements on a Full-Scale Simulated 36-Rod BHWR Fuel Element with Non-Uniform Axial and Radial Heat Flux Distribution," FRIGG-4, R4-502/RL-1253, AB Atomenergi, Stockholm.

Oye, O., Haugset, K., Holt, R., 1977, "RAMONA-3, A Program for Calculation of Transients in Boiling Water Reactors," FMS/2/RAMONA-3/A-00, Institute for Atomenergi.

Philadelphia Electric Company, 1972, "Final safety Analysis Report - Peach Bottom Atomic Power Station Units No. 2 & 3," Philadelphia Electric Company.

Roache, P.J. (1972), Computational Fluid Dynamics, Heruosa Publishers, Albuquerque, N.M. 87 108, P.O. Box 8172.

Rothenstein, W., Barken, Y. and Taviv, E., 1977, "The Revised HAMMER Code," EPRI-NP-565, Electric Power Research Institute.

Saha, P. and Zuber, N., 1974, "Point of Net Vapor Generation and Vapor Void Fraction in Subcooled Boiling," Heat Transfer 1974, Proc. 5th Int. Heat Transfer Conf., IV, pp. 175-179.

Saha, P. et al., 1984, "Further Improvements to the RAMONA-3B Code," to be published.

Sauar, T.O., Borresen, S., Haugen, J., Nitteberg, E., Nuess, H.K. and Skardhamar, T., 1972, "A Multilevel Data-Based Computer Code System for In- Core Fuel Management in Light Water Reactors," Proc. 4th Intern. Conf. on Peaceful Uses of Atomic Energy, IAEA, A/Conf. 49/p/293, 2.

Scandpower, 1977, Publication, FMS/2/RAMONA-3/C00, Institutt for Atomenergy.

Schmidt, E., 1969, Properties of Water and Steam in S1 Units, Springer Verlag, Berlin, Heidelberg, New York, R. Oldenburg, Munchen.

Serov, E.P., 1953, "The Operation of Once-Through Boilers in Variable Regimes," Trudy, Moscow Energ. Insi. 11.

Shiralker, B.S., et al., 1972, "Transient Critical Heat Flux Experimental Results," GEAP-13295, General Electric Company.

Slattery, J.C., 1972, "Momentum, Energy and Mass Transfer in Continna.

Smith, K.S., 1979, "An Analytical Nodal Method for Solving the Two-Group, Multidimensional, Static and Transient Neutron Diffusion Equations," Nuclear Engineer Degree Thesis, Massachussetts Institute of Technology.

Smith, K.S., Henry, A.F. and Loretz, R.A., 1980, "The Determination of Homogenized Diffusion Theory Parameters for Coarse-Mesh Nodal Analysis," Proc. of the Conference 1980 Advances in Reactor Physics and Shielding, American Nuclear Society.

Smith, R.A. and Griffith, P., 1976, "A Simple Model for Estimating Time to CHF in a PWR LOCA," Natl. Heat Transfer Conference, ASME paper 76-HT-9.

Solberg, K.O., 1967, Private Communication to Holt and Rasmussen (RAMONA-II Code), Institutt for Atomenergi, Kjeller Research Establishment, Kjeller, Norway.

Thorlaksen, 1976, "Analysis of Control Rod Ejection Accidents in Large Boiling Water Reactors," Riso Report No. 344, Danish Atmoic Energy Commission Research Establishment, Riso.

Tong, L.S. and Weisman, J., 1970, Thermal Analysis of Pressurized Water Reactors, American Nuclear Society.

Van Tuyle, G.J., Nepsee, T.C. and Guppy, J.G., 1984, "MINET Code Documentation," to be published.

Varga, R.S., 1962, Matrix Iterative Analysis, Prentice-Hall Inc., Englewood Cliffs, New Jersey.

Verplanck, D.M., 1981, "Methods for the Analysis of Boiling Water Reactors - Steady State Core Physics," YAEC-1238, Yankee Atomic Electric Company.

Wachspress, E.L., 1966, Iterative Solution of Elliptic Systems, Prentice-Hall Inc., Englewood Cliffs, New Jersey.

Walker, J. and Weaver, D.R., 1979, "Nuclear Physics Data for Reactor Kinetics," Advances in Nucl. Sci. and Tech., 11.

Wulff, W., 1978, "Lumped-Parameter Modeling of One-Dimensional Two-Phase Flow," Second OECD Specialists Meeting on Two-Phase Flow, Paris, France.

Wulff, W. and Jones, O.C., Jr., 1978, "THOR-1 (PWR) A Computer Code for Predicting the Thermohydraulic Behavior of Nuclear Reactor Systems," BNL-NUREG-29781, Informal Report.

Wulff, W., 1980a, "Lumped-Parameter Model for Transient Conduction in Nuclear Reactor Components," BNL-NUREG-51231, NUREG/CR-1540.

Wulff, W., 1980b, "Steam Line Dynamics, A Computer Program," Topical Report, BNL-NUREG-51186.

Wulff, W., 1980c, "PWR Training Simulator, An Evaluation of the Thermohydraulic Models for its Main Steam Supply System," BNL-NUREG-28955.

Wulff, W., 1981, "The Kinematics of Moving Flow Regime Interfaces in Two-Phase Flow," Third OECD Specialists Meeting on Transient Two-Phse Flow, Pasadena, CA.

Wulff, W., 1981, "Thermal Conductions Models for Time-Critical Simulations, BNL-NUREG-29158.

Yasinsky, J.B., 1970, "Notes on Nuclear Reactor Kinetics," WAPD-TM-960, Bettis Atomic Power Laboratory.

Zemansky, M.W., 1968, Heat and Thermodynamics, Fifth Ed., p. 42, McGraw-Hill Book Company.

Zuber, N., Tribus, M. and Westwater, 1961, "The Hydrodynamic Crisis in Pool Boiling of Saturated and Subcooled Liquids," 2nd Int. Heat Trans. Conf. Paper 27, Denver, Col.